

AD-A061 086

AIR FORCE FLIGHT DYNAMICS LAB WRIGHT-PATTERSON AFB OHIO F/G 20/4
BOUNDARY LAYER EFFECTS-PROCEEDINGS OF THE 7TH U. S. AIR FORCE/F--ETC(U)
SEP 78 A W FIORE
AFFDL-TR-78-111

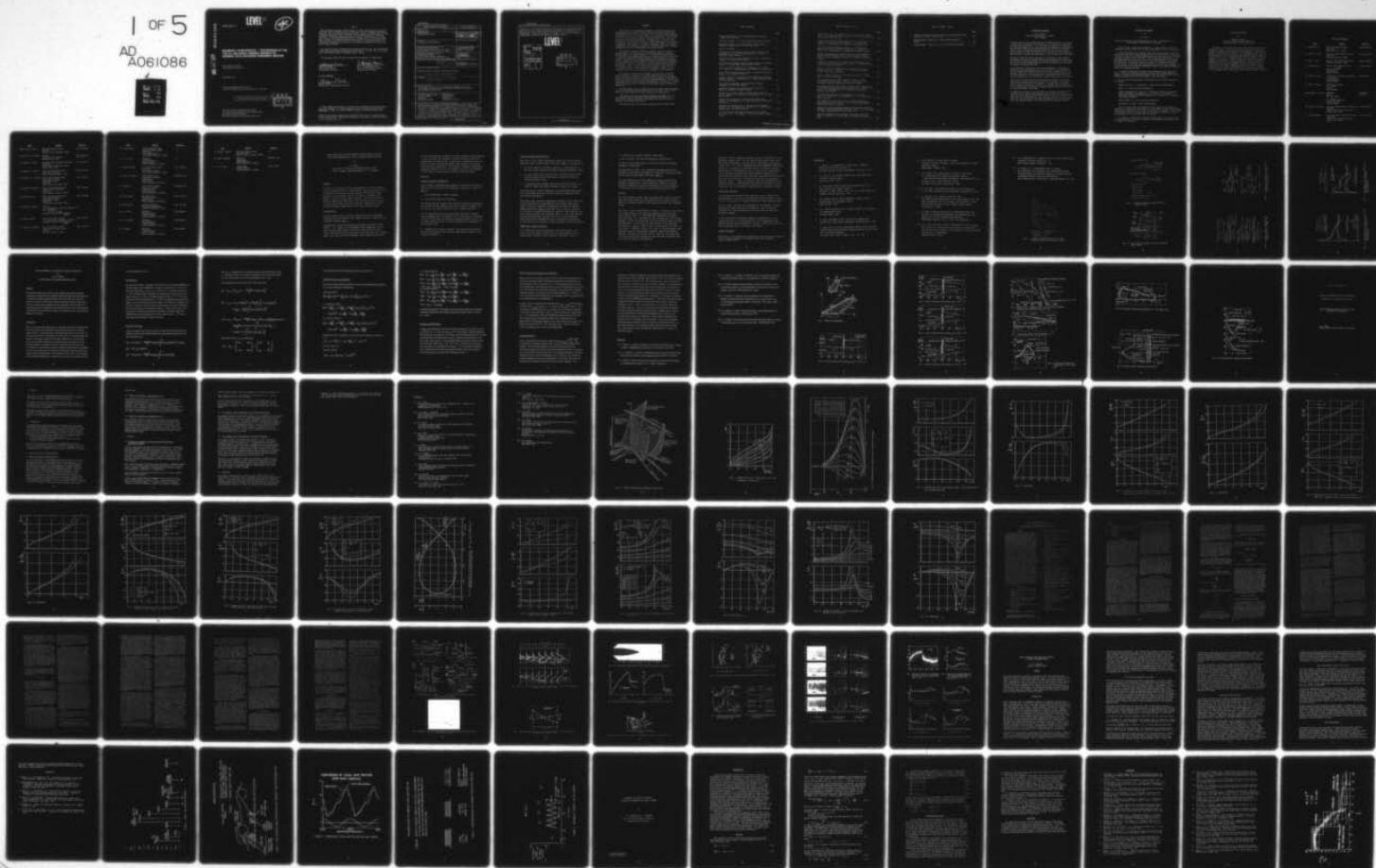
MWDDEA-AF-75-G-7440

NL

UNCLASSIFIED

1 OF 5

AD
A061086



AD A061086

DDC FILE COPY

LEVEL ^{II}

AFFDL-TR-78-111



**BOUNDARY LAYER EFFECTS — PROCEEDINGS OF THE
7TH U.S. AIR FORCE / FEDERAL REPUBLIC OF
GERMANY DATA EXCHANGE AGREEMENT MEETING**

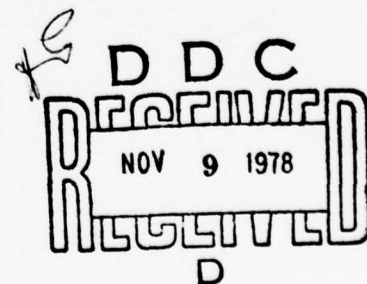
*DR. ANTHONY W. FIORE
AEROMECHANICS DIVISION*

SEPTEMBER 1978

TECHNICAL REPORT AFFDL-TR-78-111
Technical Proceedings Report for Period April 1977 — April 1978

Approved for public release; distribution unlimited.

AIR FORCE FLIGHT DYNAMICS LABORATORY
AIR FORCE WRIGHT AERONAUTICAL LABORATORIES
AIR FORCE SYSTEMS COMMAND
WRIGHT-PATTERSON AIR FORCE BASE, OHIO 45433



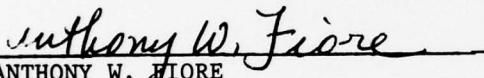
78 10 26 041

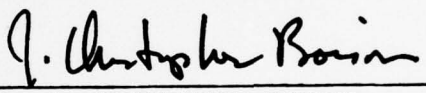
NOTICE

When Government drawings, specifications, or other data are used for any purpose other than in connection with a definitely related Government procurement operation, the United States Government thereby incurs no responsibility nor any obligation whatsoever; and the fact that the government may have formulated, furnished, or in any way supplied the said drawings, specifications, or other data, is not to be regarded by implication or otherwise as in any manner licensing the holder or any other person or corporation, or conveying any rights or permission to manufacture, use, or sell any patented invention that may in any way be related thereto.

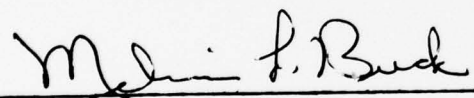
This report has been reviewed by the Information Office (OI) and is releasable to the National Technical Information Service (NTIS). At NTIS, it will be available to the general public, including foreign nations.

This technical report has been reviewed and is approved for publication.


ANTHONY W. FIORE
USAF Project Officer
Aeromechanics Division


DR. J. CHRISTOPHER BOISON
Chief, Thermomechanics Branch
Aeromechanics Division

FOR THE COMMANDER


MELVIN L. BUCK
Acting Chief, Aeromechanics Division

"If your address has changed, if you wish to be removed from our mailing list, or if the addressee is no longer employed by your organization please notify AFFDL/FXE, W-PAFB, OH 45433 to help us maintain a current mailing list".

Copies of this report should not be returned unless return is required by security considerations, contractual obligations, or notice on a specific document.

UNCLASSIFIED

SECURITY CLASSIFICATION OF THIS PAGE (When Data Entered)

REPORT DOCUMENTATION PAGE		READ INSTRUCTIONS BEFORE COMPLETING FORM
1. REPORT NUMBER AFFDL-TR-78-111	2. GOVT ACCESSION NO.	3. RECIPIENT'S CATALOG NUMBER
4. TITLE (and Subtitle) BOUNDARY LAYER EFFECTS		5. TYPE OF REPORT & PERIOD COVERED Technical Proceedings Report April 1977 to April 1978
7. AUTHOR(s) Dr. Anthony W. Fiore / Editor		6. PERFORMING ORG. REPORT NUMBER
9. PERFORMING ORGANIZATION NAME AND ADDRESS Aeromechanics Division (FXE) Air Force Flight Dynamics Laboratory (AFSC) Wright-Patterson Air Force Base, OH 45433		8. CONTRACT OR GRANT NUMBER(s)
11. CONTROLLING OFFICE NAME AND ADDRESS Aeromechanics Division Air Force Flight Dynamics Laboratory Wright-Patterson Air Force Base, OH 45433		10. PROGRAM ELEMENT, PROJECT, TASK AREA & WORK UNIT NUMBERS MWDDEA-AF-75-G-7440
14. MONITORING AGENCY NAME & ADDRESS (if different from Controlling Office) 12 478 p.		12. REPORT DATE September 1978
		13. NUMBER OF PAGES 474
		15. SECURITY CLASS. (of this report) Unclassified
16. DISTRIBUTION STATEMENT (of this Report) Approved for public release; distribution unlimited.		15a. DECLASSIFICATION/DOWNGRADING SCHEDULE
17. DISTRIBUTION 6 Boundary Layer Effects-Proceedings of the 7th U. S. Air Force/Federal Republic of Germany Data Exchange Agreement Meeting.		
18. SUPPLEMENTARY NOTES Proceedings of the 7th U.S. Air Force/Federal Republic of Germany Data Exchange Agreement Meeting, 25-27 April 1978, Naval Post Graduate School, Monterey, California.		
19. KEY WORDS (Continue on reverse side if necessary and identify by block number) Turbulent Boundary Layers Hydrodynamics Numerical Methods Separated flows Transonics Supersonics High Reynolds Number Boundary Layer effects		
20. ABSTRACT (Continue on reverse side if necessary and identify by block number) In 1975 the U.S. Air Force and the Federal Republic of Germany signed a Data Exchange Agreement numbered AF-75-G-7440 entitled "Viscous and Interacting Flow Fields." The purpose was to exchange data in the area of boundary layer research. It includes both experimental and theoretical boundary layer research at speeds from subsonic to hypersonic Mach numbers in the presence of laminar, transitional, and turbulent boundary layers. The main effort in recent years has been on turbulent boundary layers, both attached and separated in the presence of such parameters as pressure gradients, wall temperature, surface		

UNCLASSIFIED

SECURITY CLASSIFICATION OF THIS PAGE (When Data Entered)

012 070

over
gm

UNCLASSIFIED

SECURITY CLASSIFICATION OF THIS PAGE(When Data Entered)

roughness, etc. The research presented in this report covers the period April 1977 to April 1978. In the United States the research was conducted in various Department of Defense, NASA, Aircraft Corporations, and various University laboratories. In the Federal Republic of Germany it was carried out within the various DFVLR, Industrial, and University research centers.

LEVEL II A

ACCESSION NO.	
NTIS	Write Section <input checked="" type="checkbox"/>
DDI	Diff Section <input type="checkbox"/>
UNANNOUNCED	<input type="checkbox"/>
JUSTIFICATION	
BY	
DISTRIBUTION/AVAILABILITY CODES	
Dist.	AVAIL. and/or SPECIAL
A	

DDC
RECEIVED
NOV 9 1978
REGULATED
D

UNCLASSIFIED

SECURITY CLASSIFICATION OF THIS PAGE(When Data Entered)

FOREWORD

The 7th U.S. Air Force/Federal Republic of Germany Data Exchange Agreement Meeting entitled "Viscous and Interacting Flow Fields" numbered MWDDEA AF-75-G-7440 was sponsored by the Air Force Flight Dynamics Laboratory and hosted by the U.S. Navy. It was held on 25/27 April 1978 at the Naval Post Graduate School in Monterey, California. This report contains the detailed proceedings of that meeting. It contains both theoretical and experimental results covering a great variety of topics in the area of boundary layer research. The speed range is from subsonic to hypersonic Mach numbers. The types of boundary layers were laminar, transitional, and turbulent; both fully attached and separated. Similar problems in the area of hydrodynamics are also included.

The Air Force wishes to thank Mr. William C. Volz of the Naval Systems Command for his efforts in preparing the meeting. Thanks is also extended to the Superintendent of the Post Naval Graduate School for the use of his pleasant facilities. In addition the Air Force wishes to thank the following Naval Post Graduate School personnel for their efforts. Professor Louis Schmidt who made the preliminary arrangements for the meeting, Mrs. Evelyn Basham for taking care of all the necessary motel reservations and all the other clerical support rendered during the meeting. Messrs. Robert Besel and T. Dunton for their assistance in the conference room. Finally the Air Force wishes to thank all the participants from the Federal Republic of Germany for their scientific contributions and for coming such a long distance for this meeting.

This report contains the proceedings of the 7th U.S. Air Force/Federal Republic of Germany Data Exchange Agreement Meeting covering many investigations conducted in both the United States and the Federal Republic of Germany as part of the Data Exchange Agreement number AF-75-G-7440 entitled "Viscous and Interacting Flow Field Effects." The meeting was hosted by the U.S. Navy with Mr. William Volz as coordinator. It was held on 25/27 April 1978 at the Naval Post Graduate School in Monterey, California.

The contribution from the United States was research performed within the Air Force Flight Dynamics Laboratory, the U.S. Navy, the U.S. Army, NASA, and various American Aircraft Companies and Universities.

The contributions from the Federal Republic of Germany were from such organizations as DFVLR-AVA-Göttingen, DFVLR-Linden Höhe, the Universities of Berlin-Karlsruhe, and Hamberg, and such aircraft corporations as VFW-Fokker and Dornier.

The research report was conducted from April 1977 to April 1978.

TABLE OF CONTENTS

	<u>Page</u>
Introductory Comments - K. H. Gronau; German Federal Ministry of Defense; Bonn, Germany	1
Introductory Remarks - H. U. Meier; DFVLR-AVA; Göttingen, Germany . . .	2
Welcoming Statement - A. W. Fiore; Air Force Flight Dynamics Laboratory; Wright-Patterson Air Force Base, Ohio	3
List of Participants	4
Calculation of Viscous Effects on Rear-Loaded Airfoils with the Consideration of a Local Trailing-edge Solution - Thiede, P.; VFW-Fokker; Bremen, Germany	8
Transition Prediction versus Experiments on a Swept, Tapered Wing Hirschel, E. H.; DFVLR; Köln, Germany	19
Three-Dimensional Boundary Layers on Wings and Bodies of Revolution Stock, H. W.; Dornier GmbH; Friedrichshafen, Germany	32
Steady and Unsteady Transonic Flow - Seegmiller, H. L.; Marvin J. G.; Levy, L. L.; Ames Research Center; Moffett Field, California . .	57
Recent Turbulent Drag Reduction Research at Langely Research Center Bushnell, D. M.; Hampton, Virginia	71
Numerical Solution of Supersonic Interacting Turbulent Flow Along a Corner - Shang, J. S., and Hankey, W. L.; AFFDL, Wright-Patterson Air Force Base, Ohio	81
Three-Dimensional Boundary Layer Calculations on Bodies Grundmann, R.; DFVLR; Köln, Germany	95
Experimental Study of the Flow Along a Body of Revolution Bippes, H.; DFVLR-AVA; Göttingen, Germany	106
Computation of Transonic Flow Past Slender Bodies at Angle of Attack - Reklis, R. P.; Sturek, W. B.; and Bailey, F. R.; U.S. Army and NASA Ames	133
Boundary Layer Transition on Tactical Missile Seeker Domes Fyan, B. M.; and Markarian, C. F.; Naval Weapons Center; China Lake, California	153
Spherical Nose Roughness Effect on Boundary Layer Development Voisinnet, R. L. P.; Phinney, R. E. and Yanta, W. J.; Naval Surface Weapons Center, White Oaks Laboratory	164
On Full Scale Laser-Velocimeter Measurements of Ship Boundary Layer Flow - Kux, J. and Niemier, T.; Universitat Hamburg; Hamburg, Germany	173

TABLE OF CONTENTS (cont'd)

	<u>Page</u>
Measurements of the Three-Dimensional Flowfield Around a Slender Body at Large Angles-of-Attack - Yanta, W. J.; Naval Surface Weapons Center; White Oaks Laboratory	188
Pressure Distributions and Flow Visualizations on an Ellipsoid 1:6 Designed for Three-Dimensional Boundary Layer Investigations Meier, H. U. and Kreplin, H. P.; DFVLR-AVA; Göttingen, Germany	197
Wall Shear Stress Measurements, Detection of Transition and Separation by Means of Surface Hot Film Probes - Kreplin, H. P.; Meier, H. U.; and Baumgarten, D.; DFVLR-AVA, Göttingen, Germany	209
Further Investigations on Turbulence Models for Three-Dimensional Boundary Layers and Comparisons of Calculations with Infinite Swept Wing Flow Measurements - Rotta, J. C.; DFVLR-AVA, Göttingen, Germany	221
Progress in the Calculation of Three-Dimensional Boundary Layers on Bodies of Revolution at Incidence - Cebeci, T.; Douglas Aircraft Corp.; Long Beach, California	237
Influence of Surface Roughness and Mass Transfer on Turbulent Boundary Layer Flow - Voisinet, R. L. P.; Naval Surface Weapons Center; Silver Spring, Maryland	247
Further Advances in Numerical Fluid Dynamics Research at DTNSRDC Schot, J.; Bethesda, Maryland	260
An Investigation of Very Small Separation Bubbles in Laminar and Turbulent Boundary Layers - Gersten, K. and Gross, J. F.; University of Bochum, Germany and University of Arizona	271
Three-Dimensional Shock Wave Turbulent Boundary Layer Interactions - A Preliminary Analysis of Blunted Fin Induced Flows - Dolling, D. S.; Cozad, C. D.; and Bogdonoff, S. M.; University of Princeton, Princeton, New Jersey	295
Two-Dimensional Supersonic Jet Impingement on a Flat Plate Zien, T. F.; Chien, K. Y.; and Driftmyer, R. T.; U.S. Navy, Silver Spring, Maryland	329
Three-Dimensional Calculations of Vortices Behind a Missile at Large Angles of Attack - Van Teryl, A. H.; Naval Surface Weapons Center; Silver Spring, Maryland	340
Boundary Layer Fence Method for Measuring Surface Shear Stress in a Supersonic, High Reynolds Number Flow Field - Fiore, A. W. and Scaggs, N.; AFFDL; Wright-Patterson Air Force Base, Ohio	350
Supersonic Separated Turbulent Boundary Layer Over a Wavy Wall Polak, A. and Werle, M. J.; University of Cincinnati; Cincinnati, Ohio	397

TABLE OF CONTENTS (cont'd)

	<u>Page</u>
Comments on Interaction Between Theoretical and Experimental Work on the D.E.A. Topics - Walz, Alfred	462
Closing Remarks - Gronau, K. H.; German Federal Ministry of Defense	469
Closing Remarks - Fiore, A. W.; U.S. Air Force Project Manager	470

Introductory Comments

K.-H. Gronau
German Federal Ministry of Defense
Bonn, Germany

As Project Officer and representative of the Federal Ministry of Defense I should like to thank Mr. Volz on behalf of all German participants for his warm welcoming remarks. It is ten years now since German and American scientists began to hold joint meetings and embarked on collaborative efforts under a mutual data exchange program in the field of boundary layer research. During the past two years, this data exchange program has been conducted under the new caption of "Viscous and Interacting Flow Field Effects" to stress the importance of this specific area of research.

The idea to hold this year's meeting here in Monterey, a particularly picturesque place on the Pacific Coast of the United States, sprang from a desire of our American partners to combine the pleasant with the useful, and I think that by choosing Monterey as a meeting place they have fully succeeded in achieving this aim.

In my capacity as spokesman of the German delegation, I should like to express our sincere gratitude to Dr. Fiore and Mr. Volz in particular for the careful and extensive work they have done in preparation of this meeting. This year we have for the first time selected the subjects of our presentations on a reciprocal basis to take into account both the specific interests of each side and our common objectives at this meeting.

Since 1975, the benefits from our collaborative scientific activities and planning concepts have been substantially increased by the publication of the proceedings of our meetings. I am glad that we have been able to send you, in advance of this year's meeting, the proceedings of our last annual meeting held at the German Aerospace Research and Testing Institution (DFVLR) in Göttingen.

I should like to thank all participants for their keen interest which is evidenced by the long journeys they have made to join our meeting. I trust that the presentations and discussions to be held in the next three days will help to stimulate us in our research work and will lead us to reflect on the approach we have chosen and maybe give it a new direction. With this purpose in mind, I wish the meeting every possible success.

INTRODUCTORY REMARKS

by

H. U. Meier

Deutsche Forschungs- und Versuchsanstalt für Luft- und Raumfahrt E.V.
Aerodynamische Versuchsanstalt Göttingen

First of all, I would like to thank Dr. A. Fiore and Mr. W. Volz for organizing this DEA meeting and the Naval Postgraduate School for hosting it.

Rather than describe the results which have been generated by the interaction of scientists at these meetings for the past seven years, I would like to describe a new joint research project where, for the first time, scientists from both countries will be involved. This activity was agreed upon at the Göttingen meeting in April 1977 and will be an experimental and theoretical investigation of 3-D boundary layers on a body of revolution. Our interest in this project is based on long-term research at the DFVLR-AVA Göttingen for the purpose of improving and checking existing 3-D turbulence models. Our contribution will be a detailed experimental study of the turbulent boundary layer on a fuselage-like body.

It should be mentioned that these first experiments shall only be the start. Further configurations (wings, missiles) will be investigated at subsonic, transonic and supersonic speeds. Thus, the whole scope of the DEA "Viscous and Interacting Flow Field Effects" will be covered.

So far, the following research institutions are or will be involved in this project:

Douglas Aircraft Co., Long Beach, T. Cebeci (Calculation Methods).

NSWC, W. J. Yanta (Measuring Techniques).

DFVLR, Göttingen, H. U. Meier, H. P. Kreplin, H. Bippes (3-D Boundary Layer and Transition Experiments); J. C. Rotta, G. R. Schneider (Turbulence Models, Calculation Methods); E. H. Hirschel, R. Grundmann (Calculation Methods).

Dornier GmbH, H. W. Stock (Calculation Methods).

VFW-Fokker, P. Thiede (Calculation Methods).

Due to the importance and relevance of this project to a variety of aeronautical applications, and because of the manpower and high cost involved, international cooperation is not only very useful, but necessary. Thus, during this meeting we hope to convince more of our American colleagues to join us and contribute to this specific field of research.

In closing, I would like to express my appreciation to Dr. Gronau from the German Ministry of Defense for making the arrangements necessary for us to attend this conference.

Welcoming Statement

by

Anthony W. Fiore
Air Force Flight Dynamics Laboratory
Wright-Patterson Air Force Base, Ohio

On behalf of the United States Air Force and the Flight Dynamics Laboratory I want to welcome you to the 7th U.S. Air Force/Federal Republic of Germany Data Exchange Agreement Meeting. As you know the subject is "boundary layer effects." A preliminary glance at the agenda indicates that the material to be presented in this symposium is of interest to both the United States and the Federal Republic of Germany. I am sure this symposium will be as successful as the previous D.E.A. meetings. I want to thank the U.S. Navy for being so generous to the Air Force and permitting us to use the wonderful facilities of the Naval Postgraduate School. On behalf of the Air Force I wish to extend its thanks to all the participants and in particular to our German Colleagues who have come such a long distance for this meeting. Now I would like to turn the meeting over to the chairman, Mr. William Volz, so your work can begin. Thank you.

List of Participants

<u>NAME</u>	<u>ADDRESS</u>	<u>PHONE NO.</u>
Mr. William Volz	Naval Air Systems Command AIR - 320C Washington, D.C. 22202	(202) 692-2515
Dr. Joanna W. Schot	David W. Taylor Naval R&D Center Code 1843 Bethesda, Maryland 20084	(202) 227-1925
Dr. Hans J. Lugt	David W. Taylor Naval R&R Center Bethesda, Maryland 20084	(202) 227-1927
Dr. Klaus Gersten	Institut Fur Thermo-Und Fluid Dynamik Ruhr Universitat 4630 Bochum Bochum, Germany	(234) 700-2896
Dr. Alfred H. Walz	University of Berlin and Karlsruhe 7 Am Kurzarm 783 Emmendingen Baden, Germany	07-641-1202
Dr. Karl H. Gronau	Ministry of Defense Dept. RUEF04 53 Bonn Bonn, Germany	-----
Major Robert D. Powell	EOARD/LNY Box 14 FPO, NY 09510 or 223 Old Marylebone Rd. London, NW 15th United Kingdom	01-629-9222 ext 589
Mr. Richard G. Docken	Air Force Flight Dynamics Laboratory AFFDL/XP Wright-Patterson Air Force Base Dayton, Ohio 45433	(513) 255-4119
Dr. William Hankey	Air Force Flight Dynamics Laboratory AFFDL/FXM Wright-Patterson Air Force Base Dayton, Ohio 45433	(513) 255-3138

<u>NAME</u>	<u>ADDRESS</u>	<u>PHONE NO.</u>
Major David S. McRae	NASA Ames Research Center MS 206-3 Moffett Field, California 94035	(415) 965-5870
Lt Col Karl H. Schumaker	ASDC/CCE Arnold Air Force Station Tulahoma, TN 37389	(615) 455-2611 ext. 203
Dr. Anthony W. Fiore	Air Force Flight Dynamics Laboratory AFFDL/FXE Wright-Patterson Air Force Base Dayton, Ohio 45433	(513) 255-4150
Mr. Andrew H. Van Teryl	Naval Surface Weapons Center White Oaks Laboratory Silver Spring, Maryland 20910	(202) 394-1929
Mr. Robert L. P. Voisinet	Naval Surface Weapons Center White Oaks Laboratory Aerodynamics Branch Code K-81 Silver Spring, Maryland 20910	(202) 394-1928
Mr. Samuel M. Hastings	Naval Surface Weapons Center Weapons Dynamics Division Code K-80 Silver Spring, Maryland 20910	(202) 394-2094
Mr. Roland E. Lee	Naval Surface Weapons Center White Oaks Laboratory Aerodynamics Branch Code K-81 Silver Spring, Maryland 20910	(202) 394-2094
Dr. Walter B. Sturek	Director U.S. Army Ballistic Research Laboratory Attn: DRDAR-BLL Dr. W. B. Sturek Aberdeen Proving Ground, Maryland 21005	-----
Mr. Robert Reklis	Launch and Flight Division U.S. Army Ballistic Research Laboratory Aberdeen Proving Ground, Maryland 21005	(301) 278-4365
Mr. Dennis M. Bushnell	Hd. Fluid Mechanics Branch NASA Langley Research Center M/S 163 Hampton, Virginia 23369	(804) 827-4546

<u>NAME</u>	<u>ADDRESS</u>	<u>PHONE NO.</u>
Dr. Tuncer Cebeci	Chief Aerodynamic Engr. Douglas Aircraft Company Code 36-81 3855 Lakewood Blvd. Long Beach, California 90840	-----
Dr. J. C. Rotta	DFVLR-AVA 3400 Göttingen Bunsenstrasse 10 Federal Republic of Germany	-----
Dr. Frank Markarian	Hd. Aerodynamics Branch Code 3161 Naval Weapons Center China Lake, California 93555	(714) 939-2824
Dr. Ernst H. Hirschel	DFVLR-Institut Fur Angewandte Gasdynamik Linden Höhe 5000 Kolen 90 Federal Republic of Germany	(02203)6012345
Dr. Jurgen Kux	Institut Fur Schiffbau Universitat Hamburg Lammersleth 90 2000 Hamburg 60 Federal Republic of Germany	(040)291883391
Dr. Peter Thiede	VFW-Fokker GmbH Huenefeldstrasse 1-5 D2800 Bremen Federal Republic of Germany	(0421) 538-2171
Dr. Sanjoy Ghose	Stanford University Mechanical Engineering Stanford, California 94305	(415) 497-2176
Dr. H. U. Meier	DFVLR-AVA Bunsenstrasse 10 D 3400 Göttingen Federal Republic of Germany	(0551)4092269
Dr. H. P. Kreplin	DFVLR-AVA Bunsenstrasse 10 D 3400 Göttingen Federal Republic of Germany	(0551)4092258
Dr. H. Bippes	DFVLR-AVA Bunsenstrasse 10 D 3400 Göttingen Federal Republic of Germany	(0551)4092406

<u>NAME</u>	<u>ADDRESS</u>	<u>PHONE NO.</u>
Dr. Joseph G. Marvin	NASA Ames Research Center Mail Stop 229-1 Moffett Field, California 94035	-----
Dr. Roger Grundmann	DFVLR-AVA Linden Hohe 5000 Cologne 90 Federal Republic of Germany	02203/601 2055
Dr H. W. Stock	Dornier GmbH Friedrichshafen Federal Republic of Germany	07545 18 2328

CALCULATION OF VISCOUS EFFECTS ON REAR-LOADED AIRFOILS
WITH CONSIDERATION OF A LOCAL TRAILING EDGE SOLUTION

by

P. Thiede

Vereinigte Flugtechnische Werke-Fokker GmbH
D 2800 Bremen, Hünefeldstrasse 1-- 5, Germany

SUMMARY

A method is outlined for the calculation of viscous effects on rear-loaded airfoils, including the strong viscous-inviscid interaction at airfoil trailing edges. The boundary layer solution on the airfoil and in the wake is combined with Melnik's local trailing edge solution, using the method of matched asymptotic expansions. The viscous effects are simulated by the surface mass flow concept, imposing the inner viscous boundary conditions on the outer inviscid flow.

INTRODUCTION

Viscous effects have a strong influence on the aerodynamic characteristics of modern rear-loaded airfoils, especially at transonic speeds, Fig. 1.

Conventional viscous calculation methods for airfoil flows (Refs. 1, 2), based on the boundary layer approach, fail in the trailing edge region, as they do not account for the strong viscous-inviscid interaction occurring near the trailing edge. This failure of the boundary layer approximations has

a great consequence, because the local boundary layer behavior at the trailing edge directly affects the Kutta condition responsible for the airfoil circulation. Consequently an improved viscous calculation method must include the strong trailing edge interaction. The method of matched asymptotic expansions (Refs. 3, 4) is an elegant tool for the treatment of the strong interactions at airfoil trailing edges.

ANALYSIS

Viscous effects simulation

Two different mathematical concepts to simulate the viscous effects for the airfoil flow analysis, are in use (Ref. 5), Fig. 2:

1. the displacement surface concept,
2. the surface mass flow concept.

In calculating the airfoil flow with an iterative procedure, the second concept imposing the inner viscous boundary conditions on the outer inviscid flow, is more effective.

For the prediction of the laminar and turbulent boundary layer parameters on the airfoil and in the wake, an extended version of the Walz' dissipation integral method (Refs. 6, 7) is used, taking account of the non-equilibrium character of the airfoil flow.

To complete the viscous solution, the pressure variations across the boundary layer and the wake must be added to the inviscid solution.

Local trailing edge solution

The flow in the strong interaction region near the trailing edge develops a triple layer structure, Fig. 3, consisting of

1. an inner layer at the wall, which is a continuation of the wall layer from the upstream turbulent boundary layer,
2. an outer layer with inviscid but rotational flow, whose vorticity arises from the velocity profile of the upstream boundary layer,
3. a blending layer between the inner and outer layers, in order to match the shear stresses of both the layers.

The outer layer is most important as it determines the pressure deviations from the inviscid solution resulting from the strong interaction.

The outer layer solution suggested by Melnik et al. (Ref. 8), can be described as a perturbation of the basic potential flow, written as asymptotic expansions of the full Navier-Stokes equations, Fig. 4. The outer flow field is obtained by solving a Poisson differential equation. Defining the initial velocity profile by Coles' law (Ref. 9), the contribution of the trailing edge interaction to the viscous boundary conditions can be determined from a closed-form expression of the particular integral, found by analytic function theory.

Composite viscous solution

To include the strong interaction at trailing edges, the local trailing edge solution must be incorporated into the conventional boundary layer solution. The basic idea is

- to modify the viscous boundary conditions
- and to correct the inviscid pressure distribution

in the trailing edge region, using the method of matched asymptotic expansions.

As described in (Ref. 10), composite expressions for the boundary conditions are formed by correction functions, determined from the particular solution, Fig. 5.

For the completion of the composite viscous solution the pressure distribution, calculated with composite viscous boundary conditions, must be corrected by the contribution of the particular solution to the normal pressure terms.

RESULTS

The significance of the local trailing edge solution and the wake curvature terms for the prediction of airfoil viscous effects is demonstrated in test cases with sub- and transonic flows.

The Piercy 1240 incompressible airfoil is chosen as the first test case because of the precise boundary layer and wake measurements (Ref. 11). The VFW panel method with dipole covering (Ref. 12), modified for the incorporation of viscous boundary conditions evaluated from the boundary layer and wake measurements, is used for the calculation of the pressure distribution. Fig. 6 shows, that in accordance with (Ref. 13) the total 31 percent viscous lift loss is significantly under-predicted by the conventional boundary layer displacement concept. Moreover the results prove, that for the remaining lift loss the strong interaction and the wake curvature near the trailing edge are responsible.

The Korn 75-6-12 transonic airfoil, tested at the NAE at high Reynolds numbers (Ref. 14), is used as the second test case. The quasi-conservative version of the VFW finite difference method (Ref. 15), which satisfies the full transonic potential equation in streamline coordinates and the viscous boundary conditions on the matching line, is used for the calculation of the pressure distribution. The boundary conditions are evaluated from boundary layer and wake calculations prescribing the measured pressure distribution corrected by the normal pressure terms. Fig. 7 indicates that the influence of the viscous effects on the pressure distribution causing a 28 per-cent lift loss is accurately predicted by the present method.

CONCLUDING REMARKS

In accordance with Melnik the present results indicate the significance of the local trailing edge solution and the wake for the calculation of viscous effects of rear-loaded airfoils.

As the shown results are encouraging, the present viscous calculation method shall be extended to a full iterative procedure for the prediction of airfoil flows at sub- and transonic speeds.

As the principle of matched asymptotic expansions is also practicable for 2-D interactions with flow separation, the present method can be extended to airfoil flows with trailing edge separation and to airfoils with flaps.

ACKNOWLEDGEMENT

This work is encouraged and financed by the Ministry of Defence of the Federal Republic of Germany under RüFo contract T/RF 41/70022/71421.

REFERENCES

1. F. Bauer, P. Garabedian, D. Korn and A. Jameson:
Supercritical Wing Sections II.
Springer-Verlag, Berlin, Heidelberg, New York, 1975.
2. P.C. Bavitz: An analysis method for two-dimensional
transonic viscous flow.
NASA TN D-7718, 1975.
3. K. Stewartson: Multistructured boundary layers on
flat plates and related bodies.
Advances in Appl. Mech., Vol. 14, ed. by Chia-Shun Yih,
Academic Press, New York, 1974.
4. R.E. Melnik and R. Chow: Asymptotic theory of two-
dimensional trailing-edge flows.
NASA SP-347, 1975.
5. R.C. Lock: Calculation of viscous effects on aerofoils
in compressible flow.
TM Aero 1646, 1975.
6. A. Walz: Boundary layers of flow and temperature.
English Ed., MIT Press, Cambridge, Massachusetts, 1969.
7. F. Otte und P. Thiede: Berechnung ebener und rotations-
symmetrischer kompressibler Grenzschichten auf der Basis
von Integralbedingungen.
Fortschr.-Ber. VDI-Z, Reihe 7, Nr. 33, 1973.

8. R.E. Melnik, R. Chow and H.R. Mead:
Theory of viscous transonic flow over airfoils at high
Reynolds number.
AIAA-Paper 77-680, 1977.
9. D.E. Coles: The young person's guide to the data.
In: Computation of turbulent boundary layers
- 1968 AFOSR-IFP-Stanford conference. Proceedings Vol.II.
Edited by D.E. Coles and E.A. Hirst.
Stanford University, California, 1969.
10. M. van Dyke: Perturbation methods in fluid mechanics.
2. Ed. The Parabolic Press, Stanford, California, 1975.
11. H. Preston, N.E. Sweeting and D.K. Cox:
The experimental determination of the boundary layer and
wake characteristics of a Piercy 12/40 aerofoil, with
particular reference to the trailing edge region.
R and M 2013, 1945.
12. H. Jakob: Erweiterung eines 2-D Panelverfahrens auf
Profile mit dicken Hinterkanten und Kopplung des Ver-
fahrens mit einem Grenzschichtverfahren.
VFW-Fokker Bericht Ef 612, 1976, not published.
13. W.J. Piers and J.W. Slooff: Calculation of the displace-
ment effect in two-dimensional subsonic attached flow
around aerofoils; examples of calculations using measured
displacement thicknesses.
NLR TR 72116 U, 1972.

14. J.J. Kacprzyński: A second series of wind tunnel tests shockless lifting airfoil No. 1.
NAE Project Report 5X5/0062, 1972.
15. H. Jakob, K.-D. Klevenhusen and H. Struck:
Ein Verfahren zur Berechnung der zweidimensionalen transsonischen Interferenzströmung und seine Erweiterungsmöglichkeiten auf drei Dimensionen.
ZKP Flügelsektion, VFW-Fokker - Outcome Report 10, 1977.

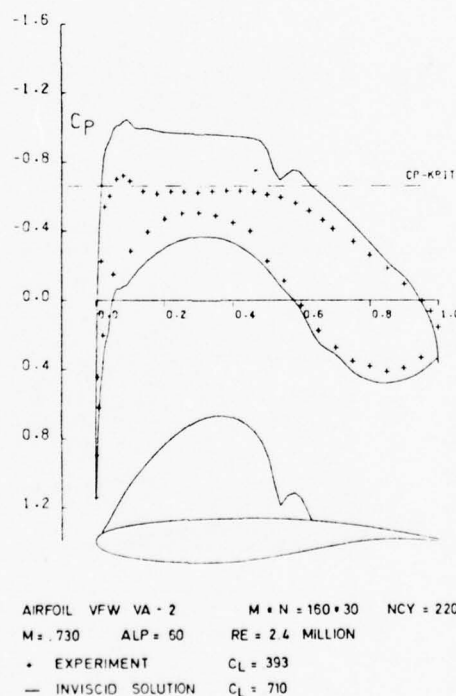


Fig. 1 Pressure distribution of a rear-loaded airfoil in transonic flow

The diagram illustrates a slender body in a fluid flow. A dashed line represents the 'DISPLACEMENT SURFACE'. A circular region on the right is labeled 'EMPIRICAL ASSUMPTIONS IN THE TE REGION'. Two vertical lines with arrows indicate distances δ_1 and $\delta_{1, \infty}$ from the body to the displacement surface.

- AIRFOIL

$$v_{n\alpha} = \frac{1}{\rho_e} \frac{d(\rho_e u_t \delta_1)}{ds}$$
- WAKE

$$\Delta v_{nW} = \frac{1}{\rho_e} \frac{d(\rho_e u_e \delta_2 w)}{ds}$$

$$\Delta v_{tW} = -x u_e (\delta_{1W} + \delta_{2W}) \quad x = \frac{d\beta w}{ds}$$

$$\Delta p_{BL,W} = p_{SURF} - p_{e,IN} = -\alpha \rho_e u_e^2 (\delta_1 + \delta_2)$$

Diagram illustrating the structure of a boundary layer flow over a flat plate, showing the development of the boundary layer from left to right. The flow is divided into three regions: Weak Interaction, Strong Interaction, and Weak Interaction. The boundary layer is divided into four layers: Outer Boundary Layer, Potential Flow, Blending Layer, and Wall Layer. The diagram shows the growth of the boundary layer thickness and the development of the wake. Key parameters are labeled: $O(\epsilon)$ for the outer boundary layer thickness, $O(\epsilon^2)$ for the wall layer thickness, and $O(1)$ for the total boundary layer thickness. The diagram also shows the potential flow region above the boundary layer and the wake region below the boundary layer.

PARAMETER

$$\epsilon = \frac{U_{\infty} \tau}{U_{\infty}} = \sqrt{\frac{C_F L}{2}} \sim O(\log Re)^{-1}$$

$$\hat{\epsilon} = (\epsilon^2 Re)^{-1} \sim O(\log Re) / Re$$

16

BASIS

- ASYMPTOTIC EXPANSIONS OF THE N-S EQUATIONS

$$\frac{u}{U_\infty} = 1 + \epsilon^{1/2} u_{0N}(\bar{x}, \bar{y}) + \epsilon f(\bar{y}) + \epsilon^{3/2} u_{1N}(\bar{x}, \bar{y}) + \dots$$

$$\frac{v}{U_\infty} = \epsilon^{1/2} v_{0N}(\bar{x}, \bar{y}) + \epsilon^{3/2} v_{1N}(\bar{x}, \bar{y}) + \dots$$

- RELATIONS FOR DENSITY AND TEMPERATURE

TRANSFORMATIONS

- SUBSTITUTION INTO THE N-S EQUATIONS
- PRANDTL-GLAUERT COMPRESSIBILITY TRANSFORMATION

$$\Rightarrow \text{INCOMPRESSIBLE POISSON EQUATION} \quad f = \begin{cases} \frac{u-u_\infty}{U_\infty} & 0 \leq \eta \leq 1 \\ 0 & \eta > 1 \end{cases}$$

$$\Delta \psi^2 = \frac{d^2 f}{d\eta^2} \psi_{0N}(x, y)$$

$$\text{BOUNDARY CONDITIONS} \quad \psi'(x, 0) = -\frac{\delta}{\delta^*} \psi' = 0$$

$$\psi'(x, y) \rightarrow 0 \text{ FOR } x^2 + y^2 \rightarrow \infty$$

PARTICULAR SOLUTION

- COMPLETE OUTER SOLUTION

$$\psi'(x, y) = \psi'_0(x, y) + \psi'_1(x, y)$$

- REPRESENTATION OF THE INITIAL VELOCITY PROFILE BY COLES' LAW

$$\frac{u(x)}{U_\infty} = \frac{1}{\pi} \left[\ln \frac{y U_\infty}{\nu} + C + \pi W\left(\frac{y}{\delta^*}\right) \right]$$

$$\Rightarrow \text{CLOSED-FORM PARTICULAR SOLUTION BY ANALYTIC FUNCTION THEORY}$$

$$\beta_{1,2}(\xi) = i \sigma_{1,2}(\xi) = \lim_{\eta \rightarrow 0} [F_{\beta,2}(z, \eta) \cdot \Delta F_{\beta,2}(z)]$$

CONTRIBUTION OF THE PARTICULAR SOLUTION TO

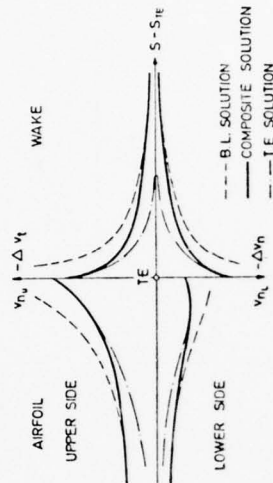
- THE NORMAL VELOCITY COMPONENT ON THE AIRFOIL AND IN THE WAKE

$$v_{0N} \sim \sigma_1(\xi) + \pi \sigma_2(\xi)$$

- THE PRESSURE JUMP ACROSS THE WAKE

$$\Delta p_p \sim \beta_1(\xi) + \pi \beta_2(\xi)$$

Fig. 4 Outer layer solution of Melnik et al. (Ref. 8)



COMPOSITE BOUNDARY CONDITIONS

- AIRFOIL

$$v_{n0} = G_n v_{nN}$$

$$G_{n0} = \frac{\delta_{0N}}{1 + \delta_1} l_{0N}$$

- WAKE

$$\Delta v_{n0} = G_{n0} \Delta v_{nN}$$

$$G_{n0} = \frac{1}{1 + \delta_1} \left(\frac{\delta_{0N}}{\delta_{0N}} \right) l_{0N} \cdot \frac{\delta_{0N}}{\delta_{0N}} \left(\frac{\delta_{0N}}{\delta_{0N}} \right) l_{0N}$$

$$\Delta v_{n0} = G_{n0} \Delta v_{nN}$$

$$G_{n0} = \frac{1}{1 + \delta_1} \left(\frac{\delta_{0N}}{\delta_{0N}} \right) l_{0N} \cdot \frac{\delta_{0N}}{\delta_{0N}} \left(\frac{\delta_{0N}}{\delta_{0N}} \right) l_{0N}$$

COMPOSITE PRESSURE DISTRIBUTION

$$p_c = p_{c0} + \Delta p_c$$

$$\Delta p_c = G_1 \Delta p_{cN}$$

$$G_{10} = \frac{\delta_{0N}}{1 + \delta_1} j_{0N}$$

WITH

$$l_{0N} = \frac{\sigma_1(\xi_{0N}) + \pi \sigma_2(\xi_{0N})}{1 + \pi_{0N}} \quad j_{0N} = \frac{\beta_1(\xi_{0N}) + \pi \beta_2(\xi_{0N})}{1 + \pi_{0N}}$$

Fig. 5 Composite viscous solution for the trailing edge region

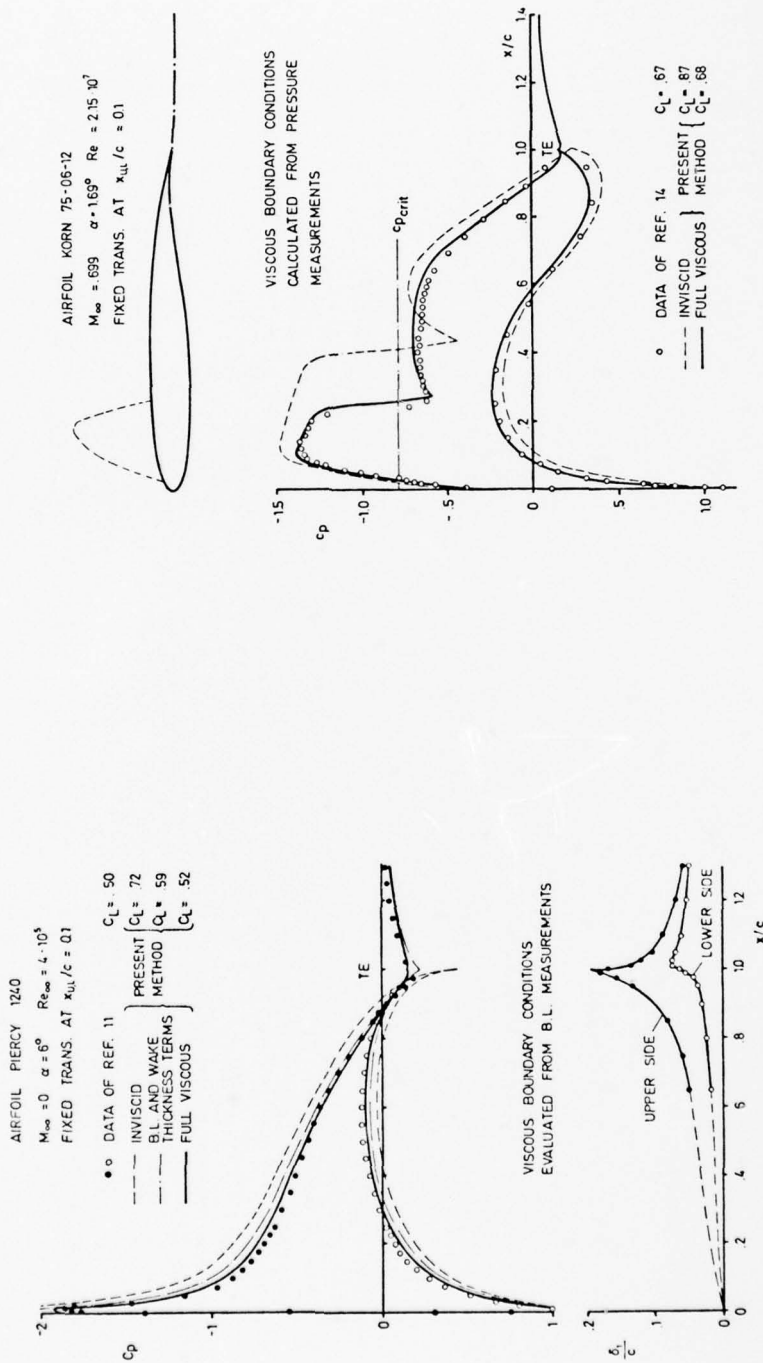


Fig. 6 Influence of viscous effects on the predicted pressure distribution

Fig. 7 Influence of viscous effects on the predicted pressure distribution

Transition Prediction vs. Experiment on a Swept, Tapered Wing

by

E. H. Hirschel

DFVLR-Institut für Angewandte Gasdynamik, Köln

Summary

The laminar boundary layer at a finite swept, tapered wing is being calculated. Comparisons are being made with available experimental data concerning the location of a spanwise extending separation bubble on the suction side of the wing. The influence of surface curvature terms in the boundary-layer equations is being shown. Transition criteria are being applied to the flow calculated. The comparison with experimental data allows judgement of the reliability of the criteria. Some parametric investigations show the qualitative influence of the Reynolds number on the transition behaviour on the wing.

Introduction

In Ref. 1 a boundary-layer experiment on a swept wing is described, and beside other results the location of the transition laminar-turbulent is given for four different angles of attack. In the present paper, which bases partly on Ref. 2, the results of a prediction of transition for the boundary-layer flow of Ref. 1 are being sketched. The boundary layer has been calculated using panel method results as outer boundary values. To the laminar boundary layer calculated stability and transition criteria have been applied, and comparisons with the experimental data have been made. It is intended to recalculate more experiments (which hopefully will become available in future), and to get by way of correlations of the data an improvement of the semi-empirical criteria available today. In this attempt the work in Ref. 3 on the stability of three-dimensional shear flows is expected to give clues how to proceed in a better

way as was possible up to now.

The Experiment

The experiment from Ref. 1 was made on a conical transonic wing model (ONERA M 6) with the symmetric airfoil ONERA "D". The span of the model was $b = 1.20$ m, the mean chord length was $t_m = 0.5(t_w + t_a) = 0.63$ m (Fig. 1). The angle of sweep was $\psi_0 = 30^\circ$, the thickness ratio 10 percent. The experiment has been made with a free-stream velocity of $v_\infty = 90$ m/s, the Reynolds number was $Re_{tm} = 3.5 \cdot 10^6$, and the relatively low free-stream turbulence $Tu_\infty = 0.002$. The weak separation bubble which appears on the suction side of the wing for angles of attack has been investigated with an oil-film technique. The location of the transition laminar-turbulent on the pressure side was found by means of a sublimation technique. In several cross sections of the wing the static wall pressure was measured. Comparisons with panel method data (ONERA) have shown a good agreement up to the angle of attack $\alpha = 15^\circ$, where larger separation areas begin to appear on the wing.

Geometry of the Wing

In Fig. 1 the geometry of the wing is given. The length elements with regard to the Cartesian reference system read (all lengths have been made dimensionless with the mean chord length t_m):

$$(1) \quad x'_1 = t_w \left(1 - \frac{t_w - t_a}{b} \cos \varphi_0 x_2 \right) \int_0^{x_1} \cos \alpha_c(\xi_1) d\xi_1 + t_w \sin \varphi_0 x_2$$

$$(2) \quad x'_2 = t_w \cos \varphi_0 x_2$$

$$(3) \quad x'_3 = t_w \left(1 - \frac{t_w - t_a}{b} \cos \varphi_0 x_2 \right) \int_0^{x_1} \sin \alpha_c(\xi_1) d\xi_1.$$

Here the x_1 - coordinate has been normalized with the local chord length, and the x_2 - coordinate with the local length of the generator of the conical wing surface. α_c is the contour angle of the airfoil measured against the x_1 - axis.

The components of the metric tensor of the surface then read:

$$(4) \quad a_{11} = \left[t_w \left(1 - \frac{t_w - t_a}{b} \cos \varphi_0 x_2 \right) \right]^2$$

$$(5) \quad a_{22} = (t_w \cos \varphi_0)^2 \left[1 + \left(\frac{t_w - t_a}{b} \int_0^{x_1} \sin \alpha_c(\xi_1) d\xi_1 \right)^2 + \right. \\ \left. + \left(t_g \varphi_0 - \frac{t_w - t_a}{b} \int_0^{x_1} \cos \alpha_c(\xi_1) d\xi_1 \right)^2 \right]$$

$$(6) \quad a_{12} = \left[t_w \left(1 - \frac{t_w - t_a}{b} \cos \varphi_0 x_2 \right) (t_w \cos \varphi_0) \left[t_g \varphi_0 \cos \alpha_c(x_1) - \right. \right. \\ \left. - \frac{t_w - t_a}{b} \left(\sin \alpha_c(x_1) \int_0^{x_1} \sin \alpha_c(\xi_1) d\xi_1 + \right. \right. \\ \left. \left. + \cos \alpha_c(x_1) \int_0^{x_1} \cos \alpha_c(\xi_1) d\xi_1 \right) \right]$$

The relation to the h_1, h_2, g coefficients is:

$$(7) \quad a_{ij} = \begin{pmatrix} a_{11} & a_{12} \\ a_{12} & a_{22} \end{pmatrix} = \begin{pmatrix} h_1^2 & g \\ g & h_2^2 \end{pmatrix}.$$

A detailed derivation of the foregoing expressions is given in Ref. 4.

Holonomic Boundary-Layer Equations

The non-dimensional holonomic equations for laminar incompressible boundary layers in curved non-orthogonal coordinates are:

continuity equation

$$(8) \quad \frac{\partial}{\partial x_1}(k_{01}v^1) + \frac{\partial}{\partial x_2}(k_{01}v^2) + \frac{\partial}{\partial x_3}(k_{01}v^3) = 0$$

x_1 - momentum equation

$$(9) \quad v^1 \frac{\partial v^1}{\partial x_1} + v^2 \frac{\partial v^1}{\partial x_2} + v^3 \frac{\partial v^1}{\partial x_3} + k_{11}(v^1)^2 + k_{12}v^1v^2 + k_{13}(v^2)^2 = k_{14} \frac{\partial p}{\partial x_1} + k_{15} \frac{\partial p}{\partial x_2} + \frac{\partial^2 v^1}{\partial x_3^2}$$

x_2 - momentum equation

$$(10) \quad v^1 \frac{\partial v^2}{\partial x_1} + v^2 \frac{\partial v^2}{\partial x_2} + v^3 \frac{\partial v^2}{\partial x_3} + k_{21}(v^1)^2 + k_{22}v^1v^2 + k_{23}(v^2)^2 = k_{15} \frac{\partial p}{\partial x_1} + k_{25} \frac{\partial p}{\partial x_2} + \frac{\partial^2 v^2}{\partial x_3^2}$$

The physical velocity components v_i can be found from the holonomic components v^i by

$$(11) \quad v_1 = \sqrt{a_{11}} v^1, \quad v_2 = \sqrt{a_{22}} v^2, \quad v_3 \equiv v^3.$$

The metric factors are:

continuity equation

$$(12) \quad k_{01} = [a_{11}a_{22} - (a_{12})^2]^{1/2}$$

x_1 - momentum equation

$$(13) \quad k_{11} = \frac{1}{2k_{01}^2} \left(a_{22} \frac{\partial a_{11}}{\partial x_1} - 2a_{12} \frac{\partial a_{12}}{\partial x_1} + a_{12} \frac{\partial a_{11}}{\partial x_2} \right)$$

$$(14) \quad k_{12} = \frac{1}{k_{01}^2} \left(a_{22} \frac{\partial a_{11}}{\partial x_2} - a_{12} \frac{\partial a_{22}}{\partial x_1} \right)$$

$$(15) \quad k_{13} = \frac{1}{2k_{01}^2} \left(-a_{22} \frac{\partial a_{22}}{\partial x_1} + 2a_{22} \frac{\partial a_{12}}{\partial x_2} - a_{12} \frac{\partial a_{22}}{\partial x_2} \right)$$

$$(16) \quad k_{14} = -a_{22}/k_{01}^2, \quad k_{15} = a_{12}/k_{01}^2$$

x_2 - momentum equation

$$(17) \quad k_{21} = \frac{1}{2k_{01}^2} \left(-a_{12} \frac{\partial a_{11}}{\partial x_1} + 2a_{11} \frac{\partial a_{12}}{\partial x_1} - a_{11} \frac{\partial a_{11}}{\partial x_2} \right)$$

$$(18) \quad k_{22} = \frac{1}{k_{01}^2} \left(-a_{12} \frac{\partial a_{11}}{\partial x_2} + a_{11} \frac{\partial a_{22}}{\partial x_1} \right)$$

$$(19) \quad k_{23} = \frac{1}{2k_{01}^2} \left(a_{12} \frac{\partial a_{22}}{\partial x_1} - 2a_{12} \frac{\partial a_{12}}{\partial x_2} + a_{11} \frac{\partial a_{22}}{\partial x_2} \right)$$

$$(20) \quad k_{25} = -a_{11}/k_{01}^2$$

A detailed representation of the equations and the auxiliary relations for the general compressible case (valid for both laminar and turbulent boundary layers) is given in Refs. 4 and 5.

Boundary and Initial Values

In Figs. 2 to 5 distributions of the external velocity components v_e^1 and v_e^2 (in x_1 and x_2 direction, Fig. 1) in the cross section $x_2/b = 0.45$ are shown, which are typical for the distributions at the larger part of the wing. Near the leading edge the flow is strongly three-dimensional. For angles of attack the v_e^1 - distribution becomes peaky on the suction side, which results in a weak separation bubble and turbulent reattachment for the experimental condition $Re_{tm} = 3.5 \cdot 10^6$. The v_e^1 - distribution on the pressure side is favourable over large parts of the wing for $\alpha > 0$. The external flow field has been computed with a first-order panel method at ONERA. The initial conditions for the boundary-layer calculation were introduced as in Ref. 6.

Results of the Laminar Boundary-Layer Calculation

Fig. 6 shows for the cross-section $x_2/b = 0.45$ the location of the stagnation line as function of the angle of attack. The agreement between panel calculation results and experimental results is very good. For $\alpha = 15^\circ$ the measured location lies closer to the leading edge, thus indicating that larger portions of separated flow exist on the wing. The location of the weak separation bubble on the suction side is calculated with good accuracy. If the surface curvature is being neglected ($\alpha_c \equiv 0$ in Eqs. 1 to 6) the calculated location of separation moves downstream, this is in accordance with two-dimensional results, for example Ref. 7.

In Fig. 7 the two components of the wall-shear stress τ_{wx1} , τ_{wx2} and the resulting wall-shear stress τ_{wges} are given ($\tau_w = c_f' \cdot Re$) for section $x_2/b = 0.45$ at $\alpha = 0^\circ$. The calculation has been made until τ_{wx1} became zero. This indicates a separation in the form of a free-vortex layer, since τ_{wx2} does not become zero. Fig. 8 shows for $\alpha = 15^\circ$ the distribution of the wall-shear stress on the suction side. The results near the leading edge of the separation bubble seem to indicate that here an approximately two-dimensional separation occurs. On the pressure side, Fig. 9, the situation is similar to that for $\alpha = 0^\circ$. Note that in Figs. 7, 8 and 9 x^*/t has its origin in the stagnation line, and not in the leading edge.

Transition Prediction

In Fig. 6 the location of the maximum external velocity $g_{e\max} = \sqrt{v_{e1}^2 + v_{e2}^2}$ is indicated for the different angles of attack. The point of neutral stability of the Tollmien - Schlichting theory applied to the mean-flow profile of the three-dimensional boundary layer (see Ref. 8) lies shortly behind this location, as would be in two-dimensional flow for the magnitude of the present Reynoldsnumber. Cross-flow instability (criterion of Owen and Randall) occurs even earlier. If one accepts the underlying hypotheses of the criteria applied (Ref. 8), the results indicate that the boundary layer is already in the process of transition when it separates. In an

experiment with higher Reynoldsnumber the separation bubble might disappear in the range of angles of attack considered. Fig. 10 shows on the suction side also calculated neutral stability results for $Re = 35 \cdot 10^6$. The locations are closer to the stagnation line, as expected. On the pressure side the situation is different. The experiment shows that the location of transition moves away from the leading edge for small angles of attack, and moves forward again for larger angles of attack. The location of neutral stability of the Tollmien-Schlichting theory for the mean-flow profile moves downstream for increasing angle of attack, Fig. 10 and Fig. 11. The cross-flow instability criterion of Owen and Randall gives locations for $\chi = 100$ which follow approximately the measured transition locations. The cross flow criterion, however, states that instability occurs at $\chi = 120 \pm 20$, and transition due to cross flow might occur at much higher values of χ . Here it can be seen that the calculated neutral stability location lies behind the measured transition location. It appears that the stability and transitional behaviour is being described qualitatively in a right way, but quantitatively the results are not satisfactory. Further studies following the work presented in Ref. 3 will possibly clarify this problem. In any case more detailed experimental data are needed in order to verify old and new stability criteria for three-dimensional flows, and to design transition criteria for three-dimensional flow, which certainly will be semi-empirical criteria like the e^9 -criterion, or Granvilles criteria.

References

- [1] V. Schmitt, J. Cousteix: "Etude de la couche limite tridimensionnelle sur une aile en flèche", ONERA Rapport Technique No. 14/1713AN, Juillet 1975.
- [2] E. H. Hirschel, V. Jawtusch: "Nachrechnung des experimentell ermittelten Überganges laminar-turbulent an einem gepfeilten Flügel", DLR-FB 77-36 (1977).
- [3] U. Dallmann: "Über die Stabilität dreidimensionaler Scherströmungen-Kriterien für reibungsfreie Störangeregung", Ph. D. Thesis in preparation.

- [4] E. H. Hirschel, V. Jawtusch, W. Kordulla: "Some considerations regarding the calculation of boundary layers on real configurations", DLR-FB in preparation.
- [5] E. H. Hirschel: "Boundary-Layer Equations in Holonomic Formulation", Proc. International Conference on Numerical Methods in Laminar and Turbulent Flow, Swansea, July 18-21, 1978, Pentech Press, London.
- [6] E. H. Hirschel, V. Jawtusch: "Some Investigations for the Evaluation of Stability and Transition Criteria for Boundary Layers on Swept Wings", Proc. 5. DEA-Meeting Boundary-Layer Effects, April 28-29, 1976, Dayton, AFFDL-TR-77-61 (1977).
- [7] R. Grundmann, K. Robert: "Krümmungseinflüsse auf das Ablöseverhalten von laminaren Grenzschichten", DLR-FB 77-36 (1977).
- [8] E. H. Hirschel: "The Influence of the Free-Stream Reynolds-Number on Transition in the Boundary Layer on an Infinite Swept Wing", AGARD R-602 (1973).

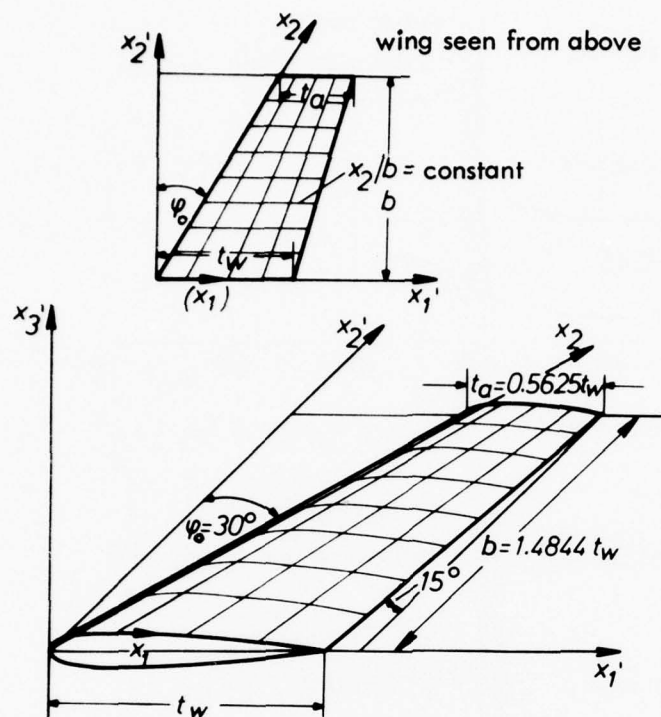


Fig. 1 Sketch of wing geometry

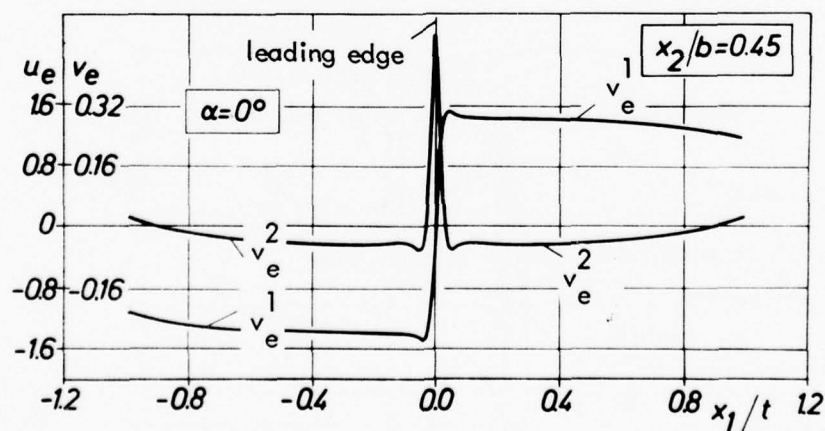


Fig. 2 External velocities in cross section $x_2/b = 0.45$, $\alpha = 0^\circ$

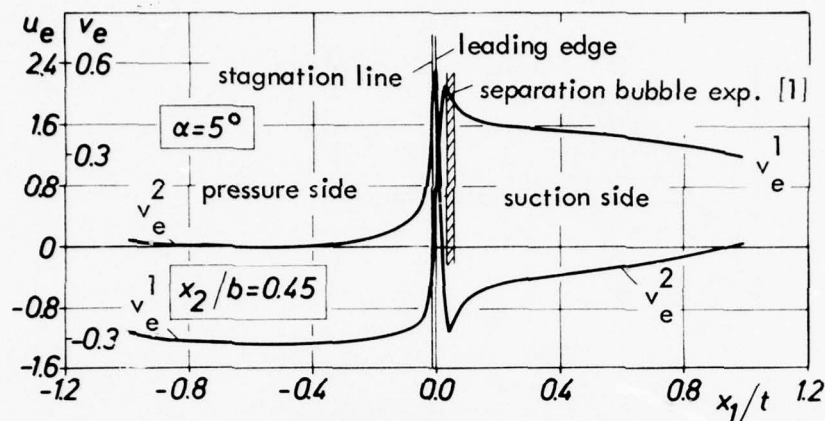


Fig. 3 External velocities in cross section $x_2/b = 0.45$, $\alpha = 5^\circ$

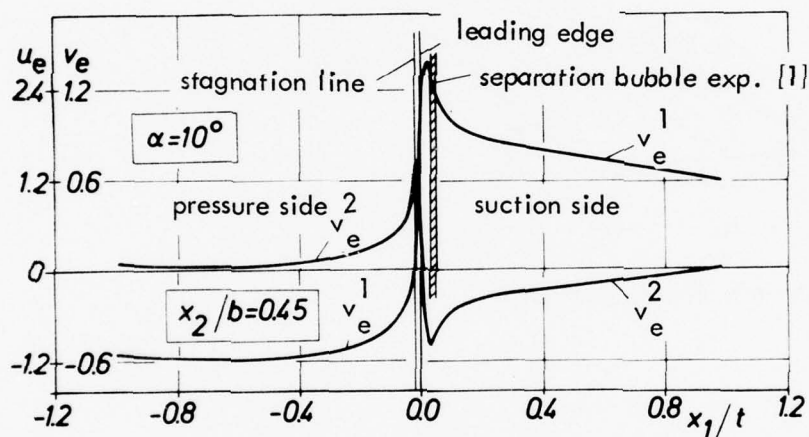


Fig. 4 External velocities in cross section $x_2/b = 0.45$, $\alpha = 10^\circ$

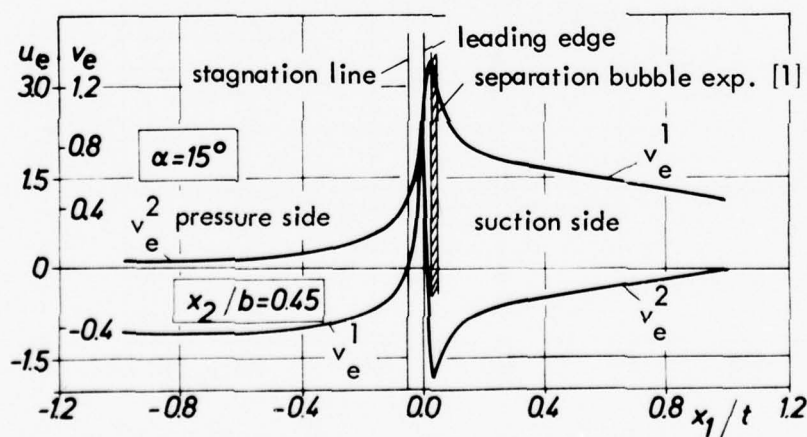


Fig. 5 External velocities in cross section $x_2/b = 0.45$, $\alpha = 15^\circ$

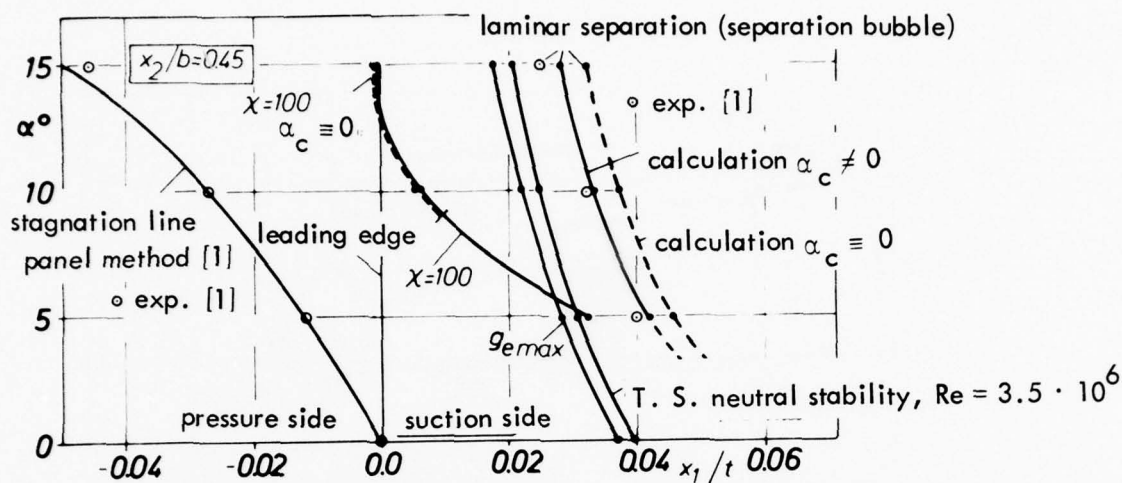


Fig. 6 Stagnation line, separation bubble - experiment and calculation, stability results - calculations at $x_2/b = 0.45$

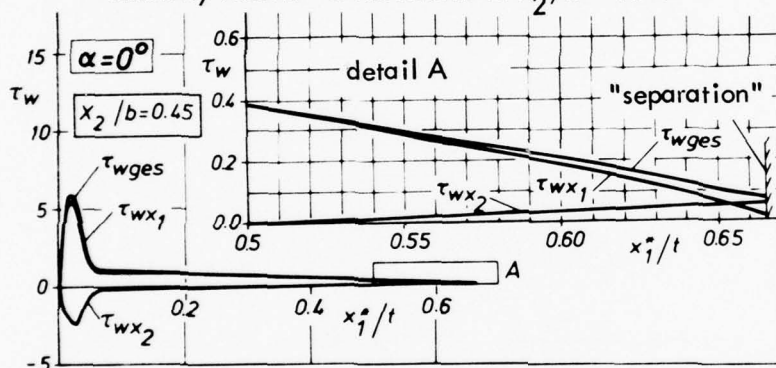


Fig. 7 Calculated wall shear-stress distributions, $\alpha = 0^\circ$

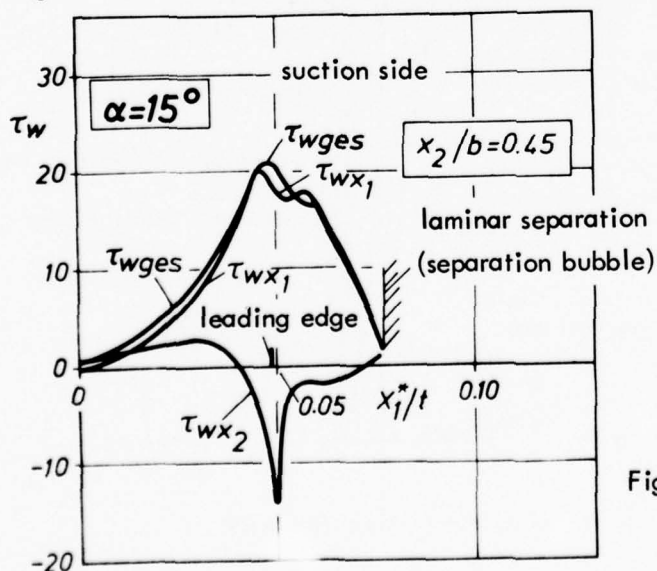


Fig. 8 Calculated wall shear-stress distributions, $\alpha = 15^\circ$, suction side

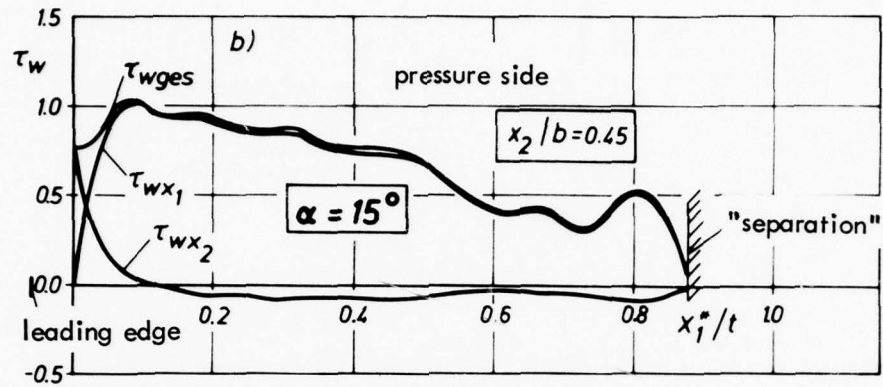


Fig. 9 Calculated wall shear-stress distributions, $\alpha = 15^\circ$, pressure side

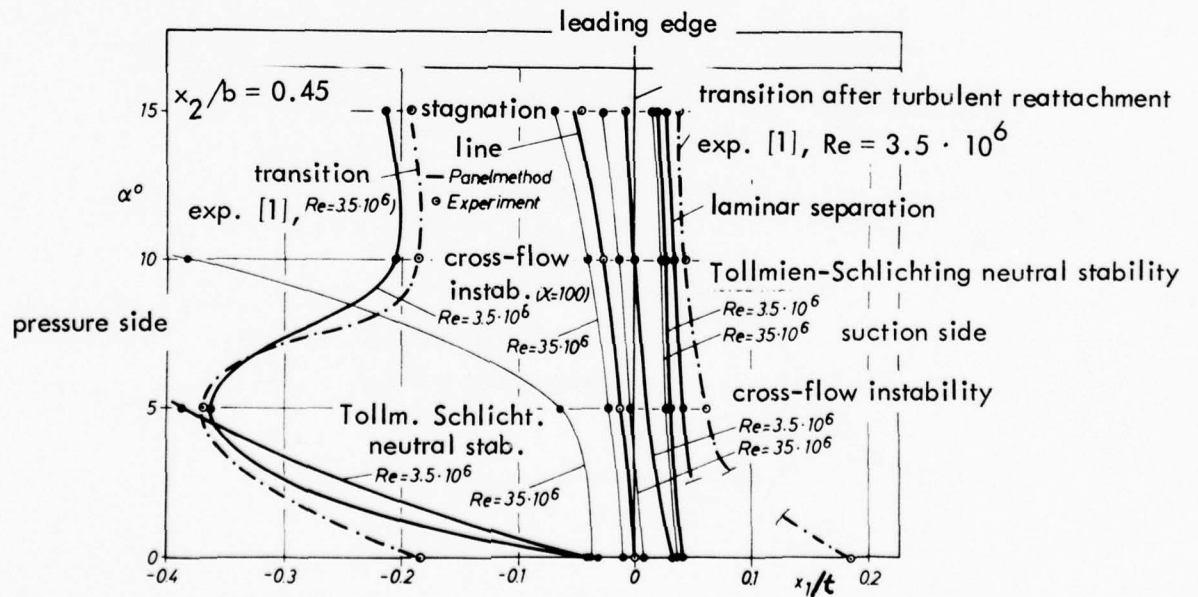


Fig. 10 Transition results - experiment and calculation

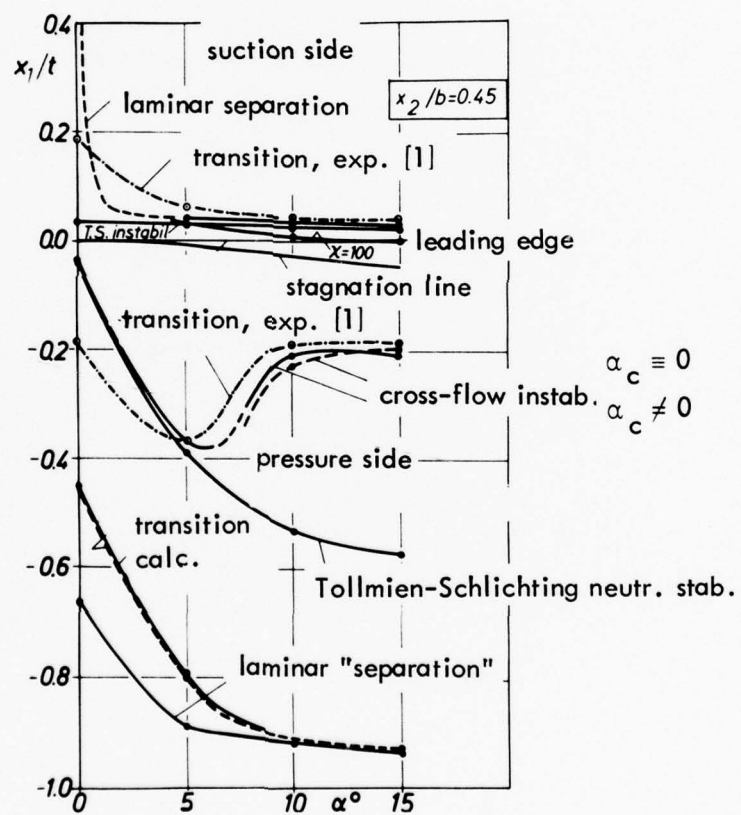


Fig. 11 Transition results - experiment and calculation

D E A - M E E T I N G

"VISCOUS AND INTERACTING FLOW FIELD EFFECTS"

Monterey, CA., USA, 25/27 April 1978

THREE-DIMENSIONAL BOUNDARY ALYERS ON WINGS
AND BODIES OF REVOLUTION

H. W. STOCK
DORNIER GMBH, Friedrichshafen, West Germany

1. ABSTRACT

The results of a newly developed integral method (Method 1) for three-dimensional, laminar, compressible boundary layers will be compared to exact solutions and to other available integral methods.

The boundary layer flow over an infinite swept wing is calculated for the laminar case (Method 1) and for the turbulent case, using the compressible version of P.D. Smith's boundary layer method together with a lag entrainment method (Method 2).

The laminar boundary layer development over an inclined ellipsoid is calculated (Method 1) and compared to the results of a finite difference solution. The turbulent flow over the same configuration is calculated using a newly developed integral method (Method 3) for incompressible flow.

2. INTRODUCTION

Three-dimensional boundary layers are often calculated in streamline coordinates, representing an orthogonal, curvilinear coordinate system. One coordinate is identical to the projection of the streamline at the outer edge of the boundary layer onto the surface and gives the mainstream direction, the other coordinate, orthogonal to the mainstream direction, gives the cross flow direction, fig. 1. Using a curvilinear, non-orthogonal coordinate system involves the following advantages:

1. The coordinate system is not fixed a priori.
2. For one configuration under different flow conditions the same coordinate system can be used.

As soon as the velocity profiles in the streamwise and crosswise direction are specified it is easy to evaluate the integral quantities in any chosen x- and y-direction, fig. 1. In the following any of the 3 integral methods is written in non-orthogonal, curvilinear coordinates.

3. DESCRIPTION OF THE INTEGRAL METHODS

3.1 Method 1 (Laminar, compressible) /1/

For the description of the streamwise velocity profiles the results of the similar solutions of Cohen and Reshotko /2/ are used, fig. 2. The integral quantities for the streamwise flow in the transformed plane are expressed as a function of one parameter. For the description of the cross-flow profiles a 6th order polynomial is employed, without using a boundary condition of the Pohlhausen type, which couples the pressure gradient to the variation of the skin friction. In fig. 3 some cross-flow velocity profiles are shown representing, a family of two parameters. (τ_2 and δ_2^* being the skin friction and the displacement thickness of the cross-flow profile in the transformed plane). Profiles of the cross-over type are included. Together with a scaling parameter of the boundary layer, the three-dimensional flow is described by four variables. The x- and y-momentum integral equations and the x- and y-moment of momentum integral equations are used for

the solution.

3.2 Method 2 (Turbulent, compressible) /3,4/

The streamwise profiles are represented by power law profiles, the cross-flow profiles by Mager /5/ or Johnston /6/ profiles. The Ludwig-Tillmann relation is used for the description of the skin friction. The influence of compressibility is represented by applying Eckert's reference temperature concept. The equations used are the x- and y-momentum equation and the entrainment equation (equilibrium entrainment). An extension of that method has been done /4/ using a lag-entrainment method for non-equilibrium entrainment.

3.3 Method 3 (Turbulent, incompressible) /7/

The streamwise profiles are described by using the two-parameter Coles profiles, which are known to produce better results in the two-dimensional case for accelerated and decelerated flows. Here the Ludwig-Tillmann relation can be dropped and replaced by the derivative of the Coles profiles at the wall. For the cross-flow profiles Mager /5/ or Johnston /6/ profiles are used. The x- and y-momentum and the entrainment equation are employed together with a lag-entrainment method.

4. RESULTS

4.1 Comparison of method 1 with exact solutions and other approximate methods

In fig. 4 the present results for a flow originating at a stagnation line are compared to the results of an exact method /8/. (Θ_{11} is the momentum thickness, H the form parameter and c_f the skin friction of the streamwise profile; β is the limiting streamline angle of the flow and δ_2^* the displacement thickness of the cross-flow profile). The point where separation is indicated is almost identical in both methods. Although β changes sign, δ_2^* remains positive and close to the exact results, which proves the quality of the employed cross-flow profiles.

Fig. 5 gives the results for a flat plate flow which is suddenly exposed at $x = 1$ to an adverse pressure gradient (decelerated U velocity component, constant V component). The agreement is acceptable, except that separation is indicated to far downstream.

Fig. 6 describes the same flow situation as fig. 5 but for a larger adverse pressure gradient.

In fig. 7 the present method is compared to exact results /9/ and other available integral methods /10-12/. The boundary layer flow starts at the leading edge, $x = 0$, and is initially accelerated (constant U velocity component, initially accelerated V component).

Cooke's integral method /10/ was estimated to be the best available /13/.

Fig. 8 gives results for the same flow situation as in fig. 7 except that the initial acceleration is larger.

In fig. 9 the boundary layer flow starts at the leading edge, $x = 0$, and is initially decelerated (constant U velocity component, initially decelerated V component). For this situation the agreement with the exact results is markedly better for the present method than for Cooke's method.

4.2 The boundary layer development on an infinite swept wing

The resultant velocity distribution U_e/U_{Ref} and the angled α for the infinite swept wing are shown in fig. 10. (α is the angle between the projection of the streamline at the outer edge of the boundary layer onto the surface and the x -direction). The laminar (Method 1) and turbulent (Method 2) boundary layer development is shown in fig. 11. (δ_1^* being the displacement thickness of the streamwise profile). As may be seen the variation of the limiting streamline angle β , which is a measure of the three-dimensionality of the flow, is much larger for the laminar case, i.e. the three-dimensionality of a flow is more pronounced in the laminar case for the same outer flow situation.

4.3 The boundary layer development on inclined ellipsoids

The laminar boundary layer development (Method 1) on an ellipsoid at 5° of angle of attack is shown in fig. 12 and compared to the finite difference solution of Geissler /14/. A comparison for the limiting streamline angle β could not be done as Geissler did not present results for cross-flow profiles. The overall agreement for an integral method in this complicate flow situation with a finite difference solution is excellent. The curves 1, which represent results close to the stagnation point, show the largest deviation from the finite difference solution. This is due to the fact that in the present method the calculation was not started in the stagnation point, but at $x/a = .04$.

Separation of the streamwise profile was predicted in almost the same location for both methods. A free vortex layer separation /15/ seems to be indicated in both methods on the side of the ellipsoid at about $\Phi = 120^\circ$. Fig. 12 gives the turbulent results (Method 3) for the same configuration. Separation occurs far downstream of the laminar one, but at almost the same angle Φ .

5. CONCLUSION

The laminar integral method is shown to give results close to the exact ones and to produce a better agreement than other existing integral methods. It is shown that for an identical potential flow situation, (infinite swept wing) the laminar boundary layer results in a high three-dimensionality than the turbulent one. The boundary layer development on an inclined ellipsoid is fairly well predicted in the laminar case

compared to a finite difference solution. In the laminar and turbulent case the separation of the streamwise profile occurs at almost the same side location ($\phi = 120^\circ$) on the ellipsoid.

REFERENCES

- /1/ H.W. STOCK
Integralverfahren zur Berechnung dreidimensionaler, laminarer und turbulenter Grenzschichten.
DORNIER-Bericht, DO 77/51 B, 1977

- /2/ C.B. COHEN, E. RESHOTKO
Similar Solution for the Compressible Laminar Boundary Layer with Heat Transfer and Pressure Gradient.
NACA R 1293, 1956

- /3/ P.D. SMITH
An Integral Prediction Method for Three-Dimensional Compressible Turbulent Boundary Layers.
ARC, R.&M., Nr. 3739, 1974

- /4/ H.W. STOCK
Results of a Calculation Method for Three-Dimensional, Compressible, Turbulent Boundary Layers.
DEA-Meeting, Dayton, Ohio, 1975
AFF DL-TR-77-61, 1977

- /5/ A. MAGER
Generalisation of Boundary Layer Momentum Integral Equations to Three-Dimensional Flow, Including those of Rotating Systems.
NACA Rep. 1067, 1952

- /6/ J.P. JOHNSTON
On the Three-Dimensional Turbulent Boundary Layer Generated by Secondary Flow.
Journal Basic Eng. Vol. 82, p. 223-250, 1960

- /7/ H.W. STOCK
Eine Integralmethode zur Berechnung dreidimensionaler, turbulenter, inkompressibler Grenzschichten.
DLR-FB 77-16, 1977

- /8/ H.P. HORTON
Numerical Solution of Incompressible Laminar Boundary Layer Problems Using Invariant Imbedding.
To be published in AIAA Journal.

- /9/ A.G. Hansen, H.Z. HERZIG
Cross-Flows in Laminar Incompressible Boundary Layers.
NACA Tech. Note 3651, 1956

- /10/ J.C. COOKE
Approximate Calculation of Three-Dimensional Laminar Boundary
Layers.
ARC, R.&M. Nr. 3201, 1961
- /11/ E.A. EICHELBRENNER, A. OUDART
Méthode de calcul de la couche limite tridimensionnelle
Application a un corps fusilé incliné sur le vent.
ONERA Publ. 76, 1955
- /12/ J.A. ZAAT
Nachprüfung der einfachen Rechenmethode für dreidimensionale,
laminare Grenzschichten mit Hilfe von exakten Lösungen.
NLL Report F202, 1957
- /13/ P.D. SMITH
Approximate Solutions of the Three-Dimensional Laminar Boundary
Layer Momentum Integral Equations.
ARC, CP No. 1064, 1969
- /14/ W. GEISLER
Berechnung der laminaren dreidimensionalen Grenzschicht an
unsymmetrisch umstromten Rotationskörpern mittels Differenzen-
verfahren.
DFVLR-IB 251-73 A 19, 1973
- /15/ E.C. MASKELL
Flow Separation in Three-Dimensions.
RAE R 2565, 1955

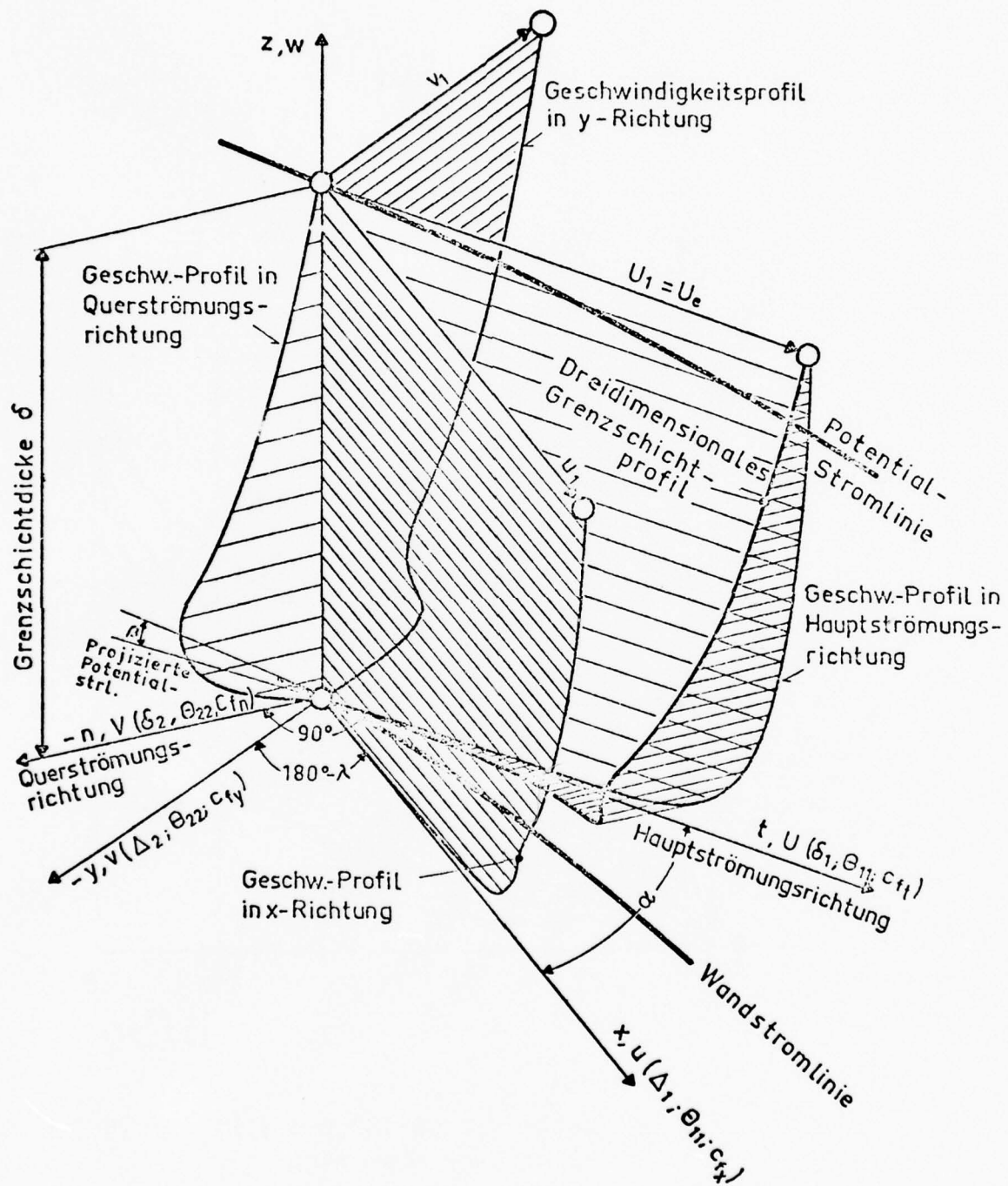


Fig. 1: THREE-DIMENSIONAL BOUNDARY LAYER FLOW

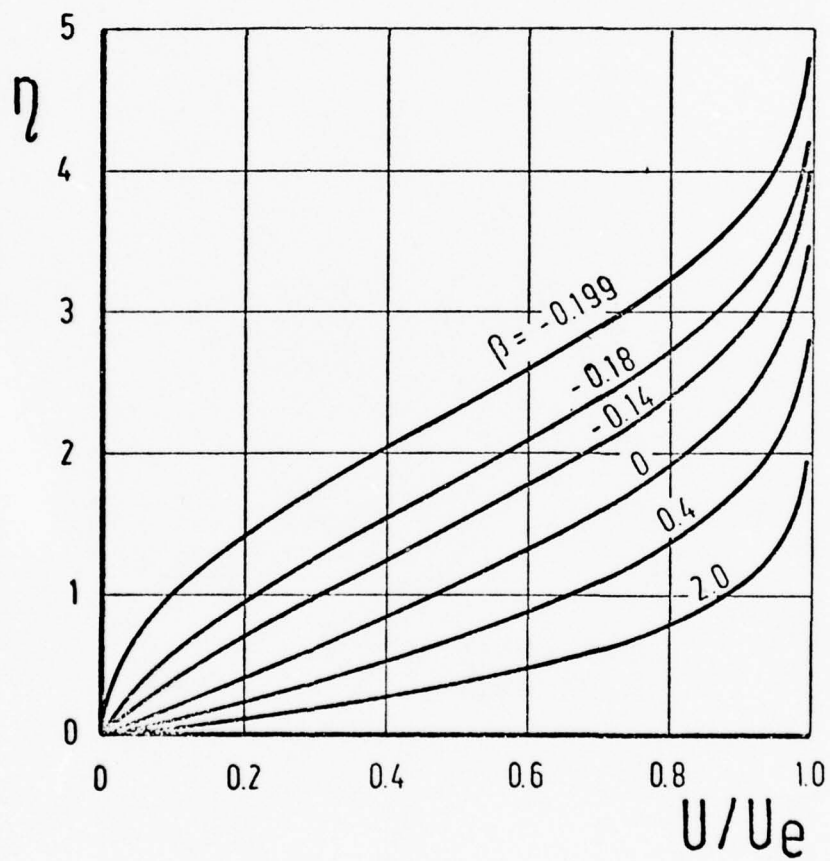


Fig. 2: LAMINAR VELOCITY PROFILES /2/ IN THE
STREAMWISE DIRECTION

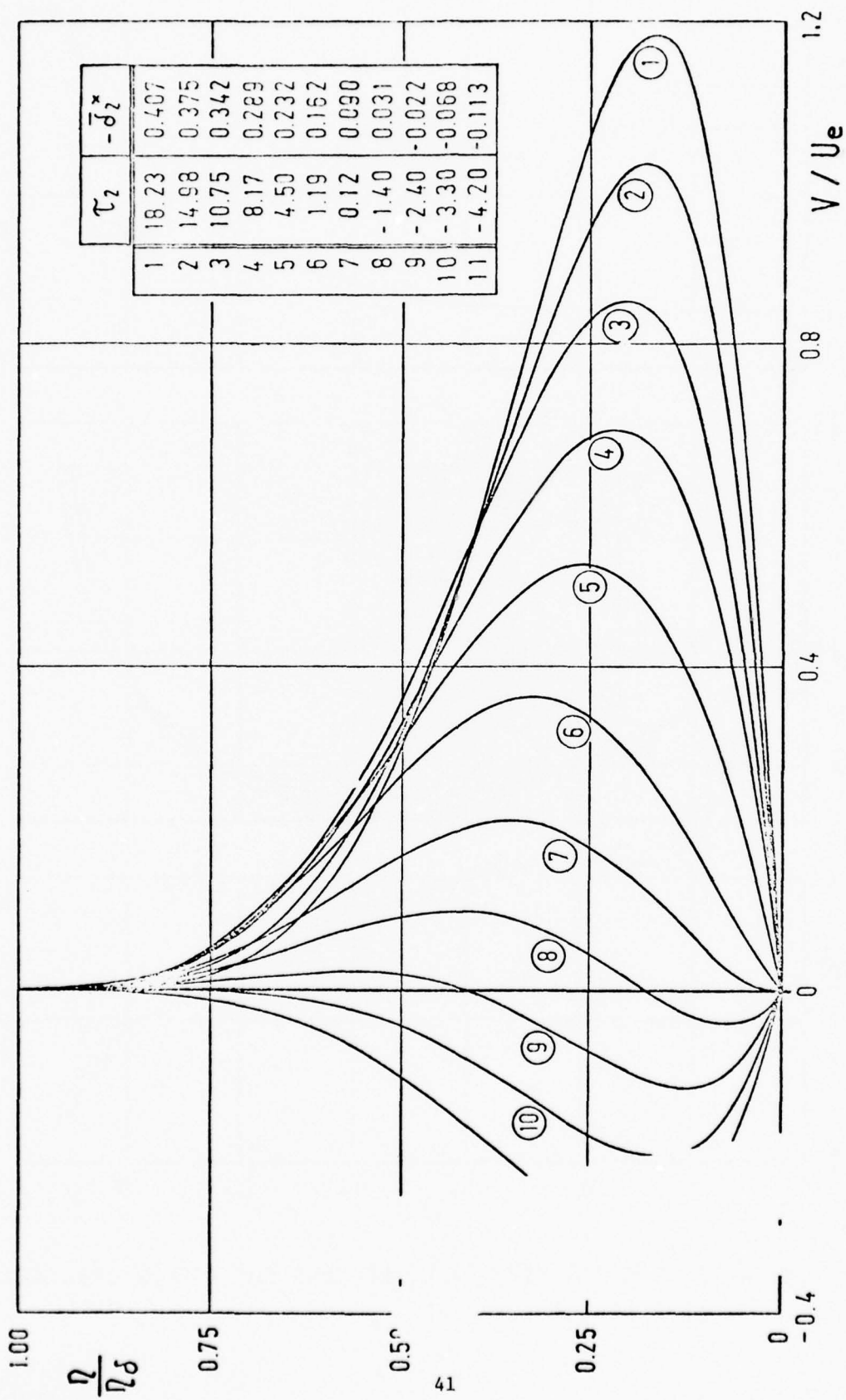


Fig. 3: LAMINAR VELOCITY PROFILES IN THE CROSSWISE DIRECTION

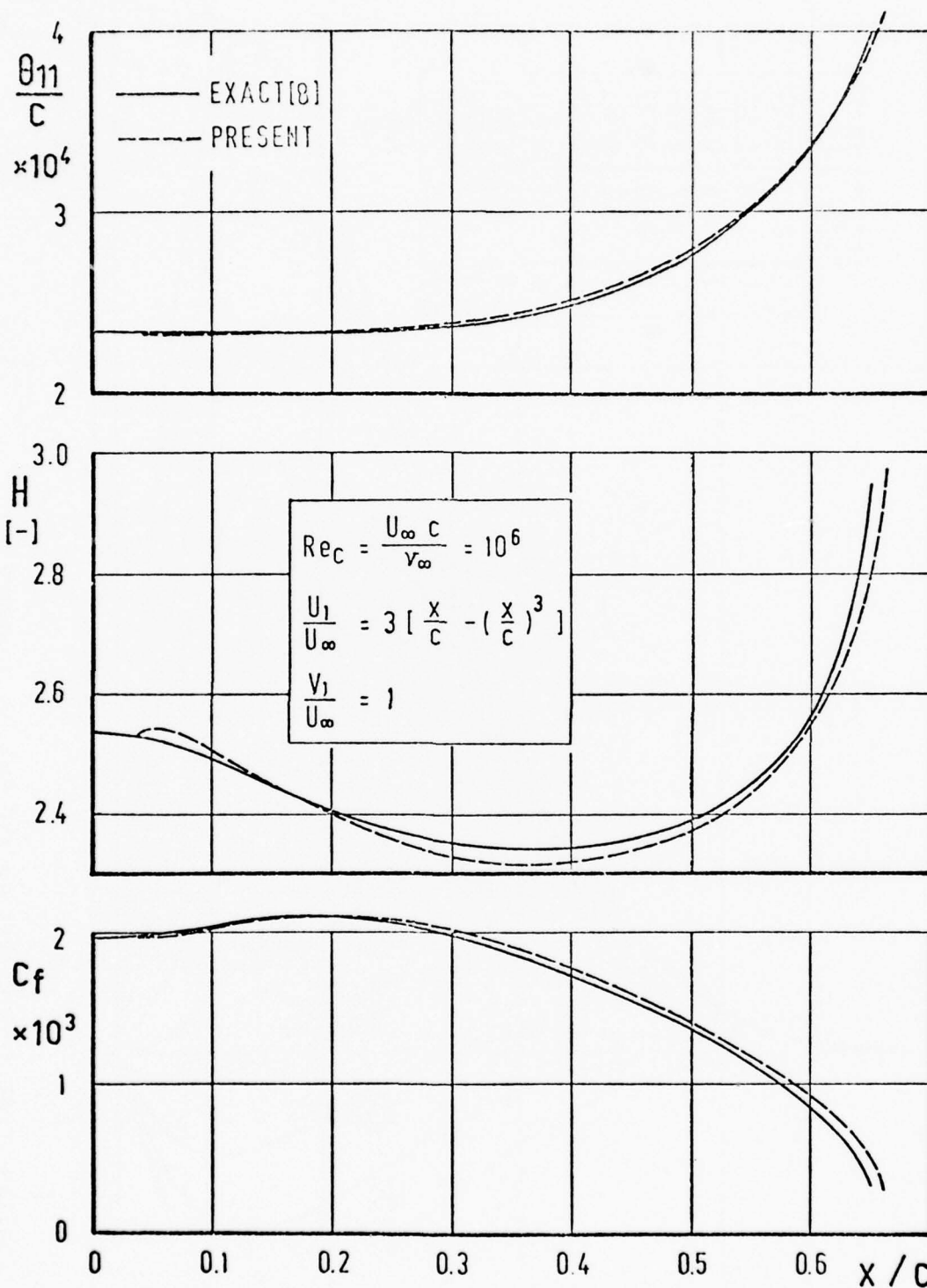


Fig. 4: COMPARISON WITH EXACT RESULTS FOR A FLOW ORIGINATING AT A STAGNATION LINE

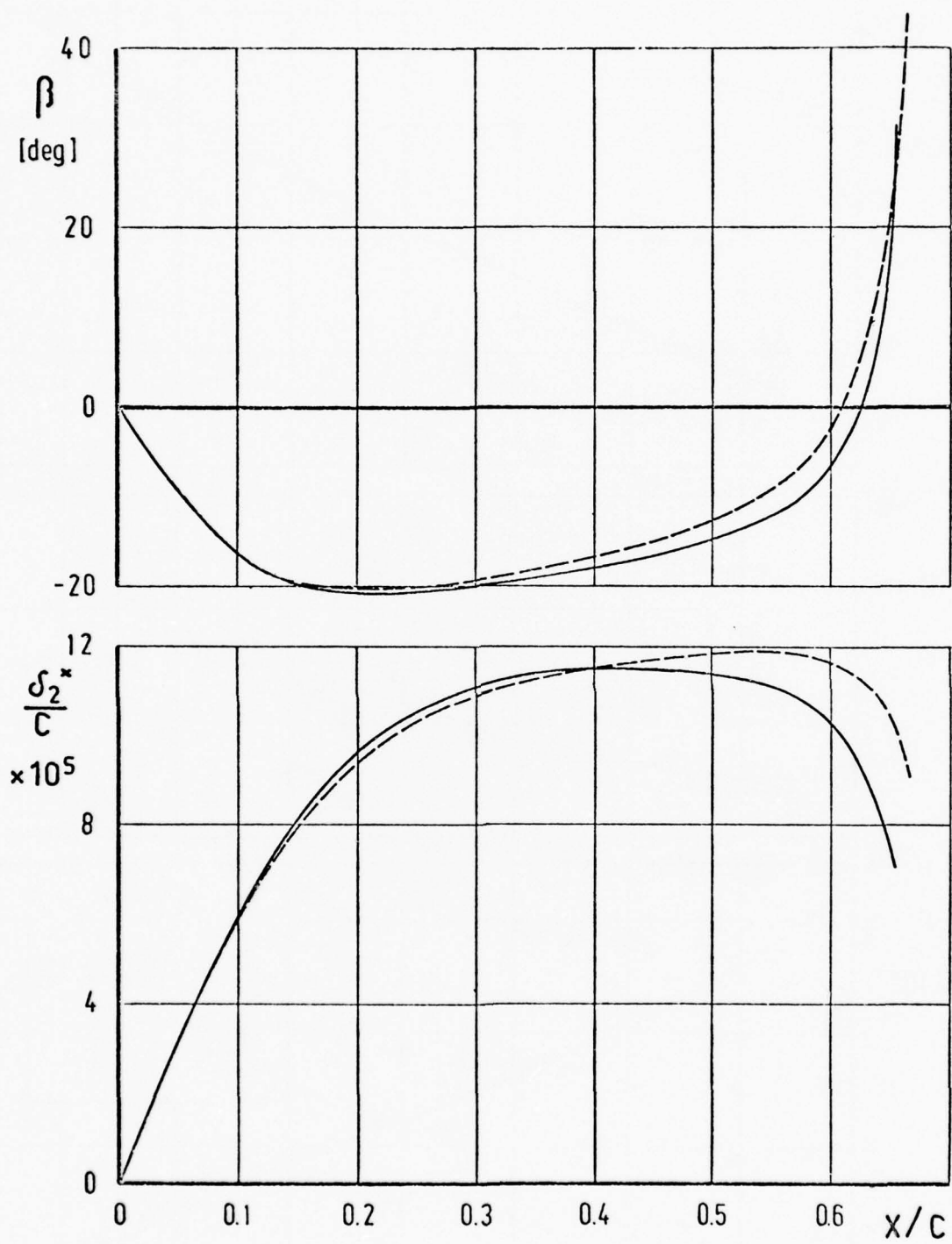


Fig. 4: CONTINUED

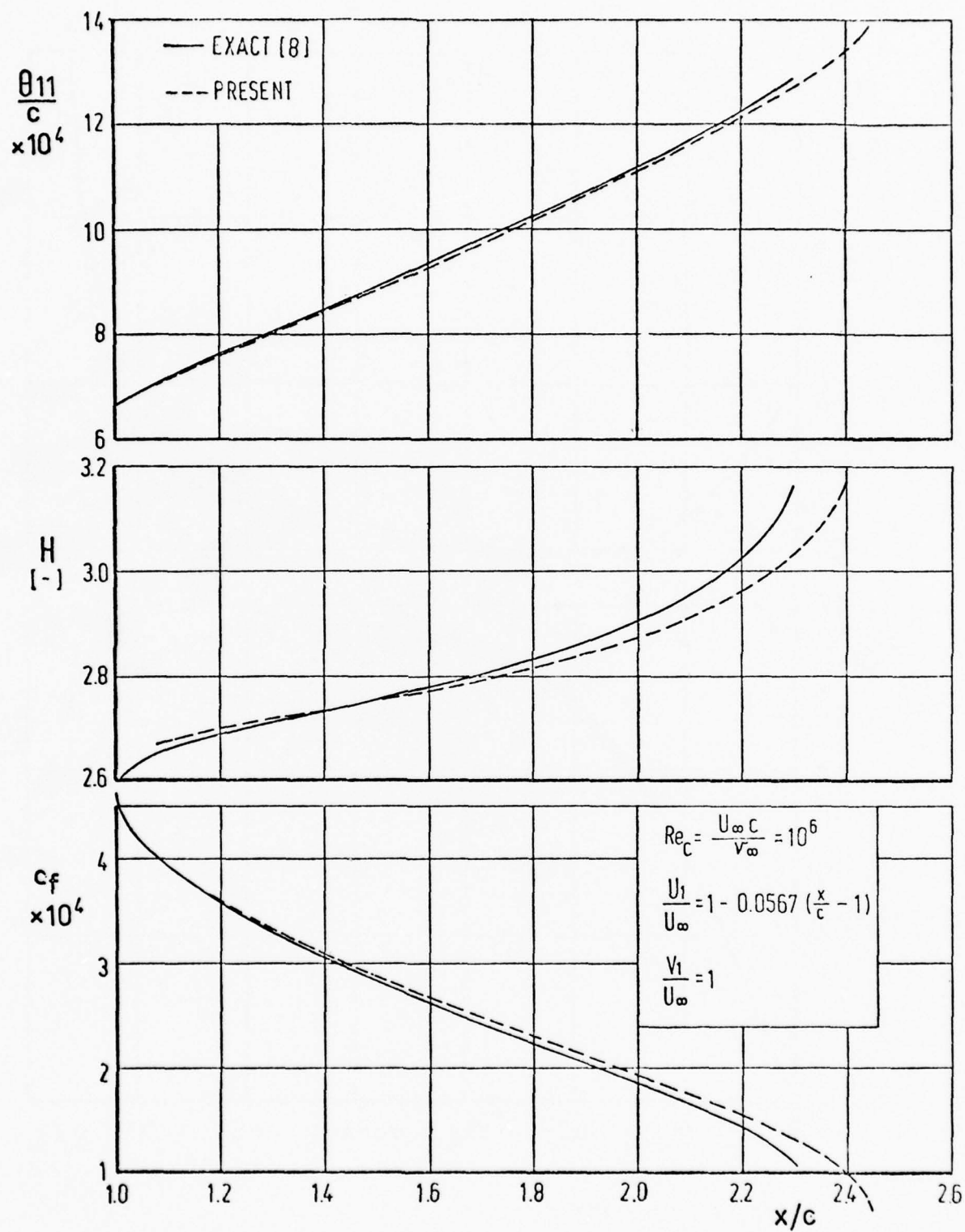


Fig. 5: COMPARISON WITH EXACT RESULTS FOR A FLAT PLATE FLOW WITH A SUDDENLY IMPOSED ADVERSE PRESSURE GRADIENT

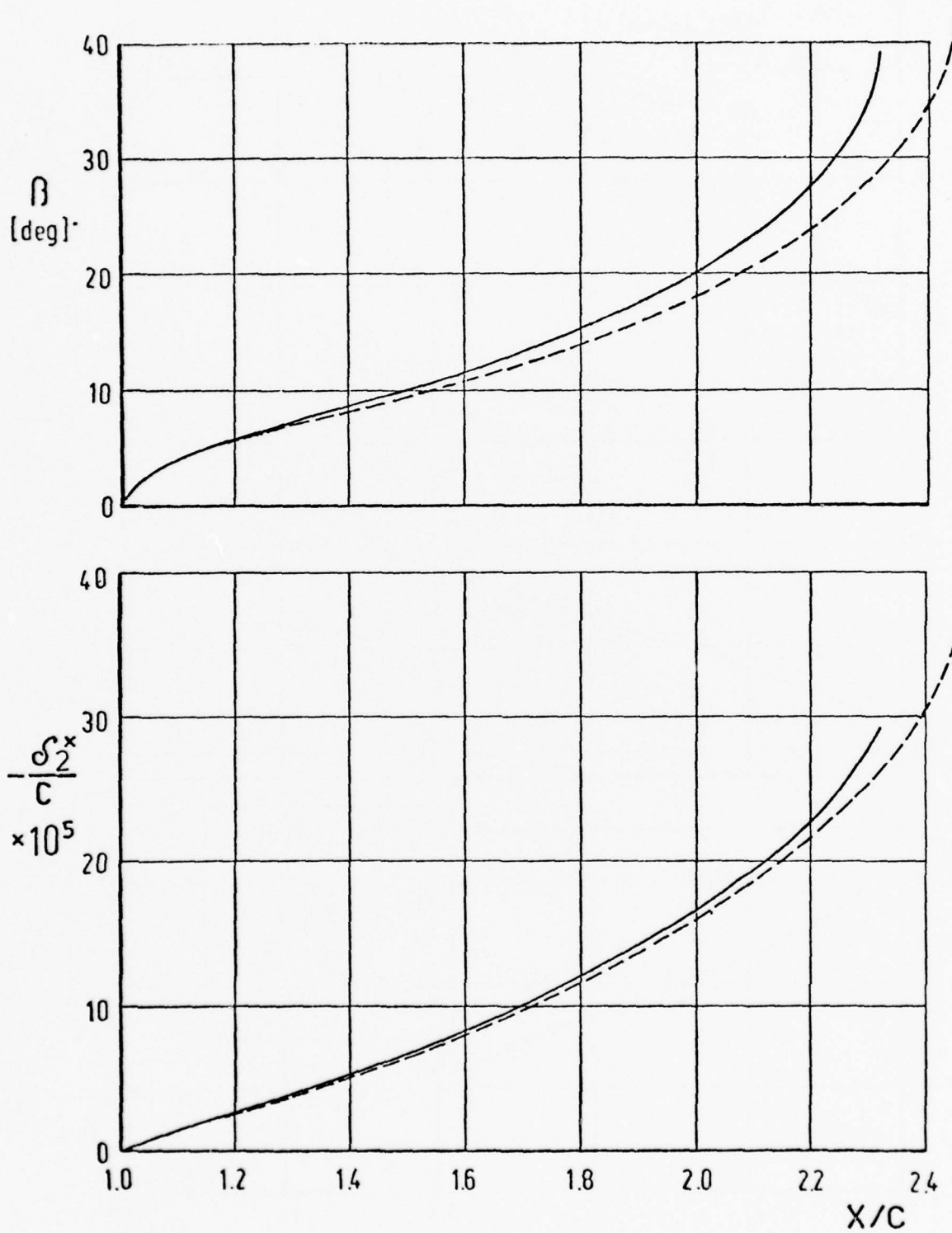


Fig. 5: CONTINUED

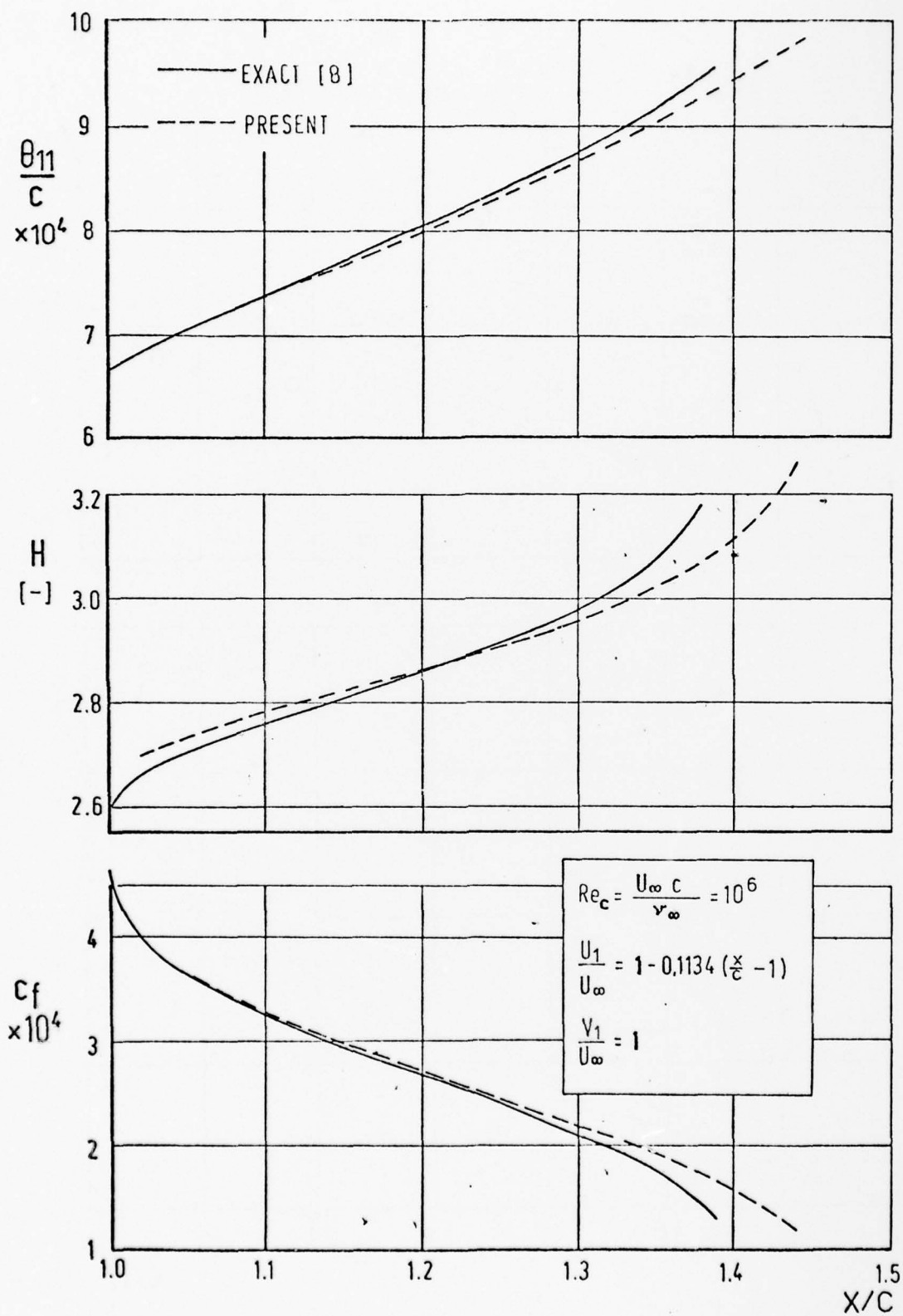


Fig. 6: COMPARISON WITH EXACT RESULTS FOR A FLAT PLATE
FLOW WITH A SUDDENLY IMPOSED ADVERSE PRESSURE GRADIENT

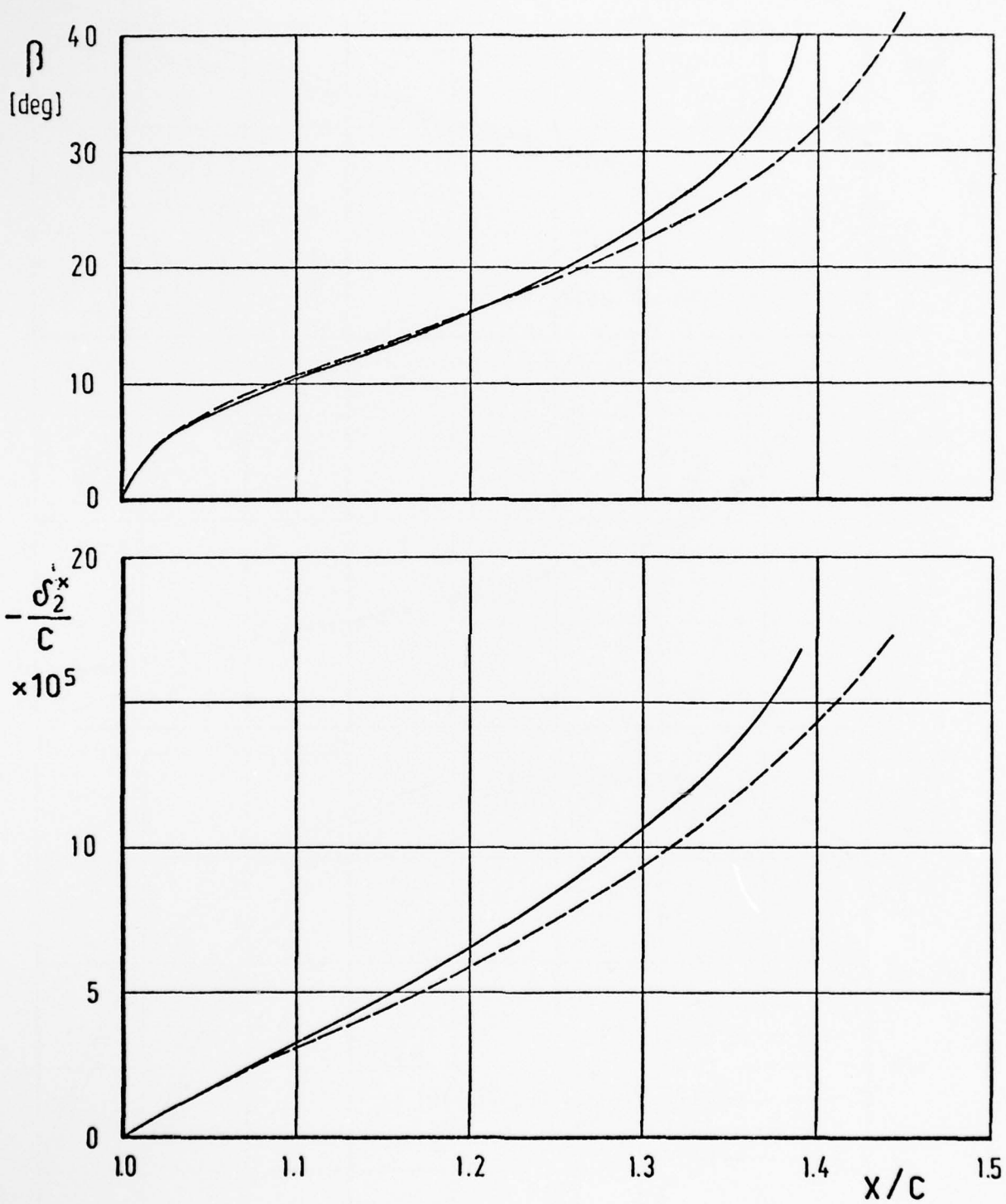


Fig. 6: CONTINUED

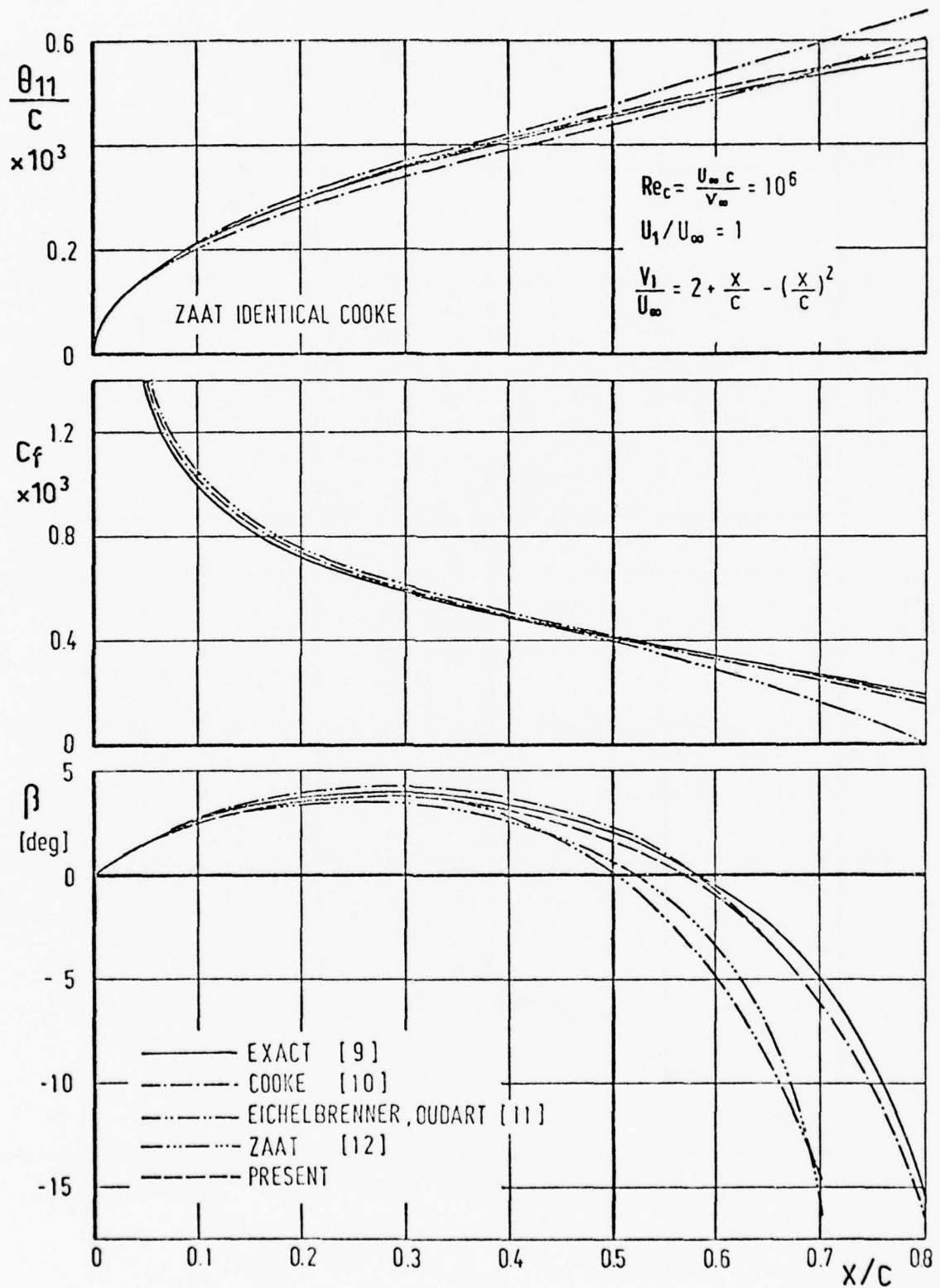


Fig. 7: COMPARISON WITH EXACT RESULTS AND OTHER INTEGRAL METHODS FOR AN INITIALLY ACCELERATED FLOW

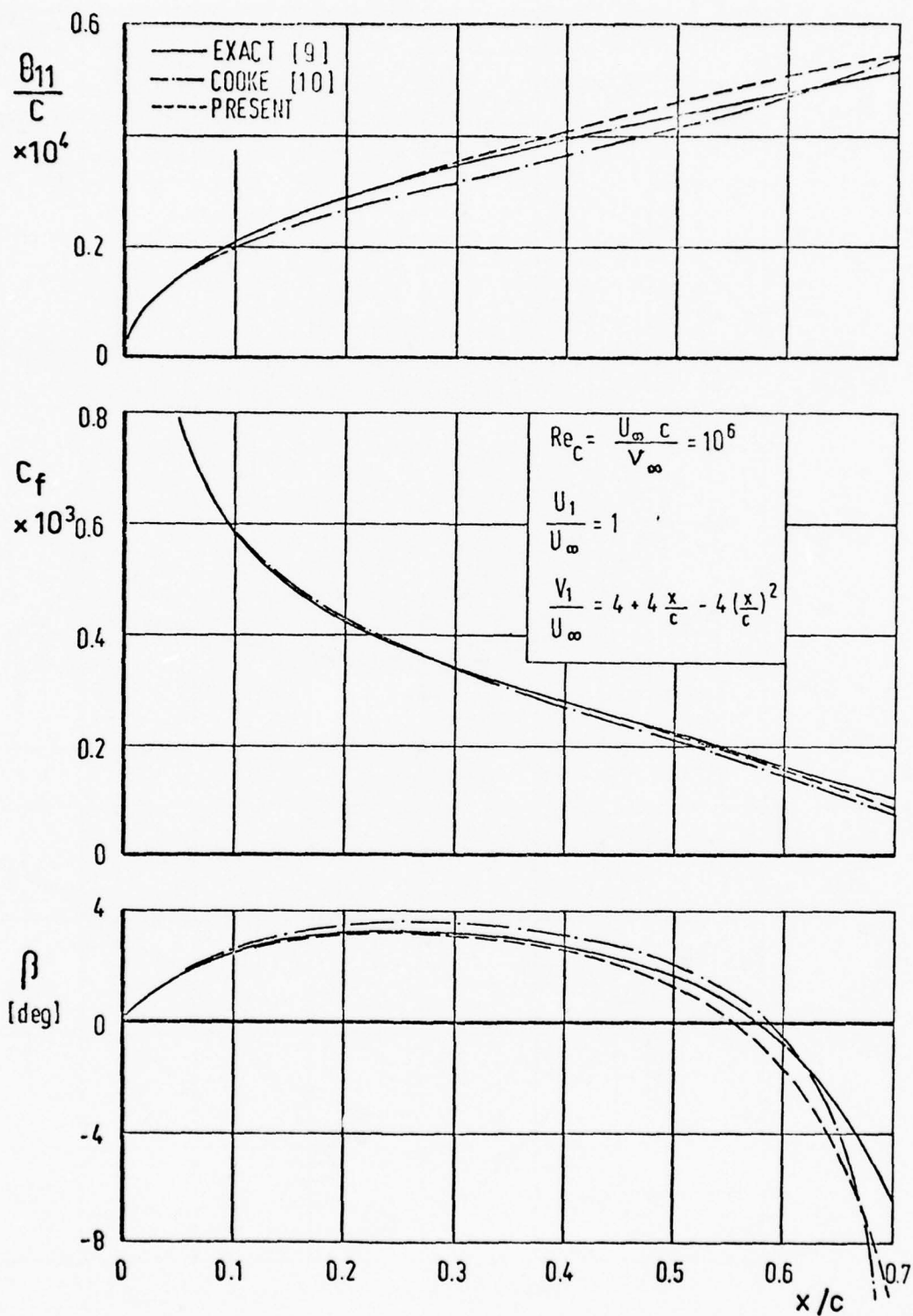


Fig. 8: COMPARISON WITH EXACT RESULTS AND COOKE'S METHOD FOR AN INITIALLY ACCELERATED FLOW

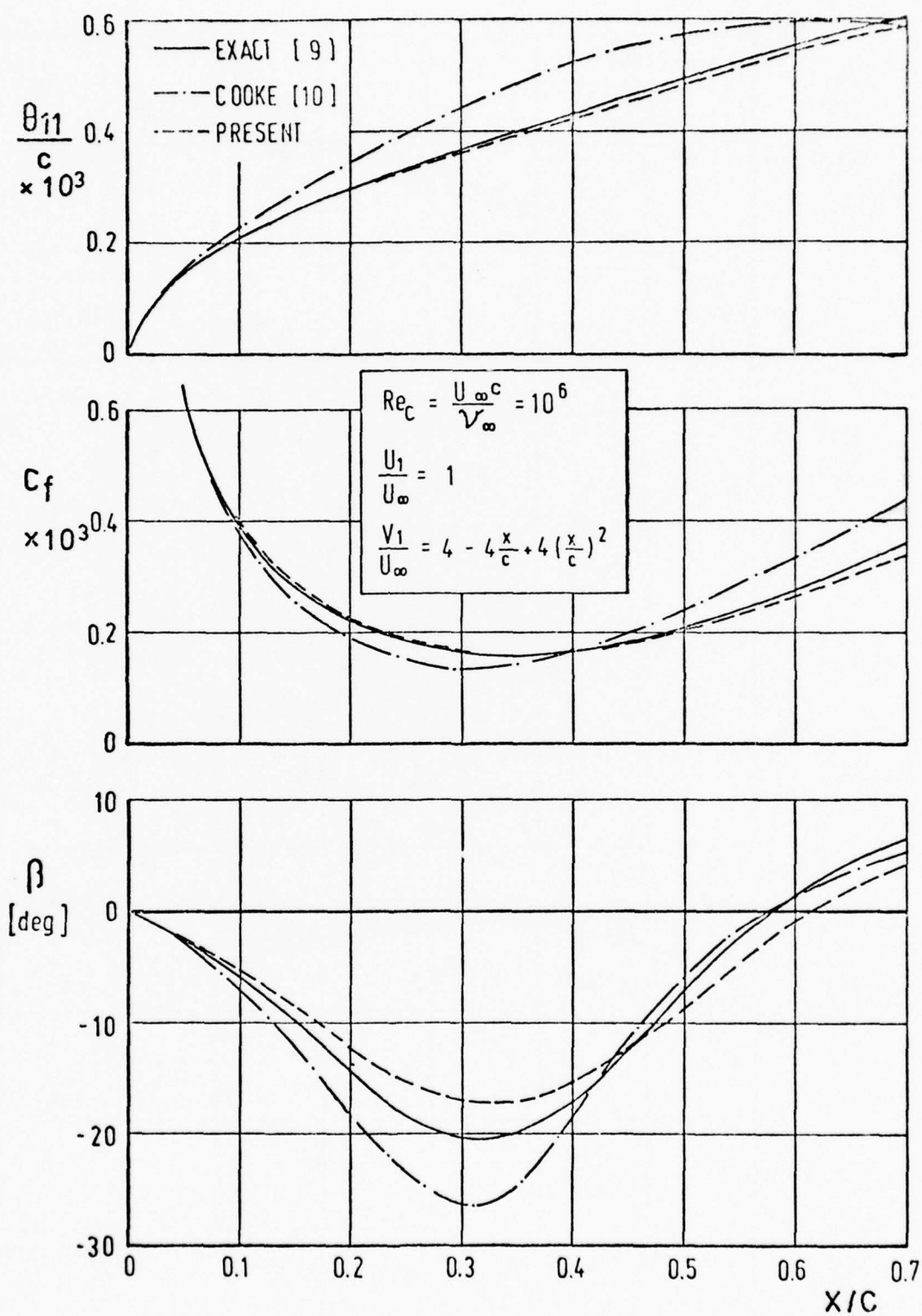


Fig. 9: COMPARISON WITH EXACT RESULTS AND COOKE'S METHOD FOR AN INITIALLY RETARDED FLOW

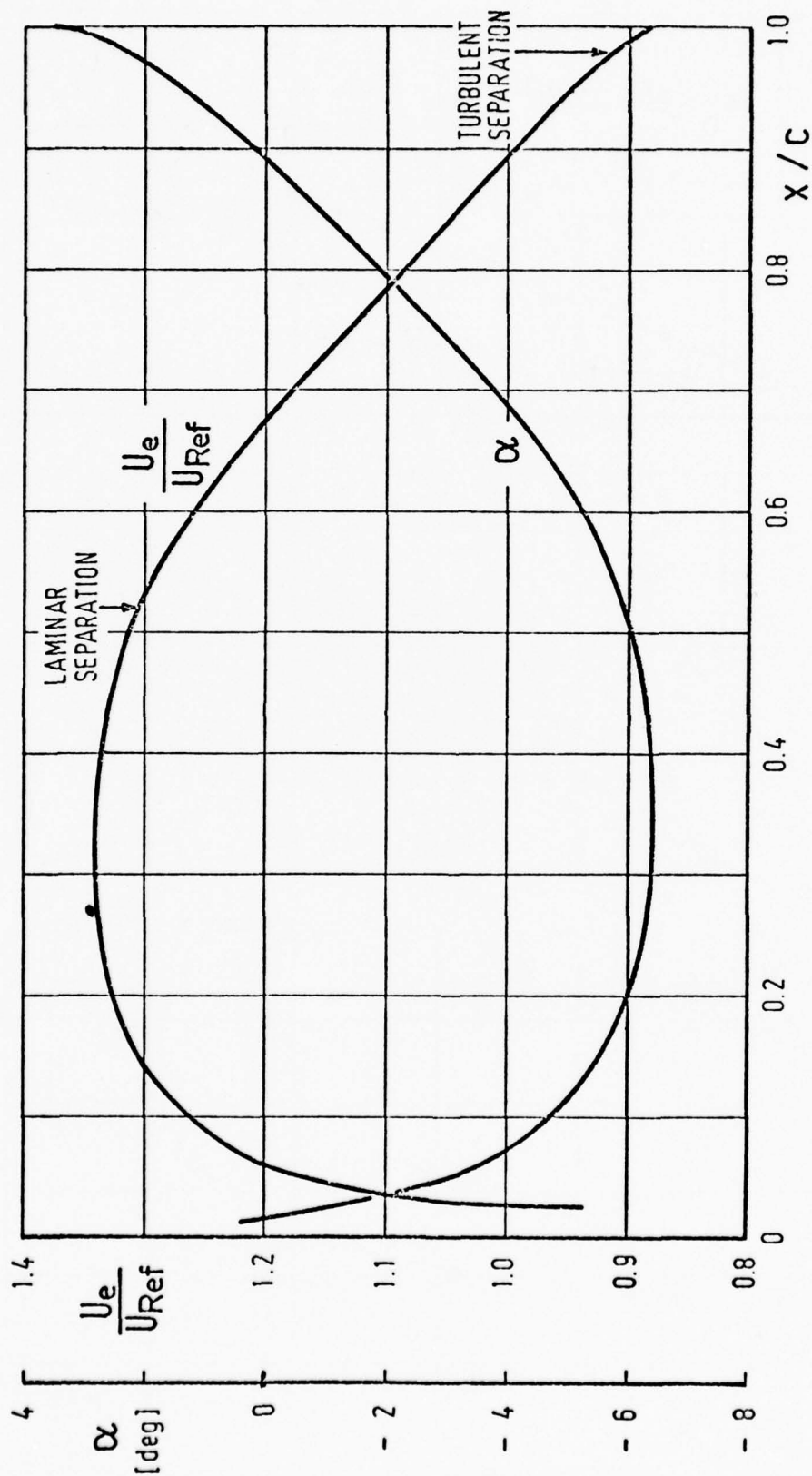


Fig. 10: DISTRIBUTION OF THE RESULTANT VELOCITY U_e/U_{Ref} AND THE ANGLE α VS. CHORD DEPTH FOR AN INFINITE SWEEP WING

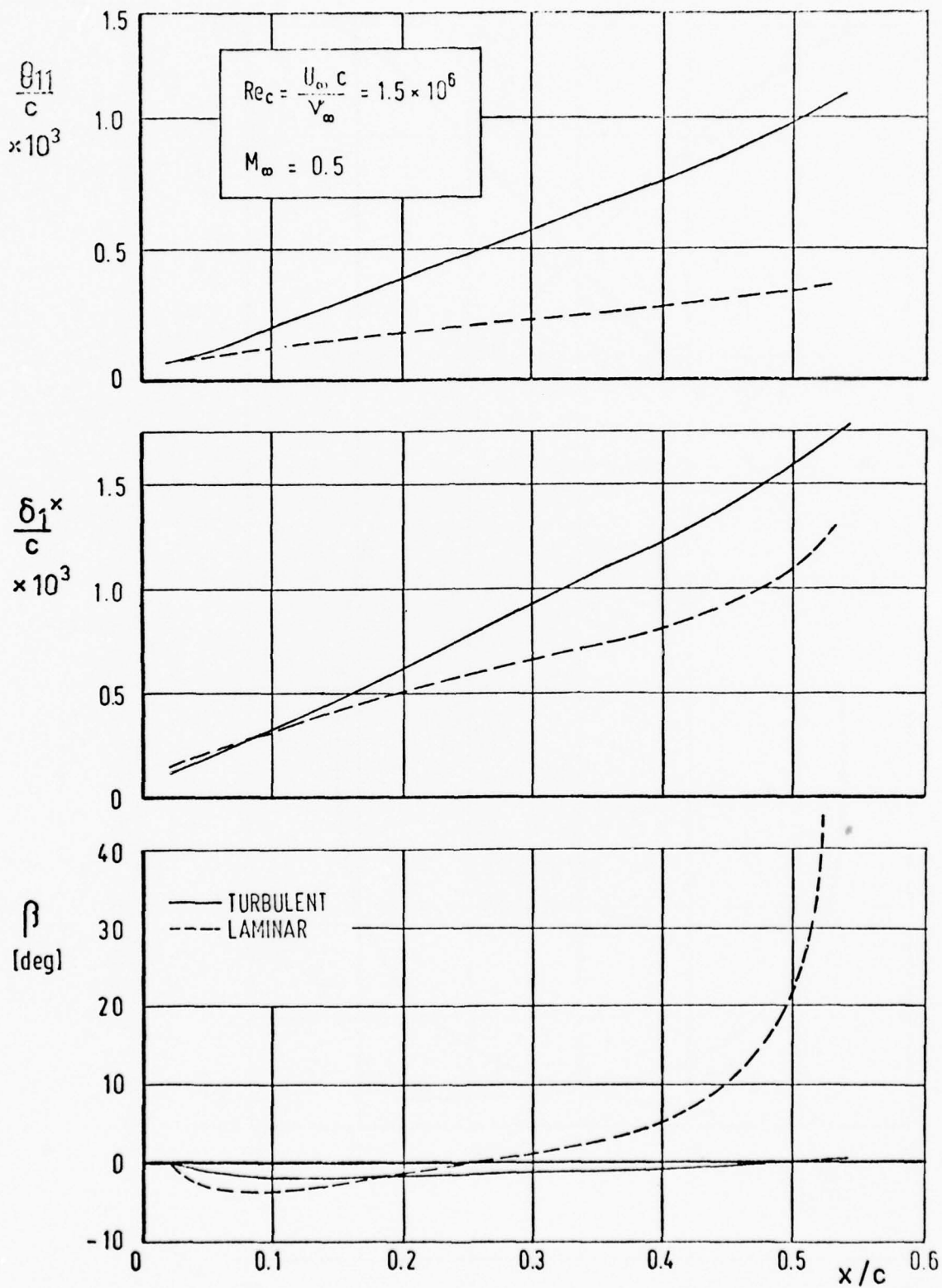


Fig. 11: LAMINAR AND TURBULENT BOUNDARY LAYER DEVELOPMENT ON THE INFINITE SWEEP WING 52

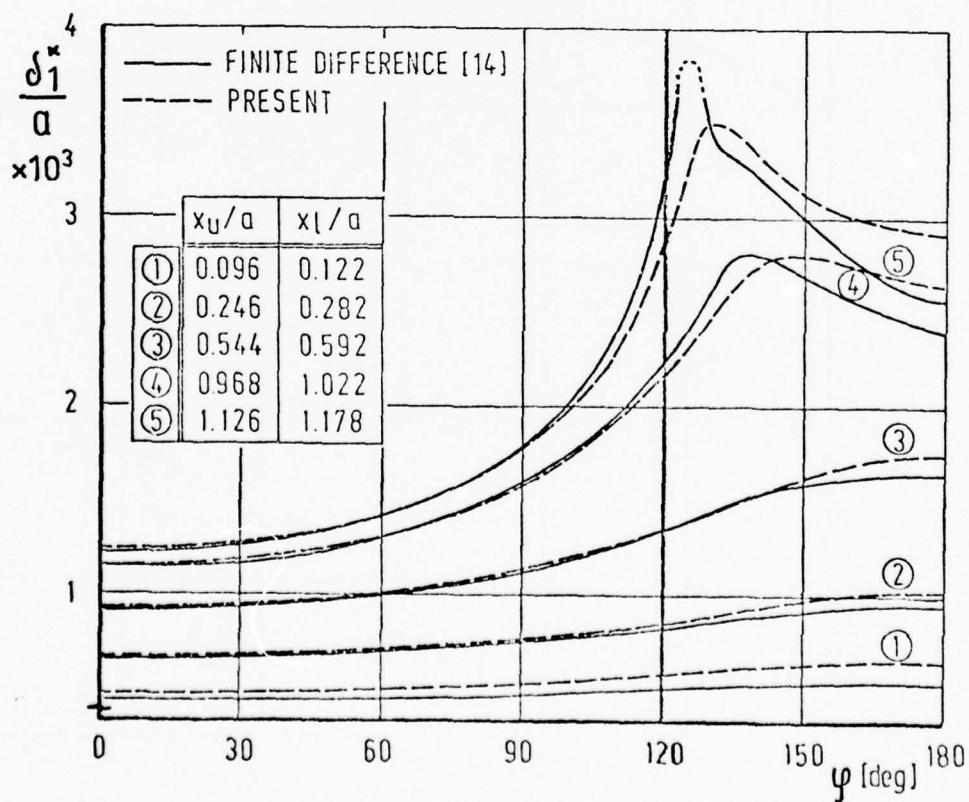
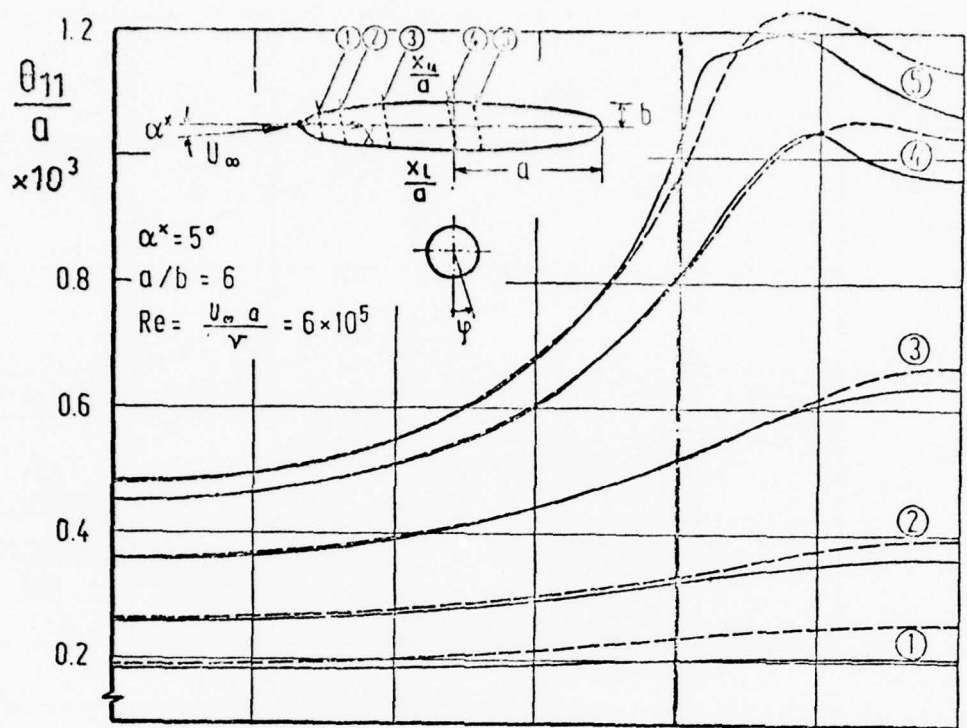


Fig. 12: LAMINAR BOUNDARY LAYER DEVELOPMENT ON AN INCLINED ELLIPSOID

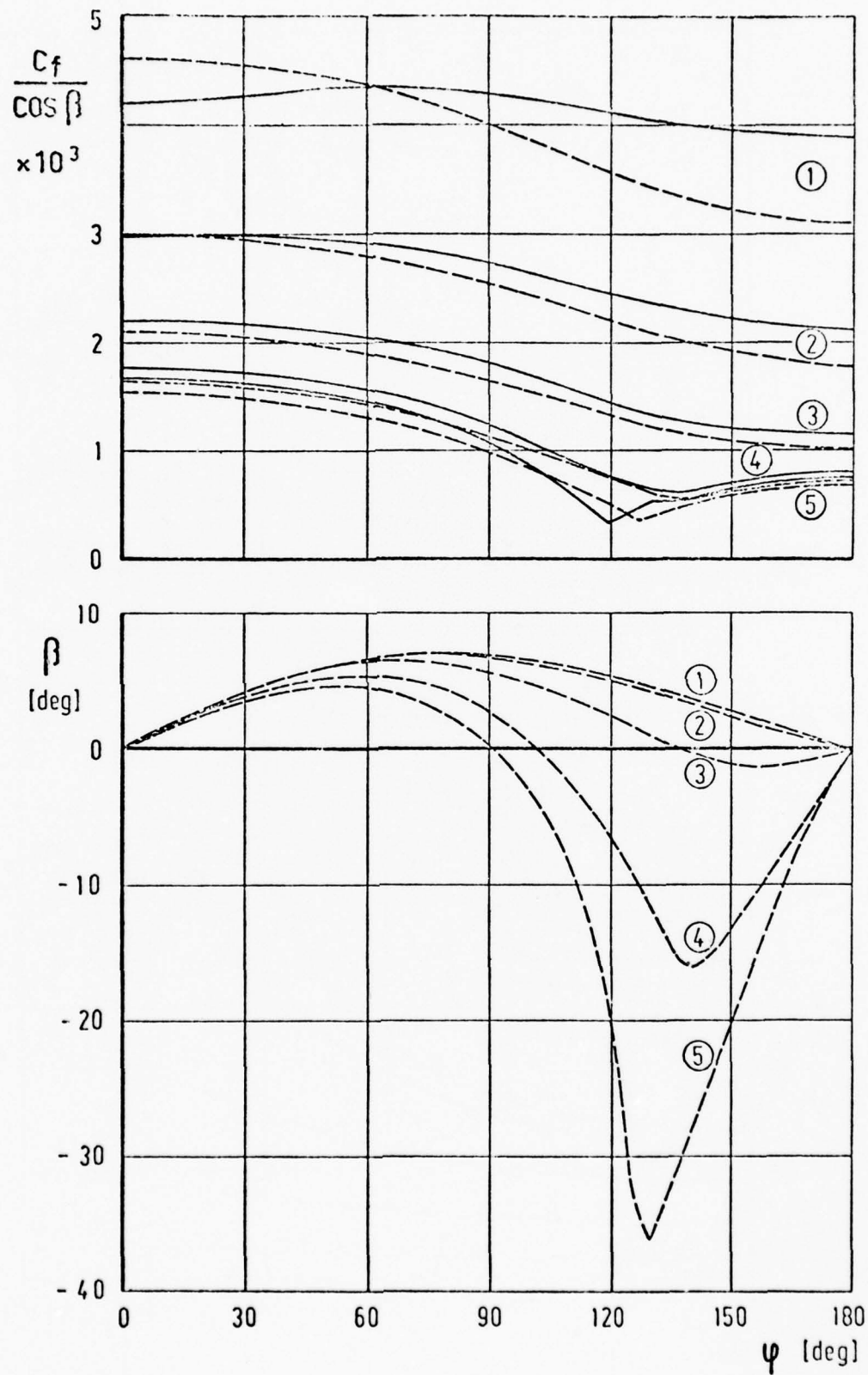


Fig. 12: CONTINUED

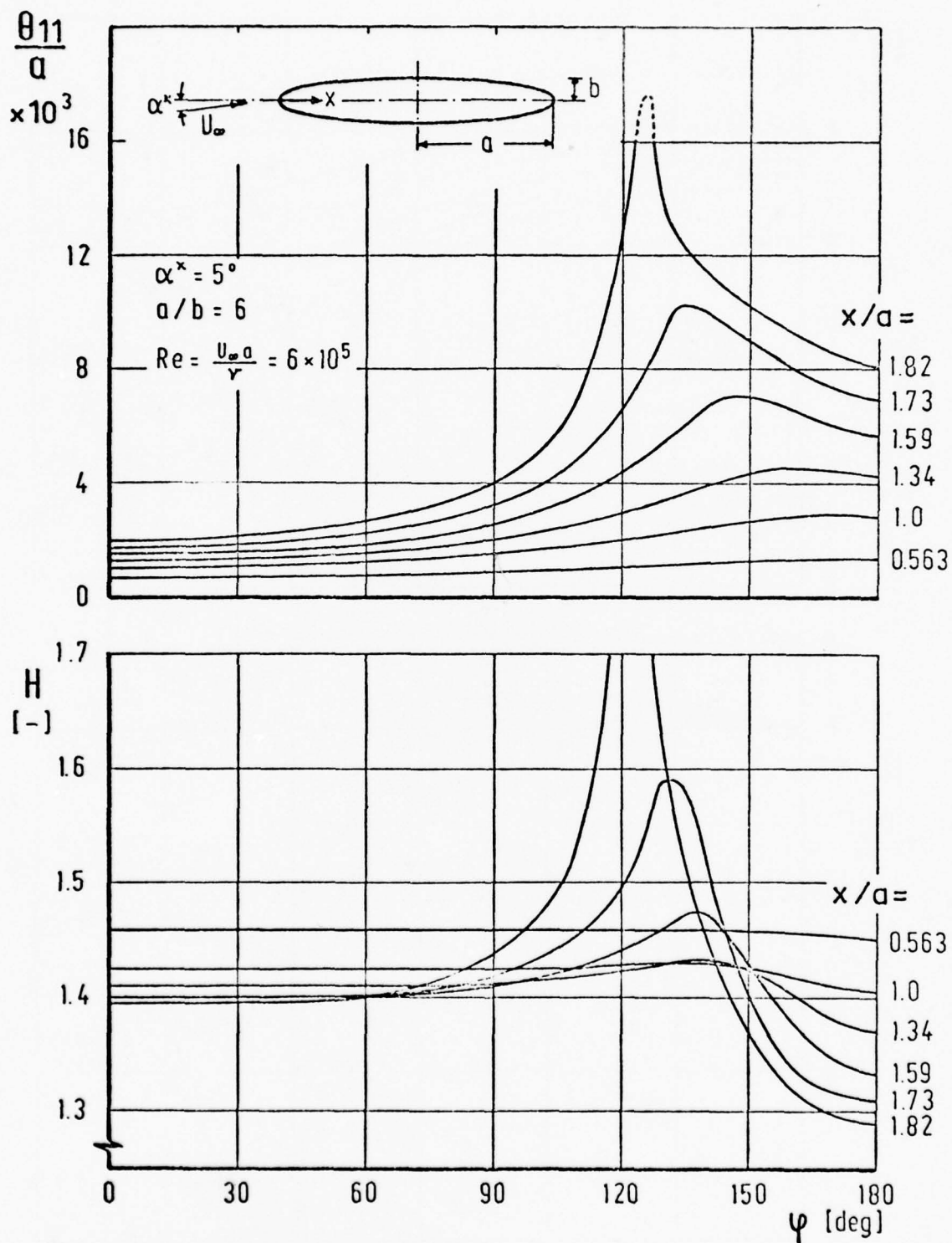


Fig. 13: TURBULENT BOUNDARY LAYER DEVELOPMENT ON AN INCLINED ELLIPSOID

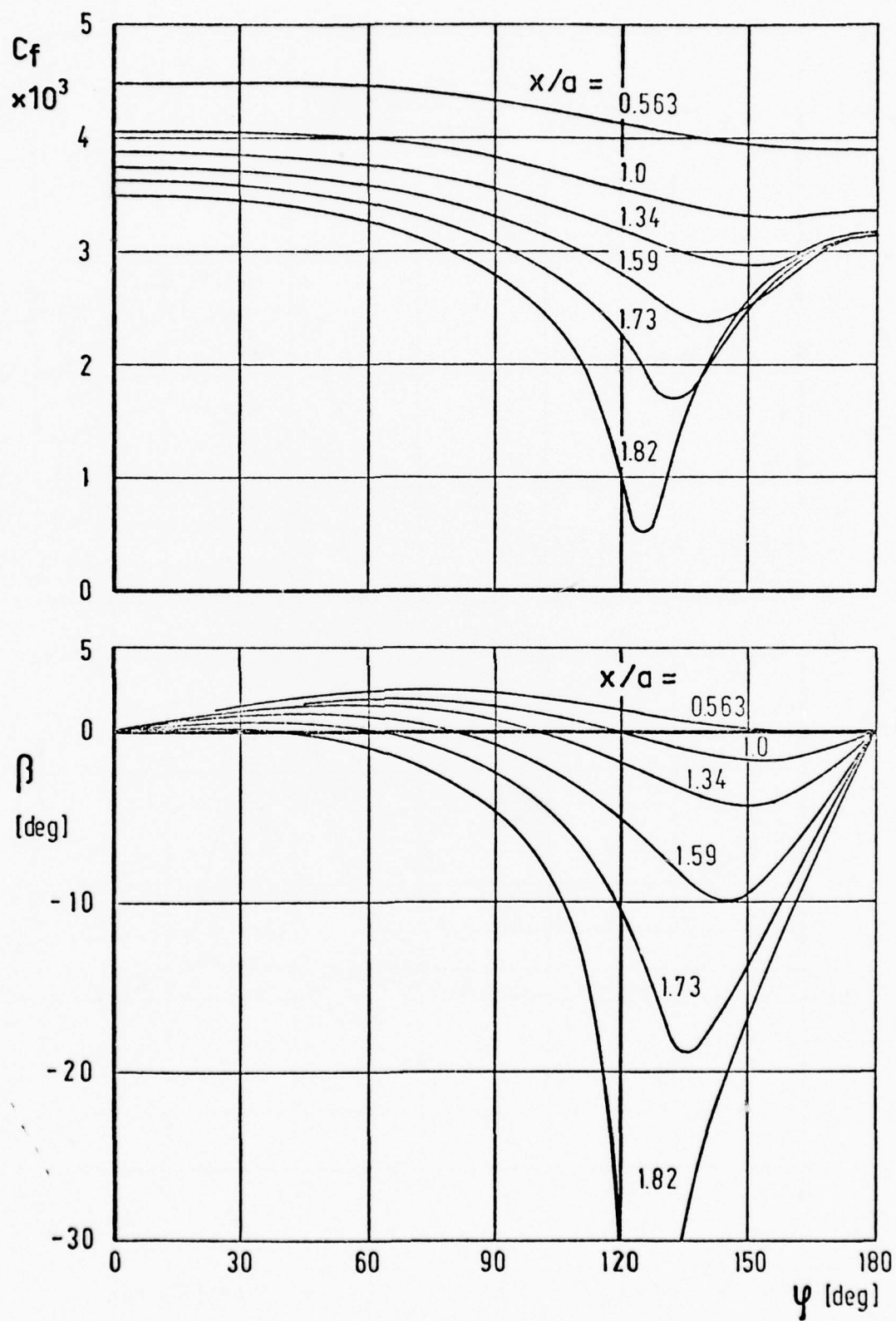


Fig. 13: CONTINUED

STEADY AND UNSTEADY TRANSONIC FLOW

H. L. Seegmiller,* J. G. Marvin,† and L. L. Levy, Jr.*
NASA Ames Research Center, Moffett Field, Calif. 94035

Abstract

The flow over an 18% thick circular arc airfoil at zero degrees angle of attack is studied at two Mach numbers, 0.76 and 0.79, and a single Reynolds number, based on chord, of 11×10^5 . At the higher Mach number, shock-induced separation occurred at the foot of the shock wave and extended downstream beyond the trailing edge. At the lower Mach number, shock-induced separation also occurred but the flow was unsteady and periodic. The mean velocity, turbulent Reynolds stresses, and kinetic energy were measured with a two-component laser velocimeter. In the outer portions of the shear layer the data for the higher Mach number suggest the appropriateness of a scalar eddy viscosity model. Using a computer code that solves the Reynolds averaged form of the compressible Navier-Stokes equations and employs a simple mixing length model for the eddy viscosity, computations are compared with the data and deficiencies are noted. Time-resolved velocity measurements for the unsteady flow were conditionally sampled relative to an initial time triggered by the onset of a periodic pressure variation at the airfoil midchord, and the velocity field for one cycle of oscillation was determined. During the initial portion of the cycle a shock wave forms near the trailing edge, strengthens, and moves toward the airfoil leading edge. The flow downstream of the shock wave separates and appears to reattach downstream on the airfoil near the trailing edge. A similar sequence takes place on the other side of the airfoil, 180° out of phase. Computations using the Navier-Stokes code reproduce the features observed experimentally. The unsteady phenomenon is believed to be initiated by a sudden increase in the extent of separation on one side of the airfoil when the separation at the trailing edge merges with the shock-induced separation. The momentary initial asymmetry in the flow causes the outer inviscid flow to slow and weaken the shock wave, thus collapsing the separation and setting up a persistent cyclic sequence alternating from one surface to the other.

Nomenclature

a_∞	= speed of sound in the free stream, 305 m/sec
a_o	= alphanumeric symbol for a set of constants from Ref. 19
b_o	= alphanumeric symbol for a set of constants from Ref. 19
C	= velocity of seed particle in the plane of two light beams normal to their bisector
\bar{C}	= average velocity of seed particles
C_p	= pressure coefficient
C_p^*	= pressure coefficient evaluated at the local speed of sound
c	= airfoil chord

c_f	= skin-friction coefficient $\tau_w / (1/2) \rho_\infty u_\infty^2$
f	= frequency of unsteady flow oscillation
\bar{f}_D	= doppler frequency
k	= turbulent kinetic energy, $1/2 (\langle u'^2 \rangle + \langle v'^2 \rangle + \langle w'^2 \rangle)$
L	= length scale from Glushko turbulence model
l	= Prandtl mixing length
M	= Mach number
N	= total number of instantaneous velocity measurements
p	= surface pressure
Δp	= incremental pressure from the mean surface pressure
Re_c	= Reynolds number based on free-stream conditions and airfoil chord
t	= time measured from the beginning of the oscillating pressure pulse
T	= fractional time of one cycle of flow oscillation
u	= mean velocity in x direction
V	= total mean velocity
v	= mean velocity in y direction
$\langle u'^2 \rangle$	= time average of the square of the velocity fluctuation in x direction
$\langle v'^2 \rangle$	= time average of the square of the velocity fluctuation in y direction
$\langle w'^2 \rangle$	= time average of the square of the velocity fluctuation in the spanwise direction
$\overline{u'v'}$	= time averaged velocity correlation
x	= distance from the airfoil leading edge in a direction along airfoil centerline
y	= distance from the airfoil centerline in a direction normal to the plane of symmetry
\bar{y}	= distance from the airfoil surface in a direction normal to the centerline
α	= angle of attack
$\bar{\alpha}$	= proportionally constant in Glushko turbulence model
δ	= thickness of the shear layer
ϵ	= eddy diffusivity, m^2/sec
θ	= angle of intersection of laser light beams
$\bar{\theta}$	= angle of total mean velocity vector relative to the x direction
λ	= wavelength of laser light beam
μ	= molecular viscosity
ρ	= mean density
τ_t	= shear stress
σ	= standard deviation from the mean

*Research Scientist.

†Branch Chief, Experimental Fluid Dynamics Branch.

This paper is considered a work of the U.S. Government and therefore in the public domain

Subscripts

- i = ith particle
- 1,2 = directions normal to the fringes set up by the blue and green beams, respectively
- m = mean value
- t = total value
- ∞ = free stream
- w = wall value

Introduction

The governing equations and the qualitative features of transonic flow have been known for some time. Sudden drag rise with increasing Mach number, shock-induced separation, and the occurrence of buffet are examples of phenomena associated with this flow regime. Before this decade, reliable predictive methods depended extensively on experimental data because the complexity of the governing equations made practical solutions impossible, but the advent of large-capacity, fast computers is beginning to change this picture. When viscous effects are small, solutions of the nonlinear inviscid equations are feasible and the results are quite reliable.^{1,2,3} When viscous effects are important and regions of separated flow are large, solutions to the governing equations are also possible, but the results thus far are not reliable enough for predictive purposes. The shortcomings of the latter solutions have been attributed mainly to the lack of an adequate turbulence model.⁴

A focused effort is now under way to develop turbulence models that can improve the reliability of computational techniques for situations where viscous effects are important. Both experiment and computation are being uniquely coupled to coordinate and utilize the most modern developments in experimental and computational fluid mechanics.^{5,6} One test flow being studied for this purpose is the transonic flow over a thick circular arc airfoil. The flow developed over this airfoil changes with increasing Mach number from a steady flow with trailing-edge separation to an unsteady flow with shock-induced separation and finally to a steady flow with shock-induced separation extending beyond the trailing edge. Several studies of this flow have been reported.^{4,7,8} The numerical solutions for this experiment have used the Reynolds averaged form of the compressible Navier-Stokes equations. Notable conclusions from these studies were that existing turbulence models are inadequate for quantitative predictions of flows with large separation and that the features of unsteady flow observed experimentally can also be observed computationally. Heretofore all of the evidence used to substantiate these conclusions was based on comparisons with measurements taken on the surface of the airfoil, so little insight into improving turbulence modeling has been gained and a complete picture of the unsteady flow has been unavailable.

In this paper experimental flow field data from around the airfoil are presented for both the steady and unsteady cases with shock-induced separation. Obtained with a laser velocimeter, the experimental data consist of mean velocity, shear stress, and turbulent kinetic energy profiles in the flow field downstream of the airfoil midchord where the more complicating features of the flow are present. Computations from a computer code that

solves the Navier-Stokes equations for both flow situations are compared with these measurements.

Experimental Arrangement and Test Conditions

The test model used in this investigation was a circular arc airfoil with a thickness to chord ratio of 0.18. It was tested in the Ames High Reynolds Number Channel at a Reynolds number based on chord of 11×10^6 . Above this Reynolds number no significant changes in surface pressure distributions were measured.⁷ The experimental arrangement is shown in Fig. 1. The airfoil with a chord of 20.32 cm spanned the shorter dimension of a rectangular test section with dimensions of 38.1 cm by 25.4 cm. The upper and lower walls were contoured so that the supersonic region of the flow developed over the airfoil would not extend to the walls. Glass windows 14 cm \times 14 cm were installed in the side walls of the test section for the purpose of providing optical access for the high-speed shadowgraph movies and the laser velocimeter tests. A translating wedge used in combination with choking inserts established the desired Mach number. The facility operated in a blowdown mode for run times in excess of a minute.

Results from a previous study⁷ illustrate the three distinct flow regimes determined (Fig. 2). At the test Reynolds number of 11×10^6 and at the lower Mach numbers the flow was steady and trailing-edge separation occurred on the airfoil. For Mach numbers between 0.74 and 0.78 the flow was unsteady but periodic, with shock-induced separation alternating from one side to the other. Above Mach number 0.78 the flow was steady and separation occurred on both sides of the airfoil extending downstream from the foot of the shock wave to beyond the trailing edge. The present test results were obtained at two Mach numbers, 0.76 and 0.79, and the respective flows developed were periodic and steady with shock-induced separation.

Flow Field Measurements

Mean and fluctuating velocity measurements were made with a two-color laser velocimeter. A schematic of the optical arrangement is shown in Fig. 3a. The two-component system employed a 4-W argon laser using a dispersing prism to obtain beams of 488 and 514.5 nm wavelength. The two beams were split, rotated $\pm 45^\circ$ and intersected in the flow field at a location near the midspan of the airfoil. The forward scattered light from particles passing through the volume formed by the intersection of the four beams was optically collected and transmitted to photomultiplier tubes. The probe volume was approximately 0.3 mm in diameter with a length of approximately 3 mm in the spanwise direction. Bragg cells were used to enable the system to detect velocity direction as well as magnitude. Vertical and chordwise movement of the probe volume were accomplished by remotely positioning the optical bench that supported the laser and optics.

A two-channel, synchronized counter system developed at Ames Research Center measured the velocity of particles passing through the probe volume. Pulse stretching, velocity consistency checks on the basis of particles crossing 5 and 8 fringes, and signal-amplitude limiting were employed. A diagram of the system is shown in Fig. 3b.

Two data acquisition modes were used during these tests. For the steady flow case (cf. Mode I, Fig. 3b), doppler frequencies were processed by the counters and passed into a dual channel signal analyzer which retained the data in memory. Subsequent to the completion of data acquisition, a computer with access to this memory was used to statistically determine the mean velocities and their variances. The doppler frequencies processed by the counters for the unsteady flow case (cf. Mode II, Fig. 3b) were conditioned by an interface and recorded with an analog tape recorder to retain real-time information.

The flow was seeded by introducing 0.4-micron-diameter polystyrene particles upstream of the model in the settling chamber of the facility. The lack of naturally occurring particles in the tunnel air supply system made seeding necessary. The size and density of the particles were chosen on the basis of a Stokes flow analysis which showed that particles in the submicron range could follow the flow at the test Reynolds number. For the particular arrangement of these tests a counting rate of a few thousand per second was obtained which was sufficient for this investigation.

The optical arrangement, incident beam wavelength, and the resulting doppler frequency uniquely determine the velocity of a particle passing through the probe volume. The instantaneous flow velocity in the direction normal to the fringes is given by

$$C_i = \frac{\lambda}{2 \sin \frac{\theta}{2}} \bar{f}_D \quad (1)$$

where \bar{f}_D is the relative doppler frequency obtained by subtracting the shifted frequency from the Bragg frequency, $f_b = 40$ MHz. The mean velocity is obtained statistically from

$$\bar{C} = \frac{1}{N} \sum_{i=1}^N C_i \quad (2)$$

The variance is obtained from

$$\sigma^2 = \frac{1}{N-1} \sum_{i=1}^N (C_i - \bar{C})^2 \quad (3)$$

With the two beams rotated $\pm 45^\circ$ the expressions for mean velocity, shear stress and turbulent kinetic energy become⁹

$$u = \frac{\bar{C}_1 + \bar{C}_2}{\sqrt{2}} \quad (4)$$

$$v = \frac{\bar{C}_1 - \bar{C}_2}{\sqrt{2}} \quad (5)$$

$$\overline{u^2 v^2} = \frac{\sigma_1^2 - \sigma_2^2}{2} \quad (6)$$

$$\langle u^2 \rangle + \langle v^2 \rangle = (\sigma_1^2 + \sigma_2^2) \quad (7)$$

Computations and Turbulence Models

The flow field was numerically simulated with a computer program that solves the Reynolds averaged form of the Navier-Stokes equations. The governing equations and solution procedure are

discussed in Ref. 10. The program used an explicit finite-difference method that employs operator splitting and a recently developed rapid solver technique.¹¹ The flow around the complete airfoil was computed and the outer wind-tunnel walls incorporated in the outer boundary conditions.⁸

The Reynolds stresses were related to the mean flow by introducing the concept of a scalar eddy viscosity

$$\tau_t = \rho \epsilon \left(\frac{\partial u}{\partial y} + \frac{\partial v}{\partial x} \right) \quad (8)$$

Over the surface of the airfoil ahead of the location of separation a two-layer mixing length model was used. The length scales were related to the eddy viscosity by

$$\epsilon = \ell^2 \left[\left(\frac{\partial u}{\partial y} \right)^2 + \left(\frac{\partial v}{\partial x} \right)^2 \right]^{1/2} \quad (9)$$

In the inner layer,

$$\ell = 0.41 y \left[1 - \exp\left(-\frac{y}{A}\right) \right] \quad (10)$$

with

$$A = 26 \frac{\mu_w}{\rho_w} \left(\frac{\rho_w}{\tau_w} \right)^{1/2}$$

In the outer layer, an Escudier formulation was used

$$\ell = 0.09 \delta \quad (11)$$

The outer length scale was used once the value from the equation for the inner scale exceeded the value from the outer layer equation. From the beginning of separation and downstream to a location of reattachment, either on the airfoil or where the near-wake closed, the length scale in the free-shear layer above the dividing streamline was frozen at a value of 1.7 times the immediate upstream attached flow outer-length-scale value from Eq. (11). Freezing the length scale was thought to provide better agreement with data in separated regions.⁴ Below the dividing streamline the eddy viscosity varied linearly from its value on the dividing streamline to zero at the airfoil surface; it was held constant at the dividing streamline value between the trailing edge and the point where the near-wake closed.⁴ In the far-wake the Escudier length scale from Eq. (11) was used with the shear layer thickness evaluated as the distance from the wake centerline to the outer edge of the shear layer.

Results and Discussion

Steady Flow With Shock-Induced Separation

Experimental observations. - A shadowgraph of the flow field taken through the test section windows during a test at $M_\infty = 0.79$ and $Re_c = 11 \times 10^6$ is shown in Fig. 4. At these test conditions shock-induced separation occurs near the foot of the shock wave and extends downstream beyond the trailing edge. A highly turbulent flow exists downstream of the shock wave and Mach waves appear to emanate from the interface between the turbulent shear layer and the outer flow. Superimposed on the shadowgraph are mean axial velocity profile data obtained with the laser velocimeter. The extent of the shear layer and the region of reversed flow are easily discernible.

The mean streamwise velocity, turbulent shear stress and turbulent kinetic energy for the viscous region of the flow downstream of the separation point are shown in Fig. 5. The airfoil surface has been sketched in the figure and the solid symbols indicate the respective wall values. The wall shear values were published previously.¹² Lines are sketched in the lower half of Fig. 5 through a locus of points representing the locations of the zero velocity point, the dividing streamline, and the shear-layer edge. In the upper half of the figure are lines representing the dividing streamline and the location of the maximum velocity gradient in the normal direction. The slopes of the shear profiles at the wall, obtained by evaluating the normal-momentum equation, are shown in Fig. 5 for a more complete picture of the profiles and for assistance in assessing the accuracy and interpretation of the near-wall data. The shear stress data at $x/c = 0.8$ below the location of their maximum are anomalous in that they change sign. Possibly they are in error, however, a post-run examination of the data revealed no obvious sources of error so they have been included.

An examination of the profile shapes in Fig. 5 reveals that the maximum values of the shear stress and turbulent kinetic energy are located somewhat above the dividing streamline and generally coincide with the location of the maximum normal velocity gradient. The magnitude of the maximum velocity gradient decreases with distance from the separation point whereas the magnitude of the maximum shear stress increases (Fig. 6).

The profile shapes and their behavior in the streamwise direction compare with similar data taken downstream of separation in a transonic flow over a bump on a wind-tunnel wall¹³ as well as downstream of rearward facing steps ahead of reattachment.^{14,15,16} Bradshaw¹⁷ classified the latter flows, in which the step height was larger than the upstream boundary-layer thickness, as flows undergoing an overwhelming perturbation. He postulated that the subsequent development of the free-shear-layer in such cases was not influenced significantly by its initial conditions such as upstream boundary-layer thickness or shape parameter, and that production of turbulence continued in proportion to the growth of the large-scale structure until reattachment occurred. The present shock-separated flow appears to behave similarly; the extent of the shock-induced separation and the airfoil surface pressures were unaffected by changes in test Reynolds number between 7×10^6 and 17×10^6 (Ref. 7). The shock-wave induced separation produced significant large-scale turbulence, and production continued beyond the trailing edge into the near wake until its eventual dissipation in the far wake. The recirculation region was supplied continually by the higher turbulent portion of the shear layer. Because of the limited streamwise extent of the test section windows, it was impossible to optically identify the entire near-wake region. An oil-flow photograph (Fig. 7) indicates the approximate size and location of the near-wake region.* The pattern of oil streaks was allowed to develop on a thin splitter plate located near the midspan of the airfoil in a plane normal to the spanline. In the near-wake region the oil streaks

begin to flow in the downstream direction indicating closure at $x/c \approx 1.3$. The necking down of the zero velocity and the dividing streamlines in the near wake at $x/c = 1.05$ observed in the velocity profile data is also apparent from a close examination of a number of such photographs.

The values of surface pressure and skin friction have been reported previously.^{7,12} They are shown in Fig. 8 for completeness and because they are needed to assess the computations discussed subsequently. The data show a small pressure recovery aft of the shock-induced separation point. The magnitude of the pressure coefficient downstream of separation is slightly lower than C_p^* and the flow may be slightly supersonic. This interpretation is consistent with the shadowgraph observation (Fig. 4) which revealed an oblique shock near the separation point. Additionally, the Mach number at the edge of the shear layer, evaluated by solving the energy equation using the measured velocities, shock angle, and total temperature, was found to be slightly supersonic.

The data from Fig. 5 can be used to guide turbulence model development for use in computer codes that attempt to numerically simulate complicated viscous flows. Thus far simulations using the Reynolds averaged Navier-Stokes equations have utilized a scalar eddy viscosity concept. In these applications the eddy viscosity is formed from a product of a modeled length scale and velocity. Models under development for shock-induced separated flows range from algebraic two-layer models which depend solely on the mean flow^{4,5,8} to one- and two-equation models that use the turbulent kinetic energy equation to obtain the velocity in the eddy viscosity formulation with either a prescribed length scale based on the mean flow¹⁸ or a differential equation for a length scale or dissipation rate.¹⁹ The eddy diffusivity and length scales that can be deduced from the present data are introduced next.

The shear stress and velocity profile data were used to evaluate the eddy diffusivity, and the results are shown in Fig. 9 as a function of the position within the shear layer. Since derivatives of the velocity are needed to evaluate the eddy diffusivity, no values are shown for the first measuring station away from the surface where the derivative was undetermined. Likewise no values are shown at the edge of the shear layer where accurate derivative evaluation was not possible. A general observation is that the eddy viscosity tends to increase with distance downstream from the separation point and its maximum value tends to diffuse outward through the shear layer, particularly beyond the trailing edge. At streamwise locations where the maximum value is readily distinguished it occurs at the point when the normal velocity gradient is maximum.

The algebraic mixing length deduced from the data was obtained using Eq. (9) without $(\partial v / \partial x)$ (Fig. 10a). The open symbols correspond to chordwise locations above the surface of the airfoil and the filled symbols to those downstream of the trailing edge. The length scale over the airfoil tends to correlate when normalized by the shear-layer thickness. The magnitude over the major portion of the shear layer is lower than the Escudier value normally employed for attached boundary-layer flows. Beyond the trailing edge the normalized

*This photograph, supplied by John McDevitt from Ames Research Center, was taken during a separate series of tests.

length scale tends to increase and is in closer agreement with the Escudier value. Although every attempt was made to obtain data as close to the airfoil surface as possible, the paucity of data makes it difficult to interpret the behavior of the length scale in the near-wall region.

Some improvement in modeling for a class of shock boundary-layer interaction flows was obtained by employing a modified Glushko model¹⁸ which uses the turbulent kinetic energy and an algebraic length scale based on the mean flow to formulate the eddy viscosity, i.e., $L = \epsilon \sqrt{k}$.¹⁹ (To form the total kinetic energy from the measurements of $\langle u'^2 \rangle + \langle v'^2 \rangle$ the relationship $\langle u'^2 \rangle : \langle w'^2 \rangle : \langle v'^2 \rangle = 4:3:2$ was assumed.) This length scale (Fig. 10b) correlates with boundary-layer thickness over the airfoil and is smaller than the algebraic scale employed by Glushko for boundary layers (the line labeled *ao*). The line labeled *bo* represents the modified length scale employed¹⁹ to achieve thicker separated bubbles in other shock boundary-layer interaction flows and it agrees more closely with the present data. Downstream of the trailing edge this length scale also increases.

The two length scales shown in Figs. 10a and 10b have similar trends and appear to be related by a constant. Using the definition of eddy viscosity and the length scale defining equations, the relationship between the two length scales is established as follows

$$\frac{k^2}{L^2} = \alpha^2 \frac{k}{u'v'} \quad (12)$$

The length scales would be related by a constant provided the ratio of shear to kinetic energy was constant, a hypothesis employed by Bradshaw. Indeed, the ratio evaluated from the present data is nearly constant. In the middle portions of the shear layer the constant is near 0.3 in agreement with Bradshaw's hypothesis.

The appropriateness of a scalar eddy viscosity concept cannot be established from the present data. However, in light of the similarities in the present data above the zero velocity line to those observed in free-shear layers successfully modeled through such an approach, the concept seems credible. The maximum shear occurs at the location of the maximum normal velocity gradient. A length scale model for the eddy viscosity may even be appropriate, but some means would have to be established for varying it to account for the sudden growth in the near wake.

Comparison with computations. - A comparison of numerical computations and surface pressure and skin friction is given in Fig. 8. The governing equations and the model of turbulence were discussed previously in the section on computation and turbulence models. Ahead of the shock-wave location the surface pressures are predicted well, but the pressure recovery is too large over the rear portion of the airfoil where separation occurs. The skin friction prediction shows reasonable agreement with the experiment, except near the location of separation and in the variation through the separated region. The code fails to give the appropriate pressure in the separated region because the predicted shock wave is nearly normal whereas in the experiment it is oblique in the region near the wall where separation is occurring. Whether this result is due to

failure of the turbulence model or to failure of the code to predict a weak shock-wave solution in the inviscid regions of the flow cannot be answered readily because of the complex interaction between the viscous and inviscid regions of the flow. However, it is possible to assess the appropriateness of the turbulence model in light of the experimental data introduced previously.

A comparison of the computation with the velocity and eddy diffusivity deduced from the experiment at two chordwise locations on the airfoil is presented in Fig. 11. (Comparisons at other locations show similar results.) The predicted separation height is smaller than that determined experimentally. The maximum eddy diffusivities compare, but their relative position in the boundary layer differ because the shear layer is too thin. The main deficiency of the computation is that it predicts a separation region too thin and an outer shear flow that thickens too slowly compared to experiment. In the outer shear flow, above the dividing streamline the computed shear layer does not grow rapidly enough because the model length scale over the separated region was frozen whereas the experiment suggests it should grow in proportion to the growth of the shear layer thickness. In fact, the length scale in the computation, normalized by the computed shear-layer thickness, varies from 0.12 to 0.02 between $x/c = 0.80$ and 1.0. For this portion of the airfoil the experimental value of the normalized length scale was around 0.06. In the inner layer below the dividing streamline, a comparison of the eddy diffusivities from the computer solutions and those deduced from the profile data at all stations suggests that the linear eddy viscosity relation used in the computations results in a larger eddy viscosity than was inferred from the data.

Modifications to the turbulence model to correct some of the deficiencies are proceeding. Changes are under way in the outer length scale and the inner layer model within the separated region that reflect trends in the values deduced from the experiment. However, the results thus far are not encouraging; for example, reducing the eddy viscosity in the inner region increases the height of the separation bubble somewhat. However, the extent of the growth appears limited because the thickening of the shear layer results in a higher eddy viscosity above the dividing streamline since the outer length is scaled to the shear-layer thickness. Similar results were found when the 1-equation Glushko model, suitably modified to reflect the experimental trends, was tried. It seems likely that any model employing a prescribed length scale which depends on a shear-layer thickness would behave similarly, so emphasis toward higher-order models that use a differential equation to generate the length scale seems warranted.

Considering the complexity of the flow under study, the predicted results, while deficient in some aspects, do reproduce many of the correct features of the flow and hence the numerical simulations are encouraging.

Unsteady Flow With Shock-Induced Separation

Experimental observations. - The flow over the airfoil at zero incidence was found to be unsteady for a narrow range of Mach numbers. This observation was first reported in Ref. 7 and introduced

previously in Fig. 2. A portion of the experimental surface pressure time histories taken during a Mach number sweep through the unsteady flow region for two positions on the airfoil are shown in Fig. 12. These pressures, expressed as an incremental difference from the mean, are shown as a function of a dimensionless time required for the flow to travel from the leading to the trailing edge, $t u_\infty/c$. Examination of these data show that the unsteady pressures are periodic and that the pressures on the upper and lower surface are 180° out of phase. The pressure histories, although periodic, differ with position on the surface, but the frequency of oscillation was found to be independent of position and its value was 190 Hz. The calculations shown on the figure will be discussed later.

A high-speed shadowgraph movie of the flow field was taken during a test at $M_\infty = 0.76$. A pulse triggered from the initial rise in the output of the periodic pressure signal on the airfoil at $x/c = 0.5$ was recorded on the film and used to synchronize these photographs with the pressure signal. Film speeds as high as 10,000 frames/sec were used. At the time of the initial rise in the pressure, the remnants of a shock wave passing upstream near the midchord of the airfoil were visible. Photographs taken from subsequent frames of the film are shown in Fig. 13a. A series of weak shock waves form near the trailing edge where they build in strength and coalesce into a single wave that moves toward the midchord. As the shock approaches the midchord it weakens appreciably and the cycle repeats itself periodically. A similar situation occurs on the lower surface 180° out of phase. Interesting and significant features of the flow observed in the movie sequence are the formation and strengthening of the shock wave and the subsequent thickening and probable separation of the boundary layer downstream of the shock wave. A vortex is seen to form near the trailing edge and sheds alternately upward and downward, depending on the direction of the asymmetry of the periodic flow. The remaining portions of the figure will be discussed subsequently.

The laser velocimeter was used to determine the velocity field around the airfoil during a cycle of the flow oscillation. Instantaneous u and v velocities were recorded on an analog tape recorder along with the signal from a pressure transducer located at midchord. The data were digitized and the velocities conditionally sampled relative to an initial time triggered by the onset of the steep rise in each successive pressure signal. Sampling in this way allowed data taken over many cycles to be used to reconstruct the velocities over a single cycle. An example of the conditionally sampled data for a single point in the flow field is shown in Fig. 14. The magnitude of the total velocities is shown as a function of the dimensionless fraction of time, T , for one cycle of oscillation. Over two thousand synchronous data samples were used to construct this plot and a mean value is easily discernible. The velocity increases with time and shows a marked decrease as the shock wave passes upstream. The limited sampling rate during a single flow oscillation precluded the possibility of acquiring turbulence measurements.

Velocity data at 125 points in the flow field were acquired in the manner described above. In seeking ways to keep data management tolerable, histograms of the velocity components for dimensionless

time intervals of 0.05 were examined. In general, the results showed narrowly peaked histograms for times when the measuring point was in the inviscid portion of the flow and broader histograms when the measuring point was in the shear layer. Skewed distributions were sometimes observed in regions where the velocity was near zero or reversed. Also, the total number of velocity acquisitions in any interval depended on the magnitude of the velocity; this is understandable since seed-particle concentration depends on the instantaneous mass flow. The choice was made to represent the velocities with the mean value of the velocity histogram over the discrete dimensionless time interval of 0.05. The mean and the mode values nearly coincided at most of the measuring locations.

The time history of the average individual velocity components of the data shown in Fig. 14 are given in Fig. 15 to illustrate two points. First, the data can be used to determine the direction of the flow, $\bar{\theta} = \tan^{-1} v/u$. A cursory examination of the vertical velocity component shows that for $T < 0.4$ the flow is in a direction almost parallel to the airfoil surface. As the shock passes ($T > 0.45$) $\bar{\theta}$ approaches zero and goes slightly positive; the resultant flow angle is nearly parallel to the airfoil chord and subsequently returns to its initial value. Second, the correspondence between the solid and open symbols shows that the particles are able to adjust rapidly to the instantaneous change in velocity across the shock wave. The solid symbols represent velocities calculated from simple shock theory using the measured velocities ahead of the shock wave and the shock wave angles measured from the shadowgraphs. The slight departure from the u velocity data with distance downstream of the shock wave is associated with the compression process occurring between the shock wave and measuring point as the shock moves upstream (rather than with particle lag).

The velocity field over the airfoil obtained with the laser velocimeter is shown in Fig. 13b. Data are shown during one cycle of oscillation that corresponds as closely as possible to the times for the shadowgraphs. (Space limitations preclude showing data at more time intervals, but a movie showing data for twenty equally spaced intervals was made to aid data interpretation.) The lines representing the velocity vectors are in arbitrary units. The origins of the vectors can be determined by inspection of the data for the first time interval, where all the flow is in the downstream direction. The small group of vectors near the trailing edge at $x/c = 1.007$ overlap those at $x/c = 1.0$ further away from the surface. At $T = 0.15$ the velocities near the surface show evidence of disturbances between $x/c = 0.85$ and 0.95 associated with the formation of weak shock waves which are discernible in Fig. 13a. At $T = 0.4$ the shock wave foot has moved forward of $x/c = 0.8$. The velocity vectors in the outer portion of the flow downstream of this location change direction as expected. Near the surface the velocity data show the formation of a separated region downstream of the shock that appears to reattach near the trailing edge. The velocity direction at the trailing edge is controlled by the vortex seen in the companion shadowgraph. These same features are more apparent at $T = 0.6$. The shock wave is obliquely aligned across $x/c = 0.6$ and 0.7 . Reversed velocity is observed at $x/c = 0.8$ and extends downstream possibly as far as $x/c = 0.95$. Reattachment occurs near the trailing

edge. At the last selected time the shock wave has weakened considerably and a small separation region can be inferred between $x/c = 0.7$ and 0.85 . A circulation toward the lower surface is observed downstream of the trailing edge at $x/c = 1.05$.

Examination of the velocity field data and the shadowgraphs for all twenty time intervals reveals a rather complete picture of the flow field. As the shock wave begins to form near the rear of the airfoil, it strengthens and moves upstream. Separation occurs at the foot of the shock with subsequent reattachment on the airfoil surface. Downstream at the trailing edge a small vortex is formed and circulation from the airfoil surface with attached flow to the surface with shock separated flow occurs.

Comparisons with computations. - Computations using the Navier-Stokes code and the turbulence model discussed earlier have been made in each of the flow domains shown in Fig. 2. As noted in Ref. 8, these computations reproduced flow features observed experimentally. The basis for comparison in that reference was limited to surface pressure data, unsteady cyclic frequency evaluation, and qualitative comparisons with shadowgraphs. A more thorough evaluation for the unsteady case is made herein.

A comparison with the experimental surface pressure time histories is shown in Fig. 12. The wave forms of the fluctuating pressures, obtained by computing four cycles of oscillation, compare rather well with the experimental forms. The oscillations on the upper and lower surfaces are 180° out of phase as observed experimentally. However the normalized frequency of oscillation (f_c/u_∞) is about 20% lower. On the upper surface at the mid-chord the magnitudes of the peak fluctuations on either side of the mean compare favorably with the experiment. At $x/c = 0.775$ the magnitude of the negative peak fluctuations compare, but the positive magnitudes are about twice that of the experiment. This is consistent with the fact that the computation tends to overpredict the pressure recovery downstream of the shock. Another observation is that there is an asymmetry in the predicted magnitudes of the positive and negative peak fluctuations on the upper and lower surface, believed to be caused by a computer code asymmetry.

Computed velocity fields for selected fractions of the time within a cycle of oscillation are shown in Fig. 13c. These times differ from those chosen for the experiment for reasons that will become apparent later. The spatial resolution of the computations reveals a more detailed picture of the velocity field than the experimental data. As time increases, a shock begins to form on the upper surface as evidenced by the change in magnitude of the vectors and also their direction. The shock continues to move forward and separation occurs with reattachment near the trailing edge. Subsequently, the shock continues forward and large-scale vortical flow or shedding appears just beyond the trailing edge. The shear-layer thickness is predicted to be smaller than that observed experimentally, but the difference is not as large as noted in the steady flow case.

The predicted shock formation and its subsequent movement toward the leading edge took a longer portion of the cycle time than in the experiment. Therefore the comparisons of the velocity fields in

Fig. 13 were made at somewhat different times so that similar flow features could be compared. The flow angle histories at several chordwise stations at $y/c = 0.1$ are compared in Fig. 16 to illustrate this difference. In each example the initial increase in angle can be associated with the shock-wave movement across the measuring point. In each example, the time of shock arrival is longer for the computation, but the resulting change in flow angle is more abrupt. An examination of the velocity fields on the basis of shifted time shows that the computation and experiment have essentially the same features.

The computation was studied in an attempt to explain the onset and maintenance of the unsteady flow. Sequential development of the flow field showed that the process that possibly initiated the unsteady flow depended on two conditions. The first was a slight asymmetry in the location of the separation points on the upper and lower surface caused by a code asymmetry; free-stream flow angle or model construction asymmetry may have introduced similar differences experimentally. The second was rapid development of a single separation zone on one side of the airfoil where the separated region behind the shock and the separated region at the trailing edge joined. The resulting asymmetry in the wake tends to extract mass from the trailing-edge separated region on the other side of the airfoil, momentarily preventing the development of a single separation on that side. Meanwhile the outer inviscid flow adjusts to the displacement effects as if the airfoil had been given camber, and the flow slows with a subsequent weakening of the shock wave until the separation collapses. Thus the sequence of oscillation is set; the flow on the opposite side speeds up and the stronger shock separates the flow causing the process to continue.

If this physical description is correct, the period of oscillation would then depend on the time it takes for the entire flow to adjust to the displacement effects caused by the thickening shear layers. Two important findings support this. First, the experimental reduced frequency, $\bar{f} = \pi f c / u_\infty$, compares with that observed by Finke²⁰ in another investigation using circular arc airfoils of different chord dimensions, where the Reynolds number was much lower. The second is that the reduced frequency determined from the present computation compared exactly with a different computation using the same code but with the airfoil chord dimension cut in half. These findings may also explain why a simple turbulence model, capable of reproducing the qualitative features of separation, can reproduce this unsteady flow.

Conclusions

A study of the transonic flow over a circular arc airfoil was undertaken to provide guidance for turbulence modeling of shock-induced separated flows and to verify numerical computer codes that are being developed to simulate such flows. Depending on the free-stream Mach number, the flow field developed was either steady with shock-wave-induced separation extending from the foot of the shock wave to beyond the trailing edge or unsteady with a periodic motion also undergoing shock-induced separation. Mean velocity and turbulence measurements for the steady flow case were successfully made with a laser velocimeter. Mean-flow velocities with the same instrument were also obtained in the

unsteady, periodic flow by conditionally sampling data relative to an initial time triggered by a pressure signal measured at the airfoil midchord. Comparisons with numerical simulations using a computer code that solved the time-dependent Reynolds' averaged compressible Navier-Stokes equations were made for both flow conditions.

For the steady flow case, a thick shear layer formed downstream of the shock-induced separation point. Within the shear layer the maximum turbulent kinetic energy and shear stress occurred at a location corresponding to that where the maximum normal velocity gradient occurred thus supporting the appropriateness of a scalar eddy viscosity concept in the outer portions of the shear layer. Comparing the measurements with computations employing a mixing length model to describe the eddy viscosity showed that the shear-layer thickness was underpredicted and that the resulting influence on the outer flow gave a rather poor prediction of the actual pressure recovery on the airfoil. Changes in the model guided by the experimental data are now being implemented in the computer code.

In the unsteady flow case a shock wave formed on one surface back near the trailing edge. As its strength increased, the flow separated just behind the shock wave and reattached on the airfoil. On the opposite surface a similar sequence took place, but 180° out of phase. Computations of the flow predicted most of the essential features observed experimentally, but the reduced frequency was lower by about 20%. The details of the computation were used to explain a possible sequence of events leading to the unsteady motion.

Work continues to improve the turbulence model used in the numerical simulations of transonic flows with shock-induced separation. Once this improvement is in hand, adequate predictions of both steady and unsteady transonic flow should be available for cases where viscous effects are important.

Acknowledgments

The authors acknowledge the untiring work of Mrs. Eva Pegot of Ames Research Center, who contributed substantially to the data reduction of the unsteady velocity measurements and to the techniques used to display both the experimental and computational results. Further acknowledgment is given to the group at Ames who developed the laser doppler instrumentation employed in this study: Dean Harrison, George Grant, Gill Kojima, and Roger Hedlund.

References

- ¹Murman, E. M. and Cole, J. D., "Calculation of Plane Steady Transonic Flows," *AIAA Journal*, Vol. 9, 1971, pp. 114-121.
- ²Bauer, F., Garabedian, P. R. and Korn, D., "A Theory of Supercritical Wing Sections, With Computer Programs and Examples," *Lecture Notes in Economics and Mathematical Systems*, Vol. 66, Springer-Verlag, C. 1972.
- ³Bailey, F. R. and Ballhaus, W. F., "Comparisons of Computed and Experimental Pressures for Transonic Flows About Isolated Wings and Wing-Fuselage Configurations," NASA SP-347, Vol. II, 1975, pp. 1213-1232.
- ⁴Deiwert, G. S., "Computation of Separated Transonic Turbulent Flows," *AIAA Journal*, Vol. 4, No. 6, June 1976, pp. 735-740.

- ⁵Marvin, J. G., "Experiments Planned Specifically for Developing Turbulence Models in Computations of Flow Fields Around Aerodynamic Shapes," Paper No. 14, AGARD Conference Proceedings No. 210 on Numerical Methods and Wind Tunnel Testing, Von Karman Institute for Fluid Dynamics, Rhode-St-Genese, Belgium, June 23-24, 1976.

- ⁶Marvin, J. G., "Turbulence Modeling for Compressible Flows," NASA TM X-73,188, Jan. 1977.

- ⁷McDevitt, J. B., Levy, L. L., Jr., and Deiwert, G. S., "Transonic Flow About a Thick Circular Arc Airfoil," *AIAA Journal*, Vol. 14, No. 5, May 1976, pp. 606-613.

- ⁸Levy, L. L., Jr., "An Experimental and Computational Investigation of the Steady and Unsteady Transonic Flow Field About an Airfoil in a Solid-Wall Test Channel," *AIAA Paper 77-678*, AIAA 10th Fluid & Plasmadynamics Conference, Albuquerque, New Mexico, June 27-29, 1977.

- ⁹Yanta, W. J., "Turbulence Measurements With a Laser Doppler Velocimeter," PhD Thesis, The Catholic University of America, Washington, D.C., 1973.

- ¹⁰Baldwin, B. S., McCormack, R. W., and Deiwert, G. S., "Numerical Techniques for the Solution of the Compressible Navier-Stokes Equations and Implementation of Turbulence Models," AGARD LSP-73, 1975.

- ¹¹McCormack, R. W., "An Efficient Numerical Method for Solving the Time-Dependent Compressible Navier-Stokes Equations at High Reynolds Number," NASA TM X-73,129, July 1976.

- ¹²Rubesin, M. W., Okuno, A. F., Levy, L. L., Jr., McDevitt, J. B., and Seegmiller, H. L., "An Experimental and Computational Investigation of the Flow Field About a Transonic Airfoil in Supercritical Flow With Turbulent Boundary-Layer Separation," 10th Congress of the International Council of the Aeronautical Sciences, Ottawa, Canada, Oct. 4-8, 1976. Also NASA TM X-62,465, July 1976.

- ¹³Alstatt, M. C., "An Experimental and Analytical Investigation of a Transonic Shock-Wave-Boundary-Layer Interaction," AEDC TR 77-47, May 1977.

- ¹⁴Arie, M. and Rouse, H., "Experiments on Two-Dimensional Flow Over a Normal Wall," *Journal of Fluid Mechanics*, Vol. 1, 1956, p. 129.

- ¹⁵Tani, I., Iuchi, M., and Komodu, H., "Experimental Investigation of Flow Separation Associated with a Step or a Groove," Report No. 364, Aeronautical Research Institute, University of Tokyo, April 1961.

- ¹⁶Le Balleur, J.-C. and Mirande, J., "Experimental and Theoretical Study of Two-Dimensional, Turbulent, Incompressible Reattachment," NASA Technical Translation of "Etude Experimentale et Theorique du Recollement Bidimensionnel Turbulent Incompressible," Paper presented at AGARD Meeting on Separated Flow, Gottingen, May 27-30, 1975, pp. 17-1 to 17-13.

- ¹⁷Bradshaw, P. and Wong, F.Y.F., "The Reattachment and Relaxation of a Turbulent Shear Layer," *Journal of Fluid Mechanics*, Vol. 52, Pt. 1, March 14, 1972, pp. 113-135.

- ¹⁸Rubesin, M. W., "A One Equation Model of Turbulence for Use With the Compressible Navier-Stokes Equations," NASA TM X-73,128, April 1976.

- ¹⁹Coakley, T. J., Viegas, J. R., and Horstman, C. C., "Evaluation of Turbulence Models for Three Primary Types of Shock Separated Boundary Layers," Paper 77-692, presented at AIAA 10th Fluid & Plasmadynamics Conference, Albuquerque, New Mexico, June 27-29, 1977.

- ²⁰Finke, K., "Unsteady Shock-Wave Boundary-Layer Interaction on Profiles in Transonic Flow," AGARD-CPP-168, Paper 28, 1975.

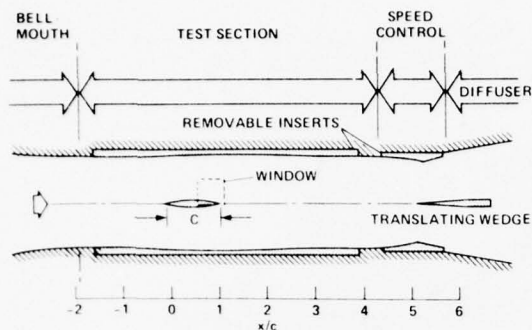


Fig. 1 Experimental arrangement.

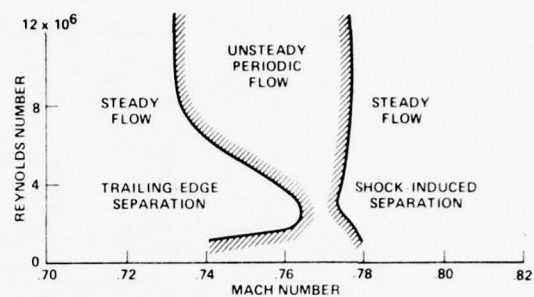
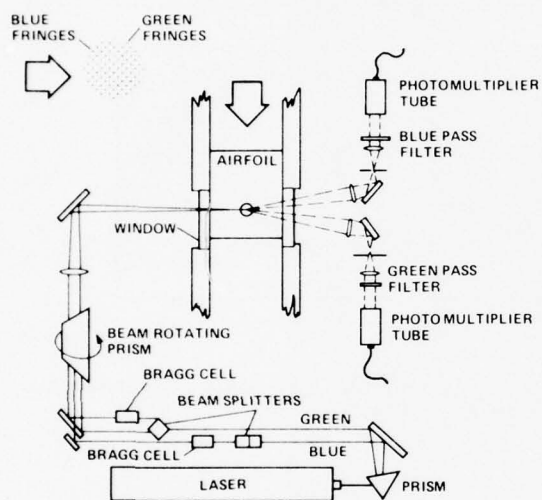
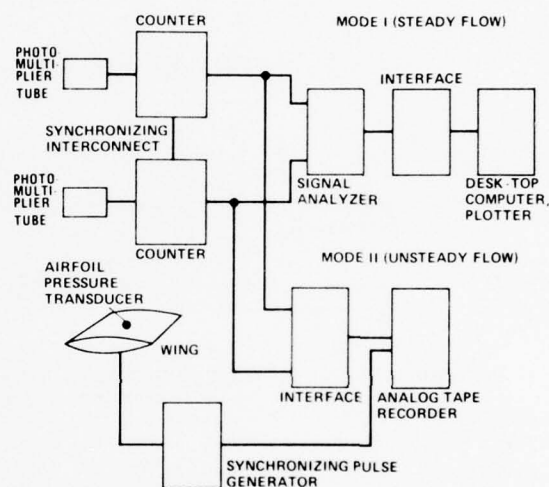


Fig. 2 Experimental flow domains.



a) Diagram showing optical arrangement



b) Diagram showing data acquisition alternatives

Fig. 3 Laser Velocimeter System.

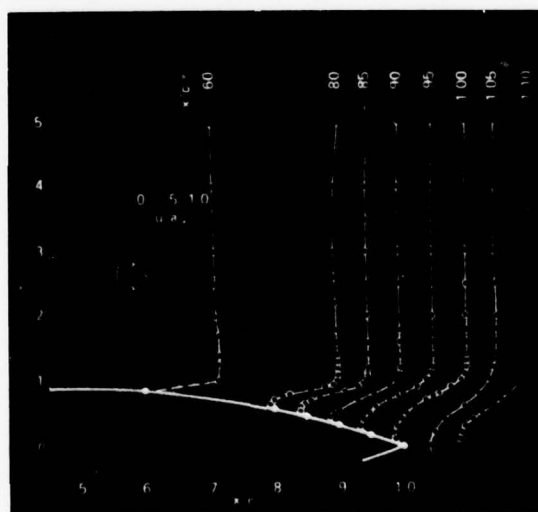


Fig. 4 Shadowgraph of steady shock-induced separation with an overlay showing mean velocity profiles, $M_\infty = 0.79$ and $Re_c = 11 \times 10^6$.

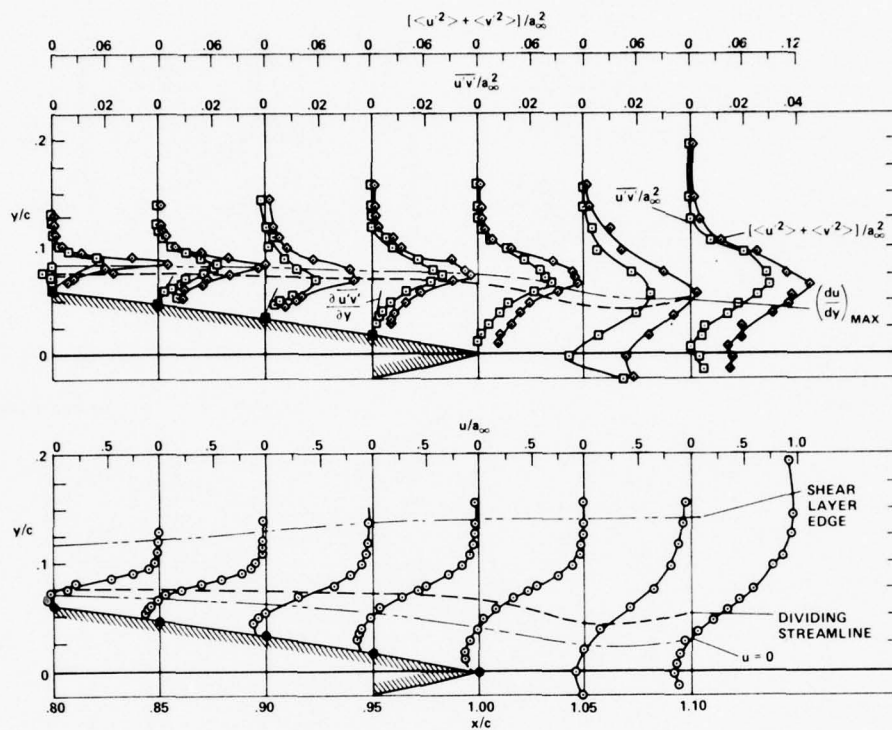


Fig. 5 Mean velocity, turbulent shear stress, and kinetic energy profiles in the shear layer downstream of separation, $M_\infty = 0.79$ and $Re_c = 11 \times 10^6$.

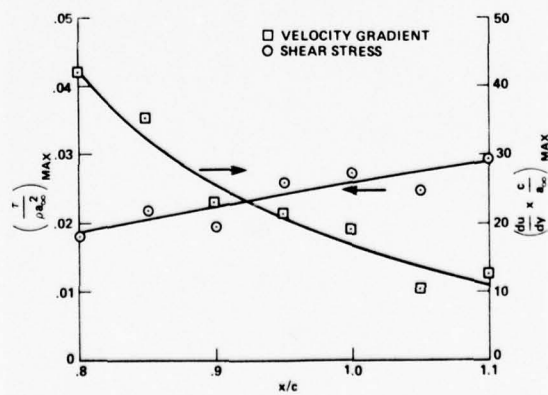


Fig. 6 Variation of maximum shear stress and normal velocity gradient in shear layer downstream of separation, $M_\infty = 0.79$ and $Re_c = 11 \times 10^6$.

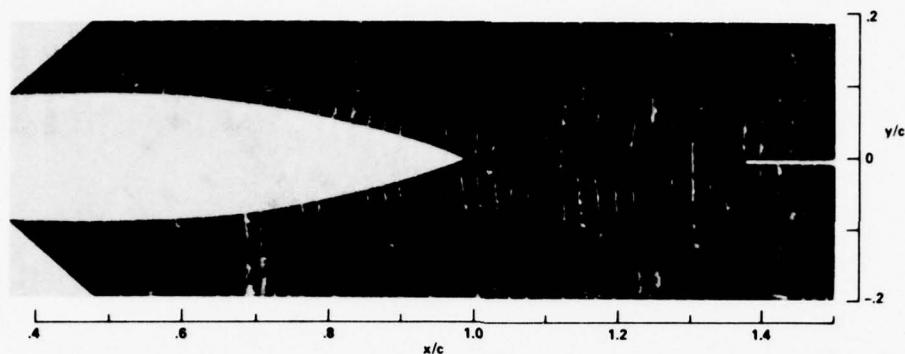


Fig. 7 Oil flow photograph showing qualitative flow features for steady shock-induced separation.

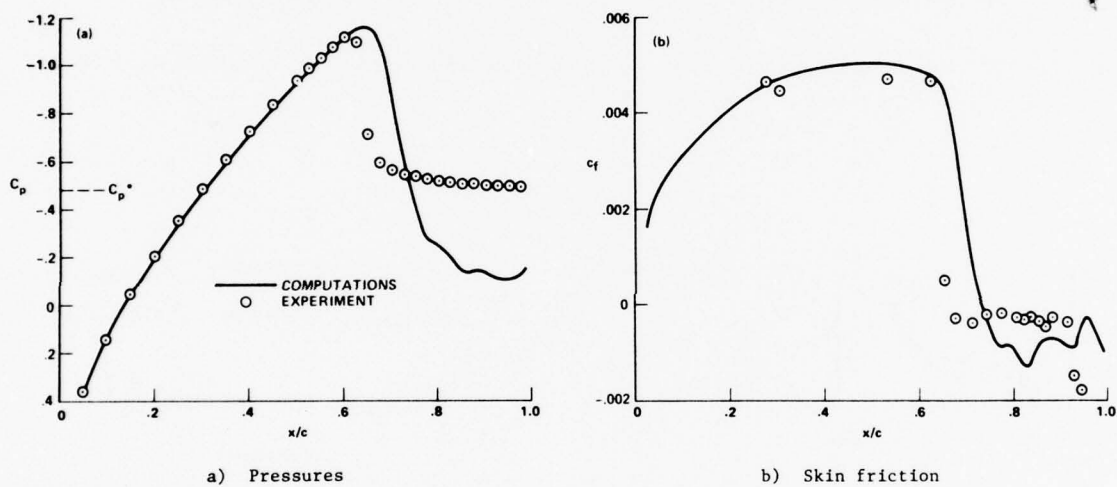


Fig. 8 Experimental and computed pressures and skin friction on the airfoil surface, $M_\infty = 0.79$ and $Re = 11 \times 10^6$.

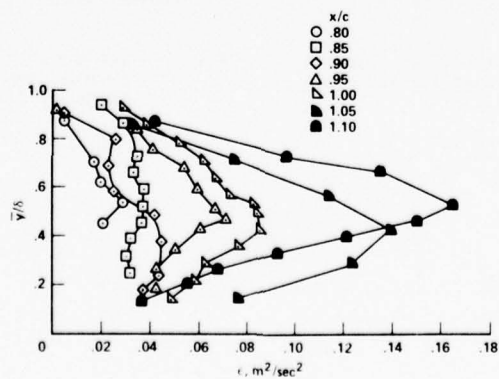


Fig. 9 Eddy diffusivity profiles in the shear layer downstream of separation, $M_\infty = 0.79$ and $Re_c = 11 \times 10^6$.

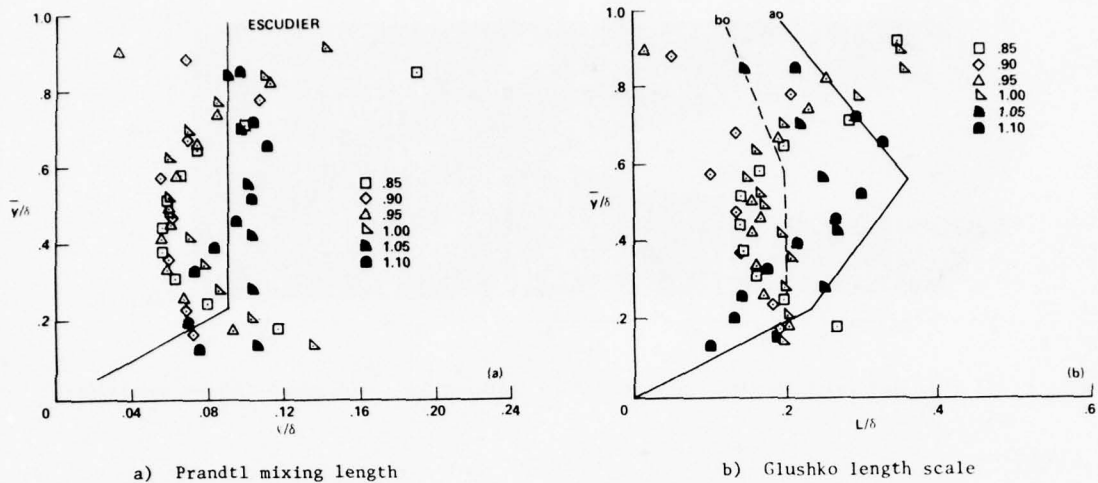
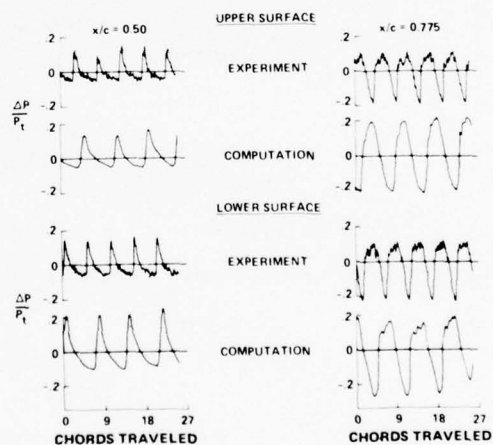
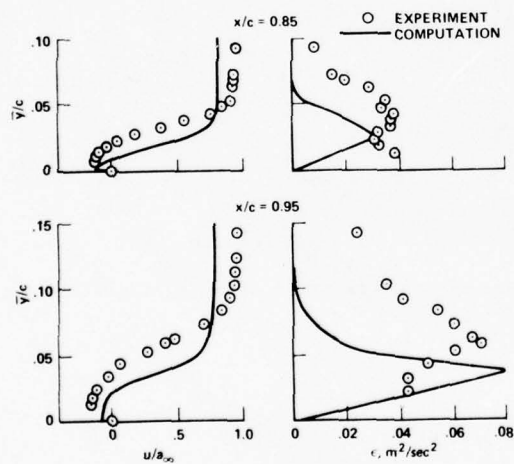
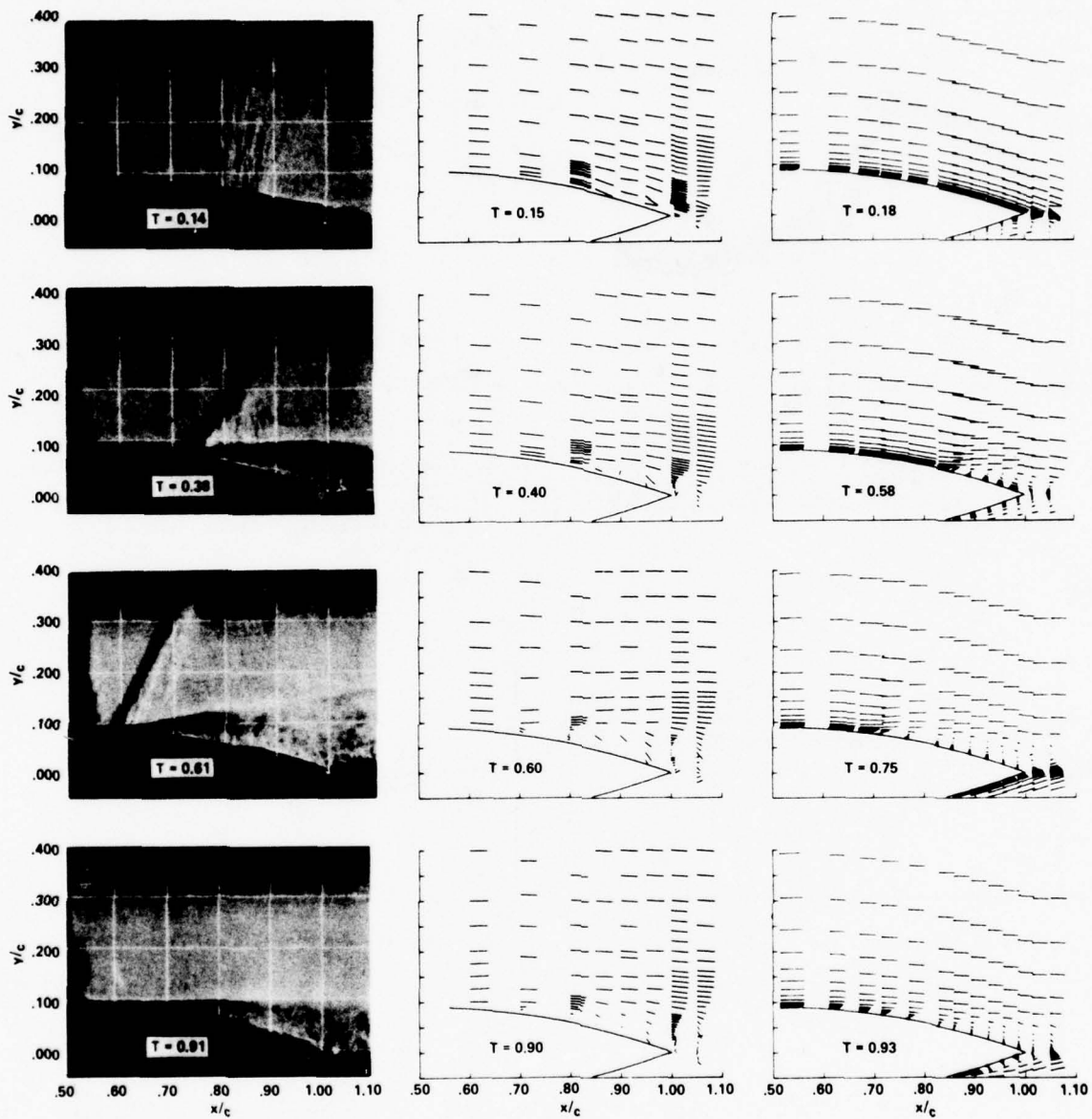


Fig. 10 Length scales measured in the shear layer downstream of separation, $M_\infty = 0.79$ and $Re_c = 11 \times 10^6$.





a) Shadowgraphs

b) Velocity field from
the experiment

c) Velocity field from
the computation

Fig. 13 Flow field over the airfoil with unsteady flow, $M_\infty = 0.76$ and $Re_c = 11 \times 10^6$.

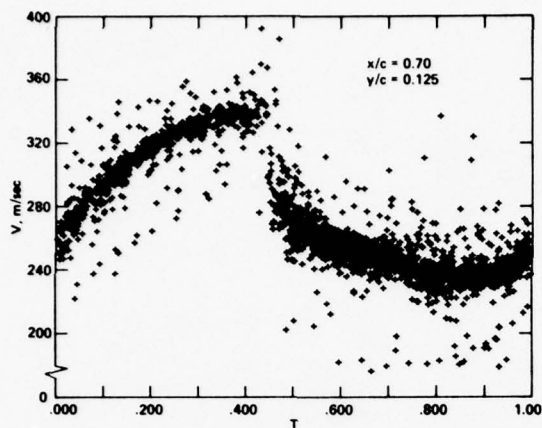


Fig. 14 Time-history of velocity from conditionally sampled data for one cycle of flow oscillation, $M_\infty = 0.76$ and $Re_c = 11 \times 10^6$; $x/c = 0.7$ and $y/c = 0.125$.

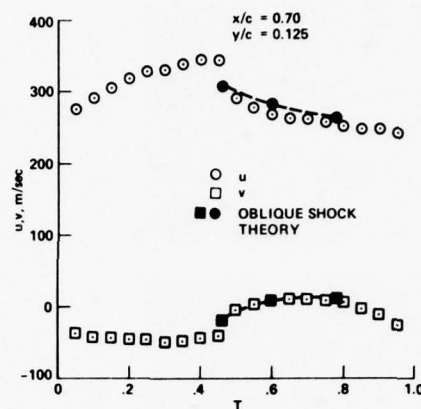
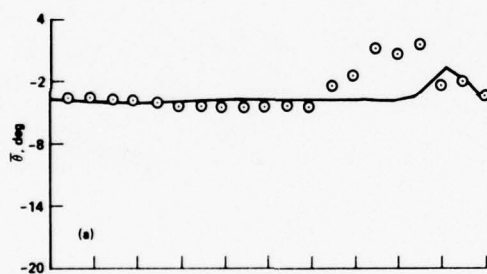
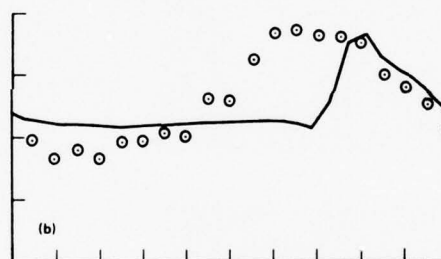


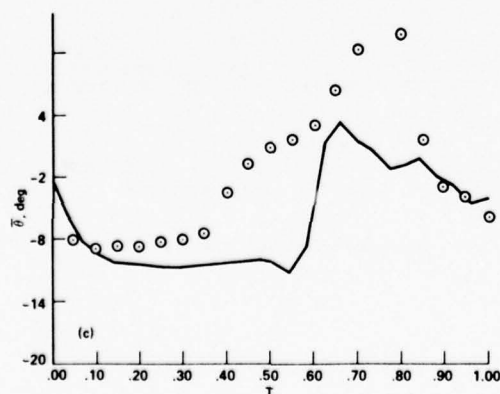
Fig. 15 Time history of averaged velocity components from conditionally sampled data for one cycle of flow oscillation, $M_\infty = 0.76$ and $Re_c = 11 \times 10^6$; $x/c = 0.7$, $y/c = 0.125$.



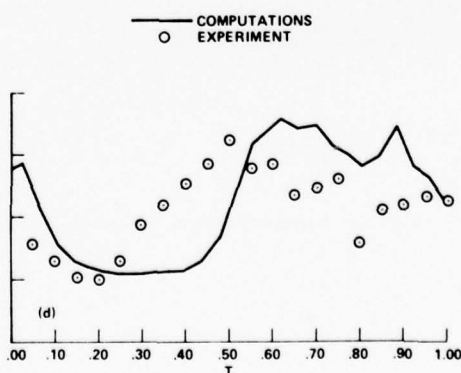
a) $x/c = 0.6$, $y/c = 0.1$



b) $x/c = 0.7$, $y/c = 0.1$



c) $x/c = 0.8$, $y/c = 0.1$



d) $x/c = 0.9$, $y/c = 0.1$

Fig. 16 Mean flow angle of velocity for one cycle of flow oscillation, $M_\infty = 0.76$ and $Re_c = 11 \times 10^6$.

RECENT TURBULENT DRAG REDUCTION RESEARCH AT LANGLEY RESEARCH CENTER

D. M. Bushnell
Langley Research Center

SUMMARY

This paper represents a report on a portion of the fuselage viscous drag reduction research at NASA Langley Research Center. The paper discusses three areas: oscillatory longitudinal curvature, large eddy breakup devices and small longitudinal surface striations. The first two concepts produce sizable local turbulent skin friction reductions, but further research is required to optimize the effect, reduce parasitic device drag, and thus provide a net increase in vehicle performance. The surface striations, due to large wetted area increases for a given planform, have not yet yielded a planform-averaged skin friction reduction. However, heat transfer data indicate such surfaces may have useful application in heat exchangers.

INTRODUCTION

One of the major goals of aerodynamic research is increased aircraft performance. Reducing drag is an obvious method of increasing performance and at the same time reducing fuel usage. Long haul aircraft drag is mainly drag due to lift and turbulent skin friction. Recent advances in technology (supercritical wings, winglets) provide sizable reductions in drag due to lift. However, while skin friction drag reduction research is currently enjoying somewhat of a renaissance, there is no generally applicable technique yet available which gives a net reduction in turbulent skin friction other than driving the flow all the way to the laminar condition (Laminar Flow Control). This forced laminar option is under active study at NASA Langley Research Center for wing application, but other methods should be examined for the fuselage, which is responsible for approximately one half of the aircraft skin friction drag. Turbulent drag reduction techniques are reviewed in reference 1 and this paper presents a progress report on research for several approaches not yet identified when reference 1 was prepared. The approaches include oscillatory longitudinal curvature (ref. 2), large eddy breakup devices (ref. 3) and small longitudinal surface striations (ref. 4 - paper accepted for presentation).

A chronology of the Langley viscous drag reduction research program is shown on figure 1. This research is based primarily on concepts derived from consideration of the coherent structures recently identified in turbulent boundary layers (fig. 2). The turbulent layer is assumed to consist of the usual outer

region with large scale motion, a wall region where turbulent production occurs, and a communication process from outer to inner layers which causes the inner layer to erupt. Obvious possibilities for turbulent drag reduction include breakup of the outer eddy structure, (thereby altering the outer-to-wall communication and perhaps decreasing the bursting activity) and stabilization of the near wall layer. However, care must be taken to consider and perhaps modify "secondary influences" of candidate drag reduction techniques to ensure that the overall effect is the net drag reduction. There are many techniques which reduce turbulence production, but actually increase overall drag, simple examples being small to moderate wall suction and favorable pressure gradients. Therefore, for each of the three candidate drag reduction techniques which will now be discussed, the effect on overall drag will be addressed, not just the influence on turbulent skin friction.

Oscillatory Longitudinal Curvature

Early results from this study are available in reference 2. The basic concept is to use transverse surface waviness in an attempt to produce periodic partial relaminarization and thus a lower average skin friction. The essence of the approach is the extreme sensitivity of turbulent flows to longitudinal curvature effects (ref. 5). Transverse wall waves produce periodic variations in two boundary conditions which strongly influence turbulent boundary layers, alternating favorable and adverse pressure gradients and concave and convex curvature. The pressure variations are phase-shifted approximately 90° from the curvature variations, but there is a region, upstream of the wave crest, where the boundary layer is subjected simultaneously to the combined influence of convex curvature and favorable pressure gradient, both of which are known to stabilize the turbulent flow. Sufficiently large and long lasting convex curvature and favorable pressure gradient effects are known to cause relaminarization of the turbulent boundary layer.

From research performed thus far, one of the keys to obtaining an average C_f reduction is the use of small wave lengths (order of the boundary layer thickness) to cause large curvature effects (small radius of curvature, proportional to wave length squared). Usual guidelines (e.g. ref. 5) indicate that δ/R values greater than 0.005 to 0.01 cause large changes in turbulence structure. In the trans-

verse wavy wall case relatively innocuous waves, $\frac{a}{\lambda} \approx 0.03$ (but small wave length,

$\lambda \sim \delta$) produce $\delta/R \sim 0(1)$ and therefore the boundary layer is subjected to tremendous oscillatory curvature influences. The pressure gradients are also not small,

with maximum $\beta \left(\frac{\delta^*}{\tau_w} \frac{dP}{dx} \right)$ values of order 10 to 15. If such influences were mona-

tonically applied to the boundary layer, the effects would be ultimately catastrophic, either complete relaminarization or separation, depending upon the sign.

The mitigating influence which keeps the turbulent flow relatively well behaved is the oscillatory nature of these influences. The turbulence is kept in a highly nonequilibrium state; as soon as the flow begins to adjust to the local gradients the spatially periodic surface condition alters them. In fact, this

nonequilibrium effect may not allow the usual Görtler vortices to form in the concave region, and delayed formation of these vortices (made probable by small λ) may be necessary for wavy walls to reduce average skin friction. If the vortices formed they would probably continue on into the area where partial relaminarization could occur and perhaps seriously disrupt the relaminarization process.

Reference 2 documents a calculation technique developed for wave-shaped walls of small wave length with first order nonequilibrium effects included via rate equations for the wall damping, wall layer and curvature modeling "constants". The method was developed and calibrated to reproduce wall shear (fig.3) and velocity profiles measured in small λ wavy wall experiments. Note that the average skin friction for figure 2 is approximately 20 percent lower than for a flat plate. This apparent reduction in average surface skin friction is not yet a net drag reduction, as the oscillatory (nonequilibrium) δ^* variation over the wall causes a phase shift in the pressure field induced by the wavy surface and therefore a form or pressure drag occurs which is larger than the C_f reduction. The calculation procedure just discussed can predict this oscillatory δ^* variation and the current Langley Research Center research is aimed at testing models of "skewed" wavy walls where the surface wave is "corrected" for this oscillatory δ^* . On paper, such optimized surfaces can produce a reasonable (10 + 20 percent) net drag reduction; even when the small additional surface area associated with the wave is included.

Large Eddy Breakup Devices

The original research on this concept is documented in reference 3. The initial basic approach was to insert across the boundary layer (but not across the entire flow) a screen or other device to break up the outer eddies (fig. 4). The usual relaxation distance for the outer flow is 60 to 100 δ , and in this region the outer eddies convalesce, heal and grow back to their usual scale. During this healing or relaxation process the outer-to-wall communication might be disrupted, resulting in less bursts and a lower C_f . The screen experiments of reference 3 show a large C_f reduction (up to 50 percent) with a monotonic relaxation to the "undisturbed level" in the order of 50 + 100 δ . The device (screen) drag in reference 3 is probably larger than the area integrated C_f reduction and therefore further research is required to determine whether the device drag can be reduced below the C_f reduction so a net drag reduction can be obtained.

As shown on figure 4, in unpublished tests at Langley by J. N. Hefner, we have used honeycombs rather than screens. These honeycombs have approximately an order of magnitude less drag than the screen of reference 3. Preliminary direct drag (balance) measurements indicate C_f reductions the order of those observed in reference 3 (0 - 50 percent), but the device drag is still larger (by a factor of 2 to 3) than the skin friction reduction. The current Langley Research Center research in this area attempts to determine whether a device such as shown on the right of figure 4 (having a smaller number of horizontal and vertical elements) can also produce large C_f reductions downstream. If so, a net drag reduction may be obtainable. The basic question of what effect various device geometries have upon suppressing the outer structures in turbulent boundary layers is essentially an entirely new line of inquiry. Most previous work

focused upon the opposite problem of using "vortex generators" or roughness to excite the turbulent boundary and keep the flow attached in adverse pressure gradient regions, or for enhanced heat transfer. Estimates based upon the form drag of four horizontal elements with an aspect ratio of 10 indicate a net drag reduction of 10 to 20 percent, if such a device produces large C_f reductions. The research on "large eddy breakup devices" is obviously in an early stage.

Small Longitudinal Surface Striations

The basic concept is described in reference 4. Early work by Eckert and Irvine (ref. 6) indicate that the apex region of isosoles triangle ducts (with small apex angle) could have laminar flow locally, although the major portion of the duct flow was turbulent. An obvious possible origin for this behavior is the local diminution in transverse scale associated with the apex region, i.e., locally the flow is highly viscous. With this experience in mind, and considering the wall scales associated with the bursting process, several walls were machined with triangular (and rectangular) shaped "riblets" having dimensions $\Delta y^+, \Delta z^+ \sim 0(50)$. These longitudinal striations are considerably smaller than any used in previous research.

Direct drag measurements indicate small drag increases (5 → 10 percent) when compared to a flat or smooth surface of the same planform. However, the actual surface (wetted) area associated with the riblets was as much as 300 percent greater than the smooth surface. Therefore, on a wetted area basis the drag was reduced considerably (but not on a planform basis, which is the only important consideration for aircraft drag reduction). Work is continuing to determine if a net drag reduction can be achieved. It should be noted that because the striations are longitudinal, there is no local pressure of form drag associated with such surfaces.

Having evidently altered the wetted surface average C_f considerably, we next checked the heat transfer behavior of these riblets. Results shown on figure 5 indicate a sizable increase in Reynolds analogy factor compared to the flat plate case. This observation may be of considerable interest for heat exchanger applications, as these small riblets evidently increase heat transfer more than they increase pumping power for non-pressure gradient (external type) surfaces. Most devices which increase heating do so at the expense of much greater pumping power compared to the heat transfer increase.

CONCLUDING REMARKS

This progress report is on a portion of the fuselage viscous drag reduction research at NASA Langley Research Center. Paper discusses three areas: oscillatory longitudinal curvature, large eddy breakup devices, and small longitudinal surface striations. The first two concepts produce sizable local turbulent skin friction reductions, but farther research is required to optimize the effect, reduce parasitic device drag and thus provide a net increase in vehicle performance. The surface striations, due to large wetter areas increases

for a given planform, have not yet yielded a planform-averaged skin friction reduction. However, heat-transfer data indicate such surfaces may have useful application in heat exchangers.

REFERENCES

1. Hefner, J. N.; and Bushnell, D. M.: An Overview of Concepts for Aircraft Drag Reduction. AGARD R-654 "Concepts for Drag Reduction," 1977.
2. Balasubramanian, R.; Cary, A. M., Jr.; Bushnell, D. M.; and Ash, R. L.: Influence of Transverse Surface Waves on Turbulent Boundary Layers. Presented at 5th Biennial Symposium on Turbulence at University of Missouri, Rolla, Oct. 1977.
3. Yajnik, K. S.; and Acharya, M.: Non-Equilibrium Effects in a Turbulent Boundary Layer due to the Destruction of Large Eddies. Symposium on Turbulence at Technische Universitat Berlin, Aug. 1977.
4. Walsh, M. J.; and Weinstein: Drag and Heat Transfer on Surfaces with Small Longitudinal Fins. AIAA 11th Fluid and Plasma Dynamics Conference, Seattle, Washington, July 10-12, 1978.
5. Bradshaw, P.: Effects of Streamline Curvature on Turbulent Flow. AGARDograph 169, 1973.
6. Eckert, E. R. G.; and Irvine, T. F., Jr.: Flow in Corners of Passages with Non-Circular Cross Sections. Transactions of the ASME, May 1956, pp. 709-718.

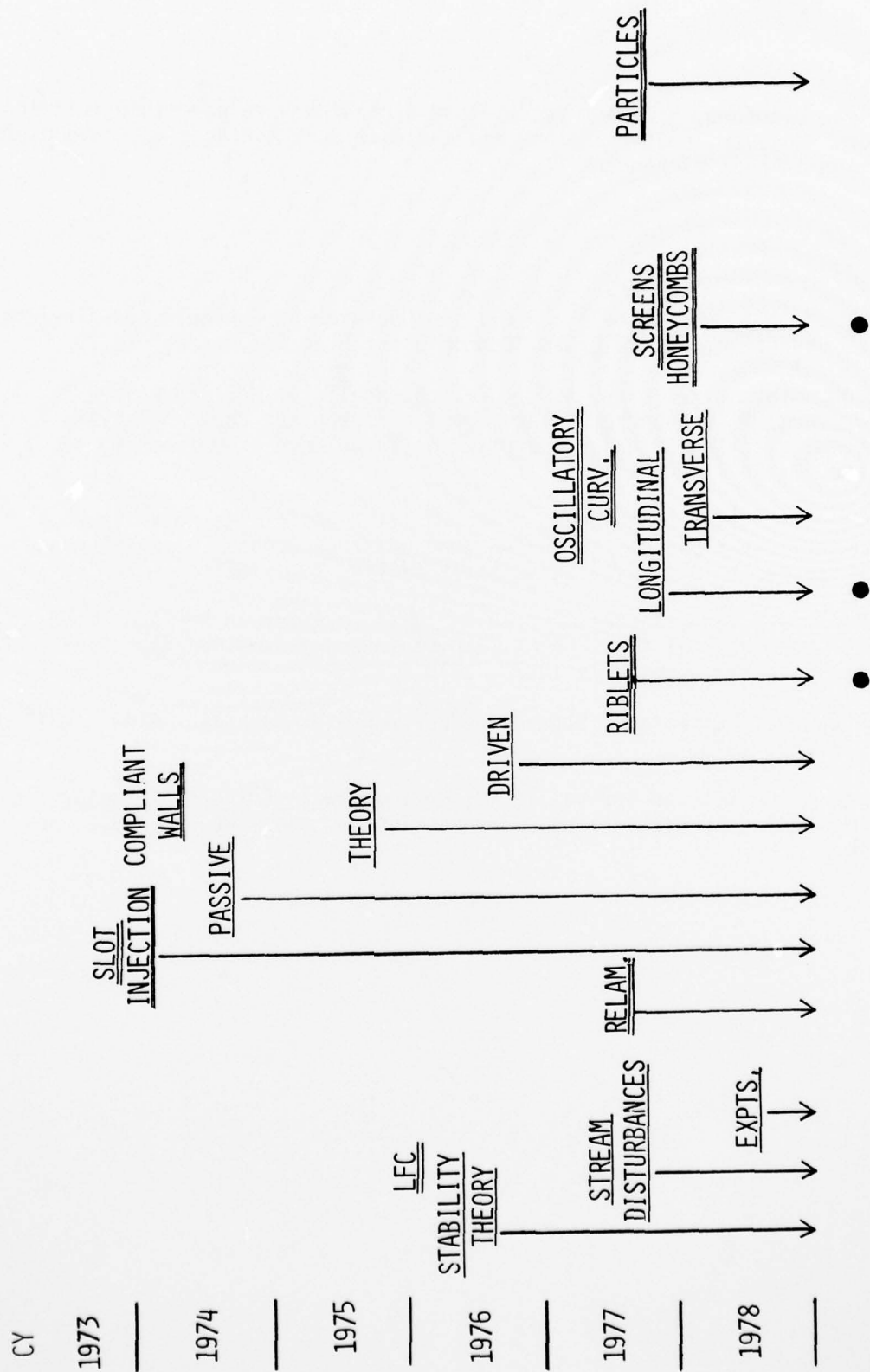


FIGURE 1.- LANGLEY DRAG REDUCTION CHRONOLOGY

OBVIOUS POSSIBILITIES

- OSCILLATORY CURVATURE,
SCREENS
 - o REDUCE SEVERITY (AMPLITUDE, TIME SCALE)
OF OUTER TO INNER COMMUNICATION BY
FRAGMENTATION OF OUTER STRUCTURES
- "RIBLETS"
 - o INCREASE STABILITY OF WALL FLOW

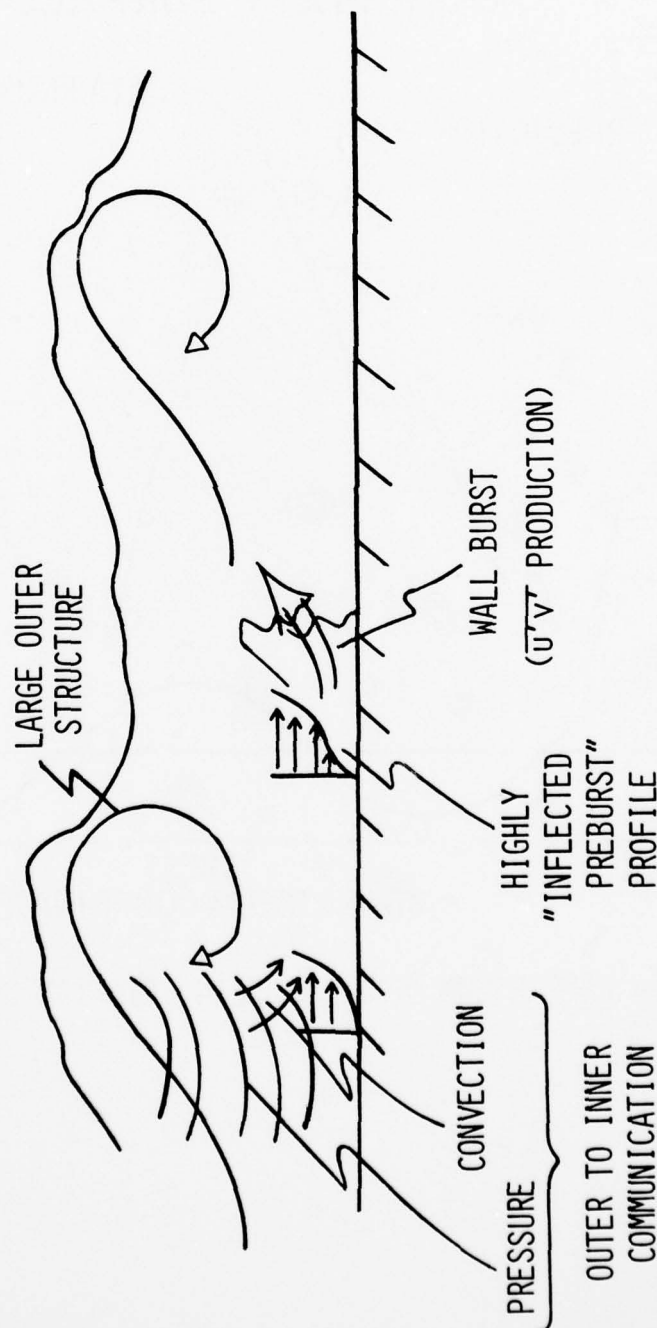


FIGURE 2.- DRAG REDUCTION THROUGH INTERFERENCE WITH TURBULENCE PRODUCTION/FEEDBACK LOOP

COMPARISON OF LOCAL SKIN FRICTION OVER WAVY SURFACE

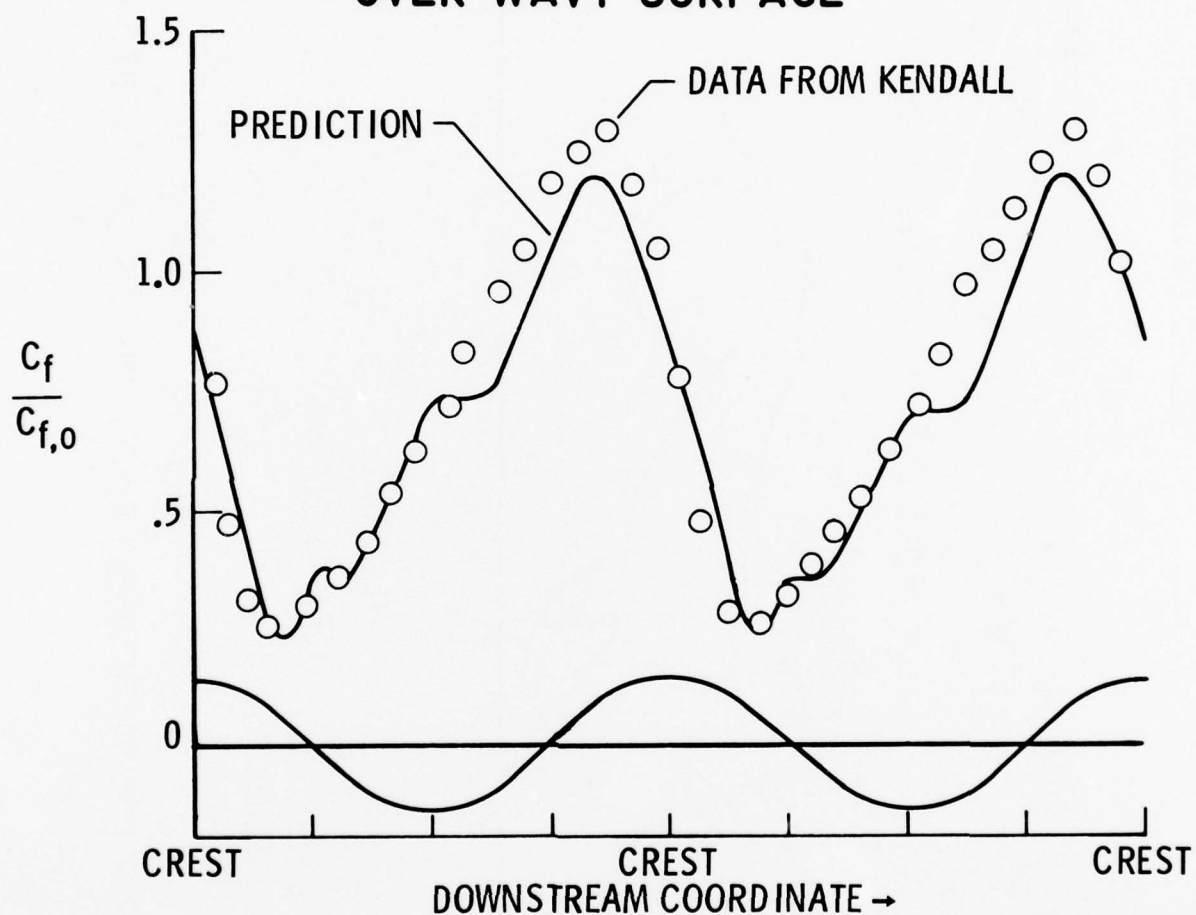
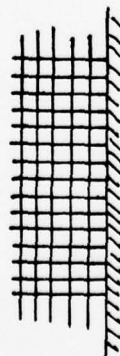


FIGURE 3.- COMPARISON OF LOCAL SKIN FRICTION OVER WAVY SURFACE

HONEYCOMBS/SCREENS FOR TURBULENT VISCOUS DRAG REDUCTION

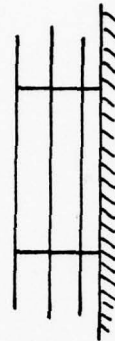
OBJECTIVE: DEVELOP A TURBULENCE "BREAK-UP" DEVICE WITH A MINIMUM NUMBER OF LOW DRAG VERTICAL/HORIZONTAL MEMBERS SUCH THAT THE DEVICE DRAG PLUS SKIN FRICTION REDUCTION DOWNSTREAM PRODUCES A NET REDUCTION IN VEHICLE DRAG



SCREENS
 $C_D \sim 0(1)$
 (YAJNIK)



HONEYCOMBS
 $C_D \sim 0(.1)$
 (CURRENT LARC)



OPTIMIZED BREAK-UP
 DEVICE
 (PRESENT CONFIGURATION
 SUGGESTED BY NAGIB)

FIGURE 4.- HONEYCOMBS/SCREENS FOR TURBULENT VISCOUS DRAG REDUCTION

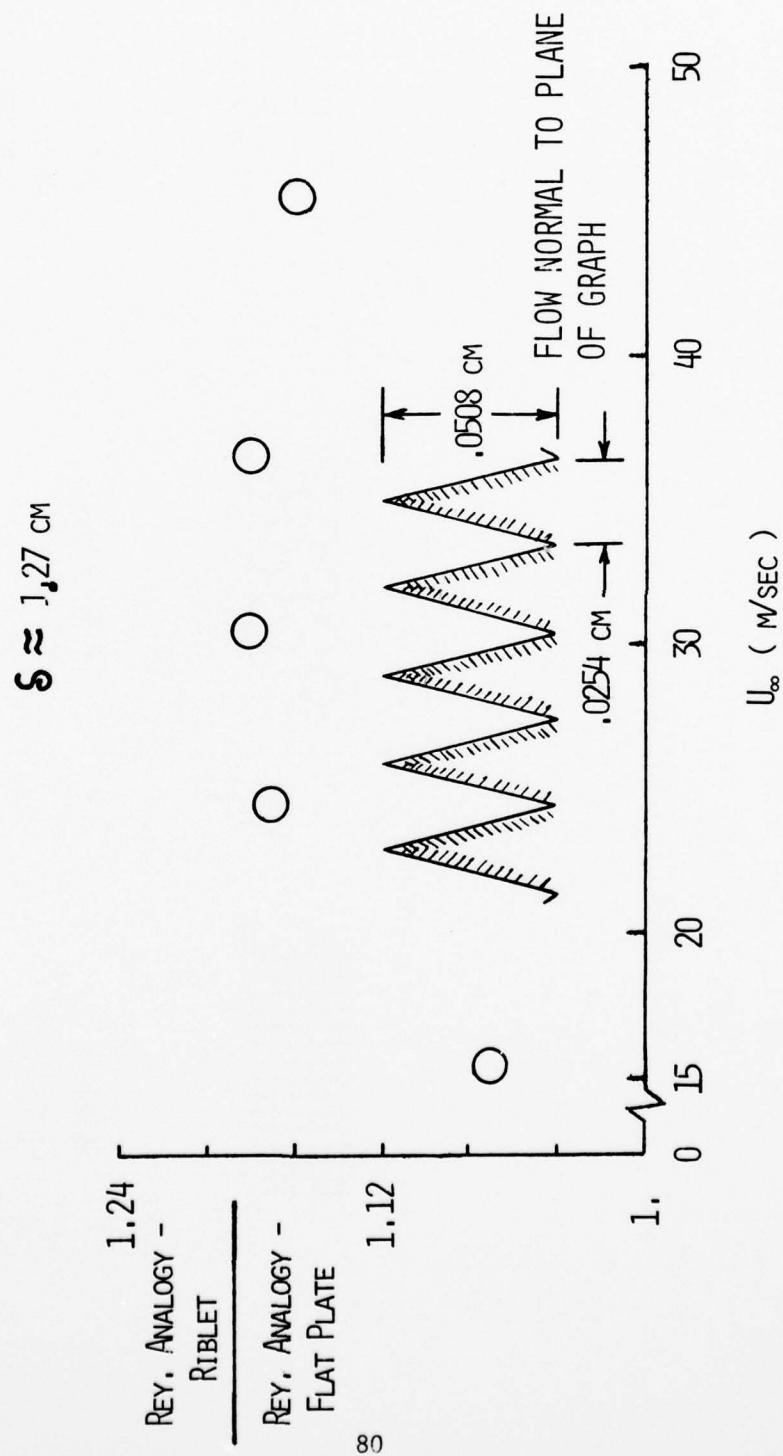


FIGURE 5.- INFLUENCE OF "RIBLETS" ON HEAT TRANSFER

NUMERICAL SOLUTION OF SUPERSONIC
INTERACTING TURBULENT FLOW ALONG A CORNER

by

J. S. SHANG* and W. L. HANKEY**
Air Force Flight Dynamics Laboratory
Wright-Patterson AFB, Ohio

*Aerospace Engineer
**Senior Scientist

INTRODUCTION

Flows along streamwise corners exist in numerous engineering applications; for example, flow along fuselage wing junction, flow in rectangular inlet diffusers and ducts, and flow in the intersection of several control surfaces. Traditionally, the flow field has been analyzed by the super-position of primary and transverse flows^{1,2,3,4}. The transverse flow has a pronounced effect on peripheral wall shear stress distribution and heat rates in the corner region. In a supersonic stream, the generating mechanism of cross flows is further complicated by the intricate shock-wave structure interacting with the viscous dominated region^{5,6,7}. In essence, this problem is amenable to a solution only through the use of the Navier-Stokes equations. This observation is reflected by the significant amount of recent numerical solutions obtained for the considered configurations. Some of the investigations are interested only in either the shock wave structure or the slip surface configuration^{8,9,10} or seek the asymptotic viscous solution under particular flow conditions^{11,12,13}. Recent work^{14,15} using the Navier-Stokes equations on the subject is currently under development in computational fluid dynamics. The sole limitations of the aforementioned efforts^{14,15} is that the flow remains laminar. The present analysis therefore, attempts to remove the last restriction in the study of the three-dimensional corner problem through the inclusion of a turbulence and transition model.

The specific case examined is a symmetrical corner formed by the intersection of two wedges with identical wedge angles of 9.48 degrees. The flow field investigated contains a supersonic leading edge with the consecutive development of laminar, transitional and turbulent viscous flow along the streamwise corner. The experimental data^{16,17} was collected at a Mach number of three, with the Reynolds number spanning a range from 0.4×10^6 to 60×10^6 . The numerical results are compared with the experimental measurements of surface pressure distribution, impact pressure survey, and oil film flow pattern. The complete flow field structure is presented in the form of density contours, cross flow velocity diagrams and surface shear distributions.

ANALYSIS

The equations of motion for the present analysis are the time-dependent Navier-Stokes equations in mass-averaged variables¹⁸ for three dimensional flows

$$\frac{\partial \rho}{\partial t} + \nabla \cdot (\rho \bar{u}) = 0 \quad (1-1)$$

$$\frac{\partial \rho \bar{u}}{\partial t} + \nabla \cdot (\rho \bar{u} \bar{u} - \bar{\tau}) = 0 \quad (1-2)$$

$$\frac{\partial \rho e}{\partial t} + \nabla \cdot (\rho e \bar{u} - \bar{u} \cdot \bar{\tau} + \bar{q}) = 0 \quad (1-3)$$

where, the stress tensor also contains components of the Reynolds stress $\langle \tau_{ij} \rangle = \tau_{ij} - \rho \langle u_i u_j \rangle$ and the heat flux also includes a convective term due to the turbulent motion $\langle \dot{q}_i \rangle = \dot{q}_i - \rho \langle e u_i \rangle$. Although, the closure problem for the system of governing equation is formidable, the approach here is to seek a simple means of effecting closure to the equations of motion. To accomplish this objective, a modification of Gessner's eddy viscosity model^{19,20} for turbulent corner flows was adopted. In this model, the component of the Reynolds stress tensor is related to the mean rate-of-deformation tensor²¹. The length scale used in the eddy viscosity formulation is the asymptotic form given by Gessner for a rectangular duct. Finally, a two-layer model is given as

$$\begin{aligned} &\text{The inner layer} \\ \epsilon_i &= \rho (K_1 L)^2 \left\{ 1 - \exp - \left[\frac{\rho \left| \frac{\partial q}{\partial n} \right| L^2}{26 \mu} \right]^{1/2} \right\}^2 \left| \frac{\partial q}{\partial n} \right| \end{aligned} \quad (2-1)$$

where K_1 is Von Karman's constant and $\left| \frac{\partial q}{\partial n} \right| = \bar{n} \cdot \nabla \bar{u}$.

The mixing length L is given by Buleev's mixing length²² model in its asymptotic form

$$L = 2yz/[y + z + (y^2 + z^2)^{1/2}]$$

The outer layerayer

In the law of the wake region, the eddy viscosity is simply the velocity defect formulation

$$\epsilon_o = \rho K_2 q_{\max} \int_0^{n_{\max}} (1 - q/q_{\max}) dn \quad (2-2)$$

In order to describe the transitional phenomenon for the corner region, the Dhawan and Narasimha's²³ transition model was extended to three dimensions. The model indeed is entirely empirical and requires specification of the zone of transition with a specific on-set point. Nevertheless, the transition model has been adequately verified^{24,25}. The Dhawan and Narasimha's laminar-turbulent transition model can be given as

$$\Gamma(\bar{x}) = 1 - \exp(-0.412 \bar{x}^2) \quad (2-3)$$

where

$$\bar{x} = (x - x_{t,i})/\Lambda, \quad x_{t,i} \leq x \leq x_{t,f}$$

The parameter Λ is a measure of the extent of the transition region defined by

$$\Lambda = x_{\Gamma} = 3/4 \quad x_{\Gamma} = 1/4$$

Once the eddy viscosity coefficient and turbulent Prandtl number are defined, the closure of the system of equations is completed. The components of stress tensor and heat flux can be summarized as

$$\tau_{ij} = (\mu + \epsilon)(\text{Def } \bar{u})_{ij} - 2/3(\mu + \epsilon)(\nabla \cdot \bar{u}) \delta_{ij} \quad (3-1)$$

$$q_i = -C_p \left(\frac{\mu}{P_r} + \frac{\epsilon}{P_{rt}} \right) \frac{\partial T}{\partial x} \quad (3-2)$$

The associated boundary conditions for the present investigations are straight forward; upstream, supersonic free stream is prescribed. The downstream boundary condition is assigned the asymptotic inviscid (conical) behavior. Away from the corner region, the flow is required to return to a two-dimensional flow.

$$\bar{U}(0, x, y, z) = \bar{U}_{\infty} \quad (4-1)$$

$$\bar{U}(t, 0, y, z) = \bar{U}_{\infty} \quad (4-2)$$

$$\frac{\partial \bar{U}}{\partial \eta} = 0 \quad \text{as } \eta \gg 0 \quad (4-3)$$

$$\frac{\partial \bar{U}}{\partial \zeta} = 0 \quad \text{as } \zeta \gg 0 \quad (4-4)$$

$$\frac{\partial \bar{U}}{\partial \xi} = 0 \quad \text{as } \xi \gg 0 \quad (4-5)$$

On the contour of the corner, the boundary conditions are the no-slip conditions for the velocity components and a constant surface temperature. The latter is intended to duplicate the experimental wall temperature. The surface pressure is obtained by satisfying the momentum equation at the wedge surfaces.

$$u = v = w = 0 \quad \text{at } \eta, \zeta = 0 \quad (5-1)$$

$$T = 530^{\circ}\text{R} \quad \text{at } \eta, \zeta = 0 \quad (5-2)$$

$$\nabla \cdot (\bar{p}\bar{I} - \bar{\tau}) = 0 \quad \text{at } \eta, \zeta = 0 \quad (5-3)$$

DISCUSSION OF RESULTS

For the present analysis two mesh-point distributions were used. The preliminary result was first obtained by a (8 x 23 x 23) system mainly to evaluate the eddy viscosity model on a CDC Cyber 74 computer. The finer resolution calculation (17 x 23 x 33) was performed on the CDC 7600 computer of NASA Ames Research Center. The rate of data processing is 0.00468 and 0.00178 seconds per grid point per time step on the Cyber 74 and the CDC 7600 respectively. The basic numerical method is the A.D.E. scheme originated by MacCormack^{26,27}, however, the numerical code also contains the option of a hybrid implicit-explicit scheme²⁷. Details of the numerical procedure will be delineated in the complete version of the manuscript.

The numerical results are presented in two categories. In the first group, a direct comparison is performed of the numerical with the experimental data. The second group is presented to delineate the structure of the corner flow. The shock wave system, slip surface and the vorticity are investigated relative to the secondary flow velocity. The surface shear stress distribution and the limiting streamline of the three-dimensional flow separation^{28,29} will also be presented.

In the first figure, surface pressure distributions for laminar and turbulent flow are presented. The agreement between the experimental measurement and calculation is excellent. The discrepancy between data and calculation is within the scatter band of the data. The computed surface pressure clearly displays the different scaling characteristic

of laminar and turbulent interacting flows while the inviscid solution fails to reveal this characteristic.

The shock wave structure of the entire flow field in terms of density contours is given in Figure 2. One observes the intersecting shock waves due to the wedges and a set of two triple points formed by further intersection of the embedded shock waves. The numerical result duplicates essentially the experimental observations. In Figure 3, two shock wave structures for laminar and turbulent conditions are presented. Good agreement is observed between the computed and experimental values. The numerical result shows the reduction in the size of the terminating embedded lambda shock as the interaction length scale decreases from laminar to turbulent flow.

The comparison of experimental impact measurement and calculated values is given in Figure 4. The agreement appears reasonable. The pressure distribution not only reveals the shock wave, but also indicates the slip surface location.

In Figure 5, the oil film flow pattern is presented. It is obvious an orderly transition from laminar flow near the leading edge to the fully turbulent flow downstream. The components of surface shear force can be obtained as $\bar{f} = \bar{n} \cdot \bar{\tau}$. According to the limiting line theory^{28,29} for three-dimensional flow separation convergence of oil film streaks represent the separation streamline. The experiment indicates asymptotic separation angles of 45° for laminar and 32° for turbulent with transition forming as 'S' shaped pattern between the two regions. The numerical results substantiate findings to within ±10%.

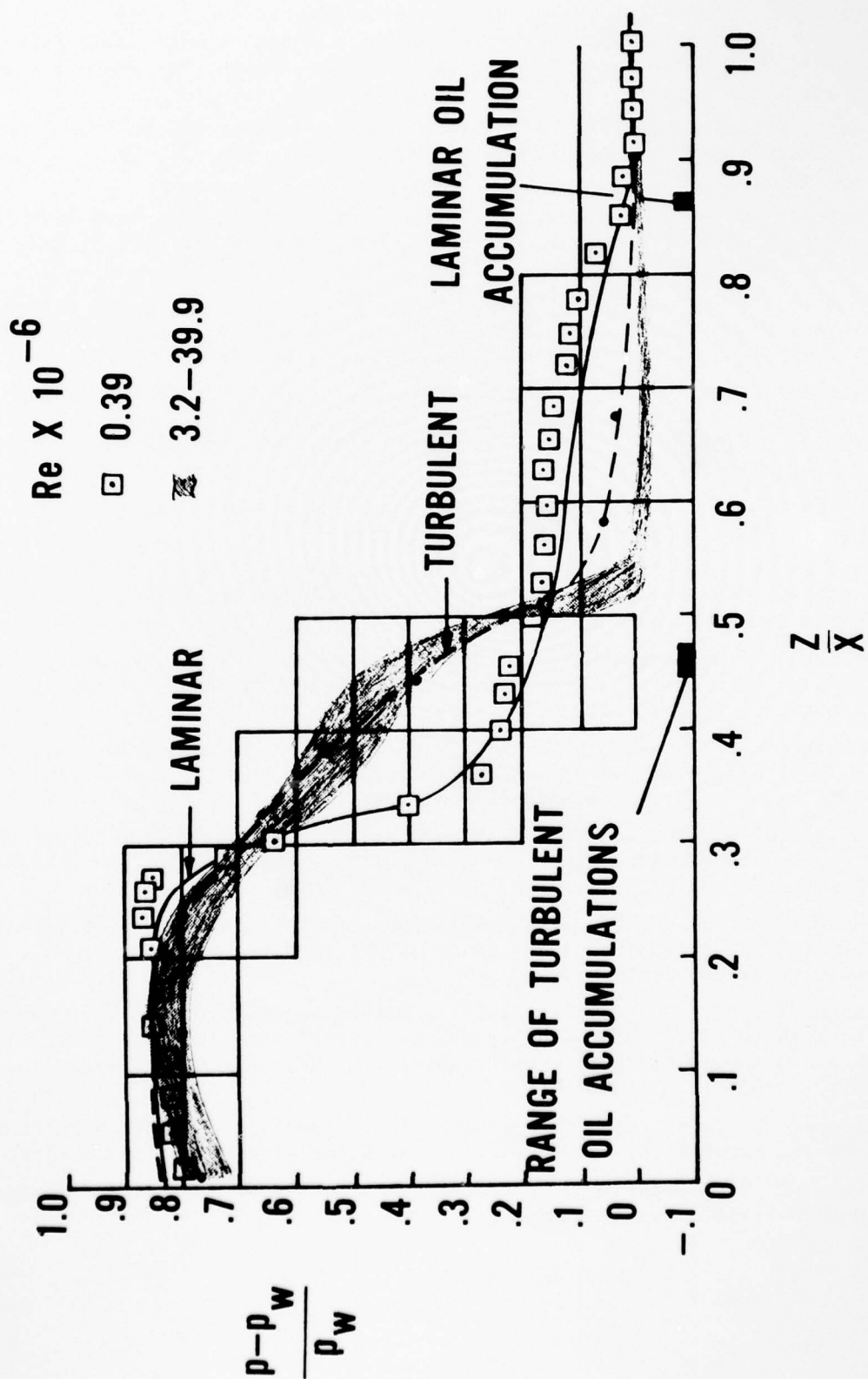
CONCLUSION

The numerical solution of a three-dimensional laminar-transitional-turbulent flow along a symmetrical corner has been obtained. The present result duplicates all the essential experimental observations. The present investigation seems to indicate that careful application of an eddy-viscosity concept is not limited to mere two-dimensional thin shear flows. Finally, the present procedure appears to offer promise for the prediction of inlets and fuselage wing junctions for practical engineering applications.

REFERENCES

1. Nikuradse, J. "Untersuchungen über die Geschwindigkeitsverteilung in Turbulenten Strömungen, Thesis, Göttingen 1926 VDI-Forschungsheft 281, Berlin, 1926.
2. Prandtl, L. "Essentials of Fluid Dynamics", London, Blackie, 1952.
3. Eichel Bremer, E. A. and Preston, J. H., "On the Role of Secondary Flow in Turbulent Boundary Layers in Corners (and Salients), J. McCanique, Vol. 10, 91-112, 1971.
4. Gessner, F. B., "The Origin of Secondary Flow in Turbulent Flow Along a Corner", J.F.M., Vol. 58, Part 1, pp 1-25, 1973.
5. Charwat, A. F., and Redekopp, L. G., "Supersonic Interference Flow Along the Corner of Intersecting Wedges", AIAA J., Vol. 5, No. 3, pp 480-488, 1967.
6. Cresei, R. J., Rubin, S. G., Nardo, C. T. and Lin, T. C., "Hypersonic Interaction Along a Rectangular Corner", AIAA J., Vol. 7, No. 12, pp 2241-2246, 1969.
7. Korkegi, R. H., "On the Structure of Three-Dimensional Shock Induced Separated Flow Regions", AIAA J., Vol. 14, No. 5, pp 597-600, 1976.
8. Kutler, P., "Numerical Solution for the Inviscid Supersonic Flow in the Corner Formed by Two Intersecting Wedges", AIAA Paper 73-675, Palm Springs, CA, 1973.
9. Shankar, V. and Anderson, D. A., "Numerical Solutions for Inviscid Supersonic Corner Flows", Engineering Research Institute, Iowa State University, Ames, Iowa, Final Rept. ISU-ERI-Ames-74090, May, 1974.
10. Shankar, V., Anderson, D. and Kulter, P., "Numerical Solutions for Supersonic Corner Flow", J. of Computational Physics, Vol. 17, No. 2, pp 160-180, July 1975.
11. Weinberg, B. C., and Rubin, S. G., "Compressions Corner Flow", J. Fluid Mechanics, Vol. 56, part 4, pp 753-774, 1974.
12. Ghia, K. N. and Davis, R. T., "A Study of Compressible Potential and Asymptotic Viscous Flows for Corner Regions, AIAA J., Vol. 12, pp 355-359, 1974.
13. Mikhail, A. G. and Ghia, K. N., "Study of Viscous Compressible Flow Along an Axial Corner", AIAA Preprint 77-685, AIAA 10th Fluid and Plasma Dynamics Conference, Albuquerque, N. Mexico, June 27-29, 1977.
14. Hung, C. M. and MacCormack, R. W., "Numerical Solution of Supersonic Laminar Flow Over a Three-Dimensional Compression Corner", AIAA Preprint 77-694, AIAA 10th Fluid and Plasma Dynamics Conference, Albuquerque, N. Mexico, June 27-29, 1977.
15. Shang, J. S. and Hankey, W. L., "Numerical Solution of the Navier-Stokes Equations for a Three-Dimensional Corner", AIAA J., Vol. 15, No. 11, pp 1575-1582, November 1977.

16. West, J. E. and Korkegi, R. H., "Interactions in the Corner of Intersecting Wedges at a Mach Number of Three (3) and High Reynolds Numbers", ARL 71-0241, Aerospace Research Laboratories, Wright-Patterson Air Force Base, October, 1971.
17. West, J. E. and Korkegi, R. H., "Supersonic Interaction in the Corner of Intersecting Wedges and High Reynolds Numbers", AIAA J., Vol. 10, No. 5, pp. 652-656, May 1972.
18. Rubesin, M. W. and Rose, W. C., "The Turbulent Mean-Flow Reynolds-Stress and Heat Flux Equations in Mass-Averaged Dependent Variables", NASA TM X-62, 248, March 1973.
19. Gessner, F. B. and Emery, A. F., "A Reynolds Stress Model for Turbulent Corner Flow - Part I; Development of the Model", J. of Fluids Engineering, Transactions of the ASME, Vol. 98, Series I, No. 2, pp 261-268, June 1976.
20. Gessner, F. B. and Po, J. K., "A Reynolds Stress Model for Turbulent Corner Flows - Part I; Comparisons Between Theory and Experiment", J. of Fluids Engineering, Transactions of the ASME, Vol. 98, Series I, No. 2, pp. 269-277, June 1976.
21. Goldstein, S., Edited, "Modern Developments in Fluid Dynamics", Vol. 1, pp. 206-208, Oxford University Press, 1957.
22. Buleev, H. I., "Theoretical Model of the Mechanism of Turbulent Exchange in Fluid Flows", AERE Translation 957, Atomic Energy Research Establishment, Harwell, England, 1963.
23. Dhawan, S. and Narasimha, R., "Some Properties of Boundary Layer Flow During the Transition from Laminar to Turbulent Motion", J. of Fluid Mechanics, Vol. 3, Part 4, pp 418-436, 1958.
24. Shang, J. S., Hankey, W. L. and Dwyer, D. L., "Numerical Analysis of Eddy Viscosity Models in Supersonic Turbulent Boundary Layers", AIAA J., Vol. 11, No. 12, pp. 1677-1683, December 1973.
25. Shang, J. S., "Computation of Hypersonic Turbulent Boundary Layers with Heat Transfer", AIAA Preprint 73-699, AIAA 6th Fluid and Plasma Dynamics Conference, Palm Springs, CA, July 16-18, 1973.
26. McCormack, R. W., "Numerical Solutions of the Interactions of a Shock Wave with a Laminar Boundary Layer", Lecture Notes in Physics, Vol. 8, Springer Verlag, p. 151, 1971.
27. Shang, J. S., "An Implicit-Explicit Method for Solving the Navier-Stokes Equations", A Collection of Technical Papers, AIAA 3rd Computational Fluid Dynamics Conference, Albuquerque, N. Mexico, pp. 141-148, June 27-28, 1977.
28. Moore, F. K., Edited, "Theory of Laminar Flows", High Speed Aerodynamics and Jet Propulsion, Vol. IV, Princeton University Press, pp 387-390, 1964.
29. Wang, K. C., "Separation of Three-Dimensional Flow", Martin Marietta Corp., MML TR-76-54C, August 1976.



AD-A061 086

AIR FORCE FLIGHT DYNAMICS LAB WRIGHT-PATTERSON AFB OHIO F/G 20/4
BOUNDARY LAYER EFFECTS-PROCEEDINGS OF THE 7TH U. S. AIR FORCE/F--ETC(U)
SEP 78 A W FIORE
AFFDL-TR-78-111

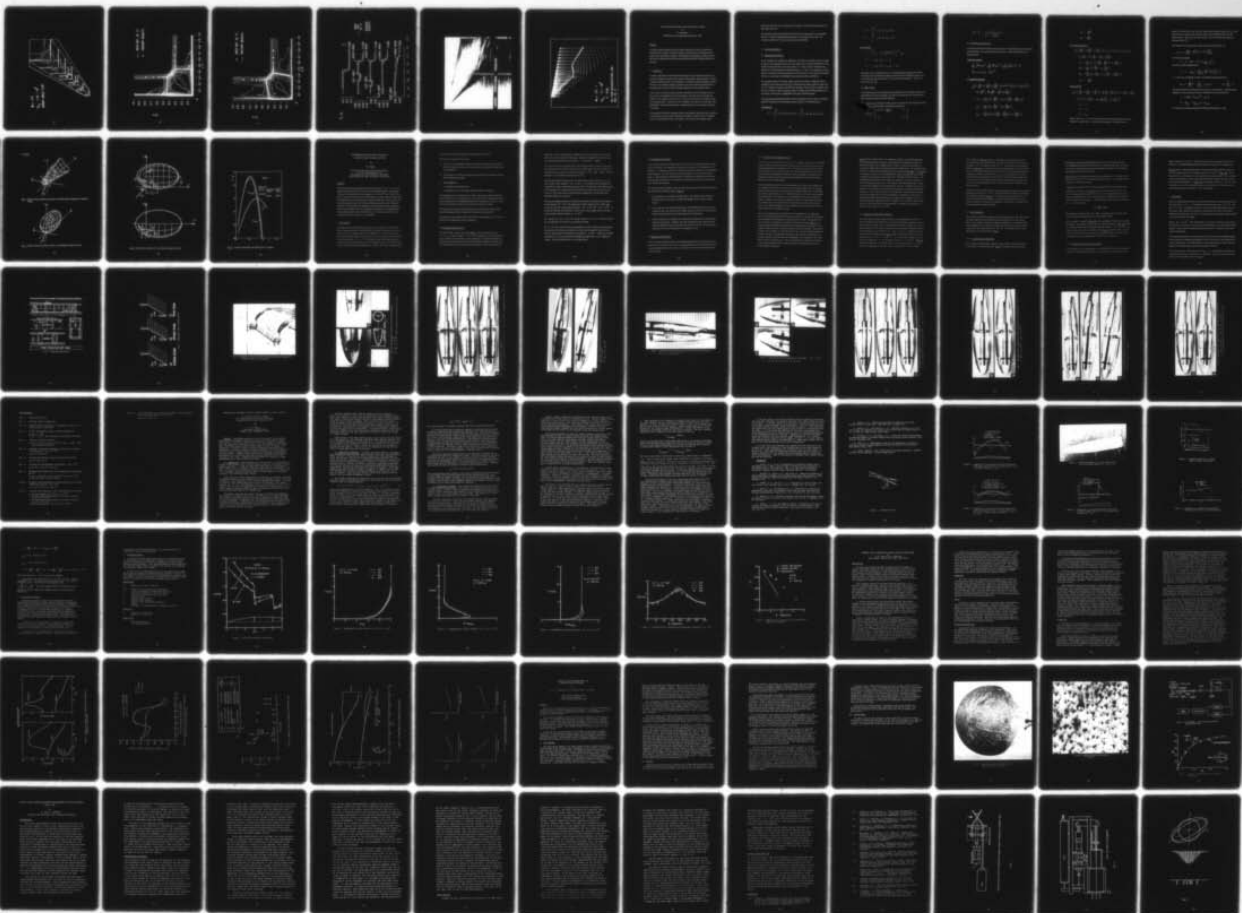
MWDDEA-AF-75-6-7440

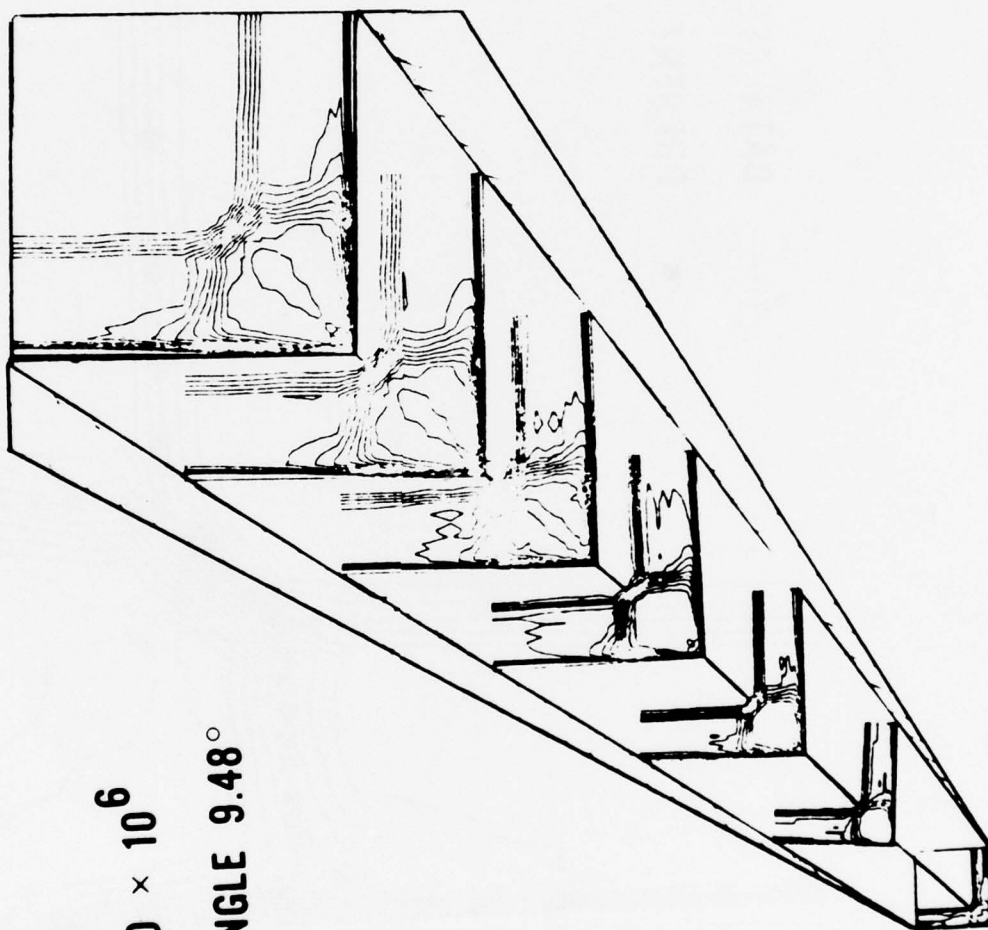
NL

UNCLASSIFIED

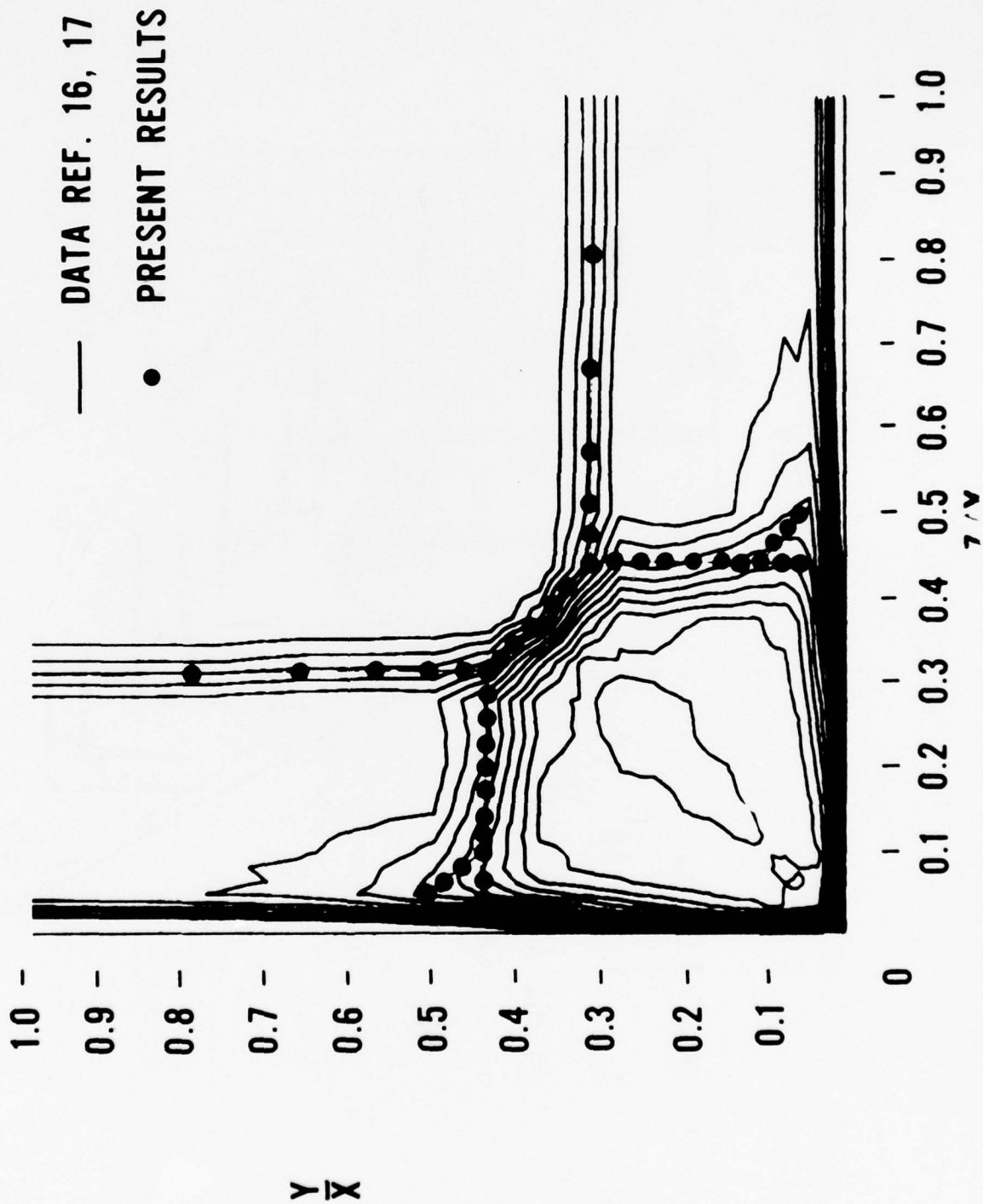
2 OF 5

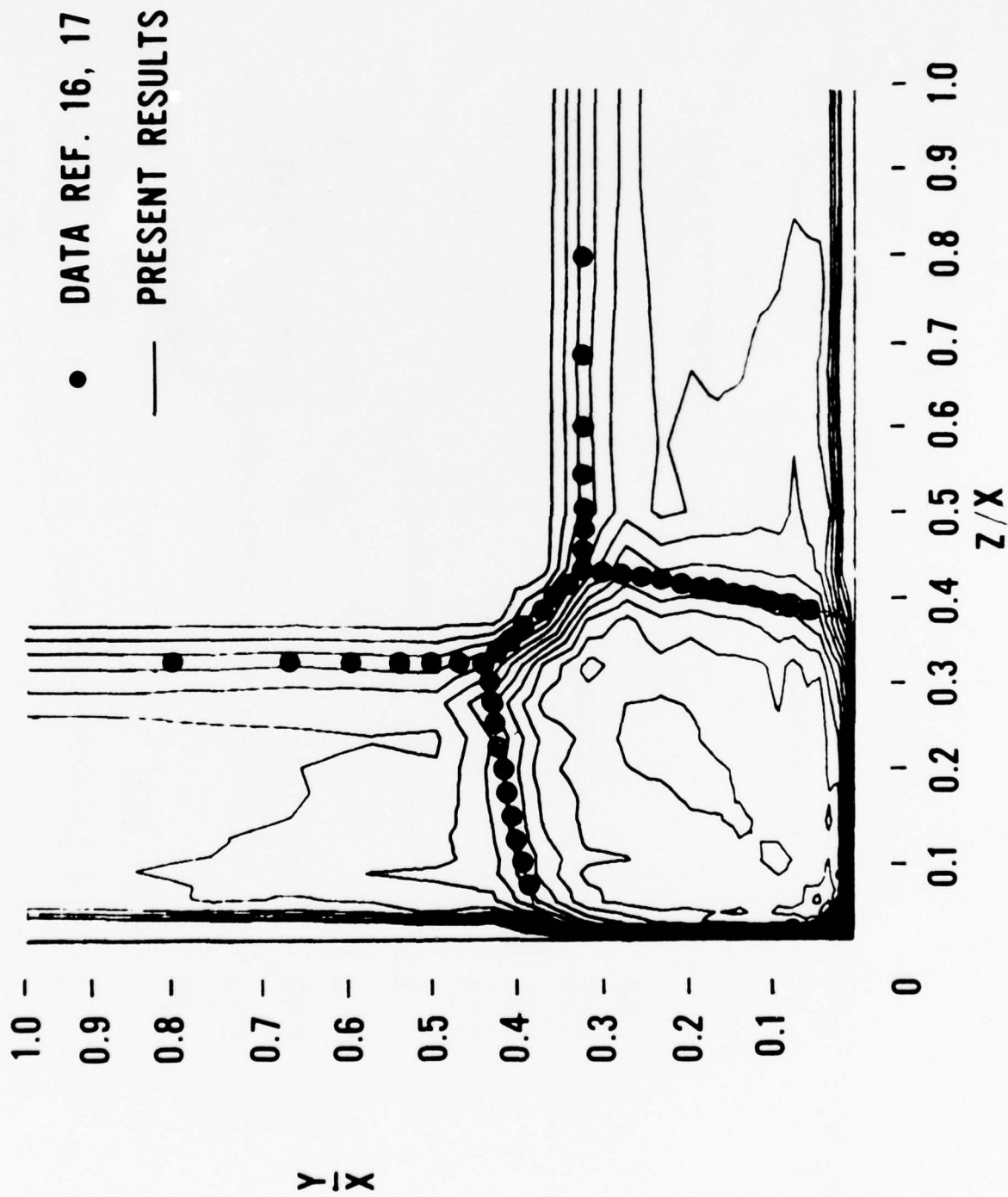
AD
A061086



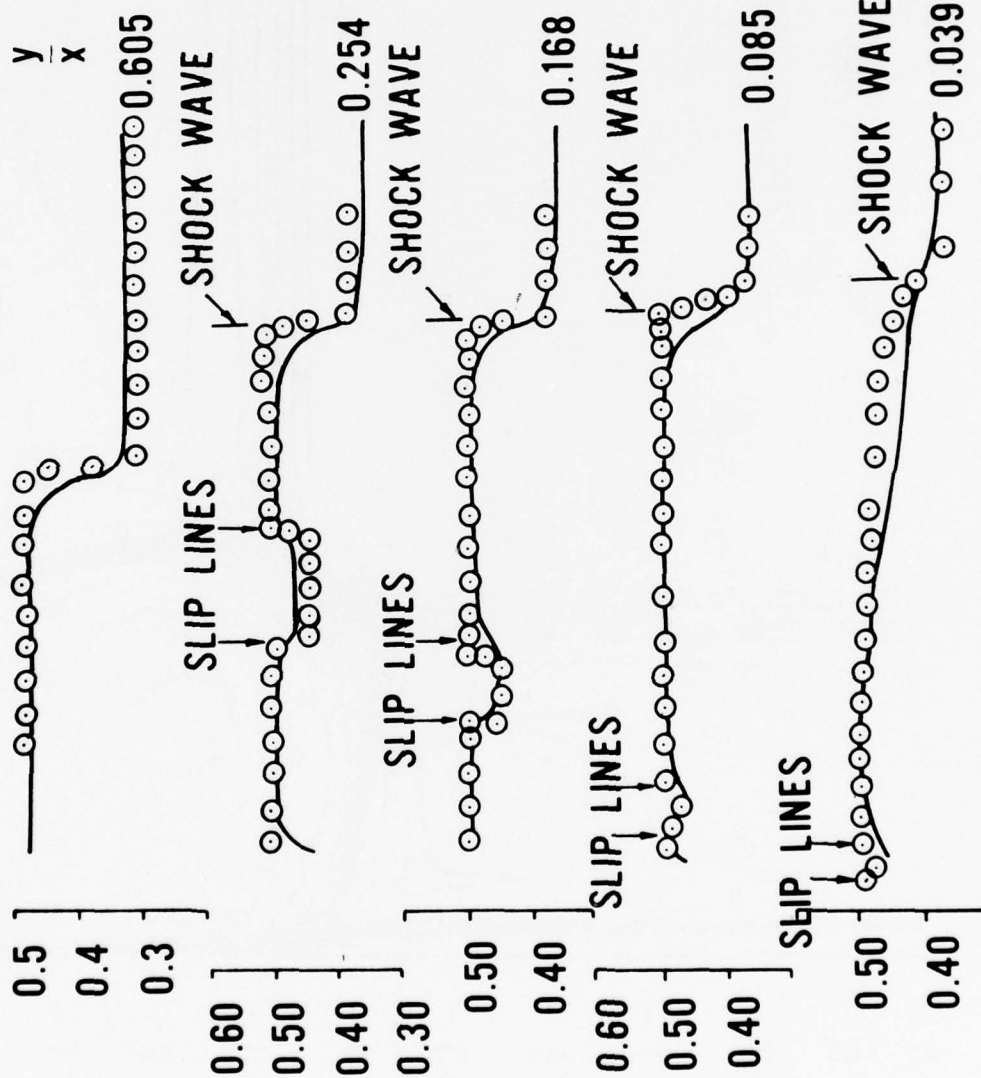


$M_{\infty} = 3.0$
 $Re_L = 1.10 \times 10^6$
 WEDGE ANGLE 9.48°





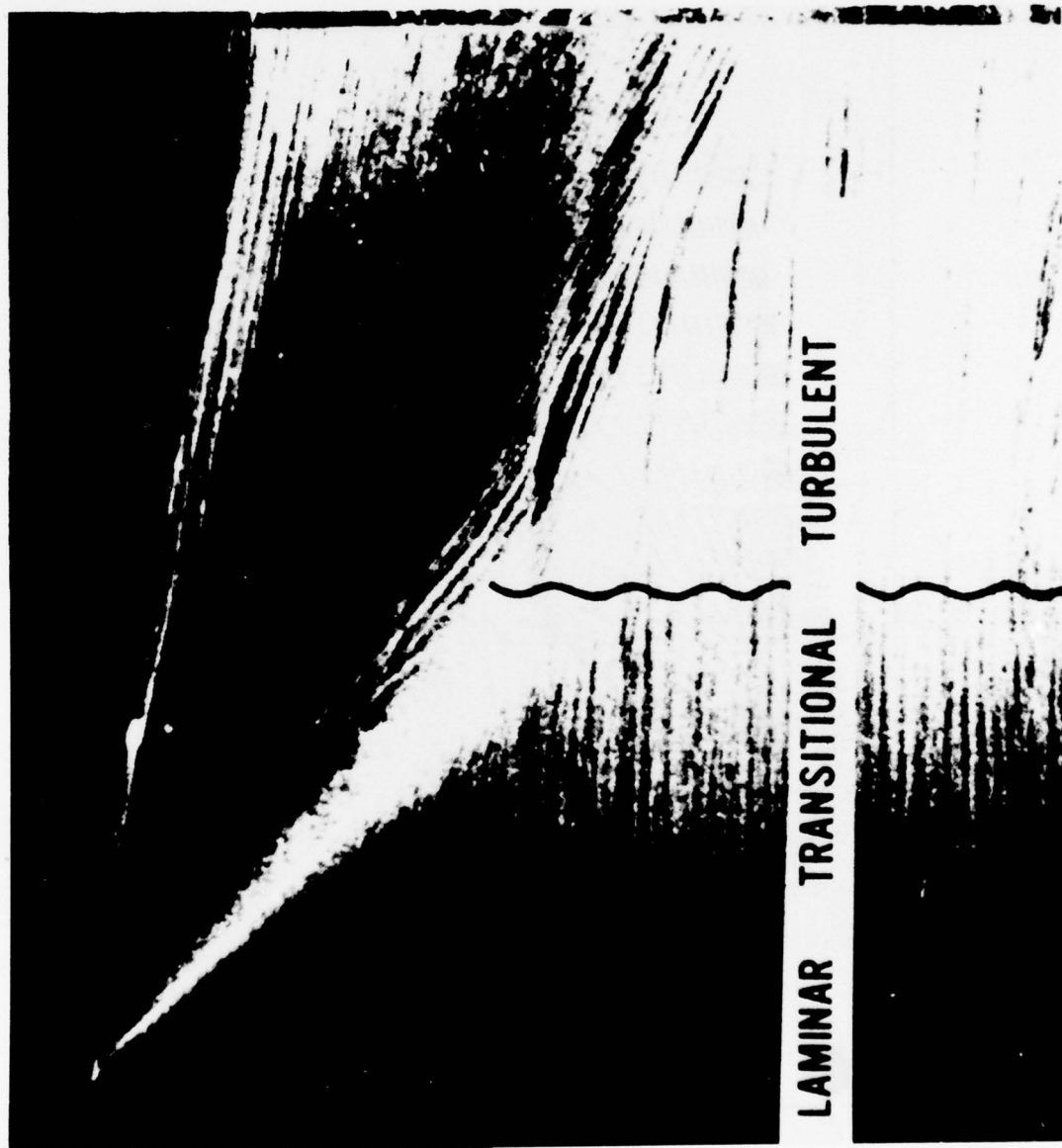
P_T/P_0

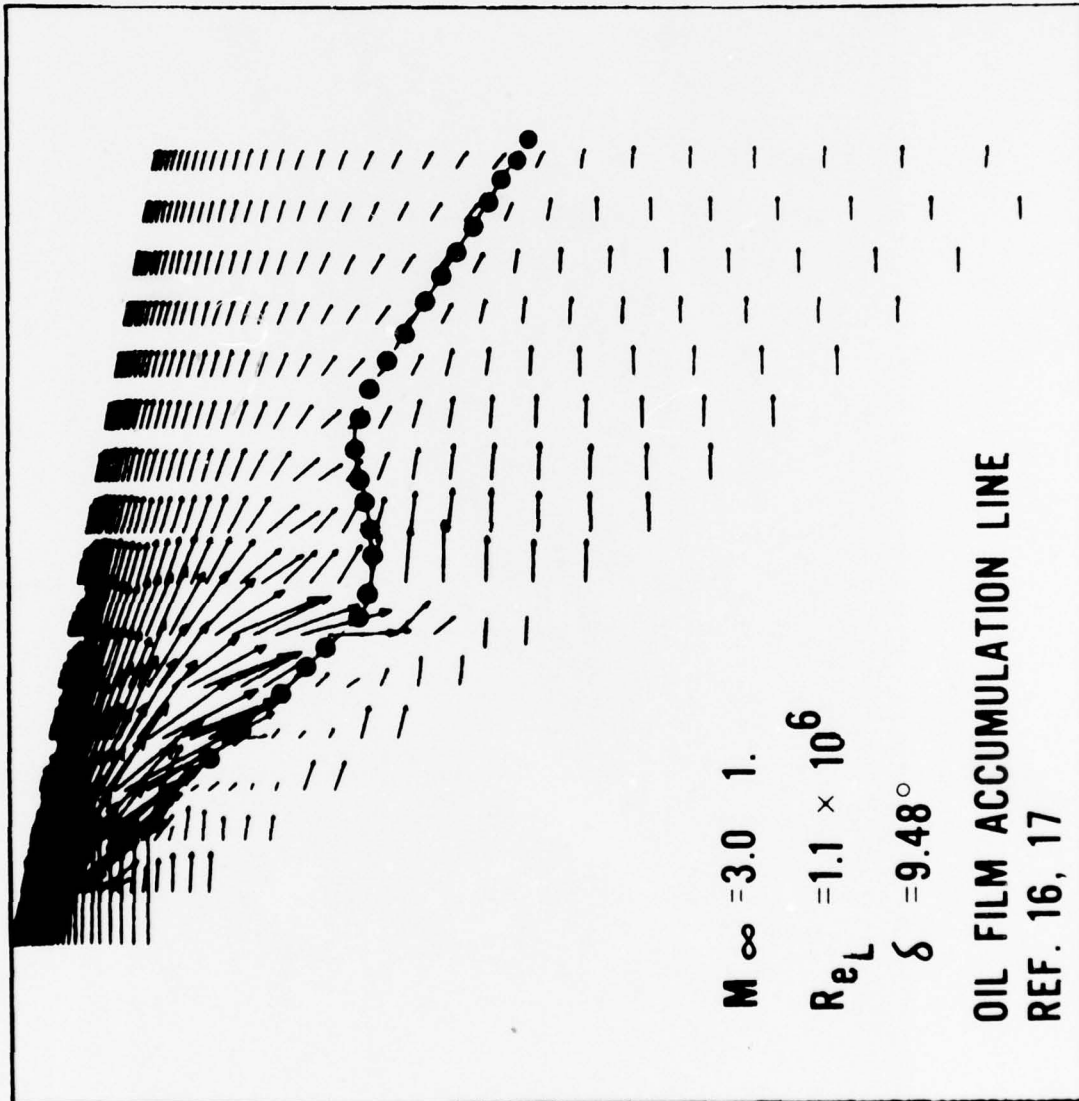


DATA
REF.
16, 17

PRESENT
RESULTS

0 0.1 0.2 0.3 0.4 0.5 0.6 y/x





Three-Dimensional Boundary-Layer Calculation on Bodies

by

R. Grundmann

DFVLR-Institut für Angewandte Gasdynamik, Köln

Summary

A surface oriented coordinate system is being constructed in order to calculate the boundary layer on bodies. A special treatment is being made in the stagnation point region and in the planes of symmetry. The boundary-layer equations in holonomic form, and the finite difference formulation are being discussed shortly. Sample calculations are given.

1. Introduction

In order to calculate the three-dimensional boundary layer on bodies at high angle of attack the attempt was made to solve the governing boundary-layer equations in surface-oriented coordinate systems. The advantage to a streamline oriented coordinate-system is that there is no interface program necessary to solve the stream and potential lines on the body surface from the inviscid flow data separately for each angle of attack.

In this study two surface-oriented coordinate systems have to be connected as shown in Fig. 1 due to the parabolic nature of the problem. Since from the inviscid data the location of the stagnation point is known, the origin of the Cartesian coordinate system can be placed there, so that the x'^1 -axis is parallel to the main axis of the body. This, additionally, means that the Cartesian coordinate system lies in the plane of symmetry of the body.

The concept of the solution procedure allows no yaw-angle, because the flow conditions on the symmetry lines are used to compute the boundary values by means of a separate quasi two-dimensional symmetry-line program. The symmetry-line program itself is

started with the data from a stagnation-point program. These additional programs are described in Ref. [1].

The governing equations are prepared to describe the incompressible or compressible, laminar or turbulent boundary-layer equations for three-dimensional flows. The turbulence model is a first order closure model by MICHEL.

2. Governing Equations

2.1 Geometrical Conditions

If one considers for simplicity an ellipsoid of revolution at an angle of attack as shown in Fig. 2, the coordinate system in the nose region consists of the coordinate lines x_N^1 that lie in planes parallel to Cartesian planes $x^2 = \text{const}$, and the coordinate lines x_N^2 that lie in planes parallel to Cartesian planes $x^3 = \text{const}$. The coordinate axis x_N^3 always is straight and erected perpendicular to the surface. So the coordinate system at the nose is curved and non-orthogonal concerning the surface coordinates.

The coordinate system in the body region consists of curved but orthogonal surface-coordinate axes, because the axes x_B^1 run along the body surface while the angle with the $x^2 = 0$ plane is constant until the end of the body. The axes x_B^2 run parallel to the Cartesian x^3 planes. Again the x_B^3 coordinate is straight and erected perpendicular to the surface. This system is comparable to the polar coordinate system.

From Fig. 3 the geometrical conditions can be formulated for both systems on arbitrary bodies in connection to the Cartesian reference system in the following way:

nose geometry

$$x^{1*} = - \int_0^{x_N^1} \cos \theta(x_N^1, x_N^2) dx_N^1 + \int_0^{x_N^2} \cos \gamma(x_N^1, x_N^2) dx_N^2$$

$$x'^2 = - \int_{x_N^1}^{x_N^2} \sin \psi(x_N^1, x_N^2) dx_N^2$$

$$x'^3 = \int_{x_N^1}^{x_N^2} \sin \psi(x_N^1, x_N^2) dx_N^1$$

body geometry

$$x'^1 = \int_0^{x_B^1} \left\{ 1 + \left[\frac{dr(x_B^1, x_B^2)}{dx'^1} \right]^2 \right\}^{-\frac{1}{2}} dx_B^1$$

$$x'^2 = -r(x_B^1, x_B^2) \sin x_B^2$$

$$x'^3 = r(x_B^1, x_B^2) \cos x_B^2 + x_M^3$$

The angles Θ and ψ are defined in Fig. 3, the lengths x_M^1 and x_M^3 give the location of the centre of the ellipsoid with regard to the location of the stagnation point, and r is the radius from the axis of rotation x'^1 to the surface of the body. Θ , ψ and r are functions of x_N^1 or x_B^2 .

2.2 Metric Tensor

In the following the case of the sphere and the ellipsoid with zero angle of attack will be described in its metric properties, and used in the numerical tests. That means the body coordinate system first will be dominate.

The components a_{ij} of the metric surface tensor are necessary for the computation of the factors k_{ij} which appear in the governing equations.

$$|a_{ij}|_B = \begin{vmatrix} \cos^2 \Omega + \left(\frac{dr}{dx_B^1} \right)^2 & 0 \\ 0 & r^2 \end{vmatrix}$$

$$\cos^2 \Omega = \frac{1}{\sqrt{1 + \left(\frac{dr}{dx^n}\right)^2}}$$

2.3 Boundary-Layer Equations

The three-dimensional boundary-layer equations for compressible flows around bodies are formulated in the contravariant tensor notation, so that the equations are in holonomic form.

continuity equation

$$\frac{\partial}{\partial x^1} (h_{01} g v^1) + \frac{\partial}{\partial x^2} (h_{01} g v^2) + \frac{\partial}{\partial x^3} (h_{01} g v^3) = 0$$

$$h_{01} = (a_{11} a_{22} - a_{12}^2)^{\frac{1}{2}}$$

x¹-momentum equation

$$\begin{aligned} & \rho \left[v^1 \frac{\partial v^1}{\partial x^1} + v^2 \frac{\partial v^1}{\partial x^2} + v^3 \frac{\partial v^1}{\partial x^3} + h_{11} (v^1)^2 + h_{12} v^1 v^2 + h_{13} (v^1)^2 \right] = \\ & = h_{14} \frac{\partial p}{\partial x^1} + h_{15} \frac{\partial p}{\partial x^2} + \frac{\partial}{\partial x^3} \left(\mu \frac{\partial v^1}{\partial x^3} \right) \end{aligned}$$

$$h_{11} = \frac{1}{2 h_{01}^2} \left[a_{22} \frac{\partial a_{11}}{\partial x^1} - a_{12} \left(2 \frac{\partial a_{12}}{\partial x^1} - \frac{\partial a_{11}}{\partial x^2} \right) \right]$$

$$h_{12} = \frac{1}{h_{01}^2} \left[a_{22} \frac{\partial a_{11}}{\partial x^2} - a_{12} \frac{\partial a_{22}}{\partial x^1} \right]$$

$$h_{13} = \frac{1}{2 h_{01}^2} \left[a_{22} \left(2 \frac{\partial a_{12}}{\partial x^2} - \frac{\partial a_{22}}{\partial x^1} \right) - a_{12} \frac{\partial a_{22}}{\partial x^2} \right]$$

$$h_{14} = - \frac{a_{22}}{h_{01}^2}$$

$$h_{15} = \frac{a_{12}}{h_{01}^2}$$

x^2 - momentum equation

$$\rho \left[v^1 \frac{\partial v^1}{\partial x^1} + v^2 \frac{\partial v^2}{\partial x^2} + v^3 \frac{\partial v^2}{\partial x^3} + h_{21} (v^1)^2 + h_{22} v^1 v^2 + h_{23} (v^3)^2 \right] =$$

$$= h_{15} \frac{\partial p}{\partial x^1} + h_{25} \frac{\partial p}{\partial x^2} + \frac{\partial}{\partial x^3} \left(\mu \frac{\partial v^2}{\partial x^3} \right)$$

$$h_{21} = \frac{1}{2 h_{01}^2} \left[a_{11} \left(2 \frac{\partial a_{12}}{\partial x^1} - \frac{\partial a_{11}}{\partial x^2} \right) - a_{12} \frac{\partial a_{11}}{\partial x^1} \right]$$

$$h_{22} = \frac{1}{h_{01}^2} \left[a_{11} \frac{\partial a_{12}}{\partial x^1} - a_{12} \frac{\partial a_{11}}{\partial x^2} \right]$$

$$h_{23} = \frac{1}{2 h_{01}^2} \left[a_{11} \frac{\partial a_{12}}{\partial x^2} + a_{12} \left(\frac{\partial a_{12}}{\partial x^1} - 2 \frac{\partial a_{11}}{\partial x^2} \right) \right]$$

$$h_{25} = - \frac{a_{11}}{h_{01}^2}$$

energy equation

$$c_p \rho \left[v^1 \frac{\partial T}{\partial x^1} + v^2 \frac{\partial T}{\partial x^2} + v^3 \frac{\partial T}{\partial x^3} \right] = \frac{1}{Pr} \frac{\partial}{\partial x^3} \left(k \frac{\partial T}{\partial x^3} \right) + E_c \left(v^1 \frac{\partial p}{\partial x^1} + v^2 \frac{\partial p}{\partial x^2} \right)$$

$$+ E_c \mu \left[h_{41} \left(\frac{\partial v^1}{\partial x^3} \right)^2 + h_{42} \frac{\partial v^1}{\partial x^3} \frac{\partial v^2}{\partial x^3} + h_{43} \left(\frac{\partial v^2}{\partial x^3} \right)^2 \right]$$

$$h_{41} = a_{11}$$

$$h_{42} = 2 a_{12}$$

$$h_{43} = a_{22}$$

Herein x^i and v^i ($i = 1, 2, 3$) are the coordinate axes and the contravariant velocity components, respectively, T , ρ and p are the temperature, the density and the

pressure. The quantities μ and k are the viscosity and the heat conductivity, c_p is the specific heat at constant pressure and Pr and Ec are the Prandtl-Number and the Eckert-Number. The k_{ij} are the metric factors. This set of differential equations is described in Ref. [2].

The turbulence first order closure model used is described in Ref. [3]

$$\mu_{turb} = \frac{\bar{\mu}_{turb}}{\mu_{\infty}} \sqrt{Re} \, g \, F^2 l^2 \left| \frac{\partial v^1}{\partial x^3} \right|$$

with the mixing length

$$l = g \cdot 0.085 \tanh \left(\frac{\kappa}{0.085} \frac{x^3}{g} \right)$$

and the van-Driest damping factor

$$F = 1 - \exp \left[- \frac{l}{26 \kappa \mu_w} \sqrt[4]{Re} \sqrt{(g\tau)_w} \right]$$

$\kappa = 0.41$ is the von-Kármán constant. The turbulent heat conductivity is

$$\bar{k}_{turb} = \frac{\bar{k}_{turb}}{\bar{k}_{\infty}} = \frac{Pr_{\infty}}{Pr_{turb}} c_p \mu_{turb} \quad c_p = \frac{\bar{c}_p}{c_{p\infty}} = 1$$

The barred quantities are dimensional, the index ∞ means infinity. In the governing equations μ and k are effective ones if turbulent flow is to be calculated:

$$\mu = \mu_{eff} = \mu_{lam}(T) + \mu_{turb}$$

$$k = k_{eff} = k_{lam}(T) + k_{turb}$$

For the laminar transport properties the Sutherland formulation is used.

3. First Numerical Results

3.1 Discretization and Solution Scheme

The in various investigations successfully used, for example Ref. [4], implicit Zick-Zack-scheme of KRAUSE, HIRSCHL, BOTHMANN is being applied in this investigation. It was preferred because it has a very large domain of dependence, and can be used even if a very strong skewing of the stream surfaces of the boundary layer occurs.

The solution scheme is the RICHTMYER algorithm applied to a three component solution vector consisting of the two velocity components and the temperature. The normal velocity component is computed separately by integrating the continuity equation. One iteration is necessary at minimum.

3.2 Laminar and Turbulent Flow around a Sphere

Although the cross flow around a sphere for the coordinate system used is zero the fully three-dimensional program was run to test its feasibility and accuracy. This was done by first computing the stagnation point solution, which was used as an initial condition for the quasi-two-dimensional symmetry-line computations. These results now were taken to be the boundary values on both symmetry lines for the body boundary-layer calculations. The procedure is started at the lower symmetry line until it meets the upper. The initial values around the half body were taken from the stagnation point solution.

The results are shown in Fig. 4 and give good agreement in the laminar case through out the whole field compared to SCHLICHTING's results. The turbulent case again is in good agreement with the expected results.

4. Concluding remarks

At present time the laminar or turbulent, incompressible or compressible three-dimensional boundary-layer calculations for a body of revolution with zero angle of attack can be carried out. Although there is no cross-flow under these conditions the fully three-dimensional procedure was run in order to prove its feasibility and accuracy.

Calculations for bodies at angle of attack are underway. In this case additionally the metric of the coordinate system fixed at the nose of the body, Fig. 3, has to be introduced. The other parts of the calculation procedure remain unchanged.

5. References

- [1] E. H. Hirschel, D. Schwamborn: "Ein Verfahren zur Berechnung von Grenzschichten in Strömungssymmetrieebenen", DLR-FB 77-16, 1977.
- [2] E. H. Hirschel: "Boundary-Layer Equations in Holonomic Formulation", Proc. International Conference on Numerical Methods in Laminar and Turbulent Flow", Swansea, July 18-21, 1978, Pentech Press, London.
- [3] R. Michel, C. Quemard, R. Durant: "Application d'un schéma de longueur de mélange à l'étude des couches limites turbulentes d'équilibre", ONERA, Note Techn. 154, 1969.
- [4] E. H. Hirschel, V. Jawtusch: "Some Investigations for the Evaluation of Stability and Transition Criteria for Boundary Layers on Swept Wings", Proc. 5. DEA-Meeting Boundary-Layer Effects, April 28-29, 1976, Dayton, AFFDL-TR-77-61 (1977).

6. Figures

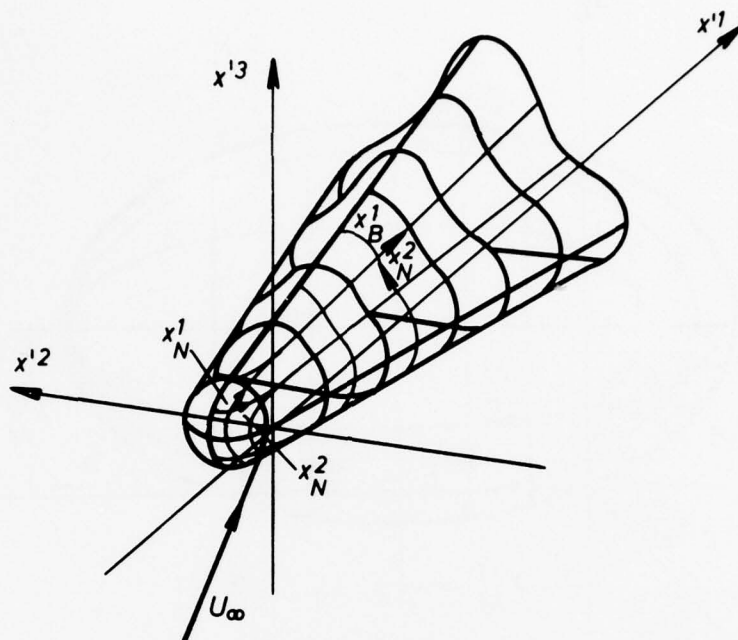


Fig. 1 Surface oriented coordinate systems on arbitrary body configuration at angle of attack.

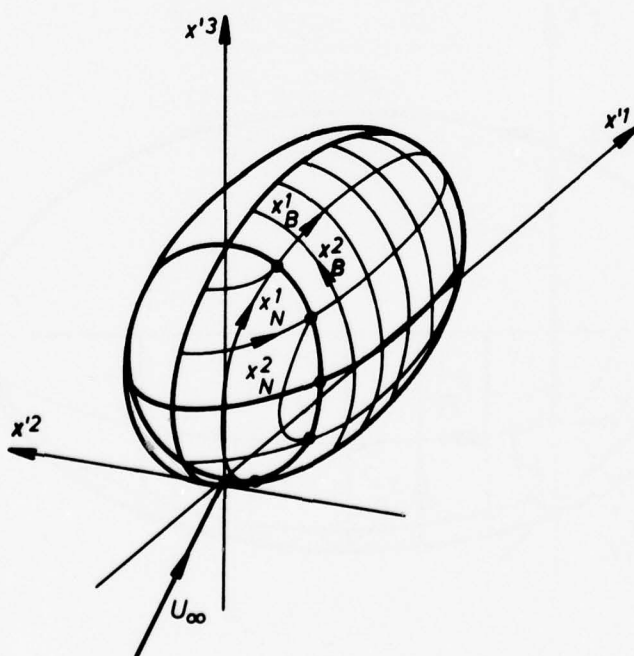


Fig. 2 Surface oriented coordinate systems on an ellipsoid at angle of attack.

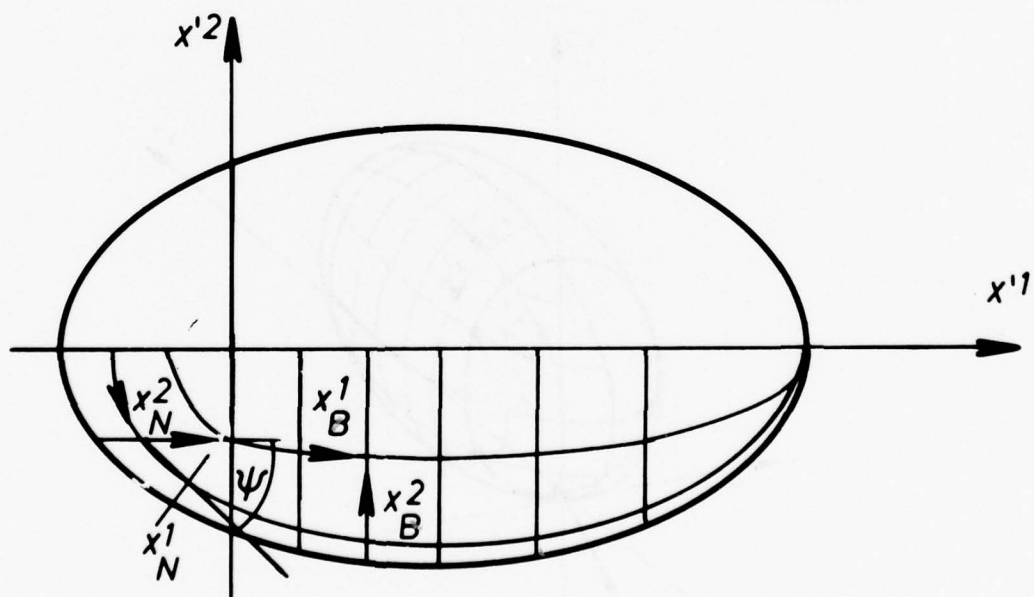
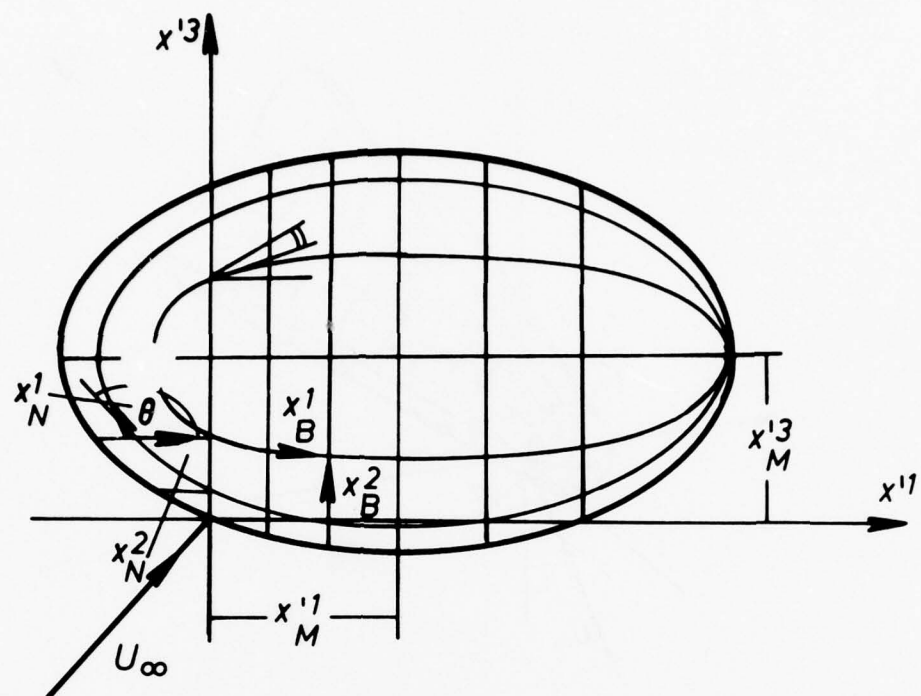


Fig. 3 Geometrical condition for an ellipsoid at angle of attack.

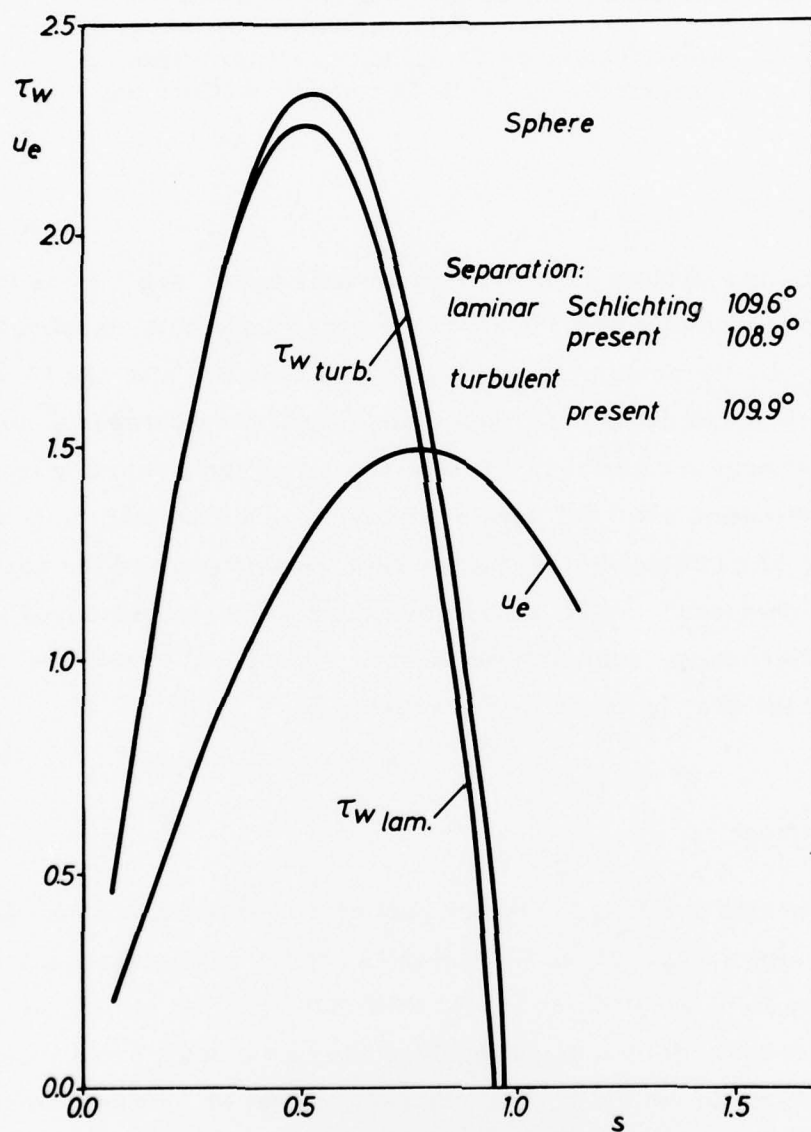


Fig. 4 Laminar and turbulent wall shear stress on a sphere.

EXPERIMENTAL STUDY OF THE FLOW ALONG A BODY OF REVOLUTION

by

H. Bippes

Deutsche Forschungs- und Versuchsanstalt
für Luft- und Raumfahrt E. V.
Aerodynamische Versuchsanstalt Göttingen
Bunsenstraße 10, 3400 Göttingen, W-Germany

Abstract

The flow along a prolate spheroid with the axis ratio $a:b = 6$ is investigated experimentally with the aid of the hydrogen bubble visualization method, in the Reynolds number range of 0.125×10^6 and 3×10^6 . For all the tests the model is set at small angles of attack between 0° and 10° . The experiments are performed in a water towing tank. Starting from the forward stagnation point the flow is followed up to the laminar-turbulent transition. The influence of stagnation flow instabilities and the angle of attack are discussed. As far as possible the results are compared with the available results from laminar theory. Theoretical results for the turbulent case are, however, not available.

1. Introduction

The experiments presented here are part of the longterm 3-d boundary layer research project of the DFVLR-AVA, which is described more extensively by H. U. MEIER and H. -P. KREPLIN [1]. The aim of the present work is essentially a visual study of the flow along a prolate spheroid with the axis ratio $a:b = 6$, i. e. the same model which was primarily chosen for practical reasons also by H. U. MEIER and H. -P. KREPLIN [1]. To give the flow around the axisymmetric body a real three-dimensionality

it was set at moderate angles of attack between 0° and 10° .

The points of special interest are:

1. The flow in the stagnation region at different angles of attack and at different Reynolds numbers as well as some associated boundary layer instabilities.
2. The laminar to turbulent transition as a function of the angle of attack and the Reynolds number.
3. Flow separation
 - a) boundary layer separation,
 - b) separation of vortex sheets along the body at incidence.

The experiments are performed in a water towing tank, which is particularly suitable for flow visualization. Furthermore the disturbance level of the oncoming flow is exceedingly small as a consequence of the fact, that in such a facility the fluid is at rest while the model is towed.

The work has just been started and therefore only initial results found with the hydrogen bubble visualization method can be reported.

The shortcoming of these tests is that it was not possible so far to fix the location of the stagnation point completely.

2. The Experimental Set-Up

The water-tank, used for the tests (Fig. 1), has a cross-section of 1.1×1.1 m and a length of 18 m. For the isolation of external vibrations the basin with the water at rest is placed on a separate foundation. In addition damping elements are used between the supports and the tank. The glass walls of the tank allow the observation of the flow at different

positions. The model towing carriage runs on rails, which are mounted above the tank on separate bearings. They are adjusted horizontally and for straightness within an accuracy of 0.02 mm/m length.

The motive force is transferred to the towing trolley by means of an endless rope drive from a DC machine of the shunttype. The controlled towing speed can be varied continuously between 0.01 and 5 m/s . At each position it is set with an accuracy of 0.1% .

The prolate spheroid chosen for the tests has a ratio of axes of $a:b = 6$ and a major axis length of $2a = 1.02 \text{ m}$. It is made of acryl glass and composed of three removable parts so that it is possible to introduce pressure transducers, surface hot films as well as ducts and cables into the interior. For accuracy smoothness and transparency the surface was finally polished on its mount.

The model supporting device allows the arbitrary variation of the angle of attack between $0^\circ - 35^\circ$. The Reynolds number based on the major axis is varied with the towing speed between $Re = 1.25 \times 10^5$ and 3×10^6 to study the laminar and transition cases. For future experiments the Reynolds number will be raised to 5×10^6 .

For fixing the strut 3% of the model length is cut off, so that the study of the separation at the end is somewhat limited.

Up to now the model is freely suspended on a strut without using any supporting wires to avoid perturbation of the flow through the wake of such wires. That means low frequency oscillations ($\approx 3 \text{ Hz}$) cannot be avoided completely. For more detailed investigations especially in the stagnation region, this oscillations have to be suppressed.

3. The Measuring Method

Up to now the results are obtained with the aid of the hydrogen bubble visualization method. The hydrogen bubbles are produced on a cathode wire of 0.03 mm in diameter which is soldered between the ends of a fork shaped probe support. In most cases the probe is placed in front of the model (Fig. 1). By shifting it perpendicular to the plane of symmetry of the flow the hydrogen bubbles can be brought into flow areas of different distances from the model surface.

For the qualitative display of the velocity distribution the hydrogen bubbles are produced in different ways (Fig. 2):

1. Continuously on a straight cathode wire: The bubble sheet then produced gives an overview on flows with sudden local velocity differences.
2. Continuously on a kinked cathode wire: The bubbles leaving only at the rearward tips, so that discrete bubble lines are formed. In stationary flows these streak lines are identical with streamlines.
3. Intermittently on a straight wire: With this method the so-called timelines are produced. Together with the streamlines the timelines display the detailed velocity distribution in the flow field. Velocity determination from the photographs is possible [2], [3].

4. Experimental Results

For the correct interpretation of detailed measurements of turbulent structures and correlation coefficients, the special features of the flow along the prolate spheroid has to be taken into account. Some of them are given in the following.

4.1 The Flow in the Stagnation Area

From the hot wire measurements of N. A. V. PIERCY [4] and A. M. KUETHE et al. [5] we know that the rms values of the velocity fluctuations are amplified while approaching the stagnation zone. Furthermore we know from numerous experiments, e. g. [6], [7], [8], that near the stagnation line of cylindrical bodies an amplified streamwise vortex instability develops several degrees around the cylinders and induces substantial three-dimensional effects into the boundary layer.

For the stagnation flow on blunt nosed bodies of revolution the experimental evidence is much less at least for the subsonic range. But the streamwise striation patterns in the coating of the models tested by L. N. PERSEN [9] and the experiments of H. HASSLER [10] on a circular cone may give some indication of the existence of this instability also in the stagnation region of bodies of revolution in subsonic flows. The reason why there has not yet been more success with blunt nosed bodies of revolution may be seen in the random wandering of the stagnation point [5] as well as in the small extent of the instability region.

Also in the experiments described here the wandering of the stagnation point could not be prevented may be as consequence of larger scale disturbances caused by low frequency oscillations of the model. Streamwise vortex streets as on cylinders in cross-flow could not be seen. Fig. 3, for instance shows the bubble configuration representing the laminar flow disturbed by Taylor-Görtler vortices across a circular cylinder. This picture is taken from a study of P. ČOLAK-ANTIĆ [7], who did his experiments in the same facility. The hydrogen bubbles are generated continuously on a straight cathode wire placed close and parallel to the stagnation line. The Taylor-Görtler instability i. e. the counterrotating vortex pairs with axes in the streamwise direction manifest themselves through the spanwise bubble density variations.

Fig. 4 shows now the flow in the stagnation region of the prolate spheroid. The hydrogen bubbles originate continuously on a cathode wire which is placed upstream of the stagnation point close to a plane of symmetry. A continuous bubble sheet develops behind the cathode wire. No striations like in Fig. 3 or any other disturbances can be visualized (Fig. 4a). For Fig. 4b a turbulence level of 1 % was superposed to the oncoming flow by towing a turbulence screen before the model like P. ČOLAK-ANTIĆ [7] did it. Correspondingly the bubble sheet behind the cathode wire shows a gross but still a homogeneous structure. That means at the Reynolds number range of these tests stagnation flow instabilities could not be observed but a final statement on this point must await future attempts to stabilize the stagnation point. If it is the Taylor-Görtler mechanism, which causes the instability on cylinders then it should also appear on bodies of revolution because this mechanism applies equally to both types of stagnation flow. If it is the mechanism explained by P. R. HODSON et al. [8] then it may be different for the two different configurations. The angle of attack has no influence in the range $0^\circ \leq \alpha \leq 10^\circ$.

4.2 Laminar to Turbulent Transition

Over the slender prolate spheroid used for these experiments after the point of maximum thickness there is only a low pressure gradient up to the last 15 % of the length. So the boundary layer must be laminar up to Reynolds numbers in the order of magnitude of the transition Reynolds number of a flat plate at zero incidence i. e. $Re_x = 2.8 \times 10^6$ (based on the distance from the leading edge). Fig. 5a shows the boundary layer at a Reynolds number of $Re = 1.5 \times 10^6$. It is completely laminar up to the rearward separation. At the Reynolds number of 2.5×10^6 (Fig. 5b) single disturbances of turbulent spots travel downstream but the final transition takes place only just at the rearmost 10 % of the model.

As a comparison Fig. 5c shows a completely turbulent boundary layer. For this picture the turbulence was forced by a trip wire. On the model at incidence, with the angle of attack $\alpha = 5^\circ$ the situation is only slightly different (Fig. 6a). On the pressure side the boundary layer remains laminar up to the highest Reynolds numbers of the tests. On the suction side the transition area has moved upstream, but as the separation point simultaneously travels upstream the region with a fully developed boundary layer is not very much extended. Only along the streamwise zones where the free vortex layer separates we have turbulence already at moderate Reynolds numbers.

At an angle of attack of 10° these turbulent zones are still more extended (Fig. 6b) compared to the case of $\alpha = 5^\circ$. The body vortices, however, create areas of different stability (Fig. 7). On the suction side between the two vortices the boundary layer stability is enhanced whereas along the streamwise zone where the vortex sheet separates, the laminar to turbulent transition takes place farther upstream.

4.3 Flow Separation

On the prolate spheroid we observe two types of separation, the usual boundary layer separation with backflow and the separation of a free vortex sheet on the model at incidence. Separation bubbles in the neighbourhood of the stagnation point could not be detected. The flow in this area is well attached up to an angle of attack of $\alpha = 10^\circ$, the highest value in these experiments, as may be seen in Fig. 8.

4.3.1 Boundary Layer Separation

The ordinary boundary layer separation takes place on the rearward part of the model. In the laminar case, Fig. 9, the separation point travels

downstream with growing Reynolds numbers, but the location found in W. GEISLER's laminar theory [11] is not reached completely. This is of course not a surprising result because Geissler introduces the boundary layer approximations in his theory.

Fig. 10 gives the rearward boundary layer separation at the angles of attack of 0° , 5° and 10° for the same Reynolds number. It illustrates the dependence on the angle of attack.

In Fig. 11 the laminar and turbulent separations for the same Reynolds number are compared. In Fig. 11b the turbulence was forced by a trip wire. No essential difference is to be seen. It is surprising that the turbulence is spreading across the boundary layer. Maybe that the diameter of the trip wire was too large. - The Reynolds number based on the diameter k of the trip wire

$$Re = \frac{k \cdot U}{\nu} \geq 1200$$

that means it is larger than $Re = 900$, the lowest value at which turbulence is produced at any position in the boundary layer.

On the model at incidence (Fig. 11c) the spreading of turbulence is further increased. The separation point has now moved upstream. Fig. 11d shows the turbulent separation at a larger Reynolds number ($Re = 3 \times 10^6$). No trip wire was used. The comparison with Fig. 11c indicates that qualitatively there is no difference between forced and natural turbulence as far as separation and the spreading of turbulence are concerned.

4. 3. 2 Separation of a Free Vortex Layer

Corresponding to the calculations of W. GEISLER [11] on a prolate spheroid a free vortex layer separates on the sides of the body already at an

angle of attack of $\alpha = 5^\circ$. This value is also in the range of that one for which E. A. EICHELBRENNER [12] predicts the begin of the separation.

Fig. 12 with a view perpendicular of the suction side shows the rollup of the free vortex sheet. At an angle of attack of $\alpha = 5^\circ$, Fig. 12a, the intensity of the vortex sheet is very low but the inward bulge of the timelines in the rearward part of the model shows that the rollup of the free vortex sheet has already begun. In Fig. 12b at an angle of attack of $\alpha = 10^\circ$ the manifestation of the rollup becomes more pronounced. In this picture the timelines show the flow closer to the vortex axes.

5. Conclusion

Near the stagnation point the flow around the slender prolate spheroid with the axis ratio $a:b = 6$ is laminar and well attached up to $\alpha = 10^\circ$ and $Re = 3.0 \times 10^6$ the highest incidence and the largest Reynolds number of the tests. Only along the streamwise zones where the free vortex layer separates the laminar to turbulent transition and the boundary layer separation moves farther upstream.

Below $Re = 3 \times 10^6$ the final laminar to turbulent transition takes place not before the rearmost 15 % of the model although at this Reynolds number single turbulent spots originating behind the point of maximum thickness travel downstream.

As already mentioned in the forward part of the model the boundary layer is well attached. Separation bubbles are not to be seen at the angles of attack of these tests. The separation on the rearward part of the model depends on the Reynolds number and the angle of attack.

The rollup of free vortex layers of finite, i. e. measureable strength are already observed at an incidence of 5 degrees. They have an asymmetric effect on the boundary layer transition.

6. References

- [1] MEIER, H. U.
KREPLIN, H. -P. Pressure Distributions and Flow Visualisations on an Ellipsoid 1: 6 Designed for Three-Dimensional Boundary Layer Investigations.
DEA-7440 "Viscous and Interacting Flow Field Effects Naval Post" Graduated School, Monterey/Calif. (1978).
- [2] SCHRAUB, F. A.
KLINE, S. J.
HENRY, J.
RUNSTADLER (Jr.), P. W.
LITELL, A. Use of Hydrogen Bubbles for Qualitative Determination of Time Dependant Velocity Fields in Low Speed Water Flows.
Report MD-10, Thermoscience Riv. Mech. Engr. Dept., Stanford University, 1964.
- [3] BIPPES, H. Eine photogrammetrische Methode zur Messung dreidimensionaler Geschwindigkeitsfelder in einer mit Wasserstoffbläschen sichtbar gemachten Strömung.
DLR-FB 74-37 (1974).
- [4] PIERCY, N. A. V.
RICHARDSON, E. G. The Turbulence in Front of a Body Moving Through a Viscous Fluid.
Phil. Mag. 9 (1930), pp. 1038-1041.
- [5] KUETHE, A. M.
WELLMARTH, W. W.
CROCKER, G. H. Stagnation Point Fluctuations on a Body of Revolution.
Phys. Fluids 2, 714 (1960).
- [6] KESTIN, J.
WOOD, R. T. On the Stability of Two-Dimensional Stagnation Flow.
J. Fluid Mech. 44 (1970), pp. 461-479.
- [7] ČOLAK-ANTIĆ, P. Visuelle Untersuchungen von Längswirbeln im Staupunktgebiet eines Kreiszylinders bei turbulenter Anströmung.
DLR-Mitt. 71-13 (1971), S. 194-220.

- [8] HODSON, P. R.
NAGIB, H. M.

Longitudinal Vortices Induced in a Stagnation Region by Wakes - Their Incipient Formation and Effects on Heat Transfer from Cylinders.

Ill. Inst. Techn. Fluids and Heat Transfer, Report R 75-2 (1975).
- [9] PERSEN, L. N.

Exploratory Experiments in Water on Streamwise Vortices

ARL 69-0160 (1969).
- [10] HASSLER, H.

Experimentelle Untersuchung von Längswirbeln im vorderen Staupunktgebiet eines Kreiskegels in axialsymmetrischer Anströmung.

DLR-FB 76-31 (1976).
- [11] GEISSLER, W.

Berechnung der dreidimensionalen laminaren Grenzschicht an schräg angeströmten Rotationskörpern mit Ablösung.

Ing. -Arch. 43 (1974), S. 413-425.
- [12] EICHELBRENNER, E. A.

Décollement laminaire en trois dimensions.

Publication ONERA Paris, No. 89 (1957).

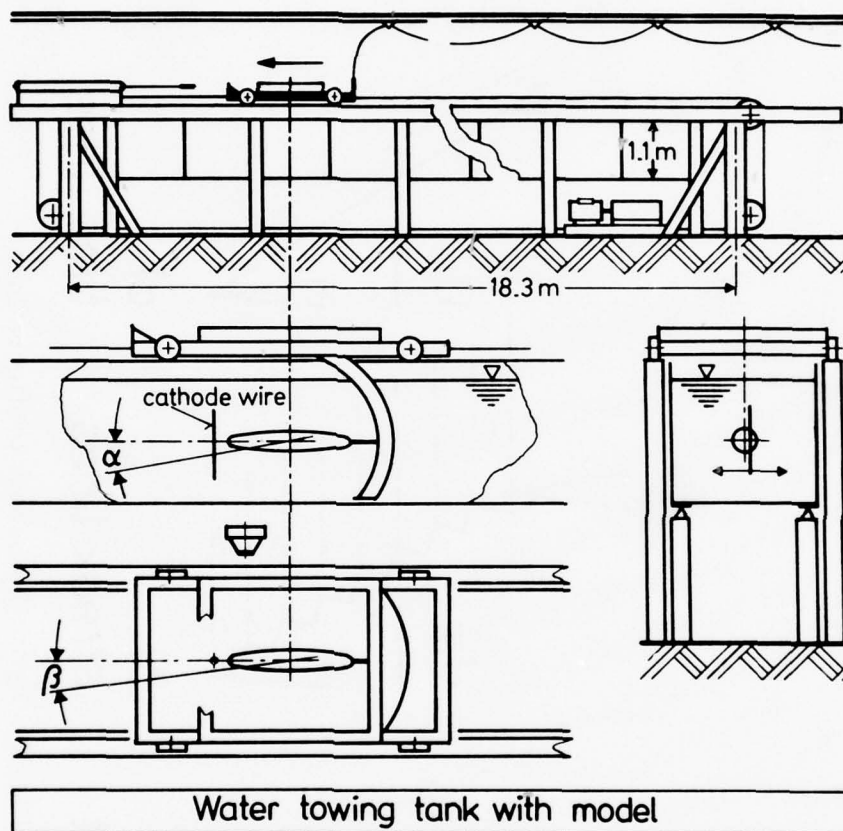


Fig. 1 Experimental set up

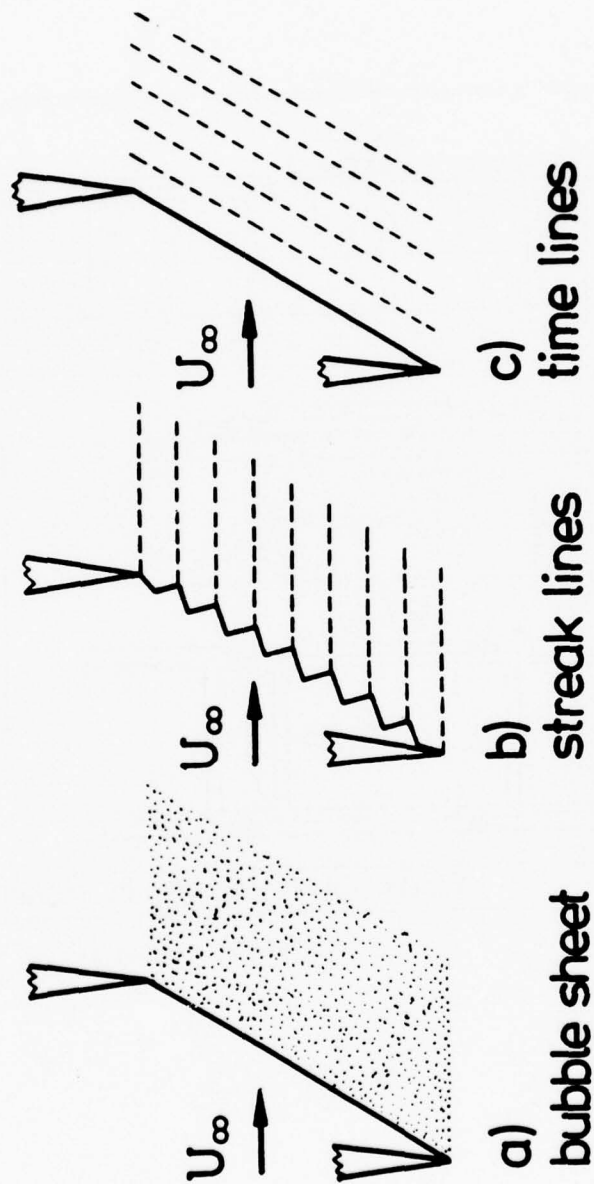


Fig. 2 Hydrogen bubble configurations

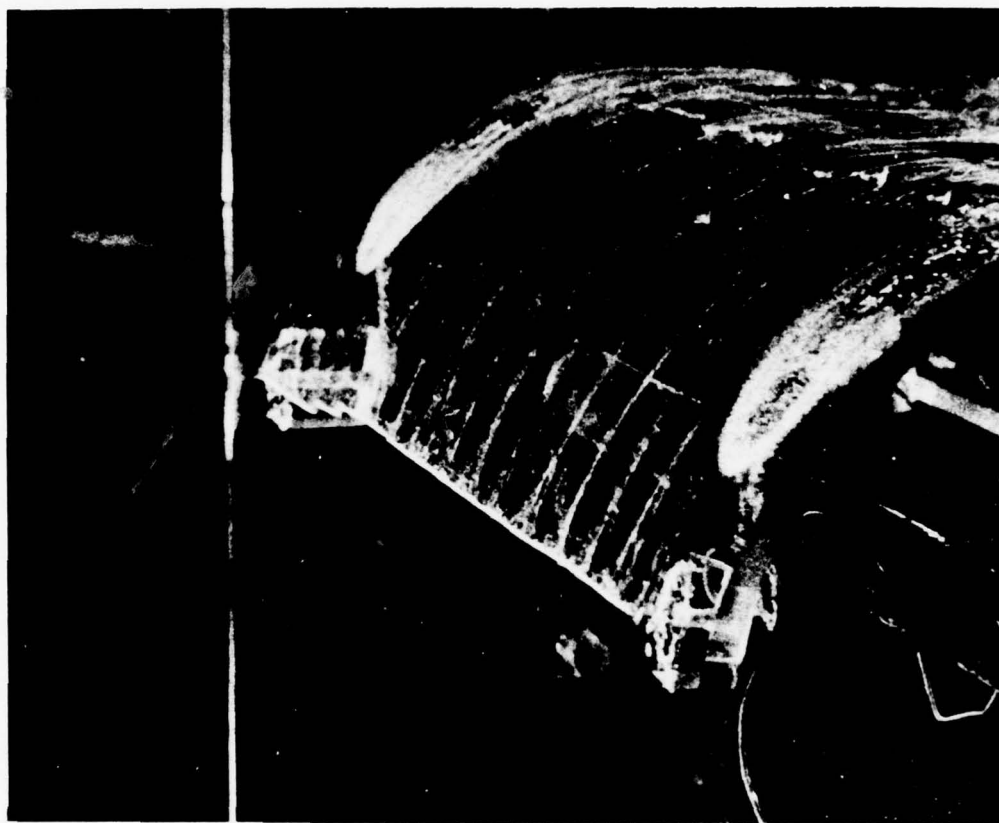


Fig. 3 Stagnation flow instabilities in the stagnation region of a circular cylinder in cross flow

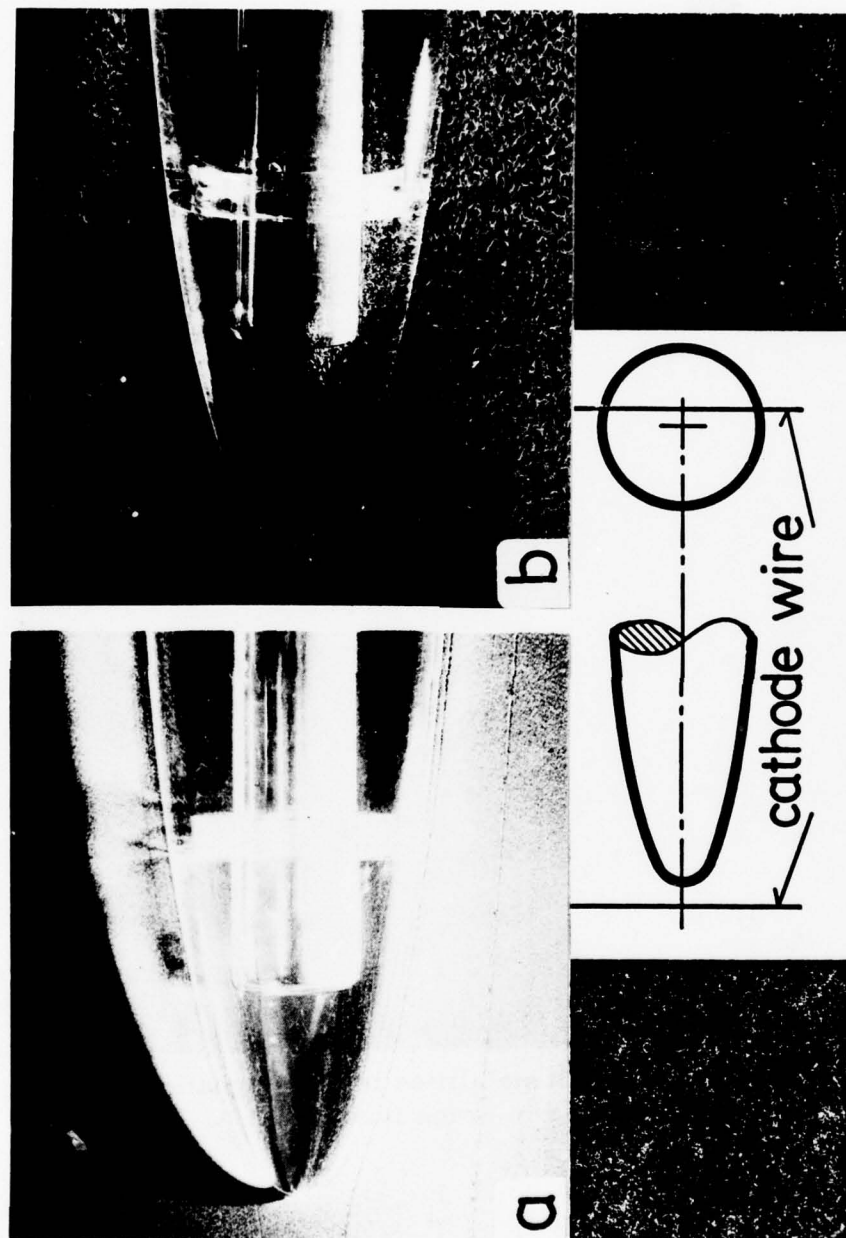


Fig. 4 Flow in the stagnation region of the prolate spheroid

- a) $Re = 1.5 \times 10^6$
- b) $Re = 1.5 \times 10^6$ (with turbulence screen before the model)

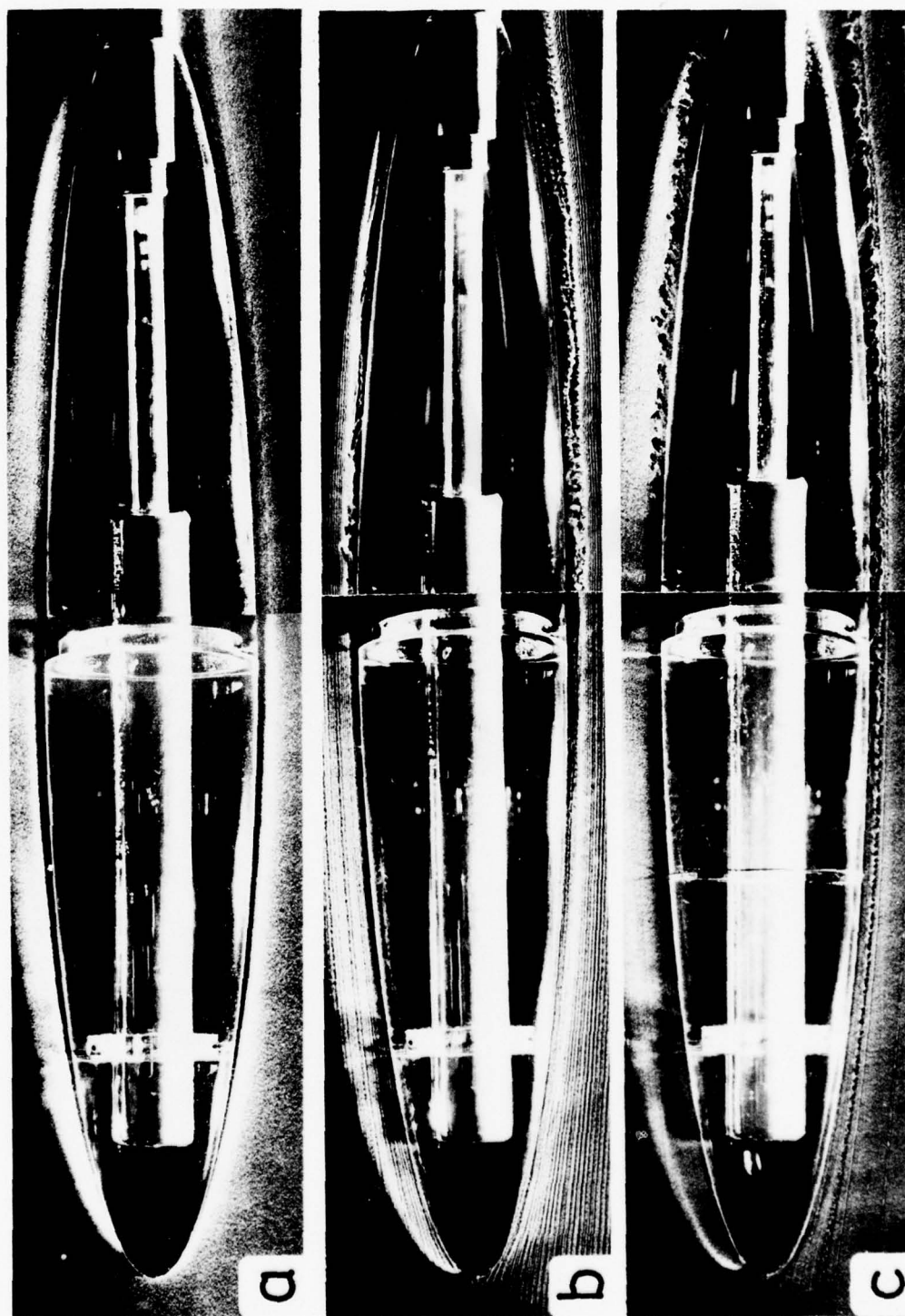


Fig. 5 Laminar to turbulent transition

a) $Re = 1.0 \times 10^6$, b) $Re = 2.5 \times 10^6$, c) $Re = 1.0 \times 10^6$ (turbulence forced by trip wire)

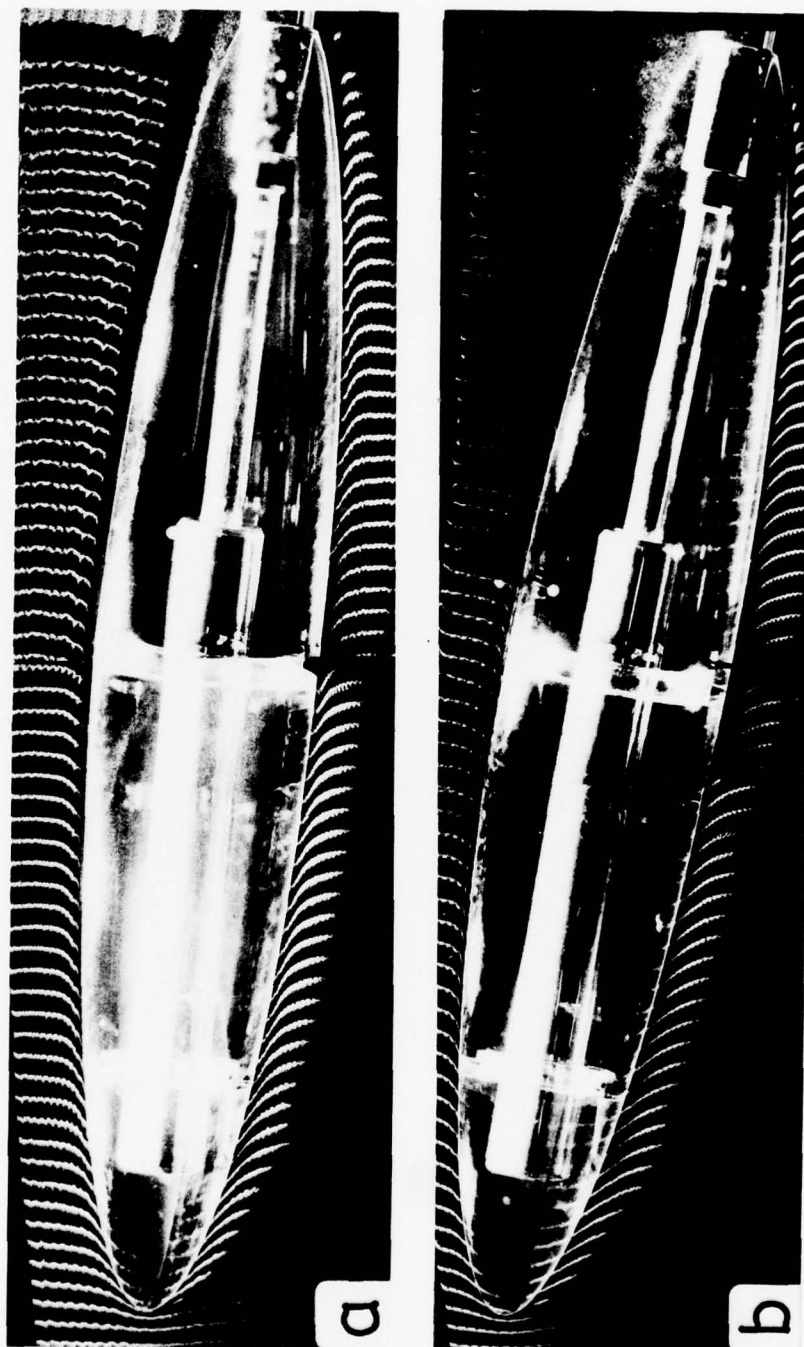


Fig. 6 Laminar to turbulent transition on the model at incidence (timeline picture)
 $Re = 1.5 \times 10^6$

a) $\alpha = 5^\circ$, b) $\alpha = 10^\circ$

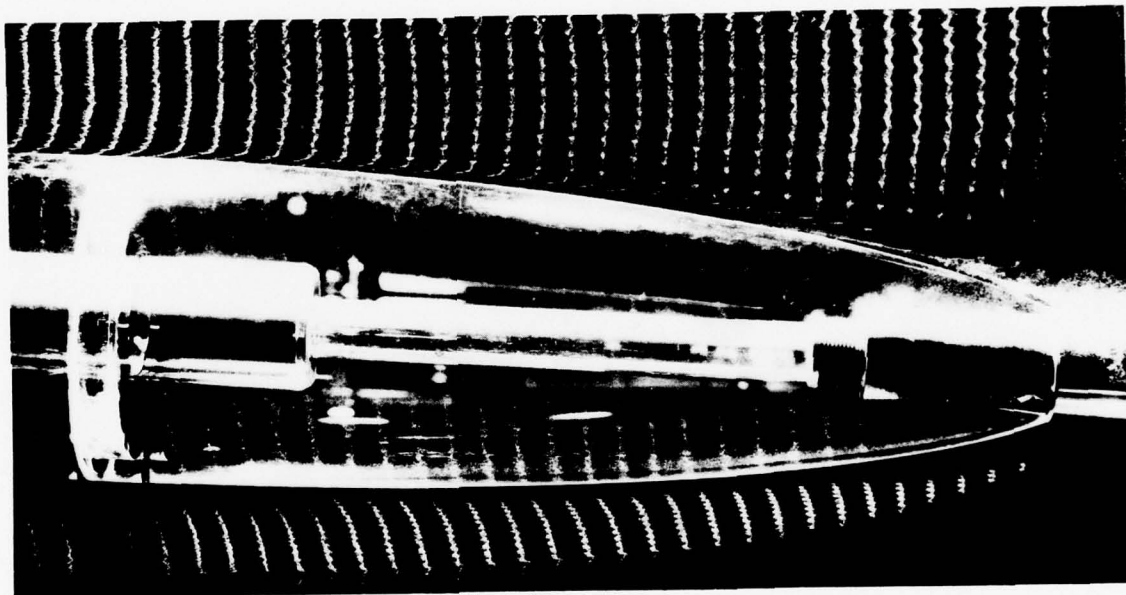


Fig. 7 Laminar and turbulent zones on the model at incidence
 $Re = 1.5 \times 10^6$, $\alpha = 5^\circ$

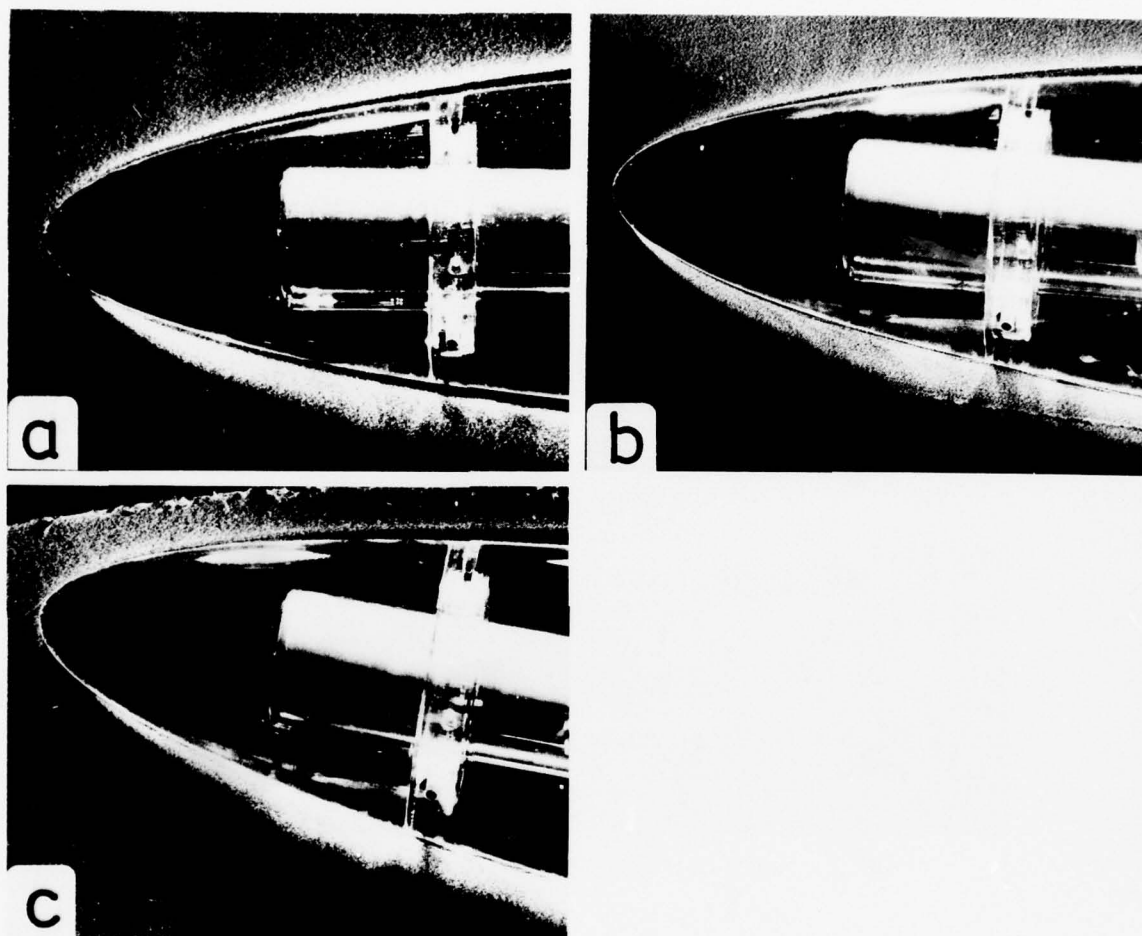


Fig. 8 The flow on the forward part of the model. $Re = 1 \times 10^6$
 a) $\alpha = 0^\circ$, b) $\alpha = 5^\circ$, c) $\alpha = 10^\circ$

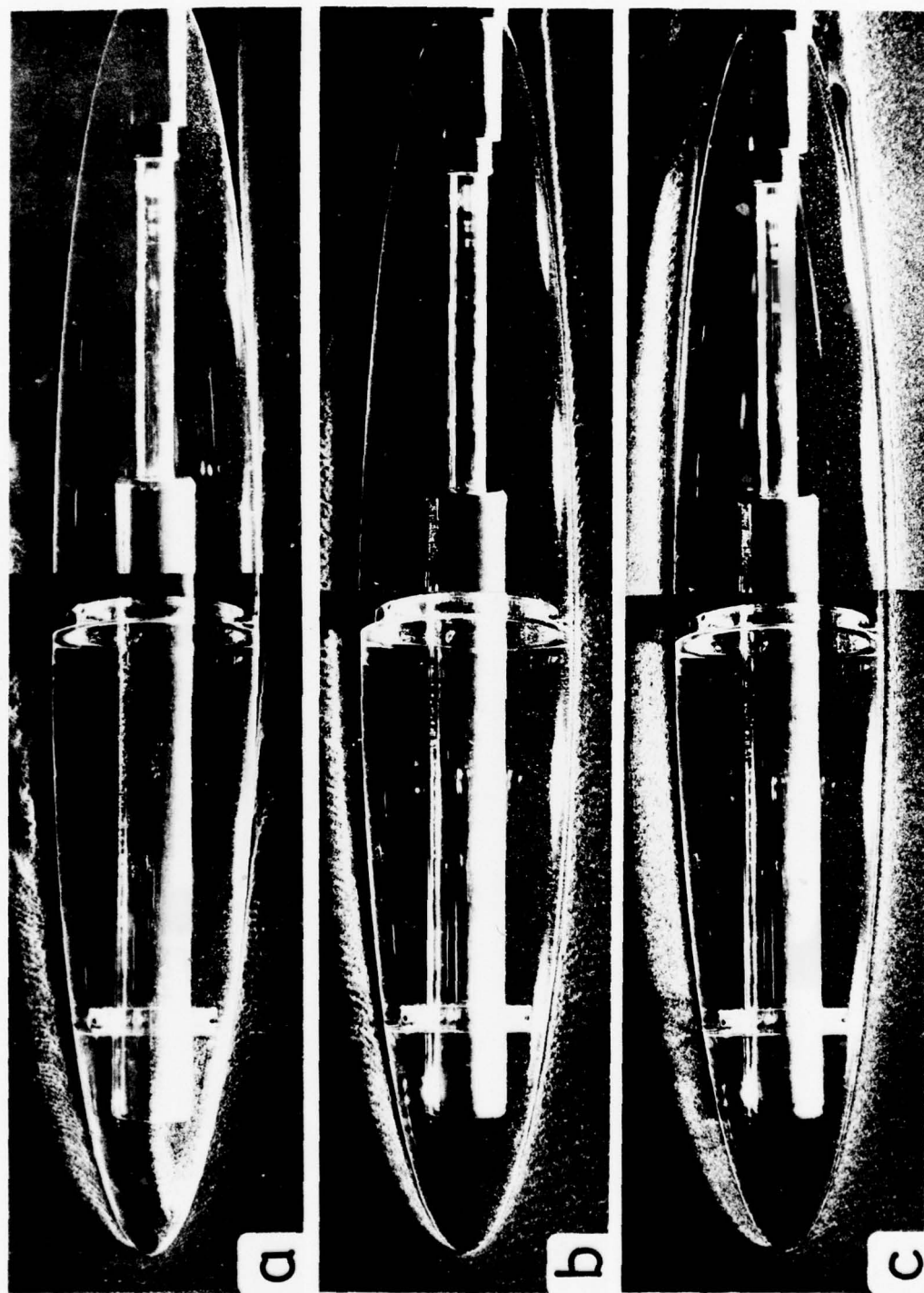


Fig. 9 Boundary layer separation on the rearward part of the model. $\alpha = 0^\circ$

a) $Re = 0.125 \times 10^6$, b) $Re = 0.25 \times 10^6$, c) $Re = 0.5 \times 10^6$,

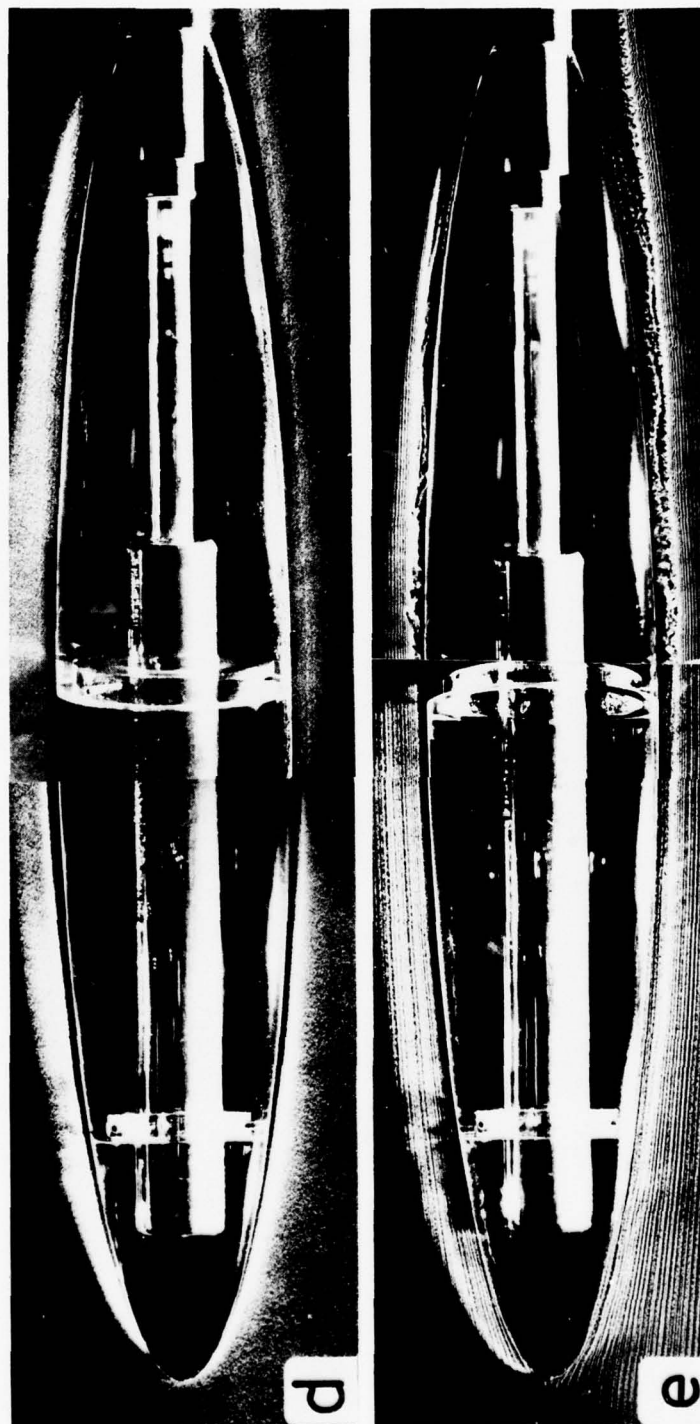


Fig. 9 Boundary layer separation on the rearward part of the model. $\alpha = 0^\circ$
d) $Re = 1.5 \times 10^6$, e) $Re = 3.0 \times 10^6$



Fig. 10 Boundary layer separation on the rearward part of the model (streak line picture). $Re = 1 \times 10^6$

a) $\alpha = 0^\circ$, b) $\alpha = 5^\circ$, c) $\alpha = 10^\circ$

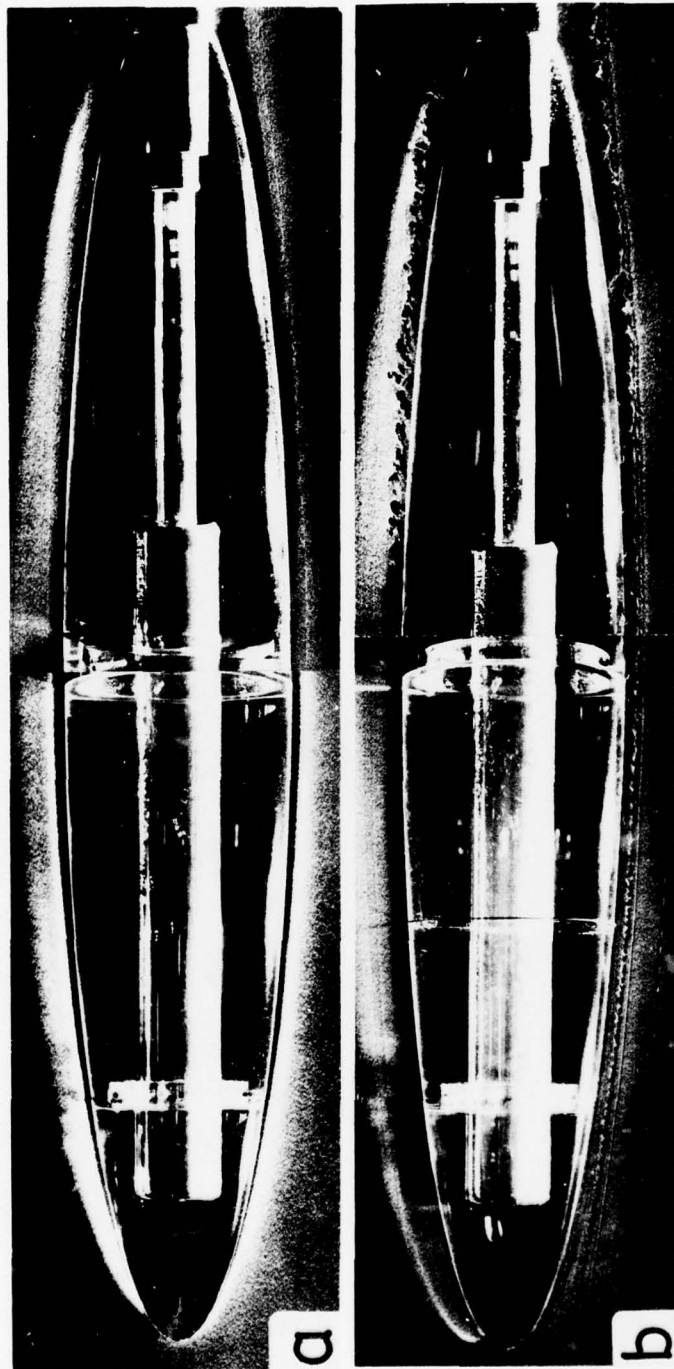


Fig. 11 Boundary layer separation on the rearward part of the model

- a) laminar separation, $\alpha = 0^\circ$, $Re = 1.5 \times 10^6$
- b) turbulent separation (turbulence forced by a trip wire)

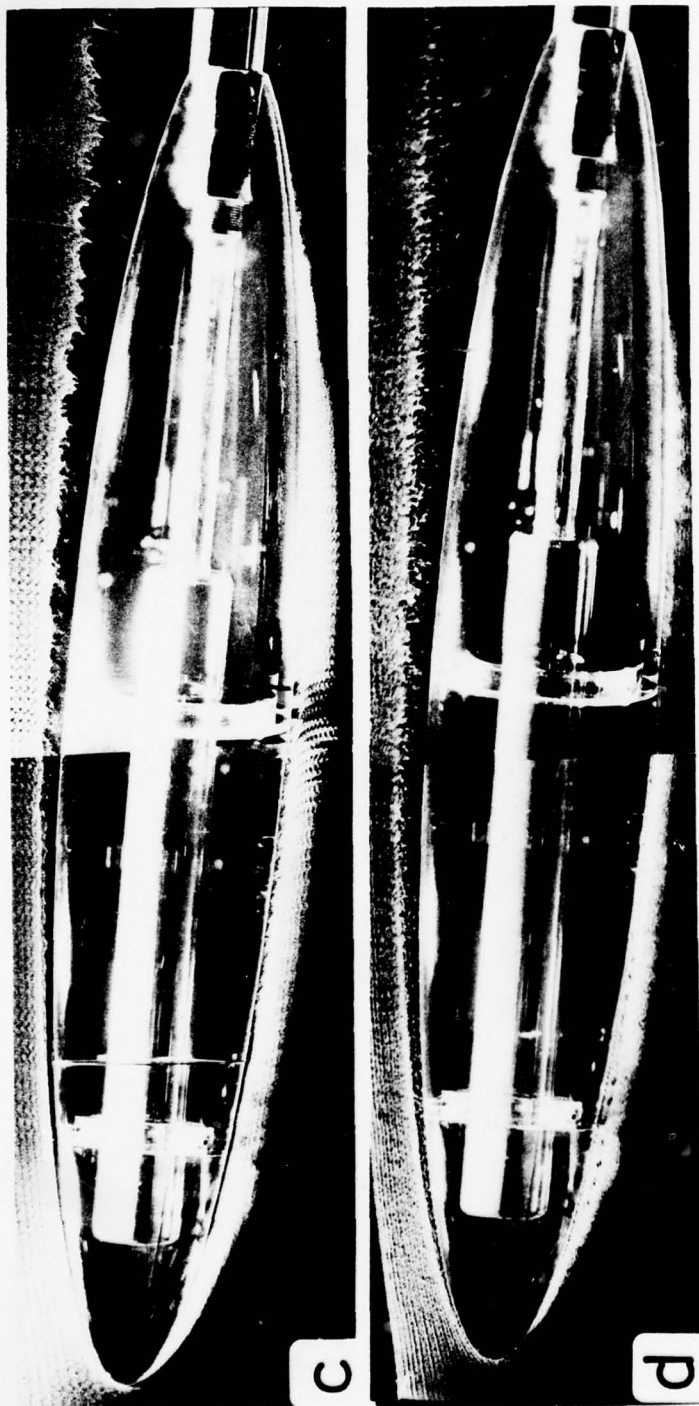


Fig. 11 Boundary layer separation on the rearward part of the model

c) turbulent separation (turbulence forced by a trip wire)

d) turbulent separation. $\alpha = 5^\circ$, $Re = 3 \times 10^6$

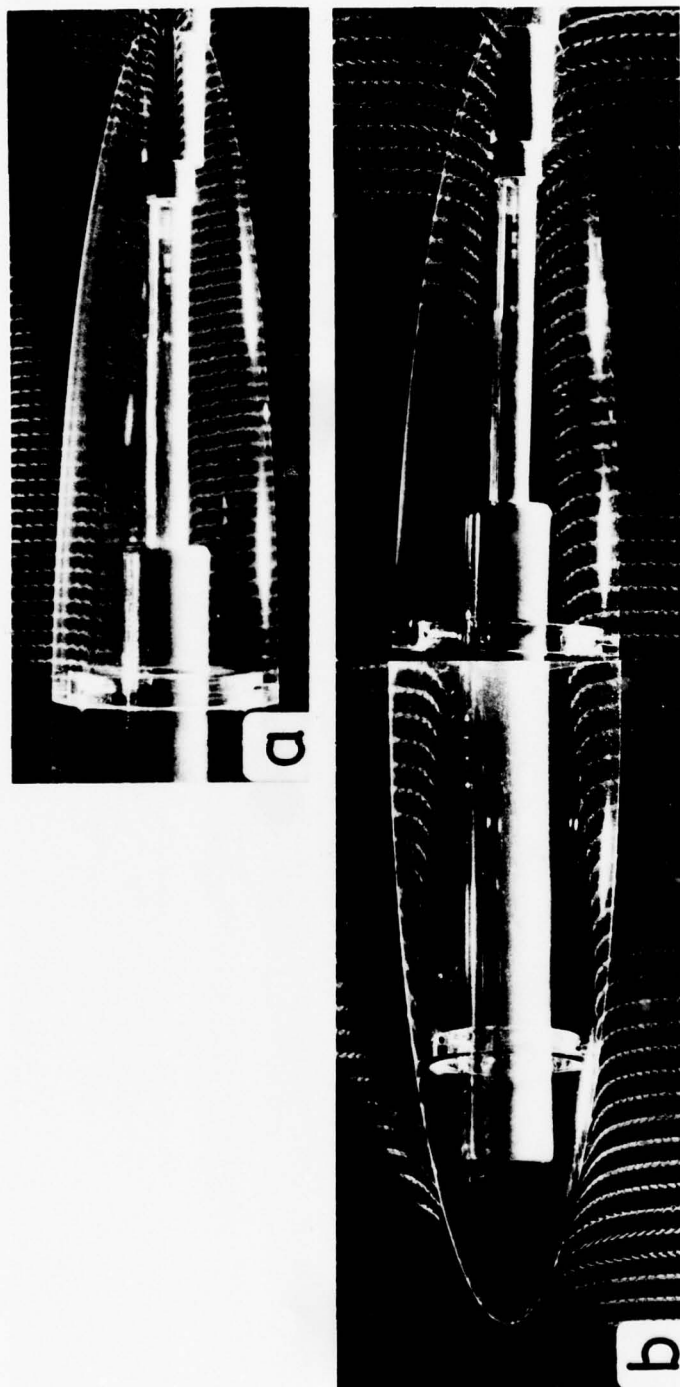


Fig. 12 Vortex separation on the model at incidence. View perpendicular to the suction side $Re = 1.5 \times 10^6$
a) $\alpha = 5^\circ$, $\alpha = 10^\circ$

List of Figures

- Fig. 1 Experimental set up
- Fig. 2 Hydrogen bubble configurations
- Fig. 3 Stagnation flow instabilities in the stagnation region of a circular cylinder in cross flow
- Fig. 4 Flow in the stagnation region of the prolate spheroid
 a) $Re = 1.5 \cdot 10^6$
 b) $Re = 1.5 \cdot 10^6$ (with turbulence screen before the model)
- Fig. 5 Laminar to turbulent transition
 a) $Re = 1.0 \cdot 10^6$, b) $Re = 2.5 \cdot 10^6$, c) $Re = 1.0 \cdot 10^6$ (turbulence forced by trip wire)
- Fig. 6 Laminar to turbulence transition on the model at incidence (timeline picture) $Re = 1.5 \cdot 10^6$
 a) $\alpha = 5^\circ$, b) $\alpha = 10^\circ$
- Fig. 7 Laminar and turbulent zones on the model at incidence $Re = 1.5 \cdot 10^6$, $\alpha = 5^\circ$
- Fig. 8 The flow on the forward part of the model. $Re = 1 \cdot 10^6$
 a) $\alpha = 0^\circ$, b) $\alpha = 5^\circ$, c) $\alpha = 10^\circ$
- Fig. 9 Boundary layer separation on the rearward part of the model. $\alpha = 0^\circ$
 a) $Re = 0.125 \cdot 10^6$, b) $Re = 0.25 \cdot 10^6$, c) $Re = 0.5 \cdot 10^6$,
 d) $Re = 1.5 \cdot 10^6$, e) $Re = 3.0 \cdot 10^6$
- Fig. 10 Boundary layer separation on the rearward part of the model (streak line picture). $Re = 1 \cdot 10^6$
 a) $\alpha = 0^\circ$, b) $\alpha = 5^\circ$, c) $\alpha = 10^\circ$
- Fig. 11 Boundary layer separation on the rearward part of the model
 a) laminar separation, $\alpha = 0^\circ$, $Re = 1.5 \cdot 10^6$
 b) turbulent separation (turbulence forced by a trip wire) $\alpha = 0^\circ$, $Re = 1.5 \cdot 10^6$
 c) turbulent separation (turbulence forced by a trip wire) $\alpha = 5^\circ$, $Re = 1.5 \cdot 10^6$
 d) turbulent separation. $\alpha = 10^\circ$, $Re = 3.0 \cdot 10^6$

Fig. 12 Vortex separation on the model at incidence. View perpendicular to the suction side $Re = 1.5 \cdot 10^6$
a) $\alpha = 5^\circ$, b) $\alpha = 10^\circ$

COMPUTATION OF TRANSONIC FLOW PAST SLENDER BODIES AT ANGLE OF ATTACK

R. P. Reklis and W. B. Sturek
U.S. Army Ballistic Research Laboratory
Aberdeen Proving Ground, Maryland 21005

and

F. R. Bailey
NASA Ames Research Center
Moffett Field, California 94035

ABSTRACT. Aerodynamic properties of artillery shell such as normal force and pitching moment reach peak values in a narrow transonic Mach number range. In order to compute these quantities, numerical techniques have been developed to obtain solutions to the three-dimensional transonic small disturbance equation about slender bodies at angle of attack. The computation is based on a plane relaxation technique involving Fourier transforms to partially decouple the three-dimensional difference equations. Particular care is taken to assure accurate solutions near corners found in shell designs. Computed surface pressures are compared to experimental measurements for circular arc and cone cylinder bodies which have been selected as test cases. Computed pitching moments are compared to range measurements for a typical projectile shape.

1. INTRODUCTION. When designing an artillery shell, it is necessary to develop a vehicle which will fly with stability under a wide variety of aerodynamic conditions. A range of propellant charges may be used giving the shell launch velocities covering a spectrum from subsonic to supersonic. The shell will also slow in flight, particularly near the apex of its trajectory. It is, therefore, important that the shell fly with stability in subsonic, transonic, and supersonic flight regimes.

Difficulties are often experienced by projectiles at transonic velocities. Aerodynamic properties such as drag and the pitching moment, which is critical to stability, will reach peak values at some transonic Mach number. This peak can form in a Mach number range which may be very limited as, for example, between $.92 < M < .94$. The sharpness of this critical behavior as well as the value of the critical Mach number are very sensitive to body geometry. A slight change in boattail length may make the difference between a successful shell and one whose behavior is unpredictable.

Aerodynamic range and wind tunnel testing are difficult and expensive, particularly at transonic velocities. Therefore, it is of great importance for artillery projectile design to develop a computational capability which can provide guidance in choosing shell configurations and reduce aerodynamic testing requirements. Techniques have been established and computers are now available which should make possible the development of useful computational design tools, particularly for the limited and usually simple geometries found in artillery projectile shapes.

The basic approach used by BRL to compute flow over supersonic projectiles¹ has been to solve for the inviscid flow field around the body and to then compute the flow in the boundary layer using turbulence modeling. This approach seems quite feasible for use in the transonic problem considering the results shown by Schmidt, Stock, and Fritz² who have coupled integral boundary layer calculations to transonic inviscid solutions. The major thrust of the transonic work reported here involves the development of numerical techniques for the computation of three-dimensional transonic inviscid flow past artillery projectiles. A three-dimensional, compressible, turbulent, boundary layer code using finite difference techniques has been developed by BRL¹ for use with supersonic flow and its carry over should be straight forward.

Complications in the body geometry such as the rotating band and rifling have been neglected. The resulting simplified shape, however, exhibits the basic aerodynamic properties of the projectile. One complication which cannot be ignored is the presence of corners at the junction of the ogive and cylindrical portions of the shell and at the junction of the cylindrical portion and the boattail. These corners are responsible for the critical transonic aerodynamic behavior of the shell.

2. COMPUTATION TECHNIQUES. Transonic techniques based on type dependent differencing have come into wide acceptance since they were developed by Murman and Cole³. There are now several schemes like that developed by Bailey and Ballhaus⁴ that will solve three-dimensional potential flow over wings and wing body combinations. Considerable simplification, however, may be achieved in the projectile problem if the code is restricted to axially symmetric bodies. Further, by using a cylindrical coordinate system which fits the body surface, no vertical or horizontal preferred directions are established. This provides an important increase in accuracy. The axially symmetric problem at angle of attack, although it is simpler than the wing body problem, does not have the range of application and has not seen as wide an interest. There has been, however, some recent numerical work by Reyhner⁵ who has studied axisymmetric inlets.

Even though techniques are available to solve the full inviscid potential equation directly⁶, the approach chosen for this study has been to solve the transonic small disturbance equation

$$[(1 - M^2) - M^2 (\gamma + 1) \phi_z] \phi_{zz} + \phi_{rr} + \phi_r/r + \phi_{\theta\theta}/r^2 = 0 \quad , \quad (1)$$

which is an approximation to the full equation. This is a nonlinear partial differential equation of mixed elliptic-hyperbolic type written in a cylindrical coordinate system (z, r, θ) as shown in Figure 1. The free stream Mach number is given by M in this equation and the ratio of specific heats (1.4 for air) is represented by γ . The solution to this equation has been shown by Bailey⁷ to give good results for the slender body case at zero angle of attack. This equation has also been studied both numerically and analytically for many years and it is simple enough that much valuable insight may be gained from it, particularly in regions near the body where it reduces to

$$\phi_{rr} + \phi_r/r + \phi_{\theta\theta}/r^2 = 0 \quad . \quad (2)$$

This last equation is a Laplace equation that may be solved analytically.

In his two dimensional solution of equation (1) Bailey⁷ used successive line over relaxation in which difference equations were solved along lines through the flow extending radially from the body axis. This line relaxation procedure has been carried a step further in the technique used here in three dimensions. The difference equations for whole planes of flow cutting the body axis have been solved simultaneously. The method thus obtained treats coupling in the r and θ directions with a direct solution technique which closely matches the physical coupling found in the flow. Flow disturbances propagate much more strongly in the r and θ directions than along the body in the z direction. This may be seen from a look at the inner equation (2). There is no z coupling in this equation. This lack of disturbance propagation along the body is a well known property of transonic flow.

The matrix equations obtained from a line relaxation procedure are in tridiagonal form which may readily be solved. The matrix equations for plane relaxation are not. It is, however, possible to make use of the periodic nature of the axisymmetric problem in such a way as to transform these matrix equations into tridiagonal form. This transformation is accomplished by a basis change which is equivalent to a Fourier transformation in θ . Reyhner⁵ has pointed out that the solution around the body is very nearly

$$\phi_1(r, z) + \phi_2(r, z) \cos \theta \quad .$$

This result appears very clearly in the Fourier transform approach and allows a considerable saving in both computer time and storage since only a few Fourier components need be treated. The use of Fourier transforms does increase, to some extent, the problem of obtaining a stable relaxation scheme. A simple stable scheme can be obtained, however, which reduces, at zero angle of attack, to the usual line relaxation algorithm.

3. DISCUSSION OF RESULTS. The results for computations of the surface pressure coefficient for bodies with circular arc profiles can be seen in Figures 2 and 3. Figure 2 shows a comparison of computed and wind tunnel⁸ pressure coefficients along the surface of a 1/10 fineness ratio body at zero angle of attack in a Mach number .99 free stream. The location of a shock can be clearly seen just aft of the center of the body.

The solid line shows the results of computations for a body generated by a perfect circular arc. The wind tunnel model, however, was supported from the rear by a sting. The effect of the sting was modeled and the resulting computed pressure coefficients are shown by the dashed line in this figure. As the angle of attack is zero in the case shown in Figure 2, the computation is two dimensional. This same case was computed by Bailey⁷ in his earlier two-dimensional work and the results are identical.

Figure 3 shows a comparison of computed and wind tunnel⁹ pressures for a slightly more slender body of fineness ratio 1/12. The Mach number in this case was .90 which is too low to allow development of a large supersonic region with strong shocks. The figure is presented to show the result of a three-dimensional computation. Unfortunately, wind tunnel data for cases showing strong shock development were unavailable at angle of attack. Discrepancies between computed and wind tunnel pressure over the aft portion of the body are the result of the presence of the wind tunnel sting.

The results presented in these two figures confirm the ability of the three-dimensional code to predict surface pressures over smooth bodies. There is little difference between the nose of a typical artillery shell which is an ogive and the front portion of these circular arc bodies. Artillery shell, however, often exhibit corners, particularly at the junction between the ogive and cylinder portions and between the cylinder portion and the boattail. Strong shocks are formed by the collapse of supersonic regions which are generated by the expansion of the flow over these corners when the shell is flown at a slightly subsonic velocity ($.8 < M < 1$). This phenomena is demonstrated in Figure 4 which shows the shadowgraph of a shell at the critical Mach number ($M = .926$). Note that the shock on the upper surface of the boattail is nearly off the end. The high pressure on the lower surface behind the shock on the boattail provides a large lift on the tail creating a powerful overturning moment. The flow pattern generated by the corner at the beginning of the boattail is largely responsible for the critical behavior of the overturning moment. Thus, the accurate treatment of corner flow is of prime consideration.

Corners create singularities in the potential. The well known incompressible result is that flow obtains infinite velocity over a corner. The speed of the flow, however, will clearly become supersonic before it becomes infinite so that an incompressible calculation is unacceptable. The corner problem is, therefore, by nature transonic and can be treated by transonic techniques. Also, the boundary layer which is well developed over the corner at the start of the boattail will tend to effectively round this corner so that a strict mathematical singularity does not exist.

The ability of the present theory to predict flow over a corner can be seen in Figure 5. Figure 5 shows a comparison of surface pressure results with wind tunnel experiments¹⁰ for flow over a cone cylinder model at Mach number 1.1. The theory shows reasonable behavior near the corner of the cone and cylinder sections. In order to achieve these results it was necessary to use care in applying boundary conditions at the body surface. An approach that is often taken is to use solutions of the simpler inner equation (2) to extrapolate the boundary conditions from the body surface to the body axis or to some other convenient location. In Bailey's two dimensional paper the boundary conditions were extrapolated to the axis where a series of sources and sinks were placed. The source and sink strengths were obtained from the solution to the inner equation.

This procedure is not feasible if accurate corner flow is to be obtained. The inner equation, which is obtained by dropping the nonlinear term from equation (1), does not apply near corners where, in fact, the nonlinear term may be large close to the body surface. Boundary conditions must be applied directly at the surface without extrapolation. Further improvement in the application of boundary conditions may also be obtained. The usual boundary condition which is applied at the body surface is given by

$$\phi_r \Big|_{\text{surface}} = dR/dz ,$$

where the left hand side is the radial derivative of the potential evaluated at the body surface and the right hand side is the slope of the body surface. This is a first order approximation to the body surface boundary condition. A second order formula is more appropriate and is given by

$$\phi_r \Big|_{\text{surface}} = (1 + \phi_z \Big|_{\text{surface}}) dR/dz .$$

The first order formula works well as long as ϕ_z remains small in comparison to 1. Near a corner ϕ_z may become large enough that it produces a noticeable effect as seen in Figure 5. Because of the iterative relaxation procedure used in solving the potential equation ϕ_z may be obtained at an old iteration. The right hand side of the second order formula may thus be evaluated. The effect of using a finer grid spacing may also be seen in Figure 5. The grid in all cases shown in this figure was made up of 64 points. In the case labeled fine grid in this figure these points were clustered so as to give twice the density near the corner. Subsequent calculations have been carried out with 128 points so as to achieve this same fine density when more than one corner is present.

The absolute necessity of the care taken with corner flow may be seen when computations of normal force and pitching moment are made. It is possible to use the inner solution found from equation (2) to predict both normal force and pitching moment. It should be noted that there is no Mach number dependence in equation (2). Because of this, both normal force and pitching moment will be constants in Mach number and will depend only on the body shape. Since it is precisely the large transonic variations of normal force and pitching moment that are desired and since the use of equation (2) will predict no Mach number dependence of these quantities, equation (2) must not be valid everywhere on the surface and it is not possible to use equation (2) to supply boundary conditions. A corollary to this argument is that it is the areas where equation (2) breaks down which are of interest in obtaining variations of normal force and pitching moment with Mach number. Such breakdowns occur near corners and it is for this reason that they are of such critical interest. Breakdowns also occur around shocks. As seen in Figure 2, accurate shock location is also vital to the computation of aerodynamic quantities because of the large pressure difference between the upper and lower surfaces in the neighborhood of the shock on the boattail.

It has been shown in the above discussion that the transonic techniques, that have been developed, will predict flow over both smooth bodies and bodies with corners. It should, therefore, be possible to obtain the solution over a body that closely resembles an artillery shell. The lift loading computed for a typical artillery shell shape is plotted in Figure 6. This graph shows the normal force per unit length plotted as a function of the position along the shell. It is felt that the features of this curve, particularly the large downward spike in the boattail region, gives an accurate representation of the aerodynamic forces on this body. Comparison of the pitching moment coefficient computed for this body and range measurements¹¹ of a similar shell are given as a function of Mach number in Figure 7. The peak shown in the computed results falls a few hundredths of a Mach number higher than the peak in the range measurements and is not as pronounced.

It is felt that this situation will improve with the inclusion of the boundary layer, the inclusion of the rotating band, and a better modeling of the wake. These improvements will be added in the very near future. At present it is felt that the techniques described above will be capable of accurate prediction of both normal force and pitching moment for practical shell configurations. With the inclusion of a boundary layer, Magnus forces may also be predicted.

REFERENCES

1. Sturek, W. B., et al, "Computations of Turbulent Boundary Layer Development Over a Yawed, Spinning Body of Revolution With Application to the Magnus Effect," BRL Report No. 1985, U.S. Army Ballistic Research Laboratory, Aberdeen Proving Ground, Maryland, May 1977. AD A041338.
2. Schmidt, W., Stock, H. W., and Fritz, W., "Numerical Simulation of Three Dimensional Transonic Flow Including Wind Tunnel Wall Effects," AGARD Specialists Meeting, "Numerical Methods and Wind Tunnel Testing," VKI, Brussels, 1976.
3. Murman, E. M., and Cole, J. D., "Calculation of Plane Steady Transonic Flows," *AIAA Journal*, Vol. 9, No. 1, January 1971, pp. 114-121.
4. Bailey, F. R., and Ballhaus, W. F., "Comparisons of Computed and Experimental Pressures for Transonic Flows About Isolated Wings and Wing Fuselage Configurations," NASA SP-347, Vol. 2, March 1975, pp. 1213-1226.
5. Reyhner, T. A., "Transonic Potential Flow Around Axisymmetric Inlets and Bodies at Angle of Attack," *AIAA Journal*, Vol. 15, No. 9, September 1977, pp. 1299-1306.
6. South, J. C., Jr., and Jameson, Anthony, "Relaxation Solutions for Inviscid Axisymmetric Transonic Flow Over Blunt or Pointed Bodies," AIAA Computational Fluid Dynamics Conference, Palm Springs, California, July 1973, pp. 8-17.

7. Bailey, F. R., "Numerical Calculation of Transonic Flow About Slender Bodies of Revolution," NASA TN-D-6582, December 1971.
8. Taylor, R. A., and McDevitt, J. B., "Pressure Distribution at Transonic Speeds for Parabolic-Arc Bodies of Revolution Having Fineness Ratios of 10, 12, and 14," NACA TN-4234, March 1958.
9. McDevitt, J. B., and Taylor, R. A., "Force and Pressure Measurements at Transonic Speeds for Several Bodies Having Elliptical Cross Sections," NACA TN-4362, September 1958.
10. Page, W. A., "Experimental Study of the Equivalence of Transonic Flow About Slender Cone-Cylinders of Circular and Elliptic Cross Section," NACA TN-4233, April 1958.
11. McCoy, Robert L., U.S. Army Ballistic Research Laboratory, Aberdeen Proving Ground, Maryland. Private communication.

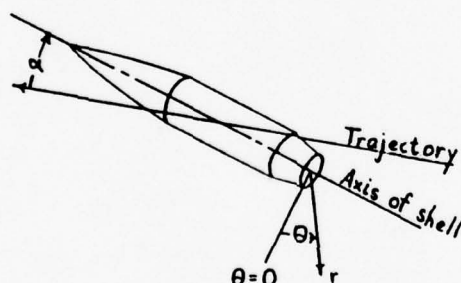


Figure 1. Coordinate System

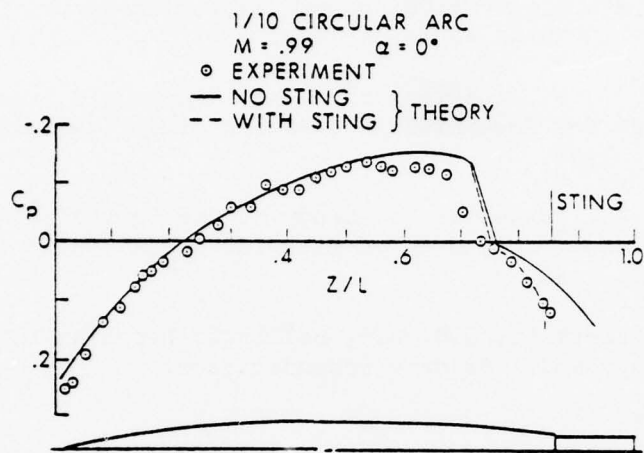


Figure 2. Comparison of Calculated Pressure Coefficients With Wind Tunnel Data for a Fineness Ratio 1/10 Circular Arc Body, $M = 0.99$

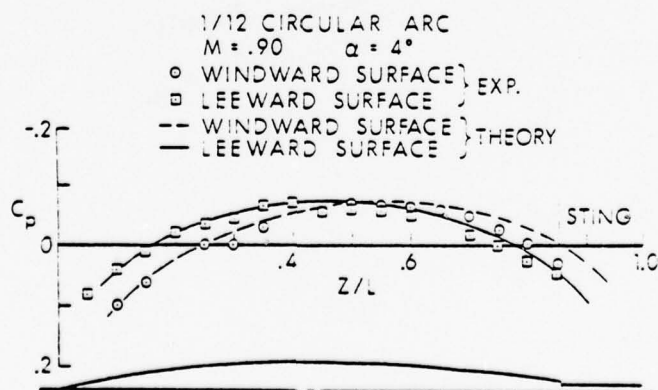


Figure 3. Comparison of Calculated Pressure Coefficients With Wind Tunnel Data for a Fineness Ratio 1/12 Circular Arc Body at Angle of Attack, $\alpha = 4^\circ$, $M = 0.90$



Figure 4. Spark Shadowgraph of a Typical Projectile at Critical Mach Number, $M = .926$, $\alpha = 8^\circ$

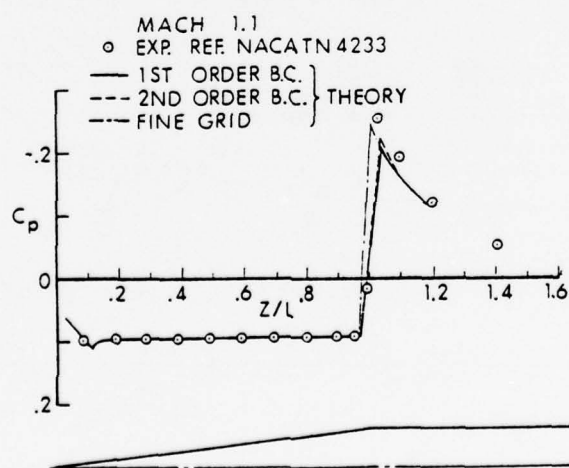


Figure 5. Comparison of Calculated Pressure Coefficient With Wind Tunnel Data for a 7° Half Angle Cone Cylinder, $M = .99$

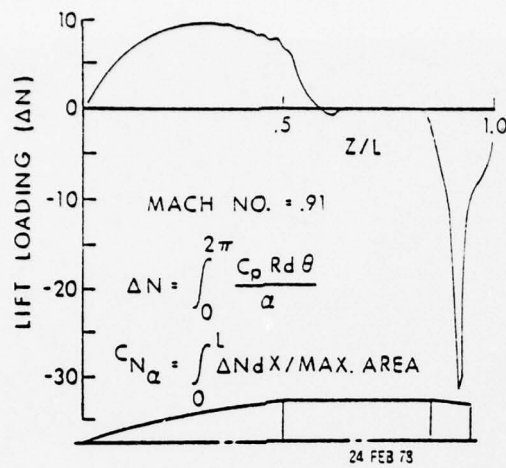


Figure 6. Computed Normal Force Loading Along a Typical Projectile

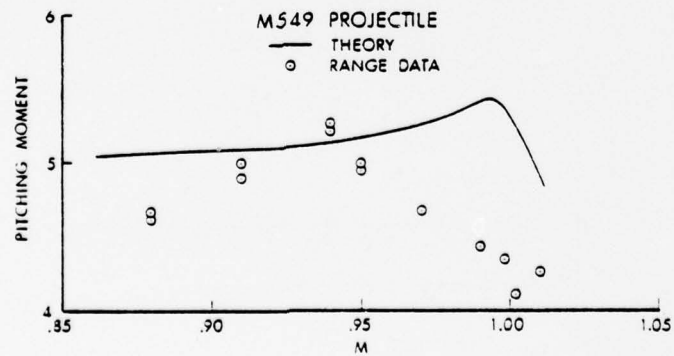


Figure 7. Comparison of Computed Pitching Moment With Range Data for A Typical Projectile

EFFECTS OF NONISOTROPIC EDDY VISCOSITY MODELS ON THE TURBULENT
BOUNDARY LAYER DEVELOPMENT ON A YAWED, SPINNING BODY OF
REVOLUTION

by

W. B. Sturek, H. A. Dwyer, C. J. Nietubicz, and L. D. Kayser

U.S. Army Ballistic Research Laboratory
Aberdeen Proving Ground, Maryland 21005

Abstract

In order to improve our capability for computing Magnus effects on yawed, spinning projectile shapes in supersonic flight, numerous numerical experiments have been carried out using the BRL finite difference computation techniques reported at previous DEA meetings. These numerical experiments involve computations of compressible turbulent boundary layer development using different models for the three dimensional eddy viscosity. Results have been obtained using three models: (1) isotropic; (2) simplified nonisotropic where $\rho \sqrt{w} \approx 0.5 \times \rho \sqrt{u} \sqrt{v}$; and (3) a modification of the nonisotropic model of Schneider and Rotta. The results of these computations are compared to experimental measurements of boundary layer profile characteristics for a secant-ogive-cylinder-boattail model. Comparisons are also made showing the impact of generalized eddy viscosity models on computations of the Magnus effect.

1. Introduction

In order to improve the accuracy of computations of Magnus effects for boattailed projectile shapes, an investigation has been carried out to examine the influence of modifications of the eddy viscosity model. As reported at last year's DEA⁽¹⁾, acceptable accuracy had been achieved for Magnus effects on ogive-cylinder bodies. However, when computations were made for an ogive-cylinder-boattail model, the computed Magnus force was greater than experiment by a factor of two.

This paper describes the effects of generalized three dimensional eddy viscosity models on the turbulent boundary layer development for a yawed, spinning model with a boattail. The computations are compared

-
1. Sturek, W. B., Kayser, L. D., and Nietubicz, C. J., "Turbulent Boundary Layer Development Over a Yawed Projectile With Boattail," DEA Meeting, Goettingen, West Germany, April 1977.

to experimental measurements of turbulent boundary layer profile characteristics for $M = 3$ and angle of attack of two degrees.

2. Eddy Viscosity Models

The numerical techniques and equations of motion have been described in reference 2 and will not be repeated here.

The basic isotropic eddy viscosity model used is described by the following equations:

$$-\rho \overline{u'v'} = -\rho \overline{v'w'} = \rho \epsilon \left(\frac{du}{dy}^2 + \frac{dw}{dy}^2 \right)^{\frac{1}{2}} \quad M0$$

$$\epsilon = \ell^2 \left[\left(\frac{du}{dy} \right)^2 + \left(\frac{dw}{dy} \right)^2 \right]^{\frac{1}{2}}$$

$$\ell = .09 \delta \tanh [(.4/.09)(y/\delta)]$$

The first nonisotropic model, designated as M1, is described by the relation

$$\rho \overline{v'w'} = \frac{1}{2} \rho \overline{u'v'} \quad M1$$

Other nonisotropic models tried consist of variation of the model described by Rotta⁽³⁾ and Schneider⁽⁴⁾.

$$\tau_x = \mu \frac{du}{dy} - \rho \overline{u'v'} = \rho \epsilon \left[(\epsilon_{xx} + \nu) \frac{du}{dy} \right]$$

-
2. Sturek, W.B., et al, "Boundary Layer Studies on a Yawed, Spinning Body of Revolution," DEA Meeting, Wright Patterson Air Force Base, Ohio, April 1976.
 3. Rotta, J. C., "Turbulence Models for Three-Dimensional Thin Shear Layers," DEA Meeting, Goettingen, West Germany, April 1977.
 4. Schneider, G. R., "A General Mixing Length Model and a General Eddy Viscosity Model for Calculating Three-Dimensional Incompressible Turbulent Boundary Layers," DEA Meeting, Goettingen, West Germany, April 1977.

$$\tau_{\phi} = \mu \frac{dw}{dy} - \rho \sqrt{vw} = \rho \epsilon [(\epsilon_{\phi\phi} + \nu) \frac{dw}{dy}]$$

$$\epsilon_{xx} = \epsilon (u^2 + Tw^2)/(u^2 + w^2)$$

$$\epsilon_{\phi\phi} = \epsilon (w^2 + Tu^2)/(u^2 + w^2)$$

$$\epsilon = \ell^2 \left[\left(\frac{du}{dy} \right)^2 + \left(\frac{dw}{dy} \right)^2 + (T - 1) \left(w \frac{du}{dy} - u \frac{dw}{dy} \right)^2 / (u^2 + w^2) \right]^{1/2} (1 - e^{-A})^2$$

where the quantity $(1 - e^{-A})$ is van Driest damping.

Computations have been run for $T = 0.5, 0.7$, and 0.9 . However, comparisons for $T = 0.5$ only will be discussed here. This model is designated as M2. Note that the off diagonal terms-

$\epsilon_{x\phi} \frac{dw}{dy}$ and $\epsilon_{\phi x} \frac{du}{dy}$ - have been dropped from the relations given in

references 3 and 4 because the computed results were physically unrealistic.

3. Discussion of Results

Computations have been run for the secant-ogive-cylinder-boattail model indicated in Figure 1 which shows the wall pressure distribution for the wind and lee sides of the model. Comparisons of the computed results for velocity profiles are shown in Figure 2 for u-velocity (streamwise) and in Figures 3 and 4 for w-velocity (circumferential). It is noted that differences are apparent, particularly for the w-velocity, indicating that the computations are sensitive to the relationship between the longitudinal and circumferential components of turbulent shear. Good agreement with experiment for the u-velocity is indicated for all eddy viscosity models.

Comparisons for the longitudinal component of displacement thickness are shown in Figure 5. Again, different results are obtained for the variations in the turbulence model. The best agreement with experiment is achieved for models M0 and M2.

The impact of the turbulence models M0 and M1 on the Magnus force coefficient is shown in Figure 6. Again, these results reveal

a sensitivity to the turbulence model. The best agreement with experiment is achieved with model M1.

4. Concluding Remarks

The results of this study indicate that the relationship between the longitudinal and circumferential components of turbulent shear stress can significantly influence the computation of 3D turbulent boundary layer development. The improved agreement between experiment and theory for Magnus effects reinforces the validity of the generalized turbulence shear stress models.

At this time, the computations have not been sufficiently comprehensive nor are sufficient experimental data available to select the most appropriate formulation for the three dimensional turbulent shear stress model. However, the results for Magnus force indicate that the generalized models do have promising engineering application.

NOMENCLATURE

C_y	Magnus (side) force coefficient
u, v, w	velocities in boundary layer coordinates
x	surface coordinate in longitudinal direction
y	coordinate perpendicular to local surface
z	cylindrical coordinate along model axis
α	angle of attack
ϵ	turbulent eddy viscosity
δ	boundary layer thickness
δ^*	boundary layer displacement thickness
ρ	density
ϕ	coordinate in circumferential (azimuthal) direction

Subscripts

x	quantity in x direction
ϕ	quantity in ϕ direction

Superscripts

$'$	fluctuating quantity
$-$	time averaged quantity

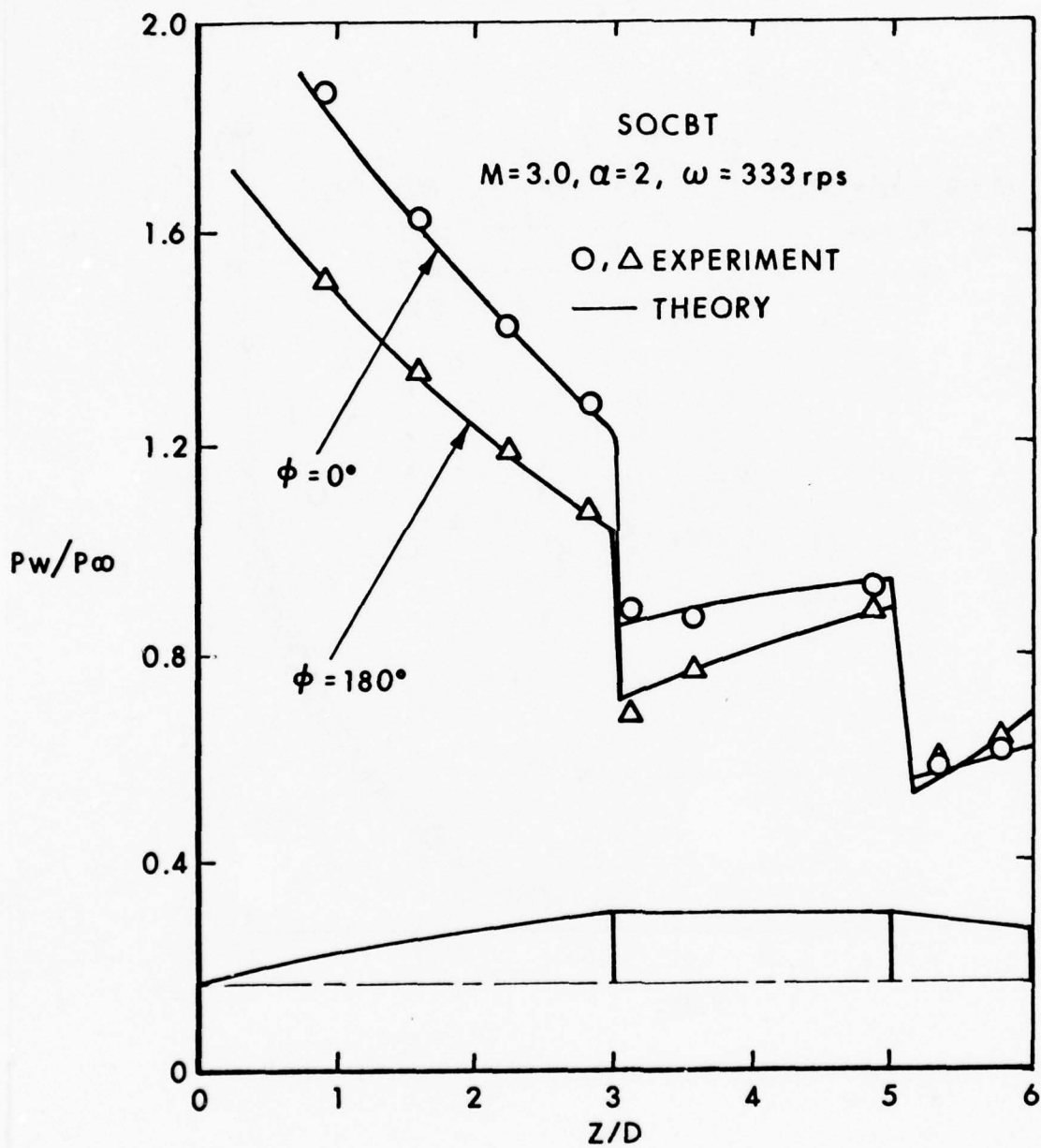


Figure 1. Wall Static Pressure Distribution

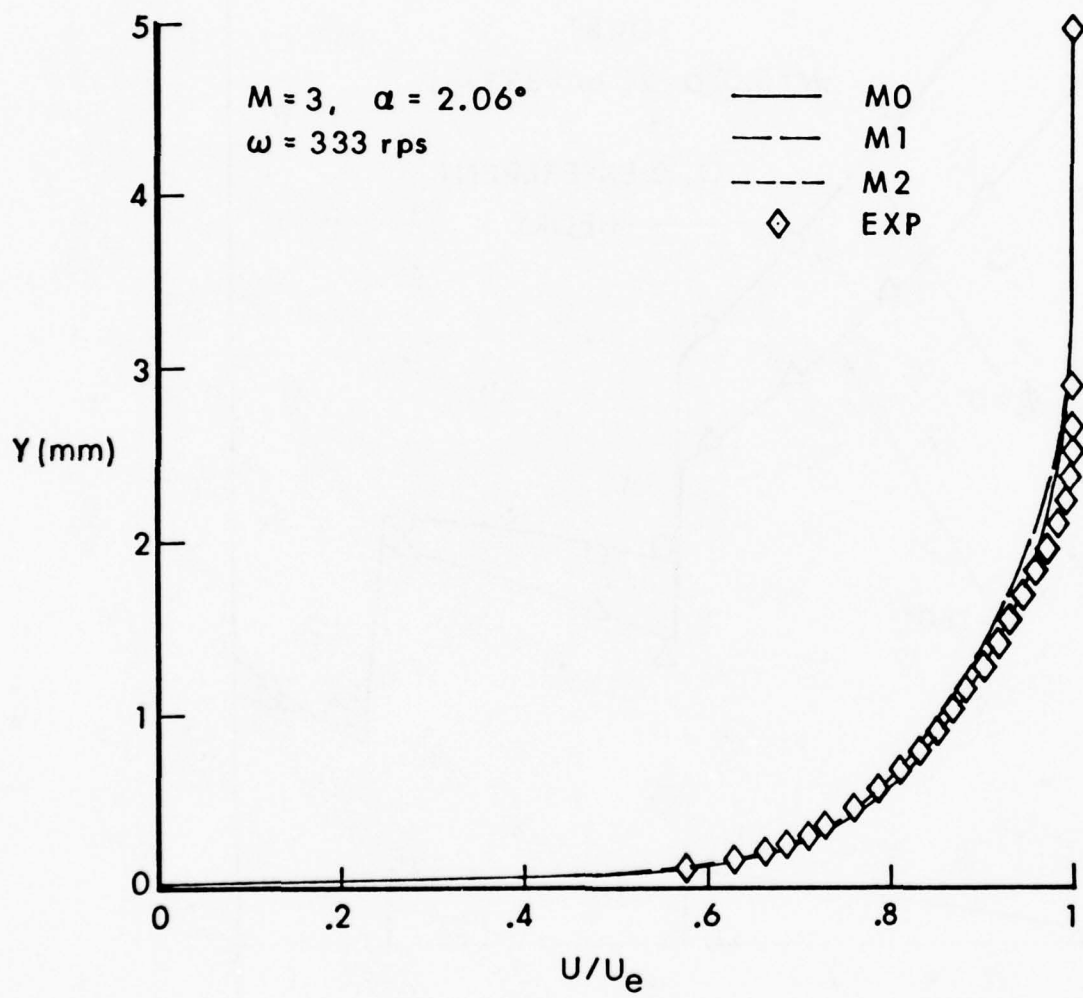


Figure 2. Longitudinal Velocity Profiles, $Z/D = 5.67$, $\phi = 180^\circ$

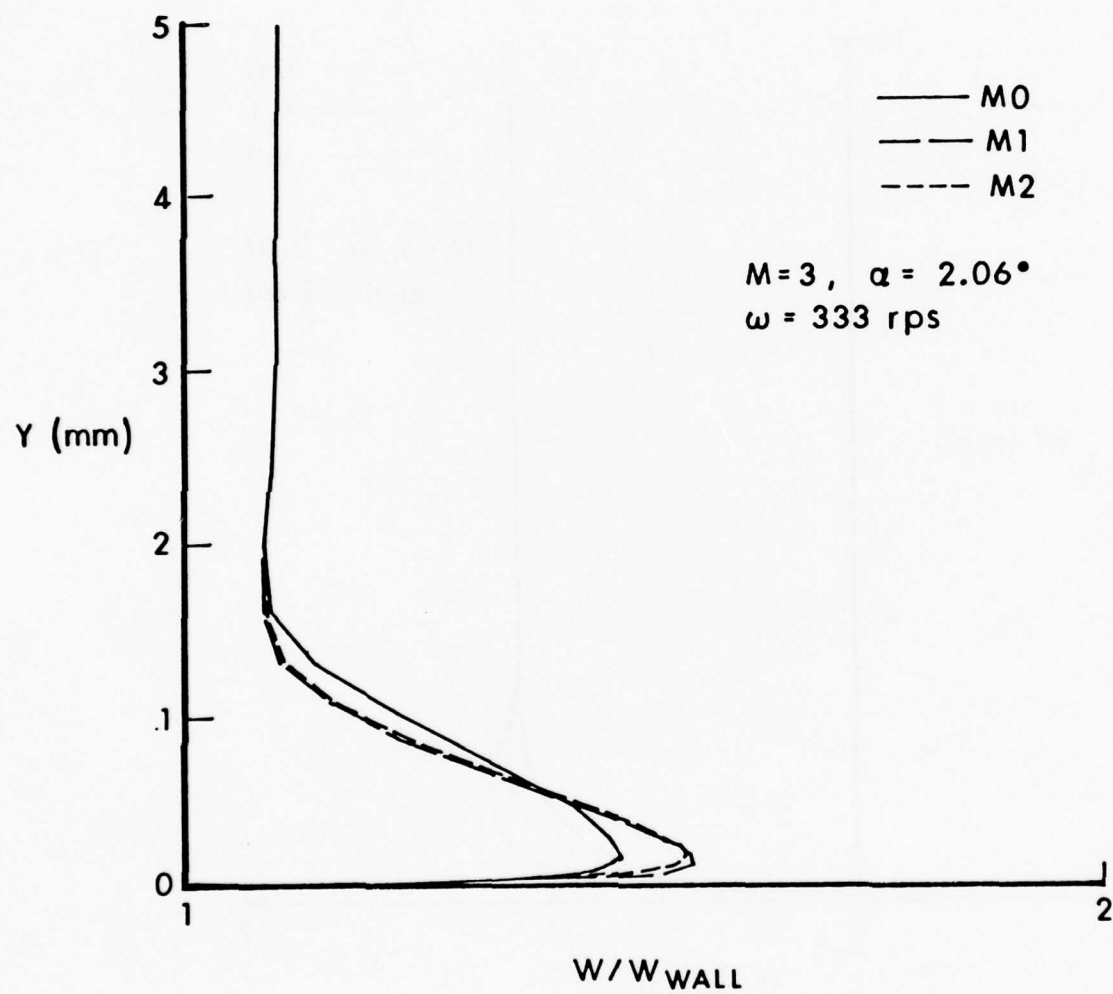


Figure 3. Circumferential Velocity Profiles, $Z/D = 5.67$, $\phi = 90^\circ$

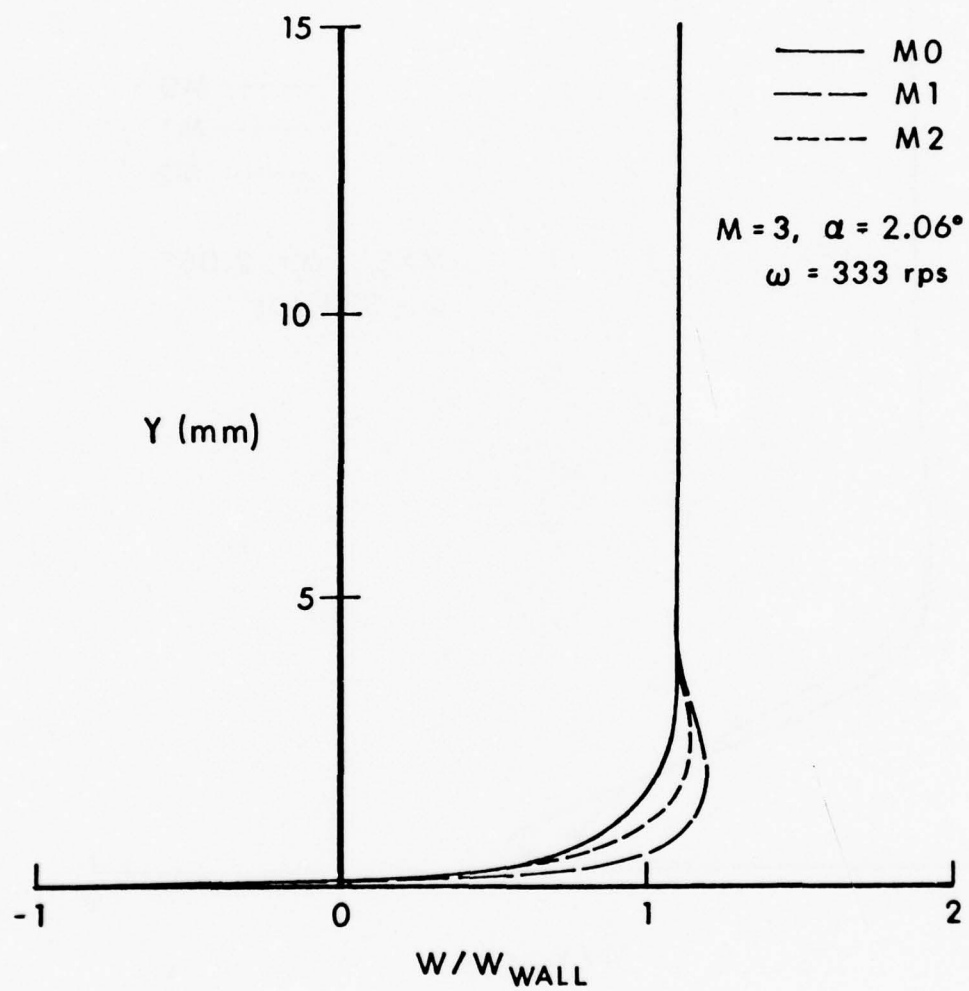


Figure 4. Circumferential Velocity Profiles, $Z/D = 5.67$, $\phi = 270^\circ$

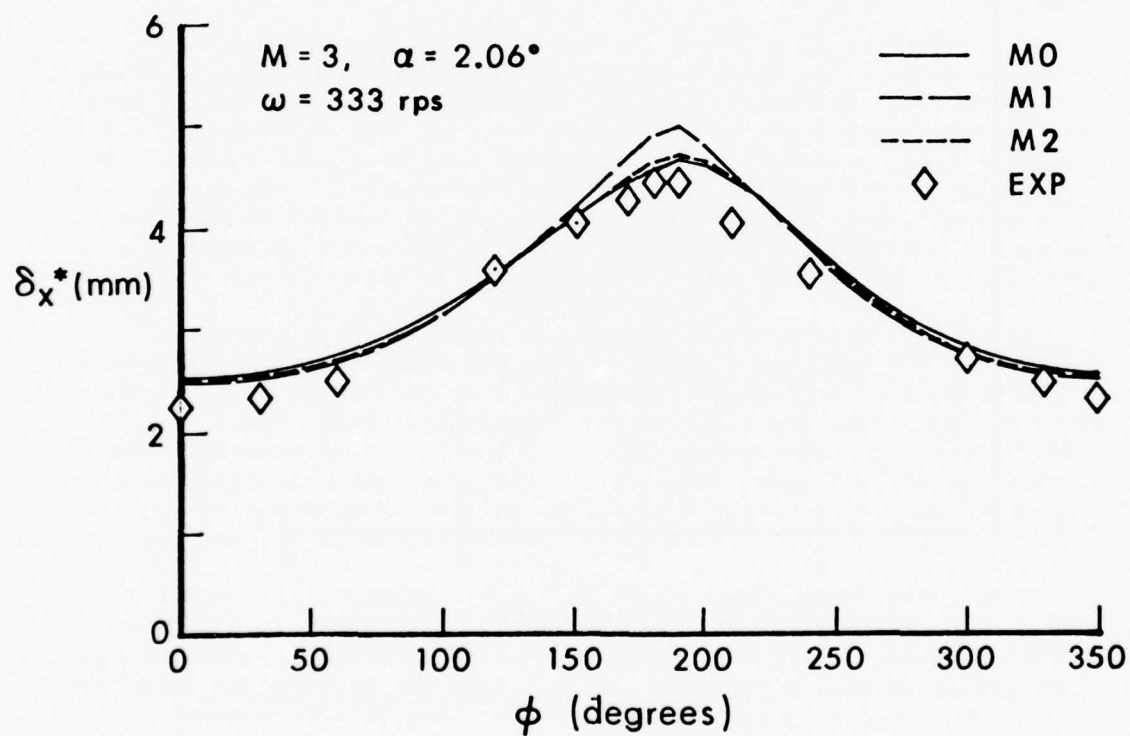


Figure 5. Circumferential Distribution of Displacement Thickness, $Z/D = 5.67$

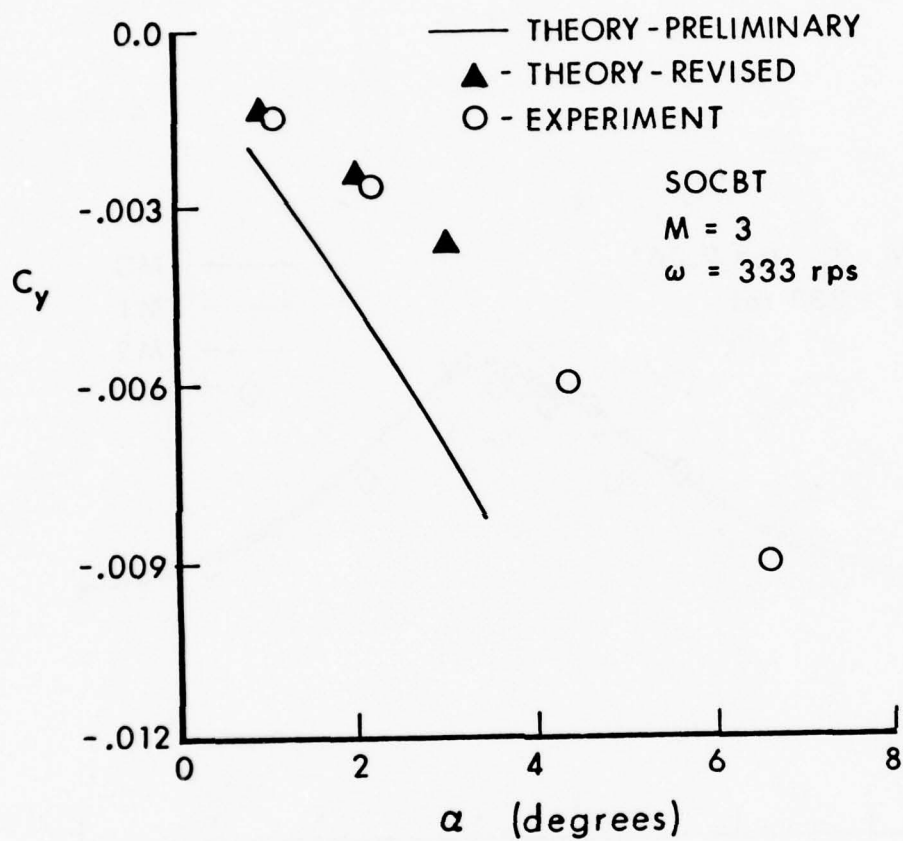


Figure 6. Magnus Force vs Angle of Attack--Computations Compared to Experiment

BOUNDARY LAYER TRANSITION ON TACTICAL MISSILE SEEKER DOMES

by

B. M. Ryan and C.F. Markarian

Naval Weapons Center, China Lake, California

Introduction

For some time the Navy has been concerned with the breakage of ceramic IR/EO seeker domes and the consequent inability of the tactical missile to perform its mission. By far the greatest current cause of such breakage is ground handling. With increased missile velocities, however, thermal stress failures caused by aerodynamic heating become a major concern. If boundary layer transition occurs on the dome, the resulting increase in heating rates and temperature gradients increases the probability of thermal stress failure of the dome.

Dome breakage causes both increased drag and inability of the guidance to perform properly. Because of uncertainties about the occurrence of boundary layer transition (and other factors), the engineer feels compelled to over-design the dome, often at greatly increased cost and sometimes even decreased operational effectiveness. An alternate, but undesirable, solution is to restrict the missile launch velocity. In addition to thermal stress problems with ceramic domes, boundary layer transition can cause longitudinal temperature gradients on radomes which can significantly affect the performance of millimeter wave seekers.

To address these problems the Naval Weapons Center instituted a program to develop engineering type criteria to predict the location of boundary layer transition on hemispherical domes in supersonic flow. In addition it was hoped to determine the severity and extent of the induced thermal stresses if transition did occur on the dome. The results of this investigation are to be used in computer codes for the analysis of seeker dome aerodynamic heating and thermal stresses on weapons systems of immediate and future concern to the Navy.

Figure 1 illustrates the effect of the temperature rise due to transition on thermal stress. If the flow remains laminar, the temperature distribution around the dome remains comparatively low and decreases uniformly as shown on the left side of the figure. The resulting tensile stress shows a similar behavior as illustrated by the lower curve on the right side of the figure. If transition occurs, however, there is a sharp increase in the temperature around the dome as the value approaches the turbulent curve. In this region of high temperature gradient there will be a peak thermal stress which could easily exceed the design strength of the dome. In the example shown, the stresses predicted in the transition region would cause failure of the magnesium fluoride dome. The extent of this region of large thermal gradients is also important in determining the magnitude of thermal stresses.

Another important consideration in the discussion of boundary layer transition is the determination of where transition takes place. Is the start of transition where the instability first begins or is it where the large scale flow characteristics have departed from laminar conditions? Does transition end where the flow is fully turbulent and what is "fully turbulent"? We favor the definition of transition as starting where the heat transfer coefficient begins to deviate from the laminar value and ending where it has reached the turbulent value. This definition allows emphasis of the practical effect on a design problem. The primary interest of the design engineer is the location of the effect of transition; i.e., where heat transfer effects are evidenced through significant increases in temperature and thermal stresses.

Background

The first step in the investigation of boundary layer transition criteria was to review the nature of the transition process as it has been understood from an historical viewpoint. A literature survey was conducted, existing flight test data were collected and analyzed, and available transition criteria were examined for applicability to the dome problem. The results of this effort are reported in NWC TN 4061-178 dated December 1975. The conclusions were (and are) that the many years of transition investigations still leaves us without a solution to the practical problem but at least more aware of the complexity and many variables involved in transition prediction.

Theory

Theoretical work is important, both to provide basic understanding and to serve as a guide for experiment. Stability theory has been applied to the transition problem to investigate the mechanism of the growth of a small disturbance in a laminar flow. Transition is basically a highly non-linear process but the stability theory can predict which flows are likely to become turbulent and what effect various parameters are likely to have on initiating instability which can lead to transition. The complex Navier Stokes equations are the basis for many attempts at studying transition. With the aid of high speed computers, it has become possible to obtain solutions to these equations which can aid understanding of the processes involved.

Ground Based Experiment

Experimental work can perhaps be classed in two categories: (1) verification and extension of theory and (2) design data. The former can lead to some understanding of the basic mechanism of transition and can also serve as a guide to further experimentation and corresponding extension of the theory. The latter is often only applicable to a particular restricted case and usually should not be generalized. Great care and patience needs to be applied in both cases, and detailed measurements of the disturbance environment must be made. There are many testing problems of which investigators are aware of today that were not

considered problems when much of the applicable data was taken. There may be other problems which are as yet undiscovered and, even those known of are not adequately understood.

All ground based experimental facilities have problems and limitations which must be understood before data obtained in them can be successfully applied and extrapolated to the real world environment. Basically the disturbance environment and the receptivity of the boundary layer to that environment must be determined. Care must be taken that transition measuring devices do not themselves contribute to transition.

Vorticity due to free stream disturbances causes problems in subsonic and low supersonic wind tunnels. Acoustic effects are also important in higher Mach number tunnels. The small models utilized in ballistic ranges can be affected by the high stress concentrations caused by the impulsive launching. The high vibration environment makes meaningful high speed sled tests difficult. These problems are but a few inherent to ground testing.

Dome transition data has been obtained in the NWC T-Range hot gas facility as part of a program to investigate thermostructural failure of IR/EO domes. This facility produces high speed, high temperature flow by burning propane with compressed air and expanding through a supersonic nozzle. While it was known the severe acoustical environment of T-Range would precipitate early transition, it was hoped something could be learned about the transition region. The results of two different tests are shown in Figure 2 where the experimentally derived heat transfer coefficient is shown for angular positions on the dome. The earlier test (June 1976) shows a rather mild effect of transition while the later test (April 1977) shows the more classic change from laminar to turbulent boundary layer conditions. Further investigation indicated changes were made to the T-Range burner that may have resulted in smoother flow conditions during the later tests. These tests and others performed by NASA indicate that the mechanism of transition may be very important in determining the behavior in the transition region. Thus, care must be taken in interpreting results and drawing conclusions even for behavior during transition.

Flight Test

Even with all the uncertainties, it is still necessary to have some guide to predict transition locations for existing problems that require immediate solution. It is important to use any such guide with care keeping in mind the limitations and perhaps restricted applicability. Nevertheless, for our purposes it was decided to develop an interim criteria based on flight test data.

Proper interpretation and use of flight test data is not without difficulty. Flight testing is also considerably more expensive than ground based testing which is in turn more expensive than computer experiments. In unmanned flight testing (and even to some extent in manned testing) it is not possible to precisely check the data or accurately control the test vehicle. It is not possible to repeat a flight

exactly and the vehicle may move between environments where many parameters vary simultaneously and the dominant cause of transition may also be changing. Free stream disturbances are important in ground testing but the effect of atmospheric turbulence in flight is unknown and the prediction and/or measurement of such turbulence is very difficult. The accurate measurement of the flight conditions and data (altitude, Mach number, angle of attack, skin temperature) is not easy and cannot be checked by repeating the experiment. Local damage or deformation in flight is usually not determinable since the test vehicle (if it is unmanned) is usually not recovered or is damaged on landing. One of the biggest problems is roughness. Many investigators have carefully measured roughness prior to flight test but later advances in roughness measurement and understanding have indicated that their measurements may not have been accurate or may have been incomplete. Even if the roughness (or lack of) should be accurately determined, what about the possible influence of fingerprints while loading, bug impact, rain or dust erosion and possible deformations under flight loads? Thus, in any flight test, the condition of the model is always in question.

Most of the flight tests applicable to the hemispherical dome problems were conducted in the middle to late 1950's. In these experiments, even within individual tests, the data are often quite scattered and meaningful correlations very difficult. The results of some of these tests are shown in Figure 3 in the form of momentum thickness Reynolds number at transition plotted against Mach number.

One flight test has been made at NWC which provided data on dome aerodynamic heating. Results of this test indicated that transition did not occur on the dome. Temperatures along the inner wall of a magnesium fluoride IR dome were measured during free flight of a boost-glide missile following a Mach 1.8 launch at an altitude of 42000 feet. Measured and calculated temperature distributions along the dome at two different times into the flight are shown in Figure 4. The calculated curves were obtained using special purpose computer sub-routines in conjunction with a large, general thermal analyzer computer code. The method of Fay and Riddell was used to compute the stagnation point heat transfer, the method of Lees to compute the laminar boundary layer aerodynamic heating and Kays techniques for turbulent heating. The specific techniques are described in NWC TN 4061-172 dated June 1974. The furthest aft sensor, at 68 degrees, is located near the junction of the hemispherical dome and ogival missile forebody. The temperature of the outer surface of the dome would give a more definite indication of transition but is impractical to measure in this type of test. Pre-flight thermal response calculations for the expected flight conditions had shown that transition could be detected by the inner wall temperature distribution if its effect were significant. Calculated streamwise temperature distributions are shown in Figure 4 for both laminar and transitional boundary layers. The data follows the predicted laminar distribution and does not show the inflection in the temperature distribution that would occur if transition were present to a noticeable extent. The maximum momentum thickness Reynolds number on the dome during this flight was 440.

Transition Criteria

There are probably almost as many transition correlation and prediction criteria as there have been investigators of the phenomena. The criteria in use currently by the Aerothermodynamics group at the Naval Weapons Center is possibly the most commonly used criteria for estimating transition on blunt bodies. Transition is assumed to be dependent on the momentum thickness Reynolds number (Re_θ) only. The momentum thickness is a measure of the decrement of momentum flux caused by the boundary layer and may be defined as

$$\theta = \int_c^\infty \frac{\rho u}{\rho_\infty u_\infty} \left(1 - \frac{u}{u_\infty}\right) dy$$

where

θ = momentum thickness
 y = direction normal to surface
 u = velocity along surface
 ρ = density

and the subscript ∞ indicates free stream conditions.

The value of $Re_{\theta_{tr}}$ for a particular problem is chosen by intuition and engineering judgement (in other words, it is a guess). Based on reported flight test results, $Re_{\theta_{tr}}$ can vary from 150 to more than 2000. One would tend to choose a low value of $Re_{\theta_{tr}}$ for a dome with a "rough" surface. Also it might be proper to raise the value of $Re_{\theta_{tr}}$ for large diameter configurations (perhaps transition is delayed due to less cross flow effect). For a smooth hemispherical dome, mid range of supersonic Mach numbers (2-5), medium diameters (about 3 inches), zero angle of attack and average wall temperature, NWC has selected $Re_{\theta_{tr}} = 750$ as a typical value for the transition criteria. This value has been chosen because flight test results have seemed to indicate that transition for these conditions usually occurs aft of the dome. A value of $Re_\theta = 750$ for these domes is aft of the hemisphere. Current effort is being directed towards trying to define trends of $Re_{\theta_{tr}}$ with various parameters as shown in Figure 5 and, hopefully, when these trends are established, assigning ranges of values. Even if such a quantification becomes possible, it is necessary to consider each case individually for any special effects due to the particular configuration. It is also urged that a range of values be considered to test the effect of the uncertainties on the final results. These trends, if confirmed, are very qualitative as the data base necessary to establish such trends, particularly flight test data, is meager.

Roughness Effects

Having tentatively concluded that transition does not usually occur on smooth domes of current and near future interest to the Navy, our investigations turned to "rough" domes. Rough domes can be a practical

case due to rain erosion and other operational effects. Wind tunnel tests on rough domes may be applicable since the roughness can dominate as the cause of transition, rather than the incompletely understood wind tunnel effects. Investigators at NSWC, White Oak, are doing wind tunnel tests on rough domes to determine the turbulence input to a computer code originally developed by Donaldson. This analytic technique works back from turbulence to find transition location.

Investigators at Aerospace have suggested a smooth dome is simply a limiting case of a rough dome and thus have developed techniques for extrapolating transition on a rough dome to transition on a smooth dome. As an extension of their effort a series of graphs have been developed relating momentum thickness Reynolds numbers to edge Mach number for various values of roughness and wall temperature. These correlations are currently being compared with experiment but there are no results as yet.

The Future, Conclusions and Recommendations

1. The theoretical studies need extension to the non-linear regime. Combined theoretical-experimental work is needed as a guide to understanding both. Correlation of the results available from stability theory would aid in establishing trends and bounds of various key parameters.
2. Further carefully done experimental work is required. Most important perhaps is the type of experimental work that can aid in developing and verifying theoretical understanding. Basic investigations of the ground based facilities are required to determine the application of those results to the flight environment. Additional flight tests are required for correlation with theory and other experiment.
3. Accurate and practical correlations and transition criteria are needed for application to specific and existing problems. The application and sensitivity to particular problems must be investigated.

All of the above are underway at various facilities and, hopefully, will lead to further understanding. The pessimist could conclude that with all the many years of effort devoted to transition we are still no farther along. But there has been a tremendous increase in the appreciation of the complexity of the problems and in understanding of the number of parameters involved and interrelated. The optimist can only conclude there will eventually be a means of predicting transition location even if only in a probabilistic form.

MAGNESIUM FLUORIDE DOME
MACH 1.6 LAUNCH AT 30K

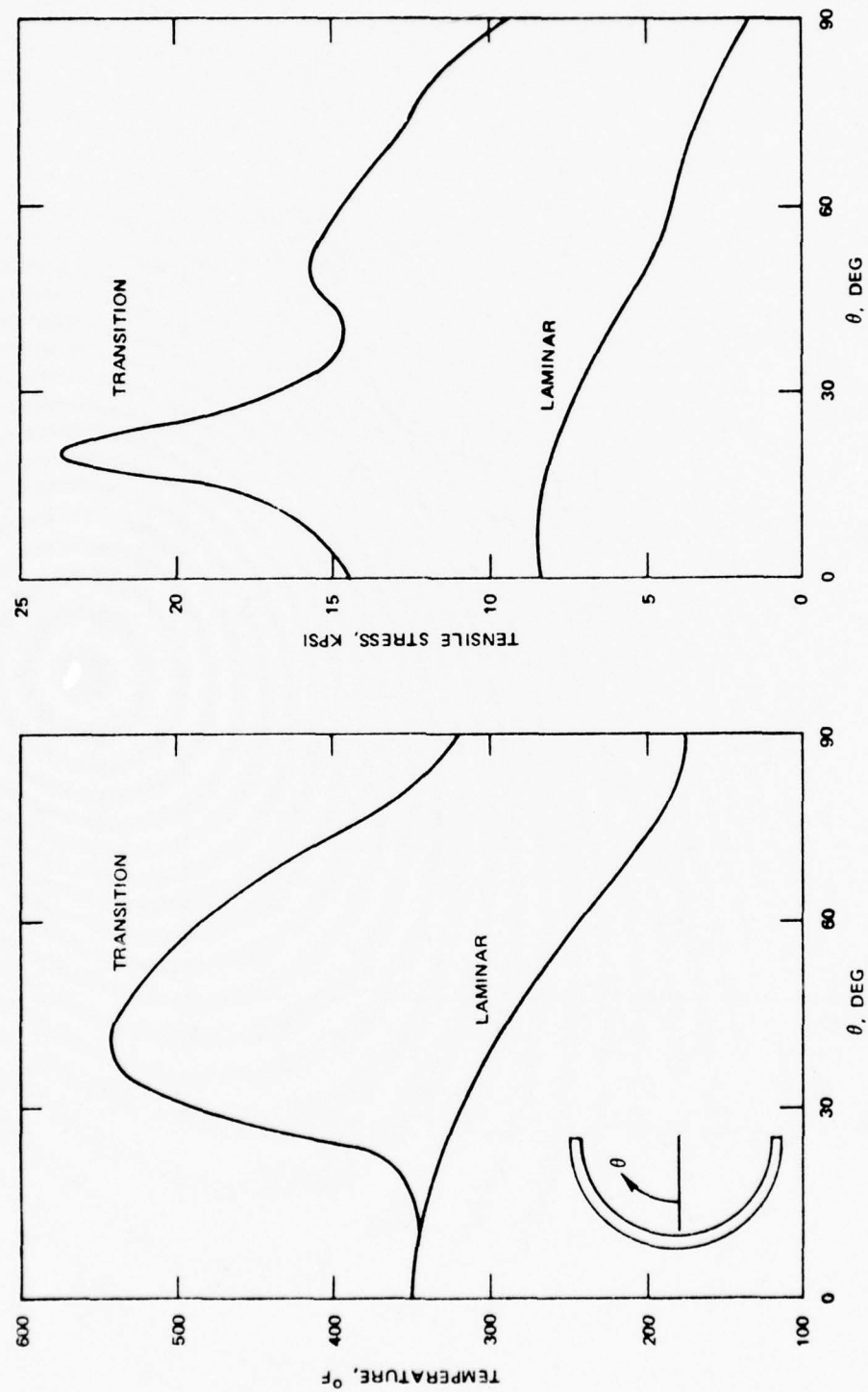


FIGURE 1: EFFECT OF BOUNDARY LAYER TRANSITION ON INNER WALL TEMPERATURE AND STRESS

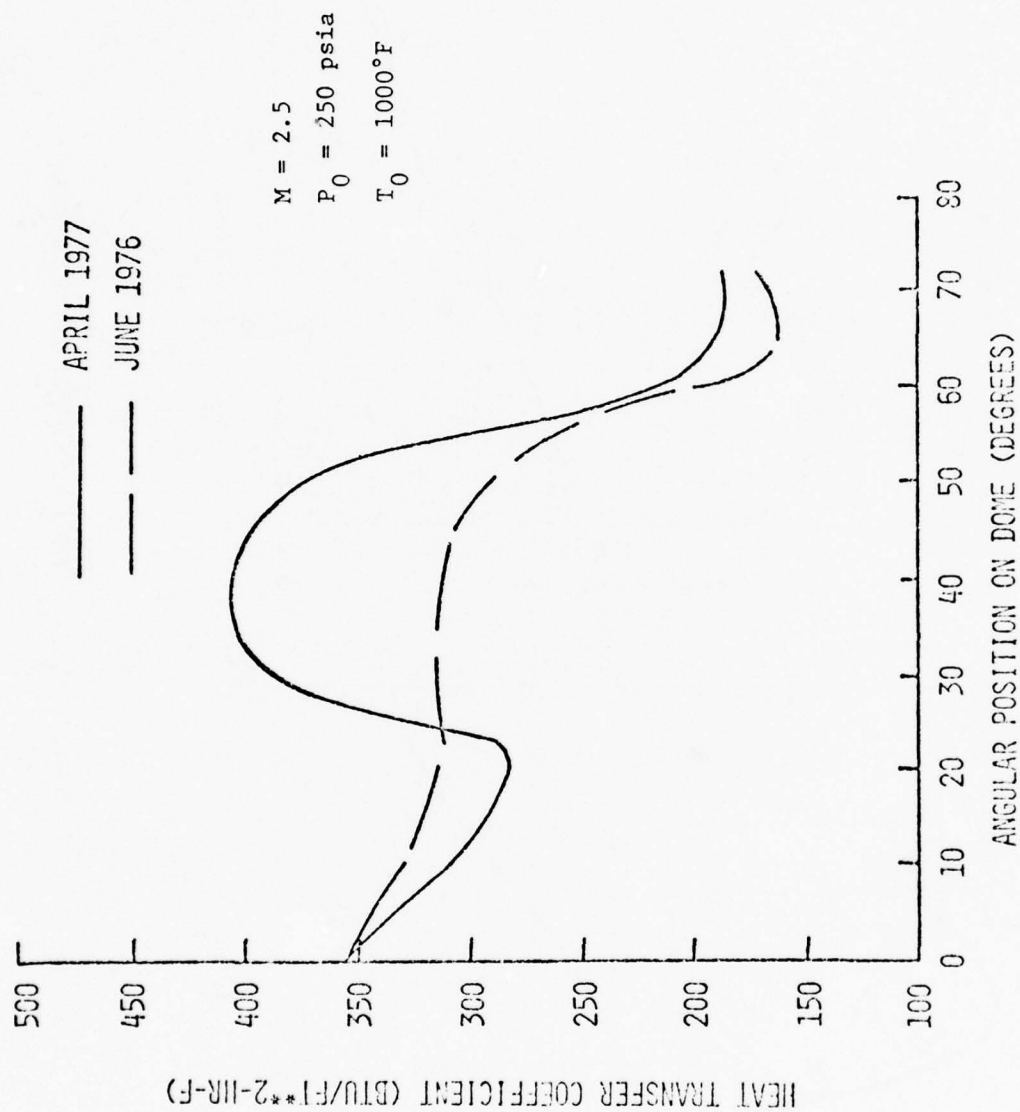


FIGURE 2: DERIVED HEAT TRANSFER COEFFICIENT DISTRIBUTIONS
FROM FREE-FLIGHT SIMULATION TESTS

SYMBOL	INVESTIGATORS	CONFIGURATION	RMS ROUGHNESS, MICROINCHES
○	HALL, SPEEGLE, PILAND	HEMISP-CYLINDER (8 IN. DIAMETER)	1-5
□	KRASNICAN, WISNIEWSKI	HEMISP-CYLINDER (9 IN. DIAMETER)	3-5
◇	GARLAND, SWANSON, SPEEGLE	1/10 POWER NOSE	6-8 (MAX 15)
△	BUGLIA	HEMISPHERE-CONE (HEMISP DIAM 12.582 IN.)	2-4
▽	GARLAND, CHAUVIN	HEMISP-CYLINDER (8 IN. DIAMETER)	25

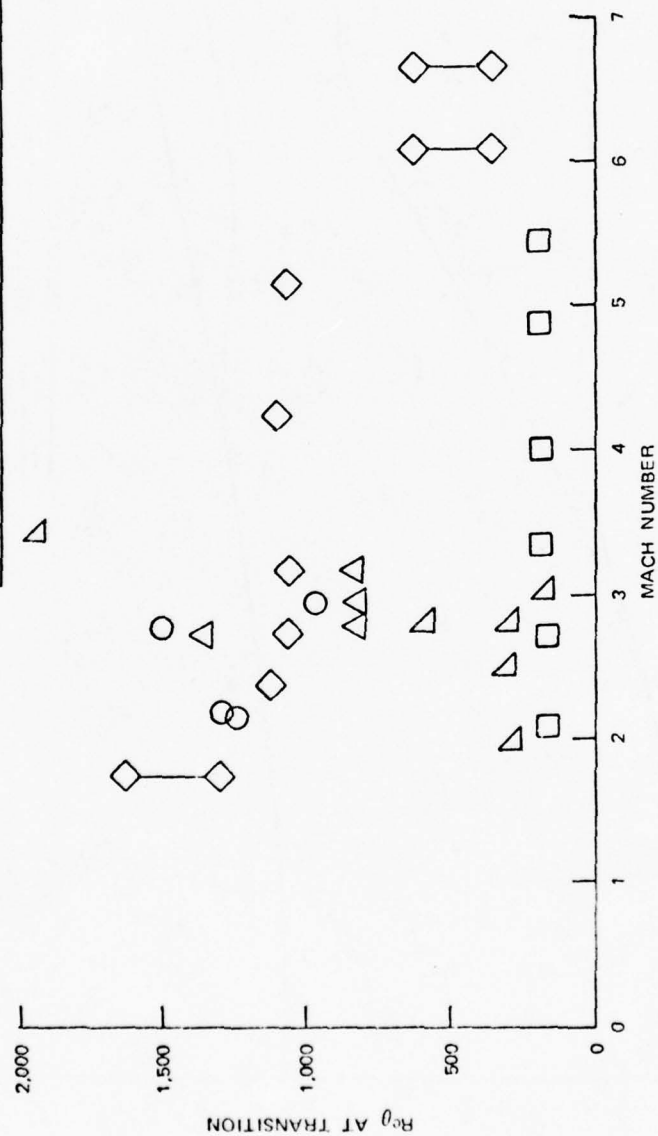


FIGURE 3: SUMMARY OF NOSE CAP TRANSITION FLIGHT TEST DATA

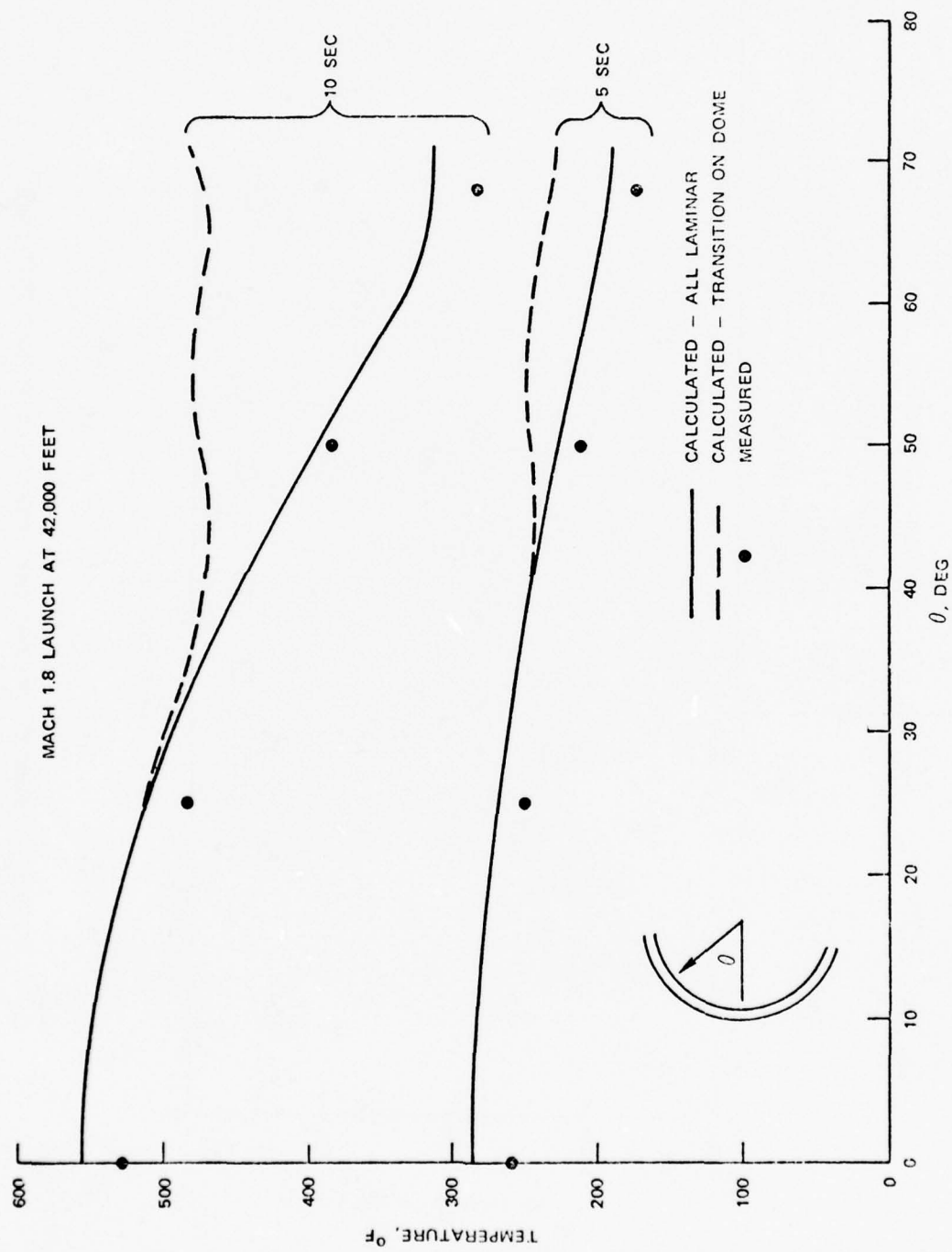


FIGURE 4: IR DOME INNER WALL TEMPERATURE DISTRIBUTION

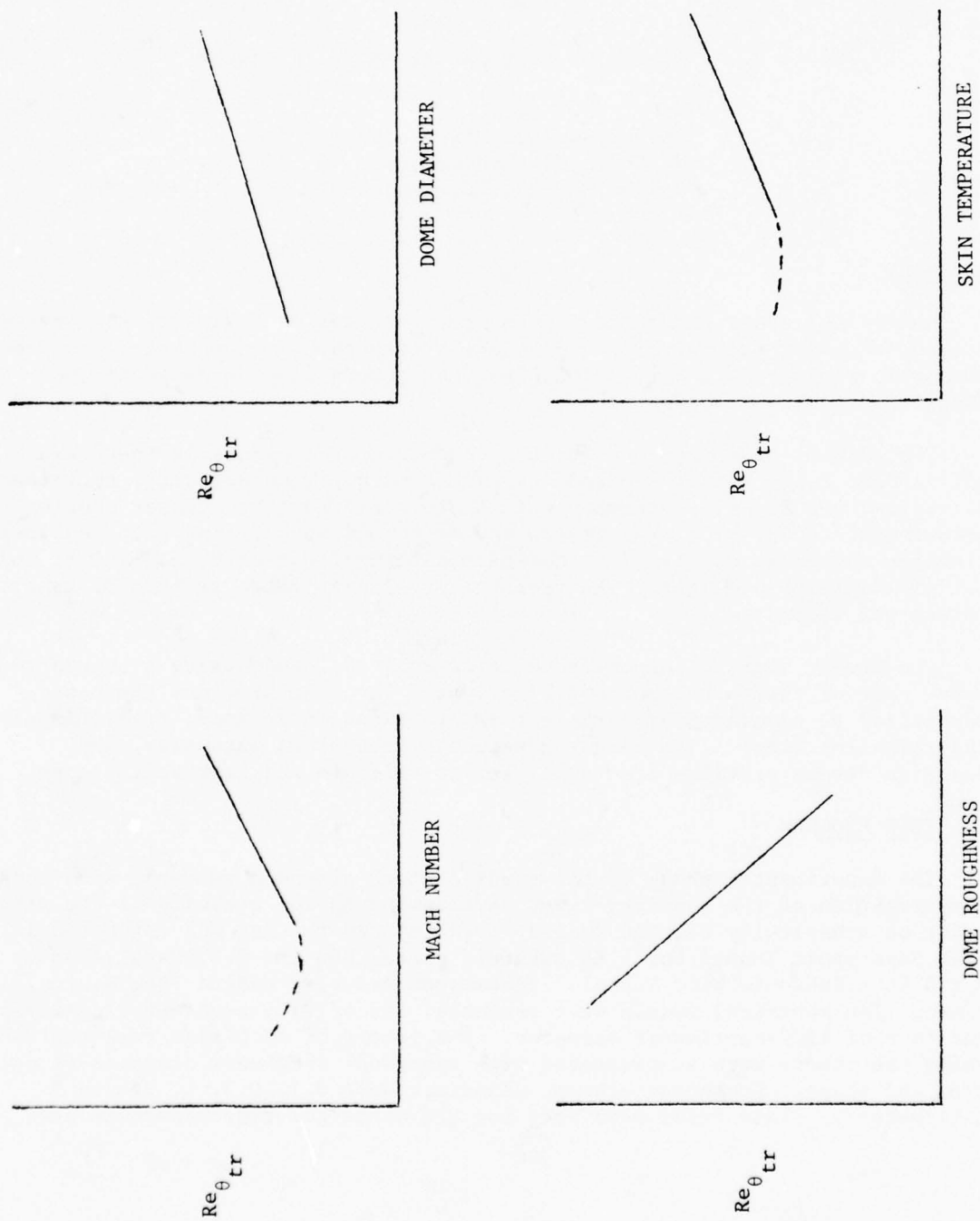


FIGURE 5: QUALITATIVE VARIATION OF BOUNDARY LAYER TRANSITION CRITERIA WITH VARIOUS PARAMETERS

SPHERICAL NOSE ROUGHNESS EFFECT ON
BOUNDARY-LAYER DEVELOPMENT

by

R. L. P. Voisinet, R. E. Phinney, and W. J. Yanta

Naval Surface Weapons Center
White Oak Laboratory
Silver Spring, Maryland 20910

ABSTRACT

Analytical and experimental exploratory studies of a simple incompressible stagnation point flow with roughness are presented. The purpose is to identify the basic parameters and relationships that govern flow development and transition on blunt bodies.

The current experiments study the cases where roughness is the dominant influence. A low turbulence wind tunnel is used. Mean velocity, turbulence intensity, and Reynolds stress profiles are measured with a Laser Doppler Velocimeter (LDV). The experiments are performed on 12.7 and 21.6-centimeter diameter spherical models with roughness distributions of 9, 3, 1, 0.3, and 0.1 millimeters in height. The freestream velocity range is from 3. to 75. meters per second.

Concurrent with the experiments is an analytic study using a boundary-layer code of the turbulence modeling type. The code provides the basic capability to simulate the turbulent interactions in laminar, transitional, and turbulent flows. The measured velocity, turbulent intensity, and Reynolds stress profiles are to be used to validate and improve the code.

I. TEST PROGRAM

The experimental phase of the study centers around a subsonic wind-tunnel investigation of the boundary-layer development in the vicinity of the stagnation point on spherically blunted bodies. Preliminary testing was conducted in the NSWC Supersonic Tunnel No. 1 at subsonic speeds and the U.S. Naval Academy 3 x 4 foot Subsonic Wind Tunnel. Freestream velocity ranged from 3. to 75. m/sec. Ten spherical models were prepared; six of 21.6-centimeter diameter and four of 12.7-centimeter diameter. One sphere of each size remained smooth while the others were instrumented with spherical roughness elements of uniform size and shape. Roughness element diameters were 0.1, 0.3, 1, 3, and 9 millimeters. Glass beads were used for the spherical roughness elements.

These were commercially available but had to be sorted as to size and spherical shape uniformity. Figure 1 shows a model which was instrumented with 1mm-diameter roughness elements. The glass beads were attached to the model by coating the surface of the model with an epoxy adhesive and sprinkling the elements onto the surface. The average surface coverage averaged 65 to 70 percent and was typical for all roughness element sizes. A close-up photograph of the roughness elements (Figure 2) shows the type of non-patterned uniformly-distributed roughness which resulted.

The combinations of roughness heights and model diameters provided for a range of roughness height to model nose radius (k/R_N) from 0.001 to 0.1 for a range of Reynolds number based on nose radius (Re_{Rn}) from 1×10^4 to 5×10^5 . For this test matrix, the roughness height to boundary-layer thickness ranged from the aerodynamically smooth to the fully rough regime with the added condition of roughness heights greater than the boundary-layer thickness.

The Laser Doppler Velocimeter (LDV) was the main diagnostic technique used for flow measurement. The LDV technique was chosen because it provided a capability for multi-component measurements of mean velocity and turbulent intensity, Reynolds stress, and turbulent energy without flowfield interference.

The LDV system is shown schematically in Figure 3. It consists of a Thermo-Systems 2-channel, 2-color optical system together with an argon-ion laser. The laser is operated in a multi-wavelength mode. The wavelengths of the laser output are separated by passing the laser light through two dispersion prisms. The two major lines (488nm and 514.5nm) are then split to form two sets of beams in two mutually perpendicular planes. All four beams are then focused to a point in the flowfield through a lens system. The scattered light from particles in the flow is collected and imaged onto a pin hole to minimize stray light and to maintain a small spatial resolution. The collecting optics includes provisions for separating the scattered light signal into two colors and focusing them onto two photodetectors. The signals from the photodetectors are then processed by two Doppler burst processors. The digital output from the processors which is the period of the Doppler frequency is then stored until a suitable number of samples are taken (typically 1,000 to 5,000 points). Finally the data are transferred to a minicomputer where the various moments of the velocity probability distribution function are computed. The focal volume diameter was 0.11mm (0.0044 inches). The aerosol was generated from olive oil using a Laskin nozzle. The mean diameter of the aerosol particles was determined to be 1.5μ .

II. RESULTS

Wind-tunnel tests were first conducted in the NSWC Supersonic Wind Tunnel 1 at subsonic speeds for the purpose of checking out the LDV capabilities. Mean and fluctuating velocity measurements were made along the stagnation streamline

and along a normal to the surface at a point 90 degrees from the stagnation point of the 21.6-centimeter diameter sphere model instrumented with 1mm-diameter spherical roughness elements. Agreement with theory was found to be excellent for mean velocity distribution (see Figures 4 and 5) and turbulence intensity (Figure 6).

Calculations were made to determine the extent of particle lag along the stagnation streamline of the sphere. It was determined that the error in mean velocity would be less than 0.5 percent for particles as large as 5 microns. However, there could be substantial errors (or the order of 10 percent) in the turbulence measurements if too large an aerosol particle were used. Large particles do not decelerate at the same rate as smaller particles, and a variation in velocities measured at the focal volume could result from the particle size distribution and not turbulence. This problem necessitated a tight control over the aerosol generator output. Aside from this problem, the LDV system performed well.

LDV verification tests resumed in the larger Naval Academy 3 x 4 foot Subsonic Wind Tunnel. The facility had just undergone modification in which turbulence reducing screens had been installed. The turbulence level of the facility was a nominal 0.1 percent. Velocity surveys were limited to (1) sweeps along the stagnation streamline, especially for low freestream velocities, and (2) boundary-layer profiles at the point 90 degrees from the stagnation point, for large freestream velocities.

Figure 7 shows the mean velocity distributions along the stagnation streamline above various roughness elements. The velocity is seen to extrapolate back to zero at some point near the mid-height of the roughness elements, as it does for flat plate boundary layers. The fluctuating components of velocity (not shown) were large and appeared well ahead of the body even for the smooth model. This unexpected phenomena appeared to be caused by a wandering of the stagnation point and was confirmed by the observation of a particle fog in the facility. The implications of such an unsteady condition have not been resolved.

The velocity profiles around the body are shown in Figure 8. The data are compared to the theoretical curve for a sphere. However, since the tests were conducted with a streamlined afterbody on the sphere, the data should not be expected to agree with theory. The data parallels the theoretical curve and breaks away near the surface to form the boundary layer. Two curves are shown for the case $K = 9\text{mm}$, $V_\infty = 30.5\text{m/sec}$ and $\phi = 90$ degrees. They correspond to surveys on opposite sides of the model. The boundary-layer profiles for these two "identical" cases appear to give measurably different boundary-layer thicknesses. The proposed explanation is that one survey is obtained above a roughness element while the other is above a space between roughnesses. This discrepancy pointed out the need for the accurate determination of the location of the focal volume in relation to the surface and roughness elements.

Turbulent shear stress distributions have been the most difficult of the measurements to make. Values are determined from the difference in the standard deviation of two nearly identical velocity histograms. The tests pointed out the stringent requirement which must be imposed on the LDV signal conditioning electronics. As a result, the LDV system is currently undergoing a major upgrading in preparation for the final testing phase. The new system will provide a greater signal-to-noise processing capability, an order of magnitude faster data-handling rate, a significant improvement in system reliability, and an increased flexibility in the types of aerodynamic experiments for which the LDV can be used.

The results of the preliminary investigation have been worthwhile in uncovering potential problem areas, especially with the LDV system. The results have also been very encouraging in that the LDV has worked with such success.

III. FUTURE PLANS

As soon as the new LDV equipment is made operational, the Naval Academy tests will be resumed and completed. By the time the experiments are completed, a stagnation point turbulence modeling code will be operational on the NSW computer, and comparisons between experiment and theory will be made.

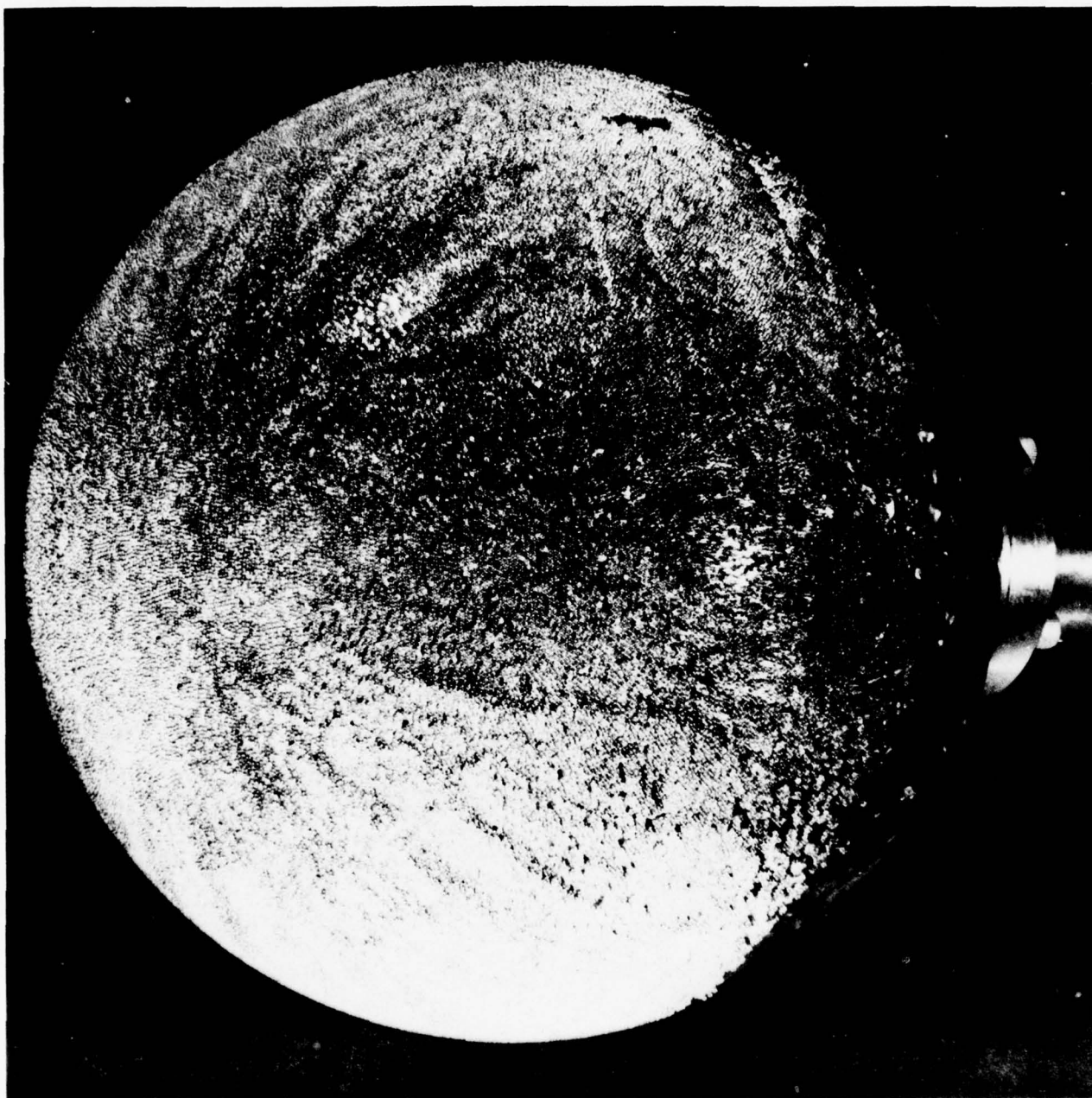


FIGURE 1 WIND-TUNNEL MODEL INSTRUMENTED WITH
1MM-DIA. ROUGHNESS ELEMENTS

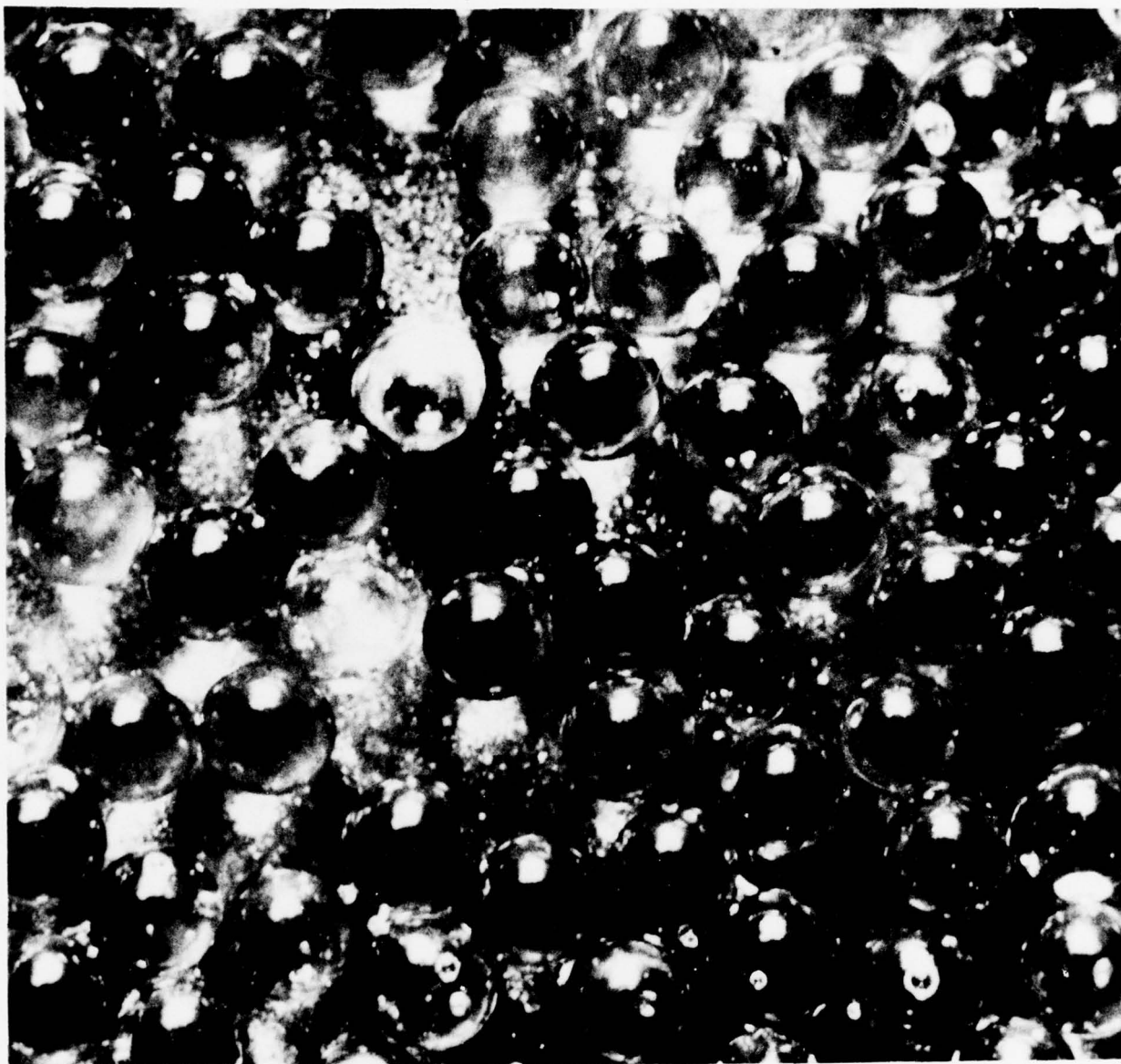


FIGURE 2 MODEL ROUGHNESS DISTRIBUTION,
K = 1MM DIA.

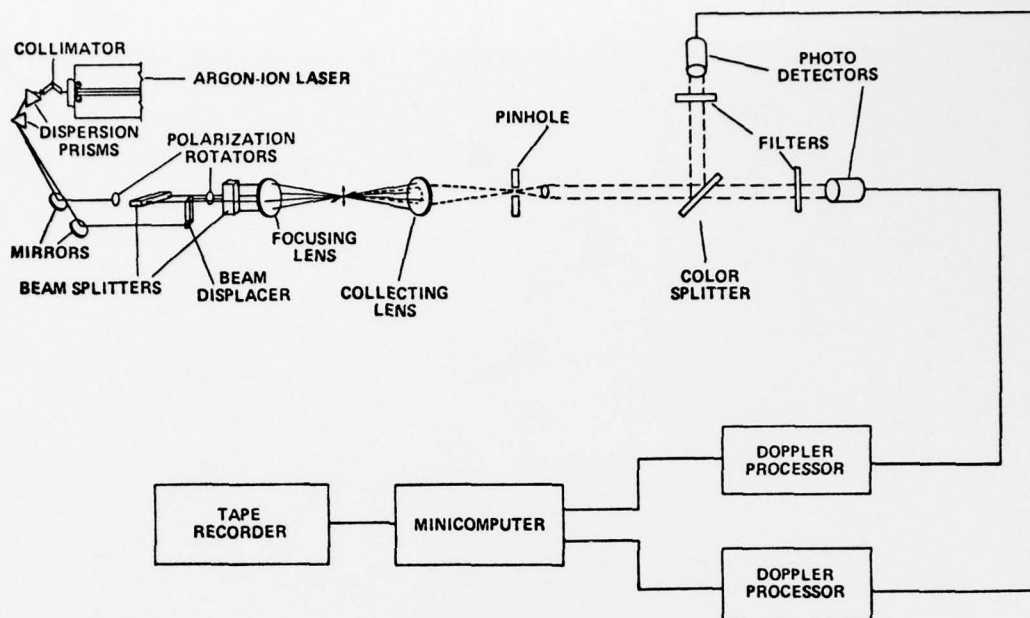


FIGURE 3 TWO COMPONENT - TWO COLOR LASER DOPPLER VELOCIMETER SYSTEM

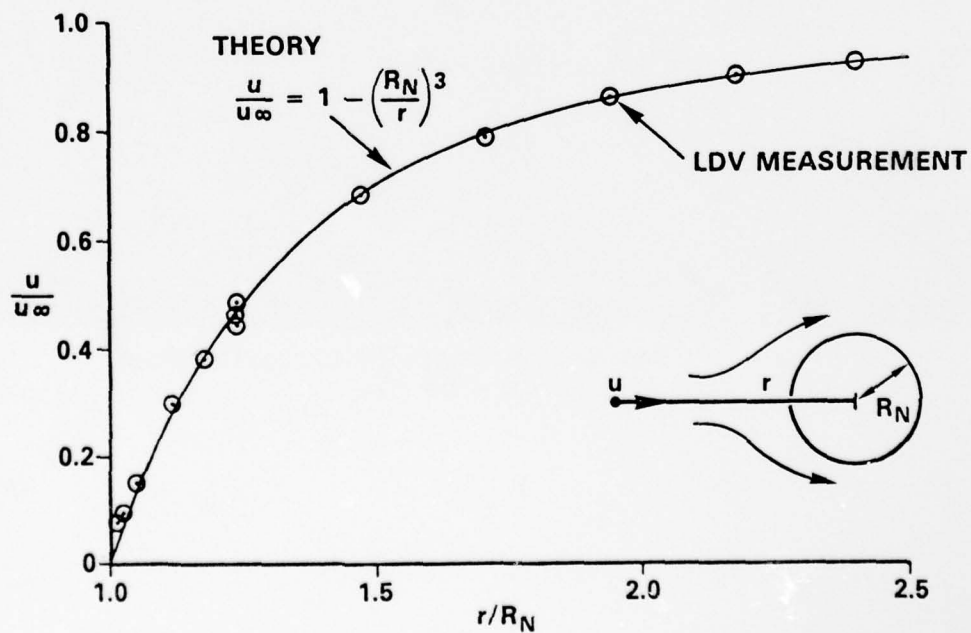


FIGURE 4 VELOCITY DISTRIBUTION ALONG STAGNATION STREAMLINE

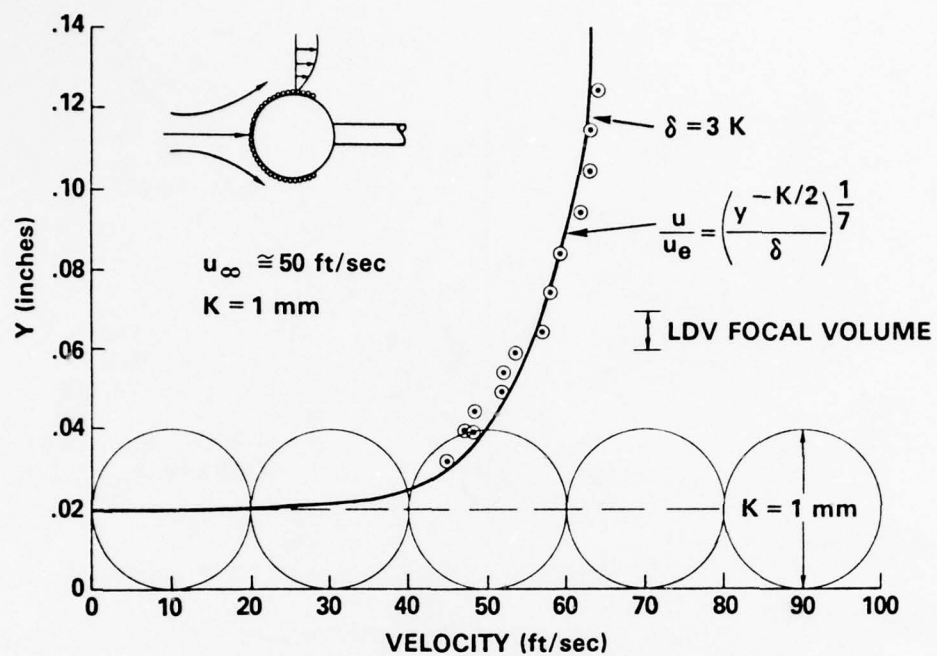


FIGURE 5 MEAN VELOCITY PROFILE ON ROUGHENED SPHERE MODEL

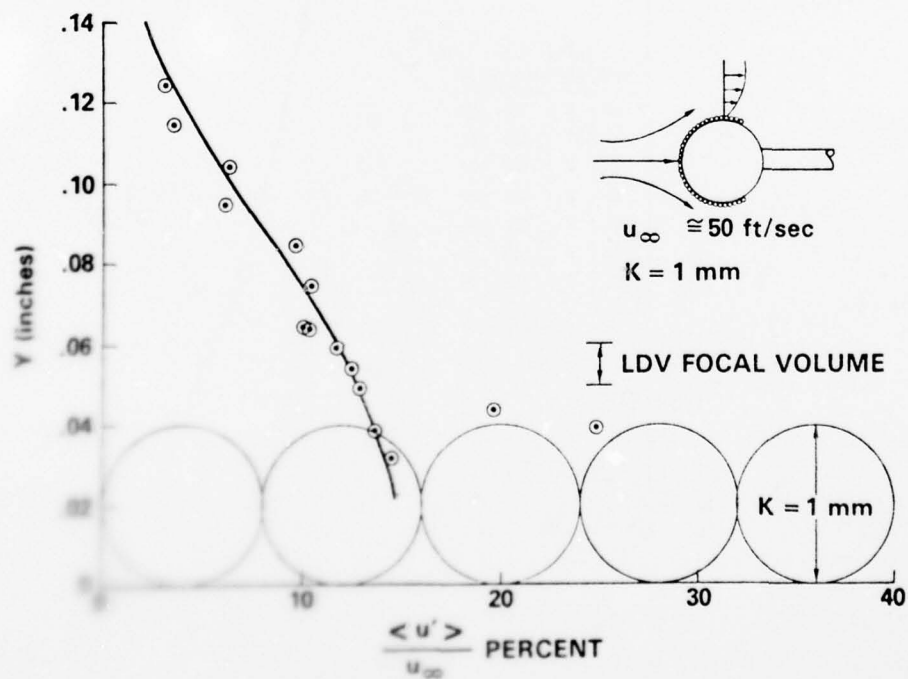


FIGURE 6 TURBULENT INTENSITY PROFILE ON ROUGHENED SPHERE MODEL

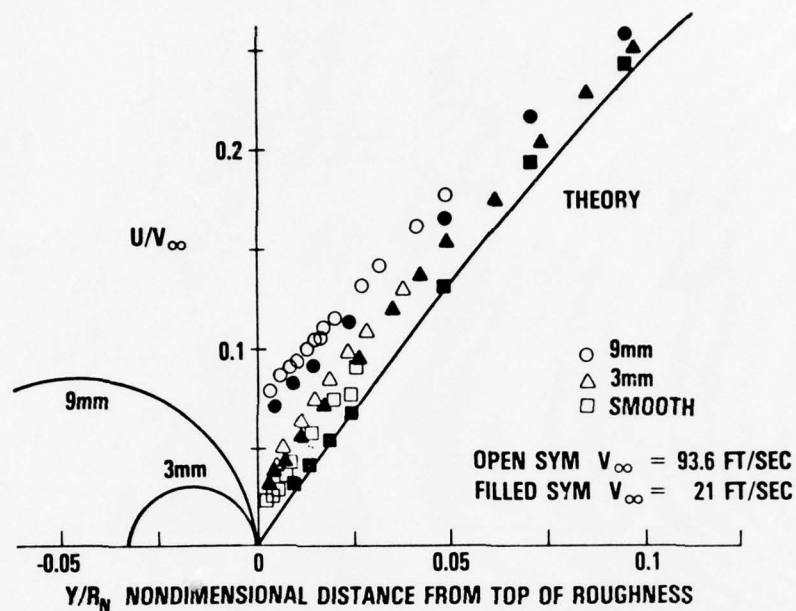


FIGURE 7 MEAN VELOCITY DISTRIBUTIONS ALONG STAGNATION STREAMLINE

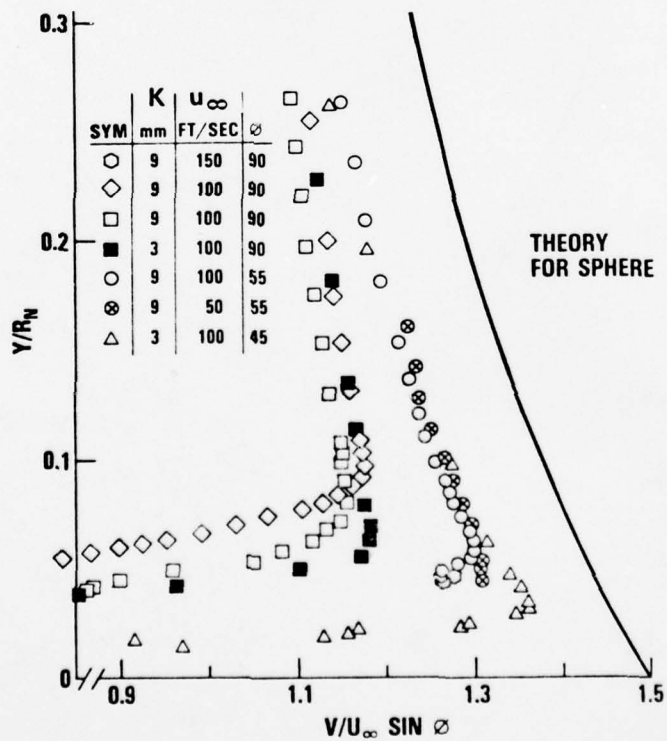


FIGURE 8 MEAN VELOCITY PROFILES AROUND THE ROUGHENED SPHERICAL MODELS

ON FULL SCALE LASER-VELOCIMETER MEASUREMENTS OF SHIP BOUNDARY-LAYER FLOW

by

J. Kux, T. Niemeier

Institut für Schiffbau der Universität Hamburg

INTRODUCTION

Full scale measurements of the flow around the ship hull are not very common [1] due to their expensiveness and to the difficulties inherent to the problem. Experimental research in ship hydrodynamics has therefore mostly been restricted to laboratory investigations at model scale (towing tanks, wind tunnels, etc.). At the last two meetings it has been reported about wind-tunnel measurements at the Institut für Schiffbau (IfS) which are typical for these model investigations. The situation is nevertheless an unsatisfactory one since Reynolds-numbers in these experiments differ from those in the full scale case by figures up to 10^3 . Extrapolation of results over such a range is more than dubious. The need for full scale measurements is evident. Several attempts have rendered a rather restricted amount of information. It is the stern region of the ship where most efforts have been concentrated due to the high interest the wake characteristics have for the understanding of propeller performance and for better propeller design techniques [1], [2]. Considering the size of modern ships one soon realizes the problems imposed on probe assemblies if pressure tubes, hot wires (or films) or other material probes are used.

This led us to the decision to develop the technique of laser-Doppler-velocimetry (LDV) in order to obtain an apparatus suitable for such measurements. First suggestions were formulated in 1973 but until the optics purchased were delivered it was fall of 1976. The LDV technique is now widely applied to flow measurements [3] but if one searches literature it readily becomes evident that most experiments are tailored

to meet the possibilities of the device at hand while the reverse would be desirable. It became our policy to design the devices ourselves to a certain degree. Of course this meant a considerable effort of development and testing. So the electronics for data reduction of the system have not yet found their final form and of course the whole device will probably have to be redesigned again and again.

Projects of this magnitude require the joint effort of many investigators. At the institute M. Scheinpflug, H. Stoermann and J. Schulz made valuable contributions. The measurements on board would not have been possible without the contribution of the Research Cooperative Programme. This cooperative with about 20 societies or institutions as members including well known ship owners joined us and contributed the financial support for the experiments. The measuring team included H. Liland and V. Vindøj from Det norske Veritas and H. Wood from Shell Intern. Marine. We acknowledge the contribution of this society which provided the ship, the liquid gas tanker "Methane Progress", and gave us all the help we needed.

EXPERIMENTAL APPARATUS

The principle of LDV is based on the detection of the frequency shift appearing when laser light is scattered from small particles moving with the flowing fluid. This shift, due to the well known Doppler effect, though being rather small, is detectable by means of interference techniques which yield the frequency shift as beat frequency at the photodetector. No more details on the basic theory shall be presented here ([3],[4],[5],[6]). Since a great number of optical arrangements is possible, first and basic decisions had to be made on the optics and the guidance of the beams. The geometry of the problem required that the detection of the radiation was to be in the backscattering mode raising intensity problems. The intensity scattered in backward direction is up to 10^3 times lower than that scattered in forward direction. Therefore the observation should be

through a lens with as high an aperture as possible. This leads to the crossed beam or differential-Doppler mode, which means the following: The laser beam is split into two separated beams of equal intensity which are focused on the point where the velocity is to be measured and where they intersect under a certain angle (Fig.1). The intersection volume of these incident beams is the sensitive volume of the device and may be depicted as an ellipsoid (Fig.3). A particle crossing this volume will scatter light (photons) from both beams. Both scattered waves, provenient from the same particle as scattering center and being coherent interfere producing the beat frequency at the detector since they have different Doppler shifts.

Three main problems had to be overcome: the long distances (order of magnitude several meters) over which the measurements should be performed, the positioning of the measuring volume and the high level of vibration to be expected. This latter difficulty demanded a so called integrated optic, an optical system where focusing of the incident beams and collection of the scattered radiation is performed by the same elements. Such a system remains focused even at high vibrational levels. In order to prevent the intersection angle of the incident beams from becoming too small and considering the low intensity of the scattered radiation a high aperture of this system became mandatory. To achieve positioning over a range of several meters a zoom lens is needed because generally there will not be enough space available inside the vessels for such displacements of the apparatus. So an arrangement emerged with a zoom comprising a front lens of 30 cm of diameter (Fig.2). The zoom was designed in such a way as to keep the angle between the incident beams constant while zooming. By this feature the calibration constant, the factor relating the detected frequency shift to the velocity, does not change with the focal length since it solely depends on this angle and the laser frequency.

Intensity considerations demand a laser of 1 to 4 Watts on the single spectral line used. In our case an Argon-ion laser was used with an over all power of 2 Watts. As these lasers may

work on two lines simultaneously, a green (514,5 nm) and a blue-green (488,0 nm) line, a two component LDV system is feasible. Such a two channel system is in fact what was built. The optics, manufactured by DISA Elektronik, Denmark allows the simultaneous measurement of two mutually perpendicular components of the velocity vector in the plane normal to the axis of the optical arrangement. In this plane the position of the two components may be varied by turning part of the optics around this axis. Finally the intersection angle of the incident beams of both colours, though constant while zooming, may be chosen within certain limits. The geometrical arrangement of laser and main elements of the optical system may be changed so as to adapt the whole device to the restrictions that the space available on board may impose. It is thought that with all these features a versatile tool for the measurement of such full scale flows has been produced.

So far nothing has been said about signal processing, neither about the electronic equipment needed nor about the computer where the final evaluation takes place. In fact there was (and still is) some uncertainty about the signals to be processed. The particle density in the sea is not well known nor is the size of the particles. Differences have to be expected at different depths, geographic regions, seasons, time of the day and state of the sea. Air bubbles of small size may or may not be present. Our knowledge about the scattering centers to be expected is thus rather poor, and therefore no decision could be taken in advance. The following methods were applied:

1. Examination of the signal on a storage oscilloscope and evaluation of the frequency by counting, the time base being known.
2. The evaluation of signals by the application of a transient recorder, its digital output being processed by a desktop computer. This method was applied by Det norske Veritas using the signals from the IfS optics. It will not be discussed here.
3. The method of photon correlation. Another electronic device known as a (4) counter was tested at the laboratory but

not on board, though it seems to be a processing device we will have to use in the future. Frequency trackers (5) were considered to be unable to process these signals. The method of photon correlation seems not yet to be in general use. As long as enough intensity of the scattered radiation is available at the detector, the signal is expected to have a Gaussian shaped envelope but modulated with the beat frequency. Such an analog signal may be processed by frequency trackers, counters, etc. Once the intensity goes down, the signal dissolves more and more into single spikes, each representing a detected photon (Fig.3). (Circuitry and photomultiplier assumed to be fast.) Such a discrete signal would disappear in the background noise if not unburied by appropriate correlation methods. The signal at low intensity is thus a stochastic train of spikes but the probability of appearance of these spikes is not constant with time but modulated with the beat frequency. This frequency may be recovered from the autocorrelation function formed in a very fast correlator with the sequence of discrete pulses as input. Details on the theory are presented elsewhere. ([7],[8],[9]) Different methods are available for the processing of the autocorrelation function with a computer including fast Fourier transform methods. We applied a method where a theoretical formula is fitted to the series of digital values which represent the autocorrelation function (Fig.4). The parameters of the fit not only give the mean value of the velocity but also its variance what means that a measurement of the turbulence-intensity is always included. This is an additional advantage of this powerful method of special usefulness for low intensity cases though a computer is always needed. The theoretical expression for the autocorrelation function was derived under the assumption of turbulence being a Gaussian process. Since this is not the case, this is just a first approximation.

FIRST RESULTS

Though the main purpose with this device is to make measu-

rements in regions of interacting flow fields of interest in ship hydrodynamics, the first step was to be a general test on a vessel at one location where a flow with boundary layer characteristics could be expected. This was done on a liquid gas carrier, the T/T "Methane Progress" on a trip between Canvey Island, England and Arzew, Algeria, and back to Le Havre, France. This vessel is fitted with a window of a diameter of 10 cm situated in the engine room 7 m below the water line, and at a coordinate estimated to be 143 m from the bow measured along the streamline through the location of the window. This small window did not allow to take advantage of the full power of the optics. Three trips had been planned, the first one (from September 20th to October 4th, 1977) had initially been appointed to serve for installation purposes only. The results obtained were considered to be so satisfactory that no more trips were made since the restricted possibilities with that window would not justify the additional expenses. Measurements could be taken at night or on the day and the ship motions and vibrations came out to be no problem. The computer had not been taken along, so the evaluation of the correlograms was performed after the voyage had been finished. Measurements were also made by the method of inspection of the signals on the storage oscilloscope and the members of Det norske Veritas applied their transient recorder and their desk-top computer. When working with the correlator, the size of the increment steps for the time lag is preset on the device, this time lag being the independent variable the correlation function depends on. So the same measurement may be repeated with different settings of this dial. In such repeated measurements no differences exceeding the expected scatter were found, increasing the confidence in the values measured.

The boundary layer is expected to be three-dimensional at this location. It was not possible to make a complete measurement since one channel of the device, the one corresponding to the blue line, did not work properly. With only one channel

working, the alignment was chosen in a direction expected not to differ too much from the outer flow direction. No additional measurement with another alignment was attempted. So no information about the cross flow has been obtained. The values found for the velocity were thus taken as if being provenient from an ordinary two-dimensional boundary layer. But even under this restriction they are far from being complete. The inner region could not be scanned down to the viscous sublayer nor was the edge of the layer reached at the outermost distance of 1.4 m. With the angle chosen the dimensions of the window precluded investigations farther away from the hull surface. With a smaller angle no systematic velocity profile measurement could be repeated. Merely one value was registered at a distance of 4 m which could be used to show the soundness of the extrapolations leading to the boundary layer thickness and the velocity values at the outer edge. Using a formula given by Winter and Gaudet [10] as discussed by Wieghardt [11], the boundary layer was found to have a thickness between 1.5 and 1.6 m.

The Re-number with respect to the above mentioned stream line coordinate was almost 10^9 , so that possibly these are the boundary layer measurements with the highest Re-number ever made.

The results (Fig.5) show an almost conventional boundary layer profile with slight differences in the outer region. This may be explained by the increased fully turbulent region toward higher values of the normal coordinate n that is found at such high Re-numbers and by the high level of the turbulence intensity still present near the outer edge of the boundary layer. Though there is considerable scatter between the values, the profile of turbulence intensity η (Fig.6) shows a clear trend toward say 6 %. Whether this is a true finding or is caused by the ship motions or vibrations remains an open question. Anyhow it would be an explanation since it means that the turbulent boundary layer has not to adjust itself to a laminar outer flow but is faced with a smaller step in turbulence intensity to overcome at its outer edge. Trying to fit a power law to these

boundary layer profiles gives a power of $1/8.7$. So the downward trend of this magnitude with raising Re-numbers also found by Wieghardt [12] in his boundary layer measurements on the "Meteor" ($Re = 8.3 \cdot 10^8$) (which fitted well as an extrapolation from other measurements at lower Re-numbers) is not confirmed by these measurements.

Analysing a boundary layer always raises questions as to the fulfillment of such laws as the law of the wall and the velocity defect law. Since there are no values at hand concerning the roughness of the hull surface, this figure must also be deduced. The values found are consistent with the usual choice for the v. Kármán constant and the additive constant in the logarithmic law of the wall. A roughness figure of 2 mm seems to fit best though it appears a bit high. But even for 1 mm a satisfactory fit is obtained.

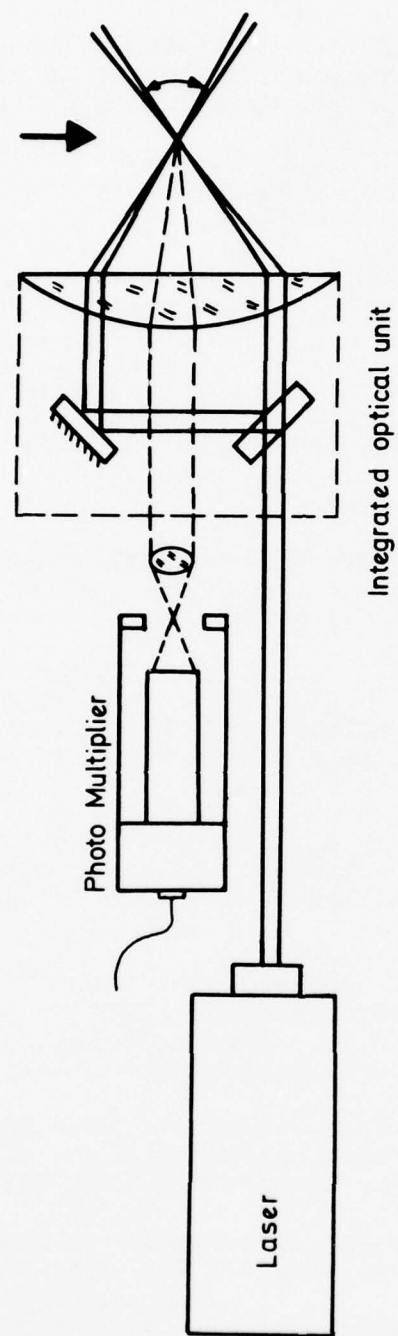
FUTURE INVESTIGATIONS

It is the purpose to use this apparatus to investigate the wake of full scale ships. Due to the velocities induced by the propeller the flow field is periodically instationary. With the aid of the computer it will be possible to analyse this by triggering according to the position of the blades in order to resolve the field with respect to its time coordinate. The pertinent changes and additions to the device are currently under progress. The deflection of the beams while keeping them intersecting will have to be managed thus enhancing the domain to be scanned from one window. A systematic search for bilge vortices may be included and more emphasis on the turbulence characteristics including Reynolds-stresses may be envisaged for the future.

REFERENCES

- [1] Yokoo, K.: "Measurement of Full Scale Wake Characteristics and their Prediction from Model Results - State of the Art", Symposium on High Powered Propulsion of Large Ships, Wageningen, Netherlands, 1974

- [2] Restad, K., Kjellberg, A.: "Full Scale Measurements on Propeller Hull Interaction", Symposium on High Powered Propulsion of Large Ships, Wageningen, Netherlands, 1974
- [3] Durst, F., Melling, A., Whitelaw, J.H.: "Principles and Practice of Laser-Doppler Anemometry", Academic Press, London, New York, San Francisco, 1976
- [4] Eliasson, B., Dändliker, R.: "A Theoretical Analysis of Laser Doppler Flowmeters", Brown Boveri Research Report KLR-73-03, 1973
- [5] Buchhave, P., Delhay, J.M., Durst, F., George, W.K., Refslund, K., Whitelaw, J.H., editors: "The Accuracy of Flow Measurements by Laser Doppler Methods", Proceedings of the LDA-Symposium Copenhagen 1975 (P.O. Box 70, DK-2740 Skovlunde, Denmark)
- [6] Eckert, E.R.G., editor: "Minnesota Symposium on Laser Anemometry", Proceedings, Department of Conferences, Continuing Education and Extension, University of Minnesota
- [7] Cummins, H.Z., Pike, E.R., editors: "Photon Correlation and Light Beating Spectroscopy", Plenum Press, New York, London, 1974 (Proceedings of the NATO Advanced Study Institute, Capri, 1973)
- [8] Cummins, H.Z., Pike, E.R., editors: "Photon Correlation Spectroscopy and Velocimetry", Plenum Press, New York, London, 1977 (Proceedings of the NATO Advanced Study Institute, Capri, 1976)
- [9] Klewe, R.C., editor: "Proceedings of the Conference on Photon Correlation Techniques in Fluid Mechanics", Cambridge, U.K., 1977, Marchwood Engineering Laboratories, Marchwood, Southampton, England, U.K.
- [10] Turbulent Boundary Layer Studies at High Reynolds Numbers and Mach Numbers between 0.2 and 2.8, Royal Aircraft Establishment Technical Report 70251, 1970
- [11] Wieghardt, K.: "Über den Reibungswiderstand der Platte", Institut für Schiffbau, Bericht Nr. 291, 1973
- [12] Schuster, S., Grothues-Spork, H., Thieme, H., Wieghardt, K.: "METEOR-Meßfahrten 1967", Jahrbuch der Schiffbautechnischen Gesellschaft, Vol. 62, 1968, pp 159-204, E.: Analyse eines Grenzschichtprofils



Measurement using the differential doppler mode on backward scattered light.

Fig. 1

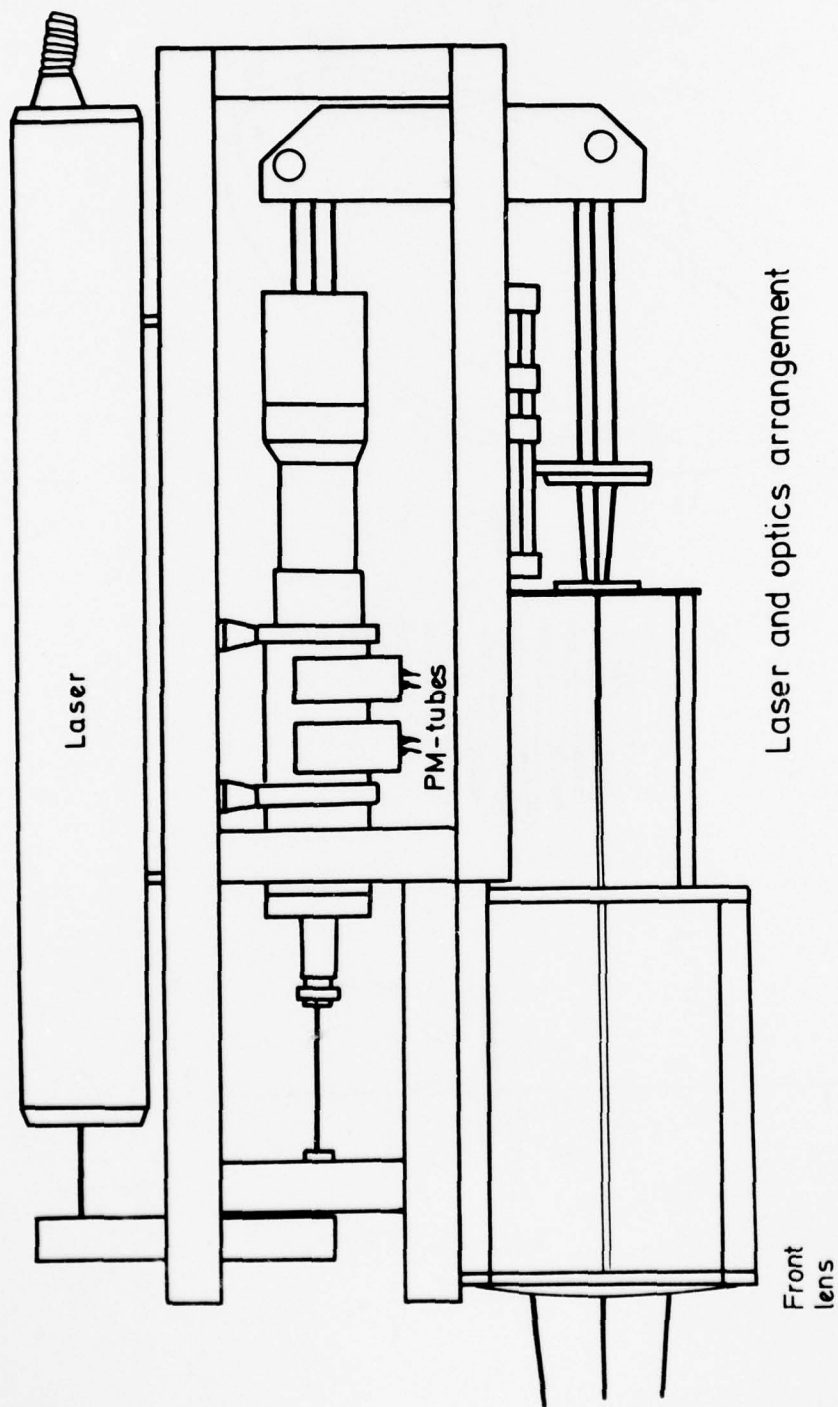


Fig. 2

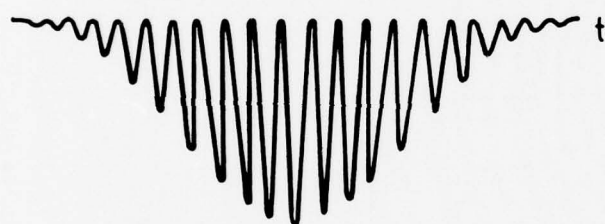
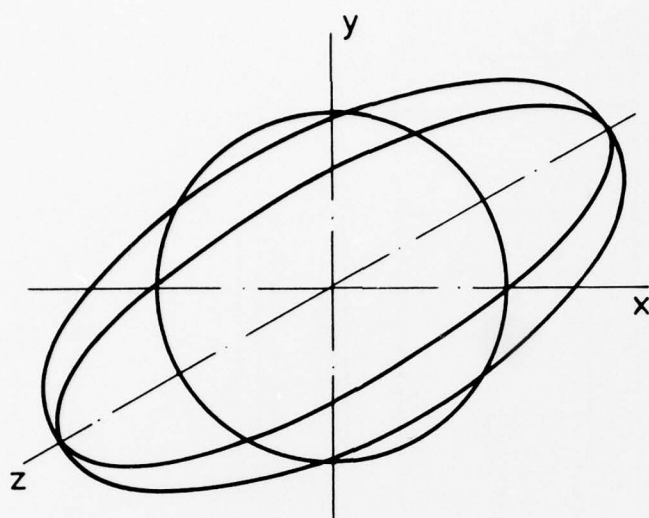


Fig. 3

AD-A061 086

AIR FORCE FLIGHT DYNAMICS LAB WRIGHT-PATTERSON AFB OHIO F/G 20/4
BOUNDARY LAYER EFFECTS-PROCEEDINGS OF THE 7TH U. S. AIR FORCE/F--ETC(U)
SEP 78 A W FIORE MWDDEA-AF-75-G-7440
AFFDL-TR-78-111 NL

UNCLASSIFIED

3 OF 5

AD
A061086



Typical correlation function

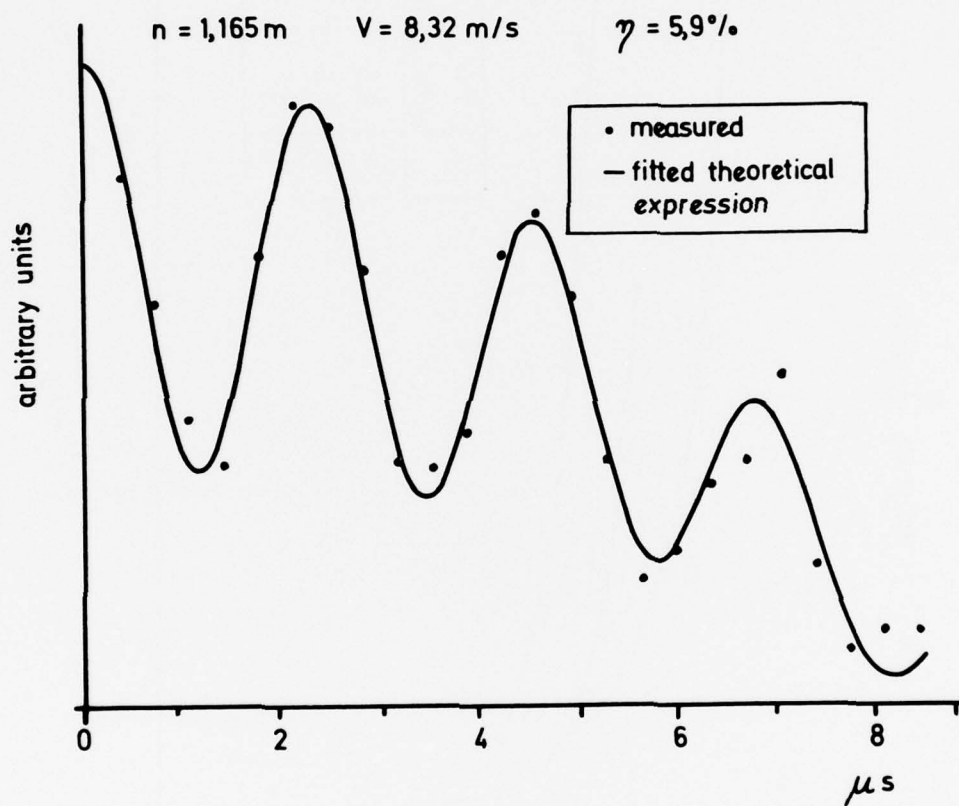


Fig. 4



Fig. 5

Turbulence intensity profile

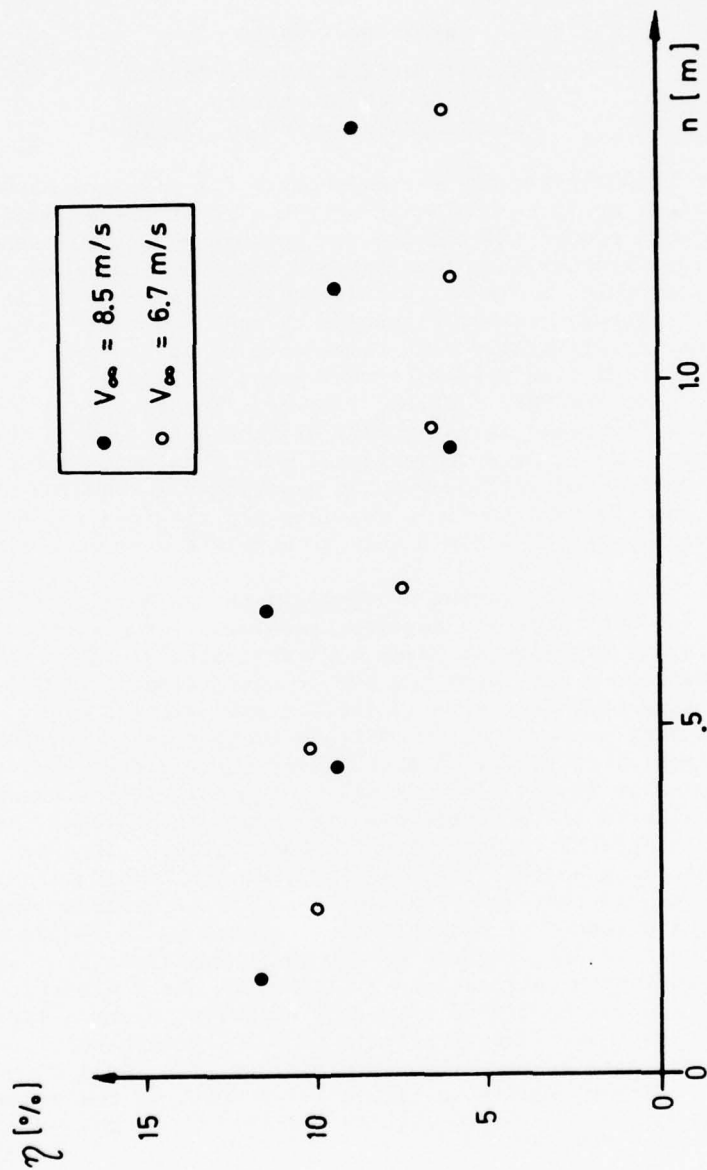


Fig. 6

MEASUREMENTS OF THE THREE-DIMENSIONAL FLOWFIELD AROUND
A SLENDER BODY AT LARGE ANGLES-OF-ATTACK

by

William J. Yanta

Naval Surface Weapons Center
White Oak Laboratory
Silver Spring, Maryland 20910

Increased flight performance requirements for missiles have resulted in a need for flight at large angles-of-attack. Under these conditions, the leeward flowfield around the missile can go through several phases. At angles-of-attack greater than five degrees the flow separates to form well-defined vortices which may be either symmetric or asymmetric in structure. The asymmetric pattern generally appears at angles greater than 25 to 35 degrees and has traditionally been considered to be steady. At incidences near 90 degrees, the flow resembles that about a cylinder in cross-flow, and is unsteady at low Mach numbers. The complicated nature of this high angle-of-attack flowfield makes it very difficult to predict theoretically the aerodynamic loads. As a consequence, most predictive methods are semi-empirical in nature and rely heavily on experimental measurements. The strength and position of flowfield vortices are required in many predictive methods, particularly those applicable to complete missile configurations.

With this in mind, a program is on-going at the Naval Surface Weapons Center/White Oak Laboratory to develop techniques for predicting the non-linear behavior of missiles at large angles-of-attack. This will be done first by developing a data base for the steady/unsteady flowfields, including resulting body forces for a slender body without fins. This will be done by mapping the external flowfields about a tangent-ogive body at angles-of-attack up to 90°, with a prototype three-dimensional Laser Doppler Velocimeter (LDV). In addition, the model is instrumented with 148 pressure taps so the pressure distributions on the model can be measured and integrated to determine the body forces. In order to investigate the resulting unsteady forces, the pressure transducers are mounted inside the model, so that the pressure lines are of minimum length. This will permit measurements of pressure fluctuations up to 500 Hz which are well within the Strouhal frequencies for these experiments. (This has been determined with insitu calibrations.) The model has a diameter of 5.7 cm (2.25 inches) and can be fitted with four different noses. They are tangent-ogive configurations with l/d 's of 0.5 (hemisphere), 3.0 and 4.0. In addition, there is a nose with a l/d of four with ten percent bluntness. These are shown schematically in Figure 1. A photo of the assembled model is shown in Figure 2. The tests will be carried out on the model initially with two noses, the 3.0 and the 0.5 l/d 's.

A 3-D Laser Doppler Velocimeter (LDV) will be used to measure the three-velocity components simultaneously. This system utilizes a two color plus polarization feature to determine the three individual velocity components and is shown schematically in Figure 3. The longitudinal (u component) and pitch plane component (w component) are measured using a polarization scheme with the 4880Å line from an argon laser. The third velocity component (v component in the yaw direction) is determined using an off-axis system at 30° to the tunnel centerline and utilizing the 5145Å line from the argon laser. This measured component of velocity is made up

of the longitudinal and yaw component. Since the longitudinal component is determined outright, the yaw component can be determined through trigonometric relations. The Doppler signals are detected by three photomultipliers and then processed by three Doppler processors. This data is then stored in a minicomputer where the three velocity components are determined. This method has been demonstrated in a wind-tunnel experiment.

In a recent paper by Lamont and Hunt (Reference 2), it was postulated that free-stream turbulence was an important factor in experiments which investigated the aerodynamics of configurations at large angle-of-attack. As part of the present program, the model will be placed in flows in which the turbulence levels are varied. Most of the data will be obtained at a free-stream turbulence level of 0.1%. Selected cases will be run at 0.7% and 1.5% turbulence levels. These levels will be generated by placing grids in the test section ahead of the model. All tests will be run at subsonic speeds, at velocities which are low enough to maintain a laminar boundary layer on the body.

Since this program is on-going, and the experimental program will begin shortly; no results on this configuration are available. However, results were obtained and reported (Reference 1) on the initial phase of this program. A small tangent-ogive model with a diameter of 2.85 cm (1.125 inches) was tested at free-stream velocities of 36.6 meters/sec (120 ft/sec) at angles-of-attack up to 50 degrees. The nose had a ℓ/d of three and a body ℓ/d of six. A single component LDV was used to measure the three components of the velocity vector. Only LDV measurements were made with no force or pressure distributions taken. Typical results from Reference 1 will be shown here. These are also typical of the kinds of results that will be obtained in the present testing program. Shown in Figure 4 are crossflow flowfield velocity distributions for an angle-of-attack of 18 degrees, at a distance of six diameters from the leading edge. This corresponds to the mid-body location. One can see the detailed flow structure of the leeward flowfield, including the two symmetric vortices. In Figure 5 are shown the isovorticity distributions for the same conditions. Again, one can see the detailed vortical structure on the leeward flowfield. Similar results for the vorticity distribution are shown in Figure 6 for an angle-of-attack of 50 degrees. The vortex strengths, streamwise vortex position, and lateral vortex positions are shown in Figures 7a, 7b, and 7c, respectively. It can be seen that the data agrees with the empirical correlation in Reference 1. In general, it was concluded that the data obtained in the first phase agreed well with existing time-averaged data.

CONCLUSIONS AND PRESENT STATUS

Time-averaged measurements have been made with a LDV of the flowfields behind a slender body at angles-of-attack up to 50 degrees. A one-component LDV was used to make these measurements and the agreement with existing data was good. These results were reported in Reference 1.

An on-going program will investigate the steady/unsteady flowfields and body forces on a body at angles-of-attack up to 90 degrees. The influence of freestream turbulence on the unsteadiness of the flowfields will also be investigated. The status of this program is as follows:

- a. A three-component LDV has been demonstrated;
- b. A pressure model has been fabricated and assembled;
- c. A low-turbulence wind-tunnel has been calibrated in preparation for tests; and
- d. Turbulence generating grids have been fabricated and these grids will be used in generating freestream turbulence.

REFERENCES

1. Yanta, W. J. and Wardlaw, A. B., "Laser Doppler Velocimeter Measurements of Leeward Flowfields on Slender Bodies at Large Angle-of-Attack," Paper 77-660, AIAA 10th Fluid and Plasma Dynamics Conference, 27-29 June 1977.
2. Lamont, P. J. and Hunt, B. L., "Pressure and Force Distributions on a Sharp-Nosed Circular Cylinder at Large Angles-of-Inclination to a Uniform Subsonic Stream" Journal of Fluid Mechanics, Volume 76, Part 3, pp 519-559, 1976.

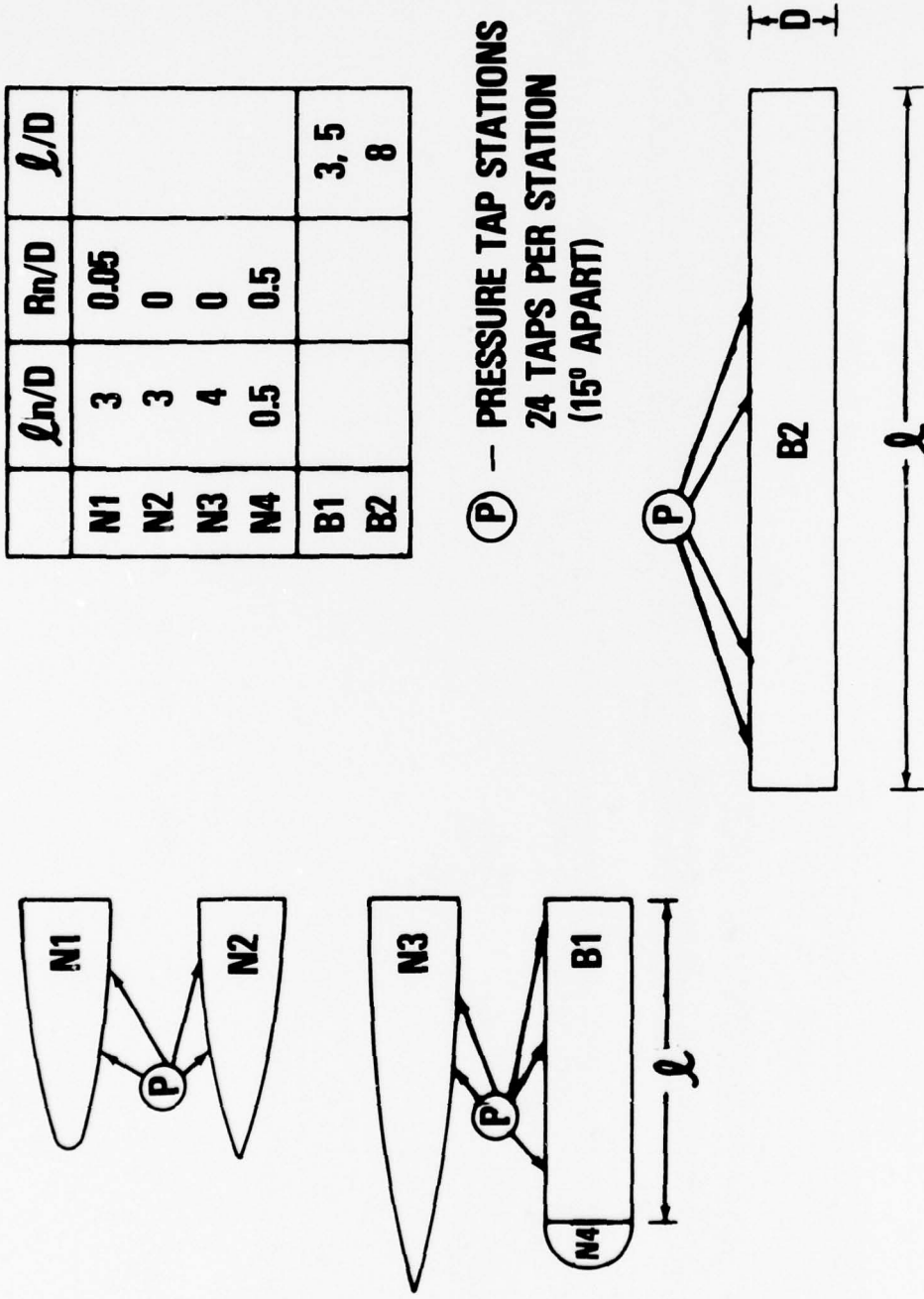


FIG. 1 MODEL CONFIGURATIONS

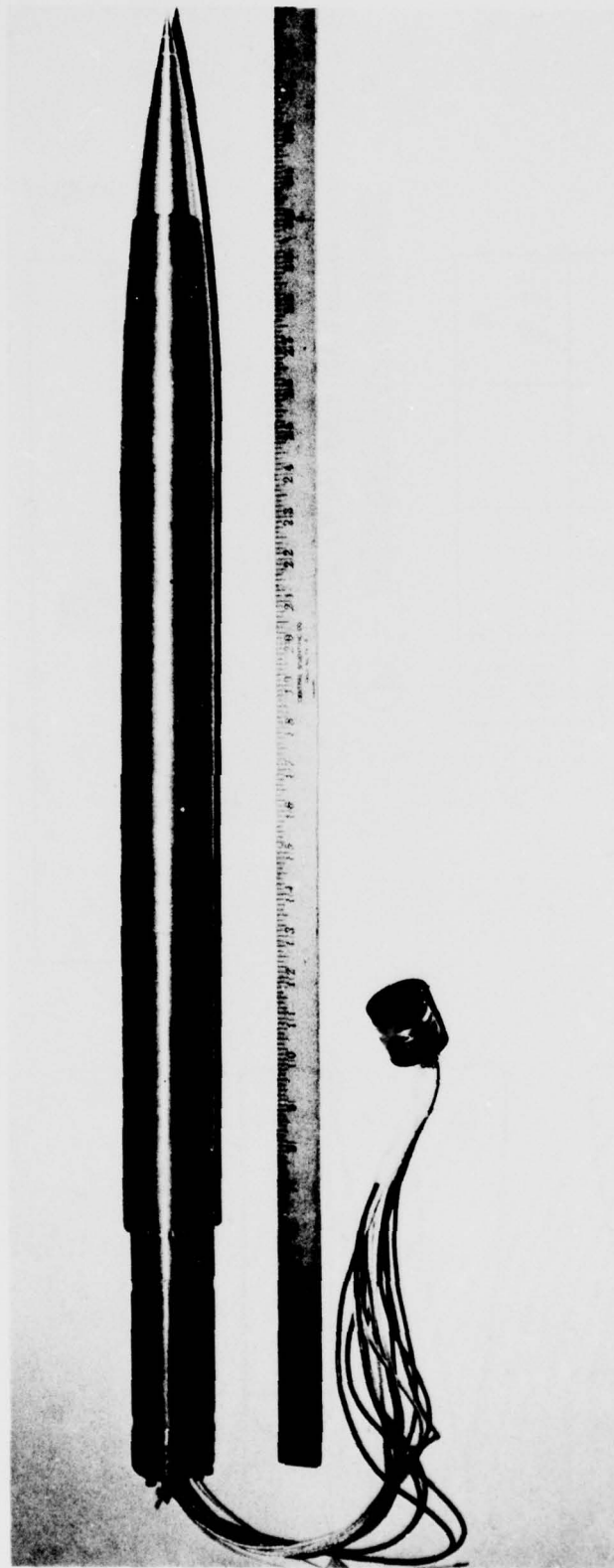


FIG. 2 PRESSURE MODEL

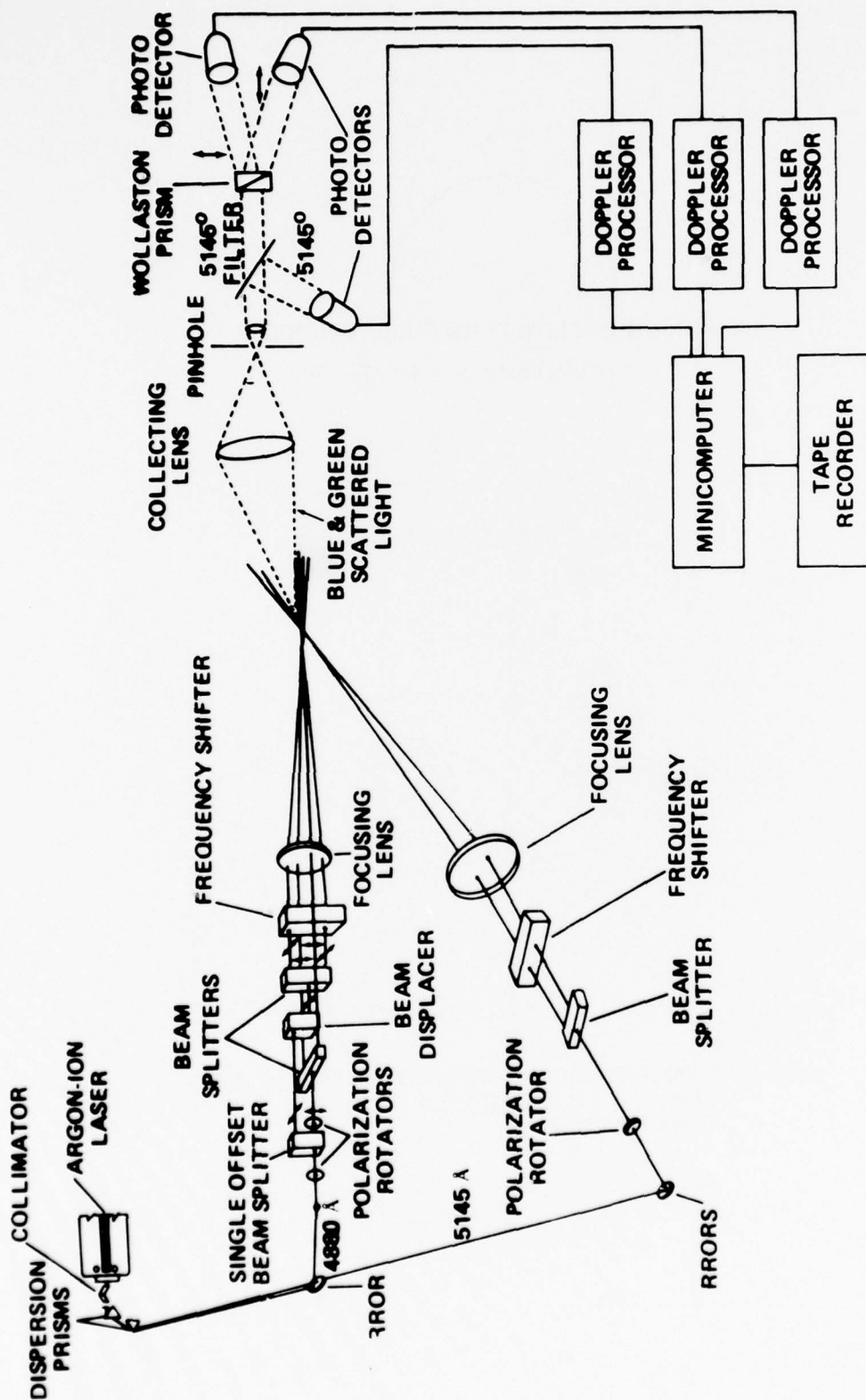


FIG. 3 SCHEMATIC OF 3-D LDV

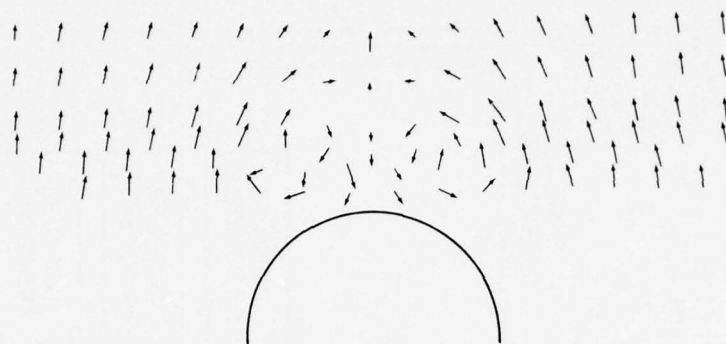


FIG. 4 CROSSFLOW FLOW FIELD VELOCITY DISTRIBUTIONS ($\alpha = 18^\circ$, $\frac{X}{D} = 6$).

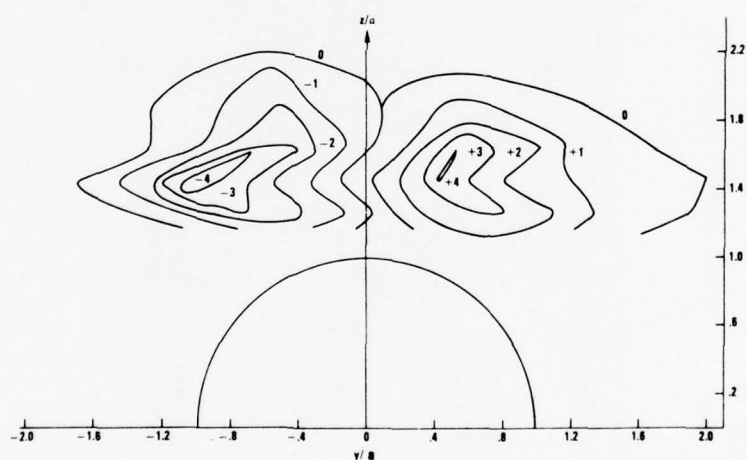


FIG. 5 NONDIMENSIONAL VORTICITY DISTRIBUTION (λ/in^2) AT $\alpha \approx 18$ DEGREES. NOSE TRIP REMOVED $X/D = 6$.

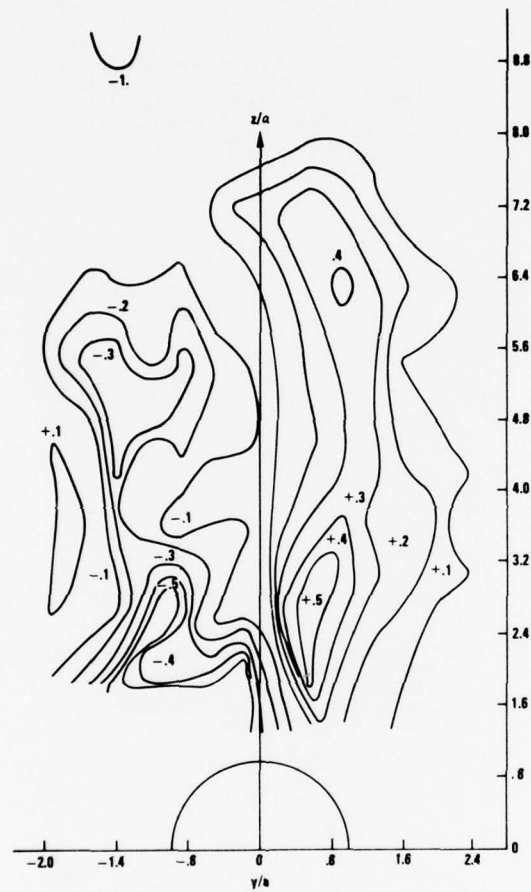


FIG. 6. NONDIMENSIONAL VORTICITY DISTRIBUTION (λ/in^2) AT $\alpha = 50$ DEGREES, $X/D = 6$.

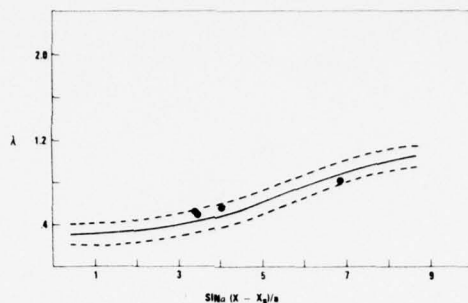


FIG. 7a. SUBSONIC VORTEX STRENGTH COMPARISON.
 • PRESENT RESULTS. — CORRELATION OF
 AVAILABLE DATA FROM REFERENCE 15. ---
 STANDARD DEVIATION OF FIT. (DETER-
 MINED IN PRESENT STUDY)

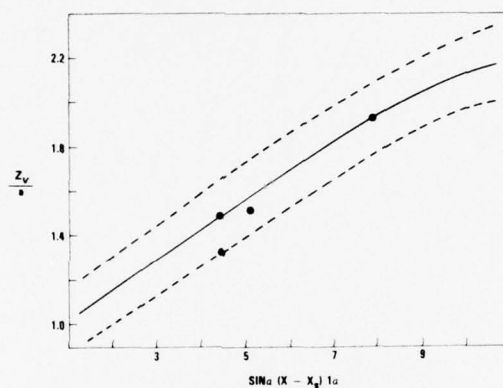


FIG. 7b. STREAMWISE VORTEX POSITION COMPARISON.
 • PRESENT RESULTS. — CORRELATION OF
 AVAILABLE DATA FROM REFERENCE 15. ---
 STANDARD DEVIATION OF FIT (DETER-
 MINED IN PRESENT STUDY).

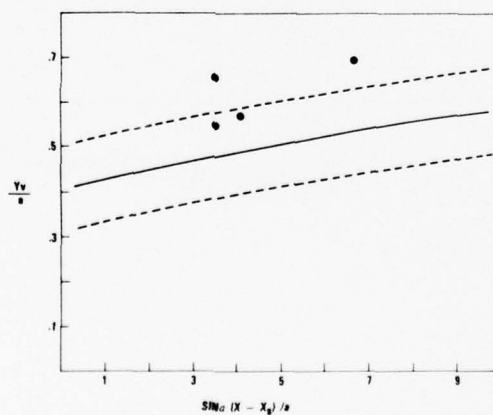


FIG. 7c. SUBSONIC LATERAL VORTEX POSITION COM-
 PARISON. • PRESENT STUDY. — CORRELA-
 TION OF AVAILABLE DATA FROM REFERENCE
 15. --- STANDARD DEVIATION OF FIT (DETER-
 MINED IN THE PRESENT STUDY)

PRESSURE DISTRIBUTIONS AND FLOW VISUALISATIONS
ON AN ELLIPSOID 1:6 DESIGNED FOR THREE-DIMENSIONAL
BOUNDARY LAYER INVESTIGATIONS

by

H. U. Meier and H. -P. Kreplin

Deutsche Forschungs- und Versuchsanstalt
für Luft- und Raumfahrt E. V.
Aerodynamische Versuchsanstalt Göttingen
Bunsenstraße 10, 3400 Göttingen, W-Germany

Abstract

The wind tunnel model designed for three-dimensional boundary layer investigations at the DFVLR-AVA is briefly described. Essentially it consists of an ellipsoid 1:6 with an overall length of 2.4 m.

Preliminary measurements of pressure distributions and flow visualisations were carried out in order to obtain an overall picture of the flow, which will be investigated by means of detailed boundary layer measurements. The results of different pressure measurements are compared with potential flow calculations.

I. Introduction

The Trondheim trials on three-dimensional boundary layers [1] clearly indicated that there is a considerable lack of experiments in this field of research. New experimental results are necessary in order to improve turbulence models as well as transition and separation criteria for the calculation methods. For this reason a long-term research project at the DFVLR-AVA was initiated, which is concerned with the providing of experimental three-dimensional boundary layer data.

Investigations on different configurations will be carried out (e. g. fuselages, wings, and missiles). For the following reasons an ellipsoid is investigated first:

- this body of revolution is relatively easy to be described applying different coordinate systems in the computer programmes,
- an ellipsoid has no sudden pressure change in the potential flow field,
- the manufacturing of the model is relatively simple,
- the complete instrumentation (e. g. probe traversing mechanism) can be stored in the model,
- the whole boundary layer flow around the model can be measured with one boundary layer probe, simply by turning the body in the range of 360° .

II. Description of the Ellipsoid-Model

A detailed description of the model is already given in Ref. [2]. The main dimensions of the model and the DFVLR-AVA Low Speed Wind Tunnel are specified in Fig. 1.

The essential construction of the ellipsoid is based on two half-shells of glass fiber reinforced resin with a wall thickness of about 4 mm.

For the first investigation the model was equipped with 8 accelerometers to measure the vibrations of 6 degrees of freedom, and 37 pressure taps on a meridian. The arrangement of the pressure taps are shown in Fig. 2. The circumferential pressure distribution of the body can be measured in arbitrary steps between $\varphi = 0^{\circ}$ and 360° in 37 cross-section because the model can be turned around its longitudinal axis. (Number of cross-

sections is equivalent to number of pressure taps.)

III. Results of First Investigations

The purpose of the first investigation on the ellipsoid was to obtain informations about the dynamic response of the model at different stagnation pressures. The dynamic control of the model is described in [2].

Pressure measurements and flow visualisations were carried out, to obtain an overall information about the flow around the ellipsoid model. Some results of these investigations are given in Figs.3 to 6. The measured pressure distributions are compared with inviscid flow calculations of W. GEISLER [3] applying a singularity method. This method is applicable to bodies of revolution with arbitrary cross-sections.

In Fig. 3 the surface pressure coefficient $c_p = (p_w - p_\infty)/q_\infty$ measured along one meridian on the ellipsoid model at an angle of incidence $\alpha = 0^\circ$ is shown. ($q_\infty = \rho_\infty U_\infty^2/2$)

As expected the agreement between measurement and theory is good. On the afterbody deviations are caused by the displacement effects of the boundary layer and the effects of truncating the model for a sting mounted through the model base. From oil flow patterns it was found that the flow separated at $x/2a \approx 0.95$. At a lower velocity ($U_\infty \sim 20$ m/s) transition detections - applying a stethoscope - indicated laminar flow up to $x/2a \sim 0.7$. A turbulence grid at the nozzle exit, which resulted in a turbulence intensity of about $Tu \approx 5\%$ at the region of the model nose, shifted the transition location to $x/2a \sim 0.15$. Due to the strong favourable pressure gradient in the nose region the boundary layer flow is very stable and remains laminar. The model was carefully adjusted in the wind tunnel, thus the reproducibility of the pressure distribution for different circumferential angles ϕ was in the order of less than 1%. As the angle

of incidence was increased to $\alpha = 5^\circ$ (Fig. 4) the deviations of the theoretical from the measured pressure distributions in the region of the leeward afterbody grows. This is due to the progressive thickening of the boundary layer flow caused by the longitudinal and circumferential adverse pressure gradients. An oil flow picture did not indicate a flow separation on the leeward side as found by W. GEISLER [4], who calculated the three-dimensional laminar boundary layer development on this body of revolution. His calculated separation line has to be interpreted as the envelope of the limiting streamlines which were obtained from an numerical instability due to sudden rise of the boundary layer displacement thickness. However, if the angle of incidence increased to $\alpha = 27^\circ$ (Fig. 5) the oil flow pattern leads to separation lines which are qualitatively similar to the calculated ones. In the experiment the leeward separation occurs at higher angles of incidence, because the separation results from a turbulent boundary layer. In addition the laminar boundary layer calculation does not take into account Reynolds number effects. The disagreement between the pressure distributions at $\varphi = 90^\circ$ and $\varphi = 270^\circ$ is caused by a misalignment of the meridian at $\varphi = 0^\circ$. In Fig. 6 the corresponding pressure distributions for the circumferential angles $\varphi = 0^\circ$ and $\varphi = 180^\circ$ are plotted. The oil flow patterns clearly indicate, that the separated flow is symmetrical to the attachment line along the leeward meridian, $\varphi = 180^\circ$. Two separation- and one re-attachment lines can be seen from the flow patterns. There is an indication that all limiting streamlines originate from the attachment region on the nose, were already a system of discrete vortices seem to exist. However, to be able to interpret this complicated flow pattern, detailed informations from measurements of the boundary layer, and the outer flow field are necessary.

IV. Conclusions

If a cross-section of the ellipsoid at $x/2a = 0.5$, and high angles of in-

cidence is considered, the circumferential flow picture can be described schematically as shown in Fig. 7. Dividing the flow around the ellipsoid in different regions, the following conclusions can be drawn from the picture:

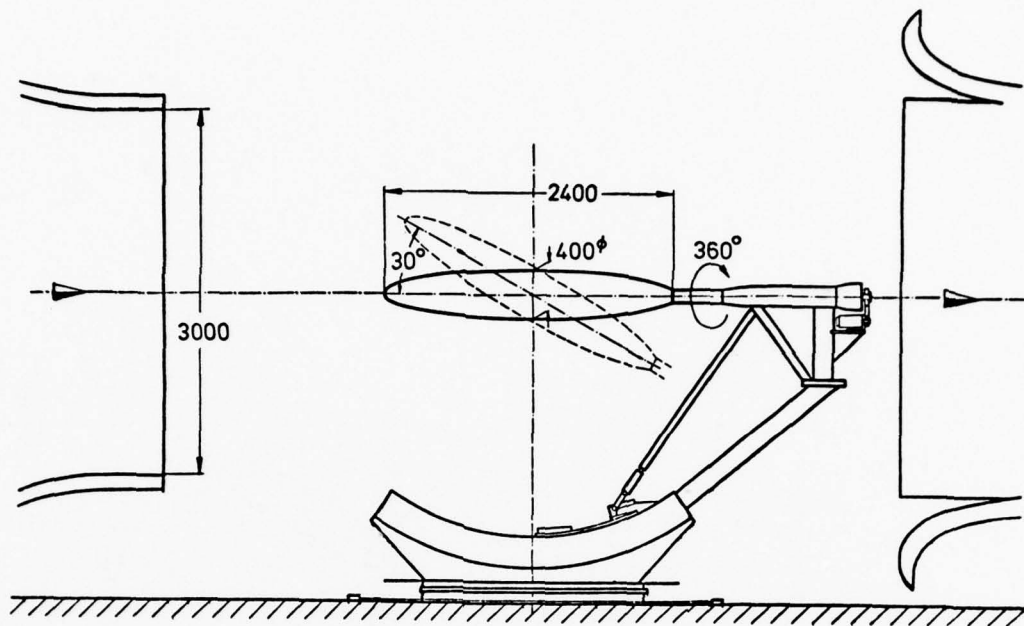
Region

- ① • Potential flow
 - panel and singularity methods are available.
- Three-dimensional laminar boundary layer
 - Integral and finite difference methods are available.
- ② • Transition from laminar to turbulent boundary layer flow
 - can only be measured, no theory available.
- ③ • Three-dimensional turbulent boundary layer
 - Integral and finite difference methods with limited accuracy are available.
 - Separation of the three-dimensional turbulent boundary layer can only be determined experimentally.
- ④ • Separated flow
 - Semiempirical methods for the estimation of normal forces are available.
 - Flow field calculations will not be available in the near future, because this postulates the solution of the complete instationary Navier-Stokes equations.

The purpose of our experimental three-dimensional boundary layer investigations is, to understand more of the physics of flows just described, and to provide theorists with new experimental data which allow improvements of the engineering calculation methods.

V. References

- [1] FANNELØP, T. K.
KROGSTAD, P. A. Three-Dimensional Turbulent Boundary
Layers in External Flows: A Report on
EUROMECH 60.
J. Fluid Mech. 71 (1975), pp. 815-826.
- [2] KREPLIN, H. -P.
MEIER, H. U.
MAIER, A. Wind tunnel model and measuring tech-
niques for the investigation of three-
dimensional turbulent boundary layers.
AIAA 10th Aerodynamic Testing Confer-
ence, April 19-21, 1978, San Diego.
AIAA Paper No. 78-781, 1978.
- [3] GEISLER, W. Berechnung der Potentialströmung um
rotationssymmetrische Rümpfe, Ringpro-
file und Triebwerkseinflüsse.
Z. Flugwiss. 20 (1972), S. 457-462.
- [4] GEISLER, W. Calculation of the Three-Dimensional
Boundary Layer Around Bodies of Revo-
lution at Incidence and with Separation.
AGARD CP 168 'Flow Separation',
33-1 to 33-11, 1975.



All Dimensions in mm

Fig. 1 Ellipsoid for the Investigation of Three-Dimensional Boundary Layers in the Low Speed Wind Tunnel of the DFVLR-AVA

Test Section: 3m x 3m, Maximum Velocity 65 m/s

Ellipsoid: $L = 2a = 2400$ mm

$D = 2b = 400$ mm

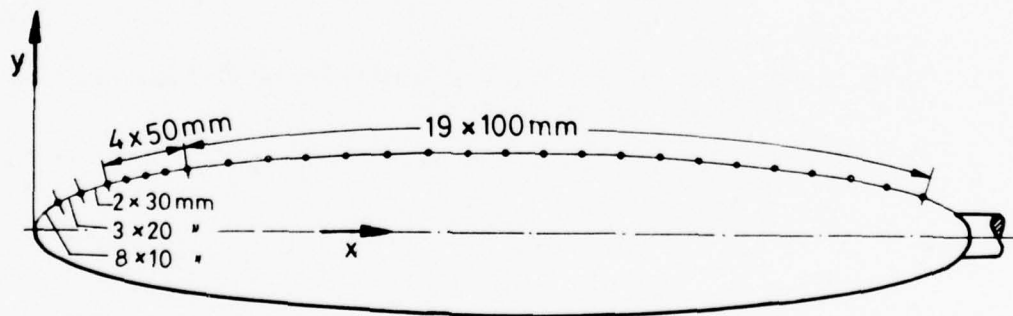


Fig. 2 Arrangement of the Pressure Taps on the Ellipsoid 1: 6

$$c_p = \frac{P_w - P_\infty}{\rho_\infty / 2 U_\infty^2}$$

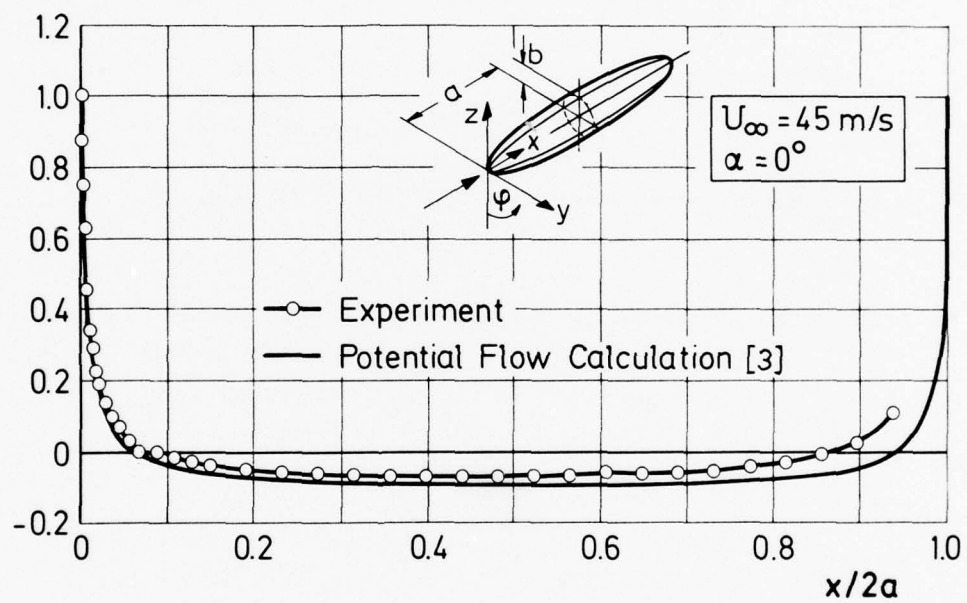


Fig. 3 Theoretical and Experimental Pressure Distributions at the Angle of Incidence $\alpha = 0^\circ$

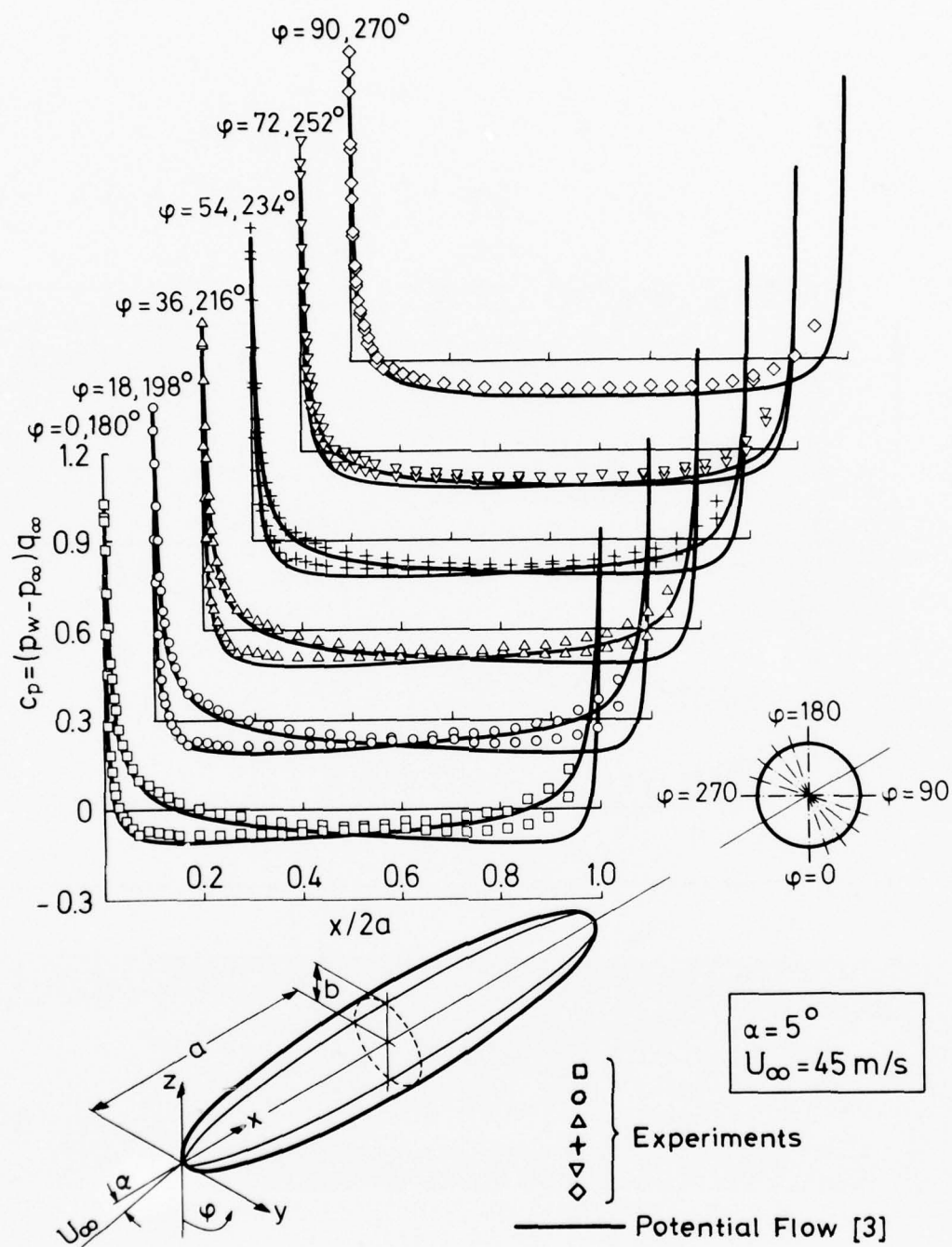


Fig. 4 Theoretical and Experimental Pressure Distributions
 $(\alpha = 5^\circ, \Delta\varphi = 18^\circ)$

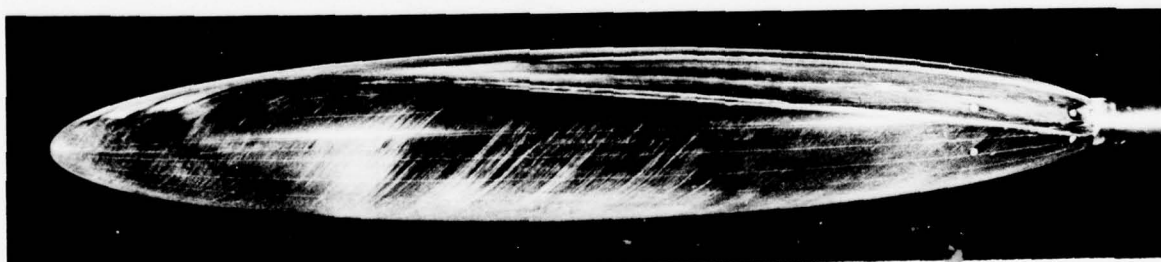
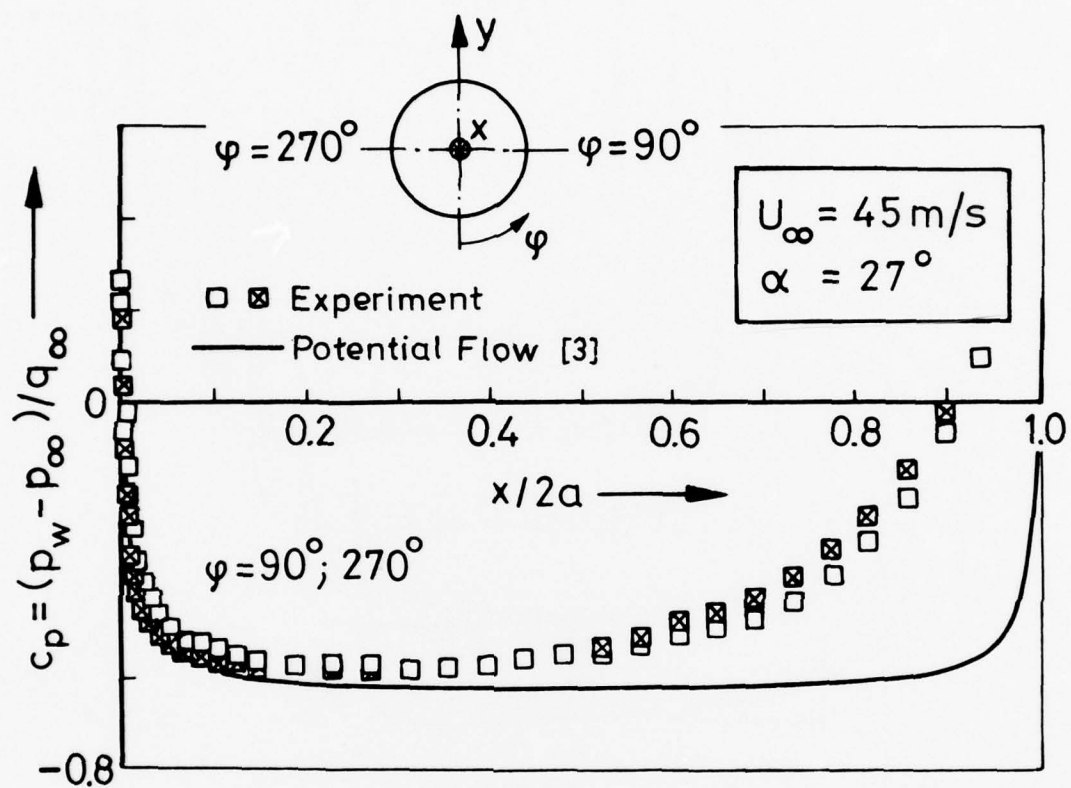


Fig. 5 Theoretical and Experimental Pressure Distribution
 $(\alpha = 27^\circ, \varphi = 90^\circ, 270^\circ)$

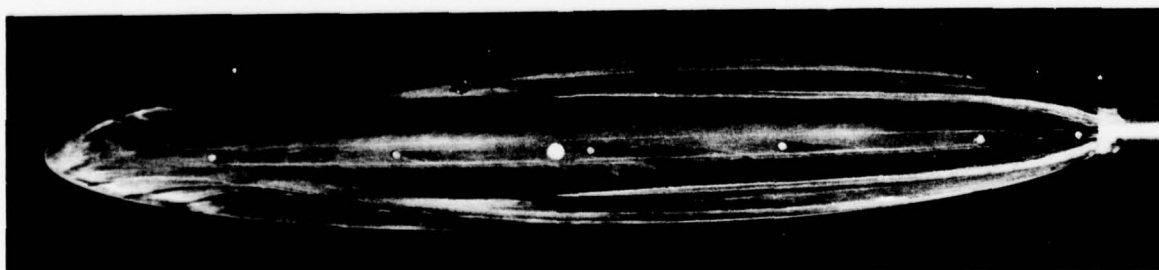
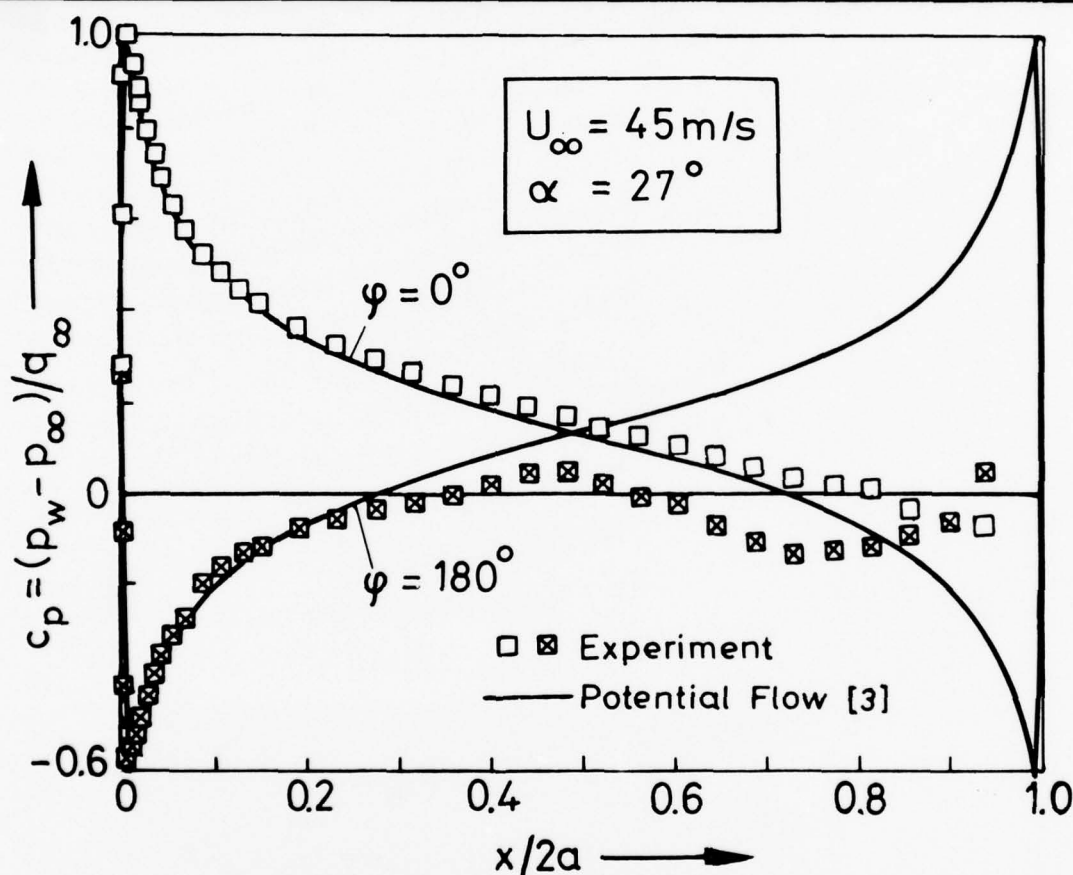
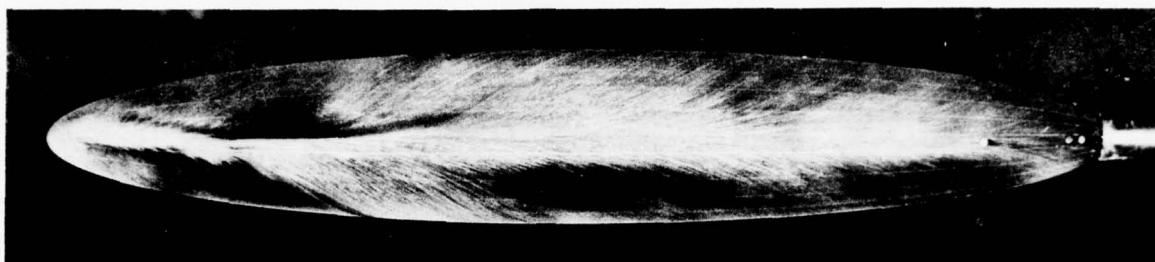


Fig. 6 Theoretical and Experimental Pressure Distribution
 $(\alpha = 27^\circ, \varphi = 0^\circ, 180^\circ)$

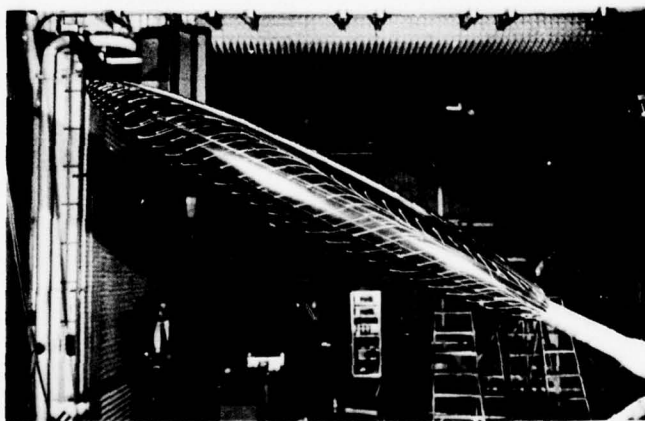
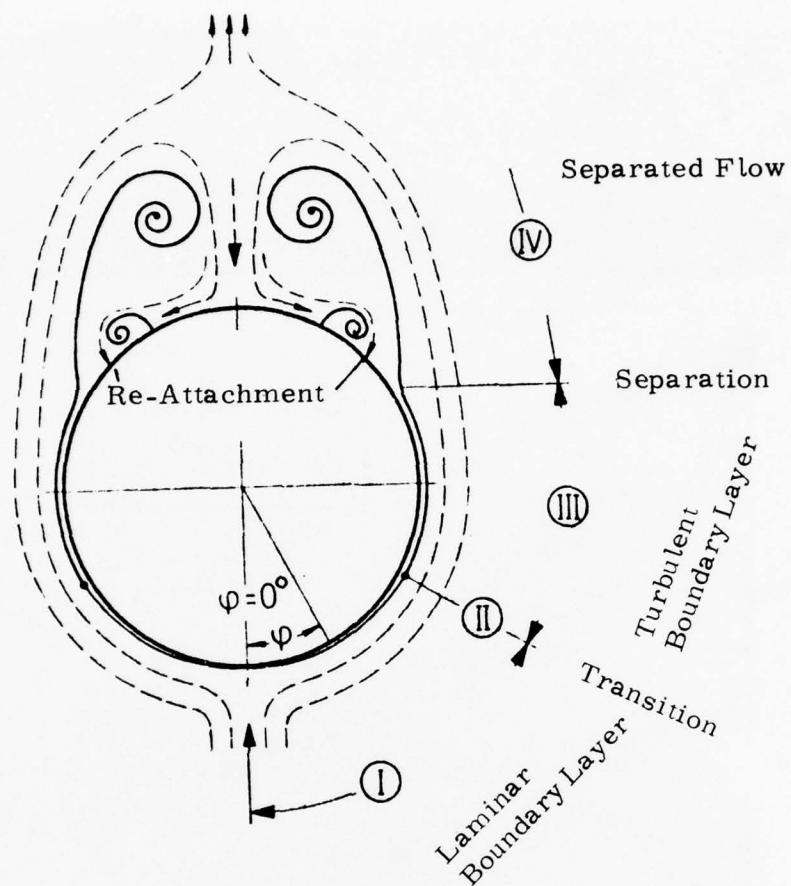


Fig. 7 Schematic Description of the Flow Field Around an Ellipsoid 1: 6 at High Incidence ($x/2a \approx 0.5$)

WALL SHEAR STRESS MEASUREMENTS, DETECTION
OF TRANSITION AND SEPARATION BY MEANS
OF SURFACE HOT FILM PROBES

by

H. -P. Kreplin, H. U. Meier and D. Baumgarten

Deutsche Forschungs- und Versuchsanstalt
für Luft- und Raumfahrt E. V.
Aerodynamische Versuchsanstalt Göttingen
Bunsenstraße 10, 3400 Göttingen, W-Germany

Abstract

Surface hot film probes are calibrated for measurements of the local wall shear stress with respect to magnitude and direction in three-dimensional boundary layers. A gauge is applied in the boundary layer of a cylinder model. The applicability of the sensors as detectors of transition and separation phenomena is studied.

I. Introduction

In three-dimensional boundary layer investigations the mean and fluctuating components of the velocity in the boundary layer profile, as well as the shear stress at the wall with respect to the magnitude and direction have to be derived from experiments. Only if the direction of the flow in the boundary layer and shear stress at the surface can be determined separately, improvements in engineering calculation procedures can be examined. For our investigations hot wire probes and surface hot film gauges will be applied, because of their minimal disturbances of the flow. The purpose of the paper will be to describe the calibration of hot film probes and the applicability for wall shear stress measurements, and detection of transition and separation.

II. Wall Shear Stress Measurements

Commercially available surface hot film gauges^{*)} designed by W. J. MCCROSKEY [1] are applied for the measurement of the magnitude and direction of the local wall shear stress. The probes shown in Fig. 1 essentially consist of two mutually perpendicular nickel films in a V-configuration on a thin plastic foil. They are operated by constant-temperature anemometers. The probes can be flush mounted even on curved surfaces with minimal disturbance of the flow. The manufacturing process of the elements allows a reproducibility at very small tolerances. For this reason the validity of a universal calibration can be expected if the same substrate material is used in each case.

The investigation and calibration of these hot film sensors, carried out in the Low Turbulence Wind Tunnel of the DFVLR-AVA, are documented in Refs. [2] and [3]. The results can be summarized as follows:

- In order to limit the heat losses to the surface, a very low thermal conductivity substrate should be used.
- It was found that a one degree change of free stream temperature results in seven per cent change of the measured wall shear stress signal. If an exact temperature control in the wind tunnel is warranted, a correction method for these temperature effects can be applied.
- From the directional calibration of the hot film probes an absolute accuracy of about two degrees for the measurement of the flow direction can be expected. Changes in the flow direction can be determined with a relative accuracy of about 0.2 degree.

In order to study the application of the hot film gauges on curved surfaces, - including favourable and adverse pressure gradients - a boundary layer

^{*)} Micro Measurements, Romulus, Mich. /USA.

on a cylinder model in cross flow was investigated. A cylinder model was chosen because the potential flow as well as the viscous flow is well documented in the literature.

For this purpose a hot film probe was glued on a plexi glass cylinder, with a diameter of 10 cm and a length of 30 cm. The cylinder was mounted rotatable around its axis between the vertical walls of the DFVLR-AVA Low Turbulence Wind Tunnel [2]. In order to minimize three-dimensional effects for the given low aspect ratio of 1:3, the cylinder was investigated 60 cm downstream of the nozzle exit. Fig. 2 shows a photograph of the model arrangement taken from the nozzle.

The measurements were carried out at free stream velocities in the range of $U_{\infty} = 10 - 20 \text{ m/s}$. The corresponding Reynolds numbers, based on the cylinder diameter, were $Re = 0.67 - 1.3 \times 10^5$, which is in the sub-critical range and consequently should result in a laminar boundary layer separation. The measured pressure distribution around the cylinder model is shown in Fig. 3 and is compared with theoretical values obtained from potential flow theory. The measured pressure drops with increasing distance from the stagnation point to a minimum at $\varphi \approx 70^\circ$, shows a weak maximum at $\varphi \approx 80^\circ$ and then decreases gradually. The pressure distribution suggests boundary layer separation somewhere between $\varphi = 70^\circ$ and $\varphi = 80^\circ$.

The wall shear stress distribution around the cylinder model is shown in Fig. 4. The measurements were carried out at a free stream velocity $U_{\infty} = 10 \text{ m/s}$ because no hot film calibration could be established on the tunnel side wall for the shear stress values expected on the cylinder at higher velocities. The hot film data are based on calibrations obtained in a flat plate turbulent boundary layer with zero pressure gradient. The results are compared with the wall shear stress distribution calculated from the measured pressure distribution applying a FORTRAN IV-boundary layer program of J. C. ROTTA [4].

The deviations between the measured and calculated wall shear stress data in the laminar boundary layer may be caused by:

- differences between laminar and turbulent calibration of the hot films,
- pressure gradient effects,
- curvature effects,
- misalignment of the cylinder at $\varphi = 0$,
- the length of the gauge relative to the cylinder diameter.

The validity of the calibration in a turbulent boundary layer applied for measurements in a laminar boundary layer can be estimated using a criterion given by M. W. RUBESIN et al. [5]. Their limiting range for the power dissipation of the heated elements is fulfilled under our test conditions. Thus the deviations between wall shear stress results in laminar and turbulent boundary layers can be expected to be small.

The effect of pressure gradients on the hot film signals can be estimated using a relation derived by B. J. BELLHOUSE and D. L. SCHULTZ [6] and applied by M. W. RUBESIN et al. [5]. Due to the relatively small effective width of our heated elements the influence of pressure gradients on the film data at the cylinder is expected to be in the order of one per cent.

The investigations can be summarized as follows:

The five possible effects - mentioned above - cannot be separated from each other. However, the good agreement between the measured and calculated shear stress distributions on the cylinder implies that the application of the surface hot films is valid without additional corrections on curved surfaces.

III. Detection of Transition and Separation

In order to study the applicability of the wall shear stress gauges for the detection of transition and separation on real configurations it was tried to identify these phenomena on the cylinder model from the hot film signals and their frequency spectra.

The laminar boundary layer on the cylinder was investigated first. Fig. 5 shows measured wall shear stress spectra together with oscilloscope traces of the corresponding hot film signals for different angular positions of the probe. For circumferential angles φ up to 70 degrees the wall shear stress indicates periodic fluctuations, which correspond to the Strouhal frequency of the v. Kármán vortex street. As expected the spectra have only low frequency components in this region. If the angle $\varphi = 70^\circ$ is increased to $\varphi \approx 80^\circ$ irregular higher frequency fluctuations appear in the hot film signal. For even larger angles φ the perturbations increase in the frequency and the amplitude. The onset of perturbations in the film signals indicates that laminar boundary layer separation begins at $\varphi \approx 80^\circ$, which agrees with the calculated separation at $\varphi = 79^\circ$, and with results of oil flow patterns.

Due to the limited Reynolds number range natural transition from laminar to turbulent flow on the cylinder could not be obtained. For this reason a tripping wire of 0.5 mm diameter placed 30° upstream of the hot film probe was used^{*)} in order to get a turbulent boundary layer with turbulent separation. Surface hot film signals and the corresponding frequency spectra for different angular positions of the probe and the tripping wire are shown in Fig. 6. For positions $\varphi \leq 105^\circ$ the signals mainly show high frequency fluctuations being interpreted as turbulent boundary layer flow. At $\varphi = 110^\circ$ there is a drastic change, the hot film signal shows an intermit-

^{*)} The tripping wire was fixed on the cylinder. Thus its position was changed with changes of the angle φ .

tent nature. In time intervals the fluctuations are of lower frequencies and amplitudes. The gauge is indicating an instationary turbulent separation. In the case $\varphi = 115^\circ$, the boundary layer is separated as indicated by the hot film signal and the lack of the higher frequency components in the spectrum.

The study of the cylinder boundary layers showed that surface hot film probes can be applied as transition and separation detectors. However, the interpretation of an individual signal of a gauge at a fixed position is difficult. Only comparative signals of e. g. laminar, transitional and turbulent flows as well as of separated regions lead to sophisticated results.

IV. References

- | | |
|--|---|
| [1] MC CROSKEY, W. J.
DURBIN, E. J. | Flow Angle and Shear Stress Measurements Using Heated Films and Wires.

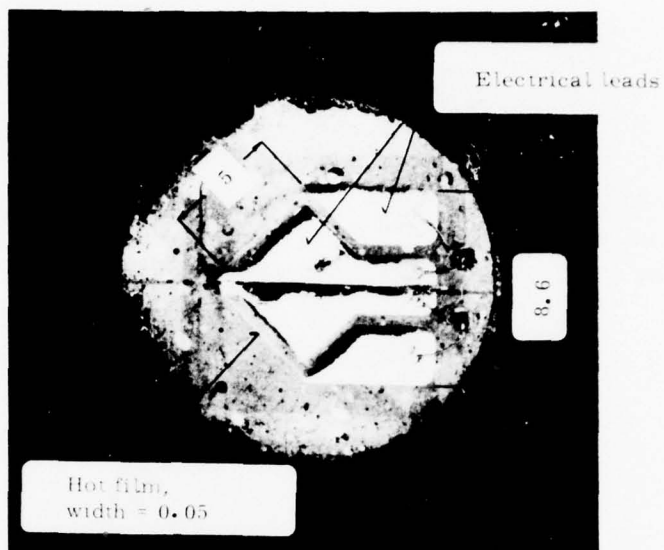
ASME J. Basic Eng. 94 (1972), pp. 46-52. |
| [2] KREPLIN, H. -P.
MEIER, H. U. | Application of Heated Element Techniques for the Measurement of the Wall Shear Stress in Three-Dimensional Boundary Layers.

DFVLR-AVA Report IB 251-77 A 15 (1977). |
| [3] KREPLIN, H. -P.
MEIER, H. U.
MAIER, A. | Wind Tunnel Model and Measuring Techniques for the Investigation of Three-Dimensional Turbulent Boundary Layers.

AIAA 10th Aerodynamic Testing Conference, April 19-21, 1978, San Diego.
AIAA Paper No. 78-781, 1978. |
| [4] ROTTA, J. C. | FORTTRAN IV-Rechenprogramm für Grenzschichten bei kompressiblen ebenen und achsensymmetrischen Strömungen.

DLR-FB 71-51 (1971). |

- [5] RUBESIN, M. W.
OKUNO, A. F.
MATEER, G. G.
BROSH, A.
Flush-Mounted Hot-Wire Gage for Skin Friction and Separation Detection Measurements.
ICIASF '75 Record (1975), pp. 108-116.
- [6] BELLHOUSE, B. J.
SCHULTZ, D. L.
Determination of Mean and Dynamic Skin Friction, Separation and Transition in Low-Speed Flow with a Thin-Film Heated Element.
J. Fluid Mech. Vol. 24 (1966), pp. 379-400.



Dimensions in mm

Fig. 1 Surface Hot Film Probe

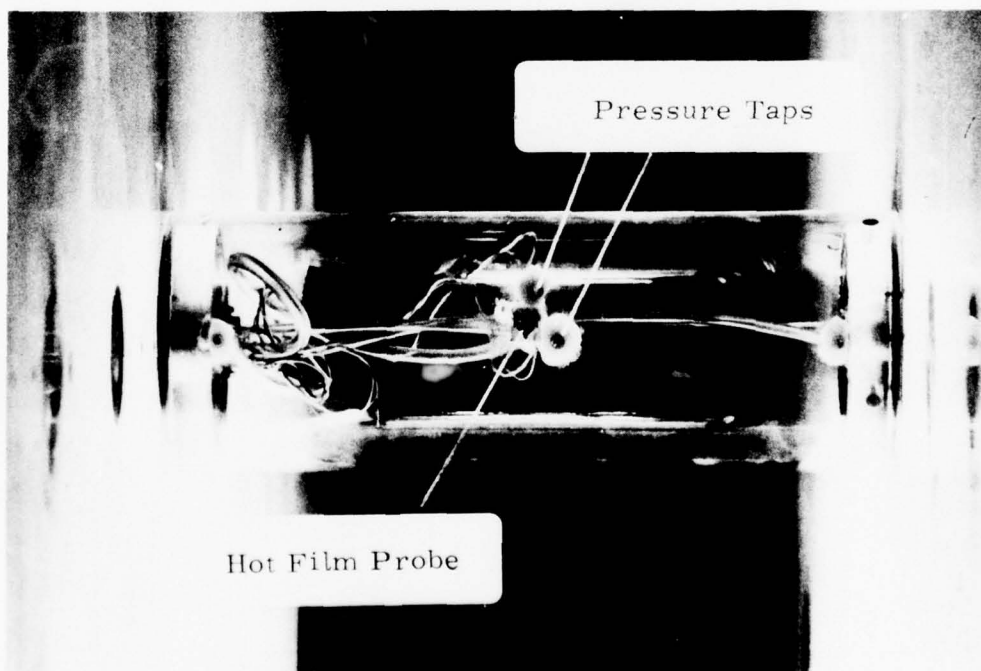


Fig. 2 Cylinder Model with Surface Hot Film Probe in the Wind Tunnel

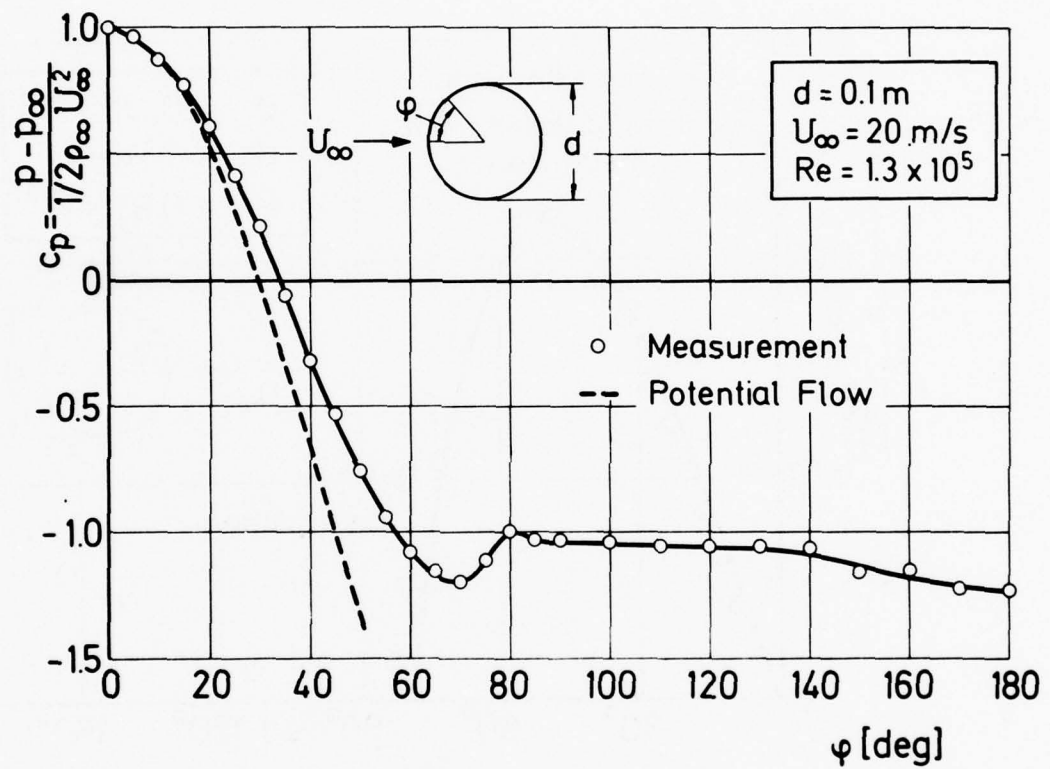


Fig. 3 Pressure Distribution Around a Cylinder Model

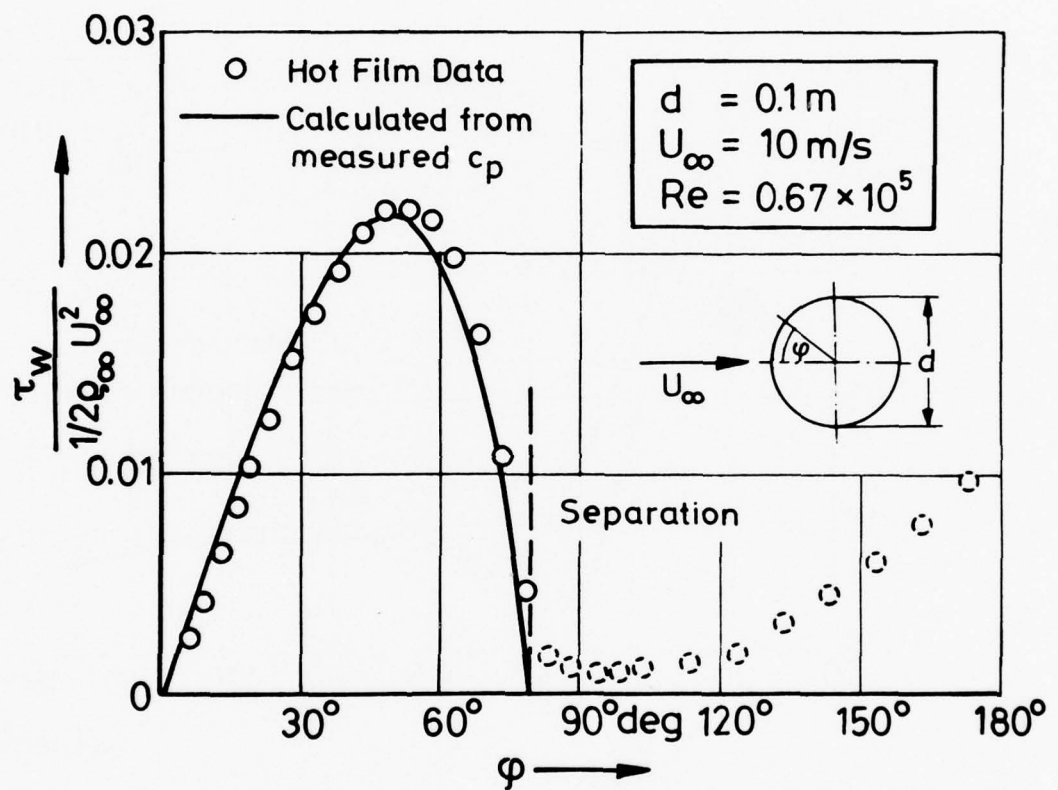


Fig. 4 Wall Shear Stress Distribution Around a Cylinder Model

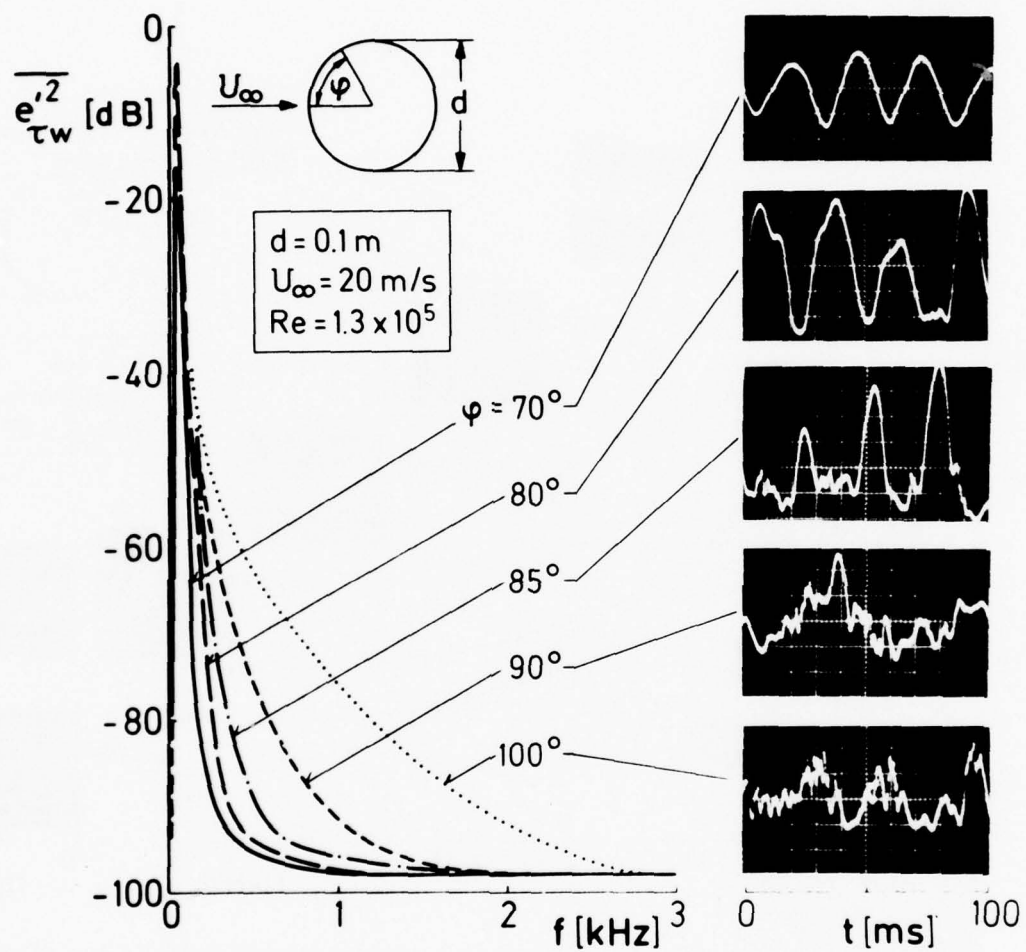


Fig. 5 Surface Hot Film Signals and Spectra on a Cylinder Model

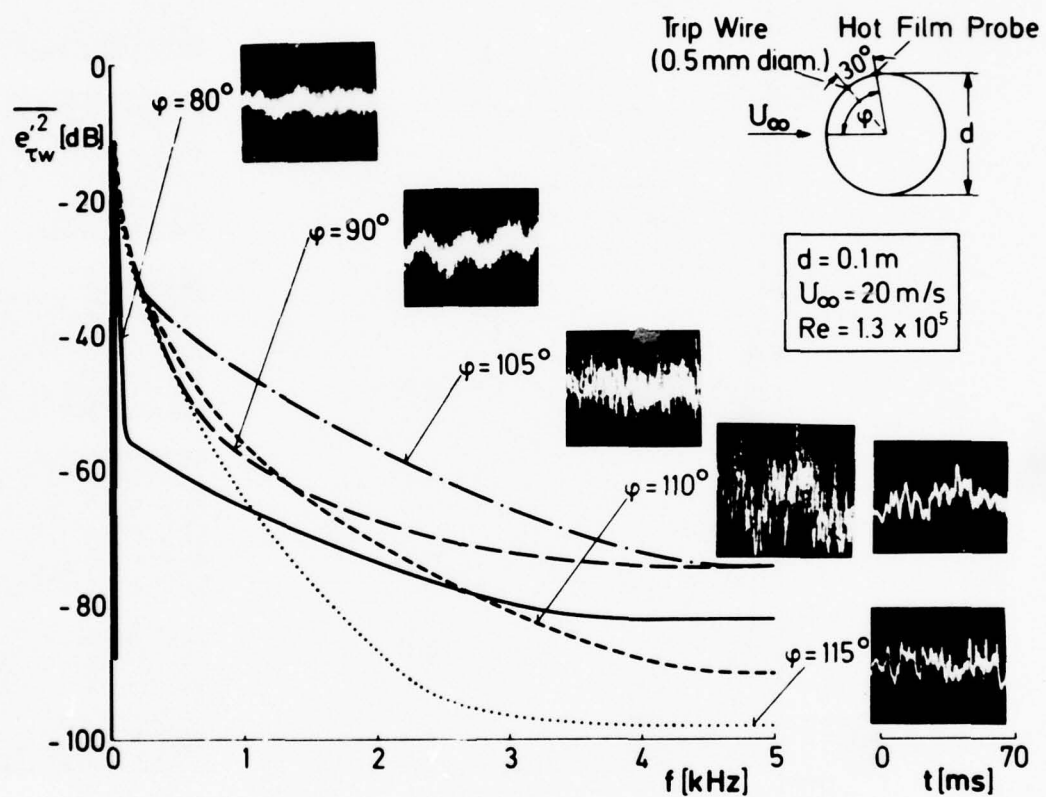


Fig. 6 Surface Hot Film Signals and Spectra on a Cylinder Model with Trip Wire

FURTHER INVESTIGATIONS ON TURBULENCE MODELS FOR THREE-DIMENSIONAL BOUNDARY LAYERS AND COMPARISONS OF CALCULATIONS WITH INFINITE SWEPT WING FLOW MEASUREMENTS

by

J. C. Rotta

Deutsche Forschungs- und Versuchsanstalt
für Luft- und Raumfahrt E. V.
Aerodynamische Versuchsanstalt Göttingen
D-3400 Göttingen, Bunsenstraße 10, W-Germany

Abstract

The pressure strain terms, which play a dominating role in the shear stress transport equations, are analyzed. Two approximative relationships are proposed. Comparative calculations of the turbulent boundary layers of infinite swept wing flows are based on the equations for mean flow and the transport equations for two shear stress components and the kinetic turbulence energy. The results of two different flow cases are compared with measurements.

List of Symbols

a_p	empirical constant, Eq. (5)
b_p	empirical constant, Table 1
E	$= (\overline{u^2} + \overline{v^2} + \overline{w^2})/2$, kinetic turbulent energy
H	$= \delta_1/\Theta_{11}$, shape parameter
L	length scale of turbulence

N	ratio of eddy viscosities with respect to direction normal and parallel to local streamline
p'	fluctuation of pressure
T	empirical constant, Table 1
U, V, W	mean velocity components (in x, y, z direction)
U_s	mean velocity component in direction of outer streamline
U_∞	velocity of undisturbed flow
u, v, w	component of velocity fluctuations
x, y, z	rectangular co-ordinates, Fig. 1
x_m	co-ordinate in direction of undisturbed flow, Fig. 1
α	$= \tan^{-1}(W/U)$, angle between U_r direction and x -axis
α_o	sweep angle of leading edge
β	$= \alpha - \alpha_c$, cross flow angle
β_w	$= \alpha_w - \alpha_e$, angle of limiting wall streamline and streamline at outer edge
β_g	$= \tan^{-1}(\frac{\partial W}{\partial y} / \frac{\partial U}{\partial y}) - \alpha_e$, angle of mean rate of strain
β_τ	$= \tan^{-1}(\frac{\overline{wv}}{\overline{uv}}) - \alpha_e$, angle of resultant shear stress
δ	boundary layer thickness (where $U_r/U_{re} = 0.995$)

δ_1	$= \int_0^{\delta} (1 - U_s/U_{re}) dy$, displacement thickness
κ_g κ_{ss}	} empirical constants, Table 1
$\kappa_{xx}, \kappa_{xz}, \kappa_{zx}, \kappa_{zz}$	
λ	dimensionless coefficients, Table 1
	empirical constant, Table 1
Θ_{11}	$= \int_0^{\delta} \frac{U_s}{U_{re}} \left(1 - \frac{U_s}{U_{re}}\right) dy$, momentum thickness in streamline co-ordinate
ρ	density

Subscripts

e	outer edge of boundary layer
r	resultant value

1. Introduction

On the previous two Meetings of the Data Exchange Agreement, G. R. SCHNEIDER and this author have reported on the efforts to find adequate and not too complicated relationships for the prediction of three-dimensional turbulent boundary layers on bodies and wings, [1] - [3]. Further investigations have been conducted in order to verify the results and to test alternative possibilities. A full report on this work is in preparation.

2. Shear Stress Transport Equations

In a plane turbulent boundary layer, the two components of the Reynolds stress tensor, $\tau_x = -\rho \overline{uv}$, $\tau_z = -\rho \overline{wv}$, are governed by the transport equations

$$(1) \quad (U \frac{\partial}{\partial x} + V \frac{\partial}{\partial y} + W \frac{\partial}{\partial z})(-\overline{uv}) = \overline{v^2} \frac{\partial U}{\partial y} - \frac{\overline{p'}}{\rho} (\frac{\partial u}{\partial y} + \frac{\partial v}{\partial x}) + \frac{\partial}{\partial y} (\frac{\overline{p'u}}{\rho} + \overline{uv^2}) ,$$

$$(2) \quad (U \frac{\partial}{\partial x} + V \frac{\partial}{\partial y} + W \frac{\partial}{\partial z})(-\overline{wv}) = \overline{v^2} \frac{\partial W}{\partial y} - \frac{\overline{p'}}{\rho} (\frac{\partial w}{\partial y} + \frac{\partial v}{\partial z}) + \frac{\partial}{\partial y} (\frac{\overline{p'w}}{\rho} + \overline{wv^2}) .$$

The left hand side represents the rate of change of the Reynolds shear stresses, caused by transport of shear stress due to mean velocity (convection). The third term on the right represents transport of shear stress in direction of the y axis due to turbulent interaction (turbulent diffusion). Usually, the first and second terms on the right hand side are the dominant terms. The first term represents generation of shear stress by the mean rate of strain and, accordingly, is a source term. The second term, which is the mean product of the fluctuating pressure and the fluctuating rate of strain (which is called the pressure strain term for brevity) acts as a sink term. We shall discuss the closure assumptions for the pressure strain terms.

3. The Pressure Strain Terms

The fluctuating pressure can be related to the fluctuating velocity field by the Poisson equation. According to the solution of this equation, the fluctuating pressure is expressed as the sum of two independent parts, the one, p'_M , being correlated with the mean rate of strain and the other, p'_T , being caused by interaction of velocity fluctuations. Consequently, the pressure strain term, too, is considered to consist of two parts.

The part of the pressure strain term, that is due to the fluctuating pressure caused by fluctuating velocity interaction, is generally assumed to effect a redistribution of kinetic energy of the fluctuating velocities and a destruction of Reynolds shear stresses. According to the empirical relationship proposed by J. C. ROTTA [2], [4], the results of these terms acts in the direction of the resultant Reynolds shear stress.

For the part of the pressure strain terms, that are correlated with the mean rate of strain, two different empirical relationships are proposed, which are referred to as the T-model and the λ -model. According to these models, the pressure strain terms can be expressed by

$$(3) \quad \overline{\frac{p'_M}{\rho} \left(\frac{\partial u}{\partial y} + \frac{\partial v}{\partial x} \right)} = E(\kappa_{xx} \frac{\partial U}{\partial y} + \kappa_{xz} \frac{\partial W}{\partial y}) ,$$

$$(4) \quad \overline{\frac{p'_M}{\rho} \left(\frac{\partial w}{\partial y} + \frac{\partial v}{\partial z} \right)} = E(\kappa_{zx} \frac{\partial U}{\partial y} + \kappa_{zz} \frac{\partial W}{\partial y}) .$$

The relationships for the 4 dimensionless coefficients κ_{xx} , κ_{xz} , κ_{zx} , and κ_{zz} are compiled in Table 1. The T-model has been given in Refs. [2], [4], and rests on the simple assumption that the turbulence structure is symmetrical with respect to the local mean streamline. This assumption is of course not generally valid and is here used for boundary layers, where the velocity is measured relativ to the solid surface. The quantity T determines the deviation between the directions of the resultants of pressure strain term and mean rate of strain. For $T = 1$, both directions collapse. This case corresponds to the solution of the Poisson equation assuming isotropic turbulence structure.

The λ -model is derived from a solution of the Poisson equation, given by B. E. LAUNDER, G. J. REECE, and W. RODI [5]. In addition higher order derivatives of the mean velocity, $\partial^2 U / \partial y^2$, $\partial^2 W / \partial y^2$, are taken into account, because the character of three-dimensionality is regarded only in

this way. The quantity b_p follows from the work of B. E. LAUNDER et al., the terms have only little influence. The angular differences between the resultants of the pressure strain terms and the mean rate of strain depends mainly on the quantity of λ . For $\lambda = 0$, both directions collapse, if the small effect of the b_p terms is neglected. In contrast to the T-model, the λ -model is applicable in every co-ordinate system.

4. Numerical Calculations

Using the two models, numerical calculations have been made for infinite swept wing cases. For those cases, the equations reduce in that the derivatives with respect to the z axis are neglected, if the x direction is in the plane of the wing and normal to the leading edge, Fig. 1. Since in the transport equation for the shear stresses, the production terms appear together with the pressure strain terms, the quantities $\overline{v^2}/E$, χ_{ss} and χ_g respectively are condensed to the quantity

$$(5) \quad a_p = \frac{\overline{v^2}}{E} (1 - \chi_{ss}) = \frac{\overline{v^2}}{E} - \chi_g,$$

for which a value of $a_p = 0.2$ is assumed. The diffusion term of (1) and (2) is replaced by a gradient expression (see [1]). The partial differential equations for the mean velocity and for the kinetic energy of turbulence are the same as used in Ref. [1]. The length scale L is approximated by a hyperbolic tangent function. The set of equations has been solved by finite difference procedures. Because of the higher order derivatives appearing with the λ -model, the numerical solutions of this model are much more expensive.

5. Results and Discussion

The first case that is treated, is the separating boundary layer on a 35 degree infinite swept wing, for which extensive experimental investigations have been made by B. van den BERG et al. [6], [7]. A quantity, which is very sensitive to the particular assumptions of the prediction method, is the angle of the limiting wall streamline, β_w . Fig. 2a shows the development of β_w in flow direction for the T-model.

According to the experiment, β_w grows continuously under the influence of the adverse pressure gradient. The separation occurs at $x_m \approx 1.3$ m. Up to values $x_m = 0.8$ m the prediction shows only small differences for different values of T . At larger x_m the calculated results with $T = 1$ (isotropic turbulence) are significantly below the experimental values and predict no separation within the range of the calculation. The agreement improves for smaller values of T and for $T = 0.7$ the deviations are a minimum. For T values still smaller, the agreement deteriorates. With $T = 0.5$ the separation is predicted at $x_m = 1.09$ m.

For the λ -model the β_w are reproduced in Fig. 2b. The predicted results for $\lambda = 0$ are almost identical with those for $T = 1$, which indicates that the terms multiplied by b_p have only insignificant effect. Furthermore, it is seen that the variation of λ has smaller influence on β_w than the variation of T . Values of λ larger than 0.8 give no improvement.

A characteristic quantity of mean velocity profiles is the shape parameter H , defined as the ratio of displacement thickness to momentum thickness, the variation of which is shown for the T-model in Fig. 3a and for the λ -model in Fig. 3b. Similarly as with two-dimensional boundary layers, the experimental values of H rise strongly under the influence of the adverse pressure gradient in flow direction. The curves for $T = 1$ and $\lambda = 0$, which are again almost identical, deviate markedly from the expe-

rimental values for $x_m > 0.9 \text{ m}$.

For smaller values of T , the curves come closer to the experiment. The value of λ has, in contrast, only little effect on H . For $\lambda = 0.2$ somewhat larger values of H result, while for larger λ the value H decreases.

Some further details shall be shown. Fig. 4a gives, for the station at $x_m = 1.095 \text{ m}$, the angle of local mean velocity, β , the angle of mean rate of strain, β_g , and the angle of Reynolds shear stress, β_τ , versus the distance from the surface, y . All angles are measured against the direction of the mean streamline at the outer edge of boundary layer. The calculation for $T = 1$ predicts a difference between β_τ and β_g , which is due to a history effect. However, this difference is much smaller than that of the experiments. For a value of $T = 0.7$ the curves for β_τ and β_g depart from each other and all three angles agree better with the experiment.

The same comparison is given in Fig. 4b for the calculations with the λ -model. The results for $\lambda = 0$ are again almost identical with those for $T = 1$. The influence of λ affects mainly the region near the surface. Here, the curves of β_τ and β_g for $\lambda = 0.8$ are further apart from each other, whereas the difference is small in the outer part of the layer. The difference between the results of the two models becomes especially clear, when the ratio

$$(6) \quad N = \frac{\tan(\beta_\tau - \beta)}{\tan(\beta_g - \beta)}$$

is considered. The values determined from the experiment and the curves resulting from the calculations for the measuring station $x_m = 1.095 \text{ m}$ are plotted versus y/δ in Fig. 5. $N = 1$ means that the shear stress and the mean rate of strain have the same directions. The calculations

with $T = 1$ and $\lambda = 0$ give $N \approx 0.9$ in the outer part. The experimental results are considerably lower. The strong scatter indicates that the determination from the experiments is rather inaccurate. For $T = 0.7$, the calculation agrees roughly with the experiments. The λ -model shows a strong variation of N with y/δ . For $\lambda = 0.8$ rather low values are obtained near the wall, increasing with y/δ up to nearly $N = 1$. The fact that N is rather independent of the value of λ in the outer part, may be assumed as the reason for the low influence of λ on the global boundary layer parameters like β_w . Therefore, the T-model gives on the whole better agreement with the experiments than the λ -model.

As a second case, the NPL experiment by P. BRADSHAW and M. G. TERRELL [8], where boundary layer measurements were made on a flat plate attached to the trailing edge of a yawed wing in the closed test section of a wind tunnel, is calculated. The three-dimensional turbulent boundary layer, generated on the 45 degree yawed wing, relaxes to a two-dimensional layer at constant pressure on the flat plate. The calculations are based on the assumption of infinite swept conditions. Fig. 6a shows the angle, β_w , of the limiting wall streamline according to the experiment and the T-model. The calculation with $T = 1$ comes closest to the measured values, whereas for $T = 0.7$ and 0.5 β_w decays more slowly. However, it is suspected that the flow conditions of the infinite swept wing are invalidated by the sidewalls of the wind tunnel, such that β_w decays faster than it would be the case on an infinite swept wing. The predicted results for the λ -model are reproduced in Fig. 6b. The curve for $\lambda = 0$, which is again identical with that for $T = 1$, comes closer to the measurement than those for $\lambda = 0.4$ and $\lambda = 0.8$. Momentum thickness, shape parameter and resulting wall shear stress are practically independent of T and λ in this flow case.

With respect to direction of mean velocity, mean rate of strain, and Reynolds shear stress a picture qualitatively similar to that of the NLR expe-

riment is obtained, i. e. the direction of the Reynolds stresses is between the directions of mean velocity and mean rate of strain. Only the diagram of N versus y for the last measuring station, $x_m = 1.67 \text{ ft} = 20 \text{ in}$ is given in Fig. 7. The curves for $T = 1$ and $\lambda = 0$ display small differences, but are higher than in the NLR case. They show that the angular difference between shear stress and mean rate of strain, as caused by the convective terms, is much smaller than determined from the experiment. The curve for $T = 0.7$ is partly above and partly below the measurements, thus giving better agreement. The curves for $\lambda = 0.4$ and $\lambda = 0.8$ are similar to those for the NLR case, showing small values near the surface, which grow towards the edge of the boundary layer.

6. Concluding Remarks

With the assumption of isotropic turbulence distributions, only small directional differences between the resultants of mean rate of strain and shear stress are caused by the convective terms of the shear stress transport equations. The relatively large directional differences, observed with the experiments, therefore must have their origin in the pressure strain terms. Neither of the two models proposed for the part of pressure strain terms, which are correlated with the mean rate of strain, is fully satisfactory. It can be stated, however, that with the T-model using $T = 0.7$ better agreement with the experimental results are achieved than with the assumption of isotropic turbulence. The λ -model has a better physical basis, but is less effective and requires much more computational expenditure. The T-model has the additional advantage, that it can be used to derive a mixing length formula for three-dimensional boundary layers. G. R. SCHNEIDER's calculations [3] for the NLR case have shown, that useful results can be obtained with the mixing length formula.

7. References

- [1] ROTTA, J. C.
SCHNEIDER, G. R. Theoretical Investigations of the Three-Dimensional Turbulent Boundary Layer on Swept Wings.

Boundary Layer Effects - Proceedings of the 5th U.S. Air Force/Federal Republic of Germany Data Exchange Agreement Meeting, A. W. Fiore (Ed.), AFFDL-TR-77-61, 1977, pp. 11-34.
- [2] ROTTA, J. C. Turbulence Models for Three-Dimensional Thin Shear Layers.

Viscous and Interacting Flow Field Effects, 2nd US-FRG Meeting, K. -H. Gronau, H. U. Meier (Eds.), BMVg-FBWT 77-20, 1977, pp. 113-119.
- [3] SCHNEIDER, G. R. A General Mixing Length Model and a General Eddy Viscosity Model for Calculating Three-Dimensional Incompressible Turbulent Boundary Layers.

Viscous and Interacting Flow Field Effects, 2nd US-FRG Meeting, K. -H. Gronau, H. U. Meier (Eds.), BMVg-FBWT 77-20, 1977, pp. 120-122.
- [4] ROTTA, J. C. A Family of Turbulence Models for Three-Dimensional Boundary Layers.

Proc. Symposium on Turbulent Shear Flow, Vol. 1, 1977, pp. 10.27-10.34.
- [5] LAUNDER, B. E.
REECE, G. J.
RODI, W. Progress in the Development of a Reynolds-Stress Turbulence Closure.

J. Fluid Mech. 68 (1975), pp. 537-566.
- [6] van den BERG, B.
ELSENAAR, A. Measurements in a Three-Dimensional Incompressible Turbulent Boundary Layer in an Adverse Pressure Gradient Under Infinite Swept Wing Conditions.

National Aerospace Laboratory NLR the Netherlands, NLR TR 72092 U, 1972.

- [7] ELSENAAR, A.
BOELSMA, S. H.

Measurements of the Reynolds Stress Tensor in a Three-Dimensional Turbulent Boundary Layer Under Infinite Swept Wing Conditions.

National Aerospace Laboratory NLR the Netherlands, NLR TR 74095 U, 1974.

- [8] BRADSHAW, P.
TERRELL, M. G.

The Response of a Turbulent Boundary Layer on an "Infinite" Swept Wing to the Sudden Removal of Pressure Gradient.

NPL Aero Report 1305, 1969,
A. R. C. 31 514, F. M. 4095.

	T-Model	λ -Model
κ_{xx}	$\frac{\sqrt{2}}{E} \left\{ \kappa_{ss} U^2 + [1 - (1 - \kappa_{ss})T] W^2 \right\} / U_r^2$	κ_g
κ_{xz}	$-\frac{\sqrt{2}}{E} (1 - \kappa_{ss})(1 - T) \frac{UW}{U_r^2}$	$-\lambda L \frac{W''U' - U''W'}{U'^2 + W'^2}$ $-b_p L \frac{(-\overline{wv})U' - (-\overline{uv})W'}{E^{3/2}}$
κ_{zx}	$-\frac{\sqrt{2}}{E} (1 - \kappa_{ss})(1 - T) \frac{UW}{U_r^2}$	$\lambda L \frac{W''U' - U''W'}{U'^2 + W'^2}$ $+b_p L \frac{(-\overline{wv})U' - (-\overline{uv})W'}{E^{3/2}}$
κ_{zz}	$\frac{\sqrt{2}}{E} \left\{ \kappa_{ss} W^2 + [1 - (1 - \kappa_{ss})T] U^2 \right\} / U_r^2$	κ_g

$$U_r = \sqrt{U^2 + W^2}; \quad U' = \partial U / \partial y; \quad U'' = \partial^2 U / \partial y^2; \quad W' = \partial W / \partial y; \quad W'' = \partial^2 W / \partial y^2$$

Table 1 Coefficients of the Pressure Strain Terms, Eqs. (3), (4)

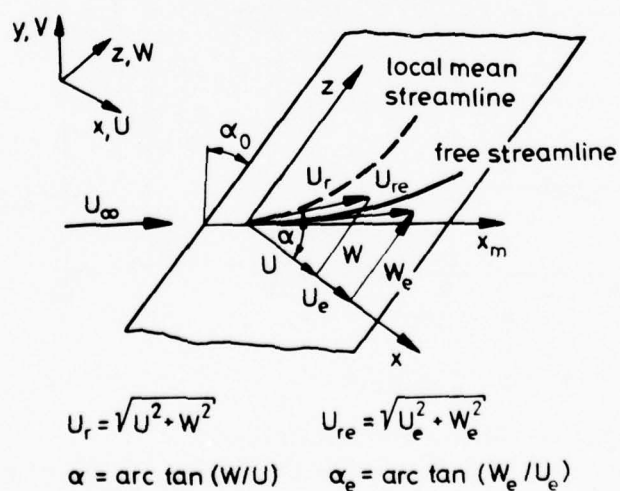


Fig. 1 Swept Wing

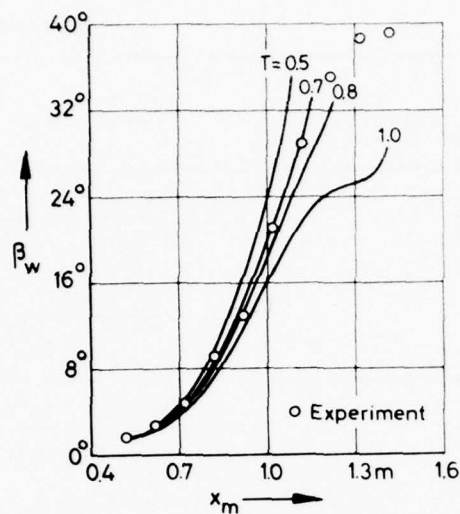


Fig. 2a T-Model

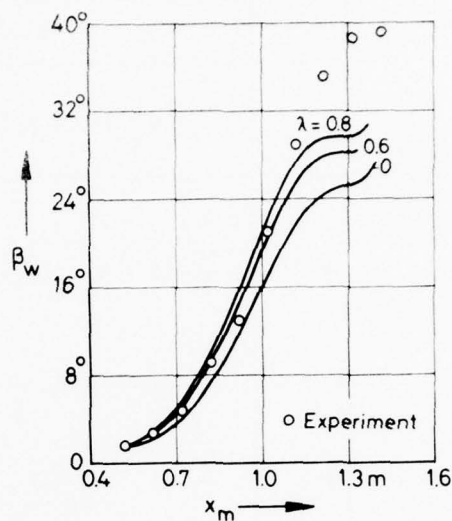


Fig. 2b λ -Model

Fig. 2 Angle of the Limiting Wall Streamline
Experiments of van den BERG et al. [6]; $\alpha_0 = 35^\circ$

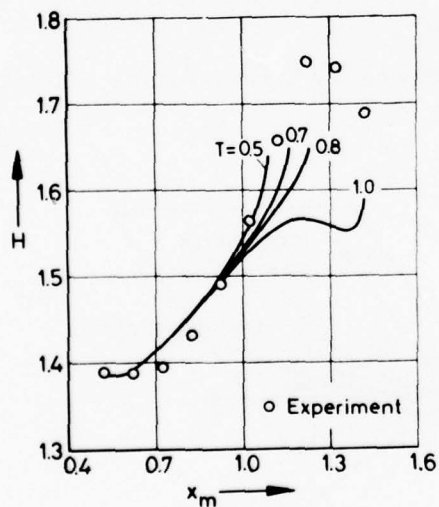


Fig. 3a T-Model

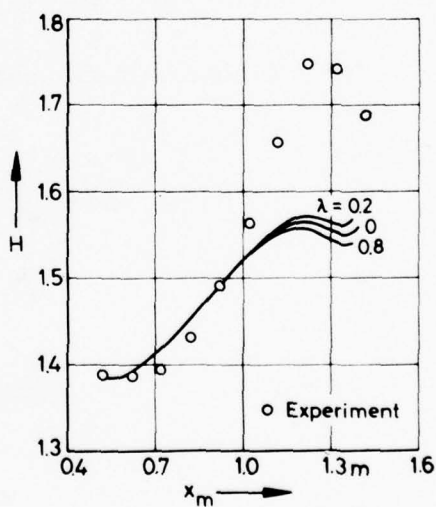


Fig. 3b λ -Model

Fig. 3 Shape Parameter
Experiments of van den BERG et al. [6]; $\alpha_0 = 35^\circ$

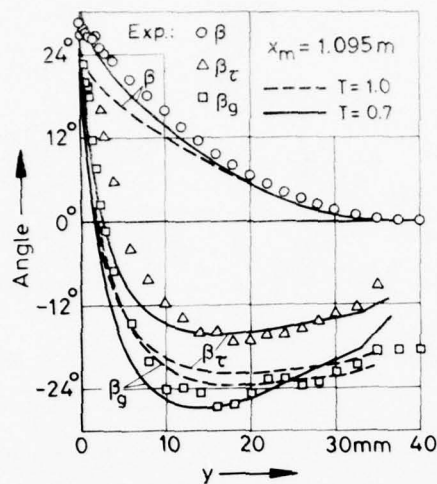


Fig. 4a T-Model

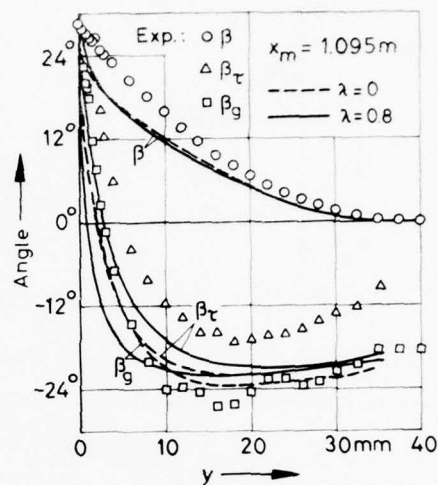


Fig. 4b λ -Model

Fig. 4 Distributions of the Directions of Mean Velocity, Mean Rate of Strain, and Shear Stress
Experiments of ELSENAAR and BOELSMA [7]; $\alpha_o = 35^\circ$

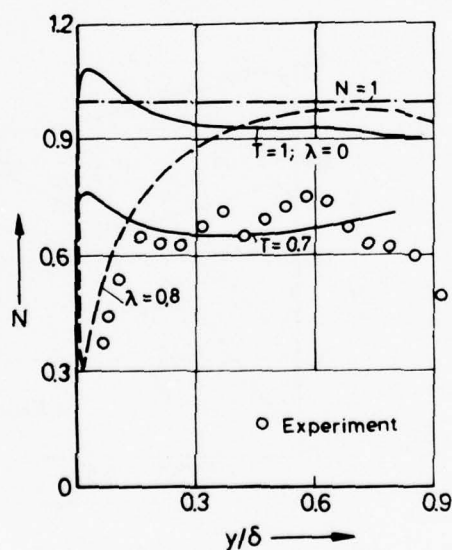


Fig. 5 Ratio N of Eq. (6) versus y/δ
Experiments of
ELSENAAR and BOELSMA
[7]; $\alpha_o = 35^\circ$

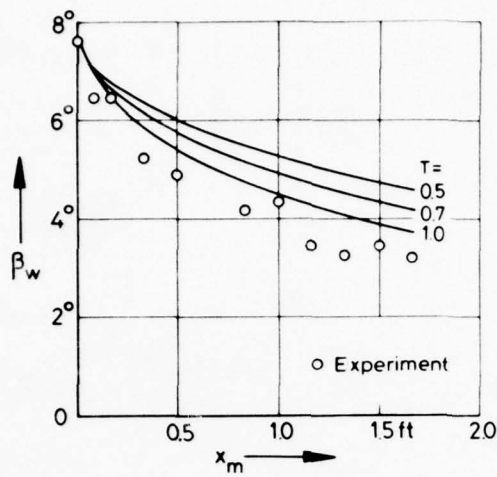


Fig. 6a T-Model

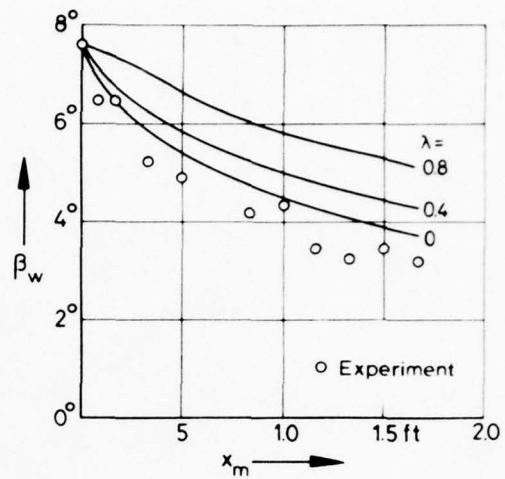


Fig. 6b λ -Model

Fig. 6 Angle of the Limiting Wall Streamline
Experiments of BRADSHAW and TERRELL [8]; $\alpha_o = 45^\circ$

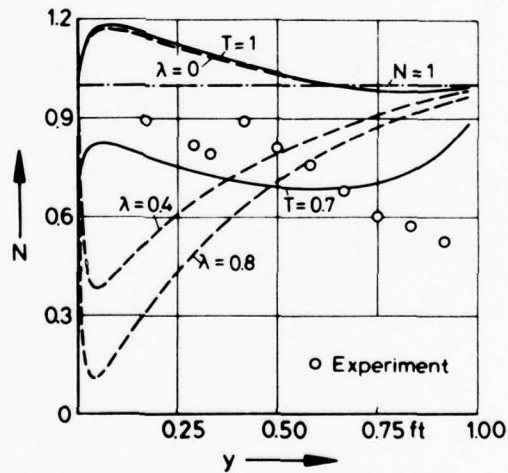


Fig. 7 Ratio N of Eq. (6) versus y
Experiments of BRADSHAW
and TERRELL [8]; $\alpha_o = 45^\circ$

PROGRESS IN THE CALCULATION OF THREE-DIMENSIONAL
BOUNDARY LAYERS ON BODIES OF REVOLUTION
AT INCIDENCE

by

Tuncer Cebeci
Douglas Aircraft Company, Long Beach, California

1. Introduction

Currently we have a considerable effort devoted to the calculation of three-dimensional boundary layers on bodies of revolution at incidence. The reasons for this effort are twofold. One stems from the need to develop a method of calculating aerodynamic forces and flow separation at small and large angles of incidence, and the other is due to our requirement to predict transition at small angles of incidence.

The boundary-layer problem is difficult for several reasons. Of these, the main ones are as follows:

- a. Nose Region: With increasing angle of incidence (α), the flow may separate on the leeward side close to the nose. There is a critical value, α_s , of the angle of incidence α such that for $\alpha < \alpha_s$ separation occurs on the leeward side near the rear of the body, but for $\alpha > \alpha_s$ separation occurs very near the nose; the change taking place in a dramatic fashion. An accurate treatment of the flow in this region is crucial for the separation problem, but has not, so far, been achieved.
- b. Negative Circumferential-Flow Velocity: Depending on the flow conditions, the circumferential flow velocity w may contain regions of flow reversal. For example, w may change from the shape shown in Fig. 1(a) to that shown in 1(b). In this event the thickness of the w -profile tends to increase rapidly with distance downstream while that for u hardly changes. Such change in w -profiles can lead to numerical instabilities resulting from integration opposed to flow direction unless appropriate changes are made in the integration procedure.

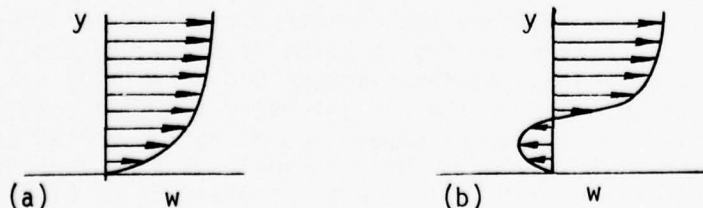


Figure 1. Variation of w -profile with pressure gradient.

- c. Turbulence Modelling: The Reynolds stresses appearing in the governing equations require closure assumptions. The extension of two-dimensional turbulence models to three-dimensional flows requires appropriate verification with experiment.

The prediction of transition is a very difficult problem. In general, transition is affected by freestream turbulence, pressure gradients, surface curvature, roughness, noise, vibration, surface temperature, compressibility, secondary-flow effects, etc. At the present time, there is no exact theoretical method that can correctly account for all — or indeed any — of these effects. The empirical method, known as the e^9 -method does, however, seem to work reasonably well for two-dimensional and axisymmetric flows. It makes use of stability theory and some experimental results, and its extension to three-dimensional flow is desirable. Three-dimensional stability calculations are, however, much more difficult than two-dimensional ones for two reasons:

- a. In the two-dimensional formulation, there is one velocity component u which is a function of x , but in three dimensions, there are two (u, w) which are functions of x and z .
- b. At each point (x, z) we must consider the propagation of disturbances traveling in all directions. We assume the disturbance has the form

$$e^{i(\alpha x + \beta z - \omega t)} \quad (1)$$

In two-dimensional flows, the wave number β in the z -direction is equal to zero and we need only find α as a function of ω and R to construct stability diagrams. In three-dimensional flows, however, we need to find appropriate values of α, β for disturbances propagating at an angle θ to the x -axis where θ is arbitrary. The condition on α and β is not

$$\tan \theta = \frac{\beta}{\alpha} \quad (2)$$

but is

$$\cot \theta = - \frac{d\beta}{d\alpha} \quad (3)$$

Calculation of transition by the e^9 -method requires the solution of the boundary-layer equations and the solution of stability equations. However, as described above, the three-dimensional stability calculations are very difficult and at the present there are some conflicting ideas. For example, in his recent paper¹, L. M. Mack reported calculations on a rotating disk, a simple three-dimensional flow for which there is some experimental data. In these calculations he picked the

condition on α and β as given by equation (2) and not by equation (3). This is incorrect for disturbances initiated at some point in the flow field and evolving downstream for the following reason. Such disturbances can be thought of as groups of waves with a particular frequency ω_0 radiating out in all directions. In order to select those which make a significant contribution along a line inclined at an angle θ to the mainstream we must remember that generally adjacent members of the group cancel each other because of the rapid oscillations. The only waves which make a significant contribution to the disturbance in the direction θ have wave numbers near to that with the property that as α and β vary

$$\alpha x + \beta z - \omega_0 t \quad (4)$$

is stationary with $z = x \tan \theta$, i.e.

$$x + \frac{d\beta}{d\alpha} z = 0 \quad (5)$$

The assumption $\beta = \alpha \tan \theta$ is equivalent to assuming that the disturbances travel with the phase velocity. Even in elementary wave theory for disperse system it is well known that the phase velocity is not directly related to the propagation of energy. It tells us that for a wave uniform with regard to x and z , the shape is unaltered if we move with the phase velocity which is quite a different thing.

At present, our efforts are directed both towards the problem of calculating boundary layers and the problem of predicting transition on bodies of revolution at incidence. However, in the latter case, we have limited ourselves first to simpler three-dimensional flows, such as rotating disks and cones, in order to explore the merits of our ideas.

The work reported here primarily deals with the boundary-layer problem and describes what we have accomplished so far and what our plans are for future work. This is discussed in section 2. We have also performed transition calculations using the e^9 -method for the body of revolution being tested at DFVLR by Dr. H. U. Meier. We include the results for zero incidence at two Reynolds numbers in section 3.

2. Boundary-Layer Problem

The three-dimensional boundary-layer equations in an orthogonal curvilinear coordinate system for an incompressible laminar flow past a general body of revolution are:

$$\frac{\partial}{\partial x} (h_2 u) + \frac{\partial}{\partial \theta} (h_1 w) + \frac{\partial}{\partial y} (h_1 h_2 v) = 0 \quad (6)$$

$$\frac{u}{h_1} \frac{\partial u}{\partial x} + \frac{w}{h_2} \frac{\partial u}{\partial \theta} + v \frac{\partial u}{\partial y} + K_2 w^2 - K_1 u w = -\frac{1}{\rho} \frac{1}{h_1} \frac{\partial p}{\partial x} + \nu \frac{\partial^2 u}{\partial y^2} \quad (7)$$

$$\frac{u}{h_1} \frac{\partial w}{\partial x} + \frac{w}{h_1} \frac{\partial w}{\partial \theta} + v \frac{\partial w}{\partial y} - K_2 u w + K_1 u^2 = -\frac{1}{\rho} \frac{1}{h_2} \frac{\partial p}{\partial \theta} + \nu \frac{\partial^2 w}{\partial y^2} \quad (8)$$

These equations are subject to the following boundary conditions:

$$y = 0 \quad u = v = w = 0 \quad (9a)$$

$$y \rightarrow \infty \quad u \rightarrow u_e(x, \theta), \quad w \rightarrow w_w(x, \theta) \quad (9b)$$

In the above equations, h_1 and h_2 are metric coefficients and are functions of x and θ ; the parameters K_1 and K_2 are known as the geodesic curvatures of the curves $\theta = \text{const.}$, and $x = \text{const.}$, respectively.

The system given by (6) to (9) has been extensively investigated by Wang² and recently by Hirsh and Cebeci³ for the specific case of a prolate spheroid (see fig. 2). Different finite-difference procedures were used by the separate authors and for low incidence (the only case treated by Hirsh and Cebeci) qualitatively similar results were obtained. In these studies the investigators assumed the nose region to be unimportant in its effects on subsequent flow development, and made an assumption about the starting profiles along line AB (fig. 2) which precluded the need to integrate through the nose at $x = -1$.

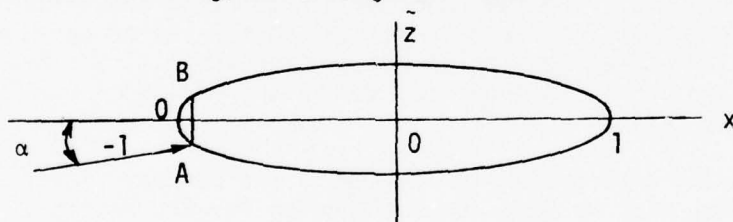


Figure 2. Prolate spheroid at incidence.

At lower angles of incidence, the stagnation point x_s is very close to the nose, for example, for $\alpha = 6^\circ$, $x_s = -0.99898$. At higher incidences, however, the stagnation point, x_s , moves aft; for example, for $\alpha = 30^\circ$, $x_s = -0.97055$. Therefore, assumptions close to the nose at small α are not important since separation occurs far downstream where the effects of the nose region have disappeared. With larger angles of incidence (i.e., $\alpha > 42^\circ$) separation occurs near the nose, upstream of the line AB of Fig. 2, and indicates that the treatment of the nose region is very important.

For the case of a prolate spheroid, $K_1 = 0$ and h_1 , h_2 and K_2 are given by

$$h_1 = \left[\frac{1 + x^2(t^2 - 1)}{1 - x^2} \right]^{1/2} \quad h_2 = t(1 - x^2)^{1/2} \quad (10)$$

$$K_2 = \frac{x}{[1 + x^2(t^2 - 1)]^{1/2}(1 - x^2)^{1/2}}$$

The avoidance of the neighborhood of $0(x = -1)$ is due to the geometrical singularity present in h_1 and hence K_2 . This is strictly a mathematical entity caused by the choice of coordinates. There is no physical singularity in the flow at $x = -1$. To prevent the integration from being stopped near the nose, we recently developed a new transformation which allows the nose region to be computed exactly. This transformation uses new independent variables X and Z defined by

$$X = s \cos \theta \quad (11a)$$

$$Z = s \sin \theta$$

and new dependent variables U , W , and V defined by

$$u = U \cos \theta + W \sin \theta$$

$$w = W \cos \theta - U \sin \theta \quad (11b)$$

$$v = V/t$$

With this transformation and with $Y = y/t$, and with $K_1 = 0$ equations (6) to (9) become:

Continuity

$$N \left(\frac{\partial U}{\partial X} + \frac{\partial W}{\partial Z} \right) + \frac{\partial V}{\partial Y} - L(UX + WZ) = 0 \quad (12)$$

X-momentum

$$N \left(U \frac{\partial U}{\partial X} + W \frac{\partial U}{\partial Z} \right) + LW(WX - UZ) + V \frac{\partial U}{\partial Y} = \beta_1 + v \frac{\partial^2 U}{\partial Y^2} \quad (13)$$

Z-momentum

$$N \left(U \frac{\partial W}{\partial X} + W \frac{\partial W}{\partial Z} \right) - LU(WX - UZ) + V \frac{\partial W}{\partial Y} = \beta_2 + v \frac{\partial^2 W}{\partial Y^2} \quad (14)$$

$$Y = 0 \quad U = V = W = 0; \quad Y = \delta \quad U = U_e, \quad W = W_e \quad (15)$$

Here N , L are parameters which are known functions of $s(\equiv \sqrt{X^2 + Z^2})$ and β_1 and β_2 are pressure gradient parameters.

For the line of symmetry where $W = 0$, equations (12) to (15) reduce to:

$$N \left(\frac{\partial U}{\partial X} + W_Z \right) + \frac{\partial V}{\partial Y} - LUX = 0 \quad (16)$$

$$NU \frac{\partial U}{\partial X} + V \frac{\partial U}{\partial Y} = \tilde{\beta}_1 + \nu \frac{\partial^2 U}{\partial Y^2} \quad (17)$$

$$NU \frac{\partial W_Z}{\partial X} + NW_Z^2 - LU(W_Z X - U) + V \frac{\partial W_Z}{\partial Y} = \tilde{\beta}_2 + \nu \frac{\partial^2 W_Z}{\partial Y^2} \quad (18)$$

$$Y = 0 \quad U = V = W_Z = 0; \quad Y = \delta \quad U = U_e, \quad W_Z = W_{Ze} \quad (19)$$

At the stagnation point where both U and W are zero, these equations reduce further and are not shown here for space limitation.

The studies dealing with the solution of equations (12) to (15) are still in progress and are not complete yet. However, the studies dealing with the solution of line of symmetry equations are complete and are briefly described below. For further details see a forthcoming paper by Cebeci, Khattab and Stewartson⁴.

The line of symmetry equations are solved by using the Box method described by Cebeci and Bradshaw⁵. The solution is obtained in the (X, Z) plane starting at the stagnation position s_0 shown in figure 3. The integration in X proceeds normally in both windward ($s > s_0$) and leeward sides $s < s_0$ and solutions obtained at the nose show no trace of singular behavior.

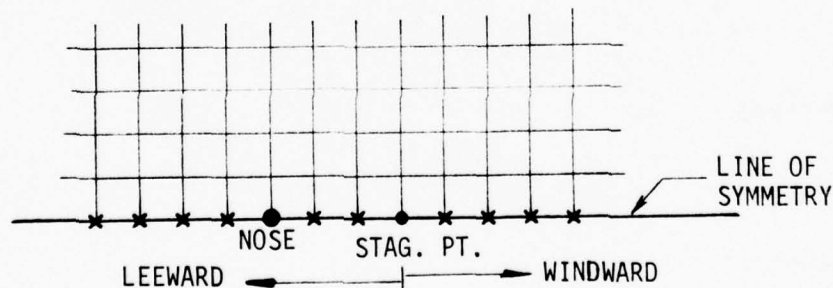


Figure 3. Sketch showing the solution procedure along the line of symmetry.

The (X, Z) plane is a nice coordinate system near the nose, but it loses its attractiveness for regions away from the nose. For this reason, at some location $x = x_0$, we switch to more appropriate variables to continue the calculations downstream. By introducing a new set of dependent and independent variables defined by

$$\eta = \sqrt{\frac{v_0}{v s_1}} y,$$

$$\psi = \sqrt{v_0 v s_1} h_2 f(x, \theta, \eta) \quad (20)$$

$$\phi = \sqrt{v_0 v s_1} h_1 g(x, \theta, \eta)$$

such that

$$u h_2 = \frac{\partial \psi}{\partial y}, \quad w_\theta h_1 = \frac{\partial \phi}{\partial y} \quad \text{and} \quad v h_1 h_2 = -\left(\frac{\partial \psi}{\partial x} + \phi\right), \quad (21)$$

we write the line of symmetry equations of (6) to (8) as

$$\frac{f'}{h_1} \frac{\partial f'}{\partial x} - f''\theta = \beta_1^* + \frac{f'''}{s_1} \quad (22)$$

$$\frac{f'}{h_1} \frac{\partial g'}{\partial x} + \frac{(g')^2}{h_2} - g''\theta - K_2 f' g' = \beta_2^* + \frac{g'''}{s_1} \quad (23)$$

$$\theta' = \frac{1}{\sqrt{s_1} h_1 h_2} \left[\frac{\partial}{\partial x} (\sqrt{s_1} h_2 f') + \sqrt{s_1} h g \right]. \quad (24)$$

Here

$$s_1 = \int_{-1}^x h_1 dx, \quad f' = u/v_0, \quad g' = w_\theta/v_0 \quad (25)$$

Comparison of solutions obtained by first solving the governing equations given by (16) to (19) then by (22) to (24) with those obtained previously by Hirsh and Cebeci³ for $\alpha = 6^\circ$ show excellent agreement (see fig. 4).

Figure 5 shows the results for $\alpha = 30^\circ$. We now note that the stagnation point is further away from the nose ($x = -0.97055$) and that on the leeward side, close to the nose, the local skin-friction coefficient has a dip followed by a rise. This is due to the angle of incidence indicating the possibility of flow separation at higher angles of incidence on the leeward plane of symmetry. Additional calculations made at $\alpha > 30^\circ$, support this conclusion and show that flow separation occurs at $\alpha = 42^\circ$ for a $t = 1/4$.

Additional calculations for different thickness ratios and angles of incidence are being performed and will be reported later.

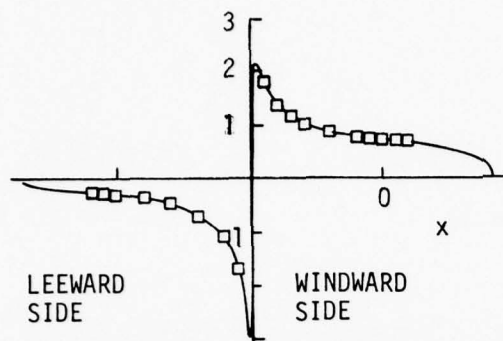


Figure 4. Comparison of present results with those of ref. 3 for $\alpha = 6^\circ$, $t = 1/4$.

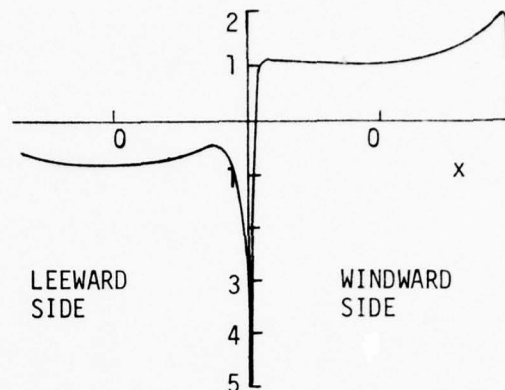


Figure 5. Computed results for $\alpha = 30^\circ$, $t = 1/4$.

An interesting question posed by the studies of the two-dimensional and axisymmetric boundary layer is whether there is significant difference between the separation phenomenon in the two cases as the nose radius tends to zero. In order to investigate this question for the prolate spheroid problem, we use the transformation defined by (11) and define

$$p = \frac{\sqrt{1-x^2}}{t} \quad (26)$$

and take the limit $t \rightarrow 0$, holding p and s finite. In this way we convert the polar form of the equations (6) to (8) near the nose into a quasi-rectangular Cartesian form which is free of singularities. After a considerable amount of algebra, the continuity and momentum equations for the line of symmetry can be written as

$$\frac{\partial U}{\partial p} + a_1 W_2 + a_2 \frac{\partial V}{\partial y} + a_3 U = 0 \quad (27)$$

$$\frac{U}{a_2} \frac{\partial U}{\partial p} + V \frac{\partial U}{\partial y} = \beta_1^* + \frac{\partial^2 U}{\partial y^2} \quad (28)$$

$$\frac{U}{a_2} \frac{\partial W_2}{\partial p} + a_4 U W_2 + a_5 W_2^2 + \frac{U^2}{a_2} + V \frac{\partial W_2}{\partial y} = \beta_2^* + \frac{\partial^2 W_2}{\partial y^2} \quad (29)$$

Here a_1 to a_5 are known functions of p and β_1^* and β_2^* are pressure gradient parameters and W_2 is defined by

$$W_2 = W_z \exp \left\{ \sqrt{1+p^2} - 1 \right\} \quad (30)$$

The results obtained from the solution of the above equations indicate that for laminar flows as the nose radius tends to zero, flow separation does not occur if α is less than 41° . By contrast, it appears that on thin two-dimensional airfoils the flow will separate right near the nose if $\alpha = 0(t)$. For further details, see Cebeci, Khattab and Stewartson⁴.

3. Transition Problem

In order to calculate the transition on the body of revolution being tested at DFVLR, we performed stability-transition calculations by using the method described in Chapter 9 of Cebeci and Bradshaw⁵. These calculations were done for zero incidence and with two Reynolds numbers based on the body length, namely 6.4×10^6 and 9.6×10^6 . Results are given below.

R_L	$(x/L)_{\text{transition}}$
6.4×10^6	0.595
9.6×10^6	0.405

Figure 6 shows the calculated amplification ratio A versus surface distance for a fixed nondimensional disturbance $\omega^* = v\omega/u^2$ for $R_L = 9.6 \times 10^6$. Here ω is the frequency in radians per second and A is the ratio of the disturbance amplitude at a given location to that at the beginning of amplification (crossing of the neutral curve). According to the e^9 -method, the first frequency whose logarithm of the amplification ratio reaches 9 somewhere on the body determines the location of transition. According to several studies

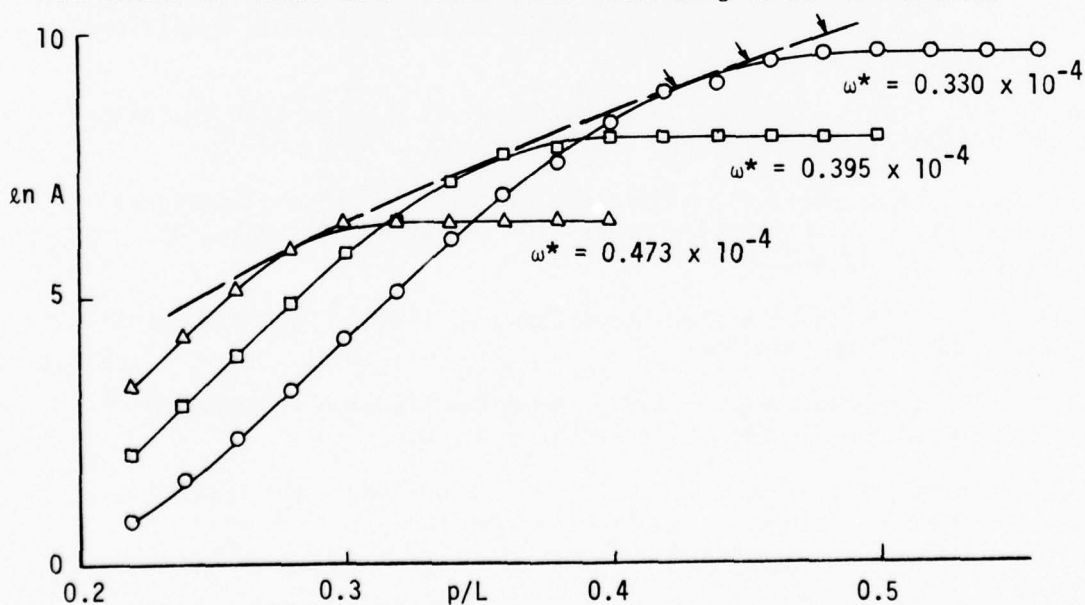


Figure 6. Computed amplification factors for the body of revolution being tested at DFVLR. Results are for $\alpha = 0$.

conducted in two-dimensional flows, however, the value of θ varies between 9 and 10. Figure 6 shows that for e^9 , $e^{9.5}$ and e^{10} , the respective transition locations are $x/L = 0.405, 0.433, 0.453$.

4. Concluding Remarks

At the writing of this progress report, the calculations dealing with off the line of symmetry are incomplete. We expect that they will soon be complete and that we will be able to extend the calculations away from the nose all the way downstream on the body. Additional computational difficulties due to flow reversal of the circumferential velocity profile will be handled by the new Cebeci and Stewartson⁶ procedure for computing three-dimensional boundary layers with the aid of backward-facing characteristics. Using this new procedure we are very hopeful that we will be able to predict the separation line very accurately.

In addition to these laminar-flow calculations, we plan to perform turbulent-flow calculations on the body being tested at DFVLR. The calculations will be made by using the eddy-viscosity formulation of Cebeci⁷ and the results will be compared with the experimental results.

The stability-transition studies dealing with bodies of revolution at incidence will begin as soon as the preliminary studies on rotating disks and cones are over. We expect this to occur early in 1979.

5. References

1. Mack, L.M. (1977) Transition prediction and linear stability theory. AGARD Fluid Dynamics Panel Symposium on Laminar-Turbulent Transition, Copenhagen, Denmark.
2. Wang, K.C. (1974) Boundary layer over a blunt body at high incidence with an open-type separation. Proc. Roy. Soc., A340, 33-55.
3. Hirsh, R.S. and Cebeci, T. (1977) Calculation of three-dimensional boundary layers with negative cross-flow on bodies of revolution. AIAA paper no. 77-683.
4. Cebeci, T., Khattab, A.K. and Stewartson, K. (1978) On nose-separation. Paper in preparation.
5. Cebeci, T. and Bradshaw, P. (1977) Momentum Transfer in Boundary Layers. McGraw-Hill/Hemisphere, Washington, D.C.
6. Cebeci, T. and Stewartson, K. (1977) A new procedure for computing three-dimensional boundary layers with flow reversal. Paper in preparation.
7. Cebeci, T. (1974) Calculation of three-dimensional boundary layers. Pt. 1. Swept infinite cylinders and small cross flow. AIAA J., 12, 779.

INFLUENCE OF SURFACE ROUGHNESS
AND MASS TRANSFER ON
TURBULENT BOUNDARY-LAYER FLOW

by

Robert L. P. Voisinet

NAVAL SURFACE WEAPONS CENTER
White Oak Laboratory
Silver Spring, Maryland 20910

ABSTRACT

The determination of the relative and combined effects of surface roughness and mass transfer on turbulent boundary-layer development, and in particular, on skin-friction drag was the prime objective of this study. Wind-tunnel tests were conducted in the NSWC Boundary-Layer Channel at a freestream Mach number of 2.9. The thick nozzle-wall boundary layer in the facility was subjected to a systematic variation of surface roughness and mass-transfer conditions. Boundary-layer surveys were made and skin friction was measured directly using a specially designed skin-friction balance which had a provision for active blowing through the drag element.

I. INTRODUCTION

The skin-friction drag on a re-entry heatshield, an important contribution to the overall drag of a re-entry vehicle, is affected by two phenomena which are interrelated through the ablation process. These are surface roughness and mass transfer. Although the relative effects of roughness and mass transfer are known with some confidence, their combined effects are not. It is for this reason that a detailed experimental program was conducted wherein direct measurements of skin-friction drag and boundary-layer velocity profiles were obtained in the presence of roughness, mass transfer, and combined roughness and mass transfer.

II. WIND-TUNNEL FACILITY

Wind-tunnel tests were conducted in the NSWC Boundary-Layer Channel.¹ The facility, shown schematically in Figure 1, consists of a two-dimensional supersonic half-nozzle which has for one wall a flat test surface on which boundary-layer measurements are made. The opposite wall is flexible and is adjusted to produce a zero-pressure-gradient flow in the test section. The lower portion of the flat test plate can be fitted with a variety of surface test plate inserts including roughened and porous test samples. Three independently controlled flow chambers exist behind the test plates and allow for active gas injection through porous test samples. The test

plate insert begins at the 1.22-meter station (distance measured downstream of the nozzle throat) and extends for 0.99 meters. A skin-friction balance with a 12.7 x 25.4-centimeter rectangular drag element is centrally located about the 1.88-meter station. The capability exists for active mass transfer through the drag element of the skin-friction balance as well as the area covered by the test plate insert. Several instrumentation ports exist downstream of the drag balance and provide for the installation of a traversing probe mechanism for boundary-layer surveying over the test sample.

III. TEST CONDITIONS

Wind-tunnel tests were conducted at a freestream Mach number of 2.9 and Reynolds number per meter from 0.1 to 3. million. The supply temperature was adjusted to maintain adiabatic-wall conditions in the test section. The nominally 2.5-centimeter thick nozzle-wall boundary layer was subjected to a systematic variation of surface roughness and mass transfer. A smooth impervious test plate was tested first to establish the baseline data followed by tests on three porous roughened samples. The porous test plates were constructed of a wire-mesh composite with the roughness character being that of the surface square-weave screen mesh. Three surface screen roughnesses were tested with nominal heights of 0.1, 0.25, and 1.0mm. These provided for a range of surface roughness conditions from the aerodynamically smooth through the fully rough regime (see Figure 2). Mass-transfer rates were 0.0146, 0.0488, and 0.146 kg/m²sec. These rates provided a range of mass transfer up to and including boundary-layer blowoff (see Figure 3). Both skin-friction and boundary-layer profile measurements were made over the full range of the testing matrix.

IV. POROUS ROUGHENED TEST SAMPLES

Present test requirements called for flat porous test samples which were uniform in porosity. In addition, a different surface roughness height was required for each panel. The porous panels were fabricated from wire-mesh materials which were diffusion bonded together (see Figure 4). A different size square-weave mesh was bonded to the surface of each panel to simulate the surface roughness. Surface screen thicknesses of 0.1, 0.25, and 1.0mm provided boundary-layer roughness effects which ranged from the aerodynamically smooth to fully rough case. In addition, the ratio of wire-mesh spacing to roughness height (twice the wire thickness) was the same for all samples in order to maintain roughness pattern similarity.

The basic porous panel on which the wire screen roughness was attached was constructed of a composite of wire screen meshes and perforated plate. This composite was designed for optimum flow uniformity and structural rigidity. A perforated metal sheet gave strength and rigidity to the composite, a 20-mesh inner screen provided flow distribution between layers, and five layers of 50 x 250 dutch weave provided the proper permeability. Permeability was selected in such a manner as to provide sufficient pressure drop across the test sample for flow uniformity, but with limitations on the pressure drop based on panel deflection considerations. It is believed that the wire mesh composite provided a more uniform porosity material than could have been attained using sintered powder technology.

V. SKIN-FRICTION BALANCE

Direct measurements of skin friction were obtained with a specially designed skin-friction balance which had a provision for active blowing through the drag element. The balance concept was based on previous NSWC/WOL experience in skin-friction balance design (References 2-5). Many of the balance components were conventional in nature, however, the test requirement for active blowing through the drag element made this skin-friction balance unique. The balance is schematically shown in Figures 5 and 6. The mechanical components of the balance are shown in the first schematic, and the mass-addition components are shown in the second. The balance is a positive displacement-type which requires the measurement of the drag-element deflection under the action of a drag force. The drag element is supported by four linkages and frictionless flexural pivots which allow movement of the drag element in the streamwise direction. Leafsprings provide a restraining force which is proportional to the deflection of the drag element. By using leafsprings with different stiffnesses, the balance can be made to accommodate a wide range of drag loading. Drag element deflections are kept small (less than 0.25mm) and are measured using a highly sensitive translational Linear Variable Differential Transformer (LVDT). A positive stop is adapted to eliminate overload damage to the balance.

Although the temperature environment of the balance is not severe in the present tests, precautions have been taken to minimize any effects which might result from ambient temperature changes. Invar and other materials with low coefficients of thermal expansion have been used for all critical balance components and supporting framework.

A drag-element counterweight is employed in the design to reduce wind-tunnel vibration effects. Structural vibration is transmitted to the drag-element via the center flexural pivot in each linkage. Since this pivot point is also the center of gravity (c.g.) of the drag-element/counterweight system, moments about the c.g. (induced drag forces) are eliminated. In addition, the counterweight relieves drag-element weight restraints and allows for an increased balance sensitivity. This is a particular necessity because of the vertical orientation of the balance in the wind tunnel. Without a counterweight, the leafsprings would have to carry the weight of the drag-element. Drag-element oscillations which are due to flow unsteadiness are damped out using a magnetic-fluid dashpot as described in Reference 6.

All critical balance components are adjusted in reference to a primary balance frame. This primary frame and associated balance components are then moved as a unit to provide the necessary alignment of the drag element with the surrounding tunnel wall. By performing the adjustment in this manner, the alignment of internal balance components is not changed, and the balance load calibration is unaffected. Air leakage through the balance from the wind-tunnel plenum chamber to the test section is eliminated by sealing the balance back housing.

Active blowing through the drag-element is accomplished by piping the injectant gas to the drag-element in such a way as to minimize the effects of the piping on the balance operation and calibration. Injectant air from a flow regulating system enters the balance from two ports at the back of the balance. The injectant air then passes through flexible metallic bellows to the drag-element for flow distribution. The drag-element houses flow deflectors and a perforated plate which disburse the injectant gas uniformly to all areas of the porous test sample. The key to the design of the active blowing system is the alignment of the primary metallic bellows with the drag element support linkages (see Figures 7 and 8). As the bellows become pressurized, the expansion forces acting along the axis of the bellows are restrained by the linkages. Because these forces act in a direction normal to the test surface, there is no component of the bellows expansion forces acting in the direction of the friction drag. When the drag element is deflected from the "null" position, a slight misalignment does occur, and a correction to the calibration must be made; however, the magnitude of this correction is small in comparison to the drag loading, and its effect can be calibrated. By designing the injectant system in this way, the injectant gas flow causes a minimum disturbance to the balance in the direction of the drag loading.

The balance drag-element design allows for replacement of the test surface. Test samples can be solid or porous, smooth or rough, and can include single or multiple roughness elements and waviness. The drag balance can also handle different injectant gases. In all cases, the surface characteristics on the drag element are closely matched to those of the surrounding test surface.

VI. BALANCE ASSEMBLY AND CALIBRATION

The successful operation of the skin-friction balance is dependent on the integration of a number of different components. Special precautions must be taken in the assembly of the balance. The balance counterweight must be adjusted to the total weight of the drag element and its attached components prior to assembly. The flexural pivots must be installed without residual torsional stress. The bellows must be aligned with the support linkages. Seals must be leakproof. Adjustment screws and linkages must be tight fitting. In addition, the alignment of components must be made in a specific manner.

The balance alignment begins by determining the balance "null" position. This position is defined as the point where the drag element does not deflect when the bellows are pressurized. It establishes the point of non-interference between load measurement and active blowing. The leafsprings are adjusted to hold this "null" position and the LVDT core is centered in this position.

The balance load calibration is performed by attaching weights to the drag element and measuring the deflection of the drag element with the LVDT. A straight line calibration between displacement and loading is typical, as shown in Figure 9 for the the different leafspring configurations. With active blowing the calibrations change slightly because the drag-element is deflected from its "null" position and a component of the bellows expansive force is felt on the drag element in the direction of the load measurement. Calibrations can still be represented by straight lines, however, because the induced loading increases linearly with the displacement of the drag element. This effect can be seen in Figures 11 and 12. There does not appear to be any difference between calibrations obtained under static pressurized test conditions and those with mass transfer through the balance. The maximum effect which was measured during tests amounted to less than three percent of the load measurement. This occurred for the lightest load range for the balance (no leafsprings installed, 50 grams maximum load). This effect was calibrated, and corrections were made in the data reduction.

VII . RESULTS

Sample boundary-layer velocity profile data for the smooth-wall, non-blowing baseline condition are shown in Figure 12 for the range of Reynolds number tested. The data are presented in law-of-the-wall coordinates and agree with theory. Sample skin-friction data for the same smooth-wall, non-blowing baseline case are shown in Figure 13. The data are below Spalding-Chi values by approximately 15 percent but show the appropriate trend with Reynolds number. The data that are presented represent several test runs, each obtained with a re-installation and alignment of the drag balance. The consistency and repeatability of the data have been excellent in all cases.

Skin-friction data for the three roughened test plates with mass transfer are shown in Figures 14 through 17. The smooth, non-blowing baseline data are shown in each figure for comparison. The relative effects of roughness and mass transfer are isolated and presented in Figures 18 and 19 as a function of roughness Reynolds number and mass-transfer ratio, respectively. The results show a marked increase in skin friction due to roughness and a marked decrease due to mass transfer. Each result is consistent with theory. The combined effects of the two phenomena are presently being analyzed further.

VIII. CONCLUSIONS

The relative and combined effects of surface roughness and mass transfer on compressible turbulent boundary-layer development were experimentally studied. Specialized test equipment was designed and validated and a data base was generated for conditions of surface roughness, mass transfer, and combined roughness and mass transfer. Analysis of the data is continuing.

IX. REFERENCES

1. Lee, R. E., et. al., "The NOL Boundary-Layer Channel," NOLTR 66-185 Nov 1966
2. Bruno, J. R., et. al., "Balance for Measuring Skin Friction in the Presence of Heat Transfer," NOLTR 69-56, Jun 1969
3. Chien, K., "Hypersonic Turbulent Cold-Wall Skin-Friction and Heat-Transfer Measurements on an Axisymmetric Sharp Cone," NOLTR 73-108, Jun 1973
4. Reda, D. C., "Compressible Turbulent Skin Friction on Rough and Rough/Wavy Walls in Adiabatic Flow," NOLTR 74-34, Feb 1974. Also AIAA Journ. Vol. 13, No. 5, May 1975, pp. 553-554
5. Horanoff, E. V. and Driftmyer, R. T., "Two-Component Force Balance for Measuring Skin Friction and Side Force," NSWC/WOL TR 75-174, Oct 1975
6. Voisinnet, R. L. P., "Temperature-Step Effects on Direct Measurement of Skin-Friction Drag," NSWC/WOL TR 77-17, Jul 1977

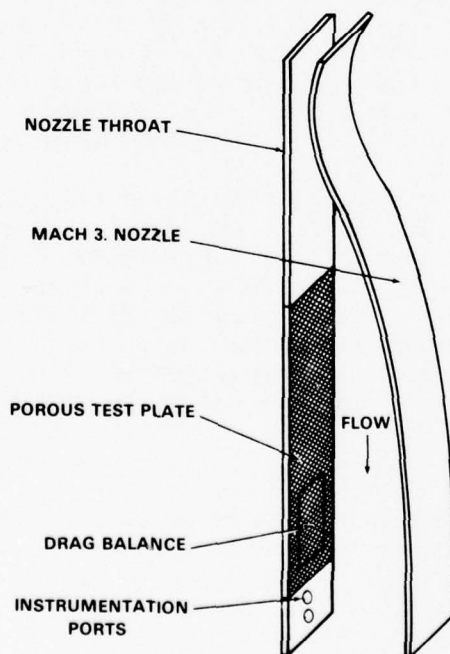


FIGURE 1 NSWC BOUNDARY-LAYER CHANNEL

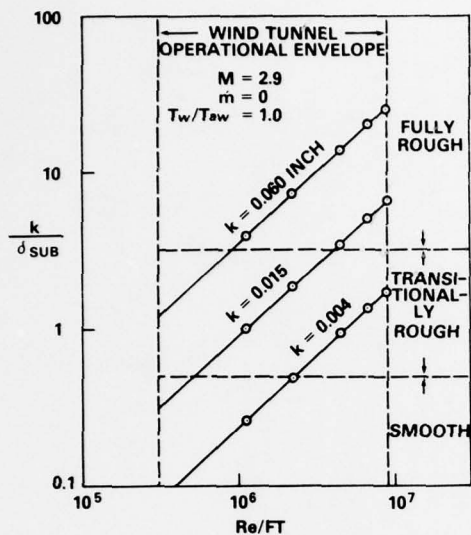


FIGURE 2 ROUGHNESS TEST MATRIX

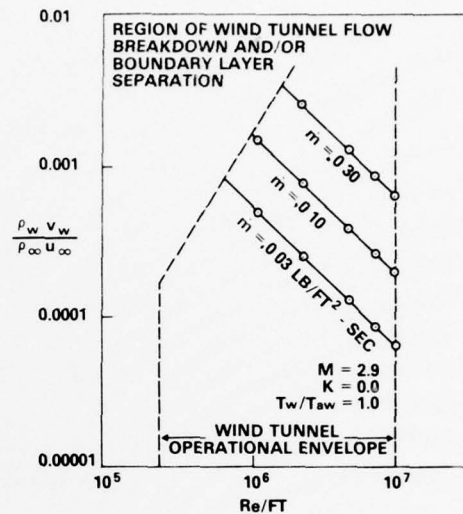


FIGURE 3 MASS-TRANSFER TEST MATRIX

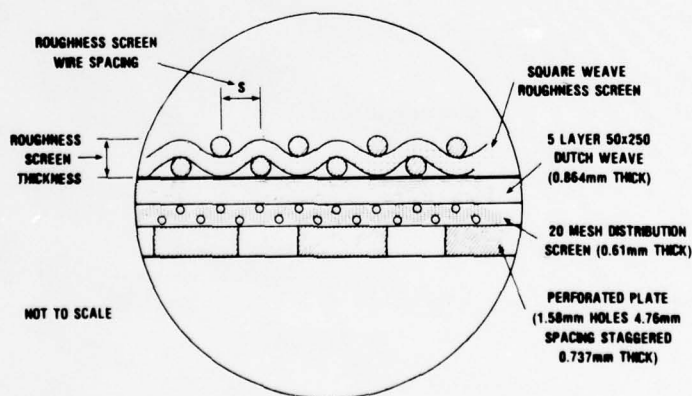


FIGURE 4 POROUS ROUGHENED TEST SAMPLE CROSS SECTION

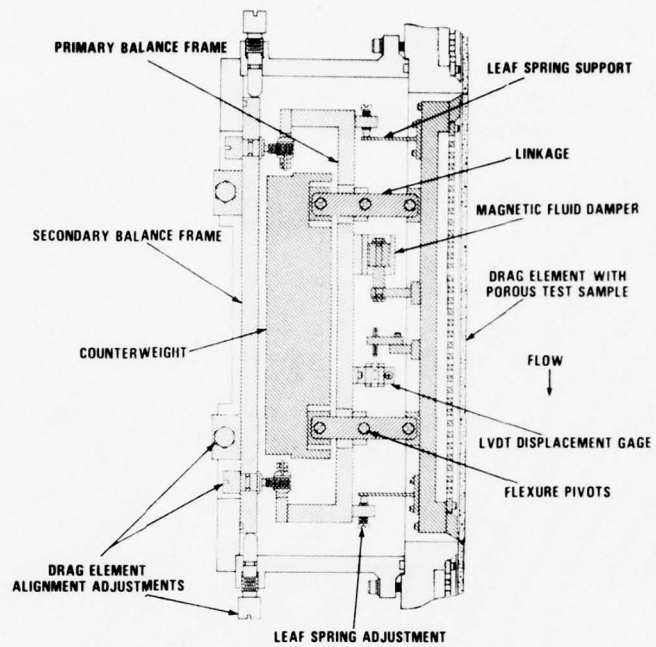


FIGURE 5 SKIN-FRICTION BALANCE SCHEMATIC,
MECHANICAL COMPONENTS

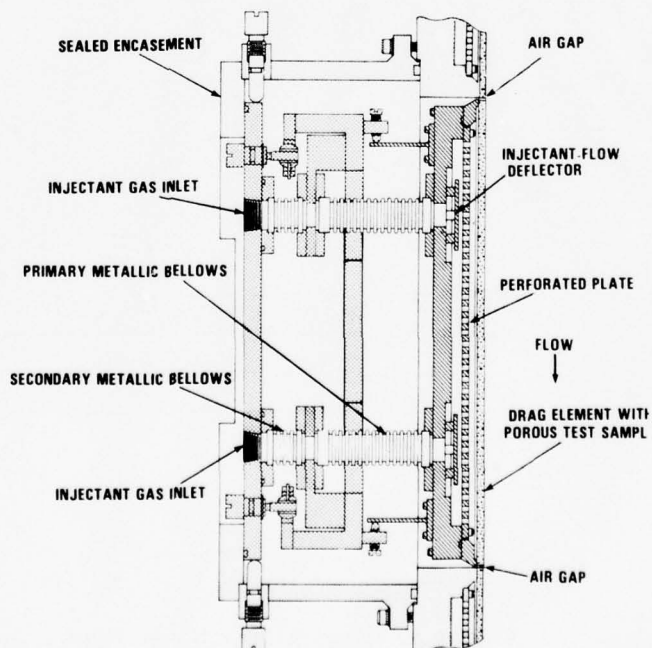


FIGURE 6 SKIN-FRICTION BALANCE SCHEMATIC, GAS
INJECTION COMPONENTS

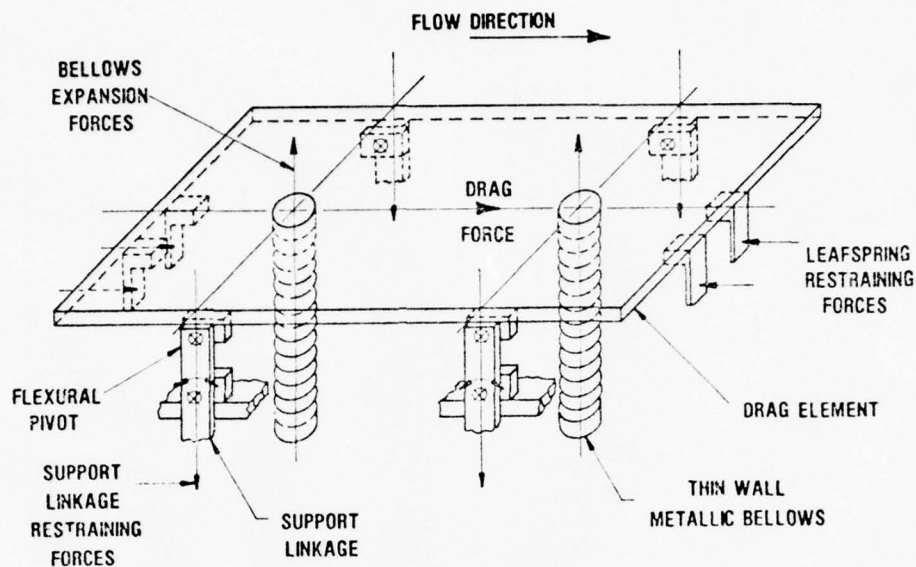


FIGURE 7 DRAG ELEMENT FORCE BALANCE

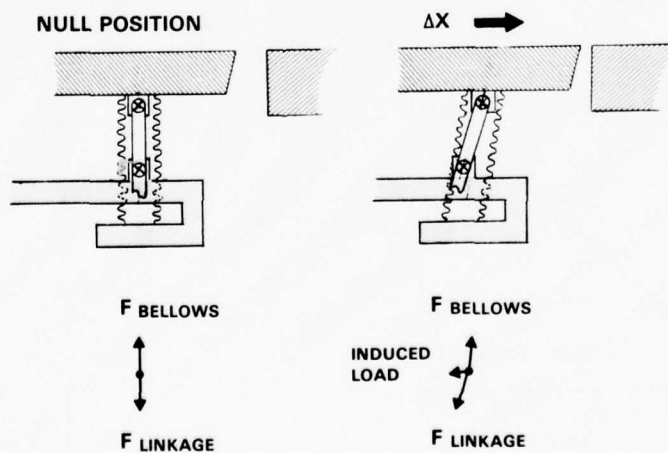


FIGURE 8 DRAG-ELEMENT BELLOWS/LINKAGE ALIGNMENT

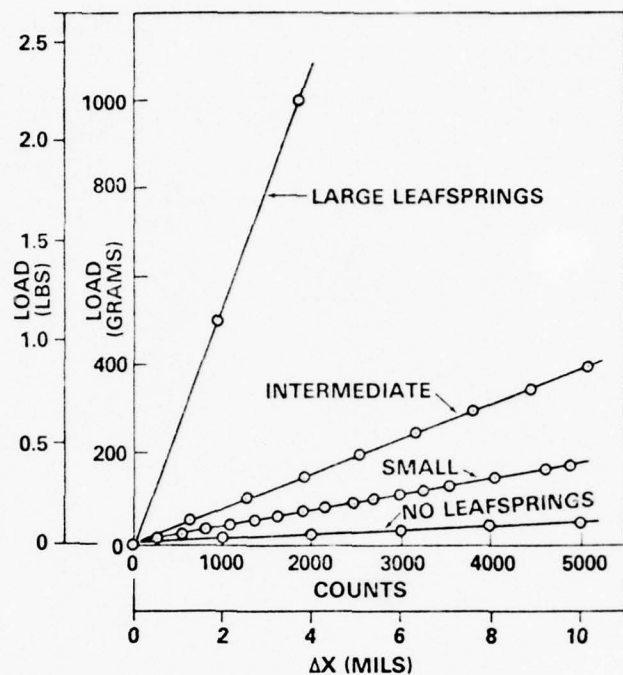


FIGURE 9 LOAD CALIBRATIONS

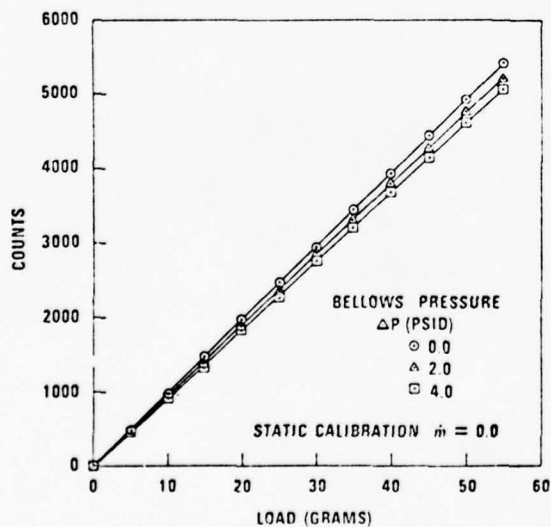


FIGURE 10 EFFECT OF BELLWS PRESSURE ON LOAD CALIBRATION

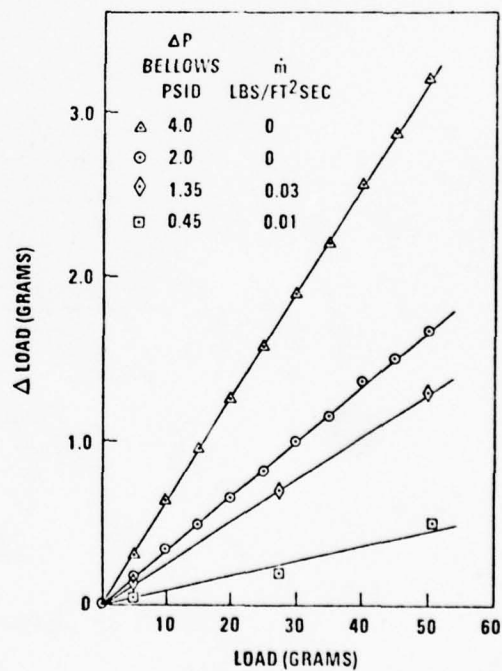


FIGURE 11 CALIBRATION SHIFT WITH GAS INJECTION

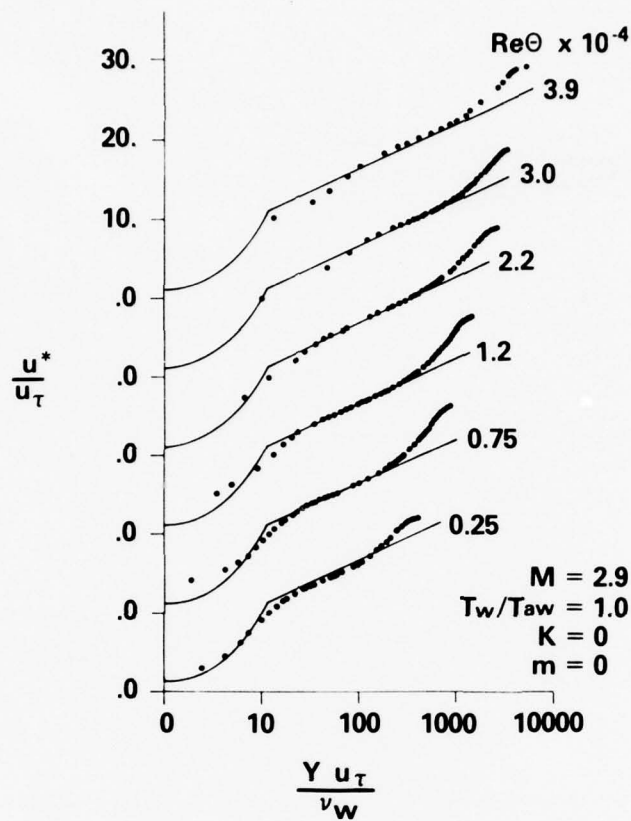


FIGURE 12 LAW-OF-THE-WALL VELOCITY PROFILES

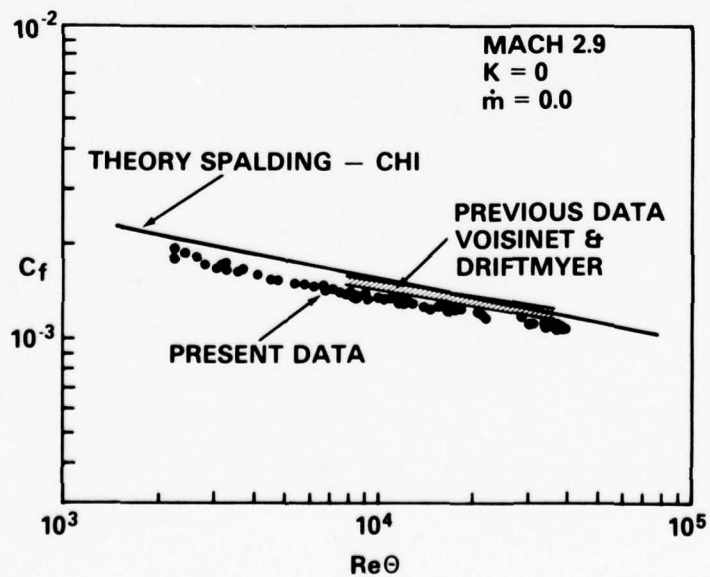
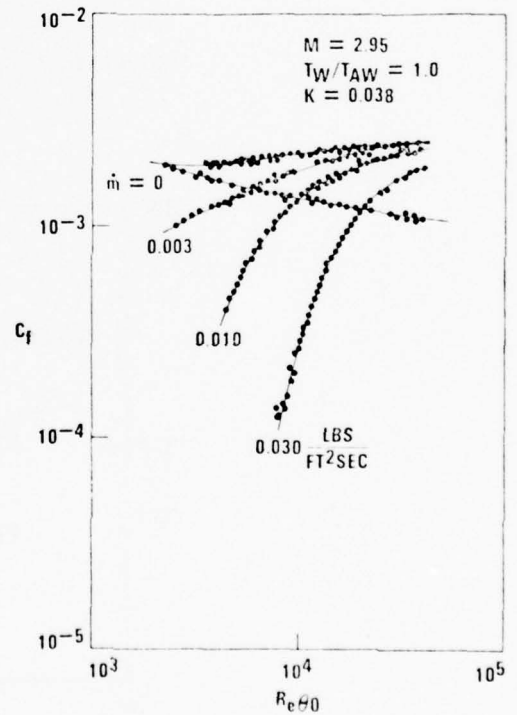
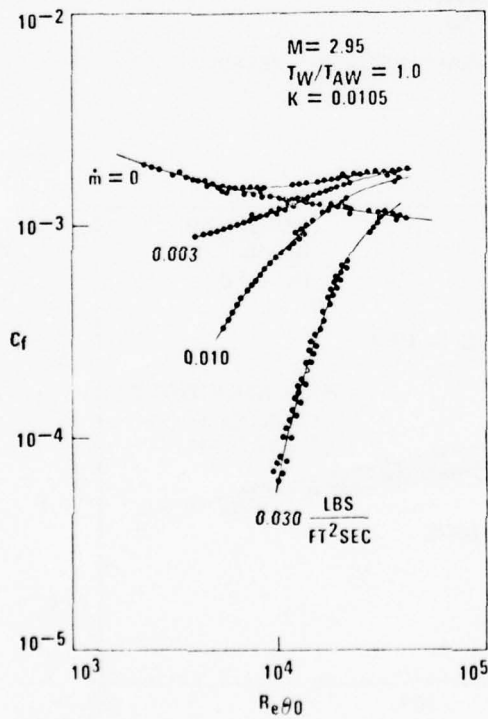
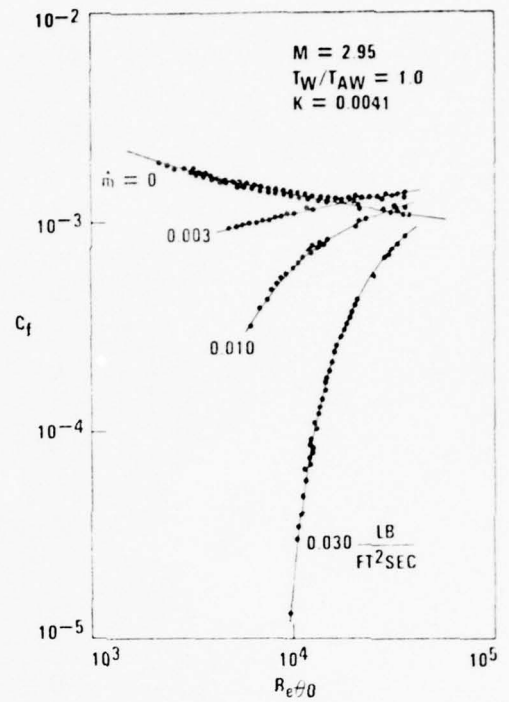
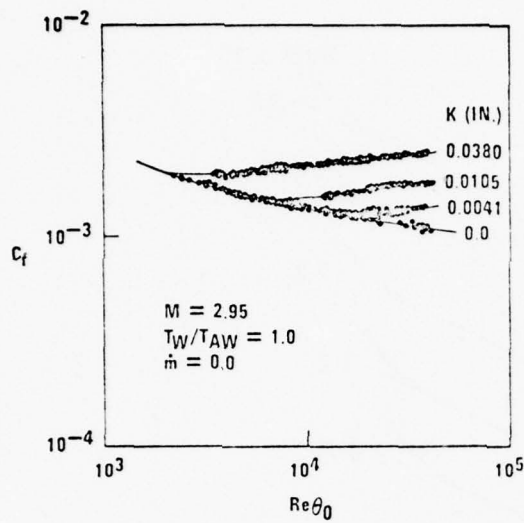


FIGURE 13 BASELINE SKIN-FRICTION DATA



FIGURES 14-17 SKIN-FRICTION VARIATION WITH ROUGHNESS AND MASS TRANSFER

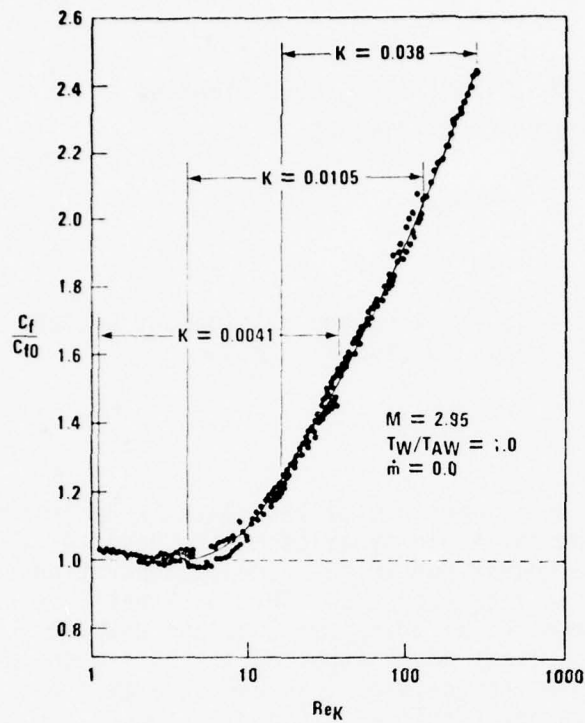
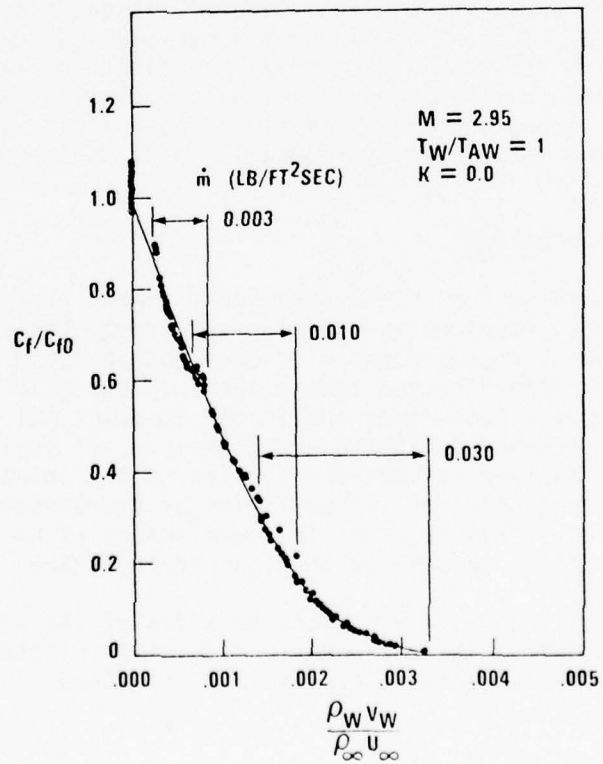


FIGURE 18 ROUGHNESS EFFECT ON SKIN FRICTION

FIGURE 19 MASS-TRANSFER EFFECT ON SKIN FRICTION



FURTHER ADVANCES IN NUMERICAL FLUID DYNAMICS
RESEARCH AT DTNSRDC

by

Joanna W. Schot

David W. Taylor Naval Ship Research and Development Center
Bethesda, Maryland 20084 U.S.A.

ABSTRACT

As reported at recent annual meetings of this Data Exchange Agreement, the research program in numerical fluid dynamics at the David W. Taylor Naval Ship Research and Development Center has been concentrating on incompressible viscous and inviscid flow problems. This work has been consistently directed toward the development of numerical methods and computer techniques applicable to problems of practical naval importance. During the past year several advances pertaining to the goals of this DEA were made and will be discussed in this paper. One new result is a contribution to the basic understanding and complete physical explanation of the phenomenon of auto-rotation of plates and airfoils obtained by means of numerical solutions of the full Navier-Stokes equations of viscous flow. Another item of progress is the development of improved numerical mesh generators for handling arbitrary flow-field geometries for finite-difference or finite-element calculations in two and three spatial dimensions. In addition, discrete vortex methods have been developed to analyze hydrodynamic noise in a shear layer and to predict hydrodynamic loads on the sidewalls of surface effect ships.

I. Introduction

The Numerical Fluid Dynamics research program at the David W. Taylor Naval Ship Research and Development Center has concentrated mainly on the solution of incompressible viscous and inviscid exterior flow problems. This work has been directed toward the development of improved numerical methods and computer techniques applicable to practical problems of naval importance. The new schemes developed are therefore not just tested on simple problems but are further refined and applied to the solution of unsolved physical or engineering problems in the fields of hydrodynamics, aerodynamics, and acoustics. This requires the development of numerical methods for handling complex flows around bodies of arbitrary shape.

This report is a summary of a few of the advances made under this program during the past year. The items selected for inclusion are examples of the development and application of methods for solving problems of

fundamental and practical importance which pertain to the goals of this Data Exchange Agreement. One advancement is a significant contribution to the basic understanding of the physical phenomenon known as autorotation in air or water. Another is the development of an improved numerical technique for generating curvilinear coordinate grid systems which produce variable concentrations of grid points in irregularly shaped flow domains. A third is the application of discrete vortex methods to solve certain hydrodynamic and acoustic flow problems. These three distinct efforts are described in the following sections.

II. The Autorotation Phenomenon

A breakthrough in the problem of autorotation has been achieved as the culmination of several years of work on two-dimensional flow about thin elliptic cylinders (plates) rotating in a parallel viscous flow. The computer program, ROTAPLATE, which solves these rotating plate problems is based on the full Navier-Stokes equations and was completely developed at DTNSRDC by Lugt and Ohring [1]. This program was discussed briefly at the DEA Meeting in 1976 [2] where the point was made that the capability of solving such a difficult time-dependent problem was due to the development of a very fast, direct Poisson equation solver. It was also stated that such a program is a powerful computational tool for investigating the phenomenon of autorotation. Lugt recently completed this investigation and has prepared a comprehensive report on the subject [3]. The following paragraphs highlight the essential facts he has elucidated and summarize his explanation of the phenomenon of autorotation.

The concept of autorotation is restricted in this investigation to the induced motion of bodies which requires an initial rotation of the body in the flow to cause self-sustained spinning. This is the most widely accepted definition in fluid dynamics. Thus, plates with fixed or freely moving axes of rotation and systems of plates such as cruciform fins are considered to be autorotating under appropriate conditions. On the other hand, it must be noted that rotating mechanisms such as windmills, anemometers, and water wheels are not considered to be autorotating because these bodies are geometrically shaped so that even under static conditions a torque is present which initiates sustained rotation when the body is released in a parallel flow. For bodies which do autorotate, the axis of rotation may be parallel or normal to the flow. The parallel case is important in the autorotation of aircraft ("spin"). The other, perpendicular, case is relevant to the control of finned projectiles and rockets, which are known to autorotate unpredictably at high angles of attack, and to the dispersion of bomblets. In either case, the axis of rotation does not need to be exactly parallel or normal to the flow, and one case may pass over into the other.

The case analyzed in detail by Lugt is for plates autorotating about a fixed axis of symmetry normal to the oncoming flow. This type of autorotation cannot be explained by quasi-steady theory (the average torque is

always zero) or boundary-layer theory (the vortex-shedding process cannot be simulated) or by discrete vortex models (these are inaccurate when the vortex sheet is close to the body). Experimental methods are difficult and relatively few experiments have been performed, but it has been established with experiments involving endplates that three-dimensional effects are not essential for autorotation. Moreover, it has also been demonstrated by E.H. Smith [4] that autorotation can occur at Reynolds numbers as low as 100 and that the angular velocity Ω of the rotating plate can be almost constant for a sufficiently large moment of inertia. Thus Lugt was led to the study of autorotation by constructing solutions of the time-dependent full Navier-Stokes equations for a thin elliptic cylinder rotating about a fixed axis normal to a parallel flow. He analyzed results for Reynolds numbers 200 and 400 and for different Rossby numbers (the ratio of translational to rotational speed of the plate).

The fact that Ω can be chosen to be constant facilitates the numerical treatment of the problem considerably. Otherwise, since an initial impulse is necessary to trigger autorotation, it would take many trial and error computer runs before real autorotation could be achieved. But by experimenting with different constant values of Ω , no matter whether autorotation occurs or not, the range of self-sustained spinning can be determined by computing the average torque. Figure 1 shows the relation between average torque (average moment coefficient \bar{C}_M) and the dimensionless angular velocity Ω . If a torque is needed to drive the body, the body will slow down without it. (See portions of the curve with positive \bar{C}_M values.) If, however, the torque has a braking, or slowing down effect (shaded area in Figure 1), then if that torque is removed, the body would rotate faster and faster until a point of stable autorotation is reached (point A in Figure 1).

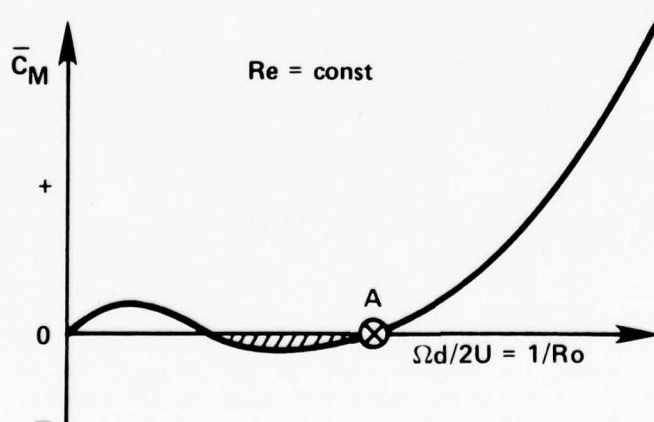


Figure 1. Average moment coefficient \bar{C}_M plotted against $\Omega d/2U$. In the shaded area the body autorotates but increases its rotation until the point A is reached. This is the condition for stable, (in the average) steady-state autorotation.

To answer the question, "What causes autorotation?", a careful analysis of the role of torque must be made. For a rotating plate, one must distinguish between a period in which the torque supports rotation and a period in which it retards rotation. The "supporting" period occurs when the angle of attack α increases from 0 to $\pi/2$, and the "retarding" period occurs where α increases from $\pi/2$ to π , approximately. Figure 2 shows a time sequence of computer-generated flow patterns during one cycle (half revolution). The Reynolds number is 200 and the Rossby number Ro is 4. The supporting period is shown in the top three positions, and the retarding period is covered in the lower three views. Based on his computed results, Lugt cites the following conditions and conclusions governing the autorotation phenomenon:

- 1) The moment of inertia must be sufficiently large to overcome the opposing torque in the retarding period. This "fly-wheel" effect has been taken care of by the constant Ω model.
- 2) Body rotation and vortex shedding must be synchronous. If the plate rotates too fast or too slowly compared to the frequency of vortex shedding, the asynchronous vortex shedding causes rotational (roll) damping.
- 3) The reduction of torque in the retarding period is essential for autorotation. This torque is reduced through the prolonged development of the boundary layer in the front of the plate. Additional assistance for autorotation is provided through boundary layer hysteresis in the supporting period; that is, the delaying of flow separation caused by an acceleration of the boundary layer.
- 4) Sufficiently strong vorticity at the edges of the plate must be present.
- 5) The combination of all these conditions induces autorotation.

A further conclusion reached by Lugt is that the above conditions are also valid for high Reynolds numbers. Not only are the flow patterns quite similar, but the lift and drag forces do not differ significantly between low and high Reynolds number values, as shown by the comparisons with experimental data given in Figure 3. Thus, this study clearly demonstrates that under certain conditions results computed using the Navier-Stokes equations at low Reynolds numbers can provide information for flows at higher Reynolds numbers. This is particularly true for flows involving vortex shedding.

III. Numerical Curvilinear Coordinate Systems

The increasing need for more accurate solutions of fluid flow problems involving arbitrarily shaped bodies and free boundaries which change with time has spurred on the work in numerically-generated boundary-fitted curvilinear coordinate systems for finite-difference or finite-element calculations. As reported at the last DEA meeting [5], these flexible

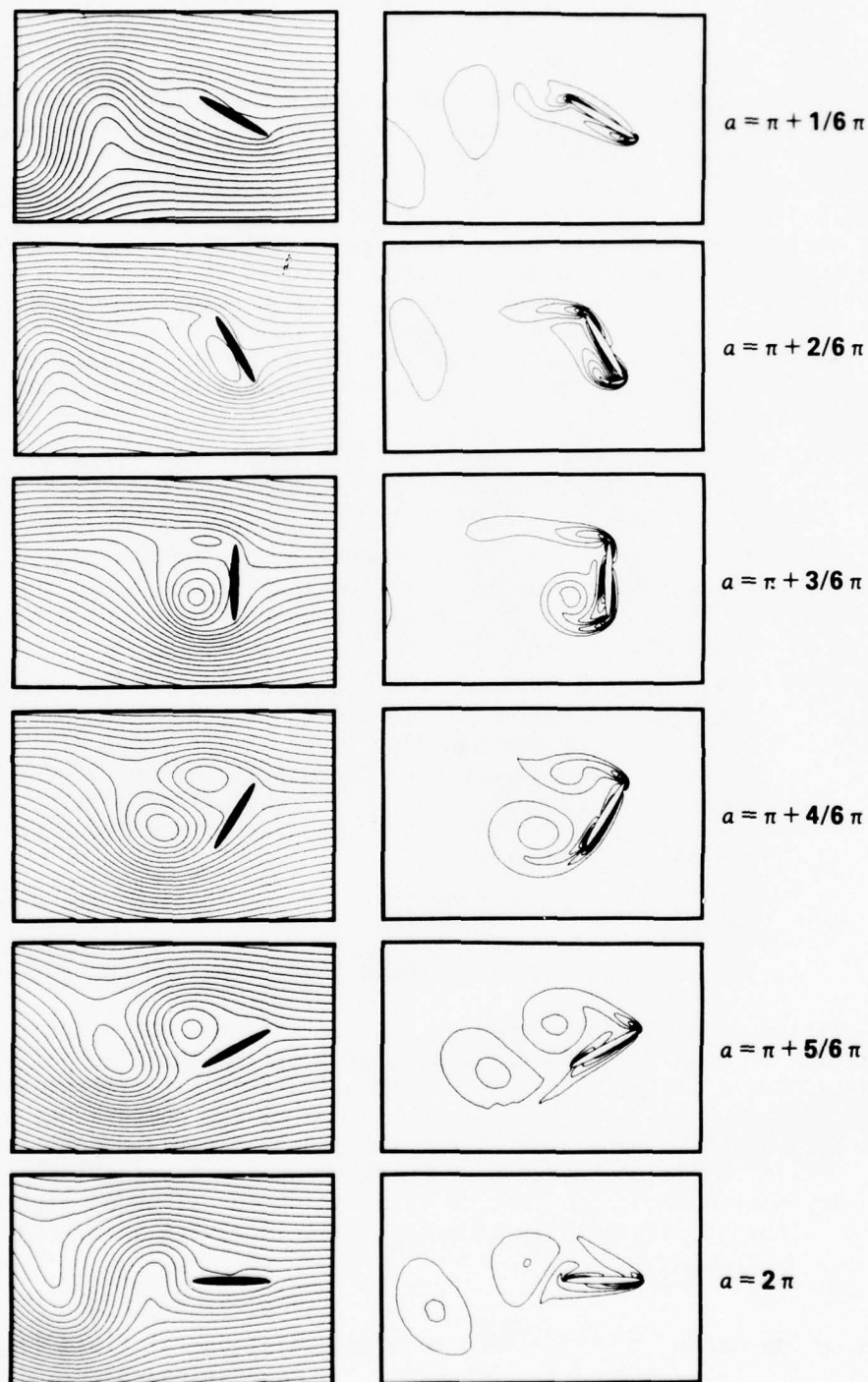


Figure 2. Time sequence of streamlines and equi-vorticity lines for a rotating plate in a parallel flow. $Ro = 4$, $Re = 200$, and $\alpha_0 = 0^\circ$. The streamlines are computed in a frame which is fixed to the body with regard to translation but which is fixed in space with regard to rotation. The fluid flow comes from the right.

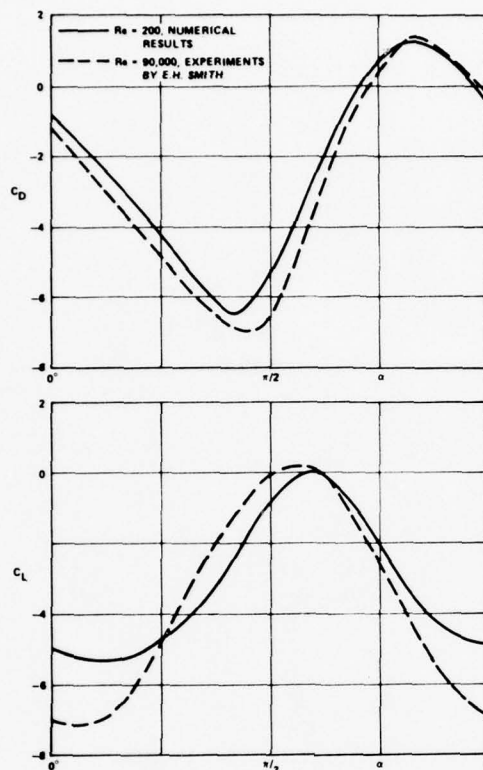


Figure 3. Comparison of numerical results at $Re = 200$ with experiments at $Re = 90,000$ for drag and lift coefficients during one half revolution of the plate.

coordinate systems are generated by numerically solving a system of elliptic partial differential equations whose solutions are the desired coordinate curves. The use of these equations is suggested by the extremum principle for elliptic boundary value problems. The grid-generating system is set up with the transformed coordinate (ξ, η) as the dependent variables and the original physical coordinates (x, y) as the independent variables. To provide for greater generality in handling arbitrary flow domains, the inner and outer boundaries of the physical flow domain may be specified to correspond to the minimum and maximum coordinate boundary values in segments of the transformed plane. The right-hand terms of the elliptic system can be selected to vary the density of the coordinate lines as desired for a given problem.

A recent development in this area of research is illustrated by the grid system computed for the case of a cylinder translating below a free surface, as shown in Figure 4. This work is an extension of the results obtained by Haussling and Coleman [6] to handle nonlinear free surface conditions. They used the following system of elliptic equations to generate these grids:

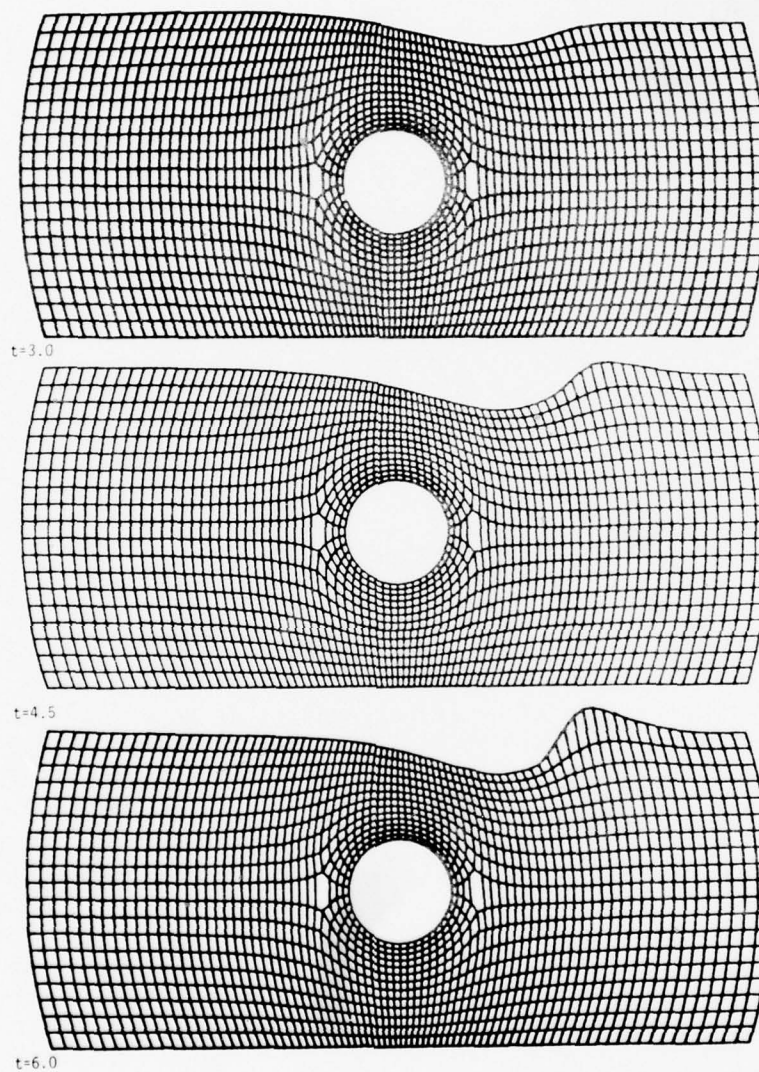


Figure 4. Time-dependent coordinate system for a cylinder translating below a free surface.

$$\xi_{xx} + \xi_{yy} = \sum_{i=1}^N C_i \exp(-\sqrt{(\xi - \xi_i)^2 + (\eta - \eta_i)^2})$$

$$\eta_{xx} + \eta_{yy} = \sum_{i=1}^N D_i \exp(-\sqrt{(\xi - \xi_i)^2 + (\eta - \eta_i)^2})$$

where C_i and D_i are parameters which control the attraction or dispersion of ξ and η lines with respect to the N specified points (ξ_i, η_i) . The boundary conditions are the coordinate values of mesh points on the boundaries of the flow field.

Coleman [7] has further extended this work to handle three-dimensional regions involving arbitrary bodies in a free surface. An early example of a grid computed for a thin ship is shown in Figure 5. Different methods for representing such three-dimensional grids for visual checking are under development. For actual flow computations, a much finer grid would be generated. For nonlinear free surface problems, once a technique has been developed for generating a curvilinear grid system, the new grids for each time step are computed simultaneously with the solution of the flow equations.

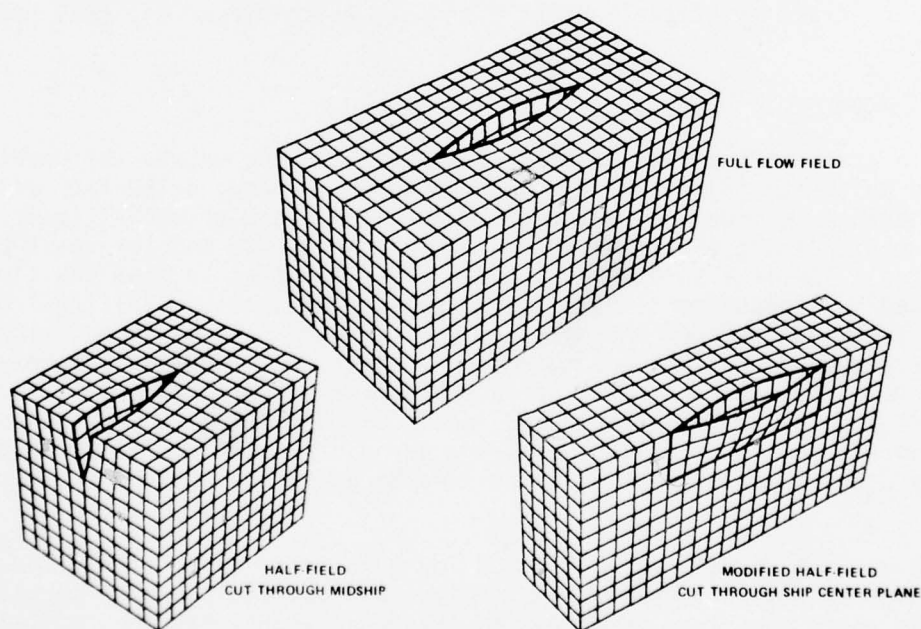


Figure 5. Views of a ship hull embedded in a body-fitted mesh.

IV. Discrete Vortex Methods

1. Hydrodynamic Noise

The use of discrete vortex methods for simulating fluid flows at high Reynolds numbers has received increased attention in recent years. Vortex lattice schemes have been used extensively for aerodynamic flow calculations by NASA researchers and other investigators. There is also an active interest in the application of discrete vortex methods in the field of acoustics. To determine the effectiveness of these methods for predicting hydrodynamic noise, a discrete vortex simulation of a two-dimensional shear layer was developed by Grabowski and Telste [8]. They represented the shear layer by a large number of vortices, namely 256 per period of length λ , to offset the inadequacies observed in models employing very few vortices. The shear layer is created by two flow streams of opposite velocity, $+U$ and $-U$, and is assumed to have been disturbed by some external force. The computed evolution of the rolling up of the shear layer is shown in the time sequence displayed in Figure 6, where time is increasing from the top to the bottom of the page. Note that the shear layer gradually rolls up into two large vortices before coalescing into a turbulent configuration. Although the flow pattern of the large scale behavior of the mixing layer is effectively simulated, the model is considered inadequate for computing the hydrodynamic sound because the point vortices, when they become too close together, twist around and generate artificial acoustic signals which exceed the real hydrodynamic noise.

2. Hydrodynamic Loads

In a separate effort, a discrete vortex lattice method was developed by Tai and Whitehead [9] for predicting hydrodynamic loads on surface effect ships. The ship is modelled by two distinct sidewalls with mutual interference. It is assumed that the effect of the air cushion pressure and the seals can be neglected. The free surface is assumed rigid and flat so that the flow can be simulated by a bound vortex sheet and free vortex sheets emanating from the sides and trailing edges of the wall. There is a pressure difference across a bound vortex sheet but not across a free vortex sheet. The normal component of velocity vanishes on either a bound or free vortex sheet. Since the flow is assumed to be inviscid and incompressible, the velocity generated by a vortex segment is determined by using the Biot-Savart law. The force induced by a bound vortex segment is calculated using the Kutta-Joukowski theory.

Numerical results were obtained for thin rectangular single and double sidewalls with different aspect ratios and yaw angles. The physical plane under water contained 40 panels in the bound vortex lattice, a single tip vortex core of 15 segments, and four wake vortex lines of 5 segments each. The results show that the method predicts higher forces in low aspect ratio cases than do other methods. The authors attribute this to the use of a



Figure 6. Time sequence of the large scale evolution of a shear layer represented by 256 discrete vortices per longitudinal period (cycle).

single tip vortex model to represent a sheet of vorticity. The dominance of sidewall edge effects reduce accuracy at low aspect ratios, but accuracy improves with increasing aspect ratios. For double sidewalls, the effect of wall interference becomes significant with increases in length-to-beam ratio, or area aspect ratio, or yaw angle.

References

1. Lugt, H.J. and S. Ohring, "Rotating elliptic cylinders in a viscous fluid at rest or in a parallel stream," J. Fluid Mech. 79 (1977), 127-156.
2. Schot, J.W., "Progress in Numerical Fluid Dynamics at DTNSRDC," Proc. Fifth U.S. Air Force/Federal Republic of Germany DEA Meeting on Viscous and Interacting Flows, Wright-Patterson Air Force Base, April 1976, Technical Report AFFDL-TR-77-61, July 1977.
3. Lugt, H.J., "Autorotation of Plates," David W. Taylor Naval Ship Research and Development Center Report (to appear).
4. Smith, E.H., "Autorotating wings: an experimental investigation," J. Fluid Mech. 50 (1971), 513.
5. Schot, J.W., "Numerical Treatment of Arbitrarily-Shaped Regions in Fluid Dynamics," Proc. U.S.-Federal Republic of Germany DEA Meeting on Viscous and Interacting Flow Field Effects, DFVLR, Göttingen, April 1977. Technical Report BMVg-FBWT 77-20, Part 1, p. 71-81.
6. Haussling, H.J. and R.M. Coleman, "Finite-Difference Computations Using Boundary-Fitted Coordinates for Free-Surface Potential Flows Generated by Submerged Bodies," presented at the Second Int'l. Conf. on Numerical Ship Hydrodynamics, Univ. of California, Berkeley, September 1977.
7. Coleman, R.M., "Numerically Generated Boundary-Fitted Coordinate Systems for Arbitrary Three-Dimensional Regions," David W. Taylor Naval Ship Research and Development Center Report (to appear).
8. Grabowski, W.J. and J.G. Telste, "A Discrete Vortex Simulation of a Two-Dimensional Shear Layer with Prediction of the Hydrodynamic Noise," Computation, Mathematics, and Logistics Department Report CMLD-77-26, December 1977. (To appear also as a revised DTNSRDC Report.)
9. Tai, T.C. and R.E. Whitehead, "A Discrete Vortex Method for Predicting Hydrodynamic Loads on Sidewalls of Surface Effect Ships," David W. Taylor Naval Ship Research and Development Center Report 77-0035, September 1977.

AN INVESTIGATION OF VERY SMALL SEPARATION
BUBBLES IN LAMINAR AND TURBULENT
BOUNDARY LAYERS

K. GERSTEN
RUHR UNIVERSITY
BOCHUM
WEST GERMANY

J. F. GROSS
UNIVERSITY OF ARIZONA
TUCSON, ARIZONA
U.S.A.

1. Introduction

Separation bubbles in a boundary layer are considered to be very small when the height of the bubble is small compared with the local boundary layer thickness. These separation bubbles are consequently found in the interior of the boundary layer in the neighborhood of the wall. The behavior of such small separation bubbles has not been studied in contrast to the extensive work done on separated regions which are relatively large compared to the boundary layer thickness. The separation region behind a circular cylinder is an example of the latter case for large separation bubbles.

The region where very small bubbles are formed is one of great practical significance. In particular, these bubbles occur near protuberant excrescences that exist on the lifting surfaces of aircraft. Consequently, they play a key role in the increase of surface friction due to these excrescences. Particular attention was paid to the importance of research in the effect of roughness and generalized excrescences immersed in turbulent boundary layers on the determination of the aircraft resistance at the AGARD Specialists Meeting in 1973, [1]

A study of very small separation bubbles is of fundamental importance because it is a limiting case of the more general problem of flows with finite

separation regions and can hence provide important insights to the more general problem.

Figure 1 shows the relationship of the limiting case of small separation bubbles to the general case of a turbulent boundary layer with separation on a backward facing step. The flow along a flat plate with a backward facing step is characterized by two Reynold's numbers Re_H and Re_L whose characteristic dimensions are the height, H , of the backward facing step and the distance, L_0 , of the step from the leading edge, respectively. The curve in Figure 1 separates the laminar from the turbulent separation regions, i.e., in the region to the right of the curve are those flows for which the separated boundary layer is turbulent. Here it is possible to identify two limiting cases. In region A, the boundary layer thickness is small compared with height of the step. In this case, it has been shown theoretically [2] that the two-parameter problem reduces to a one-parameter problem.

The present work is concerned with the region B and it will be shown that here also the two-parameter characterization can be reduced to a single parameter problem. The Figure also shows the region outlined by the dashed line in which measurements have been taken by other authors. Measurements taken at the Ruhr University are included in this region. The measurements were taken by Dipl.-Ing. P. Wauschkuhn at the Ruhr University in Bochum. The explicit purpose of these experiments was to obtain data on small turbulent separation bubbles.

The following work treats the flow along a flat plate in which the surface is distorted by an indentation or a step. The surface distortions result in a disturbance of the boundary layer and possibly a local separation. It will be shown later that an important distinction has to be made between a finite surface distortion such as indentation (see Figure 2a) or an infinite distortion such as a backward-facing step (see Figure 2b).

The present work is concerned primarily with the case of the backward facing step as a typical example for a surface disturbance or excrescence. Although the turbulent boundary layer has the greatest practical significance, the laminar flow case is also treated because of its fundamental importance and for completeness.

2. Mathematical Formulation

Consider the surface of the excrescence to be given by a function $HF(x)$ (See Figure 2). $F(x)$ is a dimensionless and generally positive function. In the case of the step, $F(x)$ is a step function with a unitstep. All distances are nondimensionalized by a characteristic length L which will be specified later but has straightforward relationship to L_0 , the distance to the leading edge. The flow velocities are non-dimensionalized

by the external flow velocity, \bar{U}_∞ , and the pressure difference with respect to the undisturbed pressure is non-dimensionalized by half the stagnation pressure, ρU_∞^2 . For turbulent flow, the Reynolds stresses are non-dimensionalized by the fictitious wall shear stress, τ_{wo} , which would obtain if no surface distortion occurred.

The following system of equations describe the flow behavior if the assumptions of stationary, two-dimensional and incompressible flow are involved.

$$u \frac{\partial u}{\partial x} + v \frac{\partial u}{\partial y} = - \frac{\partial p}{\partial x} + \frac{1}{Re} \left(\frac{\partial^2 u}{\partial x^2} + \frac{\partial^2 u}{\partial y^2} \right) + \frac{C_{fo}}{2} \left(\frac{\partial \sigma_x}{\partial x} + \frac{\partial \tau_{xy}}{\partial y} \right) \quad (1)$$

$$u \frac{\partial v}{\partial x} + v \frac{\partial v}{\partial y} = - \frac{\partial p}{\partial y} + \frac{1}{Re} \left(\frac{\partial^2 v}{\partial x^2} + \frac{\partial^2 v}{\partial y^2} \right) + \frac{C_{fo}}{2} \left(\frac{\partial \tau_{xy}}{\partial x} + \frac{\partial \sigma_y}{\partial y} \right) \quad (2)$$

$$\frac{\partial u}{\partial x} + \frac{\partial v}{\partial y} = 0 \quad (3)$$

The boundary conditions for this system are given by:

$$\begin{aligned} x = -\infty: & \quad u = u_B(y) \\ y = -\frac{H}{L} F(x): & \quad u = 0, \quad v = 0 \\ y \rightarrow \infty: & \quad u = 1 \end{aligned} \quad (4)$$

Insertion of Eqn. (5) in Eqs. (1)-(3) and collection of terms of similar order in H/L yields a system of equations for the perturbed flow:

$$u_B \frac{\partial u'}{\partial x} + v' \frac{\partial u_B}{\partial y} = - \frac{\partial p'}{\partial x} + \frac{1}{Re} \left(\frac{\partial^2 u'}{\partial x^2} + \frac{\partial^2 u'}{\partial y^2} \right) + \frac{C_{f0}}{2} \left(\frac{\partial \sigma_{x'}}{\partial x} + \frac{\partial \tau'_{xy}}{\partial y} \right) \quad (6)$$

$$u_B \frac{\partial u'}{\partial x} = - \frac{\partial p'}{\partial y} + \frac{1}{Re} \left(\frac{\partial^2 v'}{\partial x^2} + \frac{\partial^2 v'}{\partial y^2} \right) + \frac{C_{f0}}{2} \left(\frac{\partial \tau'_{xy}}{\partial x} + \frac{\partial \sigma_{y'}}{\partial y} \right) \quad (7)$$

$$\frac{\partial u'}{\partial x} + \frac{\partial v'}{\partial y} = 0 \quad (8)$$

The boundary conditions are:

$$\begin{aligned} x = -\infty: & \quad u' = 0 \\ y = 0: & \quad u' = \left(\frac{du_B}{dy} \right)_w F(x), \quad v' = 0 \\ y \rightarrow \infty: & \quad u' = 0 \end{aligned} \quad (9)$$

The condition $x = -\infty$ designates a location sufficiently upstream of the surface distortion so that an undisturbed flatplate boundary layer profile $u_B(y)$ will obtain. In addition to the velocity profile $u_B(y)$ and the surface distortion function $F(x)$, the following dimensionless parameters characterize the flow problem:

- | | |
|-------------------------------|---|
| a) relative distortion height | H/L |
| b) Reynolds Number | $Re = U_\infty L/\nu$ |
| or | |
| c) Skin Friction coefficient | $C_{f_0} = \frac{2\tau_w}{\rho U_\infty^2}$ |

An explicit relationship exists between Re and C_{f_0} . Because only small values of H/L are considered, a small perturbation solution is employed. The work of Lighthill (3) and Inger (4-7) is followed here. The solutions of the dependent variables are assumed to be expansions as follows:

$$\begin{aligned}
 u &= u_B(y) + \frac{H}{L} u'(x, y) + \dots \\
 v &= \frac{H}{L} v'(x, y) + \dots \\
 p &= \frac{H}{L} p'(x, y) + \dots \\
 \tau_{xy} &= \tau_{xyB}(y) + \frac{H}{L} \tau'_{xy}(x, y) + \dots \\
 \sigma_x &= \frac{H}{L} \sigma'_x(x, y) + \dots \\
 \sigma_y &= \frac{H}{L} \sigma'_y(x, y) + \dots
 \end{aligned} \tag{5}$$

Of particular importance is the new boundary condition for u' on the boundary $y = 0$. Instead of the no-slip condition, i.e., $u = 0$ for $y = -HF/L$, the velocity component u' assures a finite, generally positive value along $y = 0$. This condition results directly from the Taylor Series expansion for u :

$$u(y) = u(0) + \left(\frac{du}{dy}\right)_{y=0} y + \dots \quad (10)$$

$$u\left(-\frac{HF}{L}\right) = u_B(0) + \frac{H}{L} u'(0) - \left(\frac{du_B}{dy}\right)_{y=0} \frac{H}{L} F(x) + \dots = 0 \quad (11)$$

Because $u_B(0) = 0$, the boundary condition given above is obtained.

The flow along a wall with a small contour change is equivalent to the flow along an undisturbed wall which is moving in the flow direction in the neighborhood of the contour disturbance.

Figure 3 demonstrates the equivalence of the two flows. The velocity profile of the undisturbed flow satisfies the noslip condition for $x < 0$, but not on the wall downstream of the step. There it can be seen that a negative velocity exists at the level of the step height. This velocity component is compensated for by the perturbed flow. The fact that the velocity is compensated on the $y = 0$ line rather than on the wall constitutes an error that is of higher order and can be neglected.

In the formulation of Eqns. (6)-(9), assumption was made that the original velocity profile was not changed in the region of the wall disturbance. The disturbance due to the backwardfacing step results in a new asymptotic velocity profile (independent of x) that must be achieved before significant change in the original velocity profile on the wall.

This requires that certain assumptions regarding the length of the disturbance (length of the distortion) be made which are different for laminar and turbulent flows. The coordinate stretching will be discussed in detail later. The height of the distortion or step H is clearly also dependent on this condition. The basis for a perturbation analysis depends on the fact that both the ratio H/L_0 and the local variation in the contour of the wall distortion be very small. In principle, a perturbation analysis is not valid for the case of a backwardfacing step. Either the corner must be smoothed out or left out of the calculation because a perturbation analysis yields a singularity at the edge of the step.

3. The Basic Flow

Both laminar and turbulent flows will be treated simultaneously in the following section. The basic equations will be transformed to a coordinate system referred to the boundary layer thickness δ_0 . In this coordinate system, the velocity profile $u_B(y/\delta_0)$ of the basic flow is given.

The velocity profile is different for laminar and turbulent flows.

In the neighborhood of the wall, the profile can be replaced approximately by its tangent as follows:

$$u_B(\bar{y}) = u_{\tau_0}^2 \delta_0 \operatorname{Re} \bar{y} \quad \bar{y} \ll 1. \quad (12)$$

where

$$u_{\tau_0} = \sqrt{\frac{C_{f_0}}{2}} \quad (13)$$

represents the friction velocity of the basic flow.

The equation set (6)-(9) are recast using the following coordinate transformation:

$$\bar{x} = \frac{x}{\delta_0}, \quad \bar{y} = \frac{y}{\delta_0} \quad (14)$$

Distances in this coordinate system are then of the order of the boundary layer thickness.

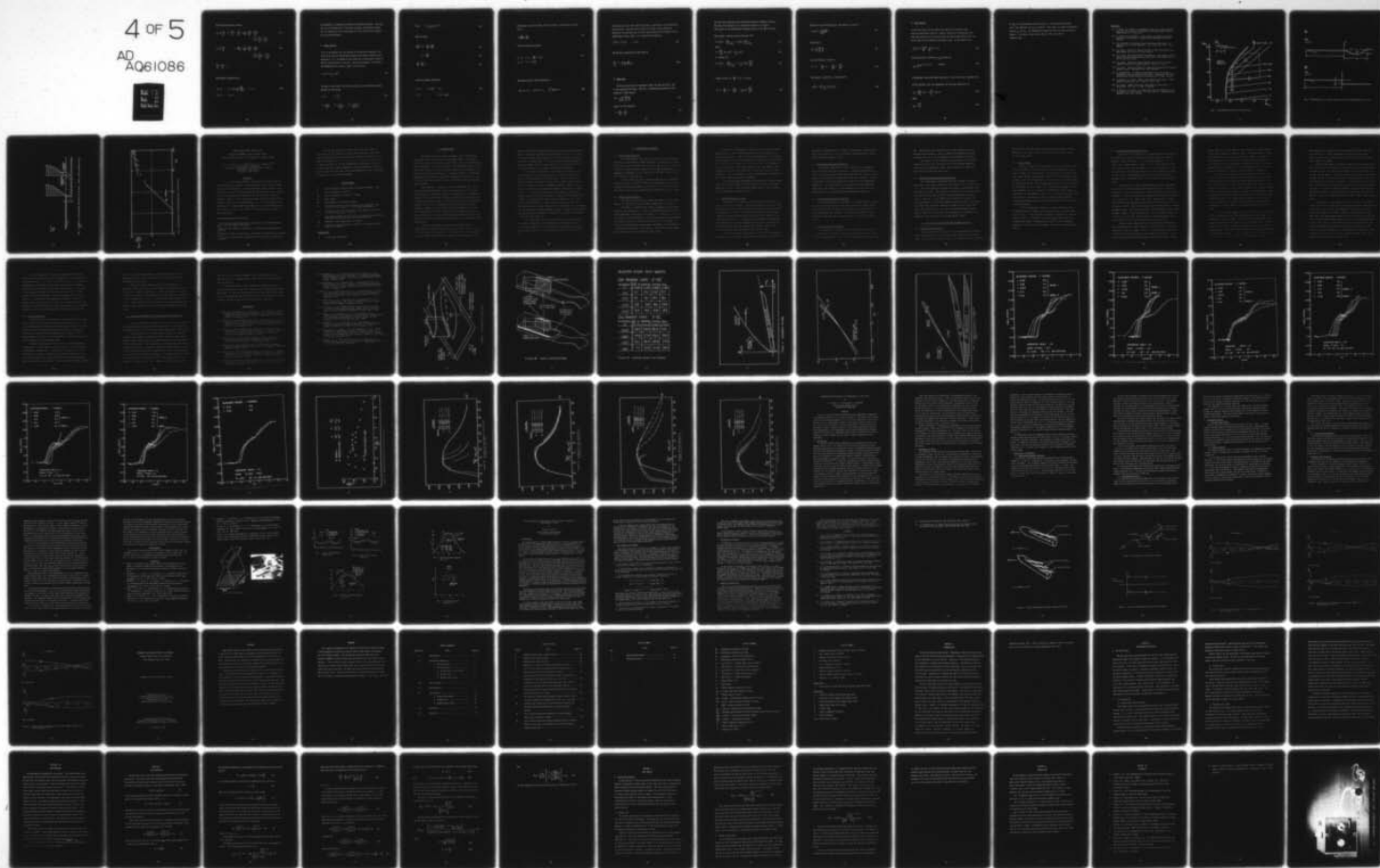
AD-A061 086

AIR FORCE FLIGHT DYNAMICS LAB WRIGHT-PATTERSON AFB OHIO F/G 20/4
BOUNDARY LAYER EFFECTS-PROCEEDINGS OF THE 7TH U. S. AIR FORCE/F--ETC(U)
SEP 78 A W FIORE MWDDEA-AF-75-6-7440
AFFDL-TR-78-111 NL

UNCLASSIFIED

4 OF 5

AD
A061086



The following equations result:

$$u_B(\bar{y}) \frac{\partial u'}{\partial \bar{x}} + v' \frac{du_B}{d\bar{y}} = - \frac{\partial p'}{\partial \bar{x}} + \frac{1}{\delta_o Re} \left(\frac{\partial^2 u'}{\partial \bar{x}^2} + \frac{\partial^2 u'}{\partial \bar{y}^2} \right) + \frac{C_{f_o}}{2} \left(\frac{\partial \sigma'}{\partial \bar{x}} + \frac{\partial \tau'_{xy}}{\partial \bar{y}} \right) \quad (15)$$

$$u_B(\bar{y}) \frac{\partial v'}{\partial \bar{x}} = - \frac{\partial p'}{\partial \bar{y}} + \frac{1}{\delta_o Re} \left(\frac{\partial^2 v'}{\partial \bar{x}^2} + \frac{\partial^2 v'}{\partial \bar{y}^2} \right) + \frac{C_{f_o}}{2} \left(\frac{\partial \tau'_{xy}}{\partial \bar{x}} + \frac{\partial \sigma'}{\partial \bar{y}} \right) \quad (16)$$

$$\frac{\partial u'}{\partial \bar{x}} + \frac{\partial v'}{\partial \bar{y}} = 0 \quad (17)$$

The boundary conditions are:

$$\bar{y} = 0: \quad u' = F(x) \frac{1}{\delta_o} \left(\frac{du_B}{d\bar{y}} \right), \quad v' = 0 \quad (18)$$

$$\bar{y} \rightarrow \infty: \quad u' = 0$$

No information is necessary to describe the Reynolds stresses. The outer flow is frictionless and, in the inner solution, the Reynolds stresses are also negligible if the step height is of the order of the thickness of the viscous sublayer.

4. Inner Solution

It is to be expected that the solution of the system of equations (15)-(17) for the case of large Reynolds numbers will exhibit boundary layer properties, i.e., the change in flow properties is much greater normal to the wall than parallel to the wall. Since the disturbance is limited to the neighborhood of the wall, $u_B(\bar{y})$ can be written:

$$u_B(\bar{y}) = u_{\tau_0}^2 \delta_0 \text{Re} \bar{y} \quad (19)$$

In order to solve Eqns. (15)-(17) near the wall, the following transformations are introduced:

$$\tilde{x} = \bar{x} \quad \tilde{y} = \frac{\bar{y}}{\hat{\epsilon}} \quad (20)$$

$$\tilde{u} = \frac{u'}{u_{\tau_0}^2 \text{Re}} \quad \tilde{v} = \frac{v'}{u_{\tau_0}^2 \text{Re} \hat{\epsilon}} \quad , \quad \tilde{p} = \frac{p'}{u_{\tau_0}^2 \delta_0 \text{Re} \hat{\epsilon}}$$

$$\text{where } \hat{\epsilon} = (u_{\tau_0} \delta_0 \text{Re})^{-2/3} . \quad (21)$$

Then we obtain

$$\tilde{y} \frac{\partial \tilde{u}}{\partial \tilde{x}} + \tilde{v} = - \frac{\partial \tilde{p}}{\partial \tilde{x}} + \frac{\partial^2 \tilde{u}}{\partial \tilde{y}^2} \quad (22)$$

$$0 = - \frac{\partial \tilde{p}}{\partial \tilde{y}} \quad (23)$$

$$\frac{\partial \tilde{u}}{\partial \tilde{x}} + \frac{\partial \tilde{v}}{\partial \tilde{y}} = 0 \quad (24)$$

with the boundary conditions

$$\tilde{y} = 0: \quad \tilde{u} = F(\tilde{x}), \quad \tilde{v} = 0 \quad (25)$$

$$\tilde{y} \rightarrow \infty \quad \tilde{v} = \tilde{y} - \tilde{y}_D(\tilde{x})$$

Eliminating \tilde{u} and \tilde{p} from Eqns. (22)-(24) yields a differential equation for \tilde{v} :

$$\tilde{y} \frac{\partial^3 \tilde{v}}{\partial \tilde{x} \partial \tilde{y}^2} = \frac{\partial^4 \tilde{v}}{\partial \tilde{y}^4} \quad (26)$$

with the boundary conditions

$$\begin{aligned} \tilde{y} = 0: \quad \tilde{v} &= 0, \quad \frac{\partial \tilde{v}}{\partial \tilde{y}} = -\delta(\tilde{x}) \\ \tilde{y} \rightarrow \infty: \quad \tilde{v} &= \tilde{y} - \tilde{y}_D(\tilde{x}) \end{aligned} \quad (27)$$

The delta function $\delta(\tilde{x})$ is defined by:

$$\delta(\tilde{x} = 0) = \infty, \quad \delta(\tilde{x} \neq 0) = 0, \quad \int_{-\infty}^{+\infty} \delta(\tilde{x}) d\tilde{x} = 1 \quad (28)$$

The solution of Eqn. (26) yields $\tilde{v}(\tilde{x}, \tilde{y})$ and, in particular, the displacement contour $\tilde{y}_D(\tilde{x})$. The outer flow behaves as if $\tilde{y}_D(\tilde{x})$ were a solid wall. Therefore, the matching with the outer flow is given by the boundary of the displacement contour $\tilde{y}_D(\tilde{x})$, i.e. along the line given by

$$\bar{y}_D(\bar{x}) = \hat{\epsilon} \tilde{y}_D(\tilde{x}) \quad \bar{x} = \tilde{x}. \quad (29)$$

The friction coefficient is then given by

$$\frac{C_f}{C_{f_0}} = 1 + \frac{H}{L} \frac{1}{\delta_0 \hat{\epsilon}} \left(\frac{\partial \tilde{u}}{\partial \tilde{y}} \right)_{\tilde{y}=0} \quad (30)$$

5. Outer Flow

If the viscous terms are neglected in Eqn. (15) and (16) and u' and v' are eliminated from Eqns. (15)-(17), a differential equation for the pressure p' (\bar{x}, \bar{y}) results

$$\Delta p' = \frac{2}{u_B(\bar{y})} \frac{du_B}{d\bar{y}} \frac{\partial p'}{\partial \bar{y}} \quad (31)$$

where Δ is the Laplacian

$$\Delta = \frac{\partial^2}{\partial \bar{x}^2} + \frac{\partial^2}{\partial \bar{y}^2} \quad (32)$$

The flow field associated with this system generally exhibits vorticity.

The outer flow behaves as if a solid wall existed at $\bar{y} = \bar{y}_D(\bar{x})$,

where $\bar{y}_D(\bar{x})$ is the displacement thickness contour of the inner solution.

The boundary condition follows from Eqn. (16)

$$\bar{y} = \bar{y}_D(\bar{x}): \left(\frac{\partial p'}{\partial \bar{y}} \right)_{\bar{y}=\bar{y}_D} = - u_B(\bar{y}_D) \left(\frac{\partial v'}{\partial \bar{x}} \right)_{\bar{y}=\bar{y}_D} \quad (33)$$

Since

$$v' = \frac{d\bar{y}_D}{d\bar{x}} \quad \text{and} \quad u_B(\bar{y}) \approx u_o^2 \delta_o \operatorname{Re} \bar{y} \quad (34)$$

it follows that

$$\bar{y} = \bar{y}_D(\bar{x}): \left(\frac{\partial p'}{\partial \bar{y}} \right)_{\bar{y}=\bar{y}_D} = - u_o^2 \delta_o \operatorname{Re} \bar{y}_D \frac{d^2 \bar{y}_D}{d\bar{x}^2} \quad (35)$$

A Taylor series for $\frac{\partial p'}{\partial \bar{y}}$ at $\bar{y} = 0$ yields

$$\bar{y} = 0: \frac{\partial p'}{\partial \bar{y}} = 0, \quad \frac{\partial^2 p'}{\partial \bar{y}^2} = - u_o^2 \delta_o \operatorname{Re} \frac{d^2 \bar{y}_D}{d\bar{x}^2} \quad (36)$$

Because of the scaling $\tilde{y}_D = \hat{y}_D / \epsilon$, the pressure is given by

$$\tilde{p}(\bar{x}, \bar{y}) = \frac{p'(\bar{x}, \bar{y})}{u_B^2 \delta_0 \text{Re} \epsilon} \quad (37)$$

This leads to

$$\Delta \tilde{p} = \frac{2}{u_B} \frac{du_B}{d\bar{y}} \frac{\partial \tilde{p}}{\partial \bar{y}} \quad (38)$$

with the boundary conditions

$$\bar{y} = 0: \quad \frac{\partial \tilde{p}}{\partial \bar{y}} = 0, \quad \frac{\partial^2 \tilde{p}}{\partial \bar{y}^2} = - \frac{d^2 \bar{y}_D}{d\bar{x}^2} \quad (39)$$

The pressure coefficient is then given by:

$$C_p(\bar{x}) = 2 \frac{H}{L} u_B^2 \delta_0 \text{Re} \epsilon \hat{p}(\bar{x}, 0) \quad (40)$$

6. Base Pressure

It has been shown that the results for laminar and turbulent flows have the same formal structure. However, because of the different boundary layer profile u_B in the outer flow, the base pressure $\tilde{p}(\tilde{x}, 0)$ will not be the same for the laminar and turbulent cases. In the laminar case:

$$u_{\tau 0}^2 \delta_0 \text{ Re} = \frac{0.332}{\sqrt{\text{Re}}} \cdot \frac{5}{\sqrt{\text{Re}}} \text{ Re} = 1.56 \quad (41)$$

The base pressure coefficient c_{pB} is given by:

$$C_{pB} = \frac{H}{L} \text{ Re}^{-1/6} \tilde{p}(0, 0) \quad (\text{laminar}) \quad (42)$$

A preliminary calculation shows that $\tilde{p}(0, 0) = 2.6$ in the case of laminar flow.

In the turbulent case, the expressions for the drag coefficient is:

$$C_{D\tau} = \frac{C_{pB}}{u_{\tau 0}^2} = \text{Re}_{\tau} \cdot 2 \frac{\delta_0 \hat{\epsilon}}{u_{\tau 0}} \cdot \tilde{p}(0, 0) \quad (43)$$

where

$$\text{Re}_{\tau} = \frac{u_{\tau 0}^* H}{\nu} \quad (44)$$

and $u_{\tau 0}^*$ is the dimensional friction velocity. For a prescribed boundary layer, the expression $\delta_o \hat{\varepsilon} / u_{\tau 0}$ is constant. This leads to a linear relationship between $c_{D\tau}$ and Re_{τ} . Our measurements demonstrate this linearity as shown in Figure 4. According to this result, $\tilde{p}(o,o) = 40$ in the case of turbulent flow.

References

- [1] L. Gaudet, K.G. Winter: Measurements of the drag of some characteristic aircraft excrescences immersed in turbulent boundary layers. AGARD-CP-124, 4-1 - 4-12, 1973.
- [2] K. Gersten, P. Wauschkuhn: On the theory for turbulent separated regions of finite length in subsonic flow. BMVg-FBWT 77-20, 1977, 145-159.
- [3] M.J. Lighthill: On boundary layers and upstream influence. II: Supersonic flow without separation. Proc. Royal Soc., A217, 1953, 478-507.
- [4] G.R. Inger: Supersonic laminar flow past a small rear-facing step. AIAA Journal Vol. 12, No. 6, 1974, 739-740.
- [5] G.R. Inger: Supersonic laminar base pressure, heat transfer, and upstream influence correlations for small steps. AIAA-Journal Vol. 12, No. 8, 1974, 1157-1158.
- [6] G.R. Inger: Supersonic laminar boundary layer flow past a small rearward-facing step including suction. VPI-E-72-17, 1972.
- [7] G.R. Inger: Upstream influence in interacting nonseparating turbulent boundary layers. BMVg-FBWT 77-20, 1977, 198-203.
- [8] E. Truckenbrodt: Die laminae Reibungsschicht an einer teilweise mitbewegten längsangeströmten ebene Platte. Abhandlungen der Braunschweigischen Wissenschaftlichen Gesellschaft Bd 4, 1952, 181-195.
- [9] K. Gersten, J.F. Gross: Higher order boundary layer theory. Fluid Dynamics Transactions, Vol 7, part II, 1974, 7-36.
- [10] F.T. Smith: Laminar flow over a small hump on a flat plate. J. Fluid Mech., 1973, Vol. 57, part 4, 803-824.
- [11] K. Gersten, J.F. Gross: A rational theory for the pressure drag of an airfoil in subsonic flow. A.W. Fiore (Editor). Technical Report AFFDL-TR-77-61, 1977, 365-381.

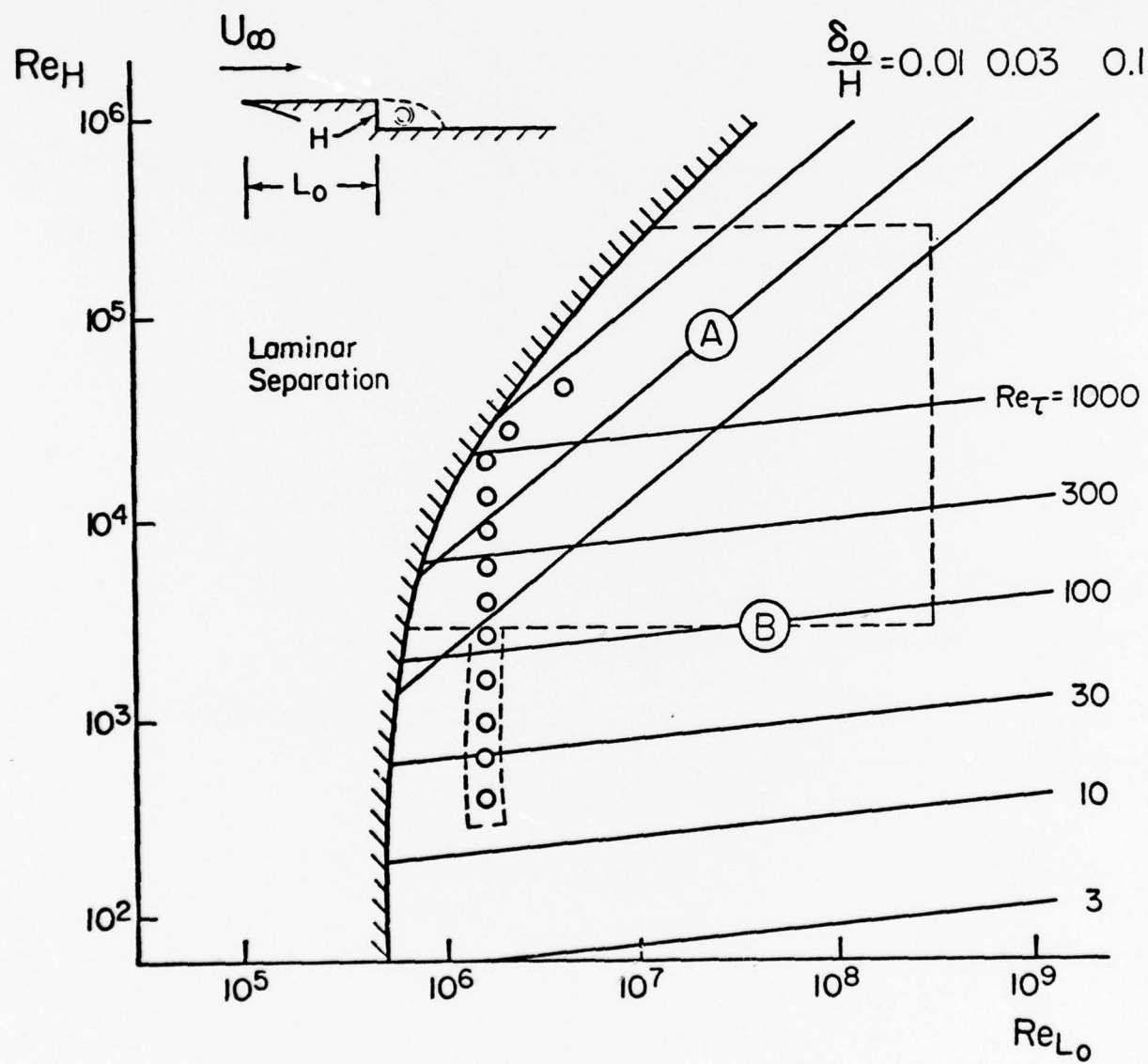


Fig. 1 Flow Regimes Characterized by Re_H and Re_{L_0} .

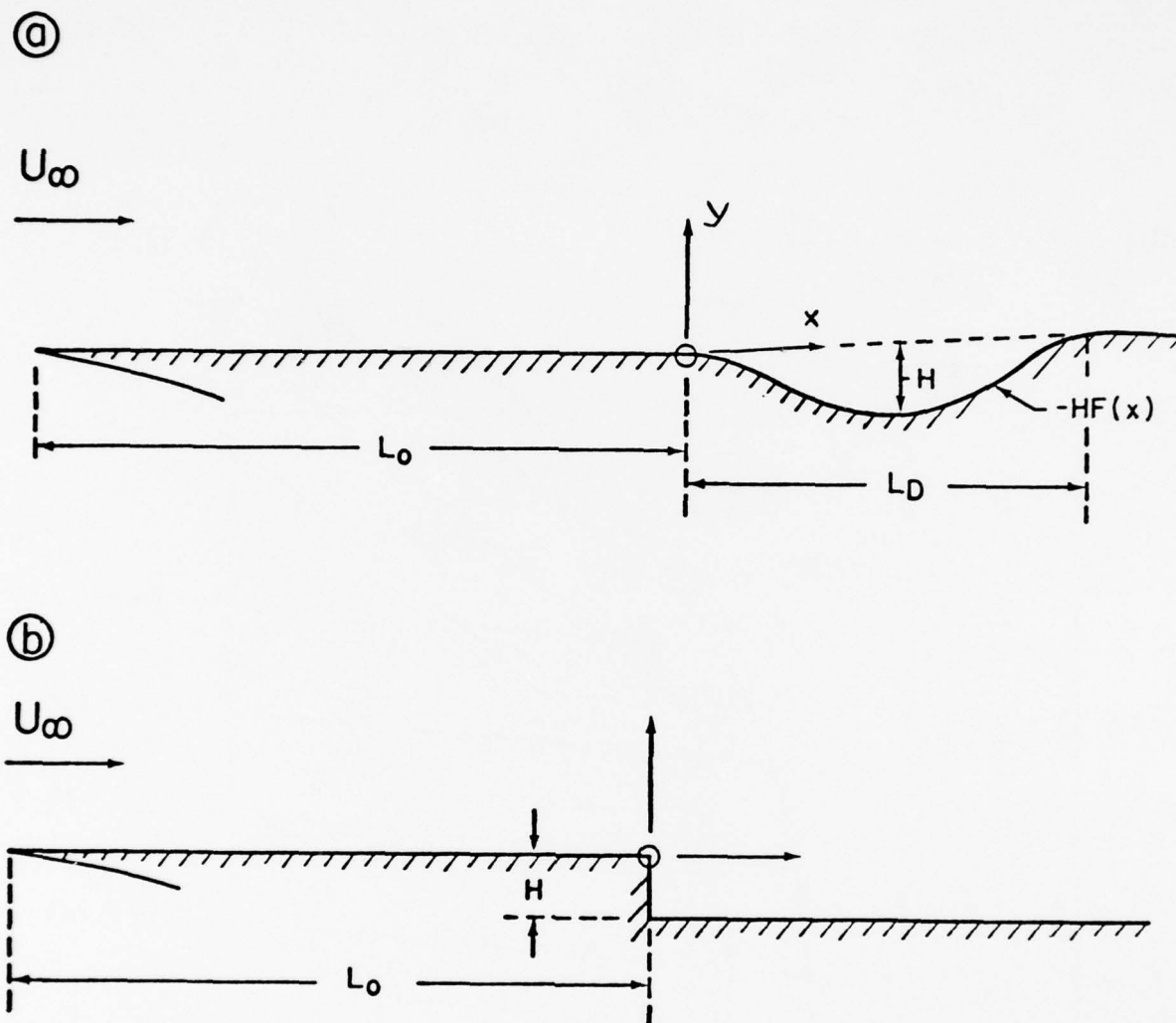


Fig. 2 Wall geometry of a Surface Distortion (a) and a Backward-Facing Step (b).

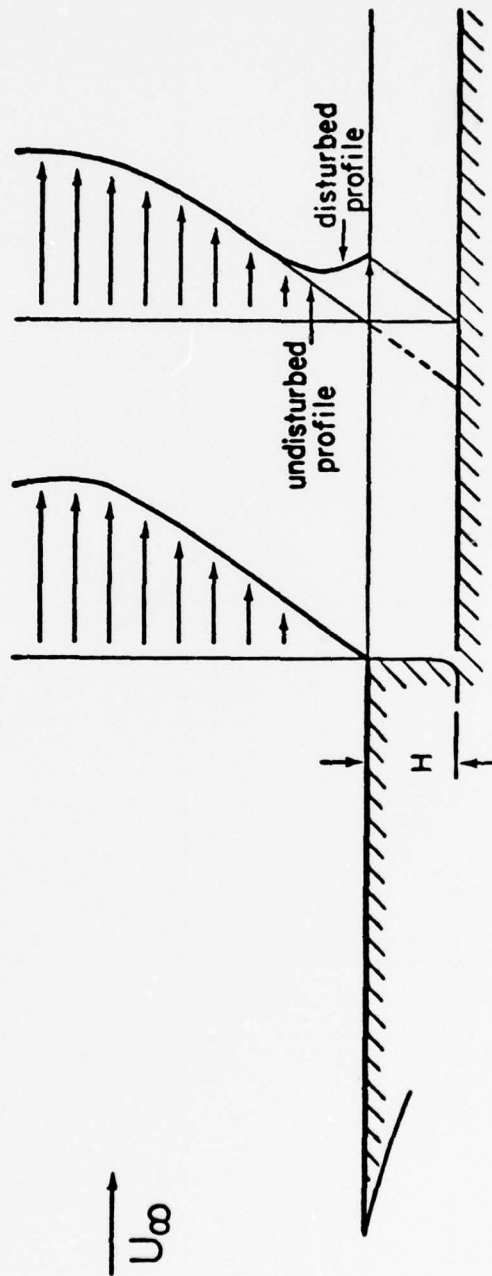


Fig. 3 Schematic of the Boundary Conditions in the Flow behind a Small Backward-facing Step.

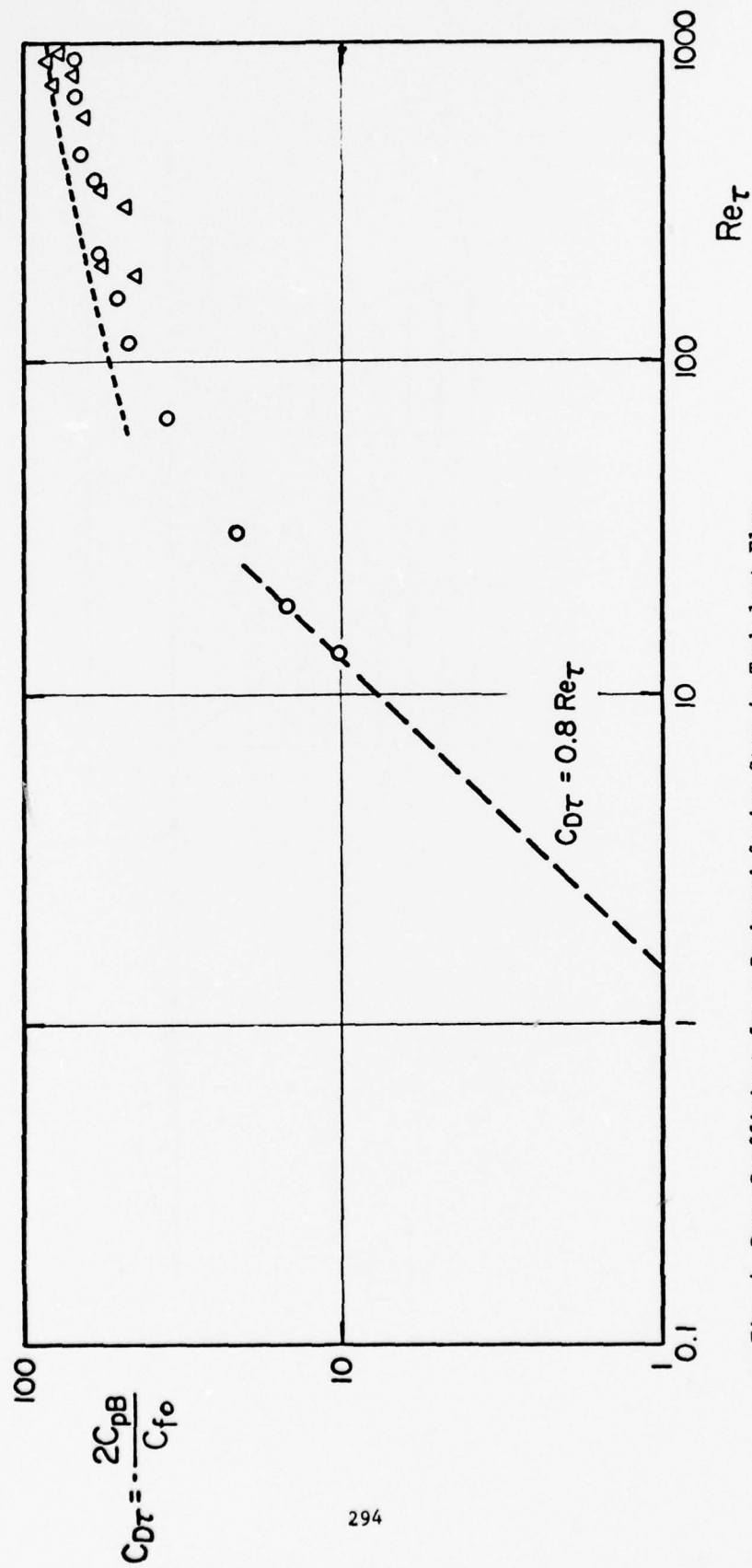


Fig. 4 Drag Coefficient for a Backward-facing Step in Turbulent Flow.

THREE-DIMENSIONAL SHOCK WAVE
TURBULENT BOUNDARY LAYER INTERACTIONS -
A PRELIMINARY ANALYSIS OF BLUNTED FIN INDUCED FLOWS

D. S. Dolling^{*}, C. D. Cosad^{**} and S. M. Bogdonoff^{***}
Gas Dynamics Laboratory
Department of Aerospace and Mechanical Sciences
Princeton University
Princeton, New Jersey

ABSTRACT

An extensive experimental investigation has been made of three-dimensional blunted fin-induced shock wave turbulent boundary layer interactions. Surface pressures, heat transfer rate distributions and oil streak patterns were obtained over a range of fin bluntnesses and incidences for two different incoming boundary layers. These incoming boundary layers had mean thicknesses in the ratio of approximately 4:1. All the measurements were made at a freestream Mach number of 3, a unit Reynolds number of $6.2 \times 10^7 \text{ m}^{-1}$ ($1.6 \times 10^6 \text{ in}^{-1}$) and with near adiabatic wall conditions.

This research was supported by the Naval Air Systems Command under Contract N60921-76-C-0053.

^{*} Research Staff Member, Department of Aerospace and Mechanical Sciences.

^{**} Graduate Student, Department of Aerospace and Mechanical Sciences.

^{***} Professor and Chairman, Department of Aerospace and Mechanical Sciences.

Preliminary analysis of these data indicates that, in the region of the interaction where the freestream shock wave shape is dominated by the fin nose bluntness, the surface property distributions correlate using purely geometric parameters. In sharp contrast to its two-dimensional counterpart, which is a highly Reynolds number dependent viscous phenomenon, the current results indicate that the three-dimensional case is governed by essentially inviscid mechanisms.

NOMENCLATURE

D	shock generator leading edge bluntness diameter = DIA
P	static pressure = P _{STATIC}
P _w	static pressure at the wall = P _{WALL}
M	Mach number
Re	freestream unit Reynolds number
X	coordinate parallel to the tunnel axis measured from furthest point forward of freestream shock wave
X _s	distance along instrumentation line measured from the freestream shock wave location
Y	coordinate normal to the X axis in plane of test surface measured from leading edge of shock generator
α_G	geometric shock generator incidence
δ	boundary layer thickness at start of interaction pressure rise = DELTA

Subscripts:

∞	freestream conditions
----------	-----------------------

1. INTRODUCTION

Two-dimensional shock wave boundary layer interactions have been studied extensively, both experimentally and theoretically, over a wide range of conditions, and are now reasonably well understood. In sharp contrast, the three-dimensional interaction has received little attention, despite its obviously important practical significance. The gross effects of systematic geometric and freestream parameter changes are known but as yet no widely applicable physical flow field model has been devised and validated.

Experimentally, neglect of the three-dimensional interaction has resulted mainly from the difficulties of resolving the flowfield. Extensive surface instrumentation is needed and optical flow visualization methods, suitable for two-dimensional flowfields, cannot be used. Flowfield details must be obtained through the difficult, expensive and time consuming task of probing. Neglect has also been partially fostered by the current computational thrust to model the two-dimensional interaction, which has directed considerable experimental effort into obtaining high quality detailed measurements for comparison with predictions.

Several experimental studies have examined three-dimensional fin induced interactions, using both sharp (i.e. Refs. 1-7) and blunted leading edges (i.e. Refs. 8-15). In the majority of blunted investigations, attention was focussed on the

region ahead of and around the fin nose, with little data being taken in the area outboard of the main body of the fin. Flow-field models have been proposed (i.e. Refs. 5,8,16), but apart from that of Oskam (Refs. 1-3) for the sharp leading edged fin, they were mainly derived from surface oil flow patterns, which in three dimensions is a highly questionable approach.

The current experimental investigation, planned as the first stage of a continuing program, is a major extension of earlier three-dimensional studies (Refs. 1-3) carried out at the Gas Dynamics Laboratory using a sharp leading edged generator. A schematic of the arrangement studied, showing the region of the interaction where measurements were made, is shown in Fig. 1. In the first phase of this program, reported on briefly here, an extensive parametric study of three-dimensional blunted fin induced shock wave turbulent boundary layer interactions has been made. Surface property distributions have been measured over a wide range of fin bluntnesses and incidences for two different incoming boundary layers. These boundary layers were generated on two model configurations and had thicknesses in the ratio of about 4:1.

The large amount of data from this study has been set up in computer compatible form suitable for detailed analysis. This current paper briefly describes the experimental program and presents details of the preliminary analysis carried out so far.

2. EXPERIMENTAL PROGRAM

2.1 Wind Tunnel Facility

The experimental study was carried out in the Princeton University high Reynolds number supersonic blowdown wind tunnel. This tunnel has a working section 20 cm x 20 cm (8 in. x 8 in.), a nominal freestream Mach number of 3 and may be operated at stagnation pressures in the range of $4 \times 10^5 \text{ Nm}^{-2}$ to $3.4 \times 10^6 \text{ Nm}^{-2}$ (60 psia to 500 psia).

In this study all tests were carried out at a stagnation pressure of $6.8 \times 10^5 \text{ Nm}^{-2}$ (100 psia) corresponding to a free-stream unit Reynolds number of $6.3 \times 10^7 \text{ m}^{-1}$ ($1.6 \times 10^6 \text{ in}^{-1}$). The models were at near adiabatic wall conditions for all tests.

2.2 Model Configurations

Two model configurations formed the basis of this experimental investigation and are shown schematically in Fig. 2.

The Model I configuration used the boundary layer developing on the tunnel wall. This is a two-dimensional fully turbulent boundary layer with a thickness $\delta \approx 1.27 \text{ cm}$ (.5 in.) in the region of the interaction. The shock generator used spanned the tunnel vertically and was 25.4 cm (10 in.) in length. A screw drive mechanism allowed manual adjustment of the angle of incidence by an external drive wheel. Four blunt leading edges were used with the thick boundary layer study.

The Model 2 configuration made use of the boundary layer developing on a sharp leading edged plate which spanned the tunnel horizontally. The incoming two-dimensional fully turbulent boundary layer had developed over a distance of about 30 cm (\approx 12 in.) to a thickness $\delta \approx .38$ cm (.15 in.) in the region of the interaction. The shock generator for the Model 2 configuration was held and controlled in the same manner as that of Model 1. As in the Model 1 study, interactions generated by four blunt leading edges were examined.

The leading edge diameters and locations of pressure tapping rows for both model configurations are given in the test matrix of Fig. 3. The coordinate system used in the presentation of the data is shown in Fig. 4.

2.3 Incoming Boundary Layers

The tunnel floor boundary layer, which served as the incoming layer for the Model 1 study, was examined in detail with both pitot and total temperature probes when the tunnel was put into operation in 1971. Calibrations spanning the available stagnation pressures were made along the entire length of the test section (2.7 m). A spanwise and streamwise examination of these data within the framework of the law of the wall combined with Coles wake law showed the boundary layer to be a fully turbulent, two-dimensional equilibrium layer.

Pitot surveys were also made at spanwise and streamwise locations in the boundary layer developing on the flat plate of

the Model 2 configuration. Analysis showed these incoming profiles to be those of a fully turbulent, two-dimensional equilibrium turbulent boundary layer.

2.4 Shock Wave Shape Determination

Of primary importance in this study was a knowledge of the freestream shock wave locations. Shadow photographs were taken of aluminum dummy models which spanned the range of bluntnesses and incidences encountered in the test program. The X-Y coordinates of the shock waves were read from the shadowgraph negatives. From these data, the locations of the freestream shock wave with respect to instrumentation stations could be determined for all experimental measurements conducted.

2.5 Surface Pressure Distributions

For both the Model 1 and Model 2 configurations, surface pressure distributions were measured along four tapping rows. Each row consisted of about 50 tappings in a line parallel to the undisturbed free stream. The locations of these instrumentation rows have been shown previously in the test matrix, Fig. 3.

2.6 Surface Oil Flow Patterns

Photographs of surface oil flow patterns were taken for all interactions studied. These were obtained by using a low viscosity commercial oil as a vehicle for a powdered fluorescent

dye. The tunnel was started and the shock generator set at the desired incidence. Once a steady flow pattern was established, usually 10 to 20 seconds, the photograph was taken.

The extent of the interactions obtainable in the downstream direction was limited by the trailing edge expansion from the shock generator and/or the reflection of the shock-wave from the opposite tunnel wall.

2.7 Estimated Measurement Uncertainties

The shadowgraph technique employed allowed for determination of the shock location to an accuracy of $\pm .13$ cm. (.05 in.). The shock generator deflection angle is considered to be accurate to $\pm .05^\circ$. The overall uncertainty of the static pressure data is less than $\pm 2\%$ of the upstream static pressure level. Surface oil flow angles are accurate to within $\pm 2^\circ$. All measurements in the test program were made under the assumption that flow variables remained "steady" at any fixed point within the interaction. No time resolved measurements were made to confirm or invalidate this assumption, although no unsteadiness was observed in the measurements taken.

3. DISCUSSION OF DATA AND PRELIMINARY ANALYSIS

3.1 General Considerations

Only a preliminary analysis of the measurements has been made, with emphasis on the surface pressure and oil streak patterns for the several blunted cases. No comparisons are presented

between data from the sharp and blunted leading edge studies, because of the lack, at this time, of accurate shock shapes for the sharp case.

3.2 Shock Shapes

Figure 5 shows the shock shapes for fin incidences of 0° and 10° plotted in the form Y/D vs. X/D on logarithmic scales. The $2/3$ power law relationship for shock shape, developed from blast wave theory, applies well from 2 to 10 tip diameters downstream of the fin leading edge. In this region the shock shape is determined by the leading edge geometry and is not influenced by incidence, up to at least 10° . The balance between the fin nose geometry and fin incidence in determining shock shape is apparent from the schematic of Fig. 6. In the nose region, the shock shape is dominated by the fin leading edge geometry. Incidence becomes progressively more important with increasing distance outboard.

In this exploratory analysis, surface pressure and oil streak patterns are shown at two locations on the shock shape plot of Fig. 5. The locations examined correspond to Y/D 's of about 9 and 31. A Y/D of 9 is in the region where the free-stream shock shape is determined by the fin nose geometry, whereas at Y/D of 31, the incidence is also an important parameter.

3.3 Surface Pressure Distributions

Similarly to the analysis of two-dimensional interactions an attempt was made to correlate the data using the incoming boundary layer thickness δ as a scaling parameter. For a fixed Y/δ , comparisons in terms of X_s/δ were made of pressure distributions from the Model 1 and 2 configurations. No correlation of the data was obtained in this coordinate system. In this type of three-dimensional interaction, the incoming boundary layer thickness alone is not a suitable scaling parameter.

The behavior of the freestream shock shapes suggested using the fin leading edge bluntness diameter D as a scaling parameter. Use of D resulted in a good correlation of the data. Figures 7, 8 and 9 each show five pressure distributions plotted as a function of X_s , X_s/δ and X_s/D respectively. These distributions correspond to a mean Y/D of 8.7 and are for a fin incidence of 10° . Four distributions are from the Model 1 (thick boundary layer) study with the other from the Model 2 study (thin boundary layer). Each distribution is for a different value of Y and D , with the only common factor, a purely geometric one, being that the ratio Y/D for each one is close to 8.7.

These figures show that for a fixed Y/D the data correlate reasonably well when plotted in terms of X_s/D . A similar series of plots, as shown in Figs. 7 to 9 was constructed over the entire incidence range for this same value of Y/D . In all cases a good correlation was obtained when scaled by D . Other

checks made at a Y/D of about 4 also resulted in a good correlation when plotted in terms of X_S/D . The predominantly inviscid character of the interaction in this region is forcefully illustrated by this correlation. Pressure distributions in this region are not influenced by large variations in incoming boundary layer thickness, in this case greater than 4:1, and can be correlated in terms of purely geometric parameters.

In Fig. 9, the data for a fin bluntness D of .318 cm (.125 in.) tend to diverge from the main body of data at about $6D$ downstream of the freestream shock wave location ($X_S = 0$). The ratio of D/δ for this case was about 0.25. There is the possibility that a critical value of D/δ exists, probably around 0.25, below which good scaling in terms of D breaks down. Some measurements from this study and others (Ref. 10) provide some tentative support, but these data are insufficient to either fully substantiate or refute this possibility. Experiments planned for the next phase of this study should clarify this point.

All of the data shown in Figs. 7 to 9 fall in the region of the interaction where the freestream shock wave shape is dominated by the fin nose. A second series of pressure distributions, plotted as functions of X_S , X_S/δ and X_S/D has been made at a Y/D of 31. These are shown in Figs. 10, 11 and 12, respectively. Here, both the fin nose and incidence determine the shock wave shape. In these figures four distributions are from the Model 2 study and one from the Model 1 study.

The correlation of the data is poor compared to that obtained at a Y/D of 8.7. With increasing distance along the shock wave (in terms of D) the strongly inviscid nature of the interaction starts to change.

Further experimental evidence supporting the premise that the interaction is governed by a predominantly inviscid mechanism is shown in Fig. 13. These two pressure distributions were obtained from the Model 1 and 2 configurations and had approximately the same values of Y and D , but the incoming boundary layers had thicknesses in the ratio of about 4:1. A good correlation of the data is obtained when plotted as a function of absolute distance X_s alone. In terms of incoming boundary layer thicknesses, the streamwise extents of these interactions are about 16δ and 55δ whereas in absolute terms they have the same length, namely about 20 cm.

Comparison of the present results with other investigations is difficult since few studies have been made under similar conditions, and of these, the emphasis has been on the region around and ahead of the nose. However, some comparisons have been made with measurements made by Price and Stallings (Ref.10) at the same freestream Mach number but with an incoming boundary layer 15 cm. thick. These data are for an incidence of 0° and for a hemicylindrically blunted fin swept back through 12.9° . Figure 14 shows a comparison of these data with the Model 1 configuration at a Y/D of 4.3. The incoming boundary layer thicknesses are in the ratio of about 12:1.

In this comparison it should be noted that Price and Stallings' data were generated by a sweptback fin, which shifts the interaction back an amount estimated by them to be about 1D. Consequently, adjustment of the data to account for sweepback would tend to bring the two distributions closer to a collapse. As seen above, the Model 1 and 2 data correlate well in this region for incoming boundary layer thicknesses in the ratio of about 4:1. Noting this and comparing the Model 1 data with those of Price and Stallings in Fig. 14, it would seem that the pressure distribution does not change significantly for incoming boundary layers having thicknesses in the ratio of about 40:1.

3.4 Oil Flow Patterns

The test matrix for surface oil streak patterns was identical to that for surface pressure distributions (Fig. 3). Oil flow photographs were taken with the pressure plates as the test surface, using the tapping locations as points of reference. Surface flow angles have been examined for values of Y/D of approximately 8.7 and 31 to check whether or not they would scale in the same way as the pressure data.

Surface flow angles at $Y/D \approx 8.7$ for a shock generator incidence of 10° are shown in Figs. 15 and 16 in X_s/δ and X_s/D coordinates, respectively. Scaling by δ does not correlate the curves. Plotted in terms of X_s/D , the correlation of the data is excellent and is consistent with the surface pressure data from identical locations. This correlation strongly supports

use of D as a scaling parameter in this region and further demonstrates the inviscid character of this type of three-dimensional interaction.

Figures 17 and 18 show surface oil flow angles at a generator angle of 10° for the five sets of data having a Y/D of about 31. Again, scaling by δ does not result in a correlation of the curves. When scaled by D , the scaling is superior to that offered by δ , but it is much poorer than that at $Y/D \approx 8.7$. These trends with Y/D for the oil flow patterns are the same as those noted earlier with the surface pressure distributions.

4. CONCLUDING REMARKS ON THE PRELIMINARY DATA ANALYSIS

From the exploratory analysis carried out so far, results have emerged which have provided new insight into the nature of different regions of this type of three-dimensional interaction.

The correlation of the data when scaled by D , even for cases having markedly different incoming boundary layer thicknesses, shows conclusively the predominantly inviscid character of the interaction. This conclusion is further supported by the correlation of data in terms of absolute distance alone for configurations having identical geometries but with incoming boundary layers of different thicknesses. It appears that this type of scaling starts to break down with increasing distance (in terms of D) away from the fin. However, it would seem certain

that use of the incoming boundary layer thickness alone as a scaling factor is inappropriate in any region of the interaction studied thus far.

A physical model of the interaction flowfield has not yet been developed, since only surface property measurements have been made. In the near future some flow visualization techniques will be attempted and hopefully the results should assist in elucidating the gross physical features of the flowfield.

REFERENCES

1. Oskam, B., Bogdonoff, S. M. and Vas, I. E., "Study of Three-Dimensional Flowfields Generated by the Interaction of a Skewed Shock Wave with a Turbulent Boundary Layer", AFFDL-TR-75-21, February 1975.
2. Oskam, B., "Three-Dimensional Flowfields Generated by the Interaction of a Swept Shock Wave with a Turbulent Boundary Layer", Princeton University, Gas Dynamics Laboratory, Report 1313, December 1976.
3. Oskam, B., "Three-Dimensional Flowfields Generated by the Interaction of a Swept Shock Wave with a Turbulent Boundary Layer", Ph.D. Thesis, Dept. of Aerospace & Mechanical Sciences, Princeton University, 1976.
4. Lowrie, B. W., "Cross Flows Produced by the Interaction of a Swept Shock Wave with a Turbulent Boundary Layer", Ph.D. Thesis, University of Cambridge, 1965.
5. Token, K. H., "Heat Transfer Due to Shock Wave Turbulent Boundary Layer Interactions on High Speed Weapons Systems", AFFDL-TR-74-77, 1974.
6. Peake, D. J., "The Three-Dimensional Interaction of a Swept Shock Wave with a Turbulent Boundary Layer and the Effects of Air Injection on Separation", Ph.D. Thesis, Carleton University, Ottawa, 1975.
7. McCabe, A., "A Study of Three-Dimensional Interactions Between Shock Waves and Turbulent Boundary Layers", Ph.D. Thesis, University of Manchester, 1963.

8. Winkelmann, A. E., "Flow Visualization Studies of a Fin Protuberance Partially Immersed in a Turbulent Boundary Layer at Mach 5", Naval Ordnance Laboratory Report NOLTR-72-33, January 1972.
9. Winkelmann, A. E., "Experimental Investigations of a Fin Protuberance Partially Immersed in a Turbulent Boundary Layer at Mach 5", Naval Ordnance Laboratory Report NOLTR-72-33, January 1972.
10. Price, A. E. and Stallings, R. L., "Investigation of Turbulent Separated Flows in the Vicinity of Fin Type Protuberances at Supersonic Mach Numbers", NASA TN D-3804, February 1967.
11. Gillerlain, J. D., "Experimental Investigation of a Fin Cone Interference Flow Field at Mach 5", Naval Surface Weapons Center Report NSWC/NOLTR 75-63.
12. Gillerlain, J. D., "Use of Phase Change Paints to Study Fin Body Interference Heating", Naval Surface Weapons Center Technical Report NSWC/WOL/TR 75-62, April 1976.
13. Young, F. L., Kaufman II, L. G. and Korkegi, R. H., "Experimental Investigation of Interactions Between Blunt Fin Shock Waves and Adjacent Boundary Layers at Mach Numbers 3 and 5", ARL 68-0214, Dec. 1968.
14. Kaufmann, II, L. G., Korkegi, R. H. and Morton, L. C., "Shock Impingement Caused by Boundary Layer Separation Ahead of Blunt Fins", ARL 72-0118, August 1972.
15. Dolling, D. S., Cosad, C. D. and Bogdonoff, S. M., "Three-Dimensional Shock Wave Turbulent Boundary Layer Interactions - A Preliminary Analysis of Blunted Fin Induced Flows", Report AMS-1354, Gas Dynamics Laboratory, Princeton University, October 1977.
16. Korkegi, R. H., "On the Structure of Three-Dimensional Shock Induced Separated Flow Regions", AIAA Jour., Vol. 14, No. 5, May 1976, pp. 597-600.

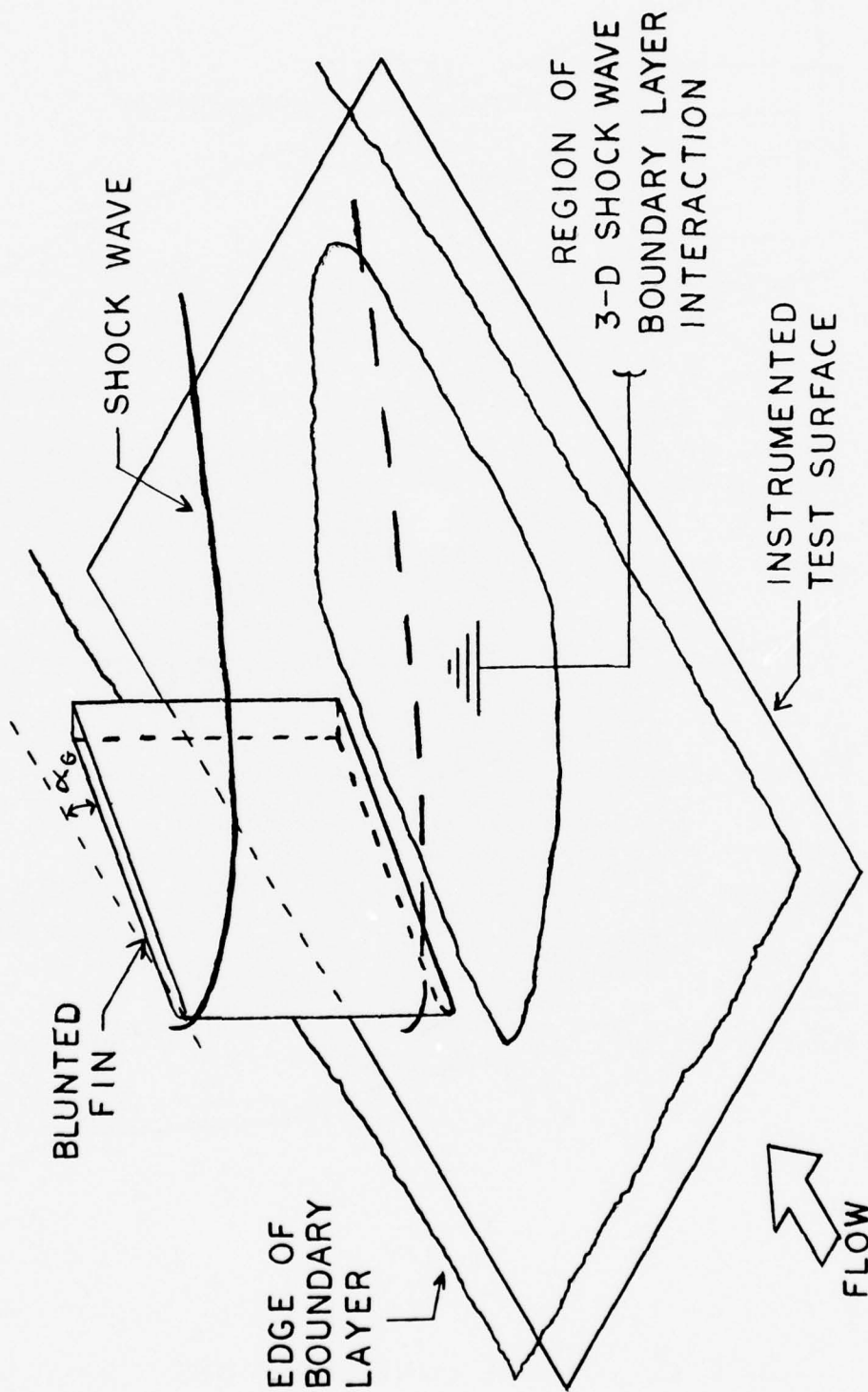


Figure 1. Configuration under study.

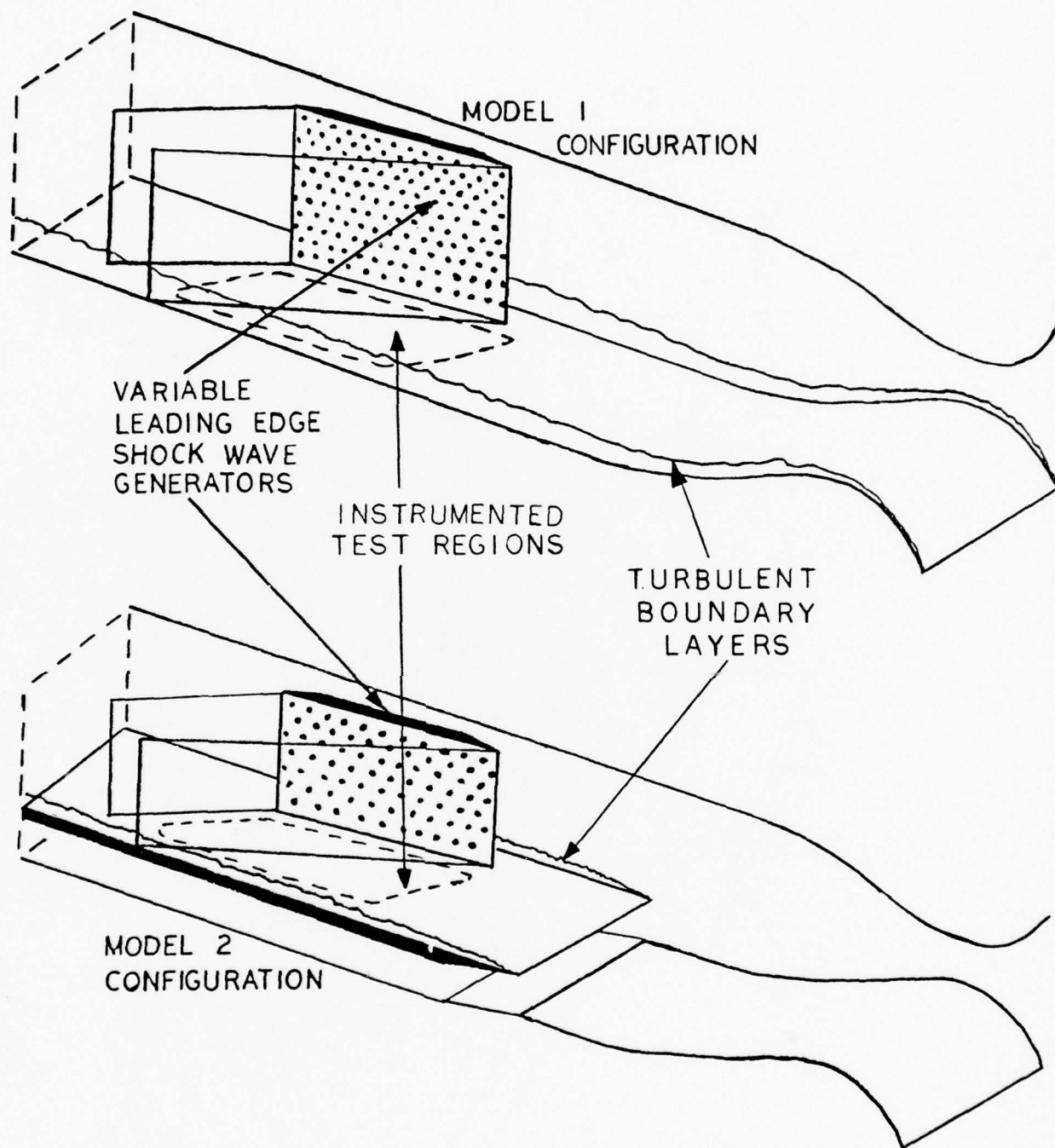


FIGURE 2 MODEL CONFIGURATIONS

BLUNTED STUDY TEST MATRIX

THICK BOUNDARY LAYER : $\delta = .50''$

BLUNTNES D	Y/D AT PRESSURE		TAPPING ROW	
	Y=0.9"	Y=1.9"	Y=2.9"	Y=3.9"
.125"	7.7	15.7	23.7	31.7
.250"	4.1	8.1	12.1	16.1
.375"	2.9	5.6	8.2	10.9
.500"	2.3	4.3	6.3	8.3

THIN BOUNDARY LAYER : $\delta = .15''$

BLUNTNES D	Y/D AT PRESSURE		TAPPING ROW	
	Y=1.15"	Y=2.15"	Y=3.4"	Y=4.4"
.040"	29.3	54.3	85.5	110.
.080"	14.9	27.4	43.0	55.5
.120"	10.1	18.4	28.8	37.2
.160"	7.7	13.9	21.8	28.0

FIGURE 3 BLUNTED STUDY TEST MATRIX

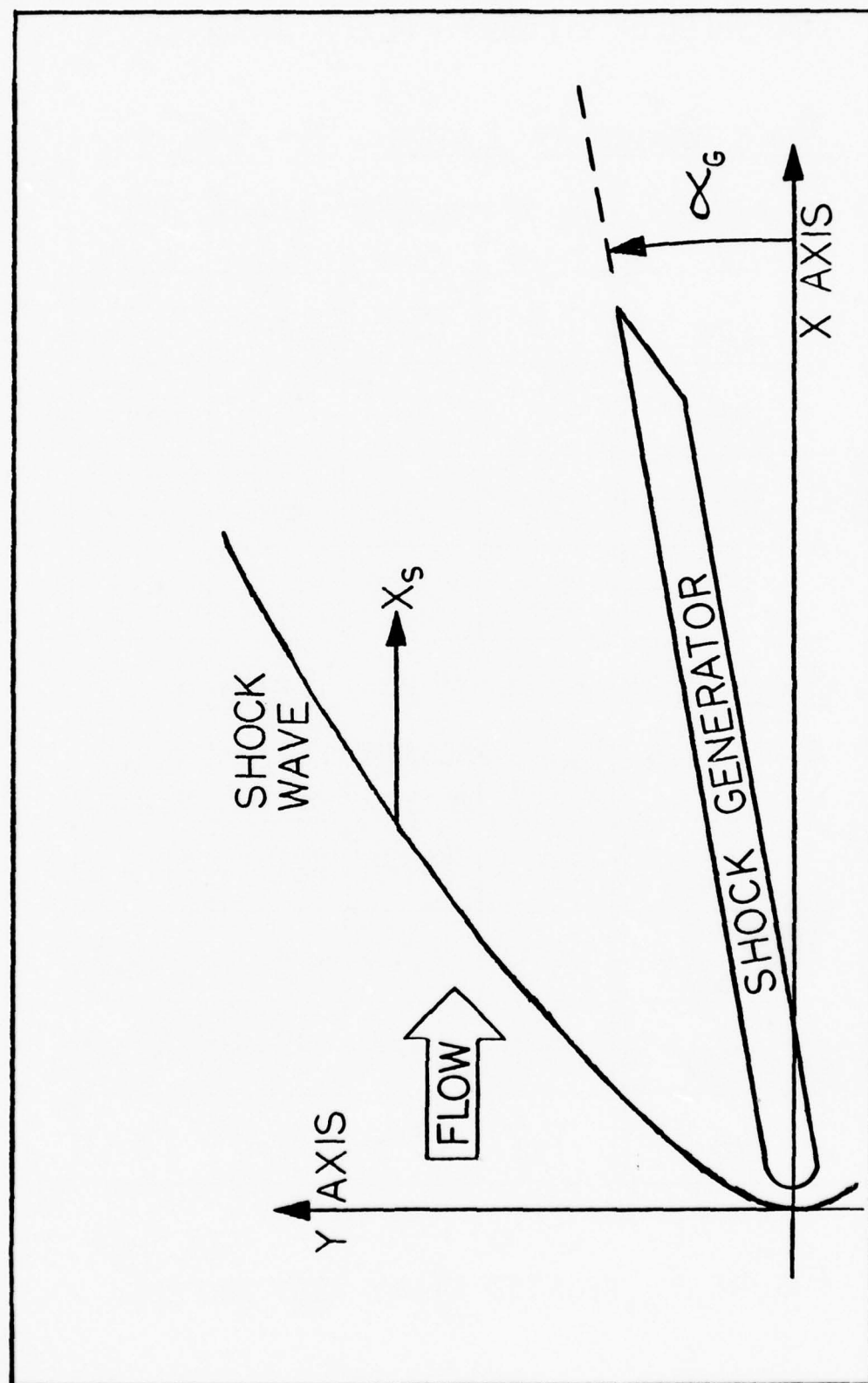


FIGURE 4 COORDINATE SYSTEMS

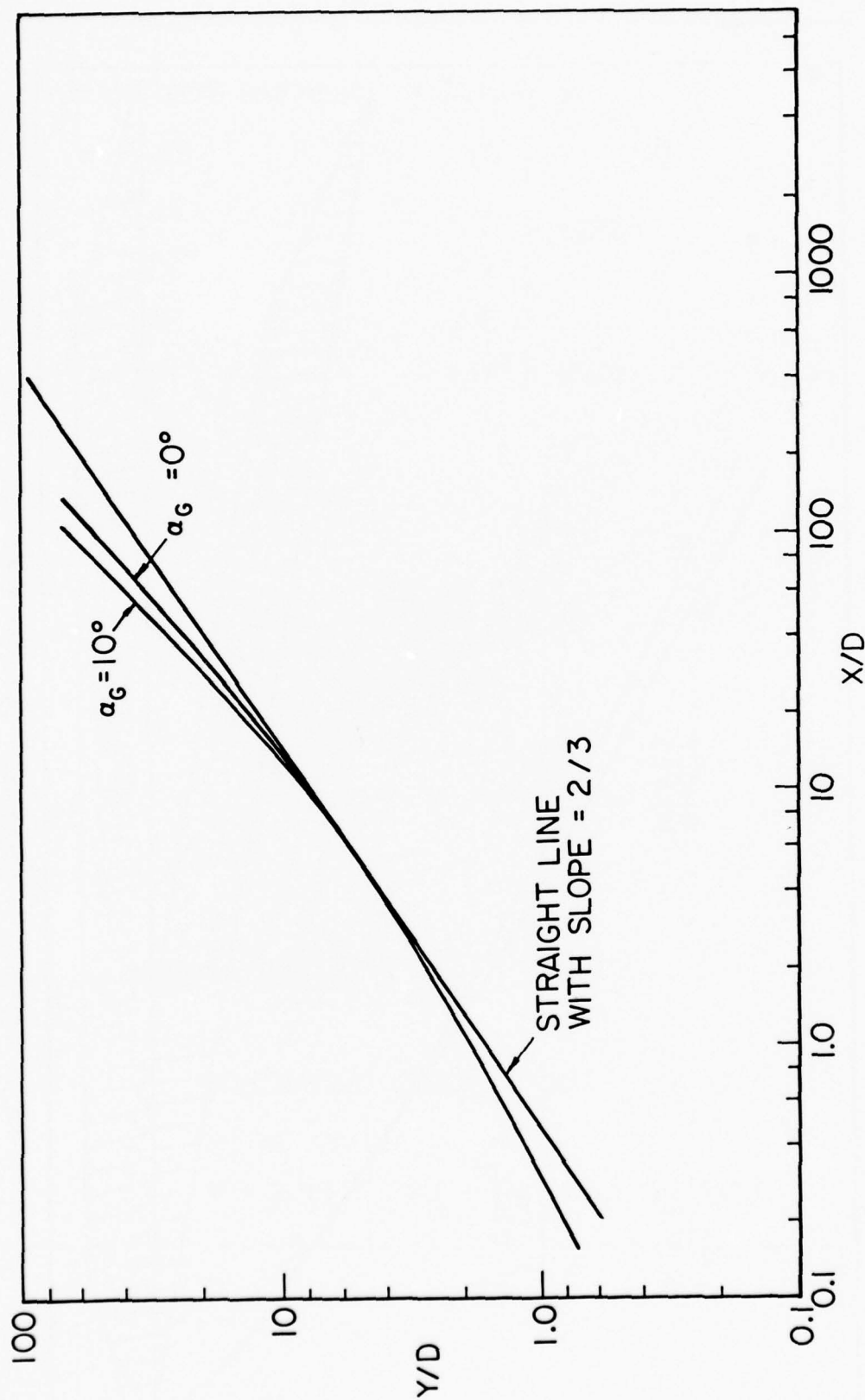


Figure 5. Shock Shapes in the form Y/D vs. X/D .

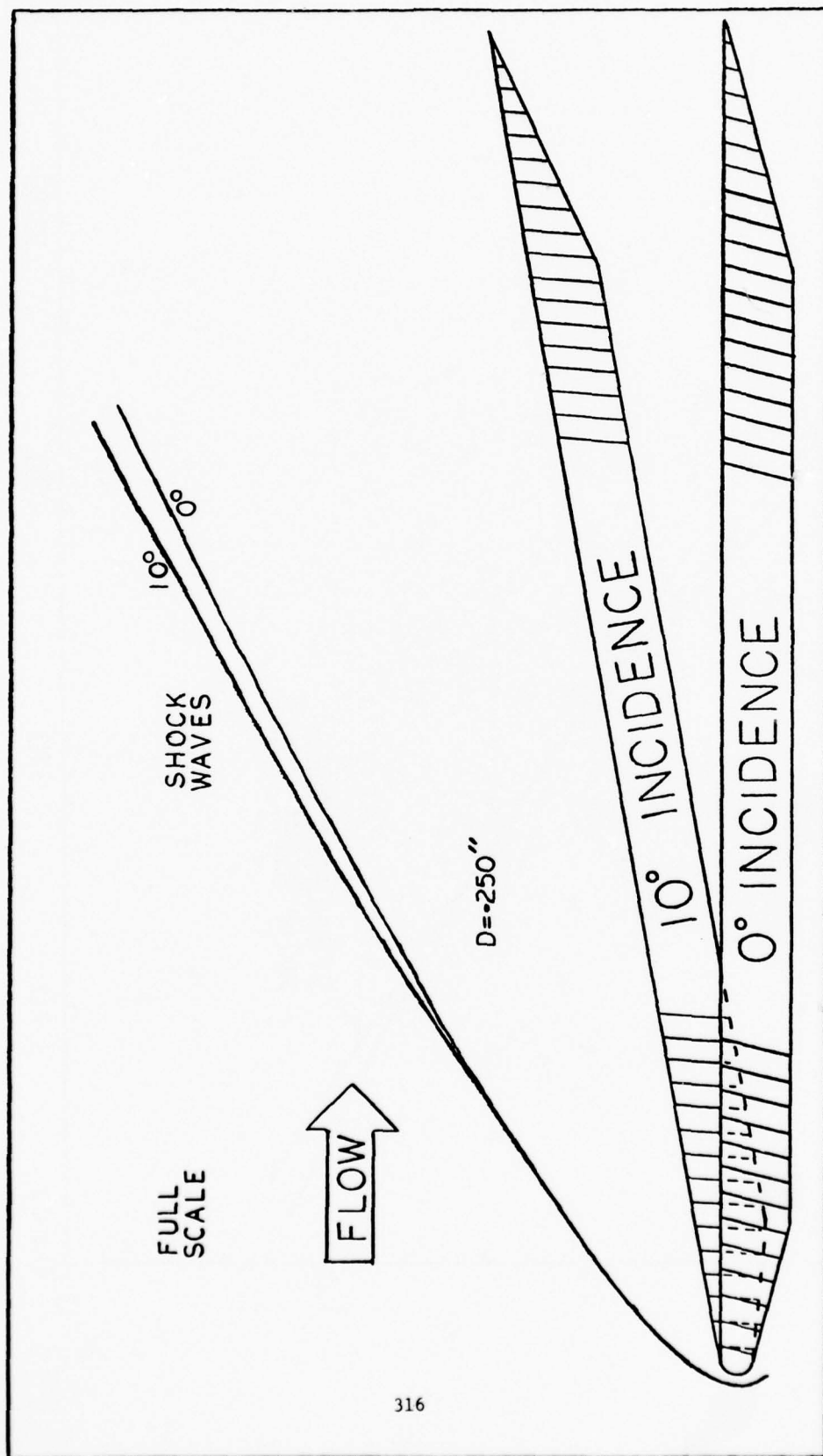


Figure 6. Effect of Incidence on the Observed Shock Wave Shape for $D = 0.635\text{cm}$ (0.250in).

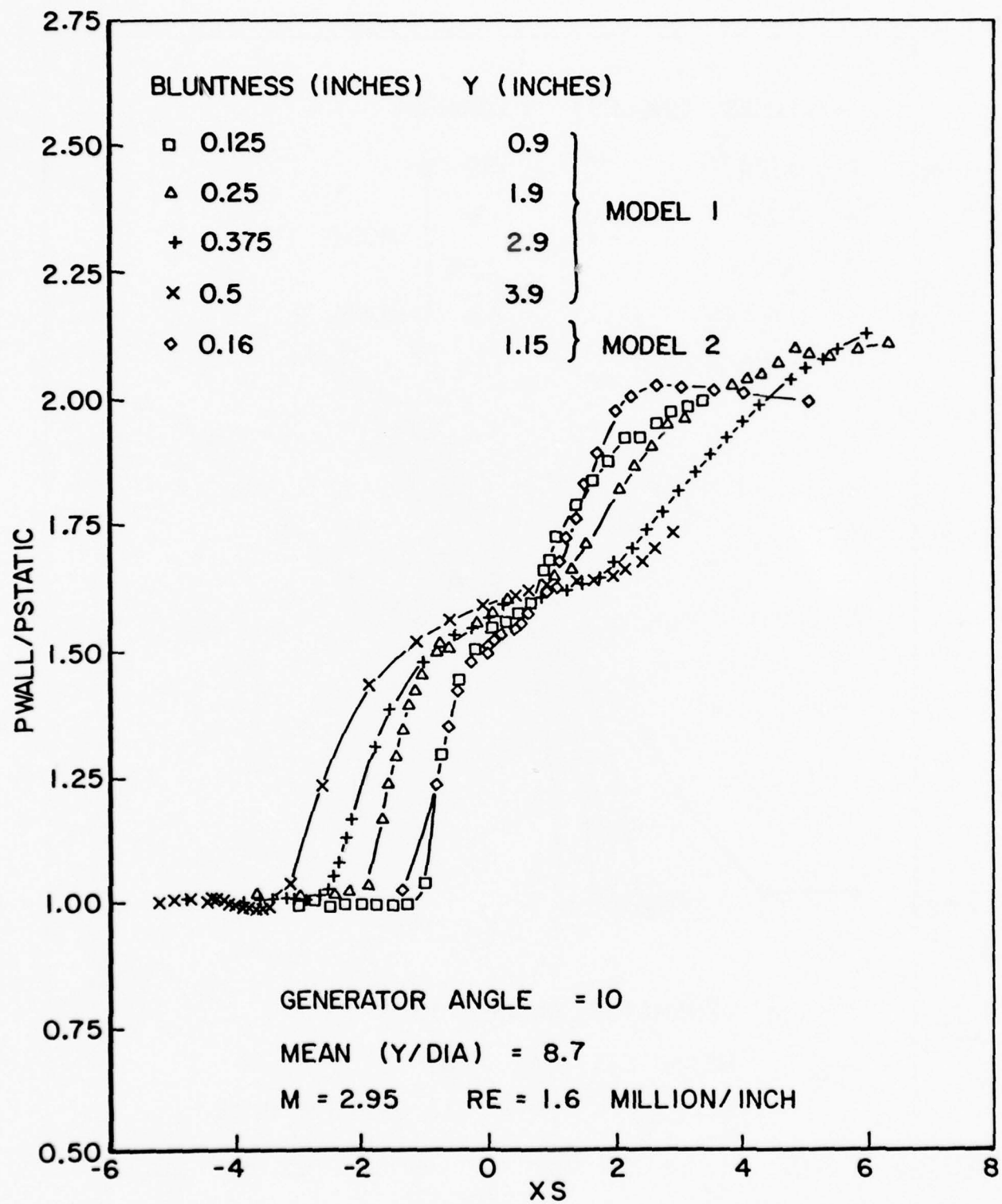


Figure 7. Pressure Distributions as a Function of X_S for $Y/D = 8.7$.

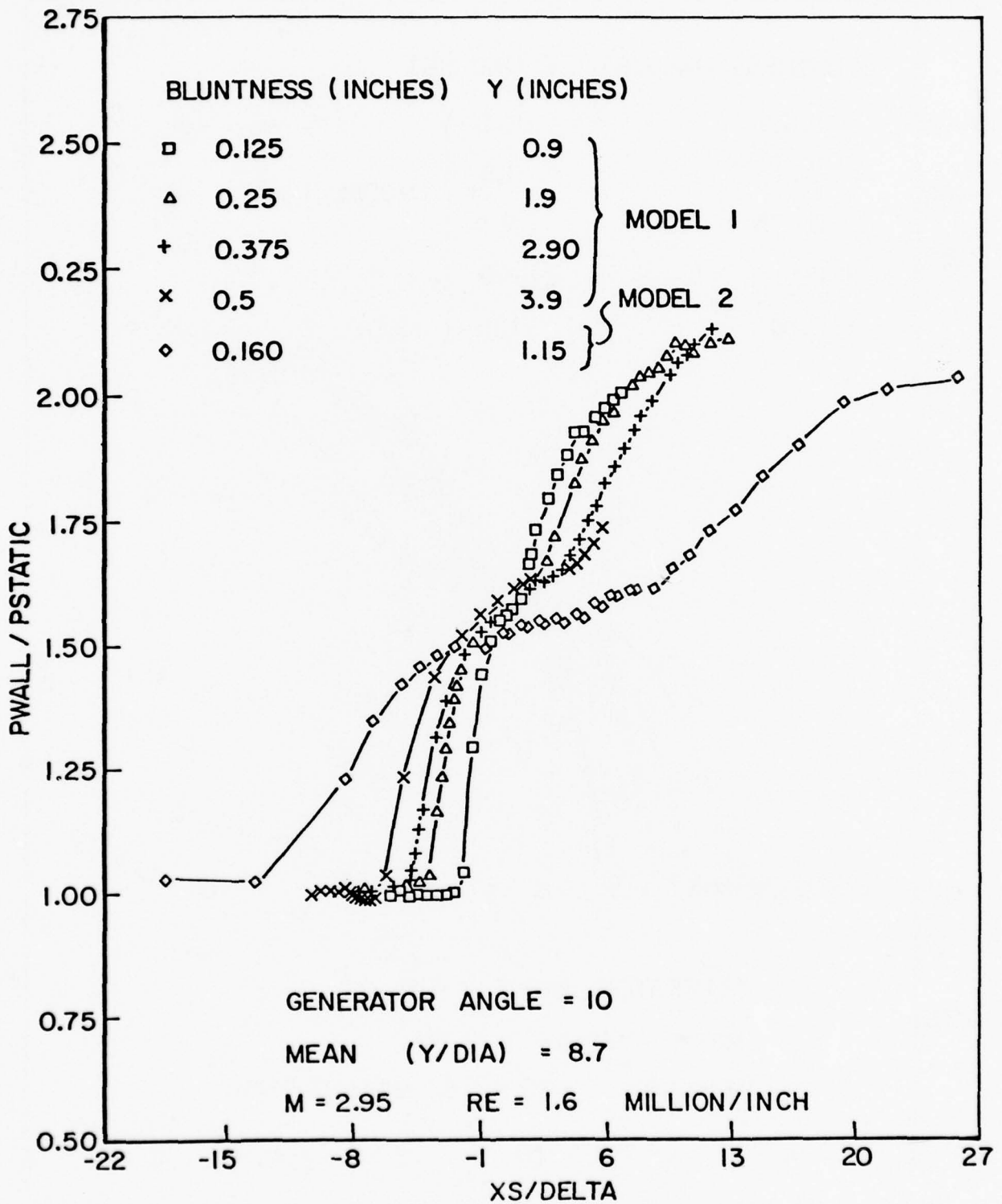


Figure 8. Pressure Distributions as a Function of X_S/δ for $Y/D = 8.7$.

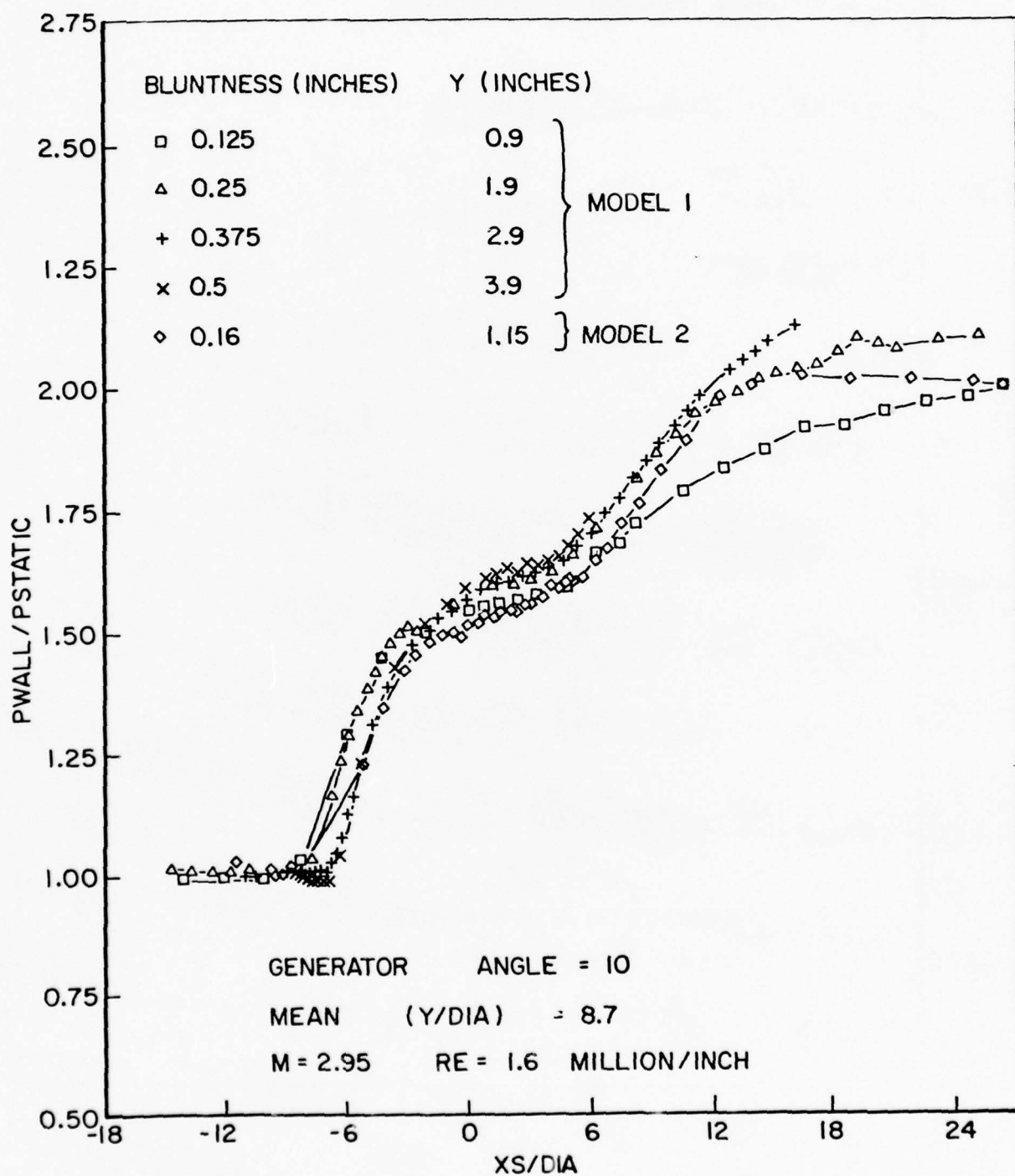


Figure 9. Pressure Distributions as a Function of X_S/D for $Y/D = 8.7$.

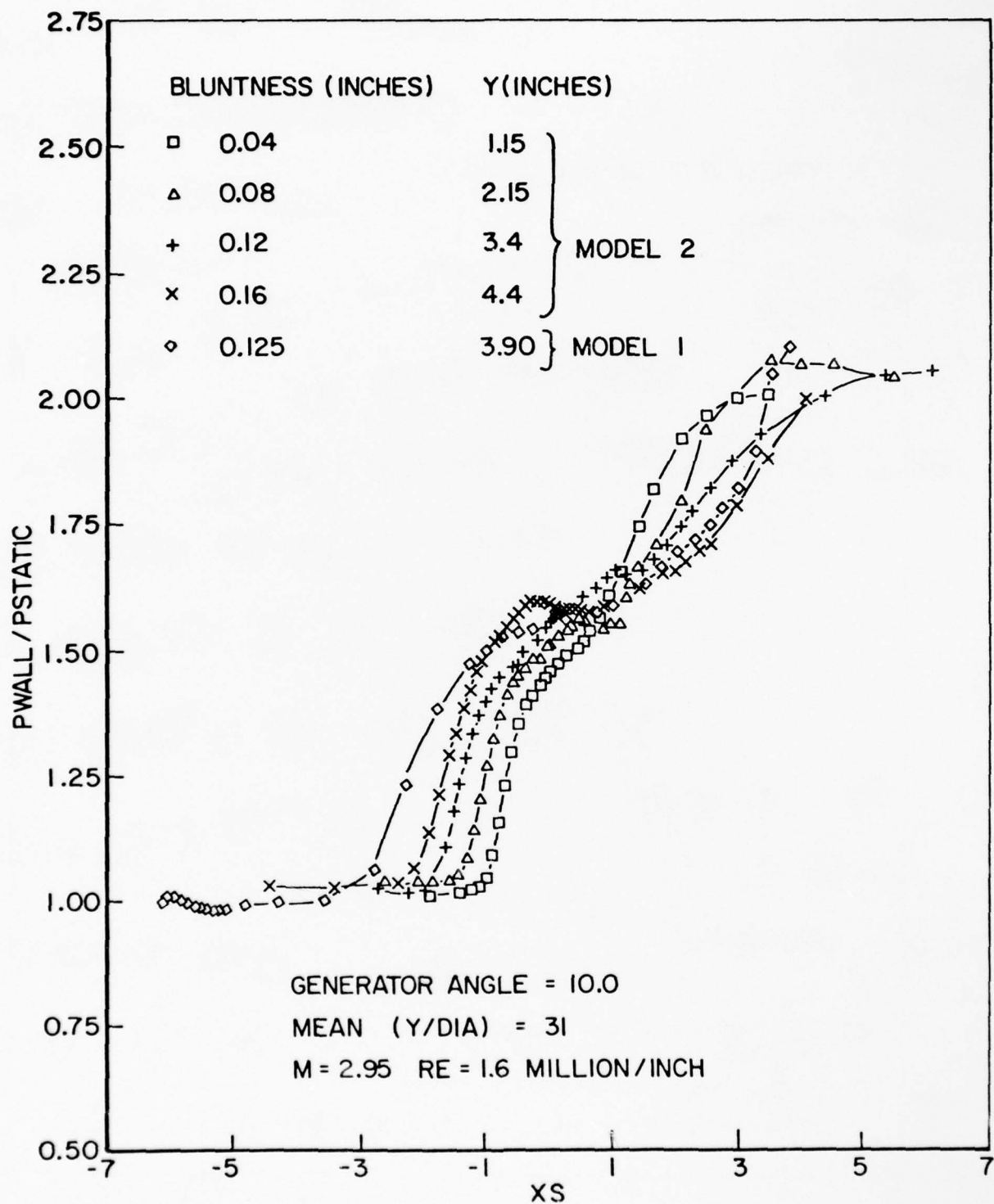


Figure 10. Pressure Distributions as a Function of X/S for $Y/D = 31$.

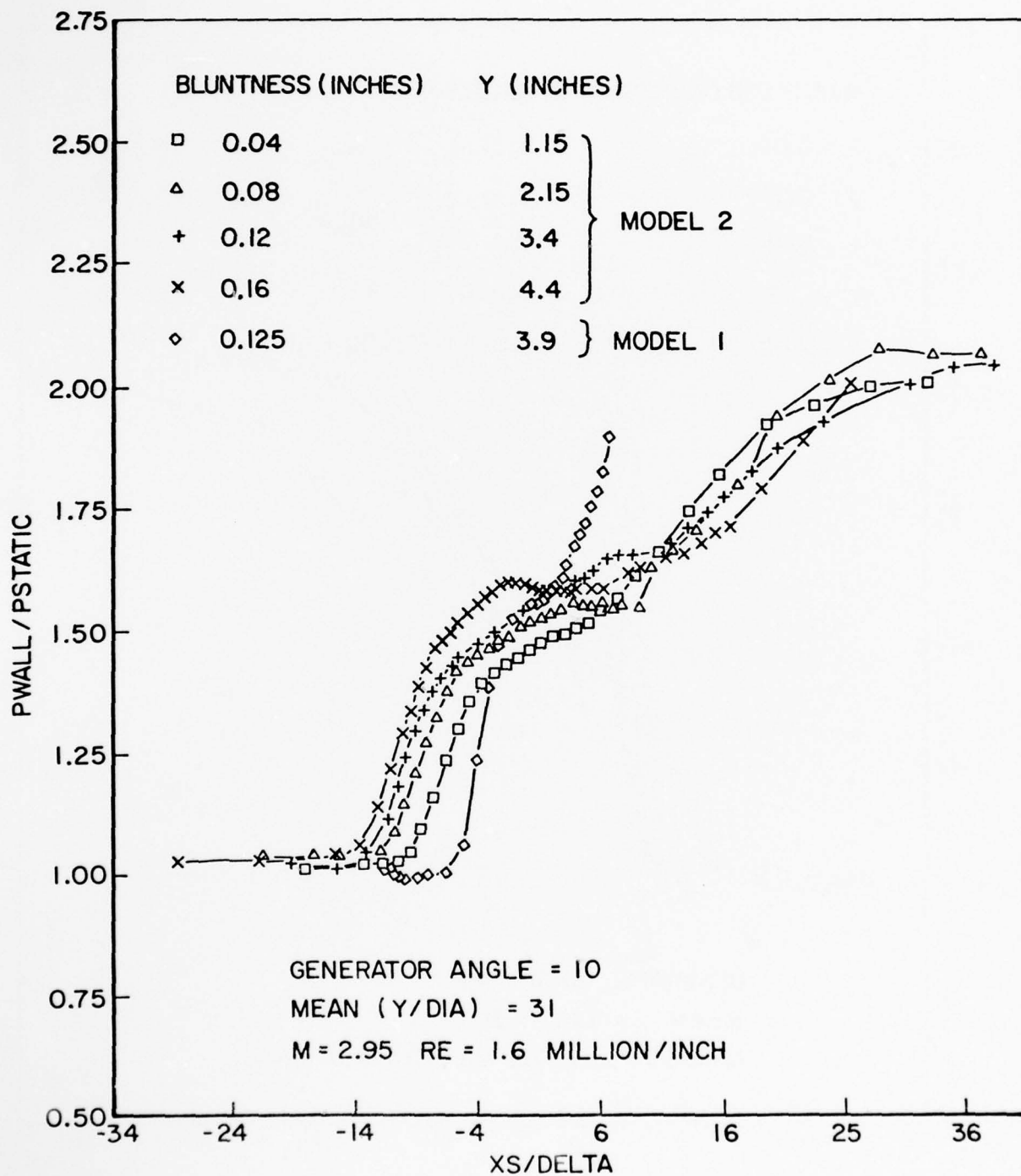


Figure 11. Pressure Distributions as a Function of X_S/δ for $Y/D = 31$.

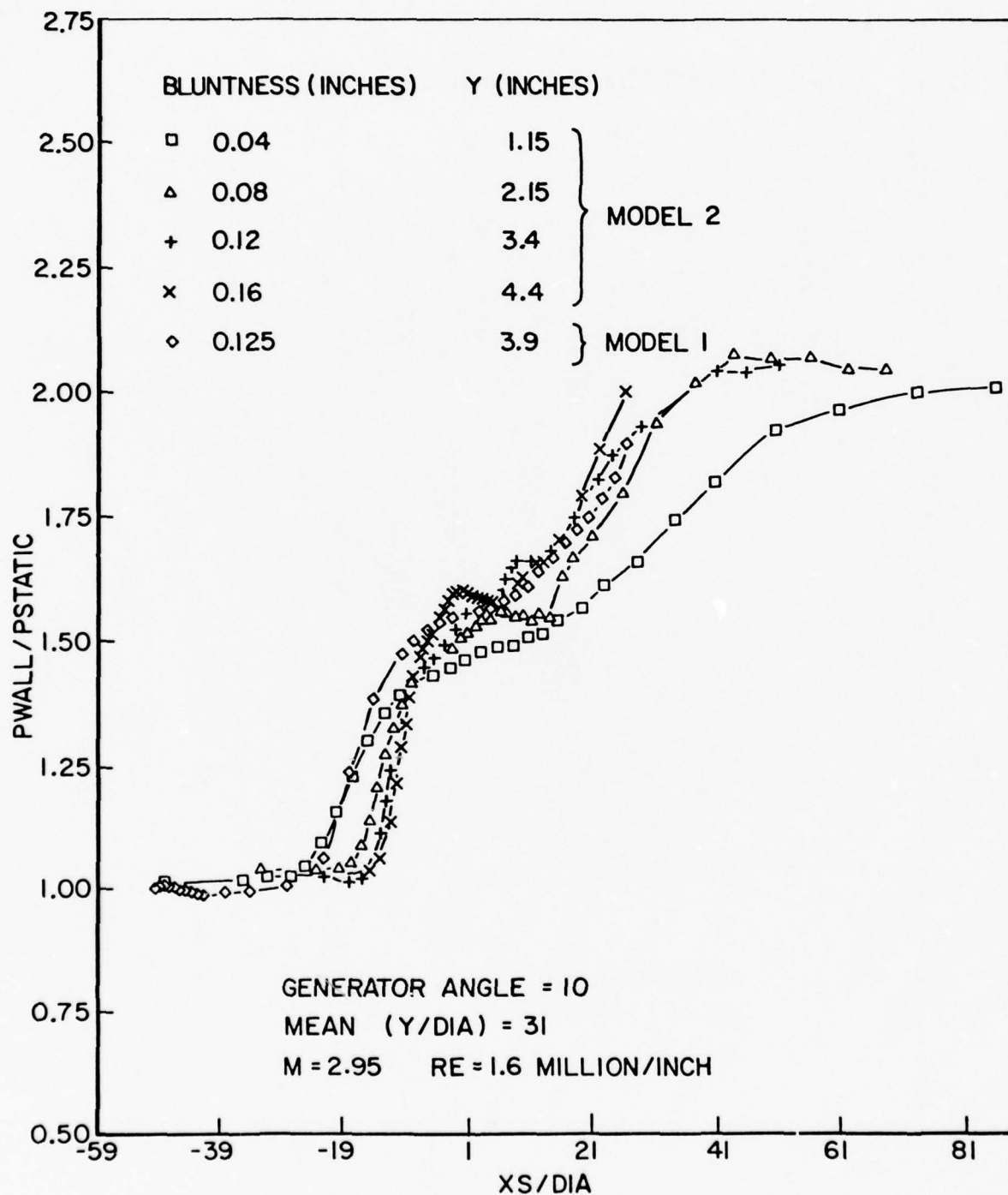


Figure 12. Pressure Distributions as a Function of X_S/D for $Y/D = 31$.

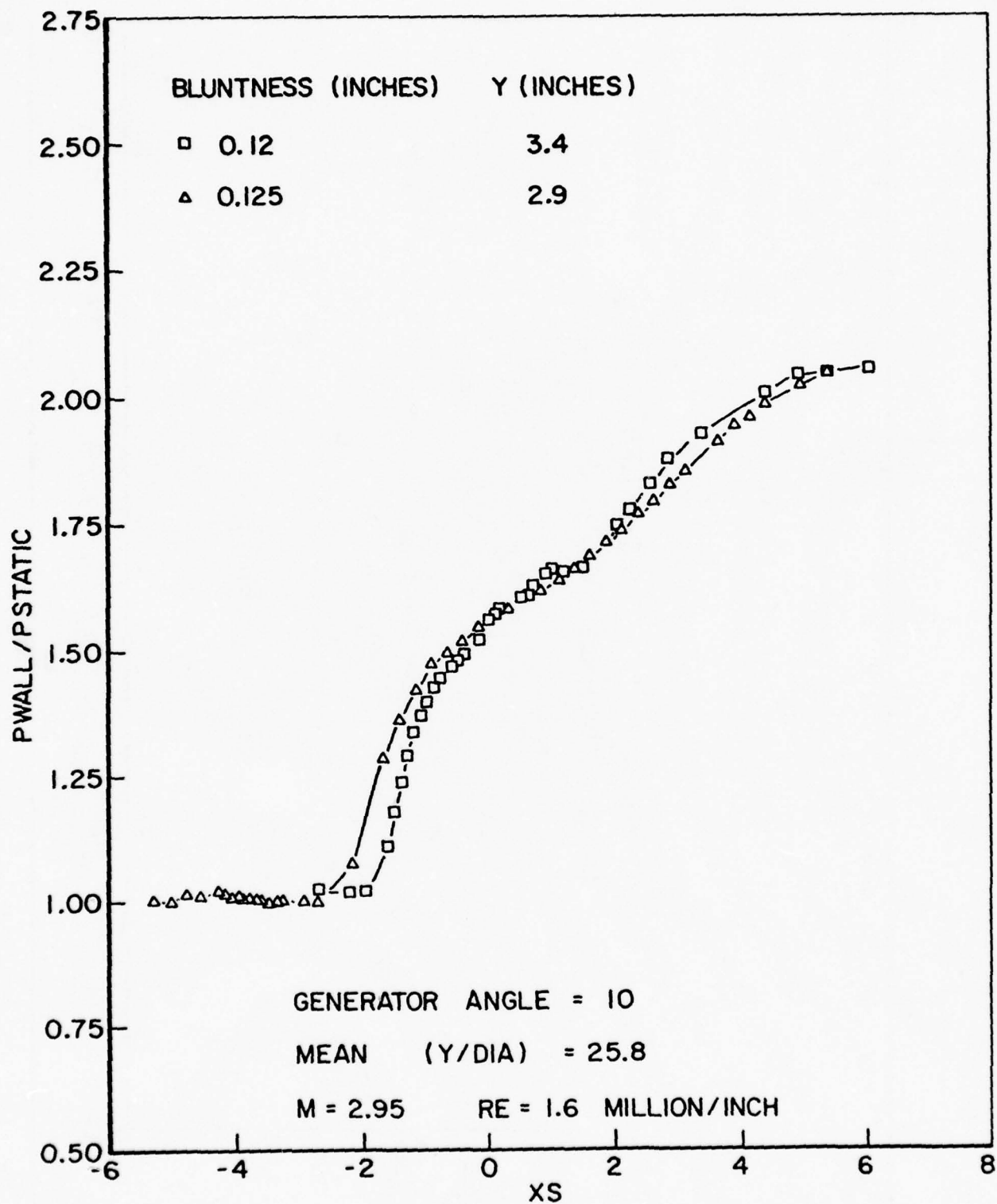


Figure 13. Influence of Incoming Boundary Layer Thickness on the Interaction Pressure Distribution.

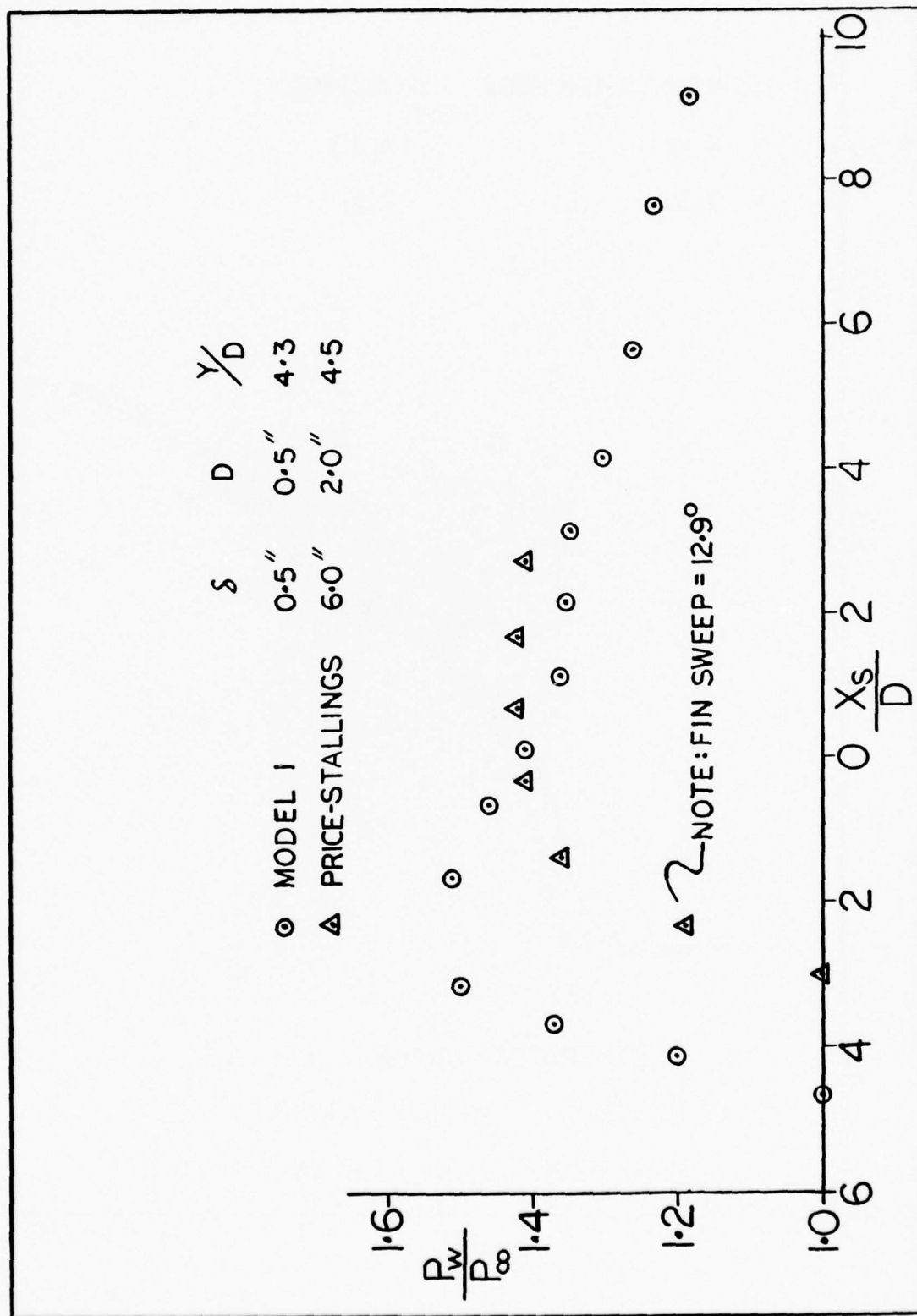


Figure 14. Comparison with Data of Price and Stallings.

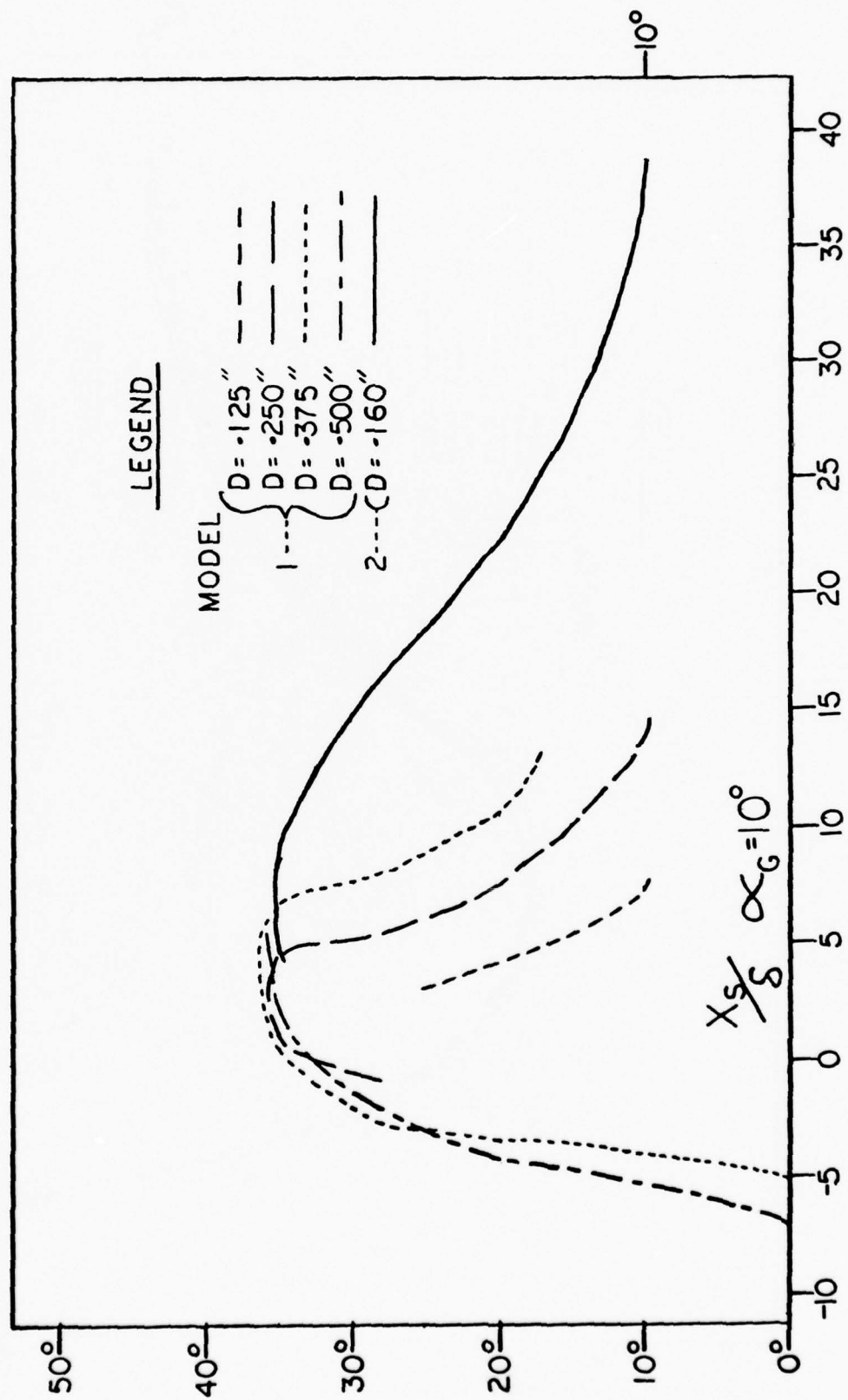


Figure 15. Surface Oil Flow Angles as a function of X_s/δ for $Y/D = 8.7$.

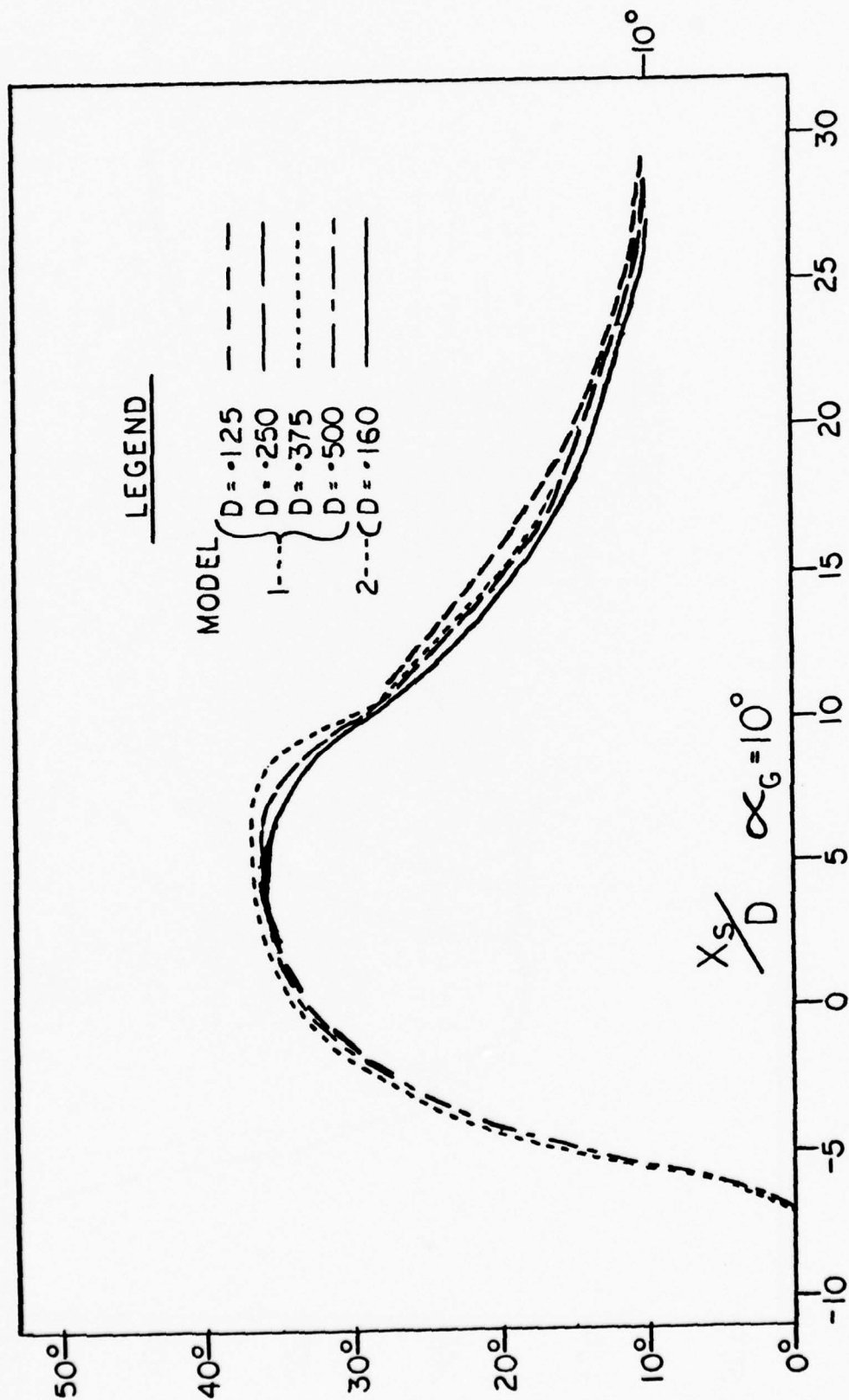


Figure 16. Surface Oil Flow Angles as a Function of X_s/D for $Y/D = 8.7$.

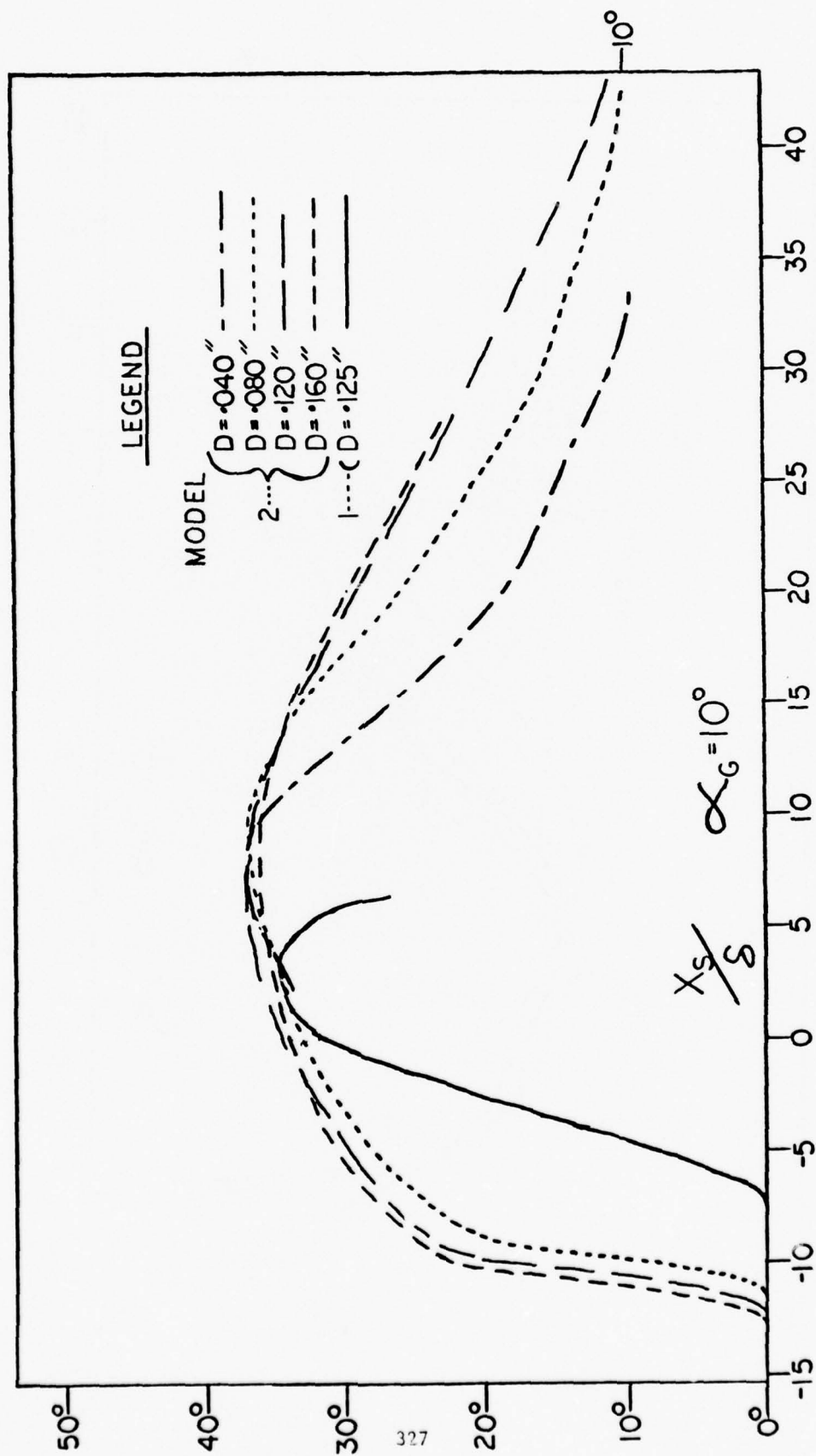


Figure 17. Surface Oil Flow Angles as a Function of X_s/δ for $Y/D = 31$.

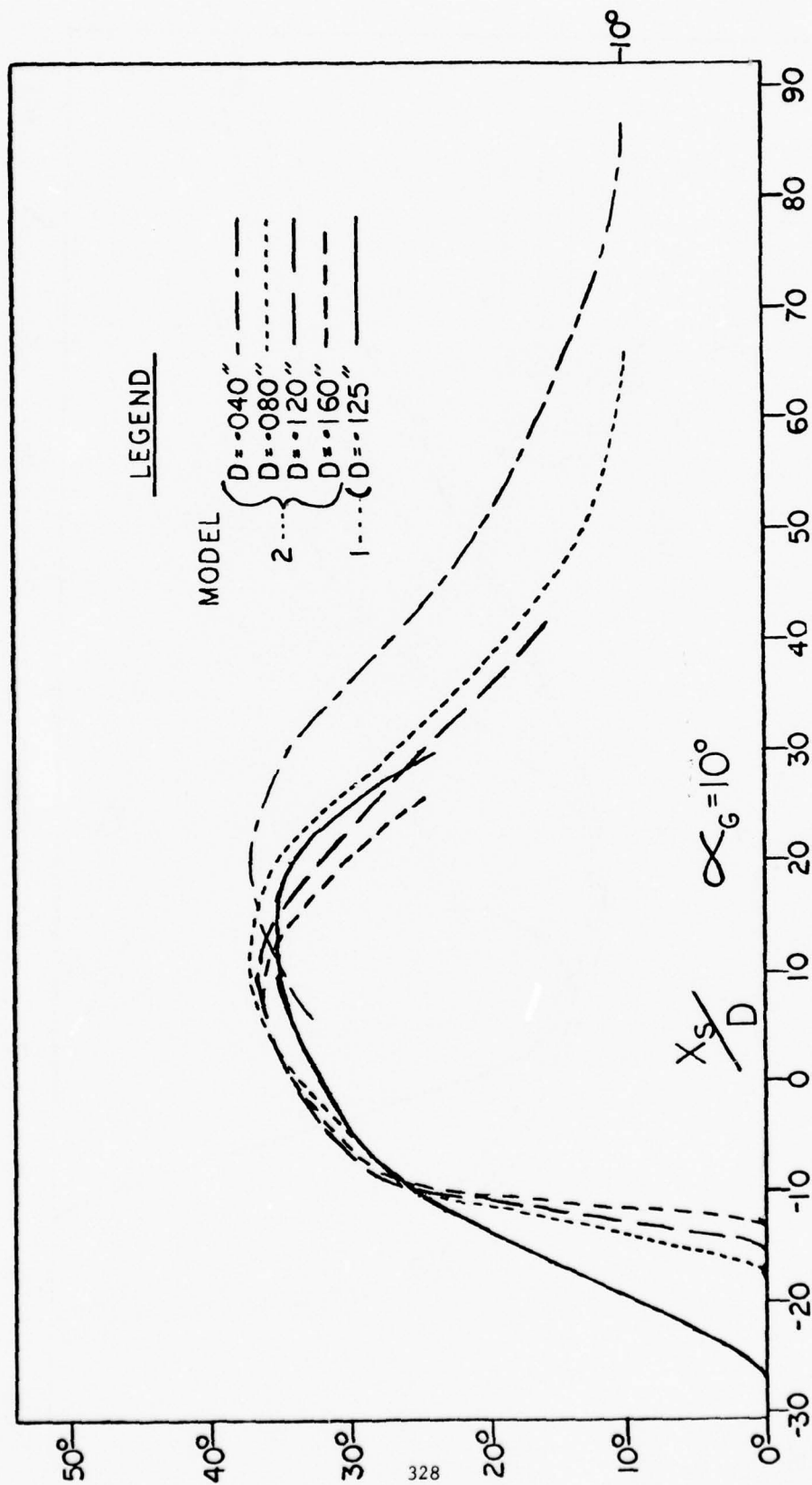


Figure 18. Surface Oil Flow Angles as a Function of X_s/D for $Y/D = 31$.

Two-Dimensional Supersonic Jet Impingement on a Flat Plate

by

T. F. Zien, K. Y. Chien and R. T. Driftmyer

Naval Surface Weapons Center
Silver Spring, Maryland

Abstract

A study of the flow field associated with a two-dimensional, supersonic jet impinging normally on a flat plate is reported. Two wedge nozzles manufactured at the design Mach numbers of 1.75 and 2.75, respectively, were used to provide the jet. Experimental results of some typical pitot surveys of the free jet are first presented to indicate the quality of free jet produced by the simple nozzles. Results of some surface pressure measurements and the shock measurements of the impingement flow are then presented and discussed. A brief description of an approximate theory based on the method of integral relations is also included, and the theory is used to compare with the experiment.

1. Introduction

It has been shown⁽¹⁾ that the impingement of a supersonic jet on an aerodynamic surface (e.g., the control fin of a missile) represents the basic mechanism responsible for the most severe case of aerodynamic heating associated with the shock-interference phenomena. However, a rational and practical theory for this basic problem of jet impingement appears lacking at the present time and, as a consequence, a reliable and practical method for predicting such heating phenomena is not yet available. To be sure, there have been recent attempts by Tannehill^(2,3) to solve the two-dimensional shock interference flow field and the associated heat transfer problem based on a time-dependent finite-difference solution of the full Navier-Stokes equations. Although their attempts are ambitious and seemingly successful, the strictly numerical nature of the approach and the excessive computer time required for a solution only reassert the continuing need for a simple, analytical method for providing physical insight into the phenomena and for practical use in the design studies. It is with the ultimate objective of fulfilling this need that the present investigation of the supersonic jet-impingement problem is undertaken. Of course, the jet-impingement flow has its basic importance in itself, and has numerous other applications.

This paper reports on the theoretical and experimental results of the supersonic jet-impingement studies. First, an approximate theory for the flow associated with an inviscid, supersonic, isentropic and uniform jet impinging normally on a flat plate is briefly described. Experimental results of the jet-impingement study in a two-dimensional configuration are then presented. Results are mainly for a jet with isentropic condition at the nozzle exit. The jet was produced by two simple wedge-nozzles at two designed Mach numbers of 1.75 and 2.75, respectively. The experimental results include surface pressure distributions and schlieren photographs of the shock wave patterns, and the results are compared with the theory whenever appropriate. Finally, some conclusions suggested by the comparison are drawn and discussed. Many details are omitted to conserve space, but appear in Ref. 4.

Related experiments of supersonic jet impingement flows previously reported include the work of Hunt and others^(5,6) for the axisymmetric jet and Pollard and Bradbury⁽⁷⁾ for the two-dimensional jet. The work of Ref. (7) was carried out in relation to V/STOL applications, and the emphasis was placed on the case of relatively large nozzle-to-surface distances when turbulent mixing and viscous entrainment by the jet were important. On the other hand, we are concerned with the situation where the ratio of the nozzle-to-surface distance to the nozzle exit width is about unity and the viscous effects are believed to be of secondary importance.

2. Description of Theory

The theoretical computations will be abstracted briefly here. More details are available in Refs. (4) and (8). The geometrical arrangement is a plane jet at normal impingement, with the origin of the coordinate system at the stagnation point of the flat surface. The problem is considered to be steady and two-dimensional, with x - and y -axes along and perpendicular to the plate surface, respectively, and the free-stream jet flow is in the negative y -direction. For simplicity, the gas is assumed to be inviscid and obeys the perfect gas law. Ahead of the shock wave, the jet is assumed to be uniform with constant static pressure equal to the ambient value.

The scheme III of the method of integral relations (MIR) was used in the formulation of the approximate theory. MIR requires that the governing partial differential equations be cast into divergence form. In the one-strip formulation, we have employed the modified continuity equation (obtained by combining the relation of constant entropy along streamlines, the energy and the continuity

equations). Since the plate surface is a streamline, an algebraic relation between the surface pressure and the surface velocity can be obtained to replace the x-momentum equation. The other governing equations are: (i) the energy equation (which is algebraic), (ii) the y-momentum equation, (iii) the geometric relation between the detachment distance of the shock wave (Δ_s) and the shock angle (σ_s), and (iv) the geometric relation between the detachment distance of the wall jet (Δ_j) and the angle of the upper boundary of the wall jet (σ_j). All angles are measured relative to the jet direction. The flow field can be divided into two regions, a shock-layer region ($0 \leq \tilde{x} \leq 1$) and a wall-jet region ($1 \leq \tilde{x} \leq \eta$), where $\tilde{x} \equiv x/R$ (R is the jet half-width) and $x = \eta$ is the location of the sonic point on the plate surface. The two regions are related by the requirements that, at $\tilde{x} = 1$, the flow variables are continuous, $\Delta_s = \Delta_j$, and σ_s and σ_j are governed by the Prandtl-Meyer expansion relation. The boundary conditions are: the symmetry conditions at $\tilde{x} = 0$, the Rankine-Hugoniot conditions at $y = \Delta_s$, and the constant entropy conditions along $y = 0$ and $y = \Delta_j$.

By integrating first the y-momentum equation and the modified continuity equation across the shock layer and then from $\tilde{x} = 0$ to $\tilde{x} = 1$, we obtain a system of nonlinear algebraic equations. The procedure is repeated in the wall-jet region. A regularity condition at the surface sonic point is imposed to close the system. Note that the numerical difficulty of satisfying the regularity condition at $\tilde{x} = \eta$ peculiar to the scheme I of MIR is completely avoided in the present scheme.

3. Description of Experiment

3.1 Experimental Hardware and Setup

Two stainless steel wedge nozzles were manufactured at the design Mach numbers of 1.75 and 2.75, respectively, to provide for the supersonic jets used in the experiment. The aerodynamic design of the nozzle was based on the simple inviscid, one-dimensional flow model for air (perfect gas, $\gamma = 1.405$). The nozzles have the same exit width of 3.81 cm ($1\frac{1}{2}$ in.) and the same exit area of 3.81 cm x 5.08 cm ($1\frac{1}{2}$ in. x 2 in.). The semi-wedge angle was $2^\circ 13'$ for the Mach 1.75 nozzle, and $5^\circ 34'$ for the Mach 2.75 nozzle. A sketch of the nozzle is shown in Fig. 1.

The test plate was made of stainless steel, and instrumented with a row of five pressure taps evenly spaced across a 2.54 cm (1 in.) span in the center portion of the plate (entire plate width = 5.74 cm (2.26 in.)). The pressure taps were aligned in the depth direction of the nozzle block in order to determine the two-dimensionality of the impingement flow field in the experiment. Two glass ported side plates were rigidly fixed to the edges of test plate to constrain the flow in order to achieve the desired two-dimensionality. These side plates were made of schlieren quality glass so that photographs could be taken of the impinging jet and the associated shock system.

The entire test plate/side plates assembly was connected to an axial traverse mechanism with controlled translational motion, and the assembly was made to slide relative to the (stationary) nozzle during the measurement. A continuous pressure signature on the test plate was thus recorded. The plate/nozzle package used in the experiment is shown in Fig. 2 (only one side plate is shown).

The nozzle/plate assembly was installed in the test section of the Supersonic Wind Tunnel No. 2 at the Naval Surface Weapons Center with the nozzle axis aligned in the vertical direction perpendicular to the (horizontal) test plate. We note that the primary reason for choosing this facility to conduct our experiment was to take advantage of the existing vacuum capacity of the tunnel to control the back pressure of the jet.

A pitot rake assembly was designed and manufactured with five 0.159 cm (1/16 in.) O.D. stainless steel tubes as pitot probes. The five probes were aligned in the same direction as the pressure taps on the test plate. The probes extended vertically upward and were spaced 0.635 cm (1/4 in.) apart, center to center. The pitot rake was used to survey the free jet, in the absence of the test plate/side plate package. When surveying the free jet, the rake was fastened to the axial traverse mechanism of the wind tunnel, and was moved across the width of the nozzle exit in a controlled manner.

All pressure measurements were made with the strain gage type pressure transducers. The stagnation temperature was measured with a copper-constantan thermocouple referenced to 0°C. The test air was supplied from bottled-filled air normally stored at pressure up to 3000 psia.

3.2 Experimental Procedure

The experiment with each nozzle began with a pitot survey of the free jet, using the pitot rake described in section 3.1, to establish the actual Mach number and to determine the uniformity and quality of the two-dimensional jet.

The survey was made at two distances downstream of the nozzle exit, $\Delta_2 = 0.3175$ cm (1 in.), in an effort to determine any possible changes in the properties of the jet during its passage through the quiescent air. For each value of Δ_2 , two values of the stagnation pressure were used.

Upon completion of the pitot survey of a wedge nozzle, the pitot rake was removed from the test cell of the wind tunnel, and the test plate/side plate package was carefully assembled and installed in the test chamber for surface pressure measurements. For each jet Mach number, two values of Δ_1 were used in measuring the surface pressure distribution.

4. Experimental Results

4.1 Free Jet Pitot Survey

Typical results of the pitot survey are shown in Figs. 3 and 4. In these figures, the Mach number distribution was deduced from the corresponding pitot pressure distribution by assuming that the total pressure upstream of the normal shock of the pitot tube is the same as the stagnation pressure, P_0 . We note that the Mach number distribution of the free jet stays practically the same further downstream at $\Delta_2 = 2.54$ cm for both nozzles (see Ref. (4)). The free jet was shown to be uniform in both width and depth directions to about 5% or better for both Mach numbers, suggesting the good quality of the jet produced by the simple nozzles.

4.2 Surface Pressure

The surface pressure results for nearly isentropic jet impingement are shown in Figs. 5 and 6, corresponding to the Mach 1.75 nozzle and Mach 2.75 nozzle, respectively.

Fig. 5 summarizes the surface pressure data obtained in the test with Nozzle No. 1. The surface pressure was measured by five pressure taps, P_1 through P_5 along the depth of the nozzle. Characteristically, the readings of the three middle taps, P_2 , P_3 and P_4 agreed to within about 3% in the region of interest, $-1 \leq \tilde{x} \leq 1$, and the readings of P_1 and P_5 generally differed by 6~10% from the three middle ones in this region. This suggests that some three-dimensional effects were still present despite the use of the side plates. Therefore, it was decided to disregard the readings of P_1 and P_5 , and use the average readings of P_2 , P_3 and P_4 for the surface pressure data. This was the procedure used in the data analysis for both nozzles.

The pressure data of the three different runs with $\Delta_1 = 5.08$ cm are seen to agree very closely, and the expected symmetry in the data with respect to the nozzle symmetry plane is clearly visible. Therefore, the good quality of the experimental results and their high reproducibility seem assured. The data with $\Delta_1 = 6.35$ cm are also included in Fig. 5 to indicate the effect of Δ_1 on the surface pressure distribution. Note that in the ideal case of a uniform, isentropic, inviscid jet as assumed in the theory, Δ_1 , should have no effect on the flow. However, in the experiment, the effect seemed to exist as the data showed a distinct, though slight, deviation from those of the other three runs. The effect of Δ_1 on surface pressure apparently becomes more pronounced for an underexpanded jet (Ref. (4)).

Fig. 6 shows the results of surface pressure measurements with Nozzle No. 2. As can be seen, the expected symmetry of the pressure distribution and the close agreement among the data for different P_0 continue to exist in this series of test.

4.3 Plate-Shock Measurements

The schlieren photographs of Run 23 and Run 37 with Nozzle No. 1 show the shock wave clearly, and were used to measure the shock shape and position. The shock measurements made from the photographs are shown in Fig. 7 where Δ_s is the vertical distance of the shock measured from the plate surface. The results of the two runs appear to be less consistent than the results of surface pressure for the corresponding runs. We only note here that the results of the shock measurement in the Nozzle No. 2 series are very similar to those of the Nozzle No. 1 series (Ref. (4)).

5. Discussion and Conclusion

The measured surface pressure distribution and shock wave patterns of the impingement flow field are all compared with the theoretical calculations.

In the comparison of the surface pressure results (Figs. 5 and 6), it is seen that the agreement is rather unsatisfactory if the theoretical results are based on the average free jet Mach numbers, $M_j = 1.85$ and $M_j = 2.77$, respectively, determined from the pitot surveys. In particular, the measured surface pressures at the stagnation point ($x = 0$) do not correspond to the total pressures behind the normal shock at the respective free jet Mach numbers. This discrepancy suggests the introduction of an "effective" jet Mach number, $(M_j)_{\text{eff}}$, in the impingement flow. $(M_j)_{\text{eff}}$ is based on the measured surface pressure at the

stagnation point, assuming isentropic flow between the plate and the downstream side of the shock caused by the plate. In fact, Gummer and Hunt⁽⁵⁾ based the determination of their jet Mach number on such a pressure measurement in their axisymmetric jet impingement experiment, in the absence of a pitot survey of the free jet. The "effective" jet Mach number was found to be 2.10 in the experiment with the first nozzle and 2.60 in the experiment with the second nozzle. The theoretical surface pressure distributions based on $(M_j)_{eff}$ show reasonably good agreement with the measured distributions, especially near the stagnation point where the most severe heating is expected to take place.

In view of the uncertainties and nonuniformities existing in the ambient conditions of the experiment, notably the difficulty in maintaining a uniform back pressure in the semi-confined configuration used in the surface pressure measurement, it is difficult to expect that the impinging jet had a constant and uniform Mach number equal to that of the freely expanding jet. Other complications such as viscous effects which could become more pronounced in a confined space than in an open space could also contribute to the deviation of the Mach number of the jet from its free expansion value. Therefore the use of $(M_j)_{eff}$ in lieu of M_j in the comparison between theory and experiment does not seem unjustified. Note that $(M_j)_{eff}$ differs from M_j only by about 7% in the Mach 2.77 experiment, although the difference is in the reversed direction relative to that in the Mach 1.85 experiment.

The experimental data of shock measurements are not as consistent as the surface pressure data, and a considerable data scatter can be seen. The scatter reflects, among other things, the optical difficulty in photographing a flow field of a depth of 5.74 cm (the width of the test plate). The shock trace can, at best, be taken as the projection of the shock envelope averaged over the field depth.

The measured shock height is greater than the theoretical predictions based on the free jet Mach number. The use of the effective Mach number would improve the agreement for the Mach 2.77 case, but further deteriorate the agreement for the Mach 1.85 case. In light of the large scatter among the experimental data themselves, the comparison between theory and experiment on the shock shapes and locations must be viewed as inconclusive at present. It provides insufficient grounds either to affirm or to negate the concept of effective jet Mach number.

In conclusion, we enumerate the following observations based on the present study: (1) the simple wedge nozzles appear adequate for providing two-dimensional

free jets of good quality; (2) the two-dimensionality of the plate pressure distribution in the jet-impingement experiment was achieved in the center portion of the plate in the present semi-confined configuration; (3) the semi-confined configuration apparently caused the Mach number of the impinging jet to deviate from its value based on the free expansion condition, and the "effective" jet Mach number of the impinging jet could be determined from the surface pressure at the stagnation point; (4) the simple approximate theory seems adequate to predict the pressure distribution on the plate surface; and (5) the considerable scatter in the measured shock shape and location makes it difficult to draw any definitive conclusions from the comparison between theory and experiment regarding the accuracy of the theory in predicting the shocks.

Acknowledgment

This work was supported by Naval Air Systems Command, AIR320C, under the cognizance of Mr. W. C. Volz whose encouragement is greatly appreciated. The authors also gratefully acknowledge some enlightening discussions with Dr. B. L. Hunt of the University of Bristol, England.

References

1. Edney, B., "Anomalous Heat Transfer and Pressure Distributions on Blunt Bodies at Hypersonic Speeds in the Presence of an Impinging Shock," FFA Report 115, The Aeronautical Research Institute of Sweden, Stockholm, 1968.
2. Tannehill, J. C., Holst, T. L. and Rakich, J. V., "Numerical Computation of Two-Dimensional Viscous Blunt Body Flows with an Impinging Shock," AIAA Journal Vol. 14, No. 2, Feb. 1976, pp. 204-211.
3. Tannehill, J. C., Holst, T. L., Rakich, J. V. and Keyes, J. W., "Comparison of a Two-Dimensional Shock Impingement Computation with Experiment," AIAA Journal, Vol. 14, No. 4, Apr. 1976, pp. 539-541.
4. Zien, T. F., Chien, K. Y. and Driftmyer, R. T., "Two-Dimensional Supersonic Jet Impingement on a Flat Plate," AIAA Paper No. 78-208, AIAA 16th Aerospace Sciences Meeting, Huntsville, Ala., 16-18 January 1978.
5. Gummer, J. H. and Hunt, B. L., "The Impingement of a Uniform, Axisymmetric, Supersonic Jet on a Perpendicular Flat Plate," The Aeronautical Quarterly, Vol. 22, Pt. 4, Nov. 1971, pp. 403-420.

6. Carling, J. C. and Hunt, B. L., "The Near Wall Jet of a Normally Impinging, Uniform, Axisymmetric, Supersonic Jet," Journal of Fluid Mechanics Vol. 66, Pt. 1, 1974, pp. 159-176.
7. Pollard, D. J. and Bradbury, L. J. S., "Impingement of a Two-Dimensional Supersonic Jet upon a Normal Ground Surface," AIAA Journal, Vol. 14, No. 8, Aug. 1976, pp. 1095-1098.
8. Chien, K.-Y., "Normal Impingement of a Supersonic Jet on a Plane--A Basic Study of Shock-Interference Heating," NSWC/WOL/TR 75-195, Naval Surface Weapons Center, White Oak Laboratory, Silver Spring, Md., 1975.

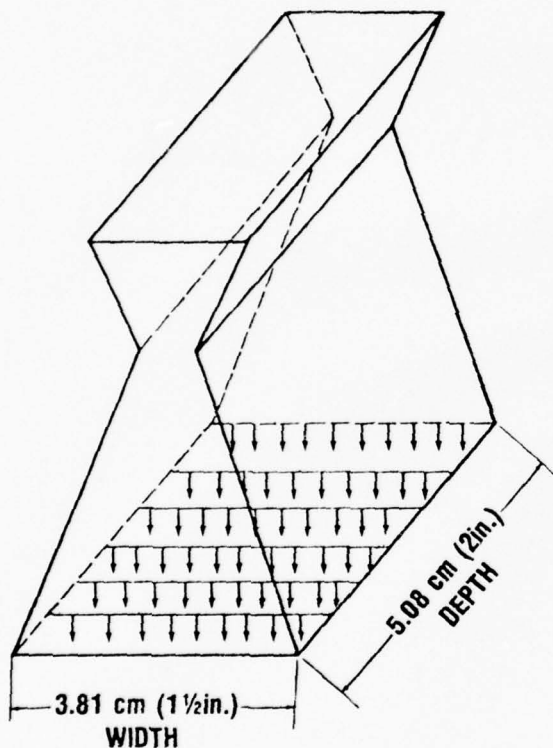


Fig. 1 Sketch of Wedge Nozzles

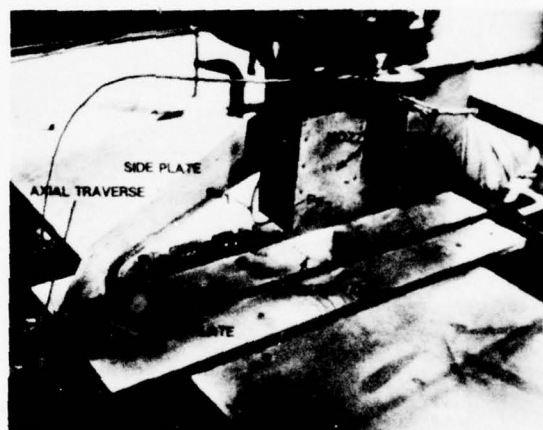


Fig. 2 Experimental Setup

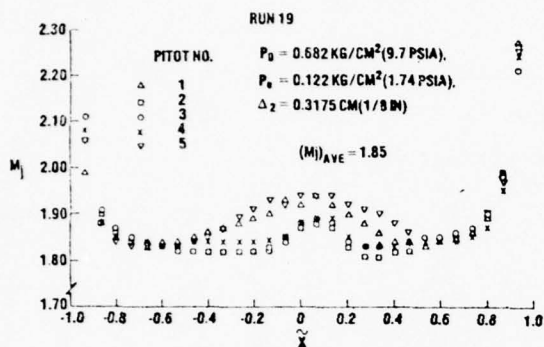


Fig. 3 Free Jet Mach Number:
Nozzle No. 1

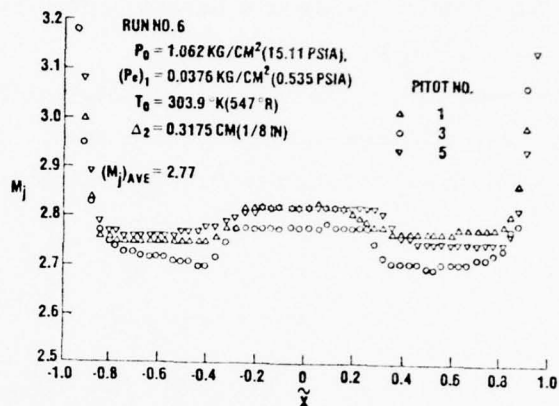


Fig. 4 Free Jet Mach Number:
Nozzle No. 2

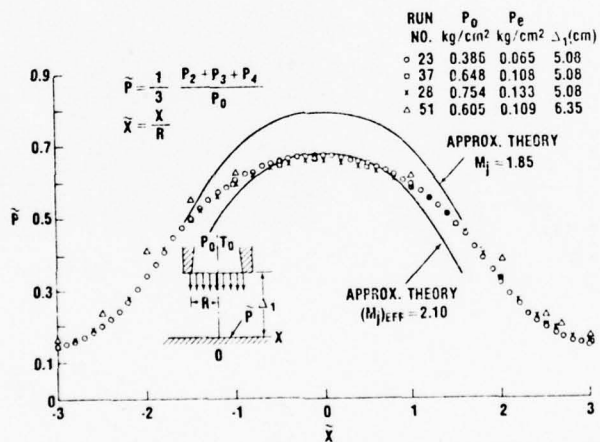


Fig. 5 Surface Pressure Results:
 $M_j = 1.85$

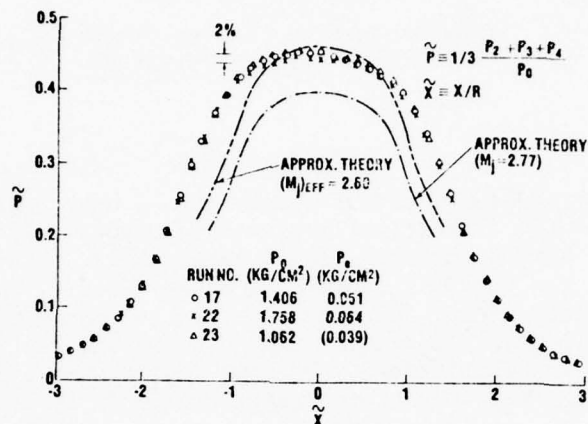


Fig. 6 Surface Pressure Results:
 $M_j = 2.77$

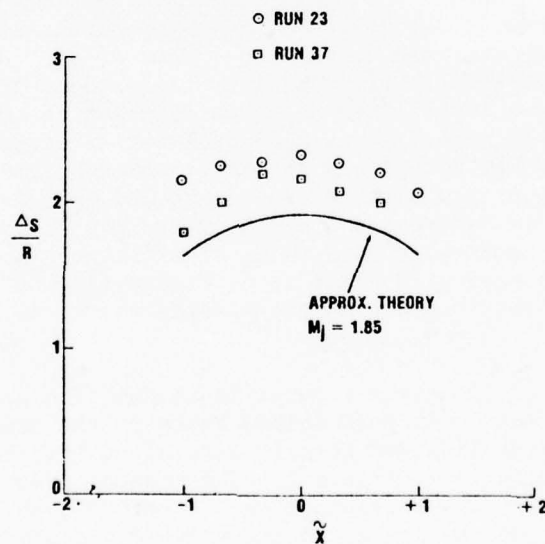


Fig. 7 Shock Measurements:
Nozzle No. 1

Three-Dimensional Calculation of Vortices Behind a Missile at Large Angles of Attack

by

Andrew H. Van Tuyl

Naval Surface Weapons Center
Silver Spring, Maryland

1. Introduction

At moderate angles of attack larger than 6 or 7 degrees, a slender missile is found to have two symmetrically placed vortices in its leeward flow field. As the angle of attack increases above about 30 or 40 degrees in the low subsonic range, the vortex pattern becomes asymmetric, and fluctuating side forces which may be larger in magnitude than the normal force are found. These side forces are most significant for Mach numbers less than about 0.8 and begin to disappear as the Mach number increases into the supersonic range. However, the effect of wake vortices on control surfaces is of importance at all Mach numbers.

The occurrence of these vortices is a viscous phenomenon, and is due to the separation of the boundary layer on the leeward side of the missile and the subsequent roll-up of the vortex sheet which forms along the line of separation. Determination of this separation line is very difficult both theoretically and experimentally. However, past work has shown that some of the main features of the vortex wake can be calculated by means of potential theory after the location of separation has been determined. Most of the computational work so far has used the impulsive crossflow analogy (References 1 through 7, for example), in which a two-dimensional time dependent problem is considered in crossflow planes. While this method gives good qualitative agreement with experiment, it is only an analogy and should not be expected to give close quantitative agreement. A comparison between experiment and calculations by the crossflow analogy is given in References 8 and 9, where the discrepancy between theoretical and experimental results is seen to be significant. A three-dimensional method of calculation is needed in order to determine flow details such as the locations and strengths of vortices behind the missile which can now be determined only by experiment.

The purpose of the present paper is to describe progress in the development of a three-dimensional inviscid method based on the use of vortex filaments, given the separation line and certain data along it. The flow fields obtained are shown schematically in Figure 1. The present treatment will be restricted to incompressible or low subsonic flow. A method such as the present one will eventually be needed as part of an iterative procedure in which it is used together with a three-dimensional boundary layer calculation.

A related problem is the calculation of the roll-up of the vortex sheet which separates from the leading edge of a delta wing of small aspect ratio. This problem is easier than the present one because of the fact that the location of separation is known. Three-dimensional calculations for a wing with leading edge separation have been made in Reference 10, where the roll-up

of the vortex sheet is calculated, and in References 11 and 12, where the vortex sheet is replaced by discrete vortex filaments.

It will be assumed in the present method that the separation line is given either by calculation or experiment, and that some component of the inviscid flow on the surface is given at each point of the separation line. In particular, when the direction of the inviscid flow is known at the separation line, the conditions to be satisfied at the intersection of each vortex filament with the separation line are that both the normal component of velocity and the component of surface velocity perpendicular to the given direction vanish. As a first approximation, we can use the crossflow analogy as in Reference 6 and use the calculated location of the separation line and the calculated value of crossflow at the separation point in each crossflow plane as input to the three-dimensional method.

2. Description of the Method

The vortex sheet will be replaced by a number of discrete vortex filaments as in References 10 and 11, where each vortex filament consists of an arbitrary number of straight line segments such that the last segment is semi-infinite and in the direction of the free stream. The boundary condition of zero normal component of velocity at the surface of the missile is satisfied by using a surface source distribution. The XYZ Potential Flow Program of Reference 13, based on a method due to Hess and Smith, is being used as a starting point in the present development. The present method can now be described as follows:

1. The surface of the missile is covered by N quadrilaterals, on each of which a constant source density is to be determined.
2. K semi-infinite straight vortex filaments with unknown circulations are placed along the given separation line so that they are oriented in the direction of the free stream.
3. The N unknown source densities and K unknown circulations are found by solving a system of $N + K$ linear algebraic equations of the form

$$a_{11} w_1 + a_{12} w_2 + \dots + a_{1,N+K} w_{N+K} = b_1$$

$$a_{21} w_1 + a_{22} w_2 + \dots + a_{2,N+K} w_{N+K} = b_2$$

.....

$$a_{N+K,1} w_1 + a_{N+K,2} w_2 + \dots + a_{N+K,N+K} w_{N+K} = b_{N+K} ,$$

where the w_i are equal to the source densities for $i = 1, 2, \dots, N$, and to the circulations for $i = N+1, N+2, \dots, N+K$. These equations express the vanishing of the normal component of velocity at the null points of the quadrilaterals, in a coordinate system fixed in the missile, and the surface velocity condition at the intersections of the vortex filaments with the separation line.

4. The positions and directions of the segments of the vortex filaments are changed iteratively until they are aligned with the flow velocity.
5. Steps 3 and 4 are repeated until the change in direction of the segments is less than a prescribed amount.

The vortex filaments are attached to the body at the null points in this calculation, since the straight vortex segment attached to a null point induces no velocity there. The velocity at the surface is calculated only at the null points, and the velocity at other points of the surface is obtained by interpolation.

It is necessary to place a small core about each vortex filament as is done in Reference 12 and by others, in order to avoid excessively large effects between closely neighboring vortices. The velocity inside such a core remains finite, while the velocity outside is that due to the vortex filament.

3. Calculation of Roll-Up

In Reference 11, calculation of the roll-up of vortex filaments in a given velocity field was carried out iteratively so that each segment becomes aligned with the direction of the velocity at its upstream endpoint. A different procedure was used in Reference 12, in which the i th segment of a filament is aligned with the velocity at the point shown in Figure 2. This point is located on the extension of the $(i - 1)$ st segment at a distance βs_i from the upstream end of the i th segment, $0 \leq \beta < 1$, where s_i is the length of the i th segment. This reduces to the method of Reference 11 when $\beta = 0$. In Reference 12, calculations using equal segment lengths were made with the initial configuration shown in Figure 3, in which two semi-infinite vortex filaments with equal circulations are parallel to a free stream with velocity magnitude unity. It was concluded that $\beta = 0.5$ and $\beta = 0.55$ are preferable to $\beta = 0$ for a given segment length, and that $\beta = 0.55$ gives the best accuracy.

In the present calculations, the procedure shown in Figure 2 is used. During each iteration, all segments are changed in a given order. Each filament is built up one segment at a time, starting at the body. The direction of the segment at the body is chosen in a special way which may depend on the geometry, and subsequent segments are added as in Figure 2. In calculating the velocity, the segment being changed is not taken into account. The velocity due to each segment is calculated by use of the Biot-Savart law. The calculation is stopped when the maximum of the distances through which the endpoints of the segments move during an iteration is less than a prescribed number ϵ .

4. Numerical Calculations

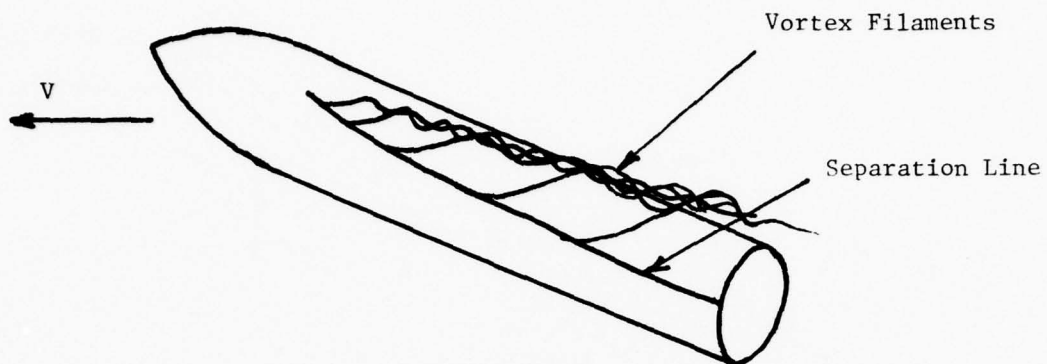
The section of the program which calculates roll-up was tested first by repeating the calculations of Reference 12. Starting from the configuration of Figure 3, calculations were carried out in which each filament consists of 24 equal segments and one semi-infinite segment parallel to the free stream. Figures 4 and 5 show the results of the calculations for $\beta = 0$ for segment lengths of 1.0 and 0.5, respectively, and Figure 6 shows the results for $\beta = 0.55$ and a segment length of 1.0. With $\epsilon = 0.001$, 6 iterations were required for $\beta = 0$ and 10 for $\beta = 0.55$. Figures 5 and 6 show that about the same accuracy is obtained with $\beta = 0.55$ and a segment length of 1.0 as with $\beta = 0$ and a segment length of 0.5, supporting the conclusion of Reference 12 that the use of $\beta = 0.55$ is the more accurate for a given segment length. Roll-up calculations involving 4 vortices lead to the same conclusion. We see that more iterations are required for $\beta = 0.55$ than for $\beta = 0$. However, a larger value of ϵ than the preceding can be used in the roll-up calculation until the final stages of the complete calculation.

The calculation of the source densities and circulations in the present method is being checked out in the case of symmetric flow past a tangent ogive-cylinder with 360 quadrilaterals on half the body. A program for subdividing the surface into quadrilaterals has been written which will allow null points to be placed on a given separation line. Vortex filaments are then attached to the body at these points.

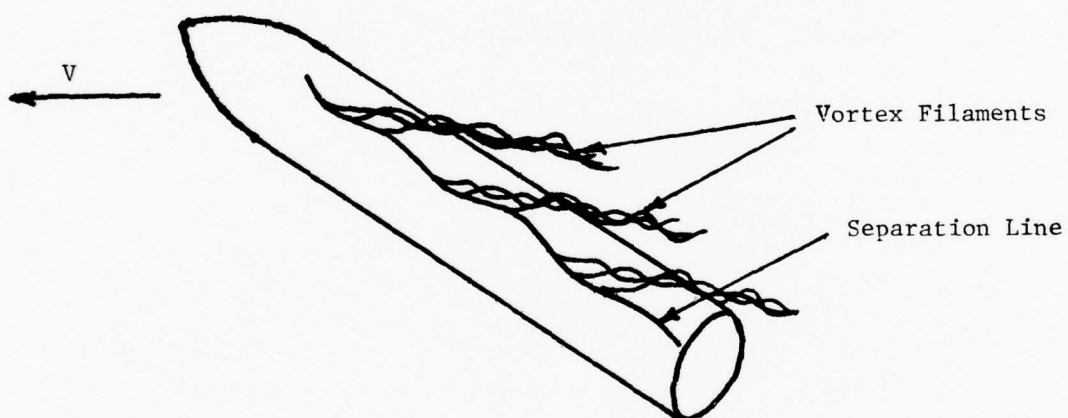
REFERENCES

1. J. A. F. Hill, "A Nonlinear Theory of the Lift on Slender Bodies of Revolution," Proceedings of the U. S. Navy Symposium on Aeroballistics, NAVORD Report 5338, Oct. 1954.
2. A. E. Bryson, Jr., "Symmetric Vortex Separation on Circular Cylinders and Cones," Journal of Applied Mechanics, Vol. 26, Dec. 1959, pp. 643-648.
3. L. H. Schindel, "Effects of Vortex Separation on the Lift Distribution on Bodies of Elliptic Cross Section," Journal of Aircraft, Vol. 6, 1969, pp. 537-543.
4. A. B. Wardlaw, Jr., "Prediction of Normal Force, Pitching Moment, and Yaw Force on Bodies of Revolution at Angles of Attack up to 50 Degrees Using a Concentrated Vortex Flow-Field Model," Naval Ordnance Laboratory, NOLTR 73-209, Oct. 1973.
5. A. B. Wardlaw, Jr., "Multivortex Model of Asymmetric Shedding on Slender Bodies at High Angles of Attack," AIAA Paper 75-123, Jan. 1975.
6. F. D. Deffenbaugh and F. J. Marshall, "Time Development of the Flow about an Impulsively Started Cylinder," AIAA Journal, Vol. 14, July 1976, pp. 908-913.
7. F. D. Deffenbaugh and W. G. Koerner, "Asymmetric Wake Development and Associated Side Force on Missiles at High Angles of Attack," AIAA Paper 76-364, July 1976.
8. P. J. Lamont, "The Out-of-Plane Force on an Ogive Nosed Cylinder at Large Angles of Incidence to a Uniform Stream," Ph.D. Thesis, University of Bristol, 1973.
9. P. J. Lamont and B. L. Hunt, "Pressure and Force Distributions on a Sharp-Nosed Circular Cylinder at Large Angles of Inclination to a Uniform, Subsonic Stream," Journal of Fluid Mechanics, Vol. 76, Oct. 1976, pp. 519-559.
10. J. A. Weber, G. W. Brune, F. T. Johnson, P. Lu, and P. E. Rubbert, "Three-Dimensional Solution of Flows over Wings with Leading-Edge Vortex Separation," AIAA Journal, Vol. 14, April 1976, pp. 519-525.
11. D. T. Mook and S. A. Maddox, "Extension of a Vortex-Lattice Method to Include the Effects of Leading Edge Separation," Journal of Aircraft, Vol. 11, Feb. 1974, pp. 127-128.

12. Vortex-Lattice Utilization, NASA SP-405, May 1976, page 163.
13. C. W. Dawson and J. S. Dean, "The XYZ Potential Flow Program," Naval Ship Research and Development Center Report 3892, June 1972.



(a) Symmetric Case



(b) Asymmetric Case

Figure 1. Vortex wake behind a missile at angle of attack.

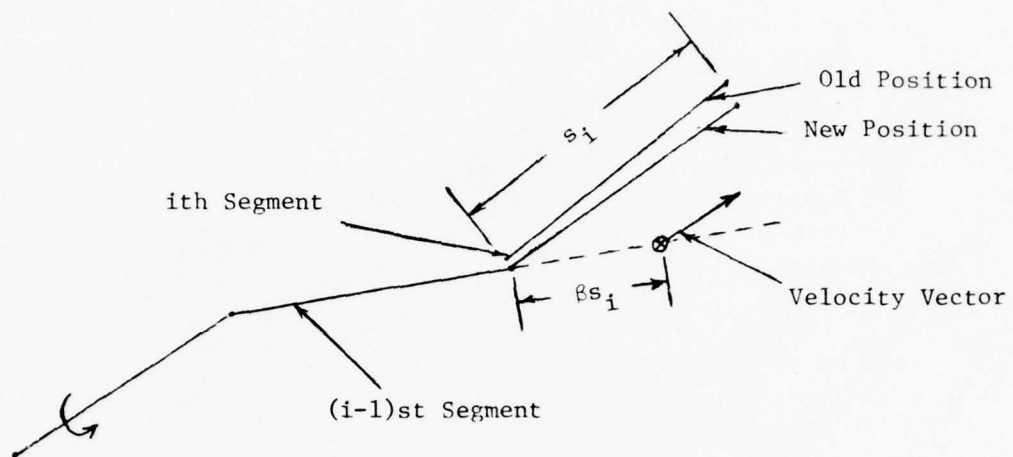


Figure 2. Procedure for roll-up calculation.

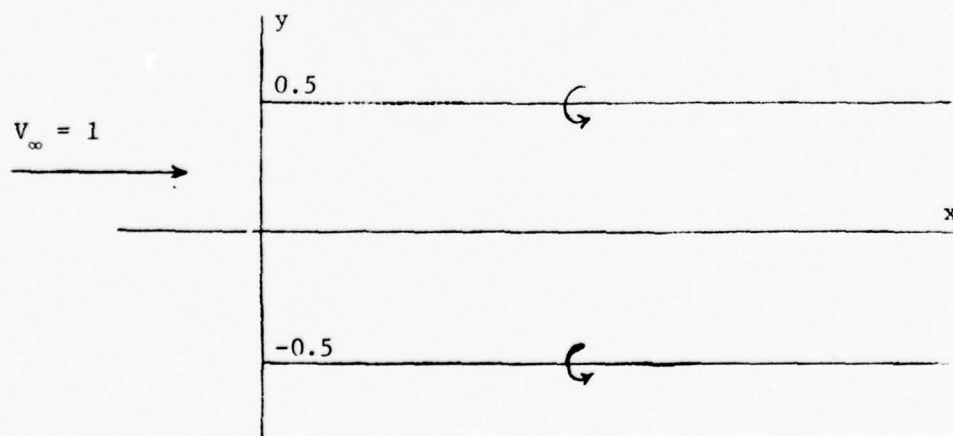
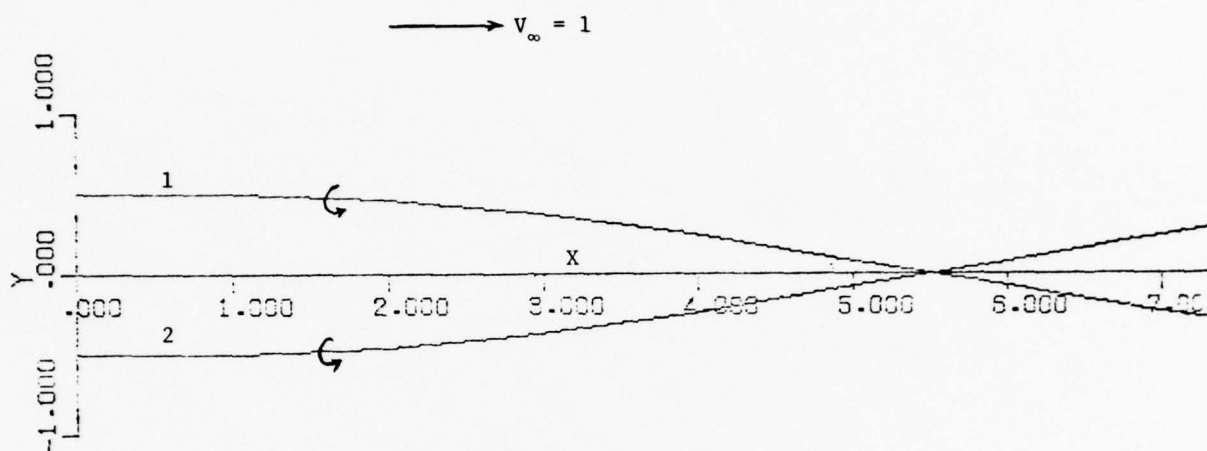
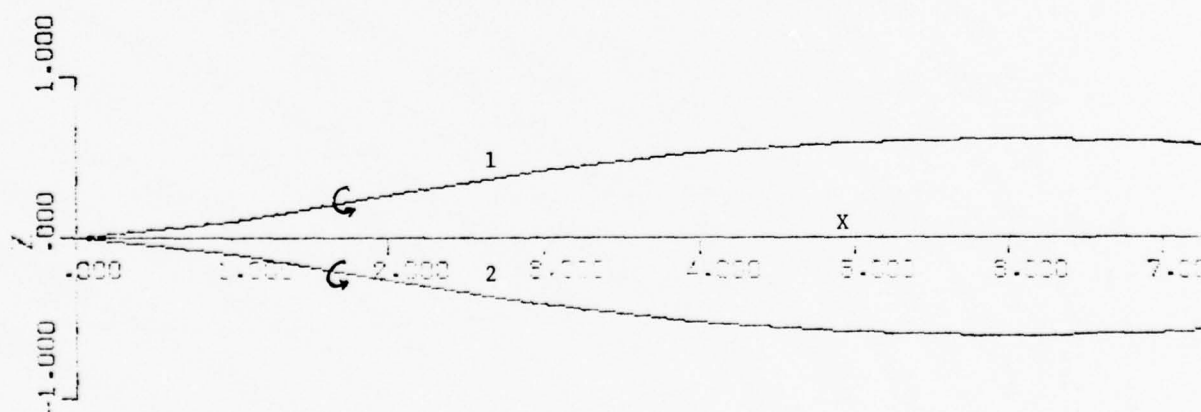


Figure 3. Initial configuration for roll-up calculation.

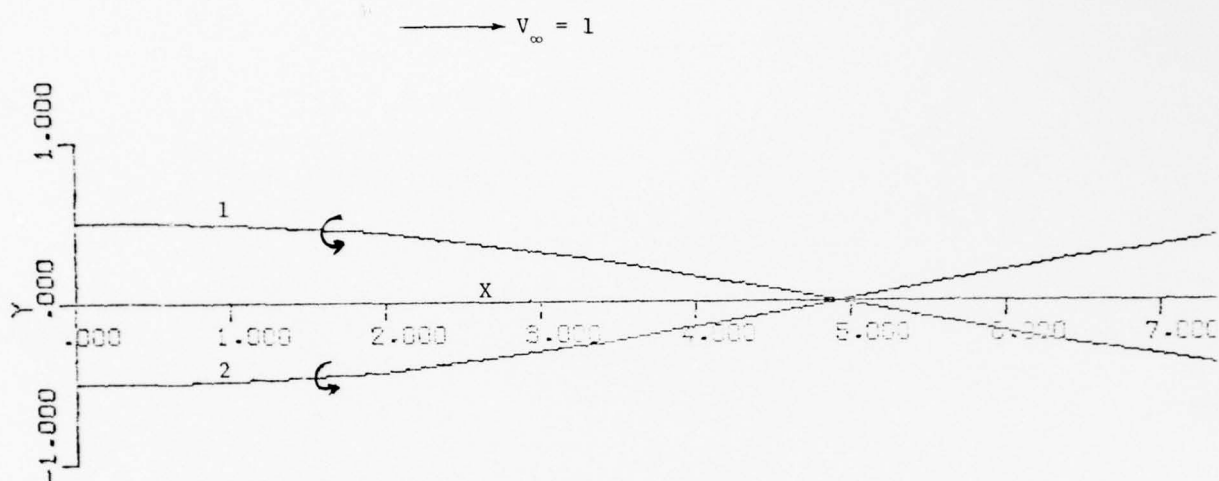


(a) Plan View

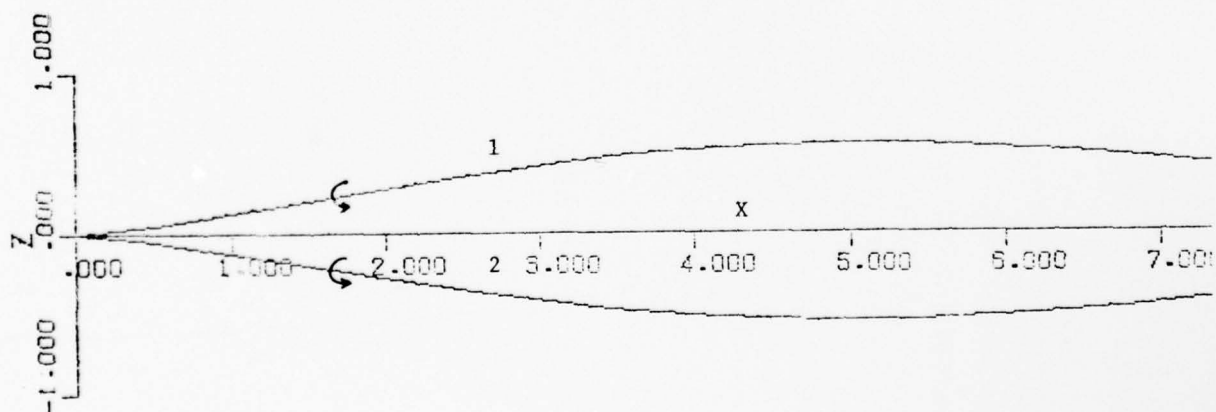


(b) Side View

Figure 4. Vortex roll-up calculation for $\beta = 0$, segment length = 1.0, and circulation = -0.4π .

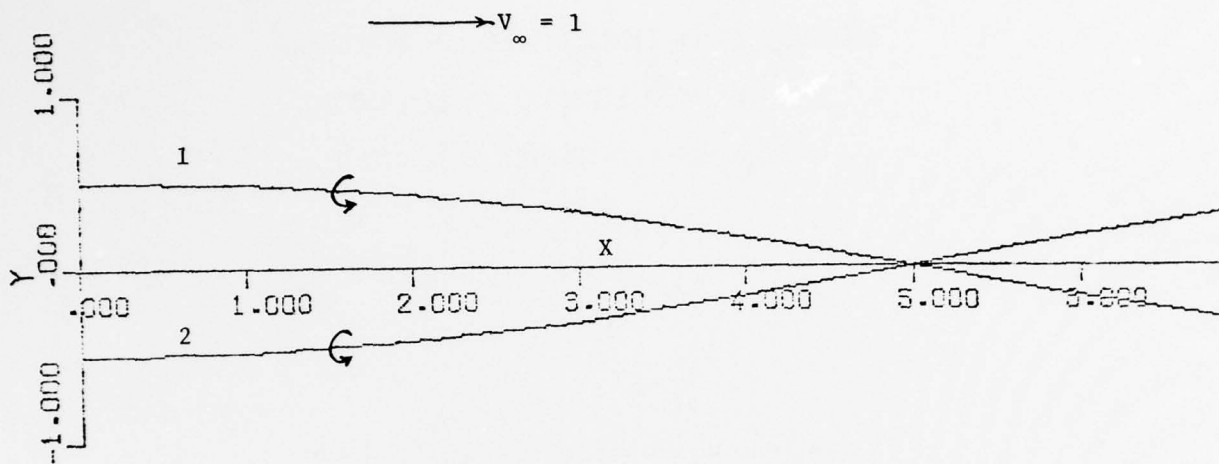


(a) Plan View

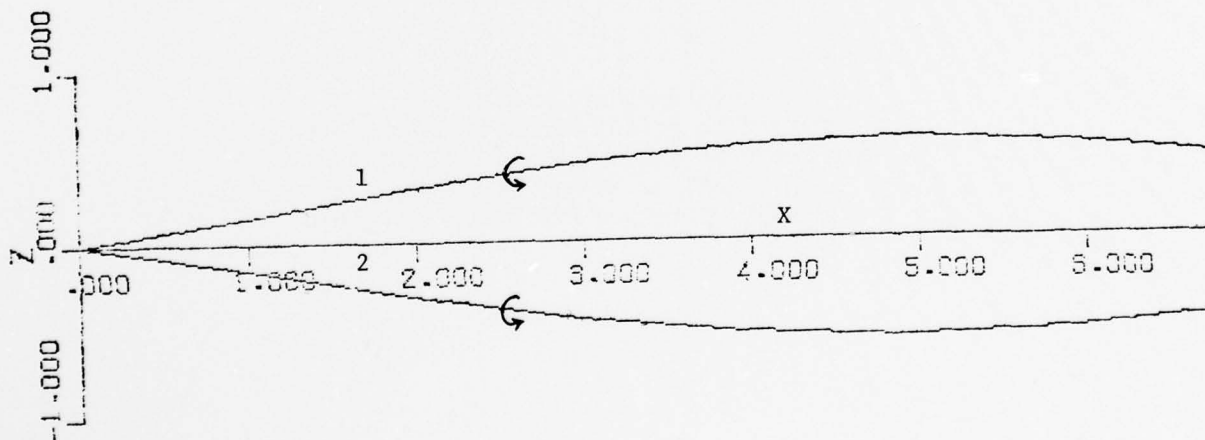


(b) Side View

Figure 5. Vortex roll-up calculation for $\beta = 0$, segment length = 0.5, and circulation = -0.4π .



(a) Plan View



(b) Side View

Figure 6. Vortex roll-up calculation for $\beta = 0.55$, segment length = 1.0, and circulation = -0.4π .

BOUNDARY LAYER FENCE METHOD FOR MEASURING
SURFACE SHEAR STRESS IN A SUPERSONIC,
HIGH REYNOLDS NUMBER FLOW FIELD

Anthony W. Fiore and Norman E. Scaggs

Aeromechanics Division
Air Force Flight Dynamics Laboratory
Air Force Wright Aeronautical Laboratories
United States Air Force
Wright-Patterson Air Force Base, Ohio

Presented at the 49th Semi-Annual
Meeting of the Supersonic Tunnel Association
Douglas Aircraft Company, El Segundo, California

17 - 18 April 1978

ABSTRACT

Experimental research on a boundary layer fence technique was conducted in the Air Force Flight Dynamics Laboratory's $M=3$ high Reynolds number wind tunnel located in Building 450, area B of Wright-Patterson Air Force Base, Ohio. The purpose of the research was to develop this technique for measuring the surface shear stress in a supersonic compressible turbulent boundary with near adiabatic wall condition for zero pressure gradient.

The measurements were made on the tunnel wall at a nominal Mach number of three. The Reynolds number was changed by two methods, i.e., changing the tunnel stagnation pressure and the measuring station. The resulting momentum thickness Reynolds number varied from 2×10^4 to approximately 60×10^4 . The recorded measurements were (a) the surface shear stress, (b) the Preston tube pressures, and (c) the static pressures ahead and behind the boundary layer fence. The corresponding skin friction coefficients were then compared with each other and the Van Driest II theory. The skin friction coefficients obtained with the fence agreed reasonably well with those obtained with a balance and the Preston tube. The skin friction coefficients resulting from all three techniques agreed very well with the Van Driest II theory.

FOREWORD

This report was prepared by Dr. Anthony W. Fiore and Mr. Norman E. Scaggs of the Aeromechanics Division of the Air Force Flight Dynamics Laboratory, Air Force Systems Command. The research was conducted under work unit numbered 23070424 entitled, "Viscous and Interacting Flow Fields about Flight Vehicles." This particular effort concerns itself with a boundary layer fence technique for measuring the surface shear stress from which the skin friction coefficient can be obtained. The experiments were performed between October 1977 and April 1978. They were carried out at a nominal Mach number of three and in the range of momentum thickness Reynolds numbers $2 \times 10^4 \leq Re_{\theta} \leq 60 \times 10^4$.

TABLE OF CONTENTS

Section No.	Title	Page No.
I	Introduction - - - - -	1
II	Experimental Apparatus - - - - -	3
	1. The Wind Tunnel - - - - -	3
	2. Instrumentation - - - - -	3
	a. Surface Shear Stress Balance - -	3
	b. Preston Tube - - - - -	4
	c. Boundary Layer Fence - - - - -	4
III	Test Procedure - - - - -	6
IV	Data Reduction - - - - -	7
V	Test Results - - - - -	12
	1. Balance Measurements - - - - -	12
	2. Preston Tube - - - - -	12
	3. Boundary Layer Fence - - - - -	13
VI	Conclusion - - - - -	16
VII	References - - - - -	17

LIST OF FIGURES

Fig.No.	Title	Page No.
1	Floating-Element Skin Friction Balance - - - - -	19
2	Boundary Layer Fence Assembly - - - - -	20
3	Boundary Layer Fence Insert - - - - -	21
4	Schematic of Tunnel Test Section and Diffuser Section - - - - -	22
5	Skin Friction Coefficient Obtained With A Balance Versus That Calculated From The Van Driest II Theory - - - - -	23
6	The Measured Shear Stress Parameter Versus The Preston Tube Parameter For $M_e=2.86$ and $2 \times 10^4 \leq Re_0 \leq 54 \times 10^4$ - - - - -	24
7	Preston Tube Skin Friction Coefficient Versus Skin Friction Coefficient Obtained With A Floating-Element Balance - - - - -	25
8	Preston Tube Skin Friction Coefficient Versus That Calculated From the Van Driest II Theory - - - - -	26
9	The Fence Wall Shear Stress Parameter Versus the Wall Static Pressure Parameter For $M_e=2.86$ and $2 \times 10^4 \leq Re_0 \leq 54 \times 10^4$ - -	27
10	Boundary Layer Fence Skin Friction Coefficient Versus Skin Friction Coefficient Obtained With a Floating-Element Balance - - - - -	28
11	Skin Friction Coefficient Obtained By The Fence Method Versus The Van Driest II Theory - - - - -	29
12	Skin Friction Coefficient Versus Momentum Thickness Reynolds Number For $M_e=2.86$, Near Adiabatic Wall and Zero Pressure Gradient Conditions - - - - -	30

LIST OF TABLES

No.	Title	Page No.
I	Recorded Measurements - - - - -	31
II	Calculated Results - - - - -	34

LIST OF SYMBOLS

- A_0 = Calibration constant see eq.(3)
 B_0 = Calibration constant see eq.(3)
 C_f = $\tau_{wg}/\frac{1}{2}\rho_e U_e^2$ = Skin friction coefficient
 d = Preston tube outside diameter in ft.
 F_3 = $\tau_{wg} \cdot d^2/4\rho \cdot v^2$ = Preston shear stress parameter
 F_4 = $\overline{\Delta P_p} \cdot d^2/4\rho \cdot v^2$ = Preston pressure parameter
 F_5 = $\tau_{wg} \cdot h^2/4\rho \cdot v^2$ = Fence shear stress parameter
 F_6 = $\Delta P_f \cdot h^2/4\rho \cdot v^2$ = Fence pressure parameter
 F_7 = $\overline{\Delta P_p} \cdot h^2/4\rho \cdot v^2$ = Coupling parameter
 h = Fence height in ft.
 M = Mach number
 P_0 = Tunnel stagnation pressure in psia
 P_{pt} = Preston tube total pressure in psia
 P = Static pressure in psia
 $\overline{\Delta P_p}$ = $\frac{\gamma}{2} P_w M_p^2$ = Preston tube dynamic pressure in psia
 ΔP_f = $P_f - P_b$ = Fence pressure difference in psia
 q = $\frac{\gamma}{2} P M^2$ = Dynamic pressure in psia
 Re_θ = $\rho_e U_e \theta / \mu_e$ = Momentum thickness Reynolds number
 \overline{Re}_θ = Incompressible momentum thickness Reynolds number given by eq.(21)
 Re_d^* = $\rho \cdot U_e d / \mu^*$ = Preston tube Reynolds number
 Re_h^* = $\rho \cdot U_e h / \mu^*$ = Fence Reynolds number
 T_0 = Tunnel stagnation temperature in °R
 T = Static temperature in °R
 U = Velocity in ft/sec.

LIST OF SYMBOLS

- X = Distance from tunnel throat to test station in inches
T = tau = shear stress in lbs/ft^2
 ρ = Density in slugs/ft^3 or lbs.sec /ft^4
 μ = Viscosity in lbs.sec/ft^2
 ν = μ/ρ = kinematic viscosity in ft^2/sec .
 θ = Momentum thickness in ft.
 γ = Ratio of specific heats (1.4 for air)
R = The gas constant taken as $1715 \text{ ft}^2/\text{sec}^2 \text{ } ^\circ\text{R}$ for air
r = Recovery factor taken as 0.88

Superscripts

- * = Value based on Sommer and Short reference temperature method

Subscripts

- b = Conditions behind the boundary layer fence
e = Conditions at the edge of the boundary layer
f = Conditions ahead of the boundary layer fence
g = Measurements made with a gauge
p = Preston tube
o = Tunnel stagnation conditions
w = Wall conditions
v.d. = Van Driest II theory

SECTION I

INTRODUCTION

In most aeronautical applications a knowledge of the total drag created when an aircraft moves through the atmosphere is essential to the understanding of the performance of such a vehicle. Because of recent energy shortages, this knowledge is becoming increasingly important. Considerable effort has been devoted to the measurement of the surface shear stress in the hope that the total drag of these vehicles can be decreased by reducing the skin friction drag. Eventually it is hoped that the skin friction drag can be controlled in order to either conserve fuel for a given flight condition or increase the flight range for a given fuel load.

Prior to conducting research on various methods for decreasing the skin friction drag, it becomes necessary to develop the instrumentation and testing techniques required for making these measurements. The purpose of this report is to develop a method referred to as the boundary layer fence technique for obtaining the wall shear stress. Like the Preston tube¹, the fence can be used to obtain the shear stress in a compressible two-dimensional turbulent boundary layer. However, its greatest advantage is its use in a three-dimensional flow field in the presence of both strong pressure gradients and separation. In this experiment the fence was calibrated in a two-dimensional flow field based on the assumption that the resultant surface shear stress vector in a three-dimensional boundary layer is related to the skewed velocity profile in a similar manner as the two-dimensional surface shear stress vector is related to its two-dimensional velocity profile. The results of this experiment indicate that this technique is a valid method for measuring the local wall shear stress in a compressible two-dimensional

turbulent boundary layer. Future research is planned in order to validate the use of this technique in a three-dimensional flow field.

SECTION II

EXPERIMENTAL APPARATUS

1. The Wind Tunnel

The facility used in the experiment was the Air Force Flight Dynamics Laboratory's Mach 3 high Reynolds number wind tunnel. It is a blowdown wind tunnel with an 8.2 x 8 inch closed test section whose upper and lower walls are contoured. It operates at stagnation pressures of 50 to 600 psia. Since the facility does not possess a stagnation temperature control system, the stagnation temperature is slightly below ambient temperature resulting from the Joule-Thompson effect. At these conditions the facility is capable of operation in the range of freestream unit Reynolds number extending from 1.12×10^7 to approximately 1.15×10^8 per foot. It is designed to run continuously for a maximum period of 10 minutes. Runs during this investigation averaged about 30 seconds. Further details on operating procedures and calibration of this wind tunnel are available in Reference 2.

2. Instrumentation

a. Surface Shear Stress Balance

The surface shear stress was measured directly with a floating-element balance shown in Fig.1. It was manufactured by the Kistler Instrumentation Company. It is a self sealed unit with a flat surface permitting flush mounting in the tunnel wall. The floating element is 0.37 inches in diameter and has a peripheral gap of 0.003 inches. The balance is self-nulling to the center position and is statically balanced about all three axes.

The electrical components were at ambient pressure and temperature during testing. Prior to installation in the tunnel the balance was calibrated

by applying known weights. Before and after each run the calibration was constantly checked with a built-in self calibration coil. The read-out and electronic calibration control is shown in Fig.1.

Primary concern was the destruction of the balance when exposed to tunnel starting and stopping loads. In order to avoid catastrophic failure the balance retraction system described in Reference 3 was used.

b. Preston tubes

Two Preston tubes and their related wall static pressure and temperature instrumentation were used to provide a second method for measuring the wall shear stress (see Fig.2).

These Preston tubes consisted of round pitot tubes placed tangential to the surface. They were constructed from #304 annealed stainless steel tubing with an outside diameter of 0.062 inches and an inside diameter of 0.0472 inches. The streamwise lengths of these pitot tubes were 0.125 inches. In this investigation a new form of the Keener and Hopkins Preston tube⁴ equation was used in arriving at the surface shear stress. This relationship will be described in detail in a later section.

c. Boundary Layer Fence

The design of the boundary layer fence is relatively simple and is shown in both Fig.2 and Fig.3. It has been determined that the best fence configuration should have square corners⁵. This feature was incorporated in the design used in this investigation. The fence had a span of 0.2 inches while its height and width was 0.01 inches. On either side of the fence there is a pressure port, in the form of a slot, used to measure the lateral pressures when the fence is aligned with the flow field velocity vector.

These same ports yield the pressure differential $\Delta P_f = P_f - P_b$ when the fence is rotated ninety degrees to the local velocity vector near the wall. The former gives the direction of the surface shear stress vector while the latter is related to the magnitude of the surface shear stress vector. These pressure slots are shown in Fig.3. They are the same length and width as the fence. The pressures sensed by these slots are transmitted to the proper recording instrumentation through isolated chambers on both sides of the fence. The fence and the main body are fabricated as a unit thus insuring the fence will have a high degree of structural integrity. As shown in Fig.2 this unit is placed in the base of the test plate and attached to a shaft which is connected to an external drive motor used to rotate the fence. The previously mentioned Preston tubes, the two wall static pressure orifices, and the two wall temperature thermocouples are also shown in Fig.2. The Preston tubes were placed sufficiently far apart so no aerodynamic interference would occur between them and the fence.

The fence operational procedure is relatively simple. It is remotely rotated until the pressure differential between the two orifices becomes zero. At this position the angle is recorded as the direction of the local velocity vector which is assumed to correspond to the local surface shear stress vector. The fence is rotated ninety degrees to this position and the two pressures, i.e., forward and aft of the fence are recorded. The corresponding pressure difference $\Delta P_f = P_f - P_b$ is then related to the surface shear stress measured with the balance at the same station and under the same tunnel test conditions.

SECTION III

TEST PROCEDURE

The experiment was conducted in two phases. The surface shear stress measurements with the balance were made during the first phase, while the Preston tubes and boundary layer fence measurements were obtained during the second phase of the experiment. These measurements were made on the upper wall of the $M=3$ high Reynolds number wind tunnel. The reason for testing on the upper surface rather than the tunnel side wall was to avoid the boundary layer distortion which occurs on the side walls resulting from lateral pressure gradients. All measurements were made at a nominal Mach number of three. The Reynolds number was varied by two methods; (1) by testing at eight different longitudinal stations as shown in Fig.4, and (2) by changing the stagnation pressure at each tunnel location. This program provided a certain amount of intentional redundancy considered to be necessary because of the difficulty in making accurate surface shear stress measurements with the balance. The combination of test stagnation conditions and wall locations along with the detailed measurements are presented in Table I.

During these tests the stagnation temperature was slightly below the ambient temperature. Under these conditions the unit Reynolds number varied from 1.12×10^7 to 1.15×10^8 per foot corresponding to a momentum thickness Reynolds number range of 2×10^4 to approximately 60×10^4 .

All the data presented is for a wall temperature near the adiabatic temperature and a near zero pressure gradient.

SECTION IV

DATA REDUCTION

A brief description of the data reduction procedure will be presented in this section. The surface shear stress measurements obtained with the floating-element balance were converted to skin friction coefficients by dividing by the dynamic pressure at the edge of the boundary layer, namely:

$$(C_f)_g = \tau_{wg} / \frac{1}{2} \rho_e U_e^2 \quad (1)$$

The corresponding momentum thickness Reynolds number was calculated from the empirical relationship obtained by Fiore³, i.e.,

$$Re_\theta = 4.513 \times 10^{-4} M_e^{1.118} Re_x^{0.949} \quad (2)$$

The data used to arrive at eq.(2) was from boundary layer profile measurements made at the same test conditions and location on the tunnel wall as the present investigation.

The Preston tubes were then calibrated for the data and test conditions of this particular experiment. As in the case of Keener and Hopkins⁴ it was assumed that the Preston tube calibration is of the form

$$\log \left(\frac{\tau_{wg} \cdot d^2}{4 \rho^* v^{*2}} \right) = A_0 \log \left(\frac{\bar{\Delta} p \cdot d^2}{4 \rho^* v^{*2}} \right) + B_0 \quad (3)$$

where the reference density, ρ^* , was calculated based on the assumption of a constant pressure boundary layer as

$$\rho^* = 144 \frac{P_w}{RT^*} \quad (4)$$

The reference temperature was calculated from the Sommer and Short expression⁶ given as

$$T^* = T_e (0.55 + 0.035 M_e^2 + 0.45 \frac{T_w}{T_e}) \quad (5)$$

The reference kinematic viscosity was calculated from the definition

$$\nu^* = \frac{\mu^*}{\rho^*} \quad (6)$$

where Keye's equation for the viscosity was used, namely:

$$\mu^* = 2.32 \times 10^{-8} \sqrt{T^*} \left[1 + \frac{220}{T^*(10^9/T^*)} \right] \quad (7)$$

In eq.(3) the value of ΔP_p was taken as suggested by Hopkins and Keener⁷ rather than the difference between the Preston tube total pressure and the wall static pressure. The purpose for this choice is based on the work of Hopkins and Keener who found that eq.(3) results in a calibration curve for the compressible turbulent boundary layer which would coincide with Preston's equation for the incompressible case¹ of the form

$$\log \left(\frac{T_{wg} \cdot d^2}{4\rho\nu^2} \right) = 0.875 \log \left(\frac{\Delta P \cdot d^2}{4\rho\nu^2} \right) - 1.396 \quad (8)$$

where $\Delta P = P_{pt} - P_w$.

The constants A_0 and B_0 in eq.(3) are determined by the least squares fit of the data.

The generalized form of the skin friction coefficient is obtained from eq.(3). This relationship can be shown to be

$$(C_f)_p = 8(1 - A_0) \cdot 10^{B_0} \frac{\left(\frac{M_p}{M_e} \right)^{2A_0}}{\left[\left(\frac{\rho_e}{\rho^*} \right) \times Re_d^{*2} \right]^{(1-A_0)}} \quad (9)$$

where the Preston Mach number, provided the flow is supersonic, is obtained from iteration of the Rayleigh pitot formula written as

$$\frac{P_{pt}}{P_w} = \left(\frac{6}{5} M_p^2 \right)^{7/2} \left(\frac{1}{\frac{7}{6} M_p^2 - \frac{1}{6}} \right)^{5/2} \quad (10)$$

for $\gamma=1.4$.

A similar method must be considered in arriving at an expression for the skin friction coefficient for the boundary layer fence technique. In this investigation it was assumed that the Preston tube diameter, d , in eq.(3) can be replaced with the fence height, h , leading to a fence calibration equation written as

$$\log \left(\frac{T_{wg} \cdot h^2}{4\rho \cdot v^2} \right) = C_0 \log \left(\frac{\Delta P_f \cdot h^2}{4\rho \cdot v^2} \right) + D_0 \quad (11)$$

where $\Delta P_f = P_f - P_b$ and the constants C_0 and D_0 are different than the Preston tube calibration constants. In order to show that these constants must be different, eq.(3) can be re-written as

$$\log \left(\frac{T_{wg} \cdot h^2}{4\rho \cdot v^2} \right) = A_0 \log \left(\frac{\bar{\Delta P}_p \cdot h^2}{4\rho \cdot v^2} \right) + (A_0 - 1) \log \left(\frac{d}{h} \right)^2 + B_0 \quad (12)$$

assuming that

$$\log \left(\frac{\bar{\Delta P}_p \cdot h^2}{4\rho \cdot v^2} \right) = E_0 \log \left(\frac{\Delta P_f \cdot h^2}{4\rho \cdot v^2} \right) + F_0 \quad (13)$$

then eq.(12) becomes

$$\log \left(\frac{T_{wg} \cdot h^2}{4\rho \cdot v^2} \right) = A_0 F_0 \log \left(\frac{\Delta P_f \cdot h^2}{4\rho \cdot v^2} \right) + \left[A_0 F_0 + (A_0 - 1) \log \left(\frac{d}{h} \right)^2 + B_0 \right] \quad (14)$$

In order for eq.(11) and eq.(14) to be identical, the following must be true

$$C_0 = A_0 F_0 \quad (15)$$

and

$$D_0 = A_0 F_0 + (A_0^{-1}) \log \left(\frac{d}{h} \right)^2 + B_0 = f_2 \left(\frac{d}{h} \right) \quad (16)$$

From eq.(16) it is noted that the intercept of eq.(11) is a function of the ratio d/h , which is a fictitious parameter, however it does serve to indicate that the calibration constants in eq.(11) are different than those in eq.(3) and must be evaluated separately.

The skin friction coefficient equation for the boundary layer fence is obtained from eq.(11) as

$$(C_f)_f = 8(1-C_0) \cdot 10^{D_0} \frac{\left(\frac{\Delta P_f}{q_e} \right)^{C_0}}{\left[\left(\frac{\rho_e}{\rho^*} \right) R_{ch}^{*2} \right] (1-C_0)} \quad (17)$$

The experimental measurements were compared with the Van Driest II skin friction theory⁶ written in the form.

$$(C_f)_{V.D.} = \frac{\left[\sin^{-1} \left(\frac{2A^2 - B}{\sqrt{B^2 + 4A^2}} \right) + \sin^{-1} \left(\frac{B}{\sqrt{B^2 + 4A^2}} \right) \right]^2}{r \left(\frac{\gamma-1}{2} \right) M_e^2 \left[17.08 (\log \bar{R}_{e_\theta})^2 + 25.11 (\log \bar{R}_{e_\theta}) + 6.012 \right]} \quad (18)$$

where

$$A = M_e \sqrt{r \left(\frac{\gamma-1}{2} \right) \frac{T_e}{T_w}} \quad (19)$$

$$B = A^2 + \frac{T_e}{T_w} - 1 \quad (20)$$

and

$$\bar{R}_{e\theta} = \sqrt{\frac{T_e}{T_w}} \left[\frac{1 + \frac{220}{T_w (10^9/T_w)}}{1 + \frac{220}{T_e (10^9/T_e)}} \right] \times R_{e\theta} \quad (21)$$

The data reduced by the method outlined above are presented in Table II.

SECTION V

TEST RESULTS

1. Balance Measurements

In Fig.5 the skin friction coefficient obtained with the floating-element balance in the Reynolds number range $2 \times 10^4 \leq Re_0 \leq 60 \times 10^4$ is compared with those calculated from the Van Driest theory⁸. Over the complete range of momentum thickness Reynolds number the measured skin friction coefficients are within $\pm 10\%$ of the Van Driest II theory. This agreement between the measurements and theory is considered to be reasonably good. Having established the validity of these measurements, they now can be used to evaluate the skin friction coefficients obtained with the boundary layer fence technique.

2. Preston tube

The Preston tube method was introduced as a second method for obtaining the local skin friction coefficient. The intent was to use the Preston tube results as a separate check on the measurements made with the floating-element balance. In order to accomplish this, it was first necessary to obtain the calibrations constants A_0 and B_0 given in eq.(3).

Figure 6 is a plot of the logarithm of the Preston shear stress parameter, $\tau_{wg} \cdot d^2 / 4\rho \cdot v^*{}^2$, versus the logarithm of the Preston pressure parameter $\overline{\Delta P_p} \cdot d^2 / 4\rho \cdot v^*{}^2$. The result is a linear function similar to eq.(3). The values of A_0 and B_0 were obtained by the least squares fit to the data and were found to be 0.86773 and -1.32283 respectively. Comparison between the measurements and eq.(3) with the proper constants is presented in Fig.6. The agreement between the two is excellent. Shown for informational purposes are the calibrations

obtained by Keener and Hopkins⁴ as well as Yanta et.al.⁹ For small values of the Preston pressure parameter, both appear to agree very well with the present measurements and the new calibration. As the Preston pressure parameter is increased the calibration of Keener and Hopkins is in excellent agreement with the present measurements while that of Yanta et.al. is somewhat lower than the new measurements. When the new calibration constants are introduced into eq.(9), the Preston skin friction coefficient equation becomes

$$(C_f)_p = 0.06261 \frac{\left(\frac{M_p}{M_e}\right)^{1.73546}}{\left[\left(\frac{\rho_e}{\rho^*}\right) Re_d^{*2}\right]^{0.13227}} \quad (9a)$$

Fig.7 shows the skin friction coefficient calculated from eq.(9a) plotted versus that obtained with a floating-element balance and Fig.8 is a plot of $(C_f)_p$ versus the skin friction coefficient calculated from eq.(18). In both cases the Preston tube skin friction coefficients are within $\pm 10\%$ of both the theory and those values obtained with the balance. The Preston tube skin friction coefficient overpredicts the theory at low momentum thickness Reynolds numbers while it underpredicts the theory at higher Reynolds numbers. In both Figs.7 and 8 the agreement is considered to be within acceptable limits.

3. Boundary Layer Fence

In all probability the boundary layer fence for measuring the wall shear stress was first introduced by Konstantinov and Dragnysh¹⁰ in 1955. The same technique was employed by Vagt and Fernholz¹¹ to measure the three-dimensional surface shear stress in an incompressible flow field. The purpose of this section is to show that the fence technique appears to be useful in measuring the surface shear stress in a compressible turbulent boundary layer as well.

As previously mentioned, it is assumed that the fence calibrations should be similar in form to the Preston tube calibration provided the Preston tube outside diameter is replaced with the fence height. This leads to the fence calibration equation given by eq.(11). Fig.9 is a plot of the logarithm of the fence shear stress parameter, $T_{wg} \cdot h^2 / 4\rho^* v^{*2}$, versus the logarithm of fence pressure parameter, $\Delta P_f \cdot h^2 / 4\rho^* v^{*2}$. Also shown in Fig.9 is eq.(11) where the calibration constants C_0 and D_0 are 0.903846 and -1.640385 respectively. The agreement between the measurements and eq.(11) is excellent; indicating that eq.(11) with these constants should result in a good expression for the skin friction coefficient as a function of the fence pressure differential, the edge dynamic pressure, the density ratio (ρ_e / ρ^*), and the fence Reynolds number (Re_h^*). This expression is obtained by introducing the above values for C_0 and D_0 into eq.(17), namely;

$$(C_f)_f = 0.027954 \frac{\left(\frac{\Delta P_f}{q_e} \right)^{0.903846}}{\left[\left(\frac{\rho_e}{\rho^*} \right) Re_h^{*2} \right]^{0.096154}} \quad (17a)$$

The skin friction coefficient calculated from eq.(17a) is compared with those measured with a balance in Fig.10 and with the Van Driest II theory in Fig.11. In both cases eq.(17a) gives values which are within $\pm 10\%$ of both the measurements made with the balance and those calculated from the theory. This agreement is considered to be very good since eq.(17a) is being compared with balance measurements which are no more accurate than $\pm 10\%$ when compared with theory.

Fig.12 is a plot of the skin friction coefficient versus the momentum thickness Reynolds number and summarizes the results of this investigation.

It contains the skin friction coefficient measurements made directly with the balance, those obtained with the Preston tube, and those taken with the boundary layer fence. Superimposed on Fig.12 is the Van Driest II theory. The agreement in the skin friction coefficients obtained by the various methods as well as the agreement with theory is considered to be acceptable.

SECTION VI

CONCLUSIONS

An experiment was performed for the purpose of developing the boundary layer fence technique used to measure the surface shear stress in a compressible turbulent boundary layer. Measurements were made at a nominal Mach number of three for momentum thickness Reynolds numbers extending from 2×10^4 to approximately 60×10^4 . The results for a near adiabatic wall and zero pressure gradient condition are as follows:

- (1) The boundary layer fence is a valid technique for measuring the wall shear stress in a compressible turbulent boundary layer.
- (2) The fence calibration is a linear function similar in form to the Preston tube calibration equation provided the Preston tube outside diameter is replaced with the fence height.
- (3) The skin friction coefficients obtained with the fence agree reasonably well with those obtained with a balance. For momentum thickness Reynolds numbers less than 15×10^4 those obtained with the fence were about 10% higher than the Preston tube values and they were in good agreement with the Van Driest II theory. At momentum thickness Reynolds numbers greater than 15×10^4 the fence measurements were 5% to 10% higher than either those obtained with a balance or those calculated from the theory.

SECTION VII

REFERENCES

1. Preston, J.H., "The Determination of Turbulent Skin Friction By Means of Pitot Tubes", ARC-15758 (1954).
2. Fiore, A.W., Moore, D.G., Murray, D.H. and West, J.E., "Design and Calibration of the ARL Mach 3 High Reynolds Number Facility", ARL TR-75-0012 (1975).
3. Fiore, A.W., "M=3 Turbulent Boundary Layer Measurements at Very High Reynolds Numbers", AFFDL TR-77-80 (1978).
4. Keener, E.R. and Hopkins E.J., "Use of Preston Tubes for Measuring Hypersonic Turbulent Skin Friction", NASA TND-5544 (1969).
5. Winter, K.G., "An Outline of the Techniques Available For The Measurement of Skin Friction in Turbulent Boundary Layers", Progress in Aerospace Sciences, Vol.18, No.1 (1977).
6. Sommer, S.C. and Short, Barbara J., "Free-Flight Measurements of Turbulent-Boundary-Layer Skin Friction in the Presence of Severe Aerodynamic Heating at Mach Numbers From 2.8 to 7.0", NACA TN-3391 (1955).
7. Hopkins, E.J. and Keener, E.R., "Comments on 'Calibration of Preston Tubes in Supersonic Flow'", AIAA Journal, Vol.4, No.4 (1966), pp.760-761.
8. Van Driest, E.R., "On Turbulent Flow Near a Wall", J.Aeronaut.Sci., 23, (1956), pp.1007-1011 and 1036.
9. Yanta, W.J., Brott, D.L. and Lee, R.E., "An Experimental Investigation of the Preston Probe Including Effects of Heat Transfer, Compressibility, and Favorable Pressure Gradient", AIAA paper 69-648.
10. Konstantinov, N.I. and Dragnysh, G.L., "Energomashinostroenie", Trudy L.P.I. 176 (1955), pp.191-200.

11. Vagt, J.D. and Fernholz, H., "Use of Surface Fences to Measure Wall Shear Stress in Three-Dimensional Boundary Layers", Aeronaut.Q., XXIV, 2 (1973), pp.87-91.

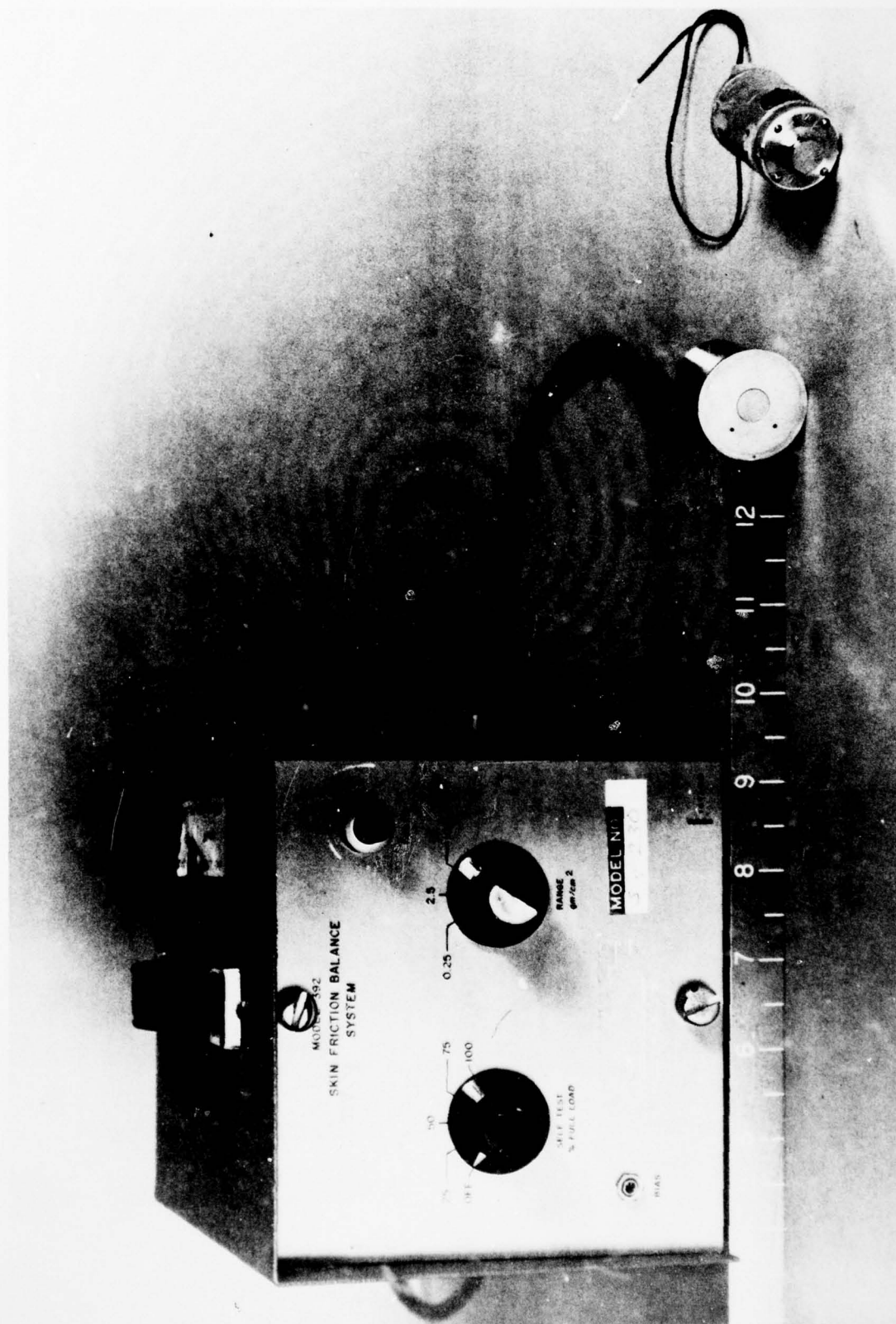


FIG. 1 FLOATING-ELEMENT SKIN FRICTION BALANCE

AD-A061 086

AIR FORCE FLIGHT DYNAMICS LAB WRIGHT-PATTERSON AFB OHIO F/G 20/4
BOUNDARY LAYER EFFECTS-PROCEEDINGS OF THE 7TH U. S. AIR FORCE/F--ETC(U)
SEP 78 A W FIORE MWDDEA-AF-75-G-7440
AFFDL-TR-78-111 NL

UNCLASSIFIED

5 OF 5

AD A061086



END
DATE
FILMED
2 79
DDC

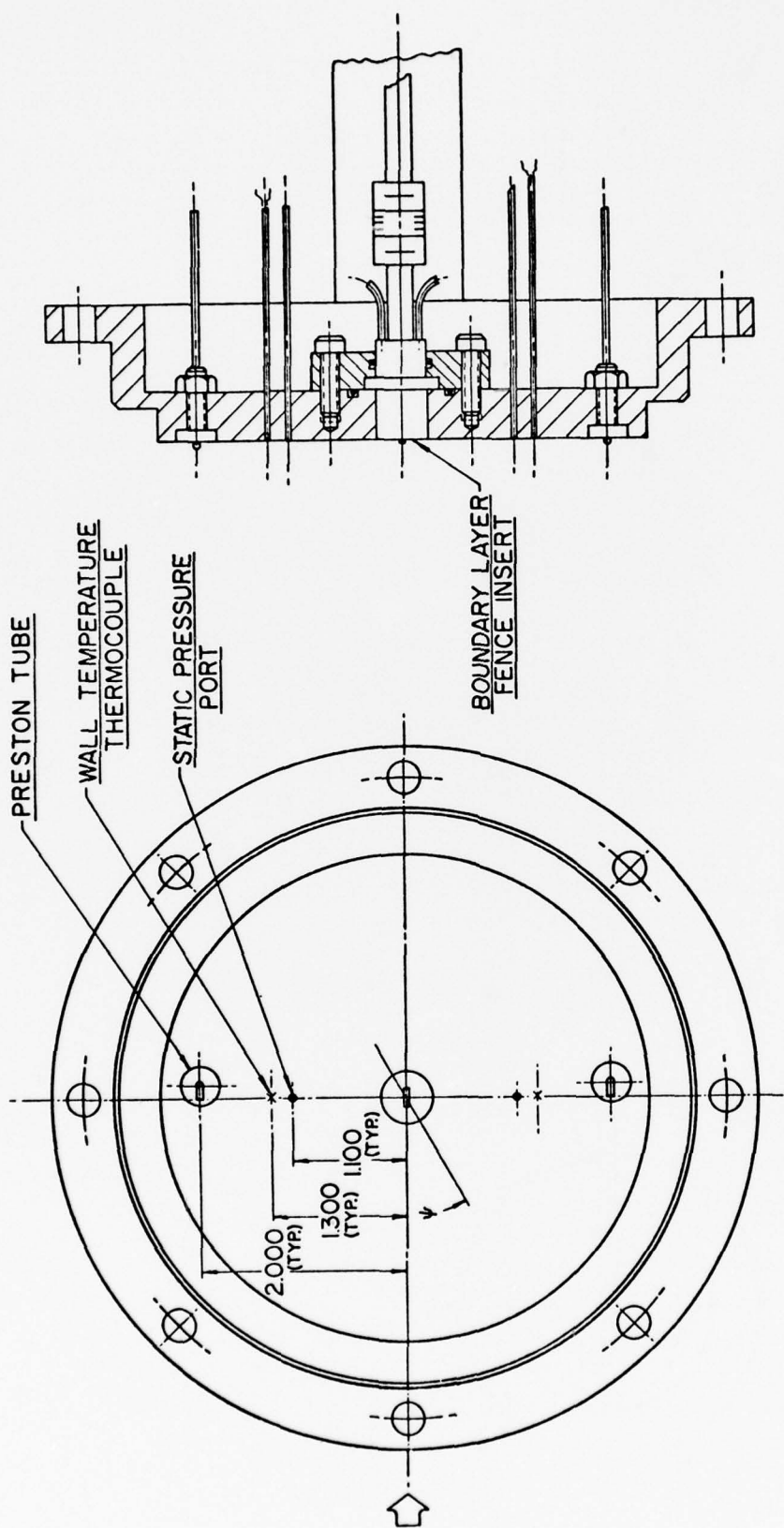


FIG. 2 BOUNDARY LAYER FENCE ASSEMBLY

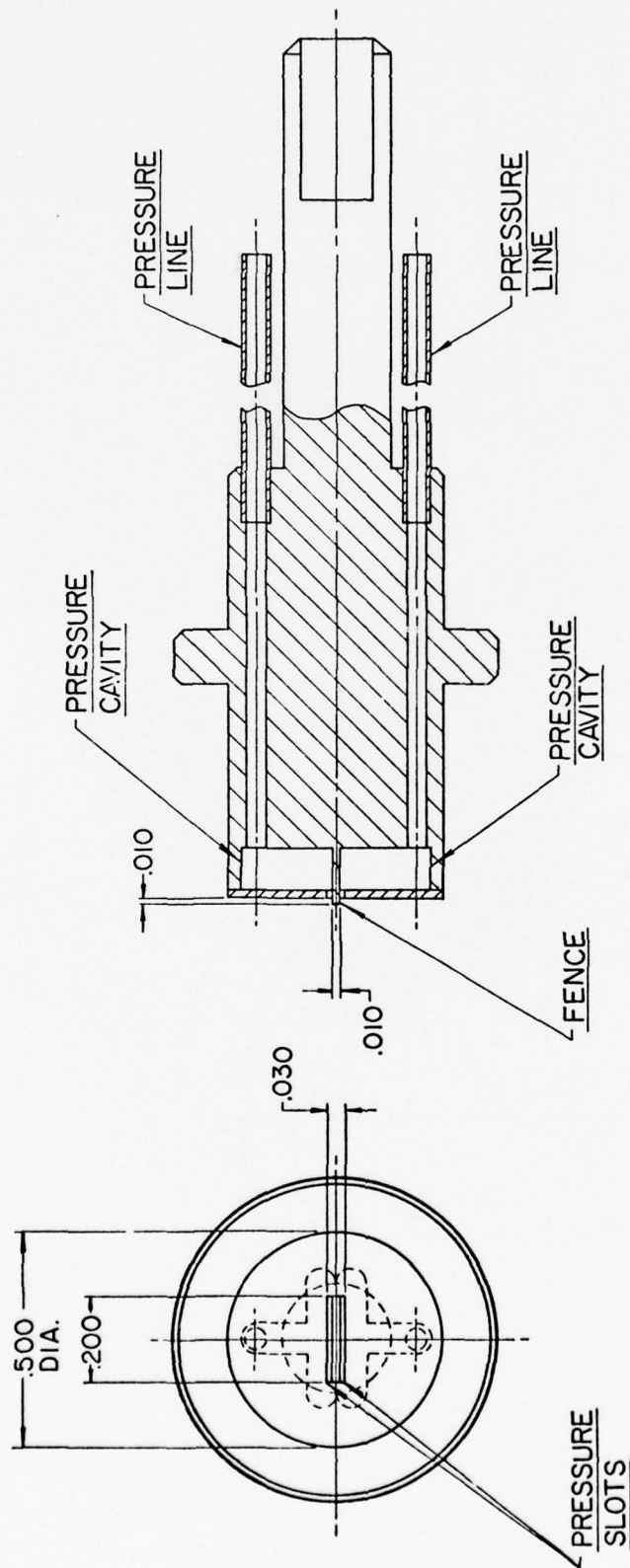


FIG. 3 BOUNDARY LAYER FENCE INSERT

STATION NUMBER	DISTANCE FROM NOZZLE THROAT (INCHES)	STATION NUMBER	DISTANCE FROM NOZZLE THROAT (INCHES)
1	27.28	5	82.28
2	43.28	6	94.28
3	58.28	7	106.28
4	70.28	8	118.28

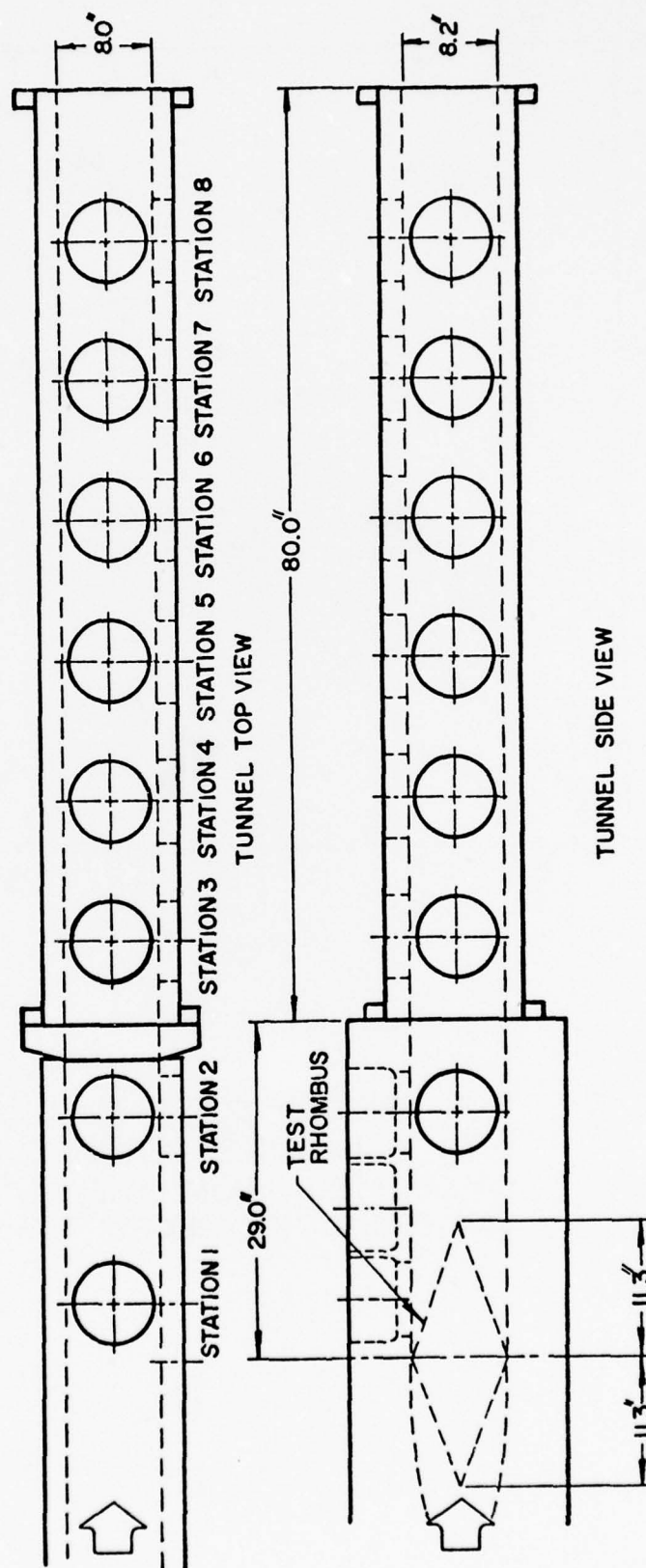


FIG. 4 SCHEMATIC OF TUNNEL TEST SECTION AND DIFFUSER SECTION

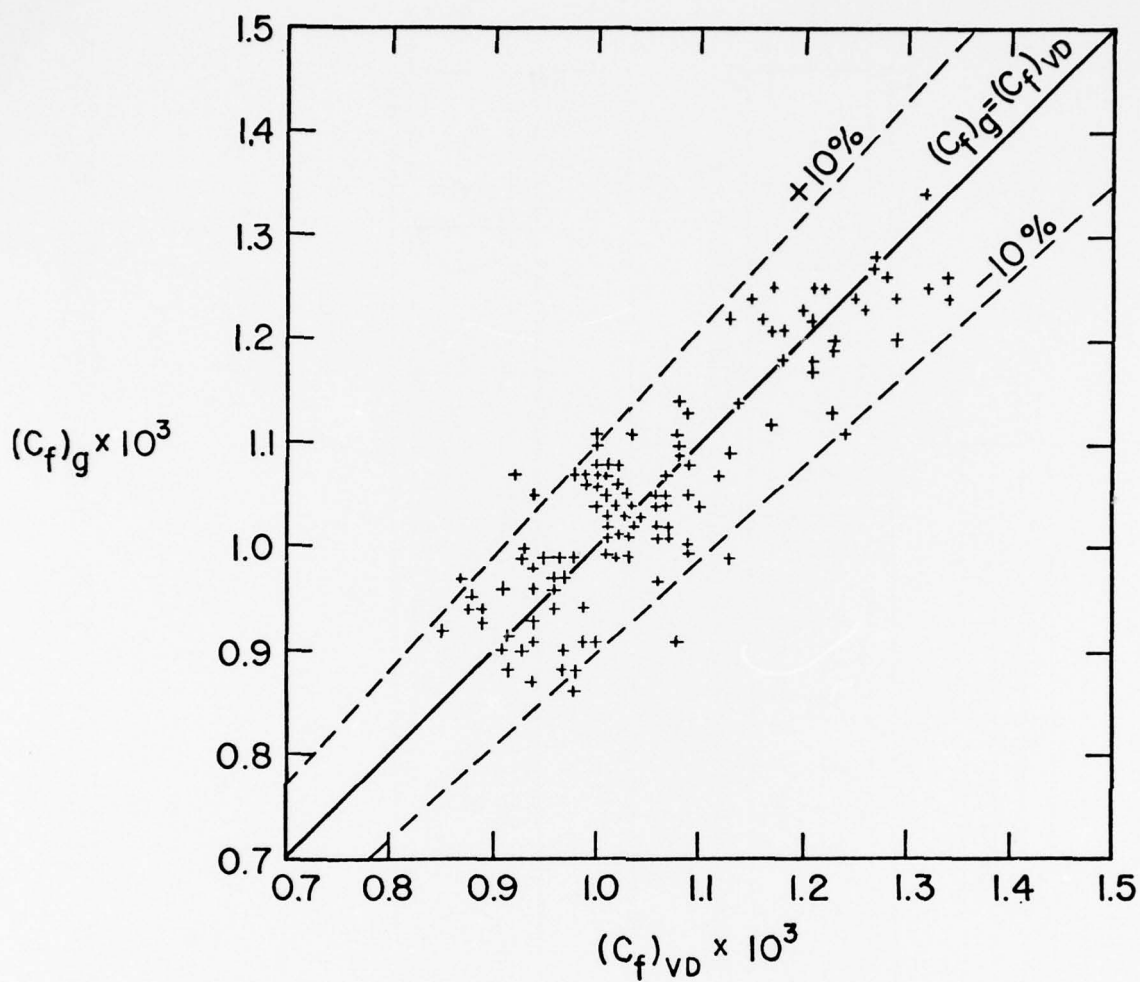


FIG. 5 SKIN FRICTION COEFFICIENT OBTAINED WITH A BALANCE VERSUS THAT CALCULATED FROM THE VAN DRIEST II THEORY.

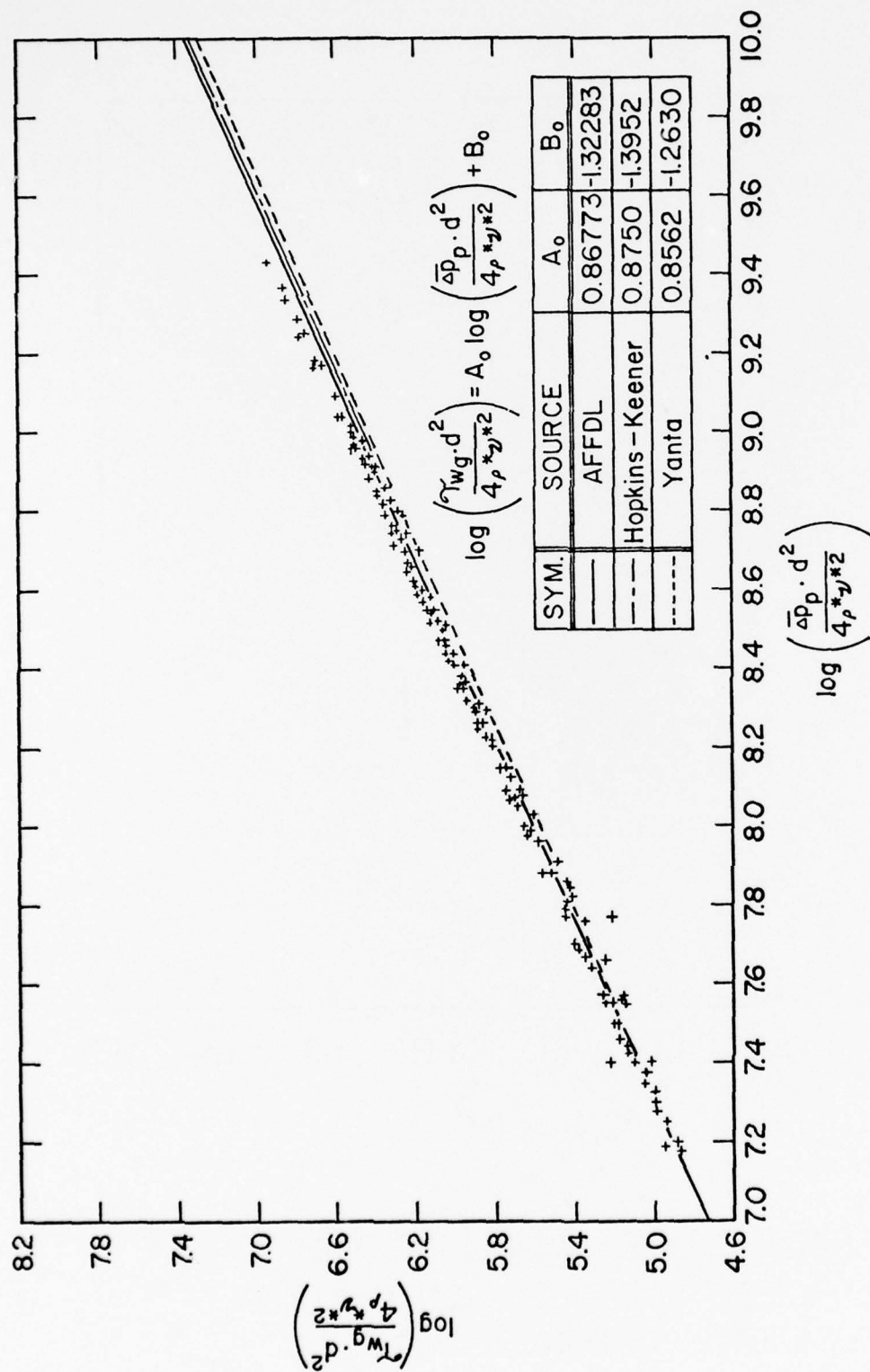


FIG. 6 THE MEASURED SHEAR STRESS PARAMETER VERSUS THE PRESTON
TUBE PARAMETER FOR $M_e = 2.86$ AND $2 \times 10^4 \leq Re_\theta \leq 54 \times 10^4$

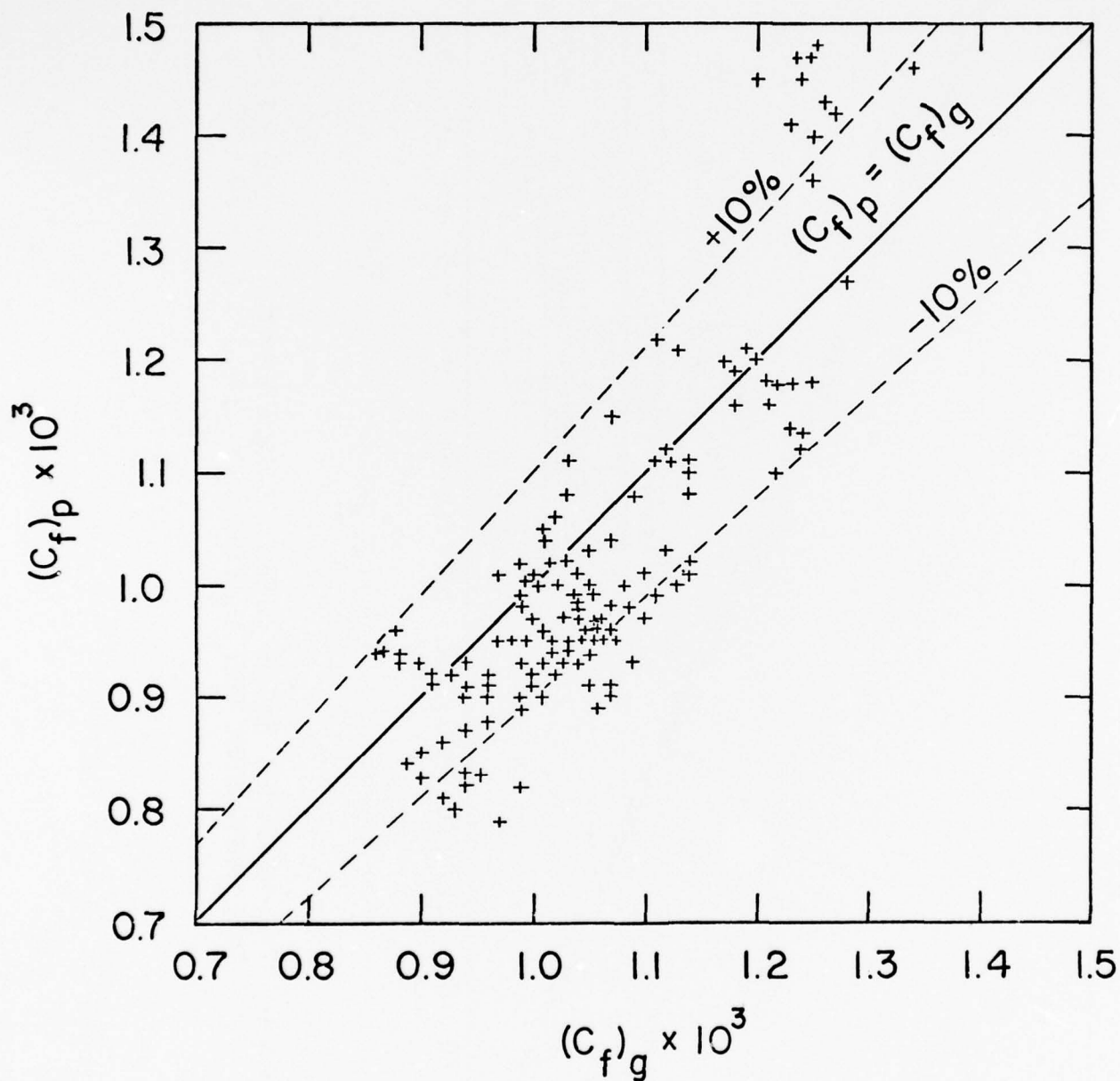


FIG. 7 PRESTON TUBE SKIN FRICTION COEFFICIENT VERSUS SKIN FRICTION COEFFICIENT OBTAINED WITH A FLOATING-ELEMENT BALANCE.

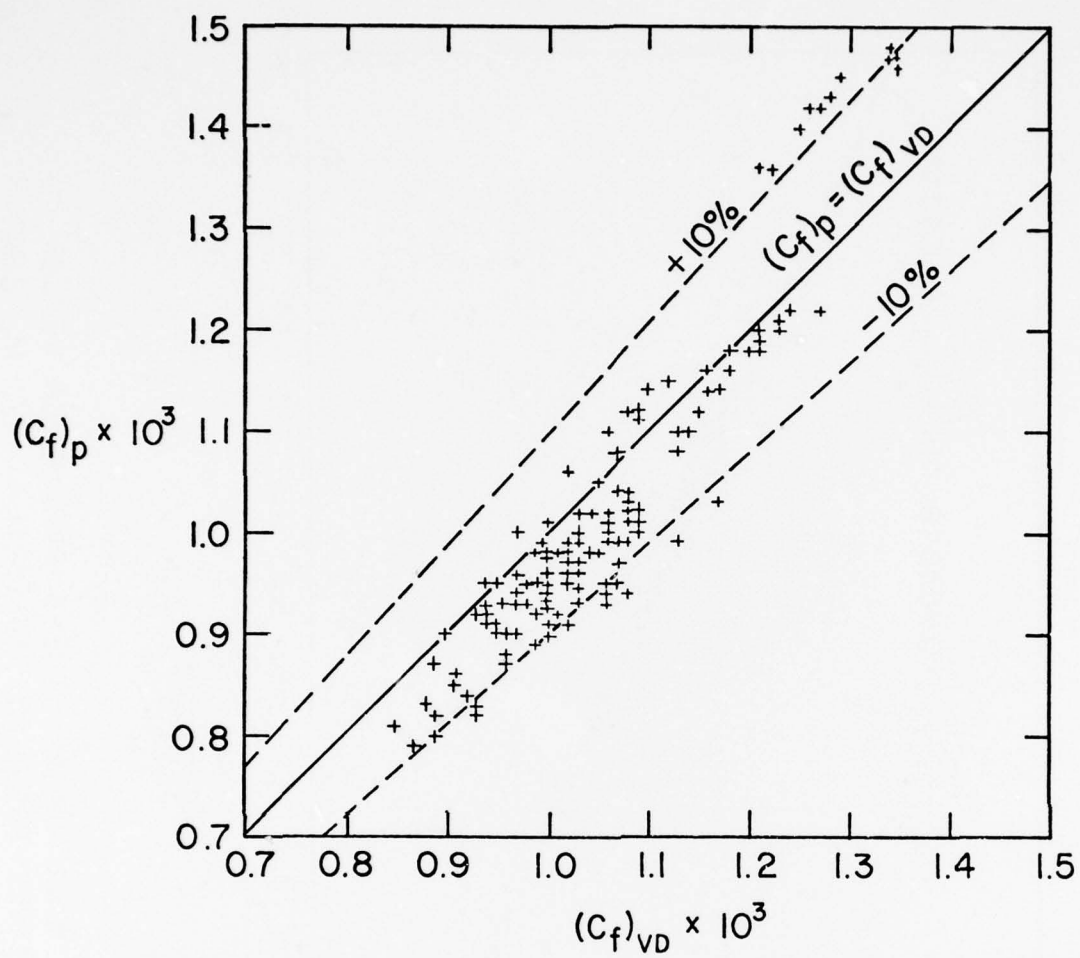


FIG. 8 PRESTON TUBE SKIN FRICTION COEFFICIENT VERSUS THAT CALCULATED FROM THE VAN DRIEST II THEORY.

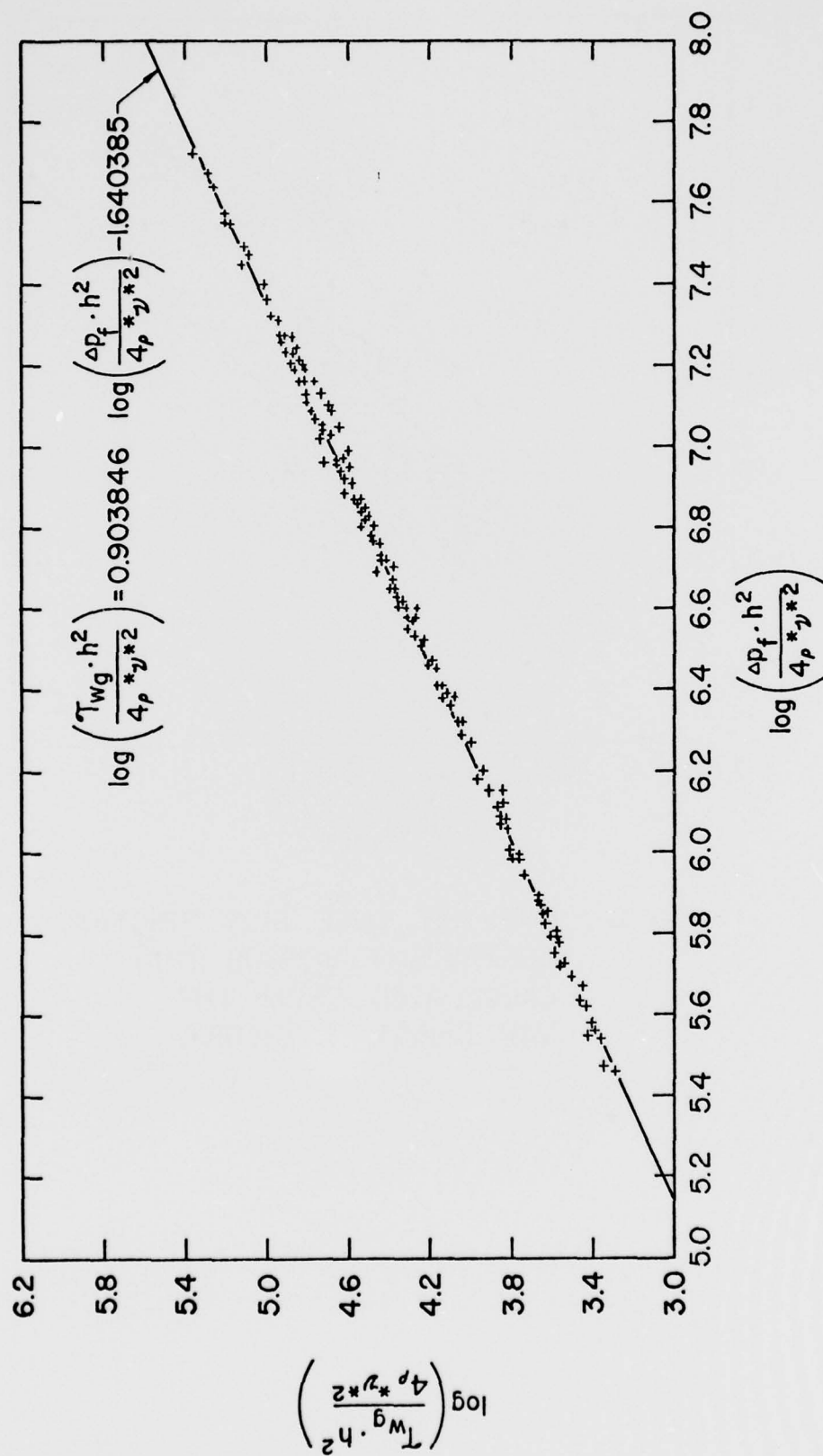


FIG. 9 THE FENCE WALL SHEAR STRESS PARAMETER VERSUS
 THE WALL STATIC PRESSURE PARAMETER FOR $M_e = 2.86$
 AND $2 \times 10^4 \leq Re_\theta \leq 54 \times 10^4$

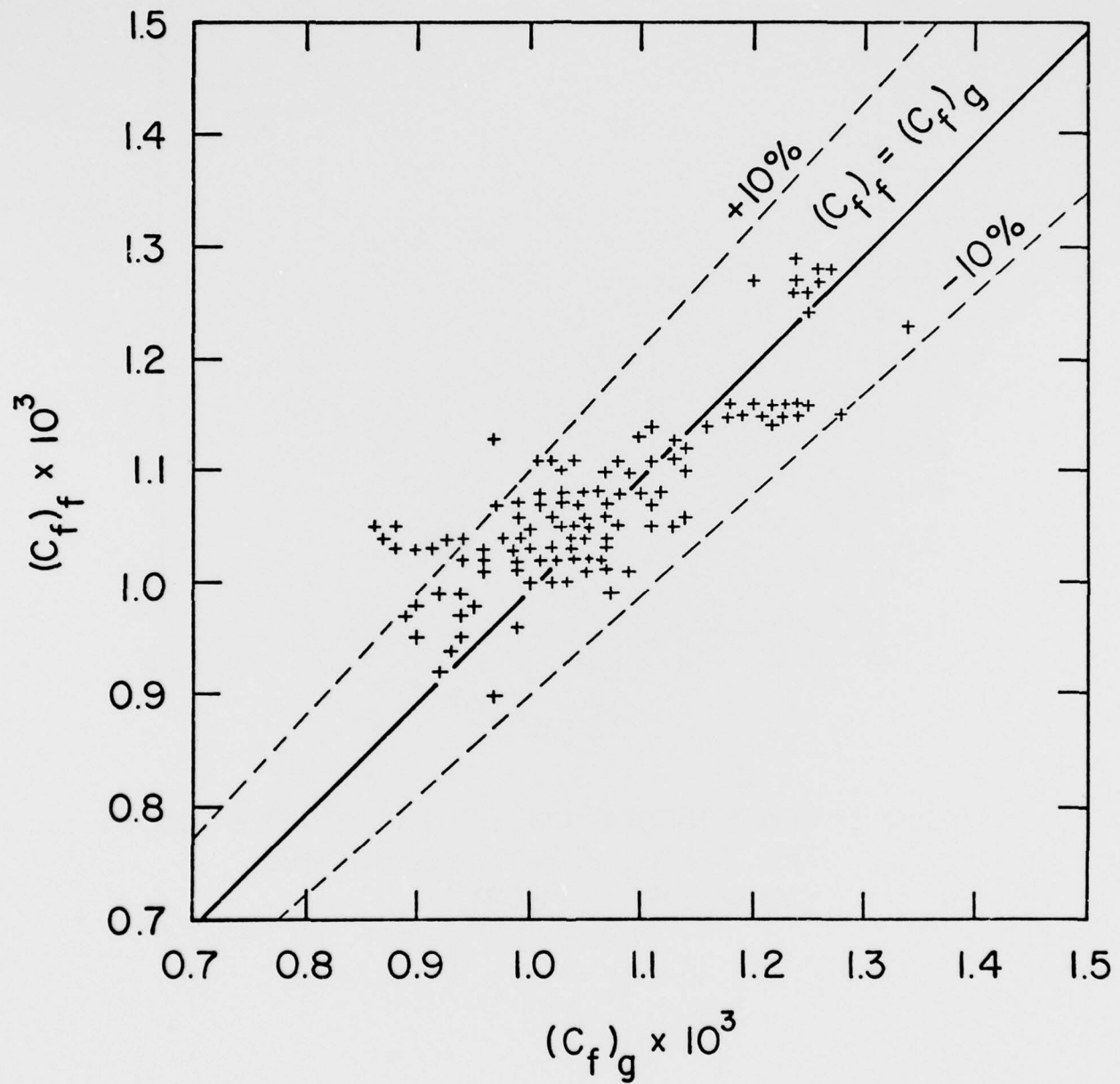


FIG. 10 BOUNDARY LAYER FENCE SKIN FRICTION COEFFICIENT VERSUS SKIN FRICTION COEFFICIENT OBTAINED WITH A FLOATING-ELEMENT BALANCE.

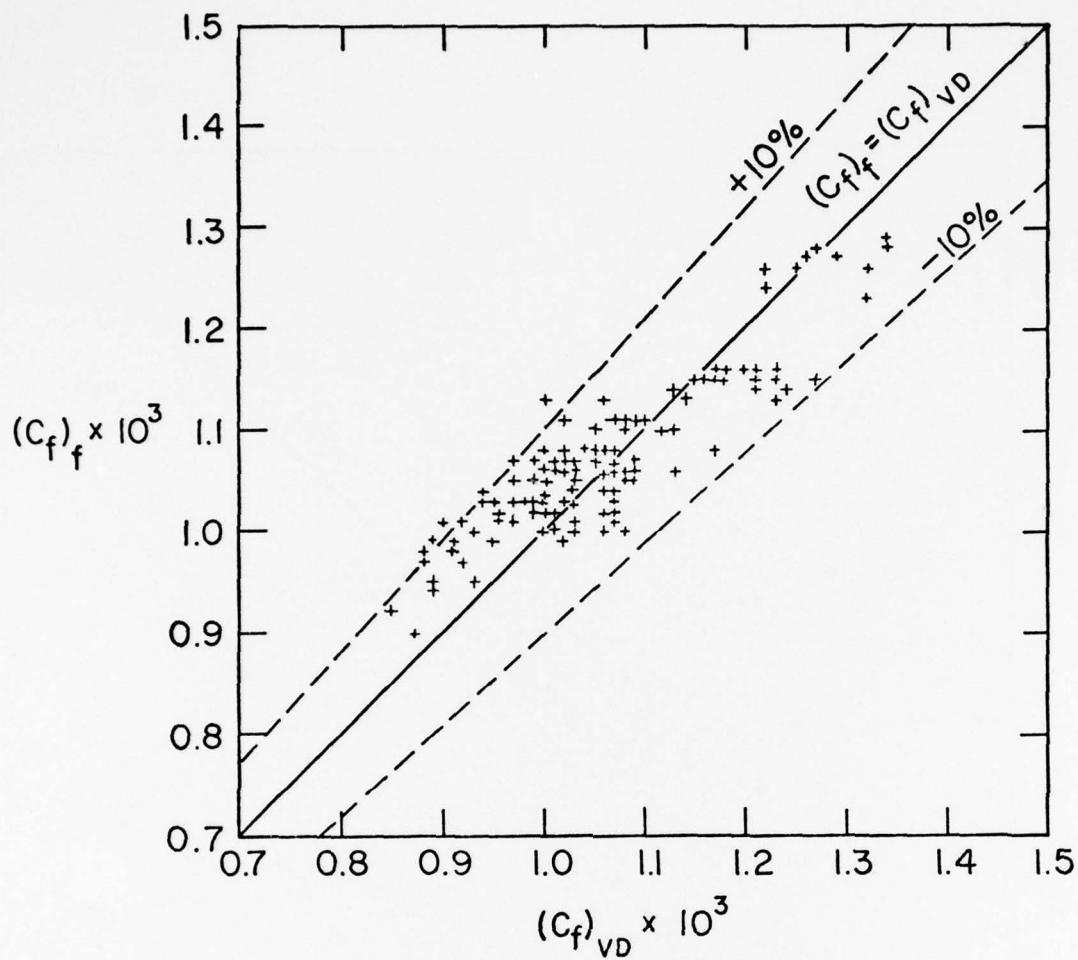


FIG. 11 SKIN FRICTION COEFFICIENT OBTAINED BY THE FENCE METHOD VERSUS THE VAN DRIEST II THEORY.

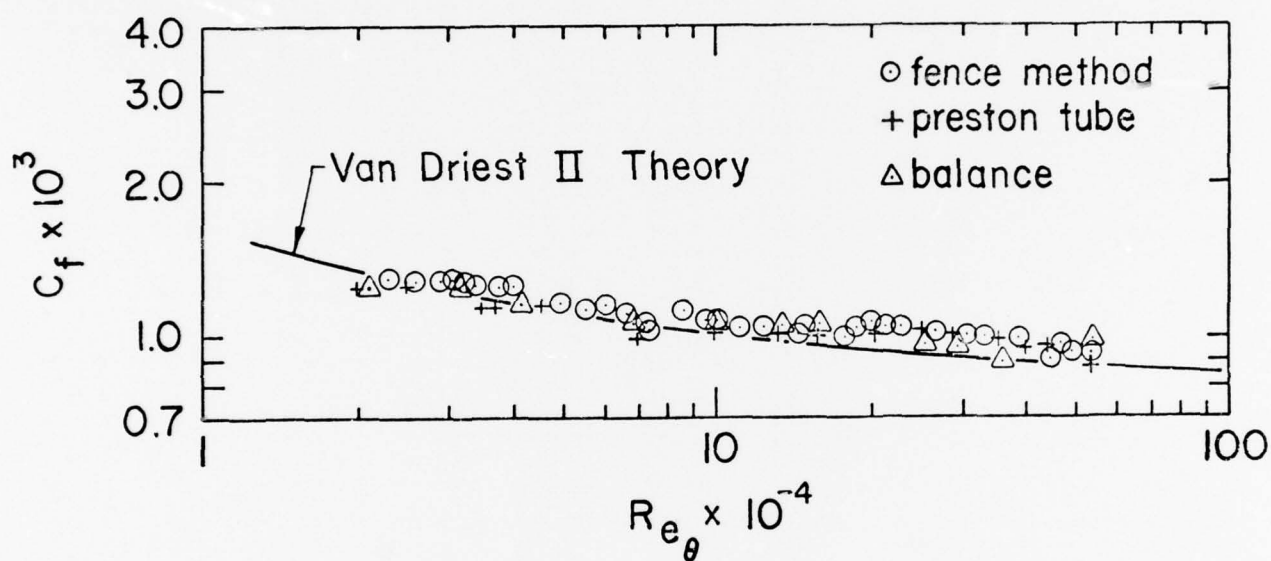


FIG. 12 SKIN FRICTION COEFFICIENT VERSUS
MOMENTUM THICKNESS REYNOLDS NUMBER
FOR $M_e = 2.86$, NEAR ADIABATIC WALL
AND ZERO PRESSURE GRADIENT CONDITIONS.

TABLE I
RECORDED MEASUREMENTS

TEST NO.	STA. NO.	X	P O	T O	P W	T H	P P T	P F	P B	TAU W G
		INCHES	PSIA	DEG R	PSIA	DEG R	PSIA	PSIA	PSIA	LBS/FT**2
1	1	27.28	75.23	472.82	2.130	497.905	8.025	3.61	1.18	2.5491
2	1	27.28	79.08	471.99	2.195	481.460	8.520	3.83	1.22	2.4577
3	1	27.28	93.18	470.80	2.550	468.995	10.285	4.59	1.39	2.7521
4	1	27.28	101.81	477.90	2.785	461.965	11.480	5.06	1.49	3.1231
5	1	27.28	112.38	477.15	3.060	456.085	12.870	5.64	1.62	3.4339
6	1	27.28	124.86	476.68	3.370	449.465	14.480	6.30	1.76	3.7376
7	1	27.28	130.68	474.41	3.510	443.845	15.115	6.61	1.83	3.9804
8	1	27.28	147.54	469.20	4.005	445.525	17.310	7.54	2.05	4.5449
9	1	27.28	86.34	466.94	2.360	441.565	9.610	4.31	1.30	2.6397
10	1	27.28	115.20	466.05	3.115	436.120	13.255	5.87	1.66	3.6056
11	1	27.28	85.73	464.52	2.335	433.110	9.595	4.27	1.30	2.5612
12	1	27.28	151.85	463.87	4.055	425.575	17.950	7.83	2.08	4.6505
13	2	44.68	161.16	474.30	5.640	473.600	18.650	9.12	2.84	4.3553
14	2	44.68	225.59	466.68	7.840	436.130	27.350	13.06	3.79	6.3429
15	2	44.68	234.90	459.76	8.170	420.200	28.480	13.60	3.94	6.6564
16	2	44.68	240.72	456.15	8.370	412.430	29.450	13.97	4.01	7.7032
17	2	44.68	242.04	464.41	8.475	453.135	29.605	13.66	3.90	7.1488
18	2	44.68	266.16	458.12	9.340	422.765	33.115	15.23	4.22	7.8943
19	2	44.68	286.26	447.45	10.050	396.535	35.065	16.41	4.40	8.3548
20	2	44.68	306.41	441.37	10.760	381.275	38.980	17.78	4.72	8.8839
21	2	44.68	324.77	437.75	11.415	372.130	41.325	18.98	4.98	9.4438
22	2	44.68	344.58	478.58	11.750	448.380	42.740	19.58	5.02	9.3331
23	2	44.68	365.16	468.91	12.480	421.030	46.020	20.90	5.37	10.7240
24	2	44.68	383.27	461.05	13.140	404.970	48.870	22.14	5.62	11.0553
25	2	44.68	421.68	452.56	14.490	388.810	54.720	24.70	6.19	12.7046
26	2	44.68	164.27	446.11	5.880	391.760	19.530	9.40	2.73	5.2690
27	2	44.68	217.38	446.90	7.700	388.360	26.400	12.53	3.46	6.1627
28	2	44.68	228.66	476.24	7.940	474.440	27.220	12.86	3.66	6.5495
29	2	44.68	237.84	474.23	8.290	450.220	28.715	13.53	3.76	7.5617
30	2	44.68	239.81	470.64	8.365	437.235	28.970	13.73	3.77	7.1157
31	2	44.68	263.40	468.84	9.205	426.910	32.305	15.13	4.12	7.8090
32	2	44.68	284.34	461.52	9.940	415.380	35.160	16.47	4.40	8.4758
33	2	44.68	301.80	457.35	10.575	406.775	37.725	17.52	4.62	9.0376
34	2	44.68	322.02	452.70	11.275	395.465	40.435	18.85	4.89	9.5814
35	2	44.68	344.04	489.42	11.510	472.925	42.470	19.58	5.08	10.2437
36	2	44.68	358.86	482.08	12.015	447.480	45.010	20.55	5.29	10.6022
37	2	44.68	379.26	473.04	12.730	427.715	47.650	21.94	5.53	11.2055
38	3	59.68	65.83	478.30	2.140	508.960	6.320	3.26	1.20	2.6137
39	3	59.68	73.13	477.83	2.365	493.515	7.150	3.66	1.29	2.3121
40	3	59.68	84.18	483.93	2.710	483.800	8.365	4.26	1.44	2.7555
41	3	59.68	91.38	482.44	2.930	475.730	9.150	4.66	1.53	2.4858
42	3	59.68	63.18	476.23	2.055	473.230	6.150	3.13	1.13	1.9032
43	3	59.68	68.58	475.77	2.225	470.200	6.715	3.44	1.21	2.2156
44	3	59.68	77.63	474.31	2.500	464.400	7.685	3.93	1.34	2.4800
45	3	59.68	79.38	474.23	2.550	461.125	7.890	4.03	1.36	2.6444
46	3	59.68	90.30	473.76	2.895	457.160	9.105	4.53	1.51	2.3536
47	3	59.68	60.54	472.86	1.975	456.780	5.870	3.02	1.08	2.1070
48	3	59.68	71.63	472.28	2.310	454.975	7.070	3.62	1.24	2.3324
49	3	59.68	80.76	471.49	2.595	452.420	8.100	4.12	1.38	2.7377
50	3	59.68	102.72	471.20	3.275	447.270	10.525	5.32	1.67	3.3936

TABLE I (CONT.)
RECORDED MEASUREMENTS

TEST NO.	STA. NO.	X	P ₀	T ₀	P _H	T _H	P _P	P _F	P _B	TAU _H
		INCHES	PSIA	DEG R	PSIA	DEG R	PSIA	PSIA	PSIA	LBS/FT**2
51	3	59.68	111.90	470.77	3.565	442.965	11.535	5.84	1.80	2.0925
	3	59.68	124.80	470.20	3.970	439.670	13.015	6.54	1.97	4.1021
53	3	59.68	81.23	467.96	2.620	438.835	8.190	4.17	1.38	2.6931
54	3	59.68	101.58	468.94	3.245	435.950	10.400	5.28	1.65	3.4021
55	4	71.68	306.41	481.32	9.815	440.615	35.270	16.78	4.36	7.2925
56	4	71.68	321.12	477.80	10.280	427.090	37.350	17.59	4.54	8.5303
57	4	71.68	323.04	474.26	10.340	419.525	37.330	17.83	4.55	7.5192
58	4	71.68	343.13	469.35	10.980	410.915	39.995	18.97	4.80	8.2907
59	4	71.68	361.55	487.38	11.530	463.675	41.595	19.85	5.09	8.4298
60	4	71.68	383.38	483.23	12.225	442.600	44.465	21.32	5.35	9.5988
61	4	71.68	398.22	474.75	12.685	427.210	46.765	22.32	5.51	11.2935
62	4	71.68	402.00	466.90	12.815	410.520	47.125	22.62	5.54	10.3599
63	4	71.68	427.32	468.70	13.545	449.635	49.800	23.70	6.02	10.9544
64	4	71.68	125.04	458.89	4.000	463.220	13.035	6.53	2.02	3.2649
65	4	71.68	157.91	453.29	5.055	455.910	16.865	8.35	2.46	4.3433
66	4	71.68	236.94	454.98	7.565	431.405	26.485	12.84	3.48	6.3445
67	4	71.68	297.30	453.26	9.480	410.920	33.900	16.37	4.25	7.0553
68	4	71.68	317.52	454.87	10.150	395.130	35.650	17.52	4.51	7.5262
69	4	71.68	337.38	459.40	10.790	382.230	39.510	18.72	4.76	8.2856
70	4	71.68	357.90	466.79	11.420	369.005	42.095	20.06	5.01	8.8069
71	4	71.68	160.13	434.38	5.160	370.860	17.765	8.56	2.41	4.3714
72	4	71.68	238.73	474.26	7.610	431.155	26.395	12.73	3.55	6.2603
73	4	71.68	319.50	467.85	10.160	448.030	36.475	17.38	4.58	8.4291
74	4	71.68	381.84	466.57	12.120	423.140	44.490	21.23	5.33	9.3640
75	4	71.68	398.48	462.18	12.595	402.000	46.870	22.22	5.51	9.3725
76	5	83.68	152.45	455.74	5.300	474.535	16.145	8.41	2.66	4.5445
77	5	83.68	159.77	450.48	5.545	446.595	17.230	8.89	2.75	4.3532
78	5	83.68	168.90	447.64	5.855	433.755	18.415	9.44	2.88	5.0916
79	5	83.68	180.16	447.45	6.240	420.760	19.815	10.19	3.02	5.3691
80	5	83.68	189.05	445.86	6.545	412.405	20.915	10.69	3.15	5.5335
81	5	83.68	198.41	441.63	6.860	398.755	22.110	11.32	3.26	5.7333
82	5	83.68	218.45	439.88	7.530	386.255	24.680	12.52	3.55	6.3329
83	5	83.68	79.38	438.05	2.785	420.705	9.145	4.33	1.50	2.5552
84	5	83.68	125.45	441.44	4.345	407.065	13.420	7.02	2.16	3.9242
85	5	83.68	132.77	444.84	4.600	400.730	14.385	7.41	2.30	4.2789
86	5	83.68	143.40	455.26	4.975	483.060	15.080	7.85	2.54	4.4571
87	5	83.68	153.54	447.53	5.320	456.610	16.345	8.49	2.67	4.8153
88	5	83.68	173.27	443.88	5.990	431.380	18.370	9.68	2.94	5.3504
89	5	83.68	180.41	439.20	6.230	417.830	19.785	10.14	3.03	5.4353
90	5	83.68	191.40	435.32	6.620	403.610	21.350	10.82	3.18	5.6455
91	5	83.68	200.52	432.30	6.930	392.730	22.560	11.41	3.30	5.9454
92	5	83.68	209.81	429.34	7.240	382.950	23.800	11.96	3.44	6.0532
93	5	83.68	219.48	427.07	7.565	375.810	24.920	12.58	3.56	6.4963
94	5	83.68	228.23	424.27	7.870	366.750	26.145	13.09	3.70	6.7497
95	5	83.68	253.50	423.02	8.930	359.330	29.950	14.94	4.16	7.7430
96	6	95.68	65.05	460.87	2.265	483.630	6.425	3.38	1.28	1.9372
97	6	95.68	73.44	456.84	2.500	469.790	7.230	3.80	1.38	2.1285
98	6	95.68	82.62	454.79	2.795	459.780	8.265	4.31	1.53	2.6035
99	6	95.68	85.27	454.32	2.910	452.140	8.670	4.52	1.58	2.5361
100	6	95.68	93.59	454.50	3.145	445.510	9.595	4.96	1.68	2.9588

TABLE I (CONT.)
RECORDED MEASUREMENTS

TEST NO.	STA. NO.	X INCHES	P O PSIA	T O DEG R	P W PSIA	T W DEG R	P P T PSIA	P F PSIA	P B PSIA	TAU W G LBS/FT**2
101	6	95.68	106.55	452.70	3.565	436.800	11.005	5.68	1.88	3.3575
102	7	107.68	108.36	456.80	4.025	455.160	11.800	6.16	2.06	3.2009
103	7	107.68	122.94	453.95	4.545	435.520	13.500	7.09	2.30	3.6857
104	7	107.68	135.72	449.85	5.025	427.070	15.375	7.77	2.51	3.32+3
105	7	107.68	143.04	447.20	5.290	414.360	16.230	8.22	2.62	4.2418
106	7	107.68	151.91	445.55	5.605	406.800	17.395	8.80	2.73	4.4783
107	7	107.68	155.70	443.80	5.740	400.570	17.890	9.03	2.80	5.0325
108	7	107.68	163.26	442.56	6.010	395.270	18.860	9.44	2.97	4.6932
109	7	107.68	172.50	440.88	6.335	388.750	19.930	10.18	3.05	5.0077
110	7	107.68	181.62	449.60	6.690	466.945	20.240	10.39	3.33	5.2567
111	7	107.68	193.02	442.34	7.085	435.815	22.020	11.10	3.48	5.4118
112	7	107.68	202.02	437.67	7.410	418.360	23.210	11.74	3.60	5.7790
113	7	107.68	211.08	433.90	7.725	406.310	24.410	12.38	3.71	5.3504
114	7	107.68	222.30	429.27	8.130	391.760	25.935	13.14	3.67	6.2025
115	7	107.68	231.41	426.21	8.460	331.630	27.120	13.73	4.01	6.3214
116	7	107.68	236.76	422.10	8.655	370.200	28.040	14.07	4.08	7.3339
117	7	107.68	240.72	419.20	8.800	362.675	28.655	14.35	4.12	6.9180
118	7	107.68	262.91	417.99	9.590	354.725	31.510	15.86	4.45	7.3422
119	7	107.68	282.54	415.52	10.290	347.430	34.345	16.95	4.78	7.7212
120	7	107.68	301.26	442.04	10.920	436.400	34.985	17.32	5.26	8.1459
121	7	107.68	321.54	436.03	11.630	406.340	38.140	19.23	5.57	8.5048
122	7	107.68	341.76	431.23	12.370	387.635	41.080	20.60	5.88	8.8440
123	7	107.68	361.85	424.88	13.100	367.425	44.110	21.99	6.15	9.2717
124	7	107.68	381.84	426.21	13.815	352.705	46.995	23.16	6.51	9.8775
125	7	107.68	398.45	420.31	14.400	339.230	49.445	24.47	6.72	11.4013
126	7	107.68	422.09	469.42	15.180	440.060	50.250	25.58	7.15	11.4804
127	7	107.68	440.58	447.01	15.855	404.565	54.250	26.85	7.33	11.4916
128	7	107.68	458.76	447.72	16.545	386.680	57.085	27.86	7.63	12.3613
129	7	107.68	478.91	433.01	17.295	367.035	59.895	29.20	7.90	12.8233
130	7	107.68	496.66	437.48	18.015	368.425	63.185	30.59	8.16	13.3412
131	7	107.68	520.14	453.88	18.060	423.920	64.540	31.13	8.86	13.7505
132	7	107.68	549.90	443.80	19.885	381.455	69.835	33.12	9.12	15.3302
133	8	119.68	82.62	449.39	3.100	452.355	8.415	4.64	1.73	2.5976
134	8	119.68	91.73	453.00	3.410	437.585	9.530	5.16	1.86	2.8100
135	8	119.68	102.72	450.91	3.775	427.680	10.670	5.80	2.01	3.1325
136	8	119.68	113.70	459.66	4.150	417.830	11.945	6.41	2.16	3.3323
137	8	119.68	124.73	451.50	4.515	409.030	13.220	7.08	2.30	3.6887
138	8	119.68	135.59	462.03	4.885	401.570	14.570	7.67	2.46	4.0729
139	8	119.68	144.12	451.02	5.170	395.605	15.860	8.18	2.58	4.2697
140	8	119.68	155.70	453.44	5.600	401.305	17.050	8.72	2.81	4.5030
141	8	119.68	161.34	453.37	5.785	340.365	17.775	9.06	2.89	5.0312
142	8	119.68	168.26	448.67	5.855	334.025	18.040	9.17	2.92	4.7558
143	8	119.68	172.44	449.56	6.190	378.710	19.210	9.75	3.05	5.0585
144	8	119.68	183.36	440.70	6.555	372.695	20.425	10.41	3.16	5.3291
145	8	119.68	192.23	448.31	6.860	368.005	21.525	10.93	3.29	5.5869
146	8	119.68	203.52	454.17	7.250	363.530	22.940	11.54	3.48	5.8283
147	8	119.68	212.76	453.26	7.570	359.200	24.070	12.12	3.59	6.1335
148	8	119.68	220.02	447.23	7.820	355.090	24.885	12.55	3.71	6.3452
149	8	119.68	231.12	448.45	8.145	350.660	26.425	13.21	3.87	6.5519

TABLE II
CALCULATED RESULTS

TEST NO.	ME ME	DELTA-PF QE	RHO-E RHO*	R*ED * 10 ** -4	R*EH * 10 ** -4	LOG F3	LOG F4	LOG F5
1	.5349	.1843	2.1715	1.6580	.2674	5.0007	7.3294	3.4159
2	.5419	.1904	2.1404	1.7800	.2871	5.0233	7.3901	3.4385
3	.5524	.1997	2.1174	2.1349	.3443	5.1594	7.5660	3.5746
4	.5594	.2039	2.0806	2.3610	.3808	5.2543	7.6507	3.6695
5	.5653	.2085	2.0693	2.6334	.4247	5.3531	7.7584	3.7683
6	.5712	.2130	2.0573	2.9512	.4760	5.4416	7.8638	3.8568
7	.5713	.2149	2.0503	3.1225	.5036	5.4920	7.9115	3.9072
8	.5738	.2173	2.0629	3.5526	.5730	5.6091	8.0301	4.0243
9	.5553	.2028	2.0545	2.1141	.3410	5.1516	7.5490	3.5668
10	.5682	.2139	2.0473	2.8345	.4572	5.4176	7.8221	3.8328
11	.5578	.2019	2.0394	2.1401	.3452	5.1665	7.5603	3.5817
12	.5796	.2232	2.0301	3.8018	.6132	5.4175	7.8458	3.8328
13	.5193	.1981	2.0020	4.4607	.7195	5.7337	8.1280	4.1489
14	.5354	.2097	1.9301	6.8099	1.0984	6.0472	8.5063	4.4624
15	.5393	.2097	1.9056	7.4121	1.1955	6.1183	8.5805	4.5335
16	.5383	.2110	1.8943	7.7626	1.2520	6.2091	8.6165	4.6243
17	.5369	.2049	1.9751	7.0683	1.1400	6.1091	8.5510	4.5243
18	.5419	.2100	1.9122	8.4143	1.3571	6.2462	8.6950	4.6614
19	.5454	.2139	1.8648	9.7328	1.5698	6.3593	8.8175	4.7750
20	.5490	.2163	1.8427	10.9221	1.7616	6.4484	8.9181	4.8636
21	.5489	.2186	1.8262	11.9105	1.9210	6.5207	8.9894	4.9359
22	.5466	.2178	1.9414	9.8745	1.5927	6.3906	8.8494	4.8058
23	.5513	.2190	1.8343	11.2670	1.1173	6.4992	8.9609	4.9144
24	.5545	.2215	1.8699	12.4104	2.0017	6.5690	9.0442	4.9842
25	.5598	.2253	1.8463	14.3535	2.3151	6.7082	9.1733	5.1234
26	.5235	.2039	1.8513	5.7613	.9292	5.9333	8.3233	4.3490
27	.5323	.2107	1.8464	7.6138	1.2280	6.1240	8.5789	4.5392
28	.5298	.2054	2.0030	6.2703	1.0113	5.9993	8.4415	4.4150
29	.5336	.2093	1.9463	6.9263	1.1171	6.1238	8.5216	4.5390
30	.5332	.2112	1.9205	7.2362	1.1671	6.1197	8.5532	4.5349
31	.5381	.2126	1.8996	8.1564	1.3155	6.2186	8.6604	4.6338
32	.5407	.2159	1.8870	9.1070	1.4689	6.3133	8.7574	4.7290
33	.5437	.2171	1.8736	9.9262	1.6010	6.3855	8.8340	4.8007
34	.5458	.2203	1.8553	10.9347	1.7637	6.4641	8.9171	4.8793
35	.5489	.2195	1.9848	9.1163	1.4704	6.3467	8.7933	4.7019
36	.5538	.2213	1.9393	10.1319	1.6342	6.4245	8.8827	4.8397
37	.5539	.2249	1.9097	11.3143	1.8249	6.5131	8.9720	4.9285
38	.4761	.1655	2.1145	1.5823	.2552	4.8725	7.1761	3.2377
39	.4826	.1719	2.0804	1.8114	.2922	4.9973	7.2984	3.4125
40	.4884	.1781	2.0428	2.1153	.3413	5.1405	7.4358	3.5557
41	.4915	.1825	2.0254	2.3331	.3763	5.2229	7.4013	3.6381
42	.4802	.1674	2.0305	1.6470	.2656	4.6823	7.2009	3.2961
43	.4825	.1722	2.0254	1.7379	.2898	4.9876	7.2796	3.4028
44	.4872	.1774	2.0164	2.0501	.3307	5.0967	7.4005	3.5119
45	.4889	.1791	2.0110	2.1088	.3401	5.1383	7.4269	3.5541
46	.4937	.1841	2.0031	2.4179	.3900	5.2380	7.5523	3.6532
47	.4785	.1692	1.9964	1.6465	.2656	4.9361	7.1900	3.3513
48	.4862	.1765	1.9982	1.9391	.3128	5.0525	7.3461	3.4677
49	.4916	.1806	1.9961	2.1338	.3538	5.1773	7.4626	3.5025
50	.4996	.1899	1.9866	2.8070	.4527	5.3808	7.6888	3.7960

$$F3 = (TAJ \ H \ G \ * \ D \ **2) / (4 \ * \ RHO \ * \ NU \ **2)$$

$$F5 = (TAU \ H \ G \ * \ H \ **2) / (4 \ * \ RHO \ * \ NU \ **2)$$

$$F4 = ((DELTA \ P) \ P \ * \ D \ **2) / (4 \ * \ RHO \ * \ NU \ **2)$$

TABLE II (CONT.)

CALCULATED RESULTS

TEST NO.	LOG F6	LOG F7	RE THETA * 10 ** -4	(CF)G * 10 ** 3	(CF)P * 10 ** 3	(CF)F * 10 ** 3	(CF)VD * 10 ** 3
1	5.5535	5.7446	2.0088	1.34246	1.4599	1.2334	1.3211
2	5.6230	5.8113	2.1076	1.24488	1.4683	1.2547	1.3220
3	5.7969	5.9812	2.4681	1.19678	1.4487	1.2662	1.2930
4	5.8860	6.0719	2.6290	1.23874	1.4449	1.2679	1.2928
5	5.9882	6.1736	2.8926	1.25687	1.4307	1.2677	1.2752
6	6.0939	6.2790	3.1981	1.23418	1.4145	1.2650	1.2573
7	6.1451	6.3267	3.3605	1.24254	1.3946	1.2616	1.2492
8	6.4453	6.4453	3.8326	1.24929	1.3572	1.2425	1.2156
9	5.7822	5.9542	2.3222	1.23516	1.4716	1.2904	1.3350
10	6.0585	6.2373	3.0581	1.27208	1.4177	1.2601	1.2725
11	5.7873	5.9755	2.3226	1.25651	1.4798	1.2833	1.3418
12	6.0834	6.2610	3.9965	1.25336	1.3593	1.2562	1.2203
13	6.4093	6.5432	6.6989	1.08782	1.0787	1.0969	1.1270
14	6.7856	6.9215	9.4223	.99624	1.0221	1.0683	1.0934
15	6.8537	6.9957	9.9971	1.00360	1.0138	1.0526	1.0932
16	6.8940	7.0317	10.3447	1.13441	.9990	1.0498	1.0920
17	6.8180	6.9662	10.1477	1.04229	1.0138	1.0366	1.0629
18	6.9659	7.1102	11.3185	1.04152	.9882	1.0280	1.0691
19	7.0894	7.2327	12.4245	1.03697	.9645	1.0189	1.0729
20	7.1891	7.3333	13.6269	1.02214	.9479	1.0077	1.0666
21	7.2652	7.4045	14.5678	1.02407	.9273	1.0016	1.0625
22	7.1274	7.2645	13.5819	1.03672	.9595	1.0288	1.0261
23	7.2336	7.3761	14.7650	1.04996	.9436	1.0102	1.0312
24	7.3170	7.4594	15.8291	1.02970	.9306	1.0035	1.0300
25	7.4452	7.5885	17.7880	1.07405	.9120	.9921	1.0213
26	6.6101	6.7385	7.4402	1.11731	1.0331	1.0601	1.1719
27	6.8554	6.9941	9.6750	.99428	.9882	1.0548	1.1247
28	6.7210	6.8567	9.2795	1.01531	1.0208	1.0615	1.0671
29	6.8030	6.9368	9.6918	1.13958	1.0104	1.0621	1.0815
30	6.8394	6.9684	9.8675	1.04793	.9992	1.0635	1.0688
31	6.9414	7.0756	10.8506	1.04728	.9851	1.0466	1.0867
32	7.0409	7.1726	11.9242	1.05268	.9657	1.0396	1.0700
33	7.1151	7.2492	12.7809	1.05257	.9539	1.0285	1.0639
34	7.2012	7.3323	13.7853	1.05004	.9372	1.0238	1.0569
35	7.0710	7.2085	13.1270	1.07735	.9841	1.0499	1.0004
36	7.1563	7.2979	13.9528	1.06770	.9743	1.0387	.9913
37	7.2524	7.3872	15.0997	1.06666	.9492	1.0335	.9799
38	5.4547	5.5913	3.7020	1.12658	1.2117	1.1320	1.2325
39	5.5817	5.7136	4.0975	1.16462	1.1998	1.1434	1.2098
40	5.7242	5.8510	4.5989	1.20875	1.1784	1.1481	1.1842
41	5.8165	5.8165	4.9921	1.21042	1.1620	1.1525	1.1688
42	5.4769	5.6161	3.5842	1.10909	1.2236	1.1395	1.2432
43	5.5633	5.6948	3.8792	1.18649	1.2058	1.1498	1.2281
44	5.6892	5.8157	4.3719	1.17944	1.1851	1.1520	1.2064
45	5.7167	5.8421	4.4733	1.23159	1.1838	1.1560	1.2039
46	5.8459	5.9675	5.0616	1.18188	1.1617	1.1552	1.1816
47	5.4738	5.6052	3.4775	1.27598	1.2188	1.1524	1.2651
48	5.6347	5.7613	4.0824	1.20153	1.1999	1.1603	1.2268
49	5.7513	5.8778	4.5839	1.25309	1.1839	1.1569	1.2054
50	5.9854	6.1048	5.7603	1.22828	1.1414	1.1534	1.1626

$$F6 = (\text{DELTA } P \cdot F * H ** 2) / (4 * \text{RHO} * \text{NU} ** 2)$$

$$F7 = ((\text{DELTA } P)P * H ** 2) / (4 * \text{RHO} * \text{NU} ** 2)$$

TABLE II (CONT.)
CALCULATED RESULTS

TEST NO.	ME ME	DELTA_P QE	RHO_E RHO*	R*ED * 10 ** -4	R*EH * 10 ** -4	LOG F3	LOG F4	LOG F5
51	.5016	.1931	1.9770	3.0886	.4982	5.2141	7.7732	3.6293
52	.5054	.1960	1.9705	3.4689	.5595	5.5589	7.8793	3.9741
53	.4925	.1825	1.9674	2.2914	.3696	5.1984	7.4958	3.6136
54	.4990	.1908	1.9621	2.8611	.4615	5.3968	7.6989	3.8120
55	.5349	.2161	1.9438	8.4867	1.3688	6.1881	8.6997	4.6033
56	.5384	.2168	1.9181	9.2046	1.4846	6.3033	8.7700	4.7185
57	.5363	.2193	1.9071	9.4538	1.5248	6.2641	8.7874	4.6793
58	.5391	.2203	1.8962	10.2919	1.6600	6.3517	8.8632	4.7669
59	.5356	.2182	1.9891	9.4203	1.5194	6.2303	8.8015	4.6961
60	.5383	.2227	1.9465	10.5154	1.6960	6.3980	8.8918	4.8132
61	.5424	.2258	1.9275	11.3877	1.8367	6.5173	8.9635	4.9325
62	.5417	.2271	1.9024	12.0531	1.9440	6.5196	9.0060	4.9348
63	.5409	.2219	2.0015	11.5743	1.8668	6.5051	8.9916	4.9203
64	.5043	.1925	2.0576	3.3230	.5360	5.4390	7.6587	3.8542
65	.5116	.1989	2.0528	4.2862	.6913	5.6815	8.0913	4.0967
66	.5263	.2110	1.9847	6.8051	1.0976	6.0573	8.5028	4.4725
67	.5328	.2179	1.9352	8.9912	1.4502	6.2351	8.7445	4.6513
68	.5362	.2187	1.8886	10.0102	1.6145	6.3177	8.8327	4.7329
69	.5408	.2208	1.8441	10.9720	1.7697	6.4024	8.9093	4.8176
70	.5426	.2247	1.7951	11.9656	1.9299	6.4674	8.9759	4.8826
71	.5222	.2074	1.8671	5.5105	.8888	5.8537	8.2861	4.2589
72	.5232	.2056	2.0654	6.0189	.9708	5.9593	8.4083	4.3745
73	.5338	.2145	2.0021	8.7144	1.4055	6.2695	8.7327	4.6847
74	.5406	.2231	1.9376	11.0568	1.7834	6.4317	8.9373	4.8869
75	.5451	.2257	1.8925	12.1540	1.9603	6.5145	9.0184	4.9297
76	.4931	.1924	2.0553	4.2311	.6824	5.6864	8.0485	4.1016
77	.4990	.1962	1.9976	4.7448	.7653	5.7621	8.1461	4.1973
78	.5026	.1934	1.9718	5.1802	.8355	5.8497	8.2229	4.2649
79	.5055	.2034	1.9386	5.7348	.9201	5.9213	8.3043	4.3365
80	.5074	.2039	1.9211	6.1197	.9870	5.9789	8.3646	4.3941
81	.5099	.2078	1.8952	6.6658	1.0751	6.0375	8.4373	4.4527
82	.5148	.2104	1.8726	7.5376	1.2157	6.1408	8.5471	4.5560
83	.4816	.1810	1.9561	2.5563	.4123	5.2584	7.5690	3.6736
84	.4969	.1972	1.9171	4.2306	.6662	5.6571	8.0041	4.0723
85	.5008	.1957	1.8917	4.4353	.7154	5.7260	8.0669	4.1412
86	.4913	.1891	2.0818	3.8894	.6273	5.5374	7.9779	4.0526
87	.4953	.1937	2.0323	4.4530	.7182	5.7487	8.0920	4.1639
88	.5028	.1990	1.9750	5.3386	.8611	5.8891	8.2508	4.3043
89	.5051	.2018	1.9527	5.7730	.9311	5.9402	8.3172	4.3554
90	.5101	.2042	1.9236	6.3798	1.0290	6.0109	8.4060	4.4261
91	.5130	.2070	1.9019	6.8898	1.1113	6.0752	8.4727	4.4904
92	.5158	.2030	1.8831	7.4092	1.1950	6.1229	8.5364	4.5381
93	.5164	.2106	1.8695	7.9112	1.2760	6.1877	8.5910	4.6029
94	.5191	.2108	1.8511	8.4587	1.3643	6.2411	8.6434	4.6563
95	.5218	.2131	1.8344	9.8146	1.5830	6.3706	8.7792	4.7858
96	.4639	.1634	2.0714	1.7705	.2856	4.9403	7.2534	3.3555
97	.4749	.1700	2.0513	2.0245	.3205	5.0377	7.3746	3.4529
98	.4810	.1742	2.0328	2.3224	.3746	5.1910	7.5011	3.6062
99	.4829	.1767	2.0154	2.4645	.3975	5.2195	7.5525	3.6347
100	.4897	.1821	1.9993	2.7081	.4368	5.3203	7.6430	3.7355

$$F3 = (TAJ W G * D **2)/(4 * RHO* * NU* **2)$$

$$F5 = (TAU W G * H **2)/(4 * RHO* * NU* **2)$$

$$F4 = ((DELTA P) P * D **2)/(4 * RHO* * NU* **2)$$

TABLE II (CONT.)

CALCULATED RESULTS

TEST NO.	LOG F6	LOG F7	RE THETA * 10 ** -4	(CF) G * 10 ** 3	(CF) P * 10 ** 3	(CF) F * 10 ** 3	(CF) VD * 10 ** 3
51	6.0734	6.1884	6.2556	1.24399	1.1214	1.1517	1.1503
52	6.1794	6.2945	6.9487	1.22167	1.1024	1.1420	1.1328
53	5.7874	5.9110	4.6591	1.22301	1.1762	1.1595	1.2141
54	5.9986	6.1141	5.7389	1.24196	1.1351	1.1573	1.1735
55	6.9930	7.1149	18.7831	.88126	.9619	1.0518	.9744
56	6.9590	7.1852	19.8378	.98969	.9529	1.0395	.9757
57	7.0847	7.2026	20.1572	.86221	.9414	1.0457	.9776
58	7.1581	7.2784	21.6555	.89515	.9295	1.0337	.9712
59	7.0978	7.2167	21.5914	.86541	.9349	1.0375	.9377
60	7.1927	7.3070	23.0965	.92940	.9135	1.0557	.9430
61	7.2637	7.3787	24.5390	1.05328	.9126	1.0347	.9414
62	7.3099	7.4212	25.3430	.95766	.8985	1.0304	.9462
63	7.2866	7.4065	26.6989	.95464	.8999	1.0118	.9048
64	6.1529	6.2739	8.5730	.96753	1.1042	1.1260	1.0618
65	6.3874	6.5065	10.8834	1.01880	1.0588	1.1071	1.0231
66	6.7998	6.9180	15.9104	.99324	.9866	1.0717	.9863
67	7.0448	7.1597	19.8354	.88088	.9414	1.0483	.9707
68	7.1231	7.2479	21.0143	.87864	.9232	1.0328	.9791
69	7.2025	7.3245	21.9551	.91012	.9221	1.0259	.9893
70	7.2737	7.3911	22.7056	.91306	.9097	1.0275	1.0034
71	6.5826	6.7013	11.7114	1.00754	1.0395	1.1055	1.0825
72	6.6992	6.8235	15.1229	.97356	1.0054	1.0677	.9653
73	7.0246	7.1479	20.3574	.98074	.9478	1.0362	.9441
74	7.2352	7.3525	24.1504	.91259	.9138	1.0291	.9405
75	7.3122	7.4316	25.3607	.93556	.9069	1.0236	.9499
76	6.3621	6.4837	12.1786	1.05601	.9904	1.0767	1.0037
77	6.4578	6.5613	12.9384	1.07708	.9906	1.0750	1.0147
78	6.5333	6.6381	13.7584	1.06996	.9817	1.0691	1.0144
79	6.6205	6.7195	14.6366	1.05750	.9637	1.0750	1.0168
80	6.6786	6.7798	15.4047	1.05915	.9562	1.0639	1.0153
81	6.7553	6.8525	16.3319	1.03504	.9456	1.0601	1.0161
82	6.8622	6.9623	17.9985	1.03985	.9331	1.0541	1.0097
83	5.8764	5.9842	6.9320	1.13474	1.1003	1.1277	1.1413
84	6.3217	6.4193	10.5776	1.11036	1.0257	1.1135	1.0797
85	6.3766	6.4821	11.0444	1.14378	1.0221	1.0972	1.0822
86	6.2871	6.3931	11.5057	1.10231	1.0198	1.0760	1.0039
87	6.4046	6.5072	12.5724	1.11130	.9923	1.0733	1.0071
88	6.5622	6.6660	14.2598	1.09926	.9741	1.1248	1.0066
89	6.6305	6.7324	15.0357	1.07114	.9636	1.0840	1.0077
90	6.7159	6.8212	16.1044	1.04779	.9566	1.0965	1.0079
91	6.7837	6.8879	16.9947	1.05370	.9478	1.0950	1.0078
92	6.8446	6.9516	17.9111	1.02700	.9309	1.0450	1.0069
93	6.9039	7.0062	18.8308	1.05340	.9263	1.0454	1.0045
94	6.9581	7.0646	19.7234	1.05227	.9196	1.0336	1.0047
95	7.0679	7.1944	22.3684	1.06204	.8933	1.0154	.9921
96	5.5373	5.6686	6.1501	1.07371	1.1527	1.0974	1.1173
97	5.6671	5.7698	6.8841	1.03848	1.1350	1.1096	1.1044
98	5.7331	5.9163	7.7391	1.13283	1.1201	1.1056	1.0896
99	5.8472	5.9677	8.0733	1.08351	1.1117	1.1082	1.0865
100	5.9386	6.0582	8.7147	1.14062	1.1204	1.1191	1.0809

$$F6 = (\Delta P F * H^{**2}) / (4 * \rho * \nu^{**2})$$

$$F7 = ((\Delta P) P * H^{**2}) / (4 * \rho * \nu^{**2})$$

TABLE II (CONT.)

CALCULATED RESULTS

TEST NO.	ME ME	DELIA-PF QE	RHO-E RHO*	R*ED * 10 ** -4	R*EH * 10 ** -4	LOG F3	LOG F4	LOG F5
101	.4928	.1857	1.9831	3.1416	.5067	5.4453	7.7739	3.8605
102	.4838	.1863	1.9721	3.3187	.5353	5.4381	7.8121	3.8533
103	.4923	.1923	1.9316	3.9330	.6353	5.5854	7.9582	4.0006
104	.5017	.1912	1.9193	4.4571	.7189	5.6740	8.0792	4.0892
105	.5025	.1932	1.8936	4.8539	.7829	5.7534	8.1486	4.1686
106	.5058	.1975	1.8784	5.2542	.8475	5.8163	8.2197	4.2320
107	.5070	.1978	1.8673	5.4730	.8827	5.8893	8.2546	4.3050
108	.5090	.1961	1.8570	5.8175	.9383	5.8904	8.3086	4.3056
109	.5095	.2048	1.8448	6.2496	1.0080	5.9540	8.3638	4.3692
110	.4976	.1923	2.0247	5.3957	.8703	5.8643	8.2612	4.2900
111	.5056	.1956	1.9647	6.1897	.9983	5.9530	8.3812	4.3732
112	.5090	.1997	1.9310	6.7852	1.0944	6.0392	8.4575	4.4544
113	.5104	.2039	1.9095	7.3190	1.1805	6.0875	8.5227	4.5028
114	.5134	.2070	1.8823	8.0323	1.2955	6.1645	8.6021	4.5797
115	.5149	.2066	1.8630	8.6063	1.3892	6.2109	8.6602	4.6261
116	.5132	.2095	1.8412	9.1228	1.4714	6.3113	8.7113	4.7269
117	.5198	.2110	1.8275	9.4969	1.5318	6.3099	8.7456	4.7251
118	.5224	.2158	1.8092	10.6034	1.7102	6.3395	8.8413	4.8047
119	.5272	.2143	1.7954	11.6502	1.8791	6.4589	8.9277	4.8741
120	.5136	.2060	1.9730	9.5039	1.5329	6.3205	8.7703	4.7356
121	.5207	.2122	1.9094	11.0265	1.7765	6.4252	8.8950	4.8404
122	.5249	.2150	1.8707	12.3643	1.9942	6.5061	8.9933	4.9213
123	.5292	.2185	1.8311	13.9113	2.2438	6.5949	9.0937	5.0101
124	.5324	.2177	1.7881	15.2802	2.4645	6.6704	9.1701	5.0856
125	.5353	.2226	1.7648	16.6554	2.6864	6.7835	9.2439	5.1388
126	.5230	.2167	1.9184	12.9531	2.0892	6.5906	9.0417	4.9958
127	.5337	.2219	1.8804	14.9989	2.4192	6.6953	9.1778	5.1110
128	.5366	.2206	1.8314	16.3848	2.6427	6.7593	9.2478	5.1750
129	.5378	.2223	1.8123	16.2702	2.9468	6.8470	9.3393	5.2622
130	.5421	.2248	1.8056	18.8899	3.0468	6.8733	9.3742	5.2890
131	.5367	.2148	1.9155	16.7385	2.6998	6.7911	9.2862	5.2063
132	.5427	.2180	1.8255	20.0165	3.2288	6.9465	9.4302	5.3618
133	.4564	.1701	1.9794	2.5794	.4160	5.2456	7.5541	3.6608
134	.4743	.1771	1.9366	2.9391	.4740	5.3404	7.6725	3.7556
135	.4765	.1827	1.9217	3.3457	.5396	5.4502	7.7856	3.8654
136	.4812	.1853	1.8789	3.7512	.6050	5.5244	7.8841	3.9396
137	.4855	.1913	1.8791	4.2042	.6781	5.6290	7.9907	4.0442
138	.4907	.1916	1.8382	4.6054	.7428	5.7065	8.0694	4.1217
139	.4949	.1949	1.8493	4.9941	.8055	5.7741	8.1500	4.1893
140	.4963	.1901	1.8573	5.3183	.8578	5.8201	8.2098	4.2352
141	.4993	.1919	1.7023	6.4313	1.0454	5.9873	8.3480	4.4025
142	.5002	.1921	1.8242	5.8410	.9421	5.8975	8.2892	4.3127
143	.5025	.1948	1.8086	6.2586	1.0095	5.9565	8.3495	4.3717
144	.5033	.1987	1.8140	6.7903	1.0952	6.0255	8.4230	4.4407
145	.5052	.1999	1.7359	7.1551	1.1540	6.0646	8.4651	4.4798
146	.5094	.1994	1.7627	7.6204	1.2291	6.1075	8.5182	4.5228
147	.5090	.2020	1.7539	8.0603	1.3000	6.1574	8.5672	4.5726
148	.5092	.2025	1.7561	8.4672	1.3657	6.2011	8.6107	4.6163
149	.5130	.2040	1.7429	8.9787	1.4482	6.2413	8.6649	4.6571

$$F3 = (\text{TAU } W \text{ G } * D **2) / (4 * RHO * * NU * **2)$$

$$F5 = (\text{TAU } W \text{ G } * H **2) / (4 * RHO * * NU * **2)$$

$$F4 = ((\text{DELTA } P) P * D **2) / (4 * RHO * * NU * **2)$$

TABLE II (CONT.)

CALCULATED RESULTS

TEST NO.	LOG F6	LOG F7	RE THETA * 10 ** -4	(CF)G * 10 ** 3	(CF)P * 10 ** 3	(CF)F * 10 ** 3	(CF)VD * 10 ** 3
101	6.0727	6.1891	9.9076	1.13956	1.0820	1.1081	1.0046
102	6.1192	6.2273	11.2075	1.01009	1.0525	1.1002	1.00475
103	6.2729	6.3734	12.7395	1.02771	1.0212	1.0978	1.00418
104	6.3748	6.4944	14.1716	.99042	1.0222	1.0668	1.00292
105	6.4477	6.5638	15.0170	1.01638	1.0037	1.0610	1.00300
106	6.5224	6.6349	15.9794	1.01164	.9951	1.0654	1.00200
107	6.5561	6.6698	16.4471	1.10974	.9894	1.0481	1.00209
108	6.6023	6.7236	17.2690	.98896	.9808	1.0403	1.00223
109	6.6810	6.7840	18.2891	.99869	.9649	1.0677	1.00162
110	6.5665	6.6764	18.6330	.93411	.9513	1.0253	.9435
111	6.6392	6.7964	20.2536	.95480	.9468	1.0202	.9577
112	6.7515	6.8727	21.4625	.93474	.9336	1.0231	.9614
113	6.8313	6.9379	22.6429	.95690	.9243	1.0282	.9619
114	6.9126	7.0173	24.1415	.96201	.9125	1.0256	.9624
115	6.9713	7.0754	25.3300	.94202	.9017	1.0193	.9628
116	7.0183	7.1265	26.2378	1.06913	.8993	1.0133	.9154
117	7.0535	7.1606	26.9135	.99079	.8955	1.0134	.9678
118	7.1545	7.2565	29.3767	.96421	.8785	1.0132	.9623
119	7.2301	7.3429	31.7129	.94431	.8714	.9897	.9569
120	7.0322	7.1855	30.9035	.93683	.8679	.9923	.8940
121	7.2046	7.3112	33.5037	.91735	.8536	.9853	.9065
122	7.3010	7.4085	36.0461	.89717	.8466	.9775	.9107
123	7.4011	7.5089	38.8593	.88622	.8350	.9715	.9152
124	7.4737	7.5853	40.7143	.89704	.8257	.9533	.9250
125	7.5494	7.6591	43.2224	.99284	.8161	.9576	.9202
126	7.3538	7.4569	39.1284	.94620	.8255	.9814	.8816
127	7.4846	7.5930	43.6195	.93864	.8275	.9684	.8816
128	7.5474	7.6530	45.2334	.93507	.8190	.9494	.8943
129	7.6468	7.7550	49.3672	.92979	.7998	.9373	.8697
130	7.6730	7.7894	50.5693	.92848	.8043	.9410	.8898
131	7.5738	7.7014	49.9806	.92155	.8100	.9190	.8527
132	7.7149	7.8454	54.3029	.96700	.7923	.9042	.8733
133	5.8655	5.9693	9.8052	1.06935	1.0365	1.0634	1.0682
134	5.9838	6.0877	10.7007	1.04704	1.0337	1.0774	1.0693
135	6.1066	6.2008	11.9813	1.04872	1.0079	1.0820	1.0561
136	6.2035	6.2993	12.8397	1.01154	.9978	1.0767	1.0609
137	6.3152	6.4059	14.3644	1.02525	.9833	1.0818	1.0427
138	6.3854	6.4846	15.0539	1.04399	.9805	1.0665	1.0510
139	6.4659	6.5652	16.4891	1.03107	.9734	1.0660	1.0322
140	6.5117	6.6250	17.6150	1.00607	.9632	1.0294	1.0184
141	6.6496	6.7632	18.2208	1.08656	.9326	1.0075	1.0792
142	6.5896	6.7044	18.6834	1.01512	.9529	1.0223	1.0227
143	6.6521	6.7647	19.6388	1.02152	.9443	1.0225	1.0212
144	6.7323	6.8382	21.3963	1.01431	.9263	1.0244	1.0062
145	6.7741	6.8803	21.8461	1.01526	.9216	1.0212	1.0141
146	6.8220	6.9334	22.6464	1.00132	.9211	1.0078	.9363
147	6.8742	6.9824	23.6851	1.00805	.9068	1.0092	1.0149
148	6.9187	7.0259	24.9096	1.00961	.8953	1.0020	1.0066
149	6.9694	7.0801	25.9954	.99369	.8941	.9979	1.0057

$$F6 = (\Delta P F * H^{**2}) / (4 * \rho H * * NU^{**2})$$

$$F7 = ((\Delta P)P * H^{**2}) / (4 * \rho H * * NU^{**2})$$

SUPERSONIC SEPARATED TURBULENT BOUNDARY-
LAYER OVER A WAVY WALL*

A. Polak**

and

M.J. Werle**

Department of Aerospace Engineering and Applied Mechanics
University of Cincinnati
Cincinnati, Ohio 45221

November 1977

* This research was supported by NASA Langley Research
Center under Grant No. NSG 1208.

** Professor

FOREWORD

This research was supported by NASA Langley Grant No. NSG 1208. The NASA Technical Officer for this grant was Mr. James C. Dunavant, NASA Langley Research Center.

The authors wish to gratefully acknowledge the continued interest and technical guidance of Prof. R.T. Davis of the University of Cincinnati.

SUPERSONIC SEPARATED TURBULENT BOUNDARY-
LAYER OVER A WAVY WALL

by

A. Polak and M.J. Werle
University of Cincinnati

SUMMARY

This research is concerned with the development of a prediction method for calculating detailed distributions of surface heating rates, pressure and skin friction over a wavy wall in a two-dimensional supersonic flow. Of particular interest is the flow of thick turbulent boundary layers. The surface geometry and the flow conditions considered are such that there exists a strong interaction between the viscous and inviscid flow. First, using the interacting turbulent-boundary layer equations, the problem is formulated in physical coordinates and then a reformulation of the governing equations in terms of Levy-Lees variables is given. Next, a numerical scheme for solving interacting boundary layer equations is adapted. A number of modifications which led to the improvement of the numerical algorithm are discussed. Finally, results are presented for flow over a train of up to six waves at various flow conditions. Limited comparisons with independent experimental and analytical results are also given.

TABLE OF CONTENTS

	<u>Page</u>
INTRODUCTION	1
GOVERNING EQUATIONS	3
NUMERICAL METHOD OF SOLUTION	14
RESULTS AND DISCUSSION	20
CONCLUSIONS	28
REFERENCES	29
APPENDICES	
A. GRID SIZE EFFECT ON ACCURACY	31
B. INITIAL PROFILES FOR THICK BOUNDARY LAYERS . . .	35

NOMENCLATURE

a	Amplitude.
A	Eddy viscosity damping function.
C_f	Skin friction coefficient, $\tau_w^*/\rho_\infty^* u_\infty^{*2}/2$.
C_p	Constant pressure specific heat.
F	Normalized longitudinal velocity, $F = u/u_e$.
g	Normalized total enthalpy, $g = H/H_e$.
h	Heat transfer coefficient.
H	Nondimensional total enthalpy, $H = H^*/u_\infty^{*2}$.
K_1, K_2	Constants in eddy viscosity models.
λ	Viscosity parameter, $\lambda = \rho u / \rho_e u_e$.
$\bar{\lambda}$	Mixing length.
L^*	Reference length.
M	Mach number.
p	Nondimensional static pressure, $p = p^*/\rho_\infty^* u_\infty^{*2}$.
Pr	Prandtl number.
Pr_T	Turbulent Prandtl number.
q_T	Nondimensional turbulent heat flux rate.
Re_r	Reynolds number based on reference viscosity, $Re_r = Re_\infty \mu_\infty^* / \mu_r^* (u_\infty^{*2} / C_p^*)$.
Re	Reynolds number based on free stream viscosity, $Re_\infty = \rho_\infty^* u_\infty^* L^* / \mu_\infty^*$.
t	Time.
T	Nondimensional static temperature, $T = T^* C_p^* / u_\infty^{*2}$.
u, v	Nondimensional x_1 and x_2 velocity components, $u = u^* / u_\infty^*$, $v = v^* Re_r^{1/2} / u_\infty^*$.
V	Transformed v velocity in the boundary-layer.

x_1, x_2	Nondimensional coordinates (surface or Cartesian), $x_1 = x_1^*/L^*$, $x_2 = Re_r^{1/2} x_2^*/L^*$.
w	Wavelength.
α	u_e^2/T_e .
β	Pressure gradient parameter, $(2\xi/u_e)(du_e/d\xi)$.
γ	Ratio of specific heats, C_p/C_v .
$\bar{\gamma}$	Transverse intermittency function.
δ	Nondimensional displacement thickness.
δ_{kin}^c	Incompressible displacement thickness.
δ_T	Displacement body height.
ϵ	Eddy viscosity.
$\bar{\epsilon}$	Eddy viscosity parameter, $\bar{\epsilon} = 1 + \frac{\epsilon}{u} \Gamma$.
$\hat{\epsilon}$	Eddy viscosity parameter, $\hat{\epsilon} = 1 + \frac{\epsilon}{u} \frac{Pr}{Pr_T} \Gamma$.
η	Transformed normal variable.
θ	Static temperature ratio, $\theta = T/T_e$.
θ_S	Surface inclination of the body.
θ_T	Surface inclination of the displacement body.
$\bar{\theta}$	Nondimensional momentum thickness.
Γ	Longitudinal intermittency function.
ν	Nondimensional viscosity, $\nu = \nu^*/\nu_r^* (u_\infty^{*2}/C_p^*)$.
ξ	Transformed longitudinal variable.
π_1, π_2	Functional grouping in inner region eddy viscosity model.
τ_T	Nondimensional turbulent shear stress.
ρ	Nondimensional density, $\rho = \rho^*/\rho_\infty^*$.

Subscripts

e	Conditions evaluated on the displacement body or at the outer edge of the boundary layer.
f.p.	Flat plate value.

- i Index for the longitudinal finite difference mesh.
- w Conditions evaluated at the wall.
- ∞ Conditions evaluated in the upstream freestream.

Superscripts

- * Denotes dimensional quantities.

INTRODUCTION

This research is concerned with the two-dimensional supersonic flow of thick turbulent boundary layers over a train of relatively small wave-like protuberances. Interest in this subject arises from the need to predict the extent to which an initially flat plate boundary layer has been disturbed by a regular corrugation in the wall surface. The flow conditions and the geometry considered here are such that there exists a strong interaction between the viscous and inviscid flow. The problem cannot be solved without including interaction effects because classical boundary layer methods would terminate in a separation point singularity.

To handle the present subject by boundary-layer methods, a technique for treatment of the interacting boundary layer equations as well as models for turbulence and for the viscous-inviscid interaction process must be available. A numerical method for addressing closed bubble separation regions was developed by Werle and Vatsa [1]. It was applied to a number of laminar separated flow problems including flow over a train of sine-wave protuberances [2]. This method uses the interacting boundary layer equations with a time-like relaxation concept which accounts for the boundary-value nature of the problem. This approach is adopted in the present study with the inclusion of the eddy viscosity model of Cebeci and Smith into the solution scheme. The present form of the numerical algorithm includes several modifications to that of the earlier work [2, 3] in order to accommodate the turbulent nature of the flow, the thick boundary layer, and the rather dramatic geometry variations of the wavy wall.

It was found that the method was capable of handling the interacting turbulent flows of present interest. Solutions were obtained for flow of thick turbulent boundary layers over a train of waves. The results are presented in terms of surface pressure, skin friction and heat transfer distributions. The predicted trends are compared with available analytical results based on small disturbance theory and with experimental data.

GOVERNING EQUATIONS

1. Boundary Layer Equations in Physical Coordinates

The suitability of the interacting boundary layer equations for describing the relatively strong streamwise variations in the boundary layer characteristics due to sudden changes in the body geometry has been, at least for the laminar case, verified earlier [1, 2]. This approach is used in the present study in which Prandtl's classical boundary layer equations are adopted with the only modification that the pressure variation was not prescribed but calculated simultaneously from a viscous-inviscid interaction model.

The boundary layer approximation in two-dimensional viscous flow problems implies that the pressure variation is assumed to occur only along one coordinate, taken in the general direction of the wall shear layer. The degree of this approximation depends on the choice of the coordinate system. While for very thin boundary layers over a corrugated wall, or thick boundary layers over a relatively flat wall, surface coordinates were suitable, (see Ref. 3) for thick boundary layers flowing over a small amplitude wavy wall, Cartesian coordinates were found to be more appropriate. Accordingly, the governing equations will first be written to apply to both the usual surface coordinates (s^*, n^*) and the Cartesian coordinates (x^*, y^*) using the notation (x_1^*, x_2^*) to denote either of these. Non-dimensional variables of order one are now defined according to the scheme

$$x_1 = x_1^*/L^* , \quad x_2 = Re_r^{1/2} x_2^*/L^* \quad (1a)$$

$$u = u^*/u_\infty^* , \quad v = Re_r^{1/2} v^*/u_\infty^* , \quad p = p^*/\rho_\infty^* u_\infty^{*2} ,$$

$$\rho = \rho^*/\rho_\infty^* , \quad T = C_p^* T^*/u_\infty^{*2} \quad (1b)$$

$$\text{with} \quad Re_r \equiv \rho_\infty^* u_\infty^* L^*/\mu^* (u_\infty^{*2}/C_p^*) \quad (1c)$$

and u^* , v^* , p^* , ρ^* and T^* represent the mean velocities, pressure, density and temperature respectively.

The turbulent boundary layer equations in these variables are:

Continuity Equation

$$\frac{\partial}{\partial x_1} (\rho u) + \frac{\partial}{\partial x_2} (\rho v) = 0 \quad (2)$$

Momentum Equation

$$\rho (u \frac{\partial u}{\partial x_1} + v \frac{\partial u}{\partial x_2}) = \rho_e u_e \frac{du_e}{dx_1} + \frac{\partial}{\partial x_2} (u \frac{\partial u}{\partial x_2} + \tau_T) \quad (3)$$

Energy Equation

$$\rho (u \frac{\partial T}{\partial x_1} + v \frac{\partial T}{\partial x_2}) = - \rho_e u_e \frac{du_e}{dx_1} u + \frac{\partial u}{\partial x_2} (u \frac{\partial u}{\partial x_2} + \tau_T)$$

$$+ \frac{\partial}{\partial x_2} (\frac{u}{Pr} \frac{\partial T}{\partial x_2} + q_T) , \quad (4)$$

where τ_T and q_T are the nondimensional turbulent stress and turbulent heat flux respectively.

The gas is assumed to be air with constant specific heats and constant Prandtl number, $Pr = 0.72$ with the perfect gas law,

State Equation

$$p = \frac{\gamma-1}{\gamma} T \quad (5)$$

Boundary Conditions

$$\begin{aligned} u(x_1, x_2) &= 0 \\ v(x_1, x_2) &= 0 \quad \text{at } x_2 = x_{2w}(x_1) \\ T(x_1, x_2) &= T_w(x_1) \end{aligned}$$

and (6)

$$\begin{aligned} u(x_1, x_2) &= u_e(x_1) \\ T(x_1, x_2) &= T_e(x_1) \end{aligned} \quad \text{at } x_2 \rightarrow \infty$$

where $x_{2w}(x_1)$ describes the body surface contour ($x_{2w} = 0$ in surface coordinates, $x_{2w} = y_w(x)$ for Cartesian coordinates).

2. Turbulence Model

To obtain closure of the system of equations (2-6), models for the turbulent stress and turbulent heat flux terms are needed. The eddy viscosity concept used in conjunction with Prandtl's mixing length hypothesis for the wall layer region is the most widely used algebraic model for turbulent stress. A well known representation is the two layer eddy viscosity model of Cebeci and Smith which has been very successful in modeling turbulence effects for flat plate boundary layers and other attached boundary layers with moderate pressure gradients. Less favorable results are obtained when using this model for strongly interacting and separated flow regions where it appears to fail conceptually.

In general turbulent quantities like the Reynolds stress are governed by transport equations, thus requiring that the turbulence history be accounted for. The eddy viscosity concept relates the Reynolds stress to only the local mean flow gradient. This corresponds to the physical idea that production of turbulence at a point due to interaction with the mean flow is cancelled by the dissipation due to its self-interaction (this is referred to as the "local equilibrium" concept). In other words, the eddy viscosity model is the solution to a truncated transport equation. In an effort to better align the predictions for separated flows with experimental data, previous investigators (see Refs. 4 and 5 for examples) have empirically modified the equilibrium eddy viscosity model to account for the history effect. Thus 'frozen', 'relaxation', and other models were devised and successfully applied in several of separated flow predictions. One of the present authors [6] also used the 'frozen' and 'relaxation' models in the interacting boundary layer equations for separated flows with no significant improvements in the predicted results over those obtained with the basic eddy-viscosity model. An alternate way to try to achieve more satisfactory results would be to model the turbulence via the turbulent transport equations, and then eventually introduce modifications which will account for the extra effects on turbulence occurring in the strongly interacting flows. This will, of course, further tax the computing times required for these calculations.

With the above mentioned limitations in mind, the basic form of the Cebeci-Smith eddy viscosity model was adapted for the

present study where interaction effects tend to reduce longitudinal gradients and only small separation regions are encountered.

Thus we take

$$\tau_T = \varepsilon \frac{\partial u}{\partial x_2} \quad (7a)$$

and relate q_T to τ_T by the turbulent Prandtl number as

$$Pr_T \equiv (\tau_T / \frac{\partial u}{\partial x_2}) / (q_T / \frac{\partial T}{\partial x_2}) \quad (7b)$$

The turbulent Prandtl number is here taken constant, $Pr_T = 0.90$.

The two layer (outer and inner region) Cebeci-Smith model is then given as:

Inner Region

$$(\varepsilon/\mu)_i = \frac{\rho^* \bar{l}^{*2}}{\mu^*} \left| \frac{\partial u^*}{\partial x_2^*} \right| \quad (8a)$$

$$\text{where } \bar{l}^* = K_1 x_2^* [1 - \exp(-x_2^*/A^*)] \quad (8b)$$

with $K_1 = 0.40$ and

$$A^* = 26 (\mu^*/\rho^*) (\mu_w^* \left| \frac{\partial u^*}{\partial x_2^*} \right|_w / \rho^*)^{-1/2} \quad (8c)$$

where the absolute value of $\partial u^*/\partial x_2^*$ has been introduced in equation (8c) as a modification of the Cebeci-Smith model for reverse flows.

Outer Region

$$(\varepsilon/\mu)_o = \frac{\rho^* u_e^*}{\mu^*} K_2 \bar{\gamma} \delta_{kinc} \quad (9a)$$

where $\bar{\gamma}$ is the transverse intermittency function

$$\bar{\gamma} = \{1 - \text{erf}[5(x_2/x_{2e} - 0.78)]\}/2 \quad (9b)$$

The variable x_{2e} is the value of x_2 at which $u/u_e = 0.995$, and $\delta_{\text{kin}}c$ is the incompressible displacement thickness.

3. Boundary Layer Equations in Transformed Variables

The boundary layer equations given in Section 1 are here recast using the Levy-Lees transformation.

The new independent variables are defined by

$$\xi = \int_0^{x_1} \rho_e u_e u_e dx_1, \quad \eta = \frac{u_e}{\sqrt{2\xi}} \int_0^{x_2} \rho dx_2 \quad (10a,b)$$

The normalized dependent variables are now defined as:

velocity ratio,

$$F = u/u_e \quad (11a)$$

mean static enthalpy ratio

$$\theta = T/T_e \quad (11b)$$

or, mean total enthalpy

$$g = H/H_e \quad (11c)$$

With these definitions, equations (2-4) become:

Continuity Equation

$$\frac{\partial V}{\partial \eta} + 2\xi \frac{\partial F}{\partial \xi} + F = 0 \quad (12)$$

Momentum Equation

$$2\xi F \frac{\partial F}{\partial \xi} + V \frac{\partial F}{\partial \eta} = \beta(\theta - F^2) + \frac{\partial}{\partial \eta}(\lambda \bar{\epsilon} \frac{\partial F}{\partial \eta}) \quad (13a)$$

or

$$2\xi F \frac{\partial F}{\partial \xi} + V \frac{\partial F}{\partial \eta} = (1 + \frac{\alpha}{2}) \beta(g - F^2) + \frac{\partial}{\partial \eta}(\lambda \bar{\epsilon} \frac{\partial F}{\partial \eta}) \quad (13b)$$

Static Temperature Energy Equation

$$2\xi F \frac{\partial \theta}{\partial \xi} + V \frac{\partial \theta}{\partial \eta} = \alpha \bar{\epsilon} \left(\frac{\partial F}{\partial \eta} \right)^2 + \frac{\partial}{\partial \eta} \left(\lambda \frac{\hat{\epsilon}}{\text{Pr}} \frac{\partial \theta}{\partial \eta} \right) \quad (14a)$$

or

Total Temperature Energy Equation

$$2\xi F \frac{\partial g}{\partial \xi} + V \frac{\partial g}{\partial \eta} = \frac{2\alpha}{2+\alpha} [\lambda (\bar{\epsilon} - \hat{\epsilon}/\text{Pr}) F \frac{\partial F}{\partial \eta}] + \frac{\partial}{\partial \eta} \left(\frac{\lambda \hat{\epsilon}}{\text{Pr}} \frac{\partial g}{\partial \eta} \right), \quad (14b)$$

where λ is the viscosity parameter defined by

$$\lambda = \rho u / \rho_e u_e \quad (15)$$

with μ given from Sutherland's viscosity law and the turbulent parameters, $\bar{\epsilon}$ and $\hat{\epsilon}$ are defined as

$$\bar{\epsilon} = 1 + (\epsilon/\mu) \Gamma \quad (16a)$$

$$\hat{\epsilon} = 1 + (\epsilon/\mu) \frac{\text{Pr}}{\text{Pr}_T} \Gamma \quad (16b)$$

where Γ is the streamwise intermittency function: for fully laminar flow $\Gamma = 0$ and for fully turbulent flow $\Gamma = 1$, while for the transitional region its value varies smoothly from zero to one.

The parameters α and β are obtained from the local inviscid flow as

$$\alpha = u_e^2 / T_e \quad (17a)$$

$$\beta = \frac{2\xi}{u_e} \frac{du_e}{d\xi} \quad (17b)$$

State Equation

$$\rho_e / \rho = \theta \quad (18a)$$

or

$$\rho_e / \rho = \frac{\alpha}{u_e^2} \left(H - \frac{u_e^2}{2} F^2 \right) \quad (18b)$$

Boundary Conditions

$$\begin{aligned}
 F(\xi, \eta) &= 0 \\
 V(\xi, \eta) &= 0 \\
 \theta(\xi, \eta) &= T_w/T_e \\
 \text{or } g(\xi, \eta) &= H_w/H_e
 \end{aligned}
 \quad \text{at } \eta = \eta_w \quad (19a)$$

where $\eta_w = 0$ for surface coordinates and $\eta_w = \eta_w(\xi)$ for Cartesian coordinates. Also we have that

$$\begin{aligned}
 F(\xi, \eta) &= 1 \\
 \theta(\xi, \eta) &= 1 \quad \text{as } \eta \rightarrow \infty \\
 \text{or } g(\xi, \eta) &= 1
 \end{aligned} \quad (19b)$$

The turbulence relations given in Section 2 can be expressed in transformed variables as:

Inner Region

$$(\varepsilon/\mu)_i = \sqrt{\text{Re}_r} \frac{\rho_e^2 u_e^2 K_1^2 x_2^2 \pi_1^2}{\mu_e \sqrt{2\xi} \ell \theta^3} \left| \frac{\partial F}{\partial \eta} \right| \quad (20a)$$

$$\text{where } \pi_1 = 1 - \exp(-\pi_2) \quad (20b)$$

$$\pi_2 = \frac{x_2 \rho_e u_e}{26 \ell \theta^2 \mu_e} \left(\theta \sqrt{\text{Re}_r} \frac{\mu_e \ell_w}{\sqrt{2\xi}} \left| \frac{\partial F}{\partial \eta} \right|_w \right)^{1/2} \quad (20c)$$

Outer Region

$$(\varepsilon/\mu)_o = \frac{\rho_e u_e}{\mu_e} \text{Re}_r K_2 \frac{\bar{\gamma} \delta_{\text{kinc}}}{\ell \theta^2} \quad (20d)$$

$$\delta_{\text{kinc}} = \frac{\sqrt{2\xi}}{\sqrt{\text{Re}_r} \rho_e u_e} \int_0^{\eta_e} \theta (1-F) d\eta \quad (20e)$$

Note that, as far as the form of the governing equations is concerned, the only difference between the use of surface coordinates and Cartesian coordinates is in the wall boundary condition equation (19a). This can be eliminated using Prandtl's transposition theorem by writing that

$$\bar{\xi} = \xi \quad (21a)$$

$$\bar{\eta} = \eta - \eta_w(\xi) \quad (21b)$$

$$\bar{V} = V - 2\xi\eta'_w F \quad (21c)$$

With these transformation equations (12-14) and (19) yield:

Continuity Equation

$$\frac{\partial \bar{V}}{\partial \bar{\eta}} + 2\bar{\xi} \frac{\partial F}{\partial \bar{\xi}} + F = 0 \quad (22a)$$

Momentum Equation

$$2\bar{\xi} F \frac{\partial F}{\partial \bar{\xi}} + \bar{V} \frac{\partial F}{\partial \bar{\eta}} = \beta(\theta - F^2) + \frac{\partial}{\partial \bar{\eta}} \left(\lambda \bar{\varepsilon} \frac{\partial F}{\partial \bar{\eta}} \right) \quad (22b)$$

or

$$2\bar{\xi} F \frac{\partial F}{\partial \bar{\xi}} + \bar{V} \frac{\partial F}{\partial \bar{\eta}} = \left(1 + \frac{\alpha}{2}\right) \beta(g - F^2) + \frac{\partial}{\partial \bar{\eta}} \left(\lambda \bar{\varepsilon} \frac{\partial F}{\partial \bar{\eta}} \right) \quad (22c)$$

Energy Equation

$$2\bar{\xi} F \frac{\partial \theta}{\partial \bar{\xi}} + \bar{V} \frac{\partial \theta}{\partial \bar{\eta}} = \alpha \lambda \bar{\varepsilon} \left(\frac{\partial F}{\partial \bar{\eta}} \right)^2 + \frac{\partial}{\partial \bar{\eta}} \left(\frac{\lambda \hat{\varepsilon}}{\text{Pr}} \frac{\partial \theta}{\partial \bar{\eta}} \right) \quad (22d)$$

or

$$2\bar{\xi} F \frac{\partial g}{\partial \bar{\xi}} + \bar{V} \frac{\partial g}{\partial \bar{\eta}} = \frac{2\alpha}{2+\alpha} [\lambda(\bar{\varepsilon} - \hat{\varepsilon}/\text{Pr}) F \frac{\partial F}{\partial \bar{\eta}}] + \frac{\partial}{\partial \bar{\eta}} \left(\frac{\lambda \hat{\varepsilon}}{\text{Pr}} \frac{\partial g}{\partial \bar{\eta}} \right) \quad (22e)$$

Boundary Conditions

$$F(\bar{\xi}, 0) = \bar{V}(\bar{\xi}, 0) = 0$$

$$\theta(\bar{\xi}, 0) = \theta_w(\bar{\xi})$$

$$\text{or} \quad g(\bar{\xi}, 0) = g_w(\bar{\xi}) \quad (23a)$$

and

$$F(\bar{\xi}, \infty) = 1$$

$$\theta(\bar{\xi}, \infty) = 1$$

$$\text{or} \quad g(\bar{\xi}, \infty) = 1 \quad (23b)$$

The interacting boundary layer calculations require an initial velocity and temperature profile at some station ahead of the effective interaction region (see Figure 1). This profile was obtained here from a noninteracting two dimensional laminar-transitional-turbulent boundary layer calculation by an ordinary marching technique using a prescribed pressure distribution.

4. Inviscid/Viscous Interaction Model

The interaction of the boundary layer with the isentropic supersonic inviscid flow is modeled in the pressure gradient parameter β by coupling it to the inclination θ_T . The edge pressure is obtained from the Prandtl-Meyer relation approximated here to second order in terms of θ_T as

$$p_e = \frac{1}{\gamma M^2} + \frac{\theta_T}{\sqrt{M_\infty^2 - 1}} + \frac{(M_\infty^2 - 2)^2 + \gamma M_\infty^4}{4(M_\infty^2 - 1)^2} \theta_T^2 \quad (24)$$

$$\text{where } \theta_T = \tan^{-1} (d\delta_T/dx) \quad (25a)$$

$$\delta_T = y_w + \delta \cos \theta_S \quad (25b)$$

$$\theta_S = \tan^{-1} (dx_2/dx_1) \quad (25c)$$

$$\delta = Re_r^{-1/2} \int_{x_{2w}}^{\infty} \left(1 - \frac{\rho_e u}{\rho_e u_e}\right) dx_2 \quad (25d)$$

Once p_e is obtained the isentropic relations and Euler's equation are used to obtain β in equation (17b). Thus, the inviscid and viscous flows must be solved simultaneously since they are directly connected through the displacement thickness given in equation (25c).

NUMERICAL METHOD OF SOLUTION

The numerical method used is an implicit finite difference scheme written for the similarity form of the governing equations that marches from some initial station along the surface to the terminal point of interest. To account for the boundary value nature of the problem, Werle and Vatsa [1] have added the time dependent concept, similar to the one used for the solution of elliptic partial differential equations. This results in modification of only the momentum equation (22b) by replacing the pressure parameter β with $\bar{\beta}$ defined as

$$\bar{\beta} = \beta + \frac{\partial \delta_T}{\partial t} . \quad (26)$$

This method has been successfully applied to laminar separated flow problems with various flow configurations including one with multiple interacting regions [2, 3]. The extension of this approach to turbulent boundary layers involves, aside from inclusion of the eddy viscosity model into the solution scheme, a number of modifications (see also Ref. 6). Specifically, the following steps were taken.

1. The numerical stability and convergence rate has been enhanced by introducing a new differencing in the continuity equation. It has only recently been recognized [7, 8] that the longitudinal derivatives in the continuity equation provide a path for interacting flows to propagate information upstream. To accommodate this numerically requires the use of some sort of a forward difference procedure. In the present work we adopt in the continuity equation the following forward differencing

$$\left(\frac{\partial F}{\partial \xi}\right)_i = \frac{F_{i+1}^{(0)} - F_i}{\Delta \xi}$$

where the superscript (o) denotes values at the previous time step and subscript i refers to the ith station along the length of the surface.

2. The reliability of the present algorithm was enhanced by adopting the 'upwind differencing' concept for the longitudinal convection effects. In the reversed flow region upwind differencing was used in the longitudinal direction for the convective terms in order to satisfy the stability requirements. This eliminates the so-called 'artificial convection' concept used earlier [2] for the laminar case. This modification is significant because the velocities in the reversed flow regions are larger in the turbulent case than in the laminar. Thus the convection term in the momentum equation is differenced as

$$\begin{aligned} F_i \left(\frac{\partial F}{\partial \xi}\right)_i &= \frac{1}{2} \{ \tilde{F}_i + |\tilde{F}_i| \} (F_i - F_{i-1}) / \Delta \xi + \\ &+ \frac{1}{2} \{ \tilde{F}_i - |\tilde{F}_i| \} (F_{i+1}^{(0)} - F_i) / \Delta \xi \quad . \end{aligned} \quad (27)$$

\tilde{F}_i is replaced by F_{i-1} for forward flow, and by $F_i^{(0)}$ for reversed flow. By replacing the \tilde{F}_i with $F_i^{(0)}$ the occurrence of a separation point singularity is avoided [1, 6]. Note that the first term on the right hand side of equation (27) vanishes for reversed flow, and the second term vanishes for the forward flow. The same procedure was followed with the term $F \partial \theta / \partial \xi$ in the energy equation.

Furthermore, the upwind differencing was found also helpful in the η direction, in the convective dominated outer regions of the thick turbulent boundary layer. It was brought to our attention* that upwind differencing of the $\partial F/\partial \eta$ term in the momentum equation might be required to satisfy the convergence criteria of the numerical scheme (see also Ref. 9). In the boundary layer near the wall the diffusion term $F_{\eta\eta}$ dominates the convective-like term F_{η} and a central difference scheme for F_{η} is appropriate. However, in the outer reaches of the boundary layer the diffusion term decreases significantly and numerical instabilities occur. From a study of the model equation $F_{\eta\eta} + \alpha F_{\eta} = 0$ it is found that with central differencing the criteria $|\alpha \Delta \eta| \leq 2$ must be adhered to, to avoid these oscillations. Hence the term F was central differenced when $|\alpha \Delta \eta| \leq 1$ and upwind differenced when $|\alpha \Delta \eta| > 1$.

3. The convergence rate of the time relaxation solution method for the thick boundary layers has been found much slower than for thin boundary layers. The two cases differ largely in that for the thick boundary layer the disturbance of the total displacement body from the flat plate value is very small. It was argued that the numerical truncation error can be of the same order as this relative change per one iteration, thus leading to very small convergence rate. We introduced therefore a new variable D_T in place of the total displacement body δ_T . The D_T is defined as $D_T \equiv [\delta_T(\xi, t) - \delta_i(\xi_i)]/h_s$, where $\delta_i(\xi_i)$ is the displacement thickness at the initial station and h_s is a constant

* R.T. Davis, Personal Communication.

of the order of the maximum protuberance height. Calculations performed with this modification show improvement in the convergence rate.

The accuracy of the calculated solutions depends on the degree of precision of the finite-difference approximation and the step size. In turbulent boundary layers, large changes occur in the velocity profile in the inner layer very near the surface. A sufficient number of mesh points are needed near the wall in order to get a good resolution in the predictions of wall shear and surface heat transfer. At the outer edge of the boundary layer where the Levy-Lees variable η acquires large values, the changes are, on the other hand, very small. This is especially pertinent in the case of a thick turbulent boundary layer disturbed by a relatively small protuberance. Thus, for reasons of efficiency and accuracy a variable mesh size in the η direction is used in solving most turbulent boundary layers. A mesh growing in size from the wall as a geometric progression is used in the present algorithm. Blottner [10] has shown that in terms of a transformed normal variable $N(\eta)$ replacing the stretched Levy-Lees variable η , the truncation error is proportional to ΔN^2 as $N \rightarrow 0$, or the method of calculation is second order accurate. At the j th grid point the physical coordinate is obtained from

$$\eta_j = \eta_{j_{\max}} \frac{K^{N_j/\Delta N_0} - 1}{(K^{1/\Delta N_0} - 1)} \quad (28)$$

where $K = \Delta \eta_j / \Delta \eta_{j-1}$, $N_j = (j-1)\Delta N$, $(j_{\max}-1)\Delta N = 1$, and where ΔN is the constant step in the transformed plane. The second order accuracy is achieved by varying j_{\max} and holding ΔN_0 fixed [10].

It was found here that if instead one replaced ΔN_0 by ΔN , where ΔN is of course varying with j_{\max} , while holding K fixed the error diminishes with ΔN as $K^{-1/\Delta N}$, i.e. much faster than ΔN^2 . Further details are given in Appendix A. Figures 2 show the surface heating parameter's dependence on ΔN and thus provides an accurate error estimation procedure. Based on this step size study it was found that with values of $n_{\max} = 200$, $j_{\max} = 55$, and $K = 1.254$, a 7% truncation error was incurred in the calculation of wall heat transfer. This represents an acceptable compromise between the accuracy and the efficiency of calculations.

The governing equations were linearized and the partial derivatives were replaced by finite differences. The eddy viscosity term ϵ/μ , appearing as a nonlinear term in the governing equations, is approximated by its previous station value. Central differences were used to represent partials with respect to η (except as noted above where upwind differencing for F_η was required in the outer region of the boundary layer) as well as for the streamwise derivatives of the displacement body height, δ_T . Upwind differencing was used in the convective terms in the momentum and energy equations and forward differencing with respect to ξ in the continuity equation.

The calculation commences with certain initial conditions and then through the time dependent approach [1] the steady state solution for a given set of boundary conditions is sought. In the present calculations the initial conditions were set by taking the zero time displacement body to correspond to a flat plate boundary layer and the surface protuberance to be of zero height. Subsequent time sweeps are conducted with the wave amplitude

increasing gradually by a small amount. After the desired geometry is reached (after the first 10-15 sweeps) the time-like relaxation process is continued until the flow properties are relaxed to the final value. This process is shown in Figure 3a where the skin friction coefficient at one location ($s = 3.58$) is shown as a function of time iteration number. This location is near the junction of the flat plate with a single sine-wave protuberance where separation occurs. The resulting skin friction and surface heating distributions are shown in Figure 3b. For this case with a thin boundary layer, the calculation was performed in surface coordinates. Figure 3a shows that once the full protuberance height is attained (11 sweeps) it takes about 50 more sweeps for the skin friction to attain its 'steady state' value. This calculation, with 41 normal grid points and 71 longitudinal grid points were performed in 5 minutes of computer time on the IBM 370-168.

RESULTS AND DISCUSSION

A major interest of the present investigation is in the numerical predictions for thick turbulent boundary layers over a wavy wall, as those in the experiments of reference [11]. The geometry and the flow conditions were therefore chosen to coincide with those given in reference [11]. The amplitude and wave length are $a^* = 0.29$ cm, $w^* = 3.66$ cm respectively. A reference length $L^* = 15.25$ cm was chosen. The base flow conditions are defined by $M_\infty = 2.53$, $Re_\infty = 10.82 \times 10^6/m$, $T_\infty = 174^\circ K$ and $T_w/T_0 = 0.81$. Henceforth, we refer to these conditions as standard flow conditions.

To obtain the present results it is first necessary to generate initial profiles at some point ahead of the first protuberance-flat plate juncture. For the standard flow conditions this station was taken at $x = 72.90$, where the initial profiles were obtained from a noninteracting calculation to correspond to the boundary layer as it develops along the wall of the UPWT Langley Wind Tunnel [11]. The details concerning the calculation of the initial profiles are described in Appendix B. The interacting algorithm was subsequently employed between this initial station and a downstream station past the last protuberance. The problem was first formulated and solved in the customary surface coordinates. It turned out that the geometry extremes make the use of the Cartesian coordinates version of the boundary layer equations more reasonable. The results of the calculations shown here were performed with a longitudinal stepsize $\Delta x = 0.02$, and a 55 point grid across the boundary layer.

Examples from the calculated results are presented for flow over a train of up to six waves, for Mach numbers $M_\infty = 2.5$ and 3.5, for Reynolds numbers $Re_\infty = 10.82 \times 10^6/m$ and $32.46 \times 10^6/m$ and for wall to total temperature ratios $T_w/T_0 = 0.40$ and 0.81.

Figure 4 shows the contour of a train of six waves, the displacement body and the viscous and inviscid pressure distributions for the standard flow conditions. The difference in the inviscid and viscous pressures dramatically shows the effect and need for interaction. The pressure is calculated from an approximation to the Prandtl-Meyer relation, accurate to second order in flow inclination angle. The inviscid pressure is calculated using the local body slope, whereas the viscous pressure is obtained by using the slope of the displacement body ($= \delta_T = y_w + \delta$). The difference in the viscous and inviscid pressure is due to the difference in amplitudes of the actual (y_w) and displacement (δ_T) body. It is interesting to observe that the viscous pressure is almost periodic even though the average displacement thickness decreases. Figure 5 shows with the distribution of pressure the corresponding distribution of surface heat transfer and skin friction at the same base flow conditions. The pressure peaks and peaks in heating occur at about the same location ahead of the body surface peak. The peak in skin friction is shifted in the opposite direction. While the pressure distribution is nearly periodic, the heating levels and the skin friction peaks rise in the downstream direction. The rate of rise in peak heating is decreasing very slowly. These results are in contradistinction to our similar

study [3] of thin laminar flow over a train of sine-waves, where the peaks in heating decreased rapidly in the streamwise direction. Figure 6 points out the fact that the local value of the surface parameters is almost unaffected by the presence of additional downstream disturbance for turbulent boundary layers (compare also Figures 5 and 6). Simply, downstream waves have little upstream influence and the problem seems localized. Heating levels aft of waves grow as the number of waves increases, but the downstream skin friction is unaffected by the number of waves.

To demonstrate the effect on surface properties due to Mach number, wall temperature, and Reynolds number, three additional cases are shown in Figures 7A,B through 9A,B. The increase of Mach number (Figures 7A,B) from 2.5 to 3.5 causes a decrease in the ratio of $h_{\max}/h_{f.p.}$. As in the standard flow case, the location which the first wave was placed was chosen in such a way that the flat plate boundary layer displacement thickness was about the same as in the experimental study of reference [11].

The lowering of wall temperature to $T_w/T_o = 0.40$ (Figures 8A,B) shows a similar trend in $h_{\max}/h_{f.p.}$ as for the increase in Mach number. But the absolute rate of surface heating is much higher than in the previous case. Interestingly, the $h/h_{f.p.}$ curve is smoother here than in other cases.

Lastly, an increase in Reynolds number, shown in Figures 9A,B is seen to cause a slight increase in the ratio of peak heating.

An interesting aspect of the present results is the location of the peaks in pressure, heat transfer and shear. The present predictions show the peaks in pressure and heating to occur at about the same location. This is in agreement with experimental observations [11]. The location of the peak pressure in the present results is shifted to the right of the location of the inviscid peak pressure location (at $y \approx 0$) by a phase angle of about 60° . Theoretical studies by Inger and Williams [12] and by Lekoudis et al. [13] predict such a shift. Data from these studies given up to $M_\infty = 2.0$ show a shift to the left which drops off quickly towards zero at $M_\infty \approx 2$. It is therefore possible to expect a phase angle in the opposite sense for $M_\infty > 2$, as is the case in present results. The maximum wall shear location obtained from present calculations is shifted to the right of the peaks in pressure and surface heating by about 60° . According to theoretical predictions [13] qualitatively such a shift is expected. Experimental data available at the same flow conditions [11] show a periodic trend in surface pressure as well as in the surface heating distribution. The periodic trend in surface pressure is observed also in the present predictions. Pressure and heating distributions between the second and third peak are compared to the experimental data [11] for Mach numbers 2.5 and 3.5 in Figure 7B. While the heating distributions in the experiments of reference [11] are nearly repetitive over consecutive waves, the present predictions show a continuous increase over the length of the waves. Note

though that in the experimental study there is also indication that separation occurs, while a lack of separation is observed in the analytical results of Figure 5. The cause of this disagreement is not certain but it could well be due to our choice of turbulence model or in the fact that the present calculations do not simulate well enough all the test conditions (three-dimensional effects or boundary layer development on the tunnel wall). Note the calculated boundary layer displacement thickness of the initial profile at station $x = 72.90$ is 2.86 cm, close to the value given in reference [11]. However the predicted surface heating value at this station is too high when compared to experimental data of reference [11] (The predicted value is $h_{f,p.} = 96.5 \text{ watts/m}^2 \text{ } ^\circ\text{K}$ vs $62.5 \text{ watts/m}^2 \text{ } ^\circ\text{K}$ in experiments). Other prediction methods also typically over predict to about the same level the heat transfer rates for boundary layers developing along the wind tunnel walls [14] thus indicating that some final adjustments may be needed in the turbulence model for these flows.

While the present prediction method has in a certain way accounted for the boundary layer displacement effect by using the interacting boundary layer equations, the effect of surface curvature was neglected. The curvature effect in turbulent flows has been summarized in a comprehensive monograph by Bradshaw [15]. It has been found that even in cases when the longitudinal surface curvature is accounted for in the governing equations the predicted surface aerodynamic parameters (surface heating, wall shear) still deviate considerably from the experimental data. Apparently, the streamline curvature has an

effect on the turbulence structure not included in the existing turbulence models. Bradshaw therefore proposed a simple correlation scheme applicable to turbulent flows with not too large streamline curvature. For the simplest equilibrium model used in the present work this correction consists of multiplying the mixing length by a factor $f = 1 + \alpha e / (\partial u / \partial y)$, where $e = \partial v / \partial x$ is the extra rate of strain induced by the streamline curvature (and $\partial u / \partial y$ is the mean rate of strain). This correction is recommended for only $0.5 \leq f \leq 1.5$. The constant α is of order 10. Because of the time lag between the first appearance of the curvature and its full effect on turbulence the effective value of αe is calculated from the lag equation

$$10\delta \frac{d}{dx} (\alpha e)_{\text{eff}} = \alpha_0 e - (\alpha e)_{\text{eff}} \quad (29)$$

where δ is the boundary-layer thickness, and the constant α_0 is taken to be 10. This idea has been implemented here for the standard test case by evaluating $\partial v / \partial x$ along a streamline at each station x . It was then assumed that this is a representative value for all values of y at this station. The δ was taken to correspond to station $x = 73.20$. The case with base flow conditions was recalculated. It was found that a streamline had to be chosen in the lower part of the inner layer (passing the 21st grid point at $x = 73.20$) in order not to violate the condition $0.5 \leq f \leq 1.5$. The results of this calculation are shown in Figures 10A,B. Observe that the peaks in $h/h_{f.p.}$ and C_f are now lower and slightly dropping along the wall. A comparison between the detailed distribution of the surface

heating calculated with and without the curvature correction, and against the experimental data is shown in Figure 10b. The comparison with experiments is now more favorable on the compression side of the wave. Recall however that in the wind tunnel tests the boundary layer was separated.

To examine the effect of separation on the character of the heating distribution and also to demonstrate the capability of the method to solve multiple separation regions, calculations without curvature correction were performed with the base flow condition but for a boundary layer developed along a flat plate up to the junction point $x = 24.30$ (Figures 11A,B). It is noticed (Fig. 11B) that when compared to the unseparated case, the heating values are lower on the expansion side of the wave. Flow separation occurred in this case due to the different history and also because of the larger pressure gradients: the ratio δ/a is here smaller than for the standard case and therefore the slope of the total displacement body steeper. This is even more apparent for a relatively very thin boundary layer. Figure 12 shows the results from a calculation performed at the same flow condition as in Figure 11, except that junction of the flat plate and the first protuberance was moved forward to $x = 3.3$ and the wave height was reduced to one-half of the previous value. Larger pressure gradients and separation regions now appear closer to the center of the valleys are observed. Again, the peak heating rates grow in the streamwise direction.

In reference [11] it was found that unlike for thin boundary layers, the peak heating rates were insensitive to the wave amplitude. To examine this question a set of calculations were performed for different ratios of wave amplitude to wave length, a/w . According to the present predictions the heating rates change considerably with the amplitude even for the thick boundary layers (Figs. 13A,B). For both thick and thin boundary layers the peak heating values, $(h/h_{f.p.})_{max}$, are plotted in Figure 14. The present predictions show similar behavior for both thin and thick boundary layers: a stronger than linear increase in peak heating with the increase of wave amplitude. Note that the curvature effect on turbulence was not accounted for in the results shown in Figures 13 and 14. The larger curvatures corresponding to higher amplitude waves probably amplify the predicted trend observed in Figures 13 and 14.

CONCLUSIONS

A numerical method capable of handling multiple interacting flow regions was adapted to the problem of thick turbulent boundary layer over a wavy wall.

The results of calculations presented in terms of surface pressure, skin friction, and heat transfer distributions disclose features distinctly different from the laminar case. The present results show a shift in the location of the viscous pressure peaks relative to the peaks in the inviscid pressure and to the peaks in the wall shear. These phase shifts are in qualitative agreement with theoretical predictions based on small disturbance theory. The location of peaks in viscous pressure and heat transfer coincide, and the longitudinal pressure variation is periodic. This is in agreement with the experimental data. The experiments also show periodicity in surface heating distribution, while the present results predict a continuous increase in heating indicating a possible weakness in the turbulence model for a surface with rapidly varying curvature. A semi-empirical modification of the eddy viscosity model, intended to account for the longitudinal curvature effect, aligns the predictions closer to the experimental data. It is recommended that future work be carried out with a more accurate turbulence model, and that a more optimal coordinate system be adopted for this problem.

REFERENCES

1. Werle, M.J. and Vatsa, V.N., "A New Method for Supersonic Boundary Layer Separations," AIAA Journal, November 1974, pp. 1491-1497.
2. Werle, M.J., Polak, A., Vatsa, V.N., and Bertke, S.D., "Finite Difference Solutions for Supersonic Separated Flows," appearing in Flow Separation, AGARD CP 168, 1975.
3. Polak, A., Werle, M.J., Vatsa, V.N. and Bertke, S.D., "Numerical Study of Separated Laminar Boundary Layers Over Multiple Sine-Wave Protuberances," J. of Spacecraft and Rockets, Vol. 13, No. 3, March 1976, pp. 168-173.
4. Shang, J.S. and Hankey, W.L., Jr., "Numerical Solution for Supersonic Turbine Flow Over a Compressible Ramp," AIAA Journal, Vol. 13, October 1975, pp. 1368-1374.
5. Horstman, C.C., Hung, C.M., Settles, G.S., Vas, I.E., and Bogdonoff, S.M., "Reynolds Number Effects on Shock-Wave Turbulent Boundary Layer Interactions - A Comparison on Numerical and Experimental Results," AIAA Paper No. 77-42, presented at the AIAA 15th Aerospace Sciences Meeting, January 24-26, 1977, Los Angeles, California.
6. Werle, M.J. and Bertke, S.D., "Application of an Interacting Boundary Layer Model to the Supersonic Turbulent Separation Problem," Report No. AFL 76-4-21, August 1976, Dept. of Aerospace Engineering, University of Cincinnati, Cincinnati, Ohio.
7. Davis, R.T. and Werle, M.J., "Numerical Methods for Interacting Boundary Layers," Proceedings from the 25th Heat Transfer and Fluid Mechanics Institute, University of California, Davis, California, June 21-23, 1976.
8. Davis, R.T., "Numerical and Approximate Solution of the High Reynolds Number Small Separation Problem," Advances in Engineering Sciences, Vol. 4, pp. 1451-1465, NASA CP-2001, Annual Meeting Society of Engineering Science, Hampton, Virginia, Nov. 1-3, 1976.
9. Blottner, F.G., "Computational Techniques for Boundary Layers," AGARD Lecture Series No. 73, Computational Methods for Inviscid and Viscous Two- and Three-Dimensional Flow Fields, February 1975, pp. 3-1 - 3-51.
10. Blottner, F.G., "Variable Grid Scheme Applied to Turbulent Boundary Layers," Computer Methods in Applied Mechanics and Engineering, 4 (1974), pp. 179-194.
11. Brandon, A.J., Masek, R.V. and Dunavant, J.C., "Aerodynamic Heating to Corrugation Stiffened Structures in Thick Turbulent Boundary Layers," AIAA Journal, Vol. 13, No. 11, 1975.

12. Inger, G.R. and Williams, E.P., "Subsonic and Supersonic Boundary-Layer Flow Past a Wavy Wall," AIAA Journal, Vol. 10, No. 5, May 1972, pp. 636-642.
13. Lekoudis, S.G., Nayfeh, A.H. and Saric, W.S., "Compressible Boundary Layer Over Wavy Walls," The Physics of Fluids, Vol. 19, No. 4, April 1976, pp. 514-519.
14. Couch, L.M. and Stallings, R.L., Jr., "Heat Transfer Measurements on a Flat Plate with Attached Protuberances in a Turbulent Boundary Layer at Mach Numbers of 2.49, 3.51, and 4.44," NASA TND-3736, December 1966.
15. Bradshaw, P., "Effects of Streamline Curvature on Turbulent Flow," AGARDograph No. 169 (1973).

APPENDIX A

GRID SIZE EFFECT ON ACCURACY

The objective is to assess the accuracy of the predicted surface boundary layer characteristics from the standpoint of the normal mesh size. The very thick turbulent boundary layer as produced on the wall of the UPWT Langley tunnel is of interest here. The boundary layer calculation is carried out as a non-interacting 2-D laminar-transitional-turbulent boundary layer. The corresponding pressure gradient is calculated from the Mach number distribution given in Appendix B.

The free stream conditions in the test section are: $M_\infty = 2.535$, $Re_\infty/cm = 1.08 \times 10^5$, $T_\infty = 314^\circ R$, $T_w/T_0 = 0.81$ and $p_\infty = 199$ psf. And $Pr = 0.72$, $Pr_T = 0.9$ were taken. The calculation commences at $s = 0.3$ with a laminar boundary layer, which becomes fully turbulent at $s = 2.1$ ($\Delta s = 0.1$). The Mach number becomes constant at $s = 40.60$. The implicit finite-difference method (Flügge-Lotz-Blottner-Davis) with non-uniform grid size, varying according to a geometric progression law, is employed.

The truncation error in this type of calculation is proportional to the quantity $(\eta_{j+1} - 2\eta_j + \eta_{j-1}) \equiv \Delta\eta_j - \Delta\eta_{j-1}$, and therefore in general not second order accurate. Blottner has shown [10] that in terms of a transformed variable, $N = N(\eta)$, where the coordinate N is obtained by coordinate stretching such that ΔN is uniform, the error is of order ΔN^2 . Blottner substantiates his conclusion by a set of calculations using the transformation

$$\eta_j = \eta_J (K^{N_j/\Delta N_0} - 1) / (K^{1/\Delta N_0} - 1),$$

where $j = 1, 2, \dots, J = j_{\max}$ = number of grid points,
 $N_j = (j-1)/(J-1)$, $K = \Delta n_j / \Delta n_{j-1}$, and $\Delta N_0 = \text{constant}$.

A similar type of transformation, corresponding to the geometrical variation of Δn_j is also employed here:

$$n_j = n_J (K^{N_j/\Delta N} - 1) / (K^{1/\Delta N} - 1)$$

where $\Delta N = 1/(J-1)$ and $K = K_0$ ($= 1.12$) does not vary with J .

Since the local truncation error is

$$E_j \approx n_{j+1} - 2n_j + n_{j-1} = \left(\frac{\partial^2 n}{\partial N^2} \right) \Delta N^2 + O(\Delta N^4)$$

$$\text{and} \quad \frac{\partial^2 n}{\partial N^2} = \frac{n_J}{K_0^{1/\Delta N} - 1} \left(\frac{1}{\Delta N} \ln K_0 \right)^2 K_0^{N_j/\Delta N},$$

we get

$$E_j \approx (\ln K_0)^2 K_0^{N_j/\Delta N} n_{\max} / (K_0^{1/\Delta N} - 1).$$

At a fixed grid location j ($N_j/\Delta N = j-1$), and for a large $1/\Delta N$ the error should be therefore plotted versus $K^{-1/\Delta N}$.

A set of calculations was carried out with $J = 80, 85, 90, 95, 100, 125$ and 150 for $K_0 = 1.12$ and two values of n_J ($n_J = 352$ and 200). For the station $s = 54.0$ (a location on the straight section of the tunnel wall) the wall heat transfer parameter $(\partial g / \partial n)_w$ is shown in Figure 2A.

As the error term suggests, the error decreases with decreasing of n_{\max} , and plots linearly with $K^{-1/\Delta N}$ as $\Delta N \rightarrow 0$. It is also observed that the two point formula [10] (used in conjunction with

the governing equations evaluated at the wall) for evaluating $(\partial g / \partial \eta)_w$ gives better results, especially at the excessive value of η_{\max} .

In a second set of calculations the value of K was varied together with J in a specified way:

$$K = K_0^m ; \quad (J-1)m = J_0 - 1 .$$

Here $K_0 = 1.12$, $m =$ positive integer, $J_0 = 109$, $\eta_J = 200$. We take $m = 1, 2, 3$ or 4 , so that $J = 109, 55, 37$ or 28 .

Then,

$$\eta_j = \eta_J (K_0^{mN_j/\Delta N} - 1) / (K_0^{m/\Delta N} - 1) ,$$

$$\Delta N = 1/(J-1) = m/(J_0-1) = m\Delta N_0$$

$$\eta_j = \eta_J (K_0^{(J_0-1)N_j} - 1) / (K_0^{1/\Delta N_0} - 1) .$$

Thus the transformation is independent of ΔN and the error term, as in reference [10], is now proportional to ΔN^2 . This is exhibited in Fig. 2B where the variation of the surface heat transfer parameter at station $s = 54.0$ is plotted for values $J = 109, 55, 37$ and 28 (compare with Figure 2a). These calculations were performed by first setting $K_0 = 1.12$ and $J = J_0 = 109$ for $0.3 \leq s \leq 44.3$. At $s = 44.3$, every 2nd, 3rd or 4th grid point value was used (corresponding to $m = 2, 3$ or 4) and the calculation marched (with the new value $J = 55, 37$ or 28 and $K = K_0^m$) past station 44.3 .

In summary, Blottner's interpretation of the accuracy of the variable grid size was extended by showing that the error term of the numerical scheme varies linearly with the inverse square of the number of grid spacings, $(J-1)$, when K and J are varying in a specified way, but also plots linearly with the inverse exponential of $(J-1)$ when K is fixed.

APPENDIX B

INITIAL PROFILES FOR THICK BOUNDARY LAYERS

A major aim of the present research project was to align numerical predictions for flow of thick turbulent boundary-layers over a wavy wall with the experimental program of reference [11]. For this reason a set of calculations were first performed for the boundary layer as it develops along the wall of the UPWT Langley Tunnel. The boundary-layer calculation was carried out as a non-interacting two-dimensional laminar-transitional-turbulent boundary-layer developing from ahead of the nozzle throat under a favorable pressure gradient. In the supersonic region downstream of the throat the pressure distribution was calculated from the sidewall Mach number distribution, using isentropic relations. The Mach number distribution was obtained from a characteristics net. From these data a cubic representation for M was assumed of the form

$$M = M_T - K_1 \left(1 - \frac{s}{s_T}\right)^2 \left(1 - K_2 \frac{s}{s_T}\right),$$

where M_T = test section Mach number at $s = s_T$. The above polynomial representation satisfies the condition $dM/ds = 0$ at $s = s_T$. At the location s_a of the first characteristic near the throat the Mach number was estimated to be $M_a = 1.11$. The measured distance along the wall from s_a to s_T is 39.6 (≈ 20 ft). At a location s_b , 8.86 units downstream of s_a , the Mach number is $M_b = 1.84$. Letting $s_a = 1$, $s_b = 9.86$ and $s_T = 40.6$. Using

these values, the constants K_1 and K_2 can be determined. For $K_1, K_2 > 0$ and $K_2 \leq 1$ (which is the case here) the polynomial representation given above yields monotonically increasing Mach number. The subsonic-transonic section of the tunnel was also assumed to be represented by a cubic polynomial

$$M = M_i + C_1 \left(1 - \frac{s}{s_i}\right)^2 \left(1 - C_2 \frac{s}{s_i}\right),$$

with the following properties:

$$\text{At } s = s_i = 0.3, \quad M = M_i \quad \text{and} \quad dM/ds = 0.$$

$$\text{At } s = s_a, \quad M = M_a = 1.11 \quad \text{and} \quad \frac{dM}{ds} = \left(\frac{dM}{ds}\right)_{s_a+}$$

Three different values for M_i were chosen: 0.01, 0.03 and 0.05. It turned out that the boundary layer development downstream of the throat was not sensitive to these initial values. Taking $M_i = 0.03$, a boundary layer calculation was performed for $0.3 \leq s \leq 97.4$ with boundary layer profiles punched on IBM cards. (At $s = 40.6$ the Mach number becomes constant on the side wall; at $s \geq 50.6$ the straight section begins.) These profiles were used as initial data for the interacting thick turbulent boundary layers. The table below gives the calculated boundary layer displacement thickness distribution along the constant Mach number section of the UPWT Langley tunnel wall at ten stations, for $M_T \equiv M_\infty = 2.53$, $T_\infty = 174.4^\circ\text{K}$, $T_w/T_0 = 0.81$, $Re_\infty = 10.82 \times 10^6/\text{m}$, $Pr = 0.72$ and $Pr_T = 0.90$.

s	40.6	44.6	48.6	52.6	56.6	60.6	64.6	68.6	72.6	76.6
δ^* (cm)	1.69	1.34	1.98	2.12	2.26	2.40	2.54	2.67	2.80	2.93

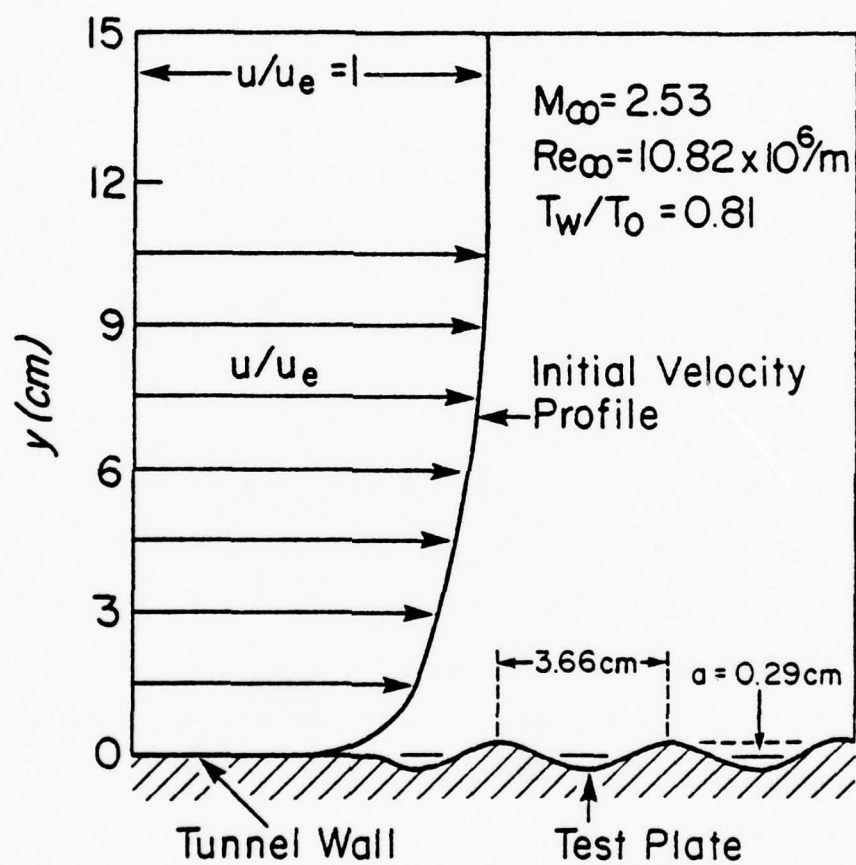


Figure 1 FLOW GEOMETRY

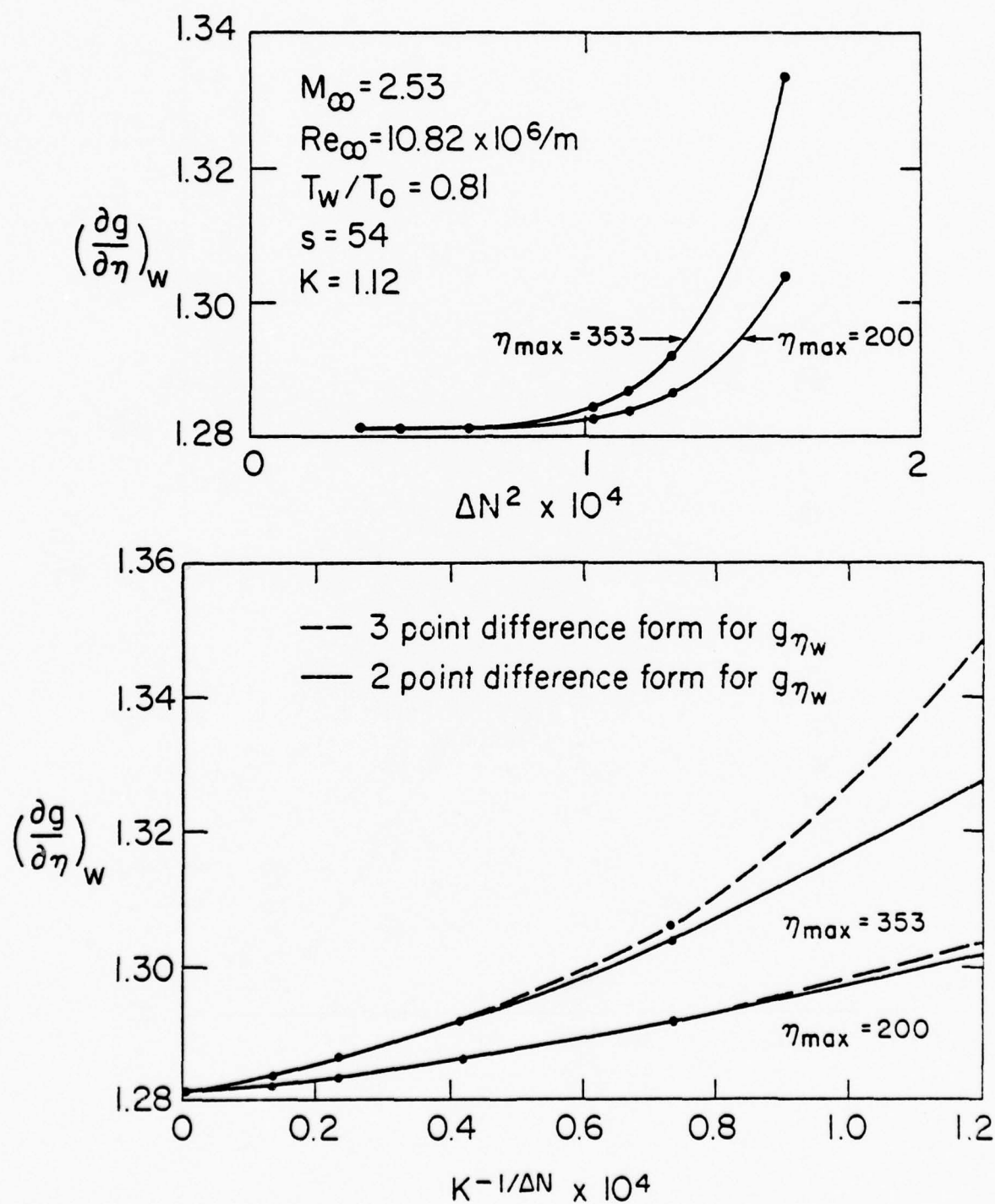


Figure 2A ACCURACY STUDY OF WALL HEATING LEVEL

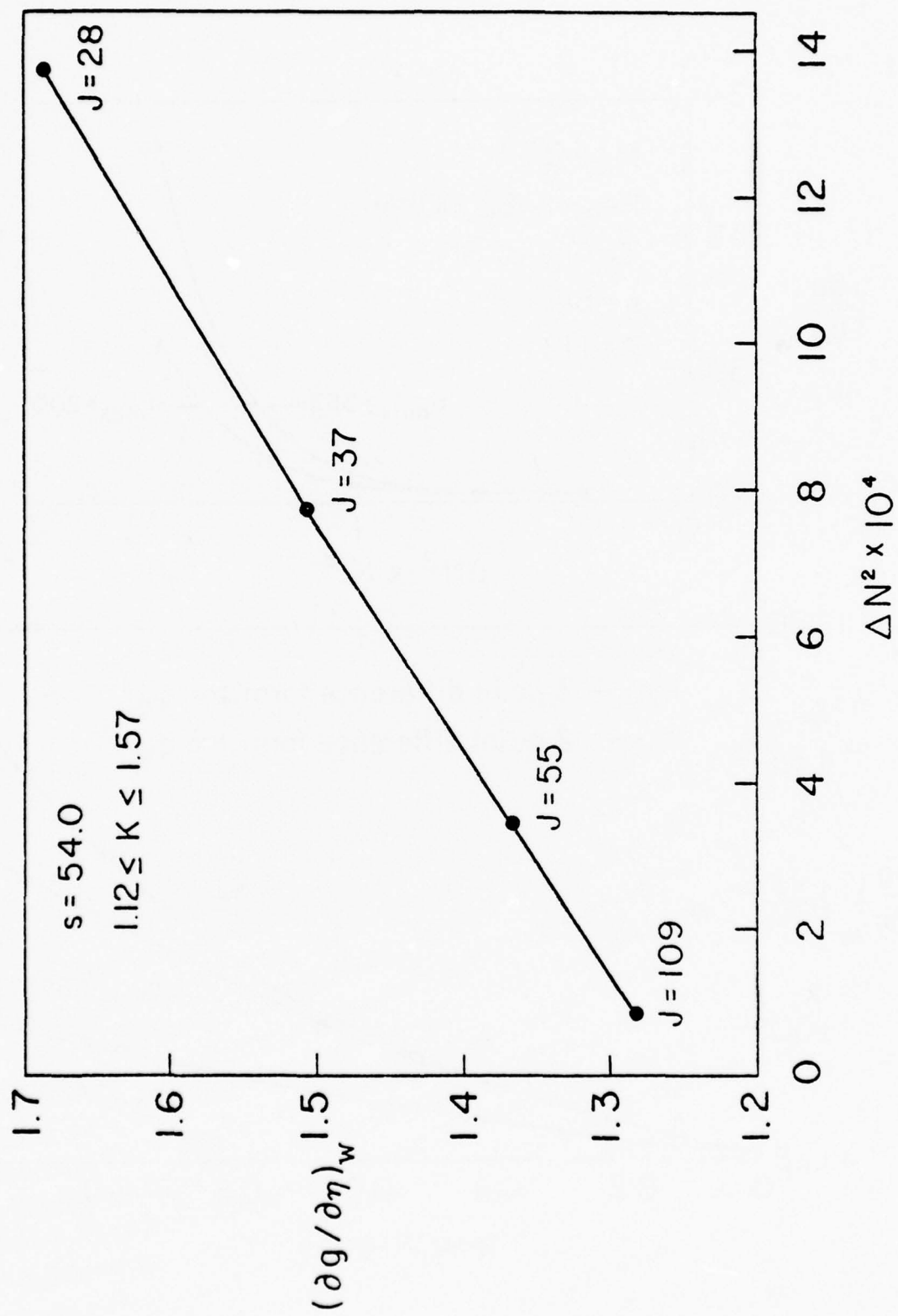


Figure 2B ACCURACY STUDY OF WALL HEATING LFVEI

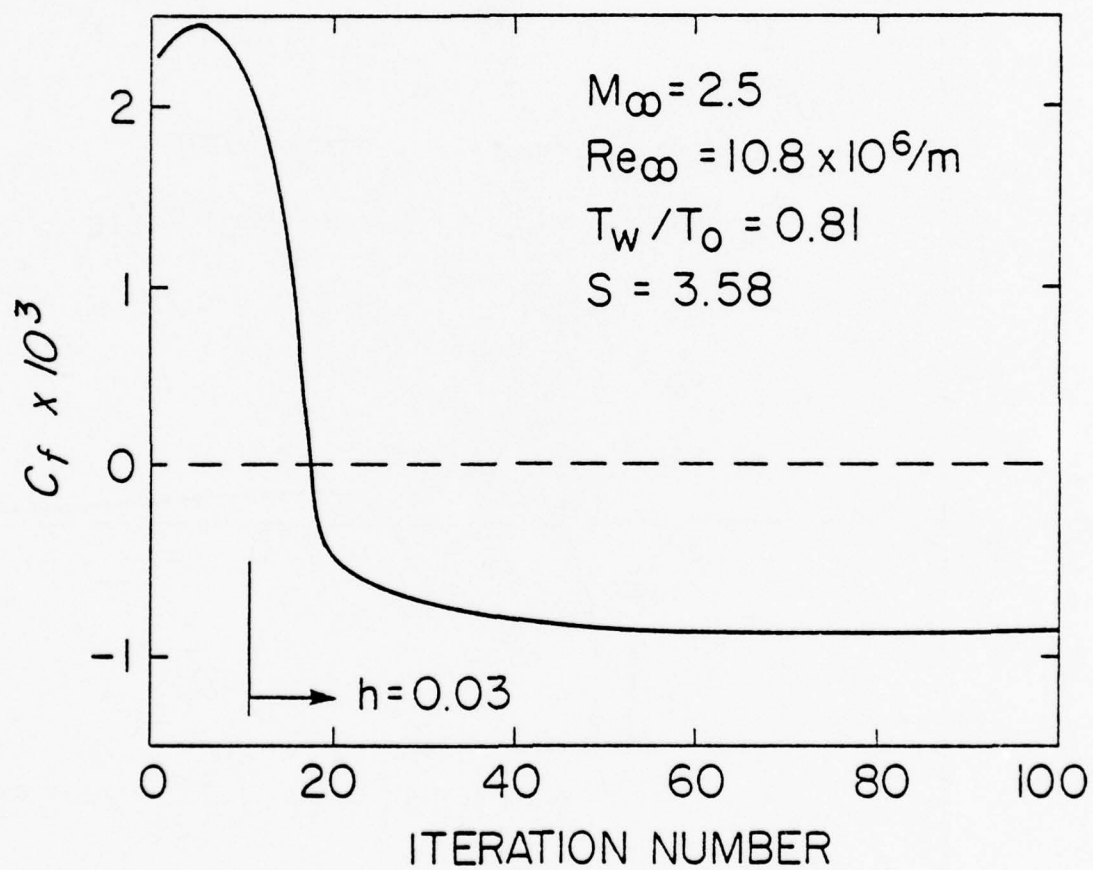


Figure 3A CONVERGENCE PROPERTY OF SKIN FRICTION

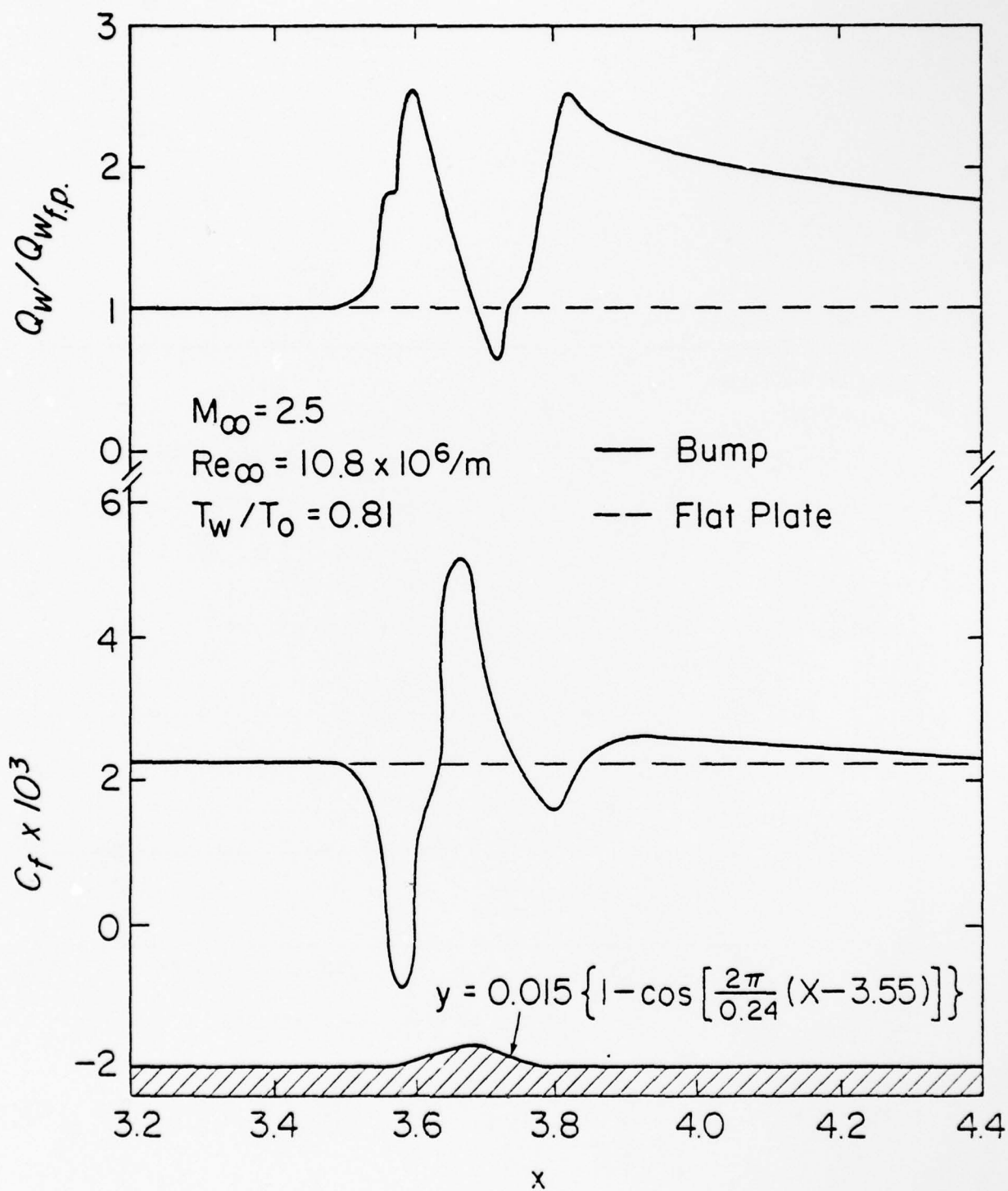


Figure 3B SURFACE PROPERTIES FOR ONE PROTUBERANCE

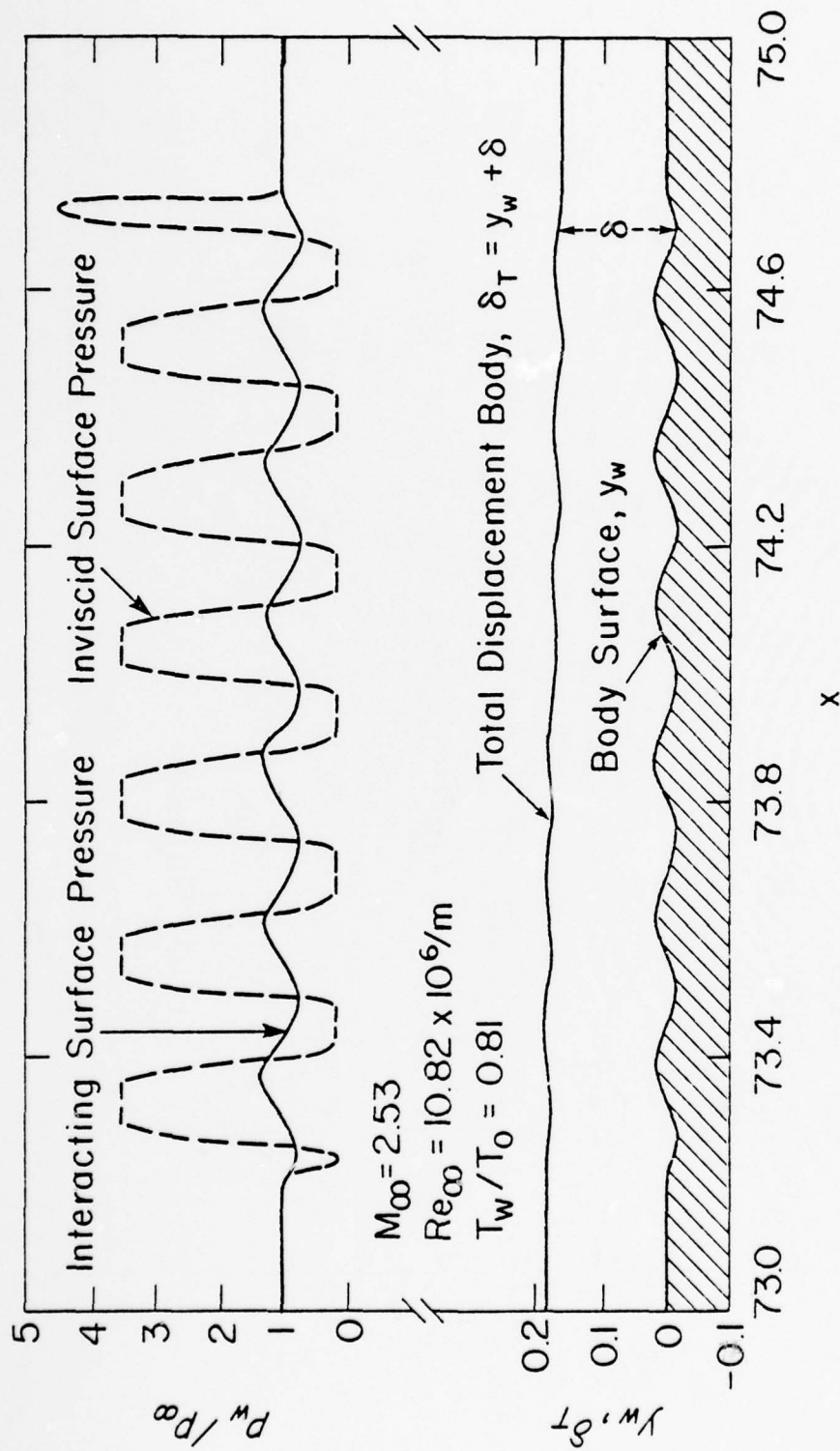


Figure 4 DISPLACEMENT BODY AND SURFACE PRESSURE - STANDARD CASE

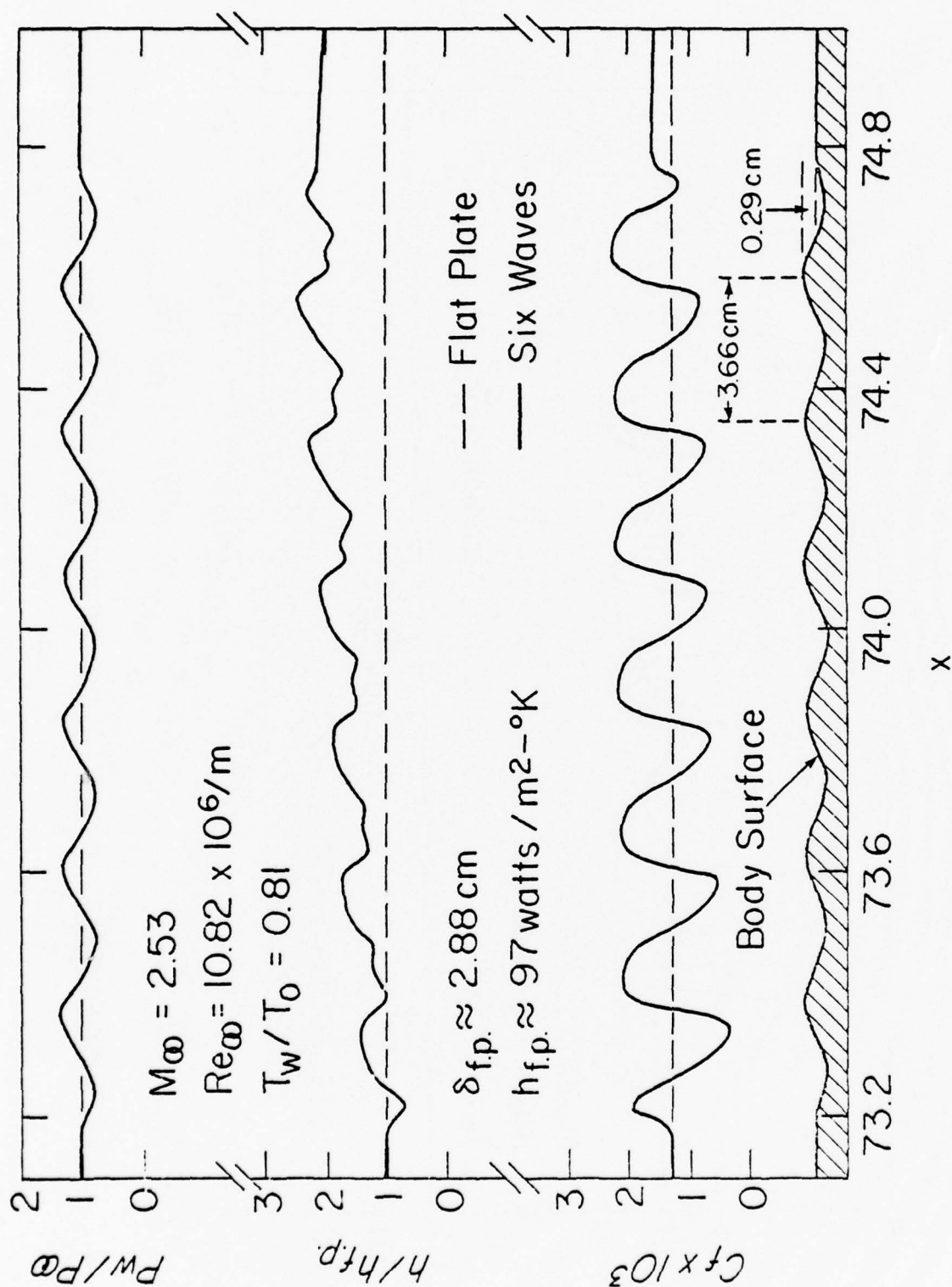


Figure 5 SURFACE PROPERTIES - STANDARD CASE

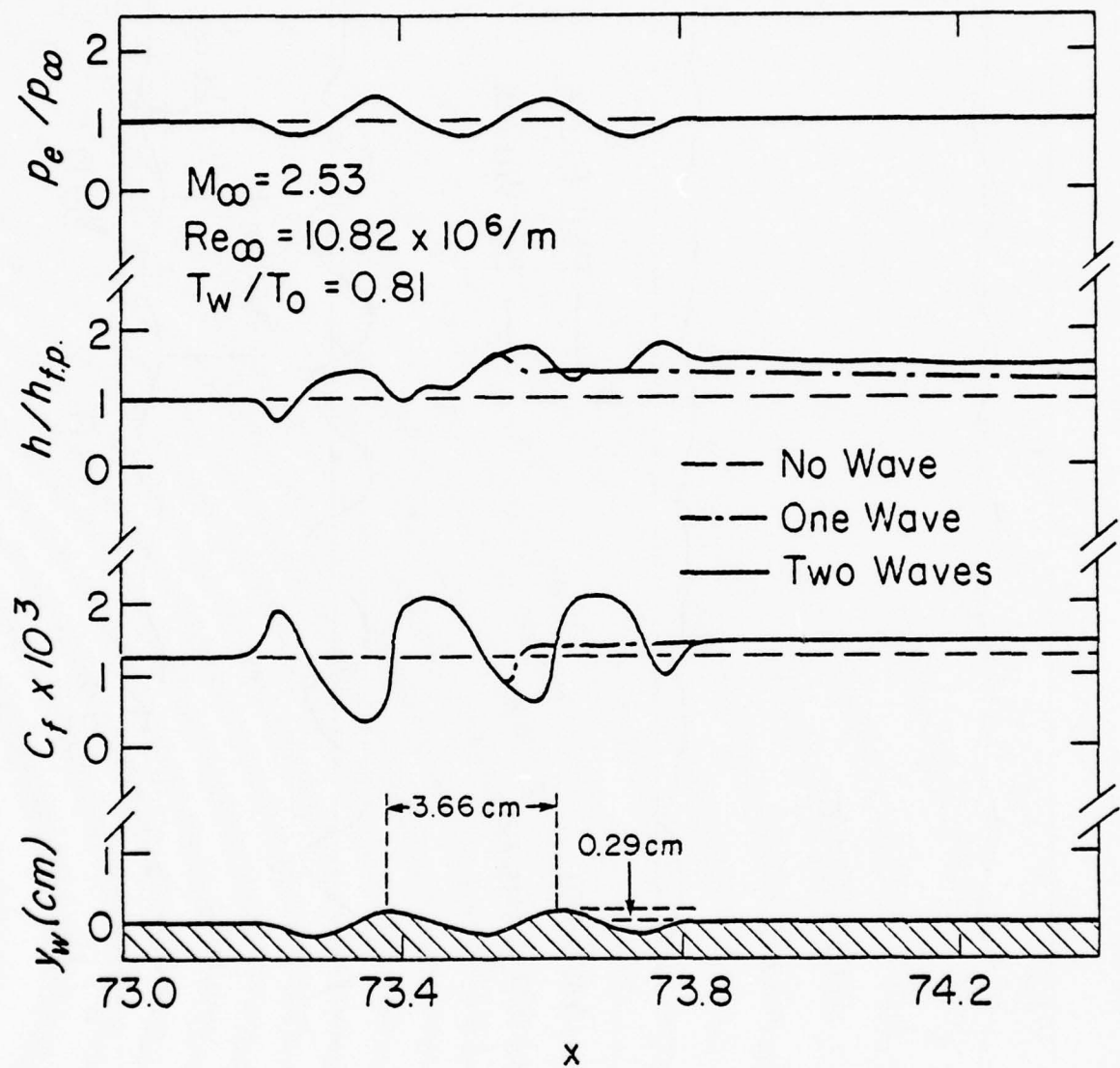


Figure 6 DOWNSTREAM EFFECT ON SURFACE PROPERTIES

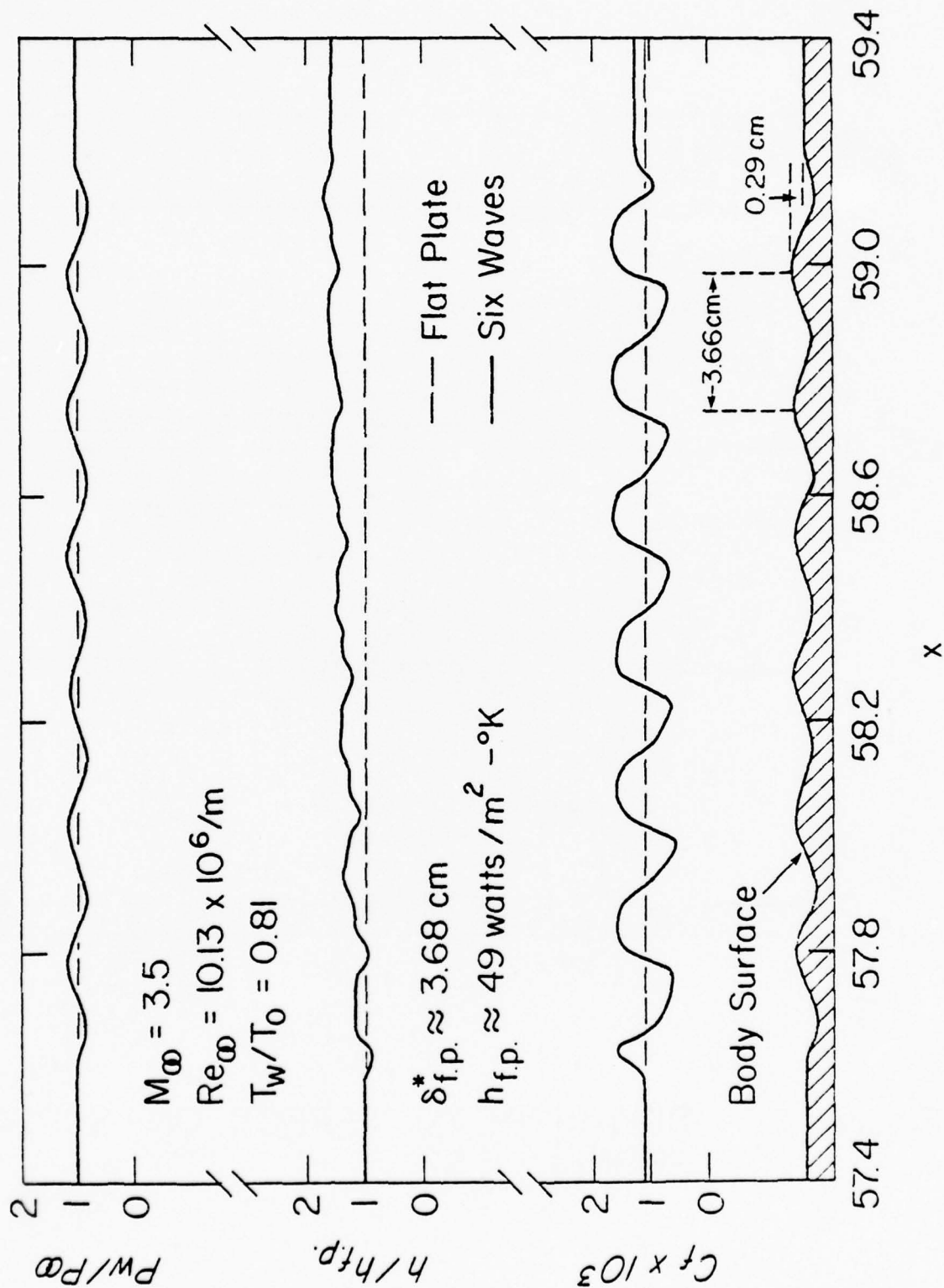


Figure 7A MACH NUMBER EFFECT ON SURFACE PROPERTIES

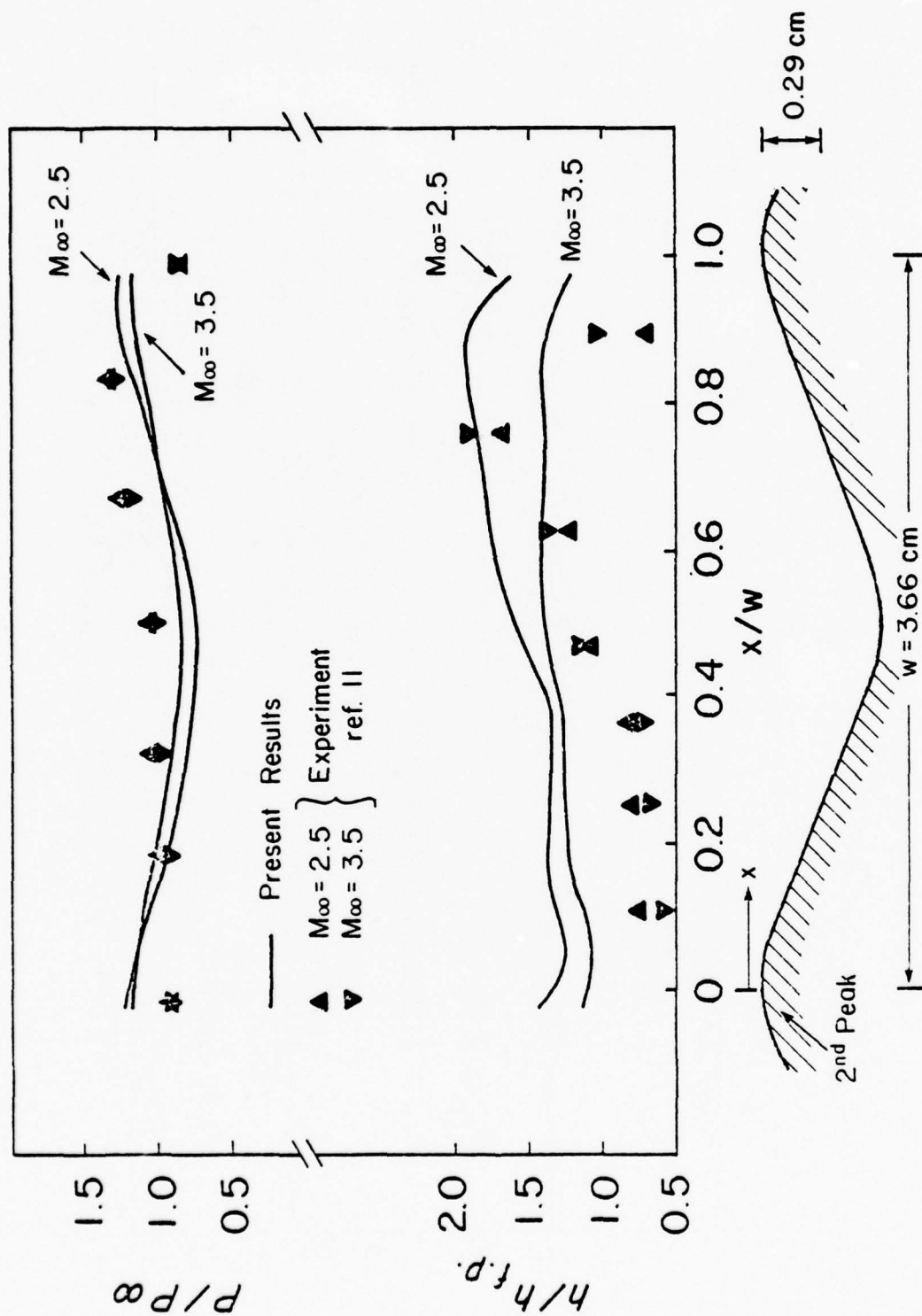


Figure 7B MACH NUMBER EFFECT ON SURFACE PROPERTIES

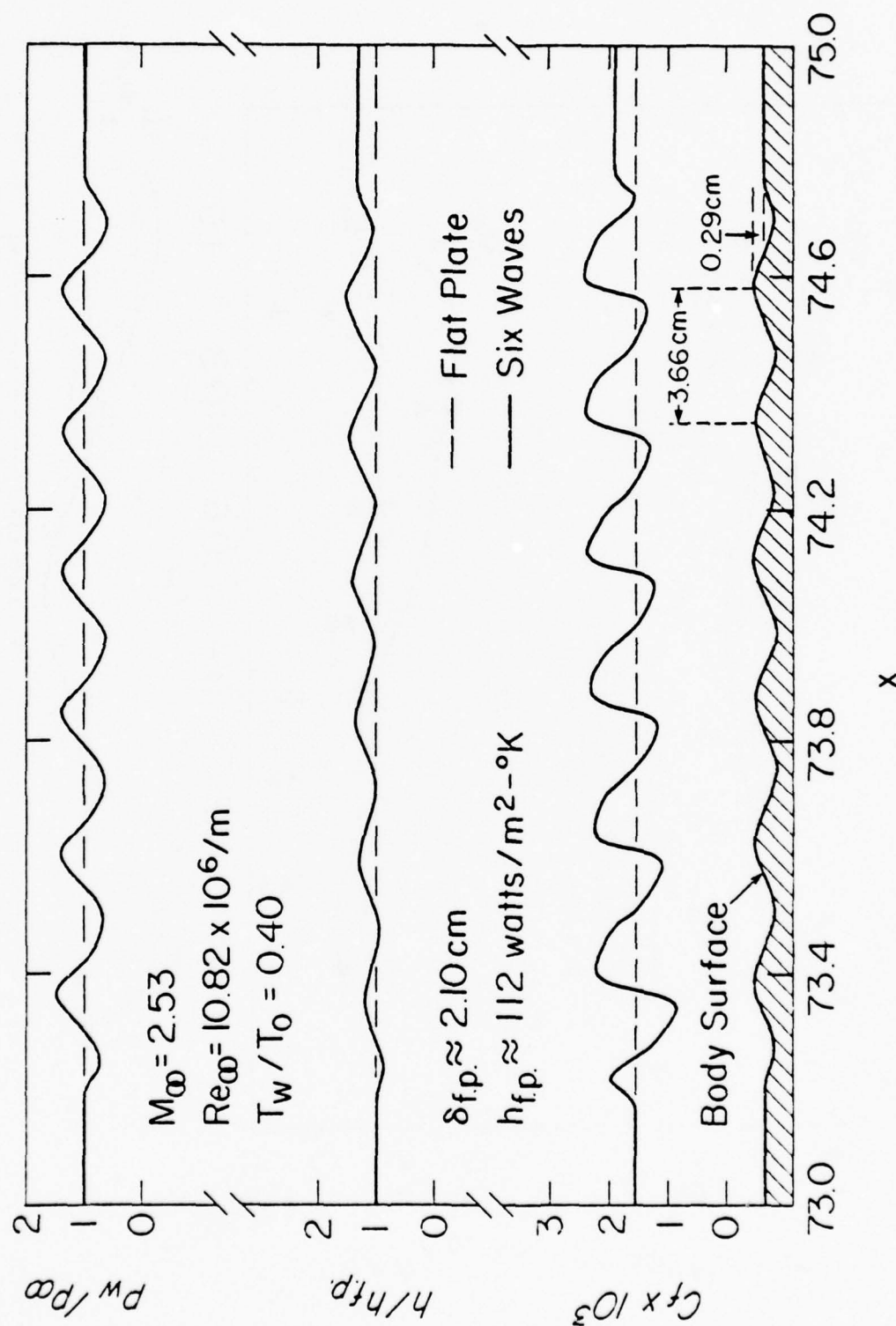


Figure 3. A. WAL: TEMPERATURE EFFECT ON SURFACE PROPERTIES

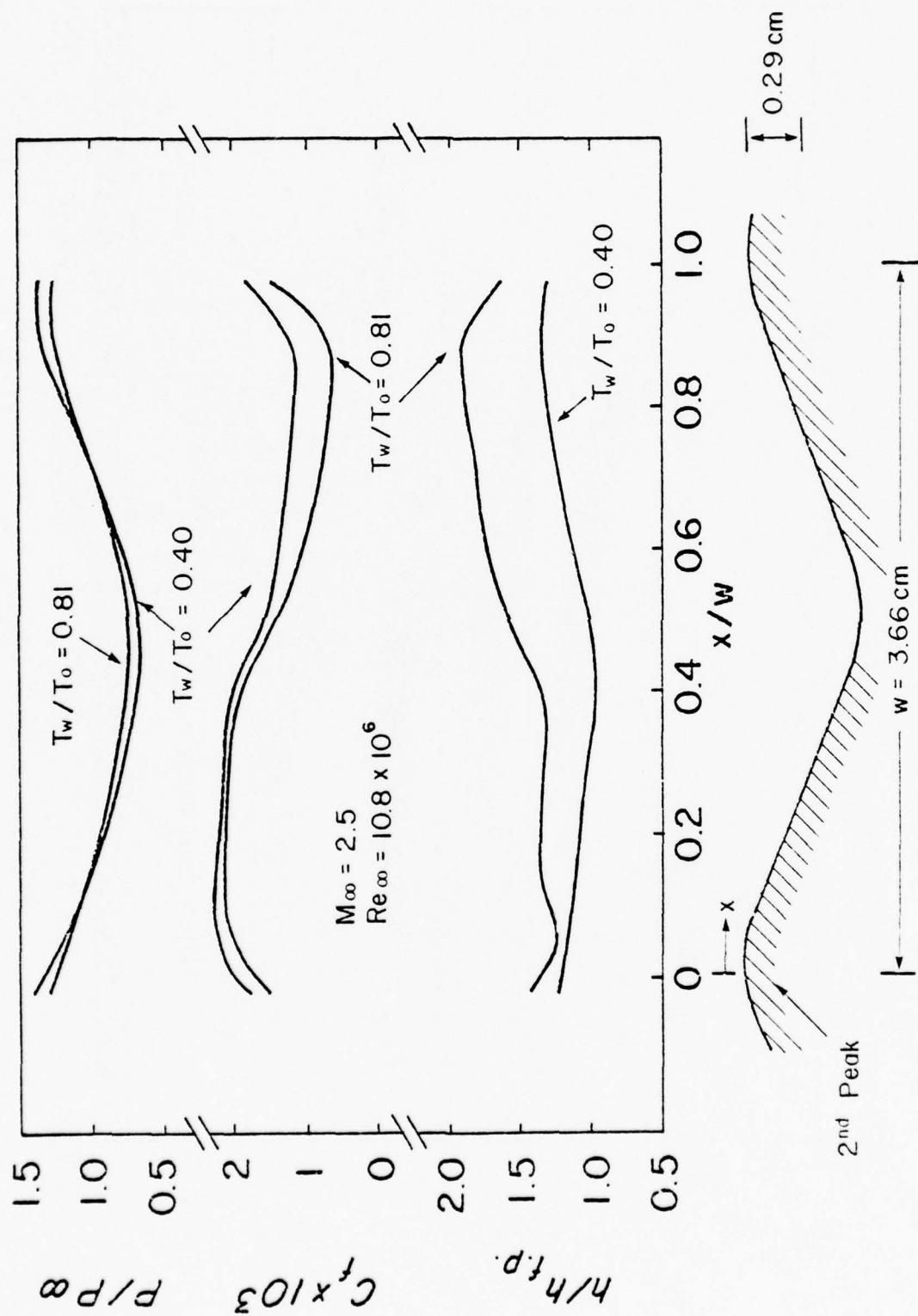


Figure 8B WALL TEMPERATURE EFFECT ON SURFACE PROPERTIES

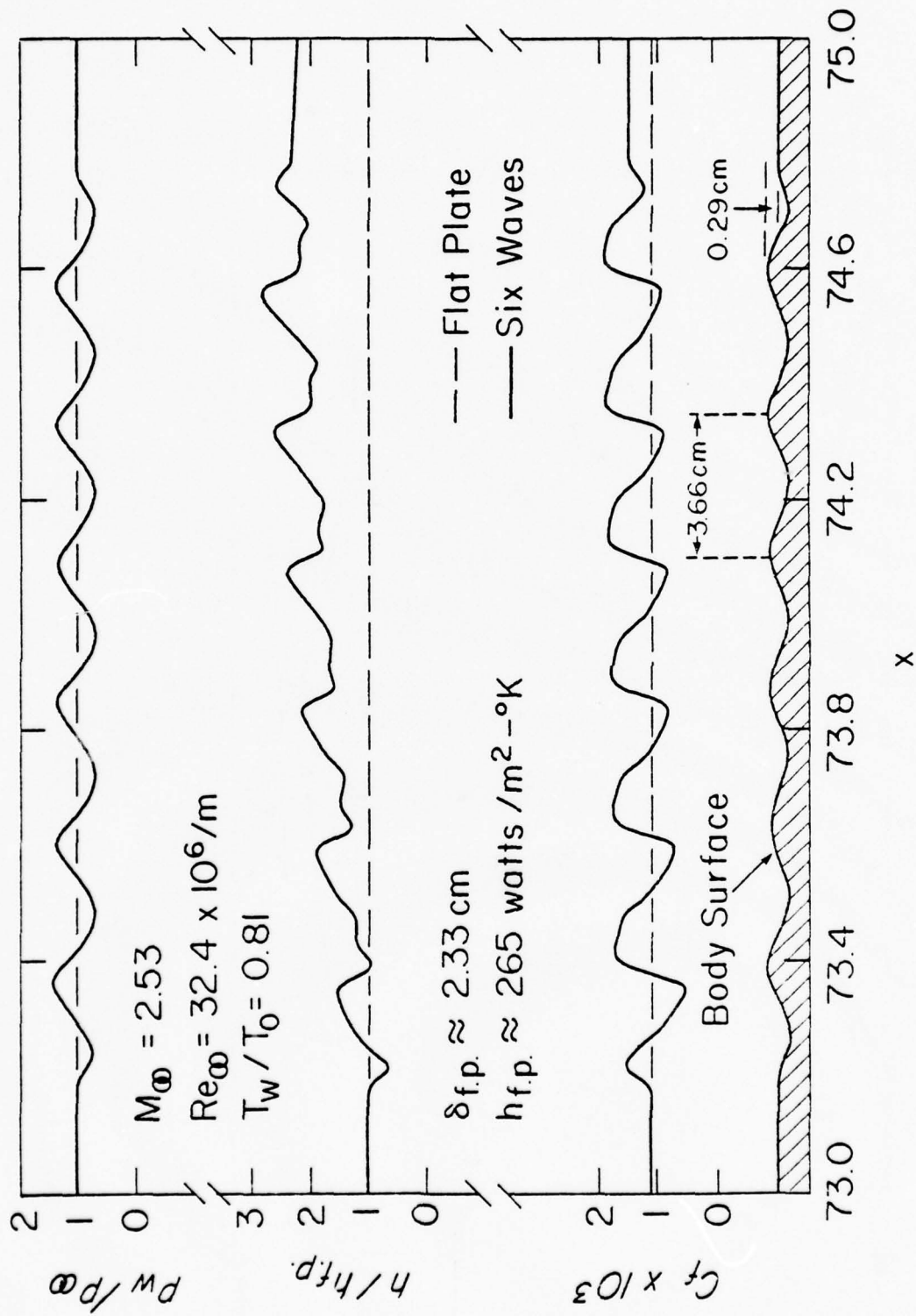


Figure 1. Aerodynamic and Thermal Properties of Six Surface Properties

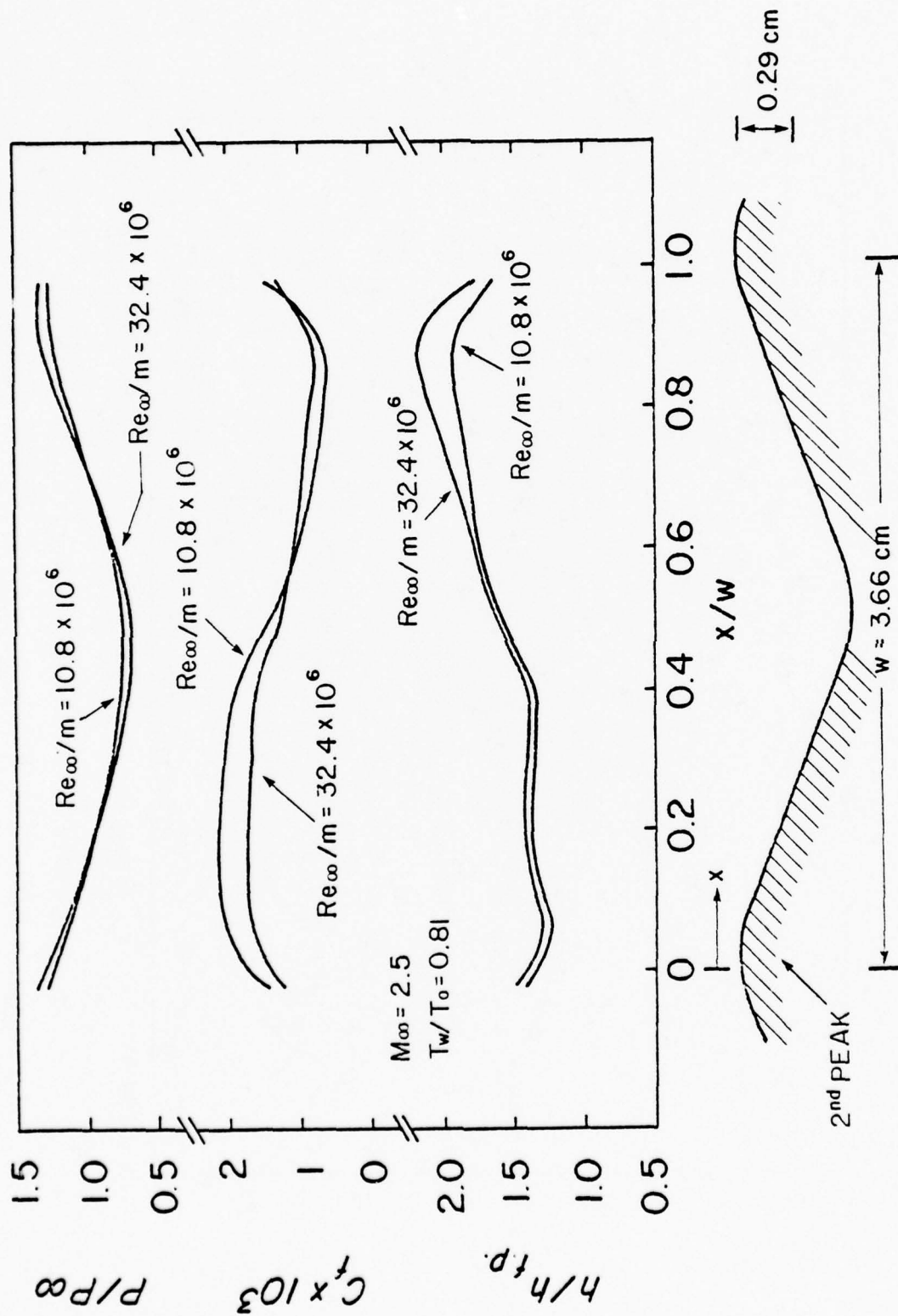


Figure 9B REYNOLDS NUMBER EFFECT ON SURFACE PROPERTIES

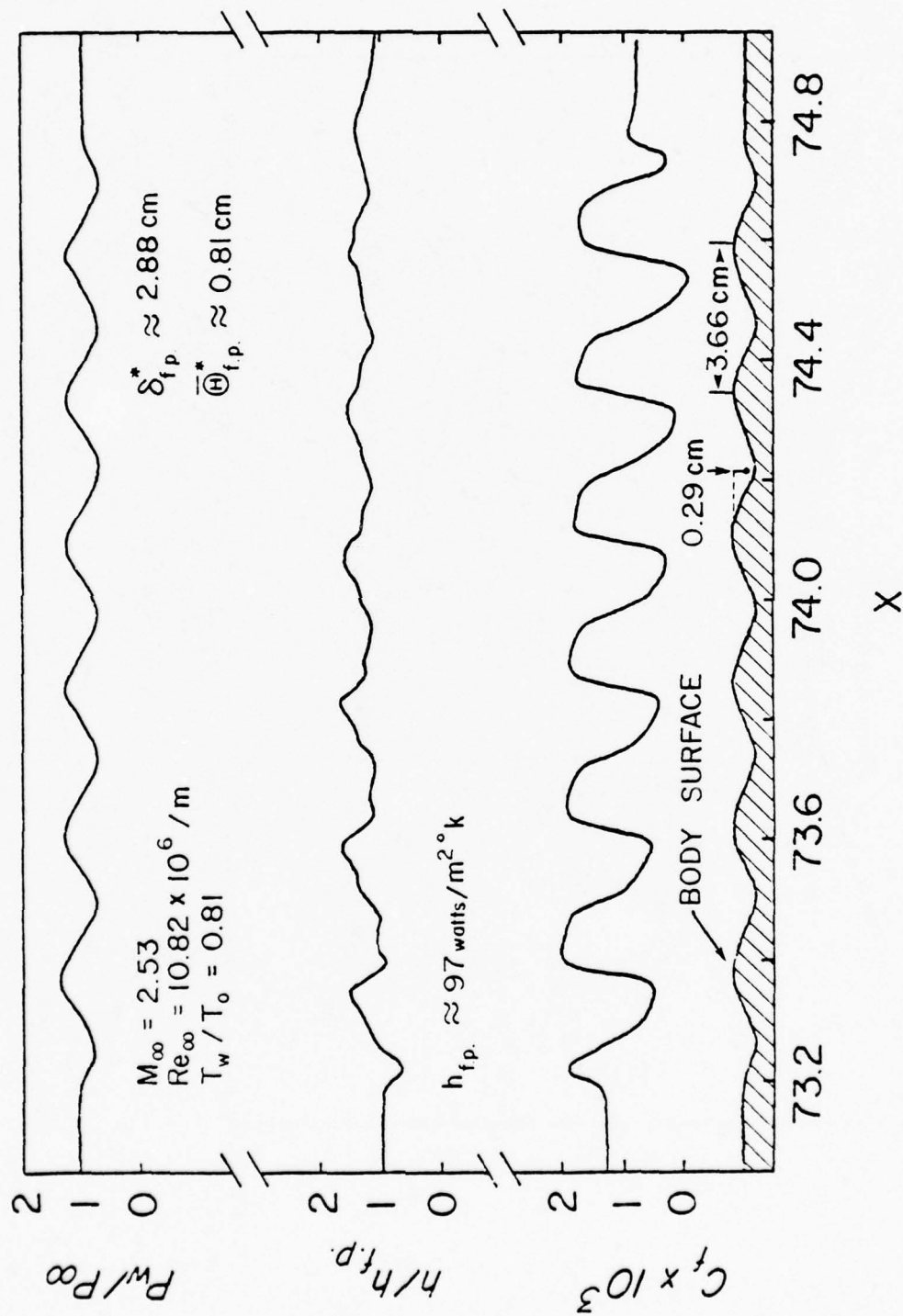


Figure 10A CURVATURE CORRECTION EFFECT ON SURFACE PROPERTIES

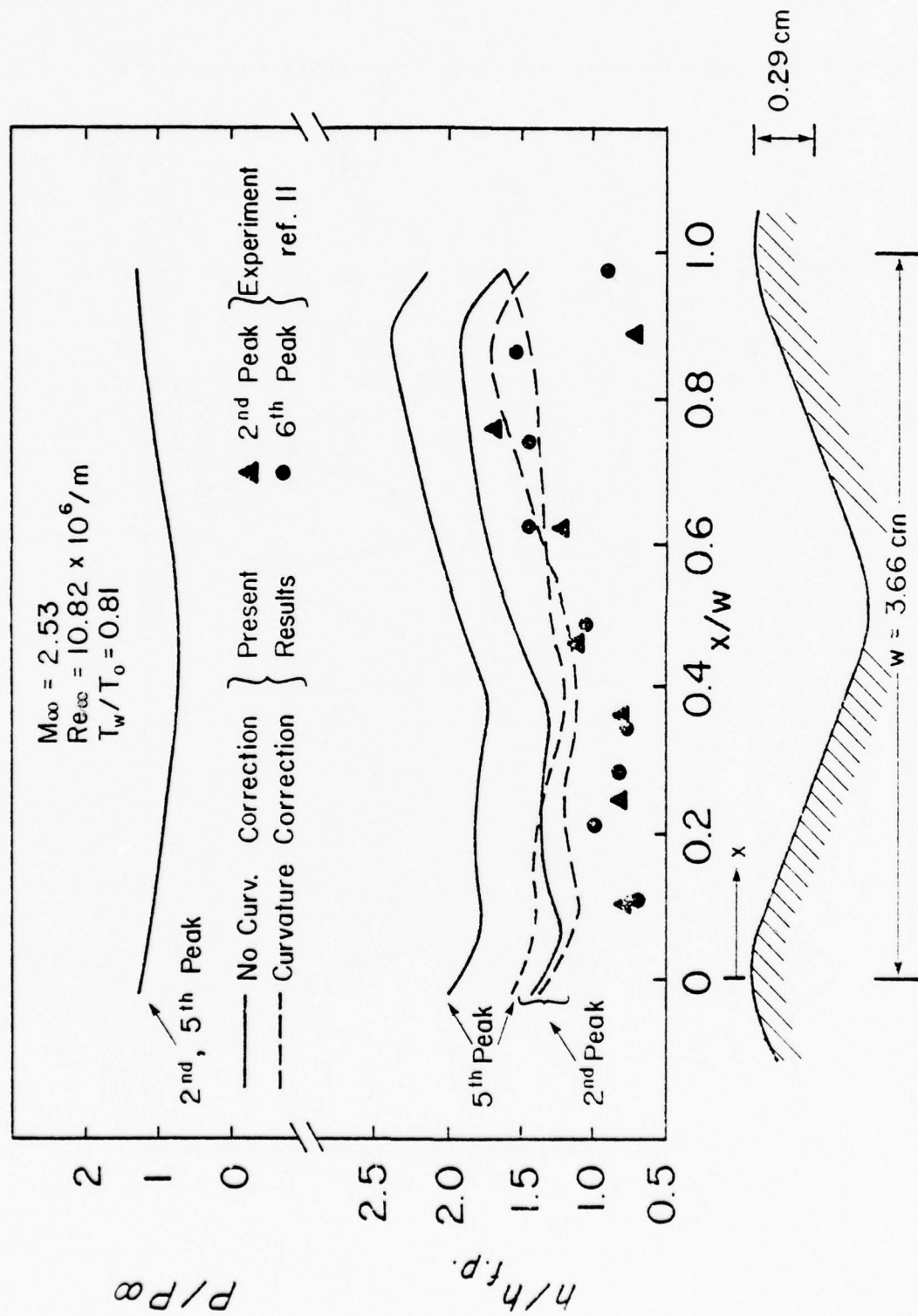


Figure 10B CURVATURE CORRECTION EFFECT ON SURFACE PROPERTIES

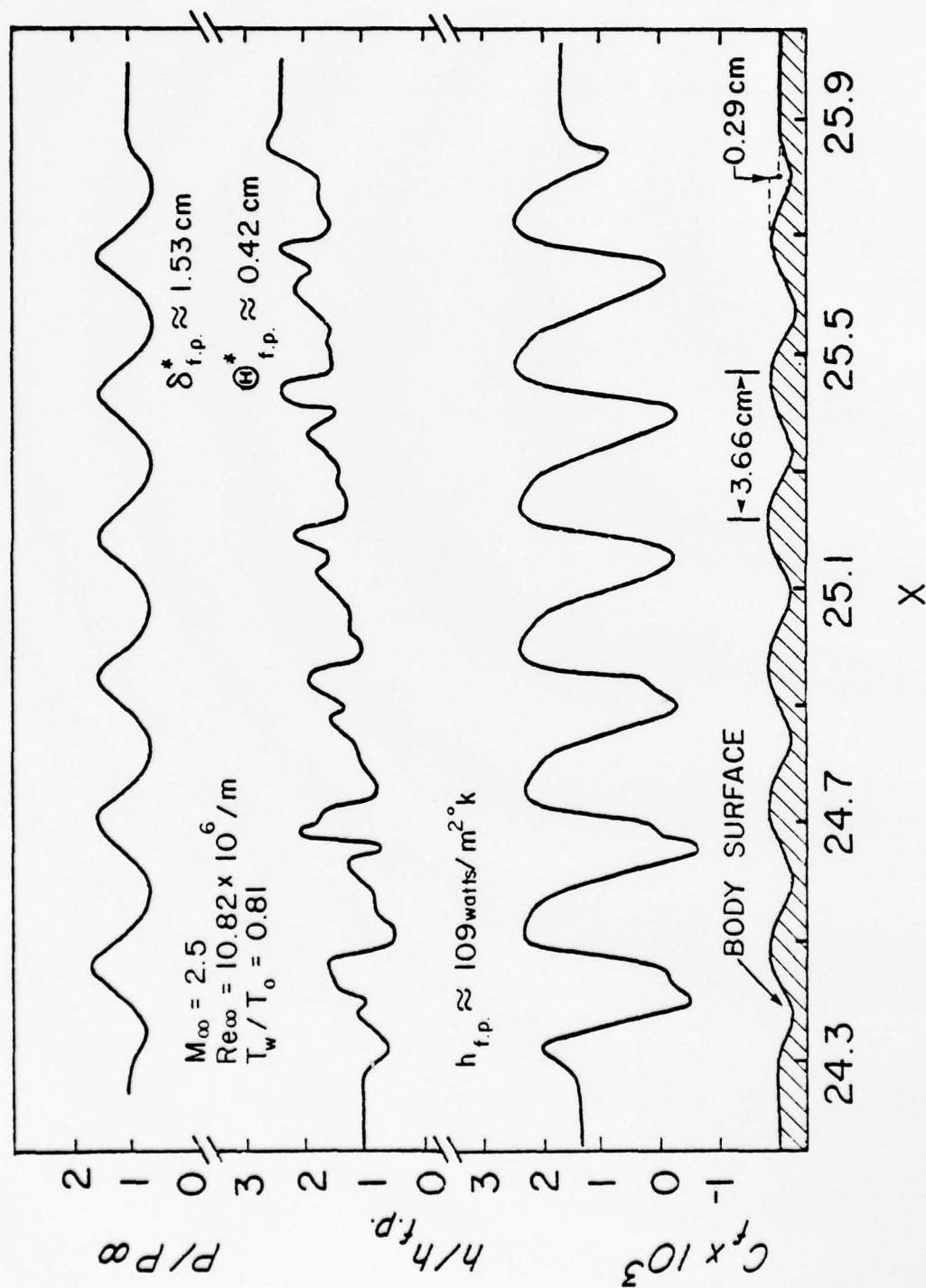


Figure 11A SURFACE PROPERTIES - SEPARATED THICK BOUNDARY LAYER

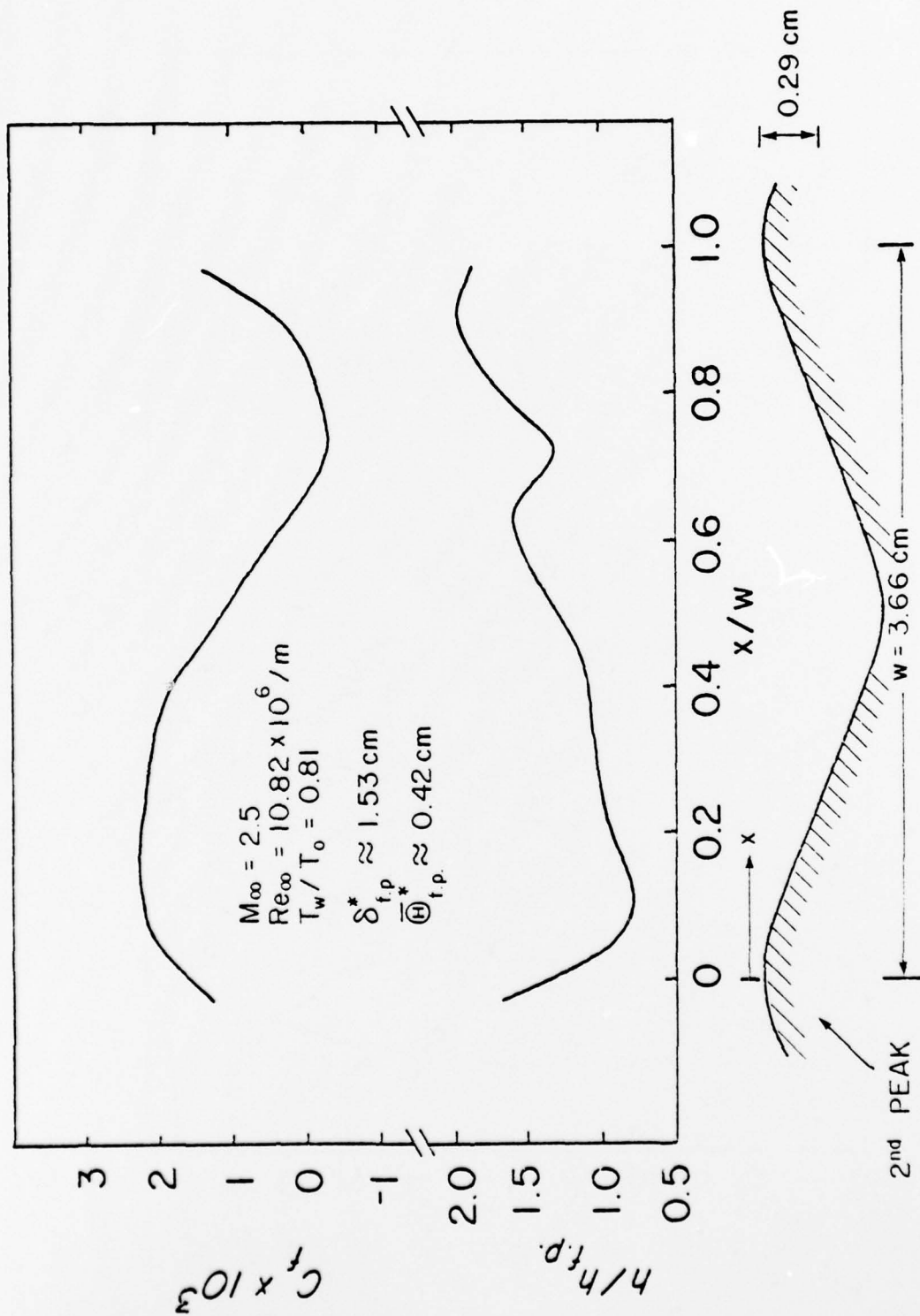


Figure IIB SURFACE PROPERTIES - SEPARATED THICK BOUNDARY LAYER

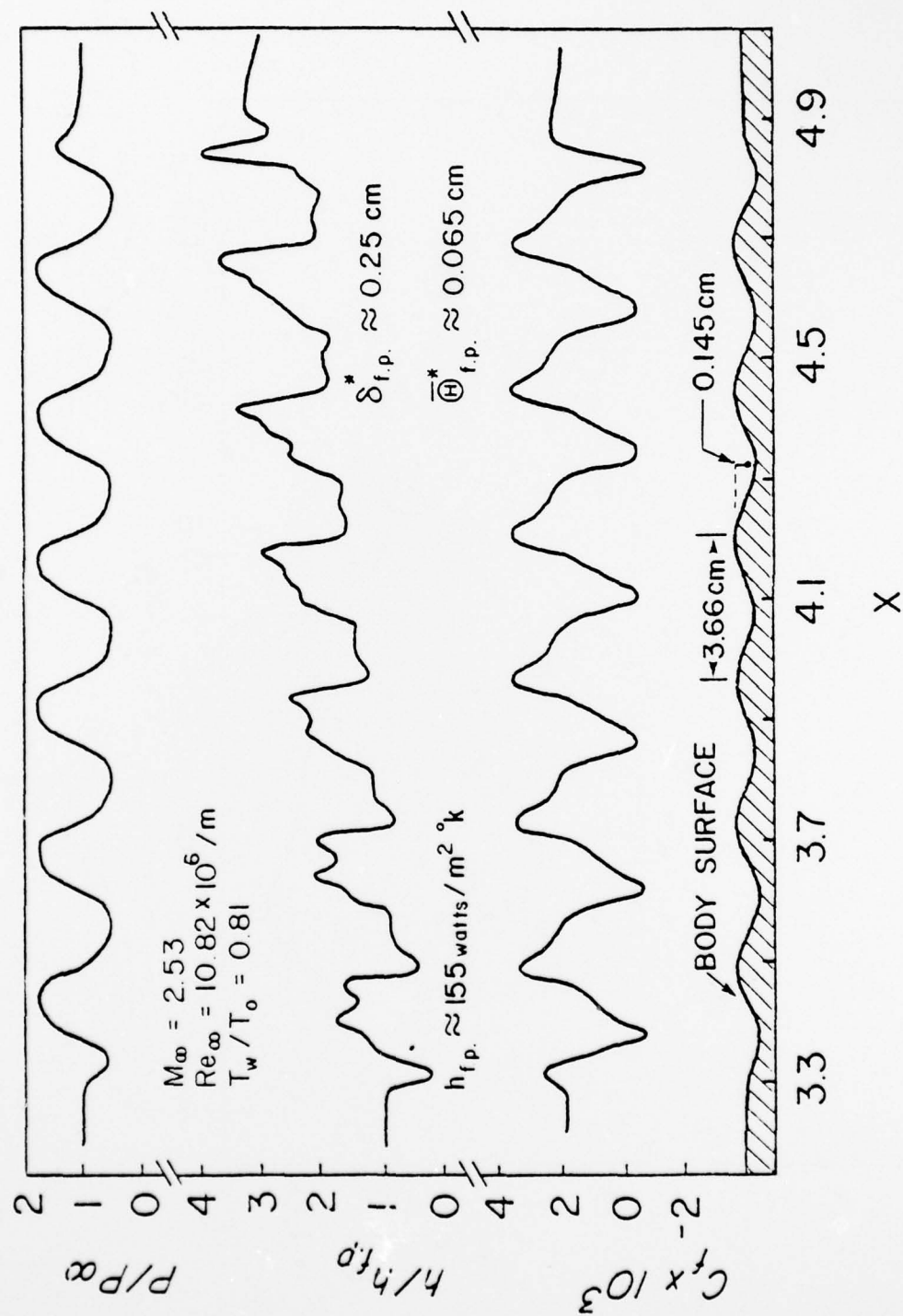


Figure 12 SURFACE PROPERTIES - SEPARATED THIN BOUNDARY LAYER

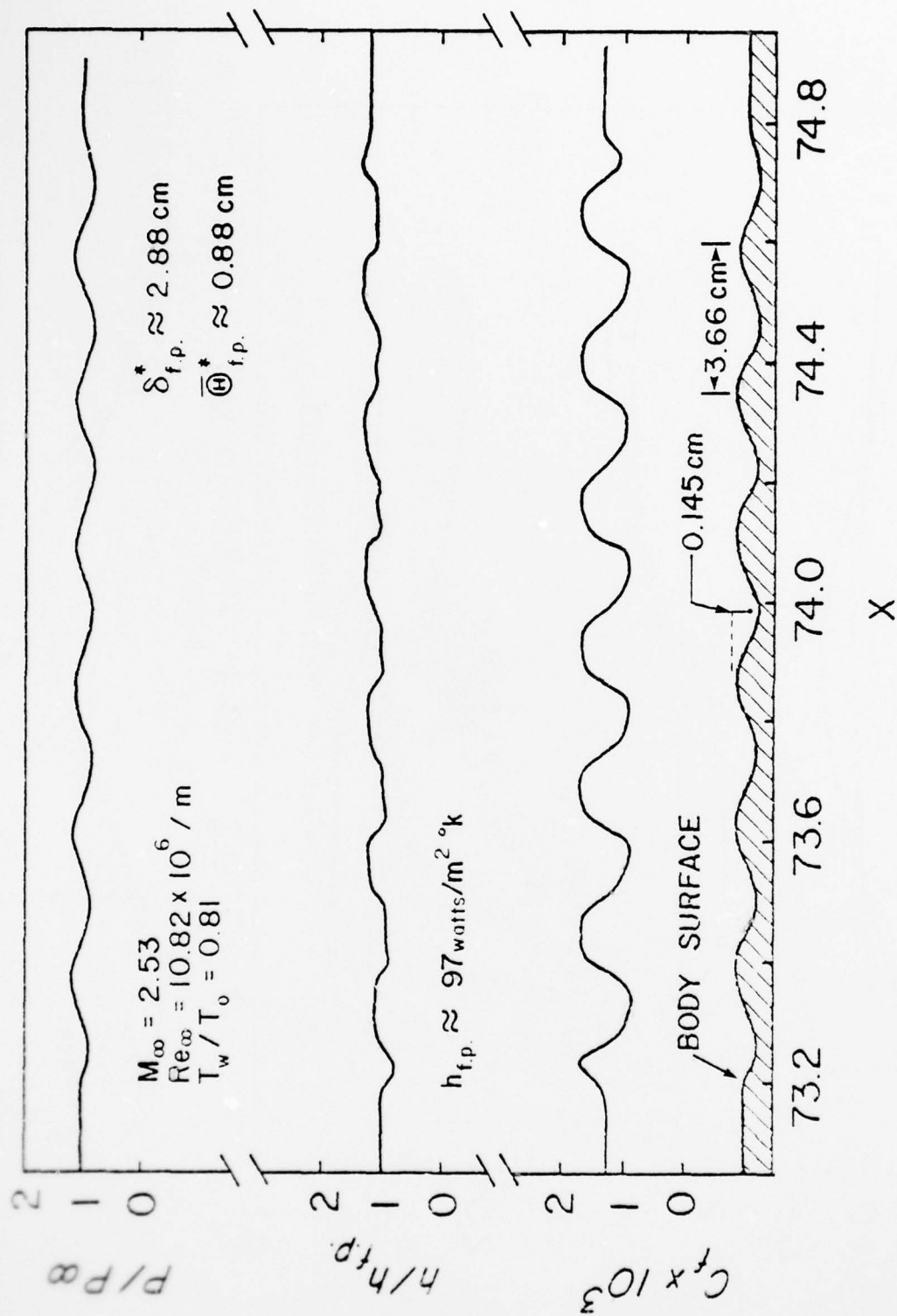


Figure 13A EFFECT OF WAVE HEIGHT ON SURFACE PROPERTIES

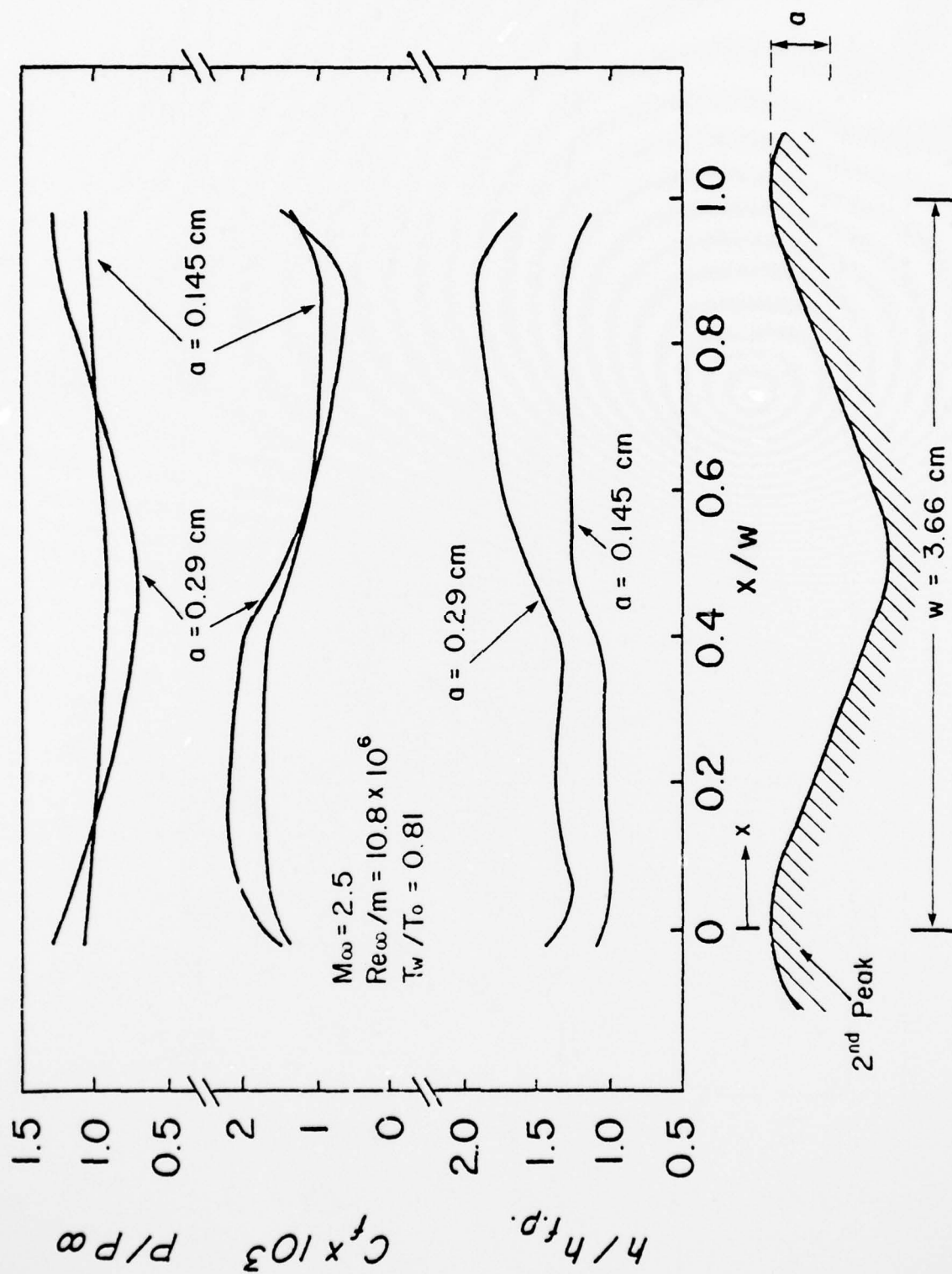


Figure 13B EFFECT OF WAVE HEIGHT ON SURFACE PROPERTIES

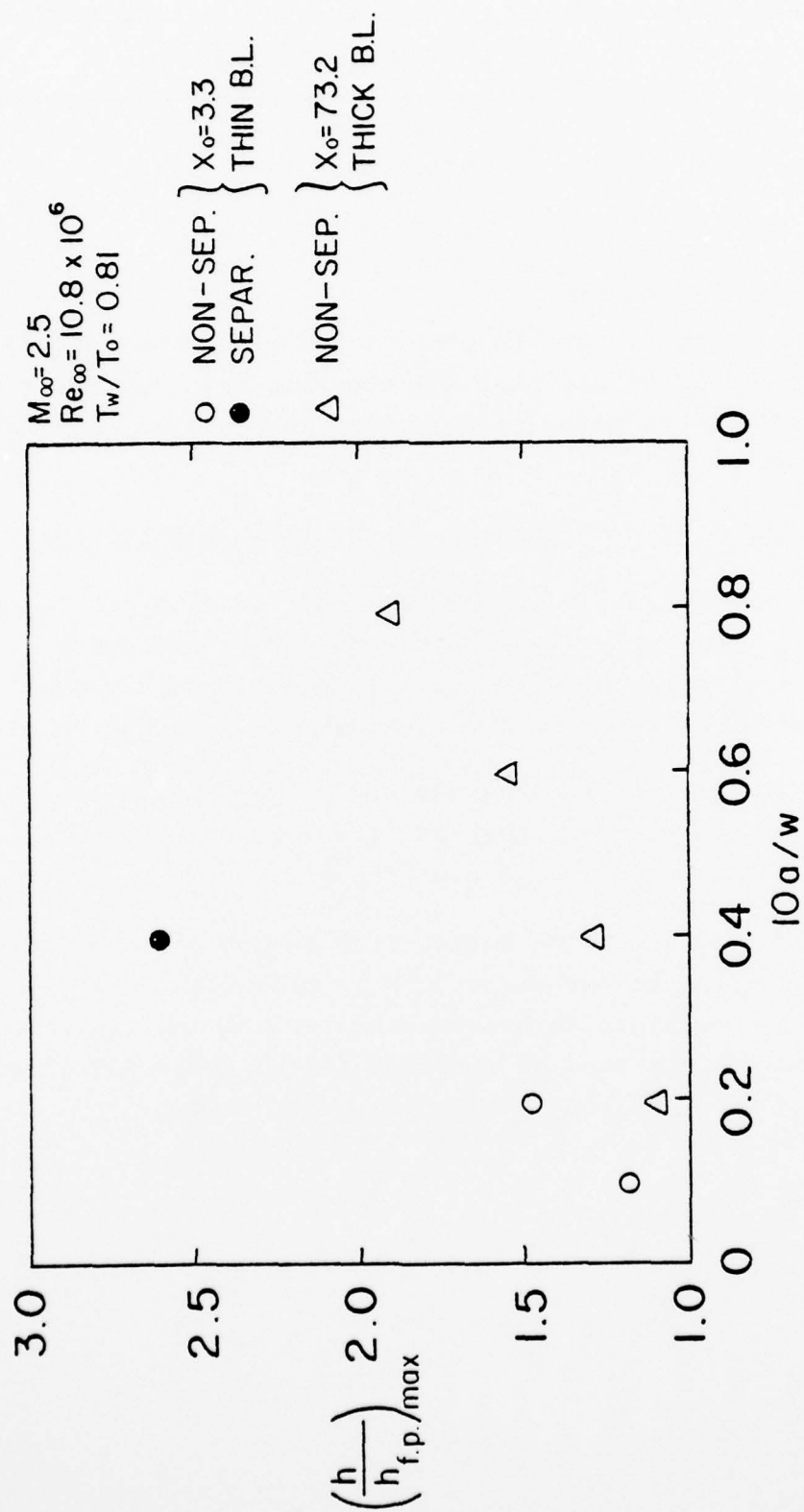


Figure 14 MAXIMUM SURFACE HEATING AT THIRD PEAK

COMMENTS ON INTERACTION BETWEEN THEORETICAL AND EXPERIMENTAL
WORK ON THE DEA TOPICS

Alfred Walz

1. Introductory Note

Research goals are in general assumed to be reached if the results of theoretical and experimental findings agree within acceptable accuracy limits. Here, an important question arises:

Which of both results is the most reliable one?

There are examples available, where this question can not be answered clearly. But the following statement seems to have general validity, basing upon a recently published "Survey of Computational Aerodynamics" in the US /4/:

If all flow configurations would keep the laminar state, experimental justification of theoretical results would no more be needed in the near future.

Since High-REYNOLDS-Number-Flow conditions are dominating, transition to turbulent flow is probable. Hence, an appropriate combination between theoretical and experimental research efforts, as outlined in the following chapter, will be needed, at last during the next decade.

2. A possible procedure of research within the near future

It is well known that any research on Technical Sciences Regimes, like Thermofluiddynamic, Aerodynamics, was formerly started from experimental observations and their evaluation, with the aim to find generalizing laws. This "prehistorical" period of research is automatically advancing to a more or less complete termination, if the interpolating or generalizing laws are recognized, formulated and proved to be the physically basic laws of the Mechanics of Continua and Thermodynamics. In this ideal case, indeed, no additional empirical information is needed to solve practical problems with arbitrary boundary and starting conditions.

The research tasks then are shifted from the physical to a pure mathematical domain: a set of partial differential equations in three-dimensional and time-dependent form, mostly non-linear, has to be solved simultaneously. Hence, to be successful in the "theoretical" research of this kind, high skillness in numerical mathematics and in using computer facilities is preferably required.

It is, indeed, surprising how many complicate flow configurations and phenomena could be completely described without any empirical input. See for instance the paper presented at this meeting by Mrs. J.W. SCHOT.

Unfortunately, such complete freedom from empirical inputs is reachable only in the case of pure laminar flow with the molecular viscosity, heat conductivity, density as known functions of temperature and pressure.

Realistic flows, however, are mostly characterized by high REYNOLDS-Numbers which means that transition to Turbulent Flow Pattern is very probable to occur, mainly in flow regions with high vorticity production, i.e. near solid

surfaces. Though this turbulent flow motions are also governed by the basic laws of the mechanics of continua, the above mentioned procedure of numerical-mathematics is not feasible (up to the present time) mainly by reasons of restricted storage and processing time requirements of the currently available computer systems.

In view of urgent actual projects, where "Viscous and Inter-acting Flow Field Effects" are present and coupled with turbulent boundary layers and other types of shear layers, a large gap of empirical information about Turbulent Flow Effects has to be closed by a "Long-Range, Professional Quality Experimentation" /1/. Prediction methods for flow simulation in the presence of turbulence have to be developed by "intelligent" consideration of available empirical informations in connection with numerical solutions of basic flow equations. Hence, an appropriate balance between theory and experiment must be practiced, which cannot be denoted as a turn-back to a prehistorical period of research.

Fortunately, the high REYNOLDS-Number conditions in modern high-speed Aerodynamics are generating not only the mentioned complications for theoretical treatments due to the occurrence of turbulent phenomena, but permit also significant simplifications:

- 1) For attached flow regions PRANDTL's Boundary Layer Concept is revalidated against the more general NAVIER-STOKES Concept and all former progress in prediction methods for laminar, turbulent, compressible, chemically reacting, three-dimensional, time-dependent boundary layers may be used. However, the pressure distribution along the attached flow surface region must be considered as known.

- 2) Separated Flow Regions (Dead-Water-Bodies) may be considered as quasi-solid parts of the flow configuration which are strongly influencing the pressure distribution at the fully-solid portion of the flow configuration /2/, /3/ and, with this, also the attached flow boundary layer development. The dead-water-inside part, however, may be considered as quasi-vortex (Turbulence)-free (see /2/).
- 3) PRANDTL's simplifying Boundary Layer Concept is entering into the prediction method scheme also in a second way: the over-all flow field is divided in a quasi-vortex-free part, including dead-water regions and in the pure and classical boundary layer part, as the only flow region where transition from laminar to turbulent flow may occur. Hence, the calculation of the solid surface pressure distribution is in principle reduced to a problem of a non-viscous flow around a three-dimensional body of arbitrary shape. Prediction methods for this problem (Panel-Methods) are available and classical.

The body shape, as argued above, has to include dead-water parts and - last but not least - for a lifting body also vortex formations due to the circulation-phenomena. Hence, the body-shape is not completely known in advance but has to be determined by iteration between "Quasi-Non-Viscous Flow-Theory" and boundary layer flow results including the prediction of flow separation lines. This means that this iteration process must be checked by an - at least averaged - solution of the 3D-NAVIER-STOKES equations.

From the above rough description of the present possibilities of predicting "Viscous and Interacting Flow Field Effects" by pure theoretical (numerical-mathematics) means we must end up with the following CONCLUSIONS:

- 1) The occurrence of turbulence at realistically high REYNOLDS-Numbers involves all well known difficulties and uncertainties in the prediction of turbulent flow pattern.
- 2) The occurrence of flow separation in the case of lifting bodies forces to apply an iteration procedure between PRANDTL's Boundary Layer Concept, non-viscous over-all-flow conditions and final check with a simplified 3D-NAVIER-STOKES-Concept.
- 3) For the near future an appropriate balance between theoretical and experimental efforts must be practiced.

3. Final Remarks

The research work in the starting period of the present DEA (about 10 years ago) was substantially simplified by the restriction of all theoretical and experimental work to non-separating flows, hence, to PRANDTL's real Boundary Layer Concept. The success in a complete theoretical treatment of the two-dimensional case including strong flow separation and interaction with the boundary layer flow /3/ gave clear directions for treating the three-dimensional lifting body case. The tremendous increase of difficulties on the computational field (numerical instabilities, large computer times and expenses), however, was underestimated.

However, recent experiences, supported by a Survey of Computational Aerodynamics in the USA by A. GESSOW and D.J. MORRIS /4/ sound very encouraging with regard to the future chances of progress in theoretical simulations on the aerodynamics field, including turbulence and separation:

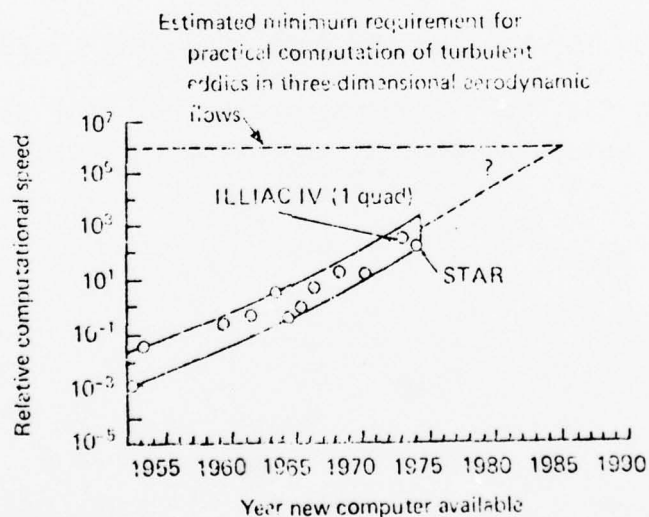


Figure 1. - Trends of computer speed
(Fig. 46 from /4/)

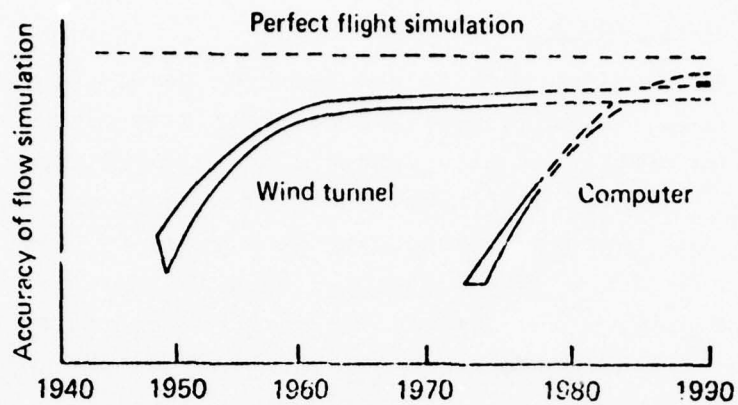


Figure 2. - Comparison of accuracy of wind tunnel testing and computer simulations
(Fig. 1 from /4/)

The realization of "LONG-RANGE, Professional Quality Experimentation" is a question of man-power and financing. The same is true for flow simulation by computer processing.

Which way will be the most accurate and economic one?

From Fig 1 and 2 we may learn that this question will permit an answer within the next 3 to 5 years.

Closing Remarks

by K.-H. Gronau

German Federal Ministry of Defense

During these two days of our common work we succeeded in pointing out the present state of research and its main directions of work. It has been attempted in many presentations and discussions to depict and sound the information obtained in the field of research and the various fields of application. Therefore, the meeting probably has fully coped with its main task, the exchange of data and special knowledge. In particular, I hope and wish that individual participants have been able to receive new suggestions and impulses for their future work.

According to the proposal of Dr. Stock from the firm Dornier-System our next meeting should be take place at Meersburg on the end of April 1978. Meersburg is a beautiful castle on the shore of lake of Konstanz in southern Germany.

We must, all of us, thank the organizers for the preparations and the troublesome spade-work for implementing the extensive program of presentation.

Not last our thanks are dure to all lecturers, chairman of the discussions and the speakers who by their presentations and discussions have essentially contributed to the success of this meeting.

Closing Remarks

by

Anthony W. Fiore
Air Force Flight Dynamics Laboratory
Wright-Patterson Air Force Base, Ohio

Gentlemen, we have reached the end of another productive D.E.A. meeting. The technical information produced in this meeting will be useful to both our nations. The results will be published in the Proceedings as soon as possible. I hope that we can get them out sooner this year than we did previously. Once again I want to thank everyone for your participation and I hope to see all of you at our 1979 D.E.A. meeting which will be in Fredrichshafen, Germany. The sponsor will be the Dornier Aircraft Corporation. Thank you.